AD-A272 915

AFOSR-TR 93-0838

DYNAMIC RESPONSE OF

MULTIPHASE POROUS MEDIA

~~FINAL REPORT~~

June 16, 1993

Prepared for

Air Force Office of Scientific Research
Bolling Air Force Base
Washington D.C. 20332-6448

Under Contract No. F49620-89-C-0037

ARA Contract No. 5535

Prepared by

Daniel E. Chitty
Scott E. Blouin
Kwang J. Kim
Alan F. Rauch

Applied Research Associates, Inc.
New England Division
Box 120A Waterman Rd.
South Royalton, Vermont 05068

93-28115

93 11 10 054

REPORT DOCUMENTATION PAGE

Form Approved
OMB No. 0704-0188

1. AGENCY USE ONLY (Leave blank)	2. REPORT DATE 930616	3. REPORT TYPE AND DATES COVERED Final 890201 to 930531

4. TITLE AND SUBTITLE
Dynamic Response of Multiphase Porous Media ~~Final Report~~

5. FUNDING NUMBERS
C - F49620-89-C-0037
PE - 61102F
PR - 2302/CS
TA - C1
WU -

6. AUTHOR(S)
Chitty, Daniel E.; Blouin, Scott E.; Kim, Kwang J., and Rauch, Alan F.

7. PERFORMING ORGANIZATION NAME(S) AND ADDRESS(ES)
Applied Research Associates, Inc.
4300 San Mateo Blvd. NE, Suite A-220
Albuquerque, NM 87110

8. PERFORMING ORGANIZATION REPORT NUMBER
5535-3

9. SPONSORING/MONITORING AGENCY NAME(S) AND ADDRESS(ES)
Air Force Office of Scientific Research
Building 410
Bolling AFB, DC 20332-6448

/NA/

10. SPONSORING/MONITORING AGENCY REPORT NUMBER
F49620-89-C-0037

11. SUPPLEMENTARY NOTES

12a. DISTRIBUTION/AVAILABILITY STATEMENT

12b. DISTRIBUTION CODE

13. ABSTRACT (Maximum 200 words)

This report presents the results of a three-year theoretical and experimental investigation of the response of multiphase porous media to strong dynamic loadings. A material element model was developed to automate the determination of parameter values for multiphase material mdoels and to predict the response of saturated porous materials to arbitrary stress, strain and fluid flow boundary conditions. Laboratory tests to measure fluid flow through porous media were conducted over a wide range of pressure gradients in granular materials and porous rock. The results of those tests were used to develop a unified fluid friction model. A laboratory apparatus was constructed for the purpose of studying wave propagation through saturated porous media. A suite of dynamic tests was performed on a porous stainless steel specimen, and the results of those tests were compared with detailed multiphase numerical simulations. The simulations were in excellent agreement with the laboratory measurements. With guidance from simulations, it was possible to identify, in the test data, the wve of the second kind. This disturbance, which propagates at a speed significantly lower than the compressionai wave, appears to be associated with a surge of pore fluid within the porous skeleton, and has previously only been

14. SUBJECT TERMS
Wave Propagation — Two-phase Modeling — Permeability
Soil and Rock Properties — Liquefaction
Geotechnical Analysis — Numerical Analysis (Geotechnical)

15. NUMBER OF PAGES
237

16. PRICE CODE

17. SECURITY CLASSIFICATION OF REPORT	18. SECURITY CLASSIFICATION OF THIS PAGE	19. SECURITY CLASSIFICATION OF ABSTRACT	20. LIMITATION OF ABSTRACT
Unclassified	Unclassified	Unclassified	None

13.　ABSTRACT (Continued)...

predicted by analysis.

Acce. for

NTIS CR&I
DTIC TAB
Unannounced
Justification

By
Distribution /

Availability Codes

Dist	Avail and/or Special
A-1	

DTIC QUALITY INSPECTED 5

EXECUTIVE SUMMARY

For more than ten years, the Air Force Office of Scientific Research (AFOSR) has supported research in the field of multiphase mechanics, i.e. the mechanical response of materials consisting of a porous skeleton of solid-phase material having its pore space filled with liquid or a mixture of liquid and gas. For the Department of Defense (DoD), the primary motivation for such efforts is the study of the effects of explosions in fully or partially saturated soils and porous rocks, which exhibit significantly different behavior than equivalent dry materials. This fundamental research in multiphase mechanics is also applicable to other problems such as earthquake induced liquefaction and shock-wave therapies for kidney stones. The results of the past decade of AFOSR-sponsored research has contributed significantly to numerous DoD studies, including:

- an evaluation of nuclear craters in the Pacific which led to a revision in the perceived cratering effectiveness of nuclear weapons;

- evaluations of the vulnerability of deep underground structures in saturated porous rock geologies;

- development of simplified weapons effects prediction techniques for use by targeting analysts throughout the DoD community;

- analysis of the vulnerability of U.S. Air Force aircraft shelters and other hardened facilities sited in saturated soils to attack from conventional weapons;

- development of countermeasures to enhance the survivability of hardened structures in/on saturated soil; and

- analysis and experimental support for the U.S. Navy's surf zone mine countermeasures research.

Analysis of the response of saturated porous materials is complicated by the fact that they are composed of multiple constituents, e.g. sand and water, having fundamentally different mechanical response characteristics. A computation of the deformation of the multiphase material under load must account for the partitioning of load between the solid and fluid phases. In addition to the deformation of the solid skeleton caused by the load it carries, it is also

iii

deformed by the pore fluid pressure acting on it. Thus, a theoretically rigorous formulation must account for the deformations of both materials and the coupling between them while maintaining full compatibility of deformations as well as tracking mass transfer of the fluid phase. All geologic and cementitions materials exhibit frictional strength characteristics, i.e. over a wide stress range, their shear strength increases with increasing normal stress. However, in the case of fluid-saturated materials, only that component of normal stress that is carried by the solid skeleton is effective in increasing its shear strength. This "effective stress" concept, which was developed by Terzaghi over 50 years ago, was largely ignored by the DoD weapons effects community until the results of the AFOSR research began to influence the community in the last few years.

The research effort described in this report, which was conducted by Applied Research Associates, Inc. (ARA), was designed to further advance the state of knowledge in multiphase mechanics. It was a rather ambitions program with three major objectives:

1.   development of a Material Element Model (MEM) to automate the determination of parameter values for multiphase material models and to predict the response of saturated undrained porous materials to specified stress and strain inputs;

2.   verification and calibration of a fluid friction model for soils and rocks covering a wide range of pore pressure gradients, and correlation of the fluid friction parameters with the microscopic structure of the pore space; and

3.   development of a better understanding of the fundamental mechanics of wave propagation in saturated porous media through theoretical, numerical and experimental studies of wave propagation in confined saturated porous bars.

While the principles of multiphase mechanics and the effective stress law have been known for many years, their application to problems of interest to the DoD community and the accomplishment of further research were impeded by the lack of analysis tools. Even the simplest problems in multiphase mechanics are analytically tractable only with numerical

iv

methods on computers. Because of the direct influence of pore fluid pressure on strength and the sensitivity of pore pressure to changes in volume, it is extremely important in multiphase calculations that the volume change behavior of the solid skeleton under shear and normal loading be modeled correctly. Under this contract, ARA developed a Material Element Model (MEM) to support constitutive modeling of multiphase materials. It is a quasi-static finite element program that was specifically designed to facilitate implementation of new skeleton constitutive models. It provides a very convenient platform for constitutive model parameter evaluation and parameter sensitivity studies. The resulting material model parameter values are directly transportable to dynamic analysis programs, a highly desirable feature in view of the fact that the modern elastoplastic constitutive models may have as many as 40 parameters. MEM includes an extremely robust set of boundary conditions, making it possible to exercise material models over virtually any combination stress, strain, and/or fluid flow conditions.

A description of the formulations implemented in MEM is presented in Section 2. An advanced three-invariant elastoplastic constitutive model which is included in MEM for modeling of multiphase materials is described in Section 3, along with a discussion of the procedures for fitting the model parameters for a granular material. An important application of MEM, presented in Section 5, involves the analysis of a conventional triaxial compression test on a porous limestone specimen in the saturated undrained condition. When the test data were interpreted using conventional approaches, the results led to the apparent paradox that the pore fluid pressure in the specimen remained constant while the volume of the specimen increased under triaxial compression loading at constant confining pressure. A study involving carefully conducted tests and a detailed analysis using MEM led to the conclusion that the conventional triaxial compression test applied to saturated undrained material is fatally flawed, and that even for dry materials, it can lead to erroneous measures of volume change under shear loading. It has long been recognized that triaxial compression test specimens deform nonuniformly owing to the additional effective radial confinement resulting from end friction. However, the traditional approach has been to assume that error occurs only at the ends of the specimen, and that the behavior of the center third of the specimen is representative of the material's response to the idealized triaxial compression loading. In fact, both the test and the MEM analysis showed that the deformation of the specimen was nonuniform in both the axial and radial

directions, with the large expansive radial deformation in the center of the specimen accompanied by a larger than average compressive axial strain. Thus, the traditional approach of volume strain computation from the radial deformation at the center of the specimen and the axial deformation averaged over the entire length substantially overstates the volumetric expansion of the specimen. In subsequent work, motivated by the results of this study, a procedure was developed to reduce end friction using lubricating membranes. Using that test technique, we have demonstrated that, at confining pressures above the brittle-ductile transition, porous limestone will undergo axial strains up to 15% with no tendency to dilate. This contrasts with the conventional approach which inferred dilation as a result of the nonuniform strain fields in the test specimen. As a result of this study of test techniques for saturated porous materials using MEM, modifications have been implemented to rock testing techniques in laboratories at both ARA and WES. These results were also presented at an international conference on constitutive modeling (Chitty, et al., 1991).

The second major thrust of this research was in the area of fluid flow through granular materials and porous rocks at high pressure gradients. Dynamic loading of a saturated porous material will induce pore pressure gradients. The development of pore pressure, and hence the strength of the saturated material, under these conditions is strongly influenced by its fluid flow characteristics. Therefor, to properly model such dynamic loading, it is necessary to analytically treat the fluid flow as well as the compressibility and strength of the material. We have proposed and validated an equation of motion for fluid flow that includes inertial terms as well as flow resistance terms that are linear and quadratic in flow velocity. While the drag equation involving the linear and quadratic terms was first proposed by Forchheimer near the beginning of this century and has been used in chemical engineering, it was virtually unknown in the civil engineering literature and had not been validated at high pressure gradients. We initially believed that the appearance of the quadratic term was related to turbulent flow, analogous to flow in pipes. However, analysis of test data for both granular materials and porous rocks has shown that, unlike pipes in which there is a change from linear to quadratic dependence on velocity at the transition from laminar to turbulent flow, both terms are present over the entire range of pressure gradients in porous materials. We now believe that the linear term is a result of drag forces related to the size of the narrow passages or throats through which the fluid must

flow, and the quadratic term is a result of changes in momentum due to direction changes as the fluid flows along a tortuous path through the material. The Darcy equation in conventional soil mechanics is equivalent to retaining the linear term and neglecting the quadratic term. This approximation has served well over the years because the effect of the quadratic term becomes small in comparison with the linear at the low velocities (pressure gradients) encountered in hydrology and in conventional civil engineering applications. We have adopted a form of the flow equation in which the flow coefficients have dimensions involving only powers of length and are functions only of the properties of the porous material, independent of fluid properties. The fluid density and viscosity appear explicitly in the equation. Flow tests were performed on granular materials with a range of sizes and shapes and, under sponsorship of the Defense Nuclear Agency (DNA), on porous limestone. Relationships have been developed to relate the fluid flow coefficients to the geometry of the porous materials. The linear flow coefficient is related to representative throat dimensions of the porous material by a dimensionless constant over the whole range of granular materials and rock tested. A similar relationship was developed for the quadratic flow coefficient, but it is found to be applicable only to the granular materials. Since the tortuosity in rock is fundamentally different than in granular materials, this is consistent with the view that the quadratic coefficient is related to the inertial forces associated with direction changes. The fluid flow test results and theoretical development of the flow model are documented in Section 4 of the report.

The final major objective of this research was to perform laboratory wave propagation tests on saturated porous materials for the purpose of validating the analytical and numerical formulations, and observing their fundamental mechanical response characteristics. The early part of the research effort involved parallel efforts to design the laboratory apparatus and perform numerical analyses of the planned experiments. The calculational portion of the effort was performed using the MultiPhase Dynamic Analysis Program (MPDAP) which was developed under a previous AFOSR-sponsored effort. For this work, MPDAP which was originally an implicit finite element program was converted to have an explicit integration option which will more efficiently treat wave propagation problems, as described in Section 2. Our approach to design of the test apparatus was similar in appearance to a Split Hopkinson Pressure Bar (SHPB). A striker bar is fired from a gas gun and impacts the incident bar inducing a

compressive wave which is propagated into the test specimen. In contrast to the SHPB, the Wave Propagation Bar (WPB) makes measurements directly on a test specimen which is many bar diameters in length. The ARA WPB uses a specimen 2 inches in diameter and up to 24 inches long. Because of the necessity to saturate the test specimen, it was originally proposed to confine the specimen within pressurized gas in a concentric pressure vessel, much like a triaxial compression apparatus. However, the MPDAP numerical calculations revealed that the experiment as planned had significant shortcomings. Because the confining pressure remained essentially constant throughout the test, the pore pressure generated by the propagating wave was prematurely relieved by a relief wave propagating in from the surface of the porous specimen. This discovery motivated further calculations to find a solution to the problem and caused a delay in construction of the test equipment. Eventually, based on the calculational results, an apparatus was designed and constructed in which the confining vessel consisted of a thick (approx. 2 inches) steel sleeve with a thin (approx. 0.2 inch) liquid filled gap between its inner wall and the test specimen. A porous metal bar was chosen as a test specimen because it appeared to have a combination of skeleton response and fluid flow properties which would accentuate the influence of relative fluid motion on the wave propagation characteristics. The design of the equipment and the preliminary calculations are presented in Section 6.

The WPB test apparatus was constructed and a series of tests was run on a specimen of porous stainless steel in both the saturated and dry states, as described in Section 7. Measurements were made of dynamic skeleton strains at three locations on the specimen and of dynamic pore pressure response at one location. The experimental apparatus produced highly repeatable measurements of excellent quality. As also documented in Section 7, the test results were analyzed using MPDAP calculations which simulated, as closely as possible, the lab tests. There is excellent qualitative and quantitative agreement between the calculations and the laboratory measurements. The calculational results clearly exhibit a secondary disturbance propagating at a relatively slow speed behind the compressional wave. This wave of the second kind is predicted by analysis to exist in saturated porous materials but has not, to our knowledge, previously been observed. Guided by the calculations, we were able to identify this phenomenon, which appears to be related to a surge of pore fluid within the porous skeleton, in the laboratory test data. Thus, we believe that we have observed a phenomenon in the

laboratory which has previously only been predicted by analysis. The excellent overall agreement between experimental wave propagation test data and the numerical calculations of these experiments provides strong validation of these analytical techniques. It should provide confidence in their application to the much more complex real-world problems of interest to the DoD and others.

TABLE OF CONTENTS

Section   **Page**

TABLE OF CONTENTS (CONTINUED)

LIST OF TABLES

LIST OF FIGURES

LIST OF FIGURES (CONTINUED)

LIST OF FIGURES (CONTINUED)

LIST OF FIGURES (CONTINUED)

LIST OF FIGURES (CONTINUED)

LIST OF FIGURES (CONTINUED)

LIST OF FIGURES (CONTINUED)

CONVERSION TABLE

angstrom	1.000 000 X E -10	meters (m)
atmosphere (normal)	1.013 25 X E +2	kilo pascal (kPa)
bar	1.000 000 X E +2	kilo pascal (kPa)
barn	1.000 000 X E -28	meter^2(m^2)
British thermal unit (thermochemical)	1.054 350 X E +3	joule (J)
calorie (thermochemical)	4.184 000	joule (J)
cal (thermochemical)/cm^2	4.184 000 X E -2	mega joule/m^2(MJ/m^2)
curie	3.700 000 X E +1	*giga becquerel (GBq)
degree (angle)	1.745 329 X E -2	radian (rad)
degree Fahrenheit	t_k = t·f + 459.67)/1.8	degree kelvin (K)
electron volt	1.602 19 X E -19	joule (J)
erg	1.000 000 X E -7	joule (J)
erg/second	1.000 000 X E -7	watt (W)
foot	3.048 000 X E -1	meter (m)
foot-pound-force	1.355 818	joule (J)
gallon (U.S. liquid)	3.785 412 X E -3	meter^3 (m^3)
inch	2.540 000 X E -2	meter (m)
jerk	1.000 000 X E +9	joule (J)
joule/kilogram (J/kg) radiation dose absorbed)	1.000 000	Gray (Gy)
kilotons	4.183	terajoules
kip (1000 lbf)	4.448 222 X E +3	newton (N)
kip/inch^2 (ksi)	6.894 757 X E +3	kilo pascal (kPa)
ktap	1.000 000 X E +2	newton-second/m^2 (N-s/m^2)
micron	1.000 000 X E -6	meter (m)
mil	2.540 000 X E -5	meter (m)
mile (international)	1.609 344 X E +3	meter (m)
ounce	2.834 952 X E -2	kilogram (kg)
pound-force (lbs avoirdupois)	4.448 222	newton (N)
pound-force inch	1.129 848 X E -1	newton-meter (N·m)
pound-force/inch	1.751 268 X E +2 .	newton-meter (N/m)
pound-force/foot^2	4.788 026 X E -2	kilo pascal (kPa)
pound-force/inch^2 (psi)	6.894 757	kilo pascal (kPa)
pound-mass (lbm avoirdupois)	4.535 924 X E -1	kilogram (kg)
pound-mass-foot^2 (moment of inertia)	4.214 011 X E -2	kilogram-meter^2 (kg·m^2)
pound-mass/foot^3	1.601 846 X E +1	kilogram/meter^3 (kg/m^3)
rad (radiation dose absorbed	1.000 000 X E -2	**Gray (Gy)
roentgen	2.579 760 X E -4	coulomb/kilogram (C/kg)
shake	1.000 000 X E -8	second (s)
slug	1.459 390 X E +1	kilogram (kg)
torr (mm Hg 0• C)	1.333 22 X E -1	kilo pascal (kPa)

SECTION 1
INTRODUCTION

This report presents the results of a research effort directed at improving the fundamental understanding of the dynamic response of fully or partially fluid-saturated porous materials. The work was performed by Applied Research Associates, Inc. (ARA) under Contract No. F49620-89-C-0037 with the Air Force Office of Scientific Research (AFOSR). The laboratory research was conducted by the Materials Testing Laboratory of ARA's New England Division in South Royalton, Vermont, which was also responsible for the data analysis and numerical simulations. An ARA subcontractor, COMTEC Research of Clifton, Virginia developed the multiphase analysis programs, MEM and MPDAP.

1.1 BACKGROUND

For more than ten years, AFOSR has supported a number of researchers in the field of multiphase mechanics, with particular emphasis on blast induced liquefaction. This research has significantly advanced the state of knowledge in this field of geomechanics and has provided strong support for Air Force and Department of Defense studies of weapons effects in saturated geologies. Studies which this work has supported include:

- an evaluation of nuclear craters in the Pacific which led to a revision in the perceived cratering effectiveness of nuclear weapons;

- evaluations of the vulnerability of deep underground structures in saturated porous rock geologies;

- development of simplified weapons effects prediction techniques for use by targeting analysts throughout the DoD community;

- analysis of the vulnerability of U.S. Air Force aircraft shelters and other hardened facilities sited in saturated soils to attack from conventional weapons;

- development of countermeasures to enhance the survivability of hardened structures in/on saturated soil; and

- analysis and experimental support for the U.S. Navy's surf zone mine countermeasures research.

1.2 OBJECTIVES

The research described in this report was designed to further advance the state of knowledge in the are of dynamic multiphase mechanics. There are three major objectives of this research:

1. development of a Material Element Model (MEM) to automate the determination of parameter values for multiphase material models and to predict the response of saturated undrained porous materials to specified stress and strain inputs;

2. verification and calibration of a fluid friction model for soils and rocks covering a wide range of pore pressure gradients, and correlation of the fluid friction parameters with the microscopic structure of the pore space; and

3. development of a better understanding of wave propagation mechanics in saturated porous media through theoretical, numerical and experimental studies of wave propagation in confined saturated porous bars.

1.3 SCOPE

Model development work under this effort is summarized in Sections 2 and 3. The formulation of the computer program, MEM, a tool for the development of multiphase constitutive models for fully and partially saturated porous materials, and the extension of MPDAP, a finite element program for multiphase dynamic analysis, to allow for explicit integration, making it more efficient for wave propagation problems are detailed. The formulations of the multiphase mechanics are presented in Section 2. Section 3 describes the constitutive relationships used to model the individual constituents in a multiphase problem, including the porous skeleton, the solid grains, and the pore fluid. The source codes and user guides for MEM and MPDAP were presented in the first two Annual Technical Reports submitted under this contract (Blouin, et. al; 1990, 1991)

Laboratory tests to support development of fluid flow models for porous media were conducted at a wide range of pressure gradients in granular materials with a range of grain sizes and in porous rock. The results of fluid flow research are presented in Section 4 along with analysis which results in a unified fluid friction model. Section 5 presents the results of an analysis of the undrained triaxial compression test on saturated undrained triaxial compression test on a porous limestone specimen using data and models from the previous sections. The test results are compared with a detailed multiphase numerical simulation of the test. In addition to exercising and validating the numerical modeling techniques, this analysis identified fundamental problems with the test and provided suggestions for correcting them.

In order to further study the dynamic response of saturated porous materials and validate procedures for numerical simulation of that response, a laboratory apparatus was designed and fabricated to study wave propagation through fluid-confined saturated porous materials. Section 6 documents the development of that apparatus, including a suite of supporting numerical simulations. A series of tests was performed on a bar of porous (sintered) stainless steel in both the dry and fully saturated conditions. Section 7 describes those tests and presents the test results along with comparisons to a numerical simulation of one of the tests that was performed using the models described in the previous sections.

1 - 3

SECTION 2
NUMERICAL MODELING OF MULTI-PHASE MEDIA

The differential equations governing wave propagation in saturated porous media are so complex that closed-form analytical solutions are totally impractical for all but the simplest one-dimensional geometries. The analytical difficulty is further exacerbated in the case of nonlinear fluid or skeleton properties. a great variety of numerical algorithms have been developed to model the mechanical deformation of materials under static and dynamic loading. However, numerical techniques that can treat saturated porous media have not been well developed. This section describes two different numerical procedures for analysis of saturated or partially saturated porous materials.

The Material Element Model (MEM) is a quasi-static finite element program that was developed under this research effort to facilitate constitutive model development for saturated porous materials. It models deformation and fluid flow under arbitrary loading, specified in terms of either stress or strain, and it is designed to simplify inclusion of new skeleton constitutive models. Because pore pressure, and hence strength, are strongly dependent on the volumetric behavior of the porous skeleton, accurate constitutive modeling of the skeleton is particularly important in the analysis of saturated materials.

Multi-phase analyses require greater computation time and computer memory than single-phase dynamic analyses because of the required additional degrees of freedom to represent the motion of pore fluid. Consequently, computational efficiencies are an essential consideration in the formulation of solution schemes for real problems of interest in weapons effects and earthquake engineering. This section describes an efficient explicit formulation for the multi-phase dynamic analysis. In contrast to implicit solution techniques, the explicit formulation does not require assembly and solution of a global stiffness matrix. For numerical stability, the explicit approach requires time steps that are no greater than the wave transit time of the smallest elements. While this is smaller than the step size required for numerical stability in an implicit calculation, wave propagation problems typically require time steps of that size to

capture the physics of interest. Thus, the explicit solution, with its greatly reduced numerical complexity, is the preferred method for real wave propagation problems.

2.1 MATERIAL ELEMENT MODEL

MEM is a finite element program that models the quasi-static response of saturated porous materials to prescribed stress, strain and pore pressure boundary conditions. As currently implemented, MEM has both single element and multiple element options. The single element option includes full three dimensional capability. The multi element option is two- dimensional, and both options model pore fluid flow between elements. MEM is written in updated Lagrangian format to enable modeling of nonlinear geometric distortions including changes in porosity.

MEM is used to compute the stress, strain and pore pressure response of saturated, nonlinear porous materials. As depicted in Figure 2.1, MEM formulates the constitutive relaitonships for 9 saturated porous materials in terms of the nonlinear response of the individual material components, including the stress-strain response of the porous skeleton in the drained or unsaturated condition, and the pressure-volume relationships for the solid grains and the pore fluid. These are combined using fully coupled two-phase theory as described by Kim, Blouin, Chitty and Merkle (1988) and Simons (1989). In the fully coupled model, the overall material response is governed by the response of the material skeleton to the applied effective stresses as well as the response of the skeleton to compression of the solid grains by the effective stresses and pore fluid pressure. In addition to the material property inputs, a set of boundary conditions and/or loading histories is input.

MEM is highly versatile in that it can handle a wide variety of input boundary conditions. As shown in Figure 2.2, individual stress, strain and pore pressure inputs can be prescribed on any face of the material element. In addition, boundary conditions can include prescribed stress followed by prescribed strain, or prescribed strain followed by prescribed stress. Pore fluid boundary conditions include drained, undrained, and prescribed pressure, as well as drained followed by undrained and vice versa. A good example of a test using a combination of these

boundary conditions is the shock consolidation test described by Kim, Blouin and Timian (1987). In this uniaxial strain test, a saturated material undergoes an undrained load-unload cycle followed by a period of drained consolidation under constant effective stress and pore pressure.

Two nonlinear skeleton material models are currently implemented in MEM, a generalized elastic-perfectly plastic model described by Kim, Piepenburg, and Merkle (1985) (and updated by Kim and Blouin, 1990), and the ARA Three Invariant Conic Model described by Merkle and Dass (1985). The elastic-plastic model requires seven material parameters to completely describe the material properties. The failure and yield surfaces are coincident and are specified as one of three options: Von Mises, linear Mohr-Coulomb, or nonlinear Mohr-Coulomb with Von Mises limit. The slope of the nonlinear failure envelope for rock is prescribed according to Hoek and Brown's empirical data table (1982) as a function of rock type and in situ rock mass quality (Kim, Blouin and Timian, 1986). Beneath the failure surface the shear behavior is linear-elastic and the pressure-volume response is nonlinear-inelastic. Along the failure surface dilatancy is prescribed according to the associated flow rule.

The ARA Three Invariant Conic Model (ARA 3-I) is a sophisticated elastic-plastic model with compressive and expansive work hardening. It requires about 40 parameters to fully describe the material model properties. These are determined by computational fits to laboratory test data as described in Section 3. Dilatancy is controlled by a plastic potential function and is generally not associated with the yield surface. Details of the current ARA 3-I model are described in Section 3, including improvements that have been implemented to better describe material behavior.

The multi-element option of MEM permits the study of two-dimensional problems with pore fluid flow, e.g., two dimensional consolidation, the simulation of saturated undrained laboratory tests to study the effects of pore fluid migration on sample response, and simulation of permeability tests. The multi-element option has all the boundary condition options listed for the single element in Figure 2.2 with the exception of the changes from one boundary condition to another.

Other applications of MEM include the following:

- provide a general-purpose tool for testing engineering material models,
- provide a means of constructing sophisticated two-phase material models from drained laboratory test data and of predicting equivalent single-phase response to prescribed loadings,
- define the shear strength of saturated porous materials for prescribed undrained loadings,
- verify the two-phase models through comparison to laboratory test data obtained from less conventional strain and stress paths,
- permit analysis and prediction of liquefaction phenomena under complex loading conditions,
- perform analysis of standard and non-standard laboratory tests to gain a better understanding of test results and to develop modifications to methods used in the determination of material model parameters.

2.1.1 Theory

The theoretical formulations used in MEM are similar to those used in the multiphase dynamic code MPDAP described by Kim, Blouin, Chitty and Merkle (1988). The formulation is briefly summarized in the following subsections.

Full documents along with MEM Users Manual and the listing of the program are presented by Blouin, et al., 1990.

Notation

Note that positive signs are used for elongation and tension. A comma denotes differentiation with respect to the subsequent indices and the superposed dot denotes differntiation with respect to time. Prime indicates effective stress or effective pressure.

$\{u\}$	:	skeleton displacement
$\{U\}$	:	absolute fluid displacement
$\{w\}$	:	apparent fluid displacement relative to the solid skeleton
$\{\sigma\}$	:	total stress
$\{\sigma'\}$	:	effective stress
p	:	total pressure
p'	:	effective pressure
π	:	pore fluid pressure
$\{\pi_{,i}\}$	:	pore fluid pressure gradient vector
$\{\epsilon\}$	:	skeleton strain
$\{\bar{u}\}_e$	:	element nodal skeleton displacement vector
$\{\bar{\pi}\}_e$	:	element nodal pore fluid pressure
$\{\bar{u}\}$	:	global nodal skeleton displacement vector
$\{\bar{\pi}\}$	:	global nodal fluid pressure
$\{T\}$	:	applied boundary traction
$\hat{Q}$	:	specified boundary flow velocity (flux)
$\{b\}$	:	body force vector (generally equals gravity force)
$[D^{ep}]$	:	elasto-plastic stress-strain matrix for skeleton
$\{1\}$	:	unit vector $(1)^T = <1\ 1\ 1\ 0\ 0\ 0>$
n	:	porosity
C_f	:	pore fluid compressibility $= 1/K_f$
C_g	:	compressibility of solid grains
C_m	:	compressibility of soil-water mixture with zero effective stress $= 1/K_m$
K_m	:	bulk modulus of soil-water mixture with zero effective stress
K_s	:	bulk modulus of skeleton
K_f	:	bulk modulus of pore fluid
M_s	:	constrained modulus
ρ	:	bulk mass density of mixture
ρ_d	:	dry mass density of skeleton
ρ_f	:	fluid mass density
ρ_g	:	mass density of solid grains

μ	: pore fluid viscosity
α	: linear pore fluid flow coefficient (defined in Section 4)
β	: quadratic pore fluid flow coefficient
$[M_t]$	: mass matrix
$[K_T]$	: tangent skeleton stiffness matrix
$[C]$	: coupling matrix between solid skeleton and pore fluid
$[E]$	: pore fluid compressibility matrix
$[H]$	: fluid friction energy dissipation matrix
$\{F\}$	: nodal force vector
$\{R\}$	: internal resistance force vector
$\{\bar{Q}\}$	: equivalent boundary flow vector

Formulations

The current version of MEM can only handle the quasi-static response of the saturated porous medium. The formulations in MEM are obtained by dropping the inertia terms out of the general equations that were derived for MPDAP by Kim, Blouin, Chitty, and Merkle (1988).

The first global equation is based on the equilibrium of the total stresses with the applied boundary tractions and is given by

$$[K_t]\,\{\Delta\bar{u}\}_n + [C]\,\{\Delta\bar{\pi}\}_n = \{P_u\}_n \tag{2.1}$$

where:

$$\{P_u\}_n = \{F\}_n - \Sigma\!\int_v\, [B]^T \{\sigma_{n-1}\}\ dv$$

$$[M_t] = \Sigma\!\int_v\, [N]^T\,(\rho-n\rho_f)\,[N]\ dv$$

$$[K_T] = \Sigma\!\int_v\, [B]^T\,[D^{ep}]\,[B]\ dv$$

$$\{F\}_n = \Sigma\!\int_s\, [N]^T\,\{T\}_n\ ds$$

$$[C] = \Sigma\!\int_v\, [B]^T \left(\{1\} - \frac{C_g}{3}\,[D^{ep}]\,\{1\}\right) <G>\ dv$$

The second global equation is based on the fact that the internal fluid movements relative to the solid skeleton are compatible with the specified boundary flux and is given by

$$[C]^T \{\Delta \bar{u}\}_n + \left(-[E] - \frac{\Delta t}{2} [H]\right) \{\Delta \bar{\pi}\}_n = \{P_\pi\}_n \qquad (2.2)$$

where:

$$[E] = \Sigma \int_v <G>^T \left(\alpha - \frac{Cg^2}{g} \{1\}^T [D^{ep}] \{1\}\right) <G> \, dv$$

$$[H] = \Sigma \int_v [A]^T \, k'[A] \, dv$$

$$\{P_\pi\}_n = \Delta t \, [H] \cdot \{\bar{\pi}\}_{n-1} - \frac{\Delta t}{2} \left(\{Q\}_{n-1} + \{Q\}_n\right)$$

$$\{Q\} = \Sigma \int_s <G>^T \hat{Q} \, ds$$

$$k' = \left(\frac{M}{\alpha} + \frac{p_f}{e} |\dot{w}_i|\right)^{-1}$$

$$\dot{w}_i = n(\dot{U}_i - \dot{u}_i)$$

$$C_m = nC_f + (1 - n)C_g$$

The shape functions , [N] and $<G>$, and their derivatives [B] and [A], respectively, in Equations 2.1 and 2.2 relate the field variables within each element to the element nodal values as follows:

$$\{u\} = [N] \{\bar{u}\}_e \qquad (2.3)$$

$$\{\epsilon\} = [B] \{\bar{u}\}_e$$

$$\pi = <G> \{\bar{\pi}\}_e$$

$$\{\pi_{,i}\} = [A] \{\bar{\pi}\}_e$$

2.3 EXPLICIT FINITE ELEMENT FORMULATIONS FOR MULTI-PHASE DYNAMIC ANALYSIS

Kim, et al. (1988) and Blouin, et al. (1991) describe the implementation of the multi-phase dynamic equilibrium equations using implicit integration schemes. In the implicit method, the element stiffness, damping, and mass matrices are assembled to form a generalized structural stiffness matrix. The linearized structural equilibrium equations are then solved simultaneously at each step in the calculation. For large scale nonlinear problems, the implicit method requires considerably longer computation at each time step, mostly for solving linear equations, and considerably more computer memory to store the generalized structural stiffness matrix, than a comparable problem solved using an explicit formulation. In many structural problems, the penalty in computation time required by the implicit approach at each step is more than offset by a greatly reduced number of time steps required to solve the problem. However, in the wave propagation problems of interest to members of the DOD community, time steps on the order of the wave transit time across an element are required to simulate the physical processes with adequate fidelity. In this, the explicit approach which requires approximately the same number of time steps, has an advantage because of the smaller computational effort at each time step.

Explicit direct integration schemes, combined with mass lumping techniques, have been successfully used to solve dynamic equilibrium equations for the single-phase media. The main advantages of such an explicit method over the implicit method are that the generalized structural stiffness matrix does not have to be formed and the structural equilibrium equations are easily solved by just inverting the diagonal components of the lumped mass matrix. However, the disadvantage of the explicit method is that the stable time step size, which depends on the smallest period of the finite element, is sometimes unduly small.

This section presents efficient explicit formulation for the multi-phase dynamic analysis along with verification problems to demonstrate the computational algorithms implemented in the Multi-Phase Dynamic Analysis Program (MPDAP).

Notation

Note that positive signs have been used for elongation and tension. A comma denotes differentiation with respect to the subsequent indices and the superposed dot denotes difdferentiation with respect to time.

$\{u\}$	:	solid phase displacement
$\{w\}$	:	apparent fluid displacement relative to solid skeleton
$\{\sigma\}$	:	total stress
$\{\sigma'\}$	:	effective stress
π	:	fluid pressure
$\{\underline{u}\}$	:	solid phase displacement vector at element nodal degrees of freedom
$\{\underline{w}\}$	:	apparent fluid displacement vector relative to skeleton at structural nodal degrees of freedom
$\{T\}$	:	applied boundary traction
$\hat{\pi}$	:	specified boundary pore fluid pressure
$[D^{ep}]$	:	elasto-plastic stress-strain matrix
$\{1\}$	:	unit vector $\quad \{1\}^T = <1\ 1\ 1\ 0\ 0\ 0>$
n	:	porosity
K_g	:	bulk modulus of solid grain
K_m	:	bulk modulus of soil/water mixture
K_s^{ep}	:	bulk modulus of elasto-plastic skeleton
ρ	:	bulk mass density of mixture
ρ_f	:	fluid mass density
μ	:	dynamic viscosity of pore fluid
α	:	linear permeability coefficient
β	:	quadratic permeability coefficient
δ_{ij}	:	Kronecker delta

Explicit Formulations

The fully coupled global equilibrium equations for the multi-phase medium have been derived by Blouin, et. al. (1991) and are given by:

$$\begin{bmatrix} M_m & M_c \\ M_c^T & M_f \end{bmatrix} \begin{Bmatrix} \bar{u}^{..}_n \\ \ddot{w}_n \end{Bmatrix} + \begin{bmatrix} 0 & 0 \\ 0 & H \end{bmatrix} \begin{Bmatrix} \dot{u}_n \\ \dot{w}_n \end{Bmatrix} + \begin{bmatrix} K_t + EE & C \\ C^T & E \end{bmatrix} \begin{Bmatrix} \Delta\underline{u}_n \\ \Delta\underline{w}_n \end{Bmatrix} \qquad (2.4)$$

$$= \begin{Bmatrix} F_n \\ G_n \end{Bmatrix} - \begin{Bmatrix} R^s_{n-1} + R^f_{n-1} \\ R^f_{n-1} \end{Bmatrix}$$

where:

$$M_m = \sum \int_v [N]^T \rho [N] \, dv$$

$$M_c = \sum \int_v [N]^T \rho_f [N] \, dv$$

$$M_f = \sum \int_v [N]^T \frac{1}{n} \rho_f [N] \, dv$$

$$H = \sum \int_v K' [N]^T [N] \, dv$$

$$G_n = \sum \int_s [N]^T \hat{\pi}_n \, ds$$

$$K_t = \sum \int_v [B]^T [D^{ep}] [B] \, dv$$

$$EE = \sum \int_v \bar{m}_1 [B]^T \{1\} \{1\}^T [B] \, dv$$

$$C = \sum \int_v \bar{m}_2 [B]^T \{1\} \{1\}^T [B] \, dv$$

$$E = \sum \int_v \bar{m} [B]^T \{1\} \{1\}^T [B] \, dv$$

$$F_n = \sum \int_s [N]^T \{T\} \, ds$$

$$R^s_{n-1} = \sum \int_v [B]^T \{\sigma'_{n-1}\} \, dv$$

$$R^f_{n-1} = \sum \int_v [B]^T \{1\} \pi_{n-1} \, dv$$

$$k' = \left(\frac{M}{\alpha} + \frac{p_f}{e} |\dot{w}_i| \right)^{-1}$$

The inertial force terms associated with the coupling mass matrix M_c and M_c^T in Equation 2.4 can be expressed in the following simple form:

$$\overline{M}\ddot{\vec{u}}_n + \overline{H}\dot{\vec{u}}_n = \overline{F}_n \qquad (2.5)$$

where:

$$\overline{M} = \begin{bmatrix} M_m & 0 \\ 0 & M_f \end{bmatrix}$$

$$\overline{H} = \begin{bmatrix} 0 & 0 \\ 0 & H \end{bmatrix}$$

$$\overline{F}_n = \left\{ \begin{matrix} F_n \\ G_n \end{matrix} \right\} - \left\{ \begin{matrix} R_n{}^s + R_n{}^f \\ R_n{}^f \end{matrix} \right\} - \left\{ \begin{matrix} M_c \cdot \ddot{\underline{w}}_{n-1} \\ M_c{}^T \cdot \ddot{\underline{u}}_{n-1} \end{matrix} \right\}$$

$$\overline{u}_n = \left\{ \begin{matrix} \underline{u}_n \\ \underline{w}_n \end{matrix} \right\}$$

Employing a central difference scheme, accelerations and velocities at step n can be expressed in terms of displacement increments at steps n and $n+1$:

$$\ddot{\overline{u}}_n = \frac{1}{\Delta t^2} (\Delta \overline{u}_{n+1} - \Delta \overline{u}_n) \qquad (2.6)$$

and

$$\dot{\overline{u}}_n = \frac{1}{2\Delta t} (\Delta \overline{u}_{n+1} + \Delta \overline{u}_n) \qquad (2.7)$$

where Δt denotes time step.

Now substituting Equations 2.6 and 2.7 into 2.5, we obtain:

$$\left[\frac{1}{\Delta t^2} \overline{M} + \frac{1}{2\Delta t} \overline{H} \right] \Delta \overline{u}_{n+1} = \overline{F}_n + \frac{1}{\Delta t^2} \overline{M} \cdot \Delta \overline{u}_n - \frac{1}{2\Delta t} \overline{H} \cdot \Delta \overline{u}_n \qquad (2.8)$$

It should be noted that for practical purposes, the mass matrix $\overline{M}$ and the dissipation matrix $\overline{H}$ in Equation 2.8 can be lumped out so that the solution can be performed on the element level without the factorization of the structural matrix.

Verification of Explicit Algorithms

Two problems are presented here to demonstrate the validity of explicit algorithms implemented in MPDAP.

The first problem considers a 12 inch hollow spherical hole in an infinite elastic medium. A 100 psi step load is suddenly applied to the internal surface of the spherical hole as shown in Figure 2.3. Material properties and time steps used for the calculation are also included in Figure 2.3. Figure 2.4 shows the radial stress profiles at 5.5 msec. The MPDAP calculation using the explicit method agrees very well with the closed-form solution.

The second problem considers a planar compression wave propagating through saturated elastic sand. The input loading, as shown in Figure 2.5, is a short rise time triangular pulse with a peak stress of 5,000 psi and a positive duration of 10 msec. Material properties and time steps used for calculations are also included in Figure 2.5. Two MPDAP calculations were performed; one with the explicit method and the other with the implicit method.

Figures 2.6 and 2.7 show profiles of effective vertical stress and pore pressure, respectively, at 20 msec. At the wavefront, there are slight differences between explicit and implicit methods. But behind the wavefront, the stress profiles are almost identical.

GIVEN: Individual Components Properties (Grain, Pore-Fluid, and Porous Skeleton) and Specified Mixture Boundary Conditions/Load Histories

PREDICT: Stress-Strain Response of Saturated Porous Materials

Individual Components Stress-Strain Relation

P_G ε_G π ε_F σ' ε'

Grain   Pore-Fluid   Skeleton

$$\{\Delta\sigma'\} = [D^{ep}]\,\{\Delta\varepsilon'\}$$

Mixture Boundary Conditions and Load Histories

Material Element Model

σ ε

Saturated Porous Material

$$\{\Delta\sigma\} = [D]\,\{\Delta\varepsilon\}$$
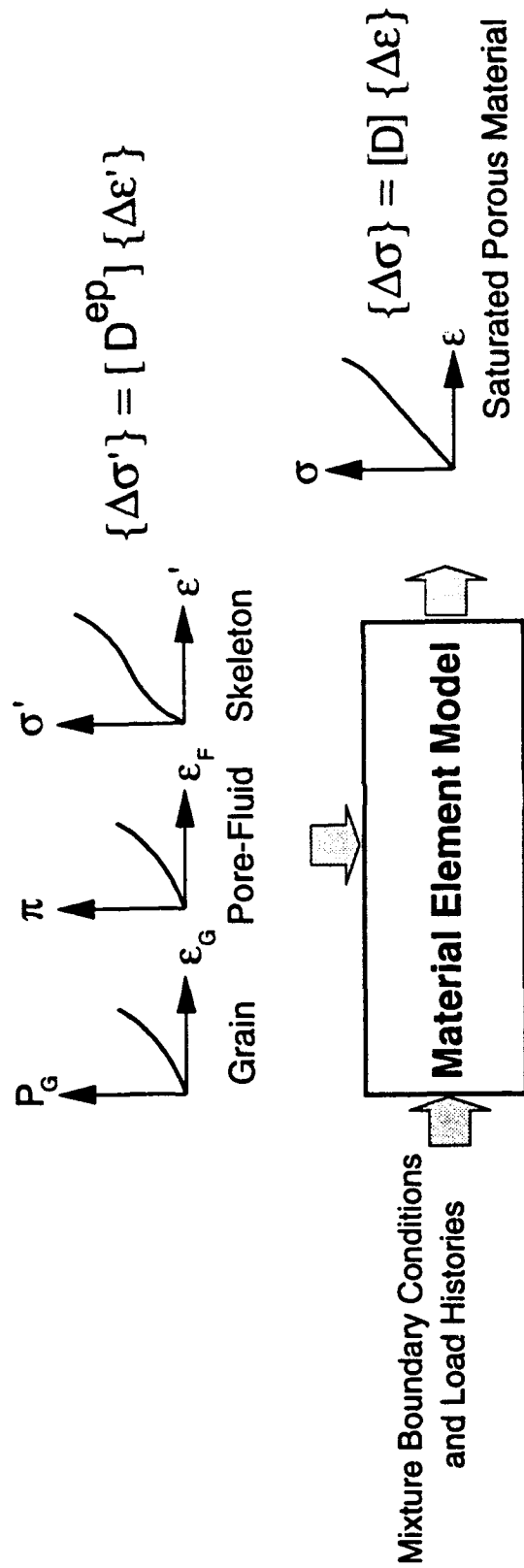
Figure 2.1. Material element model outline.

2-13

$$\sigma_x = \sigma'_x + \pi$$

(Total Stress)   (Effective Stress)   (Pore Fluid-Pressure)
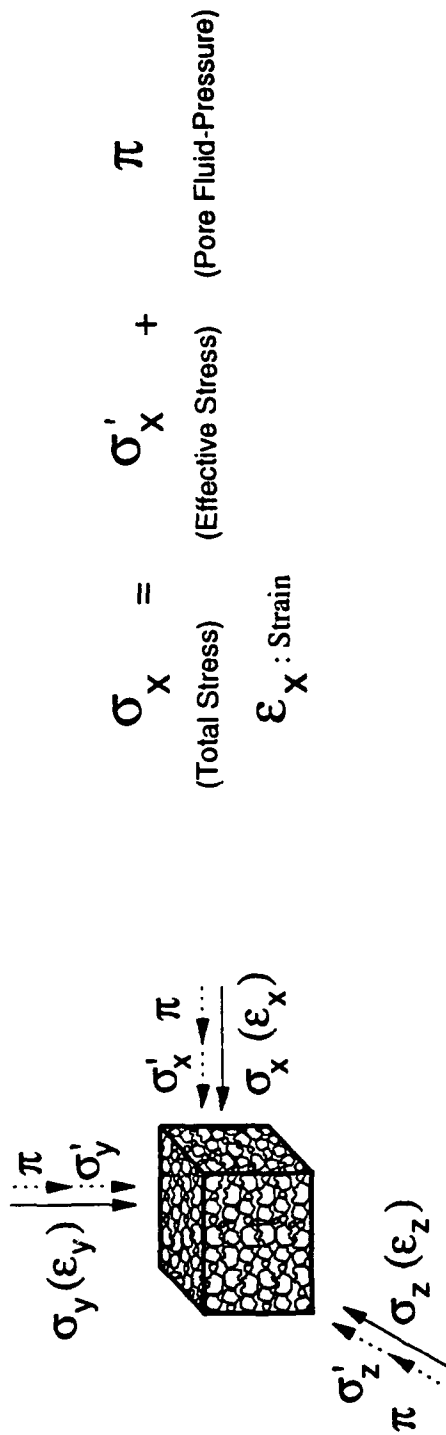
ε_x : Strain

Total Stress/Strain

- Constrained ($\varepsilon = 0$)
- Unconfined ($\sigma = 0$)
- Prescribed Stress
- Prescribed Strain
- Prescribed Strain, then Prescribed Stress
- *Prescribed Stress, then Prescribed Strain*

Pore Fluid

- Drained ($\pi = 0$)
- Undrained (π = unknown)
- Prescribed Pore Pressure
- Prescribed Pore Pressure, then Undrained
- Drained, then Undrained
- Undrained, then Drained

$\sigma_y(\varepsilon_y)$

π σ'_y

σ'_x π

$\sigma_x(\varepsilon_x)$

σ'_z

π $\sigma_z(\varepsilon_z)$

Figure 2.2.   MEM boundary conditions.
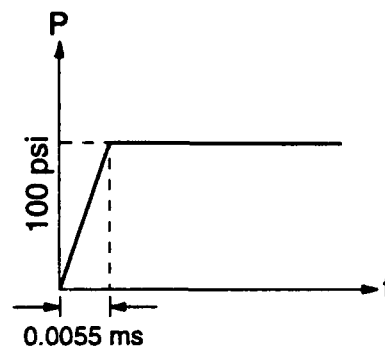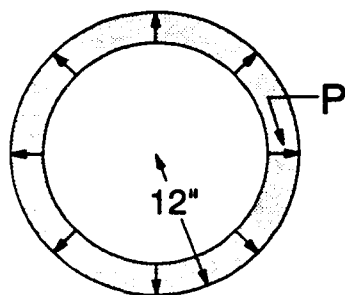
Time Step $\Delta t = 0.005$ ms

Young's Modulus $E = 12{,}457$ psi

Poisson's Ratio $\nu = 0.25$

Mass Density $\rho = 1.88 \times 10^{-4}$ lb-s^2/in^4

Figure 2.3. Verification problem 1, elastic spherical wave propagation in one-phase medium.

EXPLICIT METHOD
AT TIME .5500E-02
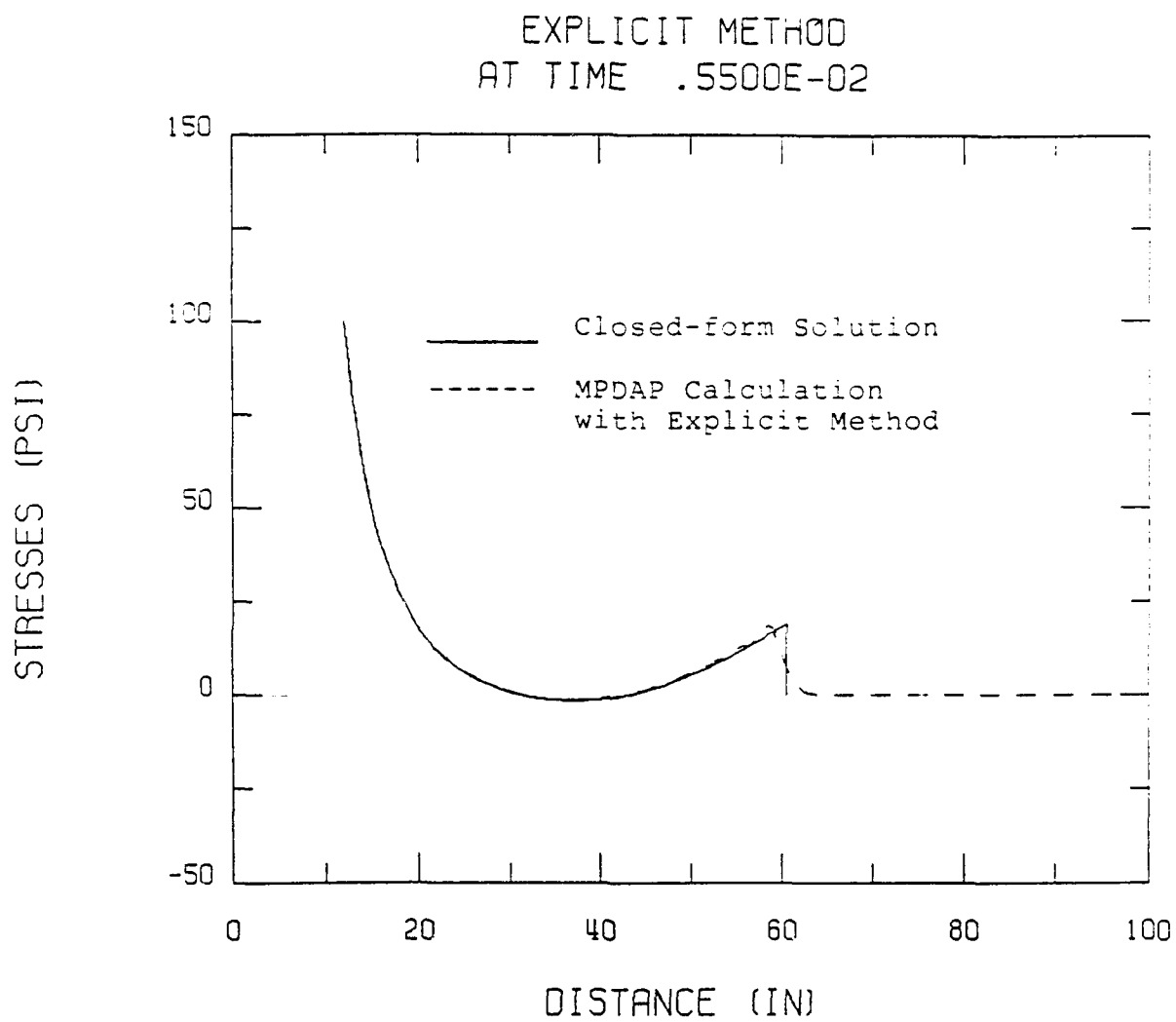
Figure 2.4. Radial stress profile at 5.5 msec, verification problem 1.

P (psi)

5000

0.01   t (s)

$\Delta t = 1.55 \times 10^{-4}$
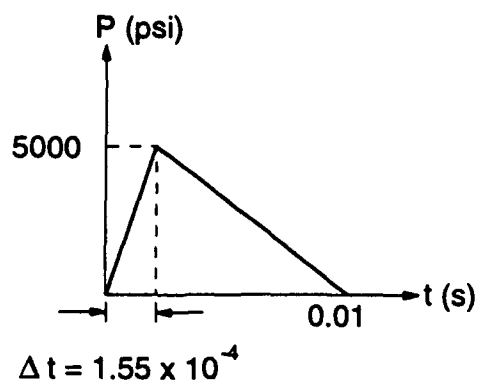
ASSUMED MATERIAL PROPERTIES

Pore Water 0.29×10^6 psi

Solid Grains
    Bulk Modulus 5.0×10^6 psi
    Specific Gravity   2.67

Drained Skeleton Properties
    Bulk Modulus   3000 psi
    Constrained Modulus   6000 psi
    Poisson's Ratio   0.20
    Porosity   0.35

Permeability   1.0 in/s

Explicit Calculation $\Delta t = 0.8 \times 10^{-5}$ sec and $C_1 = 0.8$

Implicit Calculation $\Delta t = 0.4 \times 10^{-4}$ sec, $\beta = 0.563$
    and $\gamma = 1$

Figure 2.5. Loading time history, material properties, and
    time steps used in 1-D plane strain elastic wave
    propagation for verification problem 2.

EXPLICIT VS. IMPLICIT METHOD
AT TIME   .2000E-01
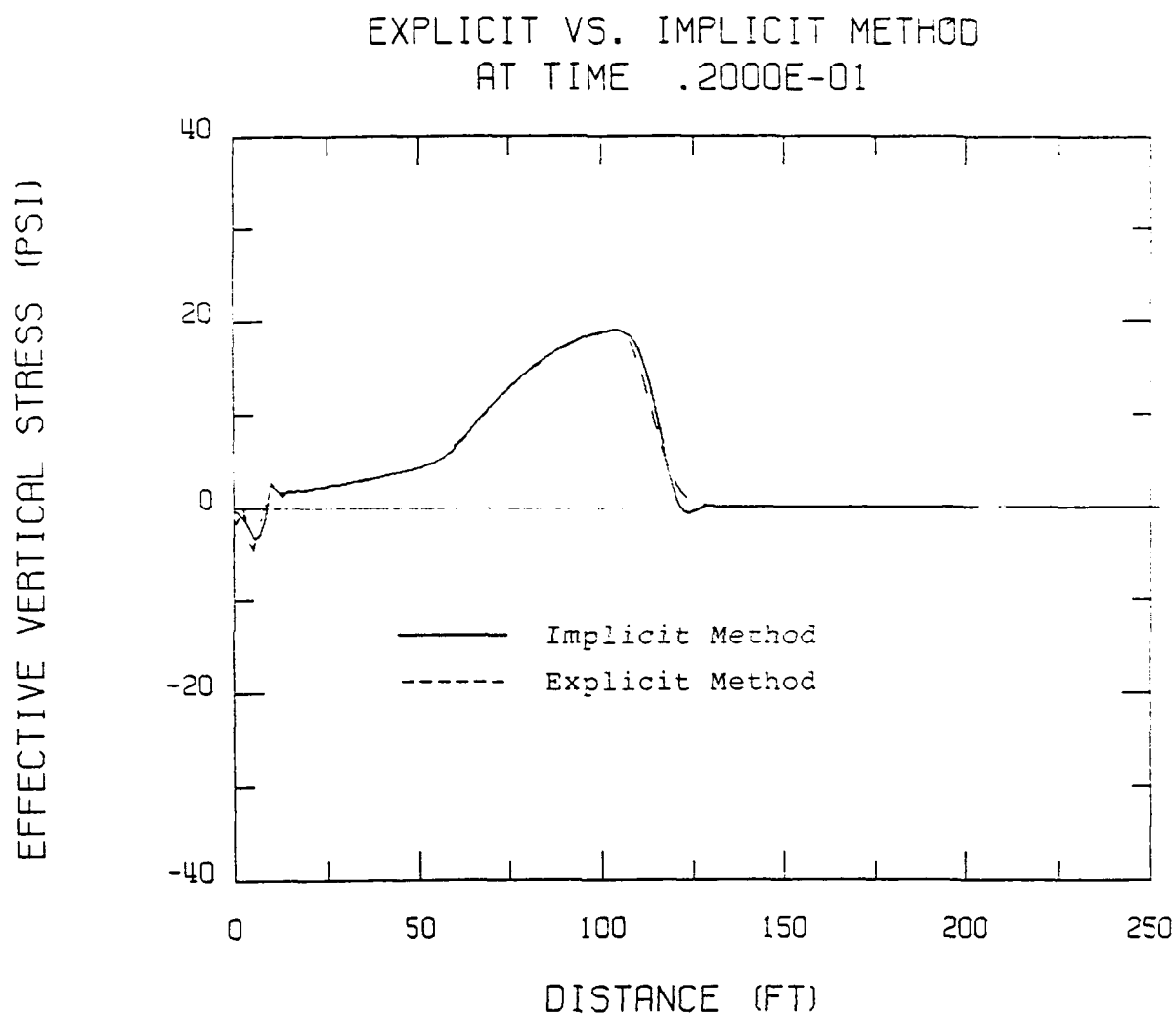
Figure 2.6.   Effective vertical stress profile at 20 msec,
verification problem 2.

EXPLICIT .VS. IMPLICIT METHOD
AT TIME   .2000E-01
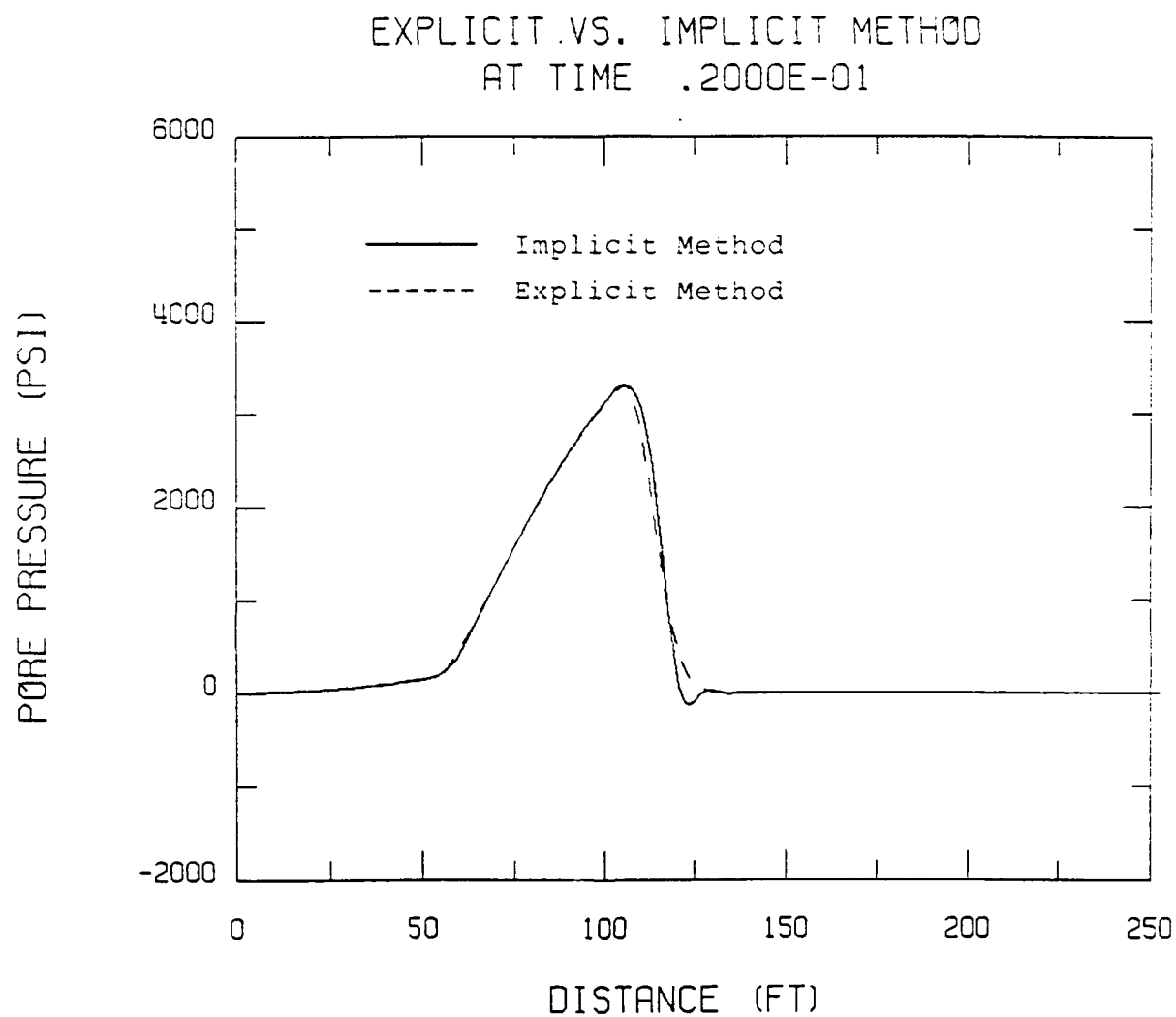
Figure 2.7. Pore fluid pressure profile at 20 msec,
verification problem 2.

2-19

SECTION 3
MATERIAL MODELS

3.1 MODELING APPROACH

To improve our understanding of the mechanical response of saturated, porous materials, we performed numerical simulations of laboratory experiments as described in Sections 5 and 7. These calculations were completed using the finite element codes MEM and MPDAP which are discussed in Section 2. Central to the success of these calculations are the numerical models used to represent the materials. These models are described in this section with the application to specific material given in later sections of this report.

In general, our approach is to model the nonlinear response of the individual material components; that is, the drained stress-strain response of the porous skeleton and the pressure-volume relationship of the solid grains, pore water, and pore air. The behavior of these constituents are combined using fully coupled two-phase theory as described by Kim, Blouin, Chitty and Merkle (1988) and Simons (1989). In a simple decoupled model, the soil or rock skeleton acts in parallel with the solid-fluid mixture such that the net compressibility is the sum of the mixture modulus and the appropriate skeleton modulus. The shortcomings of a decoupled model are demonstrated by Blouin and Kim (1984). A fully coupled approach incorporates the mixture model with the additional considerations of the strain in the skeleton resulting from the compression of individual grains by pore pressure, and the volume change in the solid-fluid mixture due to effective stresses acting on the solid grains. In addition, the flow of pore water within the porous skeleton (from element to element in a finite element mesh) is governed by a permeability law. This sophisticated formulation provides an accurate means of predicting undrained material response for many porous materials up to very high pressures.

This section describes the individual components of the material model in detail. Note that not all of these models were used in this study but are included for completeness in describing the models available in the MEM and MPDAP codes. These models include:

3-1

- ARA Three Invariant model for the drained response of the porous skeleton,
- nonlinear solid grain model,
- pore water compressibility model,
- partial saturation model that accounts for the presence of pore air, and
- permeability models.

3.2 ARA THREE INVARIANT SKELETON MODEL

In simulating the behavior of saturated materials, it is particularly important to accurately model the response of the soil skeleton. Under saturated conditions, the material strength is strongly influenced by the pore pressure response which is, in turn, controlled by the volumetric deformation characteristics of the porous skeleton. That is, collapse or compressive straining of the skeleton transfers more load to the fluid in the pore spaces which leads to reduced effective stresses and shear strength in the material. On the other hand, dilation or expansive strains reduce the pore pressures, increase the effective stresses, and generally result in greater shear strength. Consequently, the skeleton model is crucial to the performance of any saturated, two-phase material simulation.

We elected to use a relatively advanced skeleton model known as the ARA Three Invariant (ARA 3-I) model which was originally developed by ARA under sponsorship of the Air Force Office of Scientific Research and described by Merkle and Dass (1985) and Dass and Merkle (1986). This model is called the Three Invariant Model because the controlling surfaces in stress space are formulated in terms of three independent stress invariants; the octahedral normal stress, octahedral shear stress, and Lode's angle. Several modifications have been made to permit modeling both soil and rock response over a wider range of stresses, including very high stresses associated with explosive loadings.

The ARA 3-I model is a work hardening, elasto-plastic model with two independent yield surfaces, as depicted in Figure 3.1. The compressive yield surface is an ellipsoid with its center at the origin in principal stress space. It is associative, only strain hardens, and the strain

hardening parameter is the corresponding plastic work. The expansive yield surface is a hyperboloid with its apex on the hydrostatic axis in principal stress space. It is non-associative, strain hardens, and the strain hardening parameter is the corresponding plastic work. The parameters for the ARA 3-I model are summarized in Table 3.1.

Fitting and evaluating the ARA 3-I model for specific materials is accomplished using the MEM (Material Element Model) code outlined in Section 2. One portion of this code contains algorithms for fitting the model while another part is used to exercise the model under a variety of boundary conditions on a single, three dimensional finite element. The fitting portion of the MEM code outputs the ARA 3-I model parameters in the format described in Table 3.2. Other codes can then read this file directly and, hence, this is a convenient format for presenting the model parameters for a given material.

The model is fit to the measured response of the material skeleton. Usually, the model is fit directly to laboratory data obtained on drained test specimens. The minimum test data required to fit the model are:

- one hydrostatic (isotropic) compression test with at least two unload/reload cycles;
- three triaxial compression tests at confining pressures in the range of interest and with unload cycles to determine Poisson's ratio;
- one conventional triaxial extension test to establish the material strength in this mode.

Other test data, such as uniaxial strain tests, undrained triaxial compression tests, etc., are used to evaluate the performance of the model. Section 5.1.1 of this report presents an example of fitting the ARA 3-I model to test data for a porous limestone.

3.2.1. Notation

sign convention	:	Compression is POSITIVE
P_a	:	atmospheric pressure
$\{\epsilon\}$	:	total strain vector
$\{\epsilon^e\}$	:	elastic strain vector
$\{\epsilon_c^p\}$	:	plastic compressive strain vector
$\{\epsilon_p^p\}$	:	plastic expansive strain vector
ϵ_v	:	volumetric strain
γ_{oct}	:	octahedral shear strain
$\{\sigma\}$	:	stress vector
σ_{oct}	:	octahedral normal stress (mean pressure)
τ_{oct}	:	octahedral shear stress
$\sigma_{oct, max}$	:	maximum past mean pressure
$\tau_{oct, max, TXC}$	:	ultimate octahedral shear stress at infinite mean stress in triaxial compression mode
T	:	tensile strength (negative)
J_2'	:	second invariant of deviator stress tensor
J_3'	:	third invariant of deviator stress tensor
ω	:	Lode's angle
K	:	bulk modulus
K_o	:	unload/reload bulk modulus at zero pressure
K_1	:	unload/reload bulk modulus at initial unloading
ν	:	Poisson's ratio
f_c	:	compressive yield criterion
f_c'	:	compressive yield stress function
f_c''	:	compressive yield hardening function
f_p	:	expansive yield criterion
f_p'	:	expansive yield stress function
f_p''	:	expansive yield hardening function
g_p	:	expansive plastic potential function

W_c	:	compressive plastic work
W_p	:	expansive plastic work
$W_{p, peak}$	:	expansive plastic work at peak shear stress
ξ_p	:	normalized expansive plastic work
ψ	:	ratio between the triaxial compression and extension strengths at a given mean stress
η_1	:	expansive yield hardening parameter
η_2	:	expansive plastic potential parameter
$d\lambda_c$	:	compressive yield proportionality constant
$d\lambda_p$	:	expansive yield proportionality constant
α_f	:	fraction of ultimate τ_{oct} in triaxial compression mode

3.2.2. Total Strain Formulation

The ARA Three Invariant model computes the total strain in parts consisting of the elastic, compressive plastic, and expansive plastic strain components:

$$\{d\epsilon\} = \{d\epsilon^e\} + \{d\epsilon^p_c\} + \{d\epsilon^p_p\} \tag{3.1}$$

Each strain component is calculated independently within the model as described in the following subsections.

3.2.3. Elastic Response

At stress states inside the yield surfaces, the skeleton response is treated as nonlinear elastic and governed by the previous maximum peak stress. Two options are available for modeling the elastic response within the framework of the three invariant skeleton model: the ARA elastic model and the L 'e and Nelson elastic model. In both options, Poisson's ratio is assumed to remain constant.

ARA elastic model. During virgin loading, the elastic bulk modulus is given by:

$$K = \frac{K_{ur}\, P_a}{3\,(1 - 2\nu)}\left[\frac{\sigma_{oct}}{P_a}\right]^n \geq K_i \qquad (3.2)$$

where K_{ur} and n are material constants obtained in the parameter fitting. K_i represents the initial bulk modulus at low pressures and is necessary for modeling the behavior of rock-type materials that have a definite initial elastic behavior. In uncemented soils, K_i can be taken as a very small value. The initial bulk modulus is also used to determine the initial position of the compressive plastic yield function (cap) by defining the initial elastic range.

During unloading or reloading, the skeleton modulus is described by one of two segments as depicted in Figure 3.2. Between the previous peak mean stress, $\sigma_{oct,\,max}$, and the transition into the nonlinear segment at $\sigma_{oct,b}$, the elastic bulk modulus is constant and is given by:

$$K = K_1 = \frac{K_{ur}\, P_a}{3\,(1 - 2\nu)}\left[\frac{\sigma_{oct,max}}{P_a}\right]^n \qquad (3.3)$$

The transition into the nonlinear segment occurs at:

$$\sigma_{oct,b} = \lambda\, \sigma_{oct,max} \qquad (3.4)$$

where λ is a model parameter. At mean stresses less than $\sigma_{oct,b}$, the nonlinear bulk modulus is given by:

$$K = K_1 \left[1 - \gamma \left[\frac{\beta}{\gamma}\right]^{\frac{4\,\sigma_{oct}}{\sigma_{oct,b}}}\right] \qquad (3.5)$$

Referring to Figure 3.2, the model parameters γ and β are given by:

$$\gamma = 1 - \frac{K_o}{K_1} \qquad (3.6)$$

where K_o is the bulk modulus at zero pressure and

3-6

$$\beta = 1 - \frac{K_{\cdot}}{K_1} \tag{3.7}$$

where $K_{\cdot}$ is the bulk modulus at one quarter of the transition pressure $\sigma_{oct, b}$.

While this formulation allows for relatively accurate curve fitting of observed soil response, the model has three disadvantages:

a)   for certain closed-loop stress/strain paths, the model may violate the energy conservation principle;

b)   unloading at low pressures could potentially generate expansive volumetric strains; and

c)   at the transition pressure, $\sigma_{oct,b}$, the modulus is not continuous.

Lade and Nelson elastic model. The second elastic model option is based on a relationship derived by Lade and Nelson (1987). This formulation is continuous and was derived from the energy conservation principle. Lade and Nelson's model can be expressed as:

$$K = \frac{K_{ur}P_a}{3^{n+1}(1 - 2\nu)} \left[\left(\frac{3\,\sigma_{oct}}{P_a} \right)^2 + \frac{6\,(1 + \nu)}{1 - 2\nu}\,\frac{J_2'}{P_a^2} \right]^{\frac{n}{2}} \geq K_i \tag{3.8}$$

where the parameters K_{ur}, n, and K_i are the same as used in Equation 3.2. Since this model is fit strictly using the slope of an initial unload curve, it can be difficult to closely match the observed characteristic of an unload cycle.

Fitting. Poisson's ratio (ν) for a given material can be determined in a number of ways using unload/reload data which represents the elastic response of the skeleton. Lade and Nelson (1987) recommend obtaining Poisson's ratio directly from strain measurements in triaxial compression unload/reload cycles right after stress reversal at hydrostatic conditions where:

$$\nu = -\frac{\epsilon_r}{\epsilon_a} = \frac{1}{2}\left[1 - \frac{\epsilon_v}{\epsilon_a}\right] \tag{3.9}$$

where $\quad \epsilon_a \;=\;$ axial strain

$\epsilon_r \;=\;$ radial strain

$\epsilon_v \;=\;$ volume strain

In addition, since the elastic response is completely defined by any two independent elastic parameters, Poisson's ratio can be obtained from the bulk modulus, (K), measured in a hydrostatic compression unload, and any other elastic modulus. For example, a triaxial compression unload yields the shear modulus (G), an unconfined compression unload gives the Young's modulus (E), and a uniaxial strain unload produces the constrained modulus (M). Any one of these parameters can be used with the bulk modulus to obtain Poisson's ratio:

$$\nu = \frac{3K - 2G}{2\,(3K + G)} \tag{3.10}$$

$$\nu = \frac{3K - E}{6K} \tag{3.11}$$

$$\nu = \frac{3K - M}{3K + M} \tag{3.12}$$

To obtain the elastic model parameters K_{ur} and n, Equation 3.2 is rewritten in the form:

$$log\left[\frac{3K\,(1 - 2\nu)}{P_a}\right] = log\ K_{ur} + n\ log\left[\frac{\sigma_{oct}}{P_a}\right] \tag{3.13}$$

Values of K and σ_{oct}, from the initial unloading response at various pressures in the hydrostatic compression test, are then plotted as $log\ (3K\ (1\text{-}2\nu)/P_a)$ versus $log\ (\ \sigma_{oct}/P_a)$. A least squares linear regression is then applied in log-log space. The parameter n is the slope of this line while K_{ur} is the intercept where (σ_{oct}/P_a) is 1.0. The parameters λ, γ, and β for the ARA elastic unload model are determined from a single unload/reload cycle in the hydrostatic compression

test as depicted in Figure 3.2. The parameters are computed using Equations 3.4, 3.6, and 3.7.

3.2.4 Compressive Plastic Response

The compressive yield surface, or cap, is an ellipsoid with its center at the origin in principal stress space as shown in Figure 3.1. The ratio of the major axis to the minor axis is defined by the constant r, as shown in Figure 3.1, and is determined in the parameter fitting process. The compressive yield criterion is given by

$$f_c = f_c' - f_c'' = 0 \tag{3.14}$$

where the compressive yield stress function, f_c', is given by

$$f_c' = 3(\sigma_{oct}^2 + r^2 \tau_{oct}^2) \tag{3.15}$$

and the compressive yield hardening function, f_c'', is given by

$$f_c'' = P_a^2 \left[\frac{W_c}{c_i P_a} \right]^{\frac{1}{p_i}} \tag{3.16}$$

In the model, f_c'' is defined in segments with the parameters c_i and p_i determined for each segment in the fitting process. W_c is the compressive plastic work given by

$$W_c = \int \{\sigma\}^T \{d\epsilon_c^p\} \tag{3.17}$$

The compressive flow rule, which is associative, is given by

$$\{d\epsilon_c^p\} = d\lambda_c \left\{ \frac{\partial f_c'}{\partial \sigma} \right\} \tag{3.18}$$

where $d\lambda_c$ is the compressive yield proportionality constant.

3-9

Fitting. The elliptical cap ratio, r, can be determined directly from special tests following a hydro-triax-hydro type stress path (Applied Research Associates, Inc., 1991). However, this special test data is seldom available and the results are still subject to considerable interpretation. Hence, the cap ratio is generally selected to give reasonable model behavior based on experience and engineering judgement.

Other parameters which define the compressive plastic response are derived directly from the hydrostatic compression test data. At a given pressure in the hydrostatic data, the elastic component of the volume strain is computed from the elastic model and parameters described in Section 3.2.3. The compressive plastic strain is obtained by subtracting the elastic component from the total measured volume strain and the compressive plastic work is then computed according to Equation 3.17. Then, for hydrostatic compression, the octahedral shear stress is zero and Equations 3.14, 3.15, and 3.16 reduce to:

$$\frac{W_c}{P_a} = c_i \left[3 \left[\frac{\sigma_{oct}}{P_a} \right]^2 \right]^{p_i} \tag{3.19}$$

Taking the logarithm of both sides yields:

$$\log \left[\frac{W_c}{P_a} \right] = \log c_i + p_i \log \left[3 \left[\frac{\sigma_{oct}}{P_a} \right]^2 \right] \tag{3.20}$$

Plotting $\log (W_c/P_a)$ versus $\log [3 (\sigma_{oct}/P_a)^2]$ allows us to determine the parameters c_i and p_i as the intercepts and slopes, respectively, of straight line fits to the data. Since the shape of this data is usually curved in log-log space, multiple straight line segments are defined by fitting c_i and p_i over specific ranges.

3.2.5 Expansive Plastic Response

Yield surface. The expansive yield surface, or shear yield surface, is a hyperboloid with its apex on the hydrostatic axis in principal stress space as shown in Figure 3.1. The expansive yield surface has the same shape as, and approaches asymptotically to, the ultimate failure surface as shown in the same figure. The shape of the expansive yield surface in the π plane, perpendicular to the hydrostatic axis (see Figure 3.1), is a triple ellipse in polar coordinates.

The expansive yield criterion is given by:

$$f_p = f_p{}' - f_p{}'' = 0 \qquad (3.21)$$

where the expansive yield stress function, $f_p{}'$ is given by

$$f_p{}' = \left[\frac{\tau_{oct}}{P_a} \right] \left(1 - \bar{E} \, cos \, 3\omega \right) \left[\frac{P_a}{\sigma_{oct} - T} + m \right] \qquad (3.22)$$

where $\bar{E}$ and m are parameters determined in the fitting process. $\bar{E}$ is computed as:

$$\bar{E} = \frac{\psi - 1}{\psi + 1} \qquad (3.23)$$

where Ψ is the ratio between the triaxial compression and extension strengths at a given mean stress as indicated in Figure 3.1. It should be noted that Ψ must be less than 9/7 or the ultimate failure surface will become convex in the π plane thereby violating uniqueness. Lode's angle, ω, shown in Figure 3.1, is defined in the π plane and varies from 0° to 120°. An ω of 120° corresponds to the triaxial compression mode (*cos 3ω = 1.0*) and a value of 60° corresponds to the triaxial extension mode. Lode's angle is related to the second and third deviatoric stress invariants by:

$$\cos 3\omega = \frac{J_3'}{2\left[\dfrac{J_2'}{3}\right]^{1.5}} \tag{3.24}$$

The expansive yield surface hardens isotopically with the yield hardening function:

$$f_p'' = \eta_1\, \xi_p^{\bar{q}}\left[e^{\bar{q}\,(1-\xi_p)}\right] \tag{3.25}$$

The coefficient η_1 is a failure parameter representing the maximum value of f_p^* and $\bar{q}$ is an expansive hardening parameter determined in the parameter fitting process. ξ_p is the normalized expansive plastic work given by

$$\xi_p = \frac{W_p}{W_{p,peak}} \tag{3.26}$$

where the expansive plastic work, W_p, is given as

$$W_p = \int \{\sigma\}^T \left\{d\epsilon_p{}^p\right\} \tag{3.27}$$

and $W_{p,peak}$ is the peak plastic expansive work at the ultimate failure envelope for a given mean stress.

In the model, two options exist for defining $W_{p,peak}$. The first option uses a multilinear function of mean stress:

$$W_{p,peak} = a_i\, \sigma_{oct} + b_i \tag{3.28}$$

The coefficients a_i and b_i are determined in the parameter fitting process for specific ranges of mean stress. This option was added to the model to permit more accurate modeling of rock. The second option for defining $W_{p,peak}$ uses an exponential form:

$$W_{p,peak} = \bar{p} \, P_a \left[\frac{\sigma_{oct}}{P_a} \right]^l \qquad (3.29)$$

where $\bar{p}$ and l are model parameters.

Triaxial compression strength. In evaluating a model fit, it is useful to plot the strength envelope for triaxial compression stress paths. On the strength envelope, the plastic work equals $W_{p,peak}$ such that $\xi_p = 1.0$. Then, Equation 3.25 becomes

$$f_p'' = \eta_1 \, (1.0) \, e^{\bar{q}(o)} = \eta_1 \qquad (3.30)$$

In triaxial compression mode, *cos 3ω* equals 1.0 and Equation 3.22 reduces to:

$$f_p' = \left[\frac{\tau_{oct}}{p_a} \right] \left(1 - \frac{}{E} \right) \left[\frac{P_a}{\sigma_{oct} - T} + m \right] \qquad (3.31)$$

Substitution of Equations 3.30 and 3.31 into Equation 3.21 yields an equation for the triaxial compression strength envelope in the octahedral stress space:

$$\frac{\tau_{oct}}{P_a} = \left[\frac{\dfrac{\sigma_{oct} - T}{P_a}}{1 + m \left[\dfrac{\sigma_{oct} - T}{P_a} \right]} \right] \frac{\eta_1}{1 - \dfrac{}{E}} \qquad (3.32)$$

As the mean stress goes to infinity, the triaxial compression strength envelope asymptotically approaches the ultimate shear strength given by

$$\frac{\tau_{oct,max,TXC}}{P_a} = \frac{1}{m} \frac{\eta_1}{1 - \dfrac{}{E}} \qquad (3.33)$$

3-13

Expansive flow rule. The expansive flow rule, which governs the nonassociative expansive plastic flow, is given by

$$\{d\epsilon_p{}^p\} = d\lambda_p \left\{ \frac{\partial g_p}{\partial \sigma} \right\} \tag{3.34}$$

where $d\lambda_p$ is the expansive yield proportionality constant. The incremental expansive plastic strain vector is perpendicular to the expansive plastic potential function defined by

$$g_p = \left[\frac{\tau_{oct}}{P_a} \right] (1 - \frac{1}{E} \cos 3\omega) - \frac{\eta_2 \left[\frac{\sigma_{oct} - T}{P_a} \right]}{1 + m \left[\frac{\sigma_{oct} - T}{P_a} \right]} \tag{3.35}$$

The plastic potential parameter η_2 can be defined in two ways within the model. The first option defines the parameter in terms of a multi-segment function of the expansive yield hardening:

$$\eta_2 = t_i + s_i f_p'' \tag{3.36}$$

where t_i and s_i are determined for specific ranges of f_p^* in the fitting process. This option was added to the model to improve the capability for modeling rock. The second option employs a nonlinear function of the form:

$$\eta_2 = t + R \sqrt{\frac{\sigma_{oct}}{P_a}} + s f_p'' \tag{3.37}$$

where the parameters t, R, and s are constant at all ranges. This option produces a continuous function for η_2.

Potential function at high pressure. In general, the ARA 3-I model uses nonassociative flow for computing plastic strain increments related to the expansive or shear yield surface. That is, the expansive plastic strain vector, $\{\epsilon_p{}^p\}$, is computed perpendicular to the plastic potential function given in Equation 3.35. However, in the special case where $\eta_2 = f_p^*$,

Equation 3.35 can be shown to reduce to:

$$g_p = \frac{f_p{}' - f_p{}''}{m + \dfrac{P_a}{\sigma_{oct} - T}}$$

(3.38)

Thus, for the special case when $\eta_2 = f_p{}^*$, the potential function is some fraction of the expansive yield surface and plastic flow becomes associative.

At very high pressures, where the expansive yield surface is approaching the ultimate strength asymptote, the material should behave like a fluid where shear stresses do not generate plastic volume strains. To model this high pressure behavior, the plastic potential function is modified in the higher pressure regime to yield associative flow, as depicted in Figure 3.3. First, we define α_f as the fraction of the ultimate octahedral shear stress at infinite mean pressures:

$$\tau_{oct,\alpha_f} = \alpha_f \, \tau_{oct,max,TXC}$$

(3.39)

Then, using the strength envelope, the corresponding mean stress, σ_{oct}, can be found for any given fraction α_f.

As indicated in Figure 3.3, the potential function is defined in three pressure regimes delineated by α_f equal to 0.5 and 0.8. In the low pressure regime ($\sigma_{oct} < \sigma_{oct,\alpha f = .5}$), the potential function parameter η_2 is determined using the values of s, t, and R derived from the model fit. At very high pressures ($\sigma_{oct} > \sigma_{oct, \alpha f = 0.8}$), the η_2 parameters are arbitrarily set to produce associate flow. Finally, in the transition zone ($\sigma_{oct, \alpha f = 0.5} < \sigma_{oct} < \sigma_{oct,\alpha f = 0.8}$) the s, t, and R parameters are linearly interpolated.

Fitting. The first step in determining the expansive plastic response parameters is to define the ultimate failure surface and the corresponding peak expansive plastic work as functions of mean stress. In the conventional manner, the failure envelope is fit to the triaxial compression test data at the peak shear stress or the shear stress at 15% axial strain if no peak

3-15

is observed. The tensile strength T can be measured directly in an unconfined tensile test (for rocks) or inferred from the shape of the failure surface. For uncemented soils, T is generally very small. In the triaxial compression mode, the failure surface is defined by Equation 3.32 which can be rearranged to the form:

$$\frac{\sigma_{oct} - T}{\tau_{oct}} = \frac{1 - \bar{E}}{\eta_1} + m \left[\frac{1 - \bar{E}}{\eta_1} \right] \left[\frac{\sigma_{oct} - T}{P_a} \right] \tag{3.40}$$

By plotting the failure stress points from each triaxial compression test in terms of $(\sigma_{oct} - T)/\tau_{oct}$ versus $(\sigma_{oct} - T)/P_a$, a straight line fit will yield an intercept of $(1 - \bar{E})/\eta_1$ and a slope of $[m (1-\bar{E})/\eta_1]$. Then, the parameter m is obtained simply as the ratio of the slope to the intercept of this line. The parameter $\bar{E}$ is obtained directly from the ratio of triaxial compression and triaxial extension strength (Ψ) as defined in Equation 3.23. Substitution of $\bar{E}$ into the intercept value yields the parameter η_1. This completes the definition of the shear failure surface.

The next step is to determine the peak plastic expansive work as expressed in Equations 3.28 or 3.29. The plastic expansive strain is first computed by subtracting the elastic and compressive plastic strain components from the total strains in the triaxial compression tests. The plastic expansive work at the peak stress, $W_{p,peak}$, is computed by integration according to Equation 3.27. If $W_{p,peak}$ is to be modeled with Equation 3.28, the values are plotted versus the mean stress and fit with straight line segments. On the other hand, if $W_{p,peak}$ is to be modeled using Equation 3.29, we first rewrite the relationship as:

$$\log \frac{W_{p,peak}}{P_a} = \log \bar{p} + l \log \left[\frac{\sigma_{oct}}{P_a} \right] \tag{3.41}$$

A least squares, linear fit to $\log (W_{p,peak}/P_a)$ versus $\log (\sigma_{oct}/P_a)$ will then yield l and $\bar{p}$ from the slope and intercept, respectively.

The next step is to define the expansive yield hardening function of Equation 3.25. The coefficient η_1 has been obtained previously from the fit to Equation 3.40 and the peak plastic

3-16

expansive work is defined by Equation 3.28 or 3.29. Thus, only the exponent $\bar{q}$ must be obtained in order to completely define the hardening function f_p^*. Solving Equation 3.25 for $\bar{q}$ gives:

$$\bar{q} = \frac{ln\left[\dfrac{f_p''}{\eta_1}\right]}{(1 - \xi_p) + ln\ \xi_p} \tag{3.42}$$

To obtain a representative value for $\bar{q}$, a plot of f_p''/η_1 as a function of ξ_p is computed for the triaxial test data at each confining pressure. We then match the hardening function for each triaxial test at a value of f_p''/η_1 equal to 0.80 according to Equation 3.42. The $\bar{q}$ values obtained in this manner are then averaged to produce the parameter $\bar{q}$ for the model fit.

The final step remaining is to specify the expansive flow rule and expansive plastic potential function as defined in Equations 3.34 and 3.35 and illustrated in Figure 3.1. The expansive plastic strain increment is perpendicular to the plastic potential function as defined in Equation 3.35. Below 50% of the ultimate shear strength, the potential function has a form similar to the expansive yield function given in Equation 3.22, but in general the two functions are not equal and the expansive plastic strain is not normal to the yield surface; i.e., a nonassociative flow rule is used. Recall from the previous subsection that the potential function transitions to give associative flow at very high pressures as depicted in Figure 3.3. In order to define the plastic potential function, we need only to determine the parameter η_2, since all other parameters have been previously derived.

The physical meaning of parameter η_2 is depicted in Figure 3.4 at the intersection of the potential surface and the compressive yield surface. The expansive plastic strain vector ($d\bar{\varepsilon}_p^P$), compressive plastic strain vector ($d\bar{\varepsilon}_c^P$) and total plastic strain vector ($d\bar{\varepsilon}^P$) are depicted at the point of intersection. From normality, the ratio of the shear component of the expansive plastic strain vector to the volumetric component equals the ratio of the partial derivative of the expansive potential function with respect to the shear stress to the partial derivative of the potential function with respect to the mean stress as given by:

$$\frac{d\gamma^{p}_{oct.p}}{\frac{1}{3} d\epsilon^{p}_{vp}} = \frac{\frac{\partial g_{p}}{\partial \tau_{oct}}}{\frac{\partial g_{p}}{\partial \sigma_{oct}}} \tag{3.43}$$

Substituting Equation 3.35 for g_p in Equation 3.43 and solving for η_2 gives:

$$\eta_2 = \left[-\frac{1}{3} \frac{d\epsilon^{p}_{vp}}{d\gamma^{p}_{oct.p}} \right] \left(1 - \frac{1}{E} \right) \left[1 + m \frac{\sigma_{oct} - T}{P_a} \right]^2 \tag{3.44}$$

In the triaxial compression test:

$$d\gamma^{p}_{oct.p} = \frac{\sqrt{2}}{3} \left(d\epsilon^{p}_{ap} - d\epsilon^{p}_{rp} \right) \tag{3.45}$$

and

$$d\epsilon^{p}_{vp} = d\epsilon^{p}_{ap} + 2 d\epsilon^{p}_{rp} \tag{3.46}$$

where ϵ_a and ϵ_r denote the axial and radial strains, respectively. Equation 3.44 shows that the parameter η_2 is linearly proportional to the inverse slope of the plastic potential surface.

Hence, the plastic potential function parameter η_2 is computed at points along the triaxial compression response using Equation 3.44. Then, if Equation 3.36 is employed, multi-segment linear fits are determined for η_2 as a function of f_p'. If Equation 3.37 is used to define η_2, a regression analysis is used to determine t, R, and s for a single function defining η_2.

This completes specification of the ARA Three Invariant model and derivation of all model parameters from the test data. A summary of the model parameters is given in Table 3.1.

3.2.6 Tensile Failure of Skeleton

It is possible, particularly in materials around an explosive detonation, for the skeleton to fail in tension. In a soil or rock mass, the material is literally pulled apart such that individual grains are physically separated or pieces of unconnected material may form. In

3-18

modeling rocks or concrete, this is a spall condition and occurs when the tensile strength is exceeded. After failing in tension, the skeleton has no stiffness but can collapse back together to again form a contiguous mass. While the exact nature of this behavior is not easily described for the general case, particularly the characteristics of a reformed skeleton, the material model must be able to track the appropriate skeleton behavior under these conditions.

In the ARA 3-I skeleton model, the tensile strength is given by the parameter T which is the apex of the expansive plastic strength envelope. When tensile stresses exceed the tensile strength, the volume strain at which the tensile failure occurred is stored. The skeleton stiffness is set to zero and the three principal stresses are set equal to the tensile strength. The volume strains, which are initially expansive, are then tracked with respect to the volume strain at tensile failure.

At some point the volume strains may become compressive and again return to the total volume strain at which the tensile failure occurred. At this point, the material is considered to be reformed and possess the same stiffness and properties as the soil had when the tensile failure first occurred. In reality, we would expect the reformed skeleton to be significantly different from when the tensile failure occurred. While this model does not consider this altered behavior, it does ensure that the skeleton will begin to support compressive loads upon reforming.

3.3 GRAIN COMPRESSIBILITY MODEL

To model the nonlinear response of the solid grains to both the applied pore pressure and effective stress, analytic expressions for the deformation of solids at high pressure are employed. High pressure data for many rocks and minerals show a linear relationship between loading wave velocity and particle velocity (e.g. Allen, 1967). The loading wave velocity can be expressed as:

$$c_L = c_o + Sv_p \tag{3.47}$$

where: c_L = loading wave velocity

c_o = the initial wave velocity at relatively low pressure

v_p = peak particle velocity

S = experimentally determined constant relating c_L to v_p (generally equal to about 1.5 for most dense rocks and minerals).

Conservation of mass and momentum on either side of the wavefront yield the familiar relationships:

$$\sigma_p = \rho_o c_L v_p \tag{3.48}$$

$$M = \rho_o c_L^2 \tag{3.49}$$

where: σ_p = peak axial stress

ρ_o = initial material density

M = constrained secant modulus = σ_p/ϵ_p

ϵ_p = peak axial strain corresponding to the peak stress σ_p

Substitution of Equation 3.47 into 3.48 gives:

$$\sigma_p = \rho_o c_o v_p + \rho_o S v_p^2 \tag{3.50}$$

and solving for peak particle velocity as a function of peak stress yields

$$v_p = \frac{f(\sigma_p)}{2\rho_o S} \tag{3.51}$$

where:

$$f(\sigma_p) = (\rho_o^2 c_o^2 + 4\rho_o S\sigma_p)^{1/2} - \rho_o c_o \tag{3.52}$$

Substitution of Equation 3.47, 3.51, and 3.52 into Equation 3.49 gives:

$$M = F(\sigma_p) = \rho_o c_o^2 + c_o f(\sigma) + \frac{f^2(\sigma)}{4\rho_o}$$ (3.53)

The tangent constrained modulus, M_t, used in the numerical model is defined as the slope of the stress strain curve by:

$$M_t = \frac{d\sigma}{d\epsilon}$$ (3.54)

From Equation 3.53 and the definition of constrained modulus, M:

$$\epsilon_p = \frac{\sigma_p}{F(\sigma_p)}$$ (3.55)

Differentiating Equation 3.55 with respect to σ_p and inverting gives the tangent constrained modulus as

$$M_t = \frac{F^2(\sigma_p)}{F(\sigma_p) - \sigma_p F'(\sigma_p)}$$ (3.56)

Differentiating Equations 3.52 and 3.53 with respect to σ_p yields:

$$F'(\sigma_p) = c_o f'(\sigma_p) + \frac{f(\sigma_p)f'(\sigma_p)}{2\rho_o}$$ (3.57)

and

$$f'(\sigma_p) = \frac{2\rho_o S}{(\rho_o^2 c_o^2 + 4\rho_o S\sigma_p)^{1/2}}$$ (3.58)

Hence, Equations 3.51 through 3.58 can be used to define the high pressure constrained stress strain and modulus relationships for the solid grains.

For two phase, coupled calculations, the volumetric relationships for the solid grains should be specified in terms of the bulk modulus, K_g, rather than in terms of the constrained

modulus. At high pressures, the shear strength of the grain materials becomes insignificant compared to the applied stress and the materials tend to behave like fluids. At these pressures, the tangent bulk modulus equals the tangent constrained modulus with Poisson's ratio equal to 0.5. Beneath some threshold pressure, p_b, Poisson's ratio begins to decrease from 0.5 at p_b to an initial value of Poisson's ratio, ν_o, at a low value of mean stress. We have used a simple relationship to approximate the influence of mean stress on Poisson's ratio for the solid grains:

$$K_g = g(p)M_t \tag{3.59}$$

The ratio of the bulk modulus to the tangent constrained modulus, g(p) at pressures less than p_b is given by:

$$g(p) = \frac{2}{3} \frac{(1 - 2\nu_o)}{(1 - \nu_o)} \frac{p}{p_b} + \frac{(1 + \nu_o)}{3(1 - \nu_o)} \tag{3.60}$$

For pressures greater than p_b;

$$g(p) = 1 \tag{3.61}$$

Poisson's ratio can be computed as a function of the modulus ratio at a given pressure as:

$$\nu = \frac{3g(p) - 1}{1 + 3g(p)} \tag{3.62}$$

3.4 PORE WATER COMPRESSIBILITY

The model for the nonlinear, elastic compressibility of the pore water is derived from an equation of state reported by Ahrens (1988) and attributed to Bakanova, et. al. (1976). This equation relates the shock velocity in water to the peak particle velocity. In the lower pressure regime, a quadratic relation is used while a linear relation is used in the higher pressure regime. The transition point between the two regimes is defined in terms of a peak particle velocity at the transition, v_{pt}. Bakanova's equations can be expressed as:

$v_p \leq v_{pt}$:

$$c = c_1 + S_1 v_p + S_2 v_p^2 \tag{3.63}$$

$v_p > v_{pt}$:

$$c = c_2 + S_3 v_p \tag{3.64}$$

where: c = shock propagation velocity in the fluid

     v_p = peak fluid particle velocity

     c_1, S_1, S_2 = constants used to fit data below the transition

     c_2, S_3 = constants used to fit data above the transition

Equation 3.64 can also be expressed in terms of the shock velocity at the transition point, c_t. Substituting v_{pt} into Equation 3.64 yields:

$$c_2 = c_t - S_3 v_{pt} \tag{3.65}$$

Substituting 3.65 into 3.64 produces this expression for the shock velocity above the transition:

$v_p > v_{pt}$:

$$c = c_t + S_3 (v_p - v_{pt}) \tag{3.66}$$

where: c_t = shock velocity at the transition

     v_{pt} = peak particle velocity at the transition (model constant)

At the transition point, the shock velocity from Equations 3.63 and 3.66 should be equal to preserve continuity. Setting Equations 3.63 and 3.66 equal at $v_p = v_{pt}$ gives:

$$c_t = c_1 + S_1 v_{pt} + S_2 v_{pt}^2 \tag{3.67}$$

thereby defining c_t in terms of the model constants. Equations 3.63, 3.66, and 3.67 (with the constants c_1, S_1, S_2, and S_3) define the shock velocity as a function of peak particle velocity.

To derive a bulk modulus for water as a function of pressure, we first need an expression for the peak particle velocity as a function of pressure. Conservation of mass and momentum

3-23

on either side of the wavefront yields the familiar relationship from shock physics:

$$\pi_p = \rho_o c v_p \qquad (3.68)$$

where:

π_p = pore fluid pressure

ρ_o = mass density of fluid

Substitution of Equation 3.63 into 3.68 yields an expression for the transition fluid pressure (π_{pt}):

$$\pi_{pt} = \rho_o v_{pt} (c_1 + S_1 v_{pt} + S_2 v_{pt}^2) \qquad (3.69)$$

For water, the transition pressure is greater than 30,000 MPa.

Below the transition pressure, substitution of Equation 3.63 into 3.68 will give:

$$v_p^3 + \frac{S_1}{S_2} v_p^2 + \frac{c_1}{S_2} v_p - \frac{\pi_p}{\rho_o S_2} = 0 \qquad (3.70)$$

This cubic equation can be solved to yield an expression for v_p as a function of fluid pressure below the transition pressure π_{pt}:

$$v_p = m \cos \left[\frac{1}{3} \cos^{-1} \left[\frac{3\beta}{\alpha m} \right] + \frac{4\pi}{3} \right] - \frac{S_1}{3S_2} \qquad (3.71)$$

where:

$$\alpha = \frac{c_1}{S_2} - \frac{1}{3} \left[\frac{S_1}{S_2} \right]^2 \qquad (3.72)$$

$$\beta = \frac{-\pi_p}{\rho_o S_2} - \frac{1}{3} \left[\frac{S_1}{S_2} \right] \left[\frac{c_1}{S_2} \right] + \frac{2}{27} \left[\frac{S_1}{S_2} \right]^3 \qquad (3.73)$$

$$m = 2 \sqrt{\frac{-\alpha}{3}} \qquad (3.74)$$

Above the transition pressure, substitution of Equation 3.66 into 3.68 yields a quadratic equation:

$$v_p^2 + \left[\frac{c_t - S_3 v_{pt}}{S_3} \right] v_p - \frac{\pi_p}{\rho_o S_3} = 0 \qquad (3.75)$$

Solving this equation for v_p as a function of fluid pressure gives v_p for pressures above the transition pressure π_{pt}:

$$v_p = -\left[\frac{c_t - S_3 v_{pt}}{2S_3} \right] + \left[\left[\frac{c_t - S_3 v_{pt}}{2S_3} \right]^2 + \frac{\pi_p}{\rho_o S_3} \right]^{\frac{1}{2}} \qquad (3.76)$$

The elastic bulk modulus of water (K_w) is defined as:

$$K_w = \frac{d\pi_p}{d\epsilon_v} = \frac{d\pi_p / dv_p}{d\epsilon_v / dv_p} \qquad (3.77)$$

where ϵ_v is the volume strain corresponding to the pressure π_p. Taking the derivative of Equation 3.68:

$$\frac{d\pi_p}{dv_p} = \rho_o (c' v_p + c) \qquad (3.78)$$

The volume strain is given by:

$$\epsilon_v = \frac{v_p}{c} \qquad (3.79)$$

and taking the derivative yields:

$$\frac{d\epsilon_v}{dv_p} = \frac{c - v_p c'}{c^2} \qquad (3.80)$$

Substitution of Equations 3.78 and 3.80 into 3.77 gives an expression for the bulk modulus in terms of the shock and peak particle velocities:

3-25

$$K_w = \frac{\rho_o c^2 (c + v_p c')}{c - v_p c'} \tag{3.81}$$

The derivatives of the shock velocity with respect to the peak particle velocity are given by:

For $\pi_p \leq \pi_{pt}$:

$$c' = S_1 + 2S_2 v_p \tag{3.82}$$

For $\pi_p > \pi_{pt}$:

$$c' = S_3 \tag{3.83}$$

This completes the derivation of the water compressibility model. To summarize the use of the model:

1. begin by computing the transition shock velocity and pressure using Equations 3.67 and 3.69,

2. compute the peak particle velocity using either Equation 3.71 below the transition pressure or Equation 3.76 above the transition pressure,

3. compute the corresponding shock propagation velocity from Equation 3.63 or 3.66 and the derivatives from Equation 3.82 or 3.83;

4. substitute the results into Equation 3.81 to get the bulk modulus.

The material constant values for this model are given in Table 3.3 for fresh water and sea water. The fresh water values are from Bakanova, et. al. (1976) as reported by Ahrens (1988). Parameters for sea water were fit to compressibility data described by Kim, et. al. (1986) and attributed to Britt (1985). The pressure-volume response of fresh water and sea water as predicted by this model are given in two pressure ranges in Figures 3.5a and 3.5b.

Distention and Rejoining. Just as it is possible for the skeleton to separate into pieces in a tensile failure, gas-filled voids develop in the pore fluid if subjected to tensile (vacuum) pressures. These voids will contain either water vapor or air drawn in from the atmosphere and may exist as bubbles or separations between soil clumps or rock fragments. In this condition, the fluid has essentially zero stiffness and will expand indefinitely. Sufficient volumetric compression can eventually collapse the void spaces such that the pore fluid will again carry compressive pressures.

In developing a model for this behavior, several simplifying assumptions are made:

- A single pore fluid model will be used to represent the pore water and any gas-filled void that may develop under vacuum;

- No attempt is made to model the actual process of gas void formation: the voids are simply assumed to develop, without bounds, with expanding pore volumes;

- The vapor pressure required to form water vapor is neglected;

- If the pore fluid was partially saturated at the start of the problem (see the model described in Section 3.5), the fluid is assumed to return to the initial partial saturation condition when the voids created under vacuum have collapsed.

In discussing this feature of the water model, the term "distended" is used to describe the condition of the pore fluid under vacuum pressure. A "rejoined" condition is said to exist when subsequent compressive strains return the pore water to the initial condition which may, in fact, be a partially saturated condition.

Given the assumptions, distention and rejoining of the pore water can be modeled in a fairly simple manner. A negative volume strain in the pore fluid, computed with respect to the initial, unloaded condition indicates the onset of distention. While the pore fluid is distended, the stiffness of, and pressure in the pore fluid is set to zero. The fluid is considered to be rejoined (at the initial conditions) when the pore water volume strain becomes compressive (positive). The total volume strain in the pore fluid is computed from the current porosity of the material, but an adjustment is made to account for movement of water in and out of the material as simulated in the MPDAP and MEM codes.

3.5 PORE FLUID MODEL FOR PARTIAL SATURATION CONDITIONS

When rock or soil is unsaturated, compression of the pore water and solid grains is nearly insignificant when compared with the compression of pore air. Under these conditions,

material behavior is governed mostly by the skeleton model. With sufficient compression, the pore air gets squeezed out and the material becomes saturated. Rischbieter, et. al. (1977) demonstrated that even a minute amount of entrapped air drastically alters the pore pressure response in multiphase porous materials. To simulate this behavior, the pore fluid model is modified to account for the compressibility of pore air and converges to a saturated condition. Note that this model is invoked only when the initial saturation is less than 100%.

The compressibility of the air-water mixture, C_{aw}, is defined as:

$$C_{aw} = \frac{d\epsilon_{v,aw}}{d\pi_p} \qquad (3.84)$$

where π_p is the fluid pressure. The volumetric strain in the air-water mixture, $\epsilon_{v,aw}$, is the sum of volume strain in the air and water. Using the definition of the initial saturation, it can be shown that:

$$\epsilon_{v,aw} = (1 - S_o) \, \epsilon_{v,a} + S_o \, \epsilon_{v,w} \qquad (3.85)$$

where
$\epsilon_{v,aw}$ = volume strain of air-water mixture

$\epsilon_{v,a}$ = volume strain of air bubbles

$\epsilon_{v,w}$ = volume strain of water (from Equation 3.79)

S_o = initial saturation

From Equations 3.84 and 3.85 we can get an expression for the compressibility of the air-water mixture:

$$C_{aw} = (1 - S_o) \, C_a + S_o C_w \qquad (3.86)$$

Since the compressibility is the inverse of the bulk modulus, Equation 3.86 can be expressed as:

$$\frac{1}{K_{aw}} = \frac{1-S_o}{K_a} + \frac{S_o}{K_w} \qquad (3.87)$$

where:
K_{aw} = bulk modulus of air-water mixture

K_a = equivalent bulk modulus of air bubbles in the fluid

K_w = bulk modulus of water (from Equation 3.81)

3-28

Kim (1982) developed a formulation for the volume strain and equivalent bulk modulus of air bubbles in the pore fluid. This formulation, which was summarized by Kim, Blouin, and Timian (1986) explicitly modeled the dissolution of gas in liquid. This formulation was implemented and tested in MPDAP. While it is fundamentally sound, its practical application requires the evaluation of some parameters which are nearly impossible to obtain directly. Initially, the surface tension forces were assumed to remain constant. In reality, the surface tension forces are related to the inverse of the bubble radius. Thus, surface tension grows tremendously as the air bubbles are compressed and eventually collapse. If this effect is not modeled, the effective modulus of the fluid is unrealistically low. Since there is no available procedure for determination of the bubble radius, the full theoretical complexity of the formulation is not justified.

As an alternative, a much less complex model was implemented for pore air based on the adiabatic ideal gas law:

$$\pi_a V_a = \pi_{ao} V_{ao}{}^\gamma \tag{3.88}$$

where:

π_{ao} = initial air pressure (absolute pressure)

π_a = current air pressure (absolute pressure)

V_{ao} = initial air volume

V_a = current air volume

γ = ratio of heat capacity (C_p/C_v)

For non-adiabatic compression of air at constant temperature, γ has a value of 1.0 and Equation (3.88) reduces to Boyle's Law.

The volume strain of air can be defined in terms of engineering strain.

$$\varepsilon_{v,a} = 1 - \left(\frac{V_a}{V_{ao}}\right) \tag{3.89}$$

Substituting Equation (3.88) into Equation (3.89), we can express the volume strain in the air in terms of air pressure:

$$\varepsilon_{v,a} = 1 - \left(\frac{\pi_{ao}}{\pi_a}\right)^{\frac{1}{\gamma}} \tag{3.90}$$

Neglecting the influence of surface tension,

$$\pi_a = \pi + P_a \tag{3.91}$$

where: π = current pore water pressure (gage pressure)

P_a = reference atmospheric pressure

Substitution of Equation (3.91) into Equation (3.90) yields

$$\varepsilon_{v,a} = 1 - \left(\frac{\pi_{ao}}{\pi + P_a}\right)^{\frac{1}{\gamma}} \tag{3.92}$$

The tangent bulk modulus of air bubble can be defined as

$$K_a = \frac{d\pi_a}{d\varepsilon_{v,a}} \tag{3.93}$$

Differentiating Equation (3.92) with respect to π,

$$\frac{d\varepsilon_{v,a}}{d\pi_a} = \frac{1}{\gamma\,\pi_{ao}} \left(\frac{\pi_{ao}}{\pi + P_a}\right)^{\left(1 + \frac{1}{\gamma}\right)} \tag{3.94}$$

Substitution of Equation (3.94) into Equation (3.93) yields

$$K_a = \gamma \; \pi_{ao} \left(\frac{\pi + P_a}{\pi_{ao}} \right)^{\left(1 + \frac{1}{\gamma}\right)}$$ (3.95)

3.6 PERMEABILITY MODEL

The finite element code MPDAP is capable of calculating the flow of pore fluid between elements. The flow of fluid with respect to the skeleton is controlled by Forchheimer's permeability model which is described in detail in Section 4. The Forchheimer model can be expressed as:

$$\pi_{,i} = \frac{\mu}{\alpha} \; \dot{w}_i + \frac{\rho_f}{\beta} \; \dot{w}_i^2 + \rho_f \ddot{U}_i$$ (3.96)

where: $\pi_{,i}$ = pore pressure gradient

g = acceleration of gravity

ρ_f = mass density of pore fluid

μ = pore fluid viscosity

α = linear flow coefficient

β = quadratic flow coefficient

$\dot{w}$ = apparent flow velocity relative to the skeleton

$\ddot{U}$ = absolute acceleration of pore fluid

The first term in Equation 3.96 is simply Darcy's law while the velocity squared term was apparently first proposed by Forchheimer (1901). The first two terms represent the energy loss due to fluid flow while the last term accounts for fluid inertia.

Equation 3.96 can also be written in the form:

$$\pi_{,i} = \frac{\rho_f g}{k'} \; \dot{w}_i + \rho_f \ddot{U}_i$$ (3.97)

3-31

where k' represents an equivalent, high pressure permeability coefficient given by:

$$k' = \left[\frac{\mu}{\alpha} + \frac{\rho_f}{\beta} |\dot{w}_i| \right]^{-1} \qquad (3.98)$$

Hence, the flow of pore fluid in the soil skeleton is governed by Equations 3.97 and 3.98 and the flow coefficients α and β which can be determined from laboratory test data.

If the soil skeleton undergoes significant volumetric strains, the permeability of the skeleton will change. This is particularly true near an explosive detonation where large volumetric compression restricts pore fluid flow or, for some materials, expansion of the skeleton yields greater fluid flow. We have implemented a simple empirical model to account for this behavior which varies the Darcy permeability coefficient with changes in porosity

$$\alpha = \alpha_o^{C_p(n-n_o)} \qquad (3.99)$$

where:

α_o = initial linear flow coefficient

α = flow coefficient at a porosity of n

c_p = slope of straight line relationship between porosity and the logarithm of the permeability

n = current porosity

n_o = initial porosity

The form of Equation 3.99 is suggested by test data reported by Blouin and Timian (1986) and shown in Figure 3.7. A similar relationship may exist between porosity and the quadratic coefeicient β in the flow equation, but there is insufficient high pressure permeability data available to establish such a relationship. Hence, β is assumed to remain constant as the porous skeleton deforms.

Table 3.1. Parameters for the ARA Three Invariant Material Model.

Elastic Response:

ν : Poisson's ratio

K_{ur} : elastic modulus constant

n : elastic modulus exponent

K_i : initial bulk modulus at low pressure

λ, γ, β : unload/reload bulk modulus constants used in ARA elastic model

Compressive Plastic Response:

r : elliptical cap (compressive yield surface) axis ratio

c_i : compressive hardening constant for segment "i" of fit

p_i : compressive hardening exponent for segment "i" of fit

Expansive Plastic Response:

T : apparent tensile strength (negative)

$\bar{E}$: expansive yield constant

m : expansive yield exponent

a_i, b_i : constants for segment "i" in a multilinear fit for defining $W_{p, peak}$

$\bar{P}, l$: constants in an exponential fit for defining $W_{p, peak}$

$\bar{q}$: expansive hardening exponent

s_i, t_i : constants for segment "i" in a multilinear fit for defining η_2

s, R, t : constants in a single line fit for defining η_2

Table 3.2. Format of input data file specifying the ARA Three Invariant Model parameters for a given material.

Model Parameter	Input Variable	Description
Stress units used in fit	IUNITS	IUNITS = 1 Pa = 2 dynes/cm^2 = 3 psi = 4 psi = 5 ksi = 6 MPa = 7 kg/cm^2 = 8 Mbar
T, P$_a$	APEX, ATMO	APEX = apparent tensile strength (negative) ATMO = atmospheric pressure in units of the calculation
K$_{ur}$, n, ν	AKUR, AN, APOI	AKUR = elastic modulus constant AN = elastic modulus exponent APOI = elastic Poisson's ratio
r	AR, ACRV	AR = elliptical cap major/minor axes ratio ACRV = Number of pairs of c$_i$ and p$_i$ describing compressive hardening function (max ACRV = 4)
c$_i$, p$_i$ (i = 1 to ACRV)	AACC(i), AAPC(i) _____ , _____ _____ , _____ AACC(ACRV), AAPC(ACRV)	AACC(i) = compressive hardening constant for segment "i" AAPC(i) = compressive hardening exponent for segment "i"
$\bar{E}$, m, η_2	AEY, AMY, AETA1	AEY = expansive yield constant AMY = expansive yield exponent AETA1 = expansive yield hardening constant
Option for plastic potential definition	NETA2	NETA2 = 1 multi-segment, linear fit of η_2 as function of f$_p$" NETA2 = 2 nonlinear fit of η_2 as function of f$_p$" and σ_{oct}
t$_i$ s$_i$	If NETA2 = 1: NPTS SOCTA(i), i = 1 to NPTS ATGA(i), i = 1 to NPTS ASGA(i), i = 1 to NPTS	NPTS = number of pressure points defining linear ranges of η_2 SOCTA(i) = pressure points, σ_{oct} ATGA(i) = η_2 constant t$_i$ at SOCTA(i) ASGA(i) = η_2 constant s$_i$ at SOCTA(i)

Table 3.2. Format of input data file specifying the ARA Three Invariant Model parameters for a given material (continued).

Model Parameter	Input Variable	Description
t, R, s	If NETA2 = 2: AATG, AARG, AASG	AATG = constant t in nonlinear η_2 definition AARG = constant R in nonlinear η_2 definition AASG = constant s in nonlinear η_2 definition
Option for specifying $W_{p.peak}$	NWPPK	NWPPK = 1 multi-segment, linear fit for $W_{p.peak}$ as a function of σ_{oct} NWPPK = 2 nonlinear fit for $W_{p.peak}$ as a function of σ_{oct}
a_i, b_i	If NWPPK = 1 PDPK(i), i = 1 to 4 WPDPK(i), i = 1 to 4	PDPK(i) = pressure points, σ_{oct} WPDPK(i) = $W_{p.peak}$ at PDPK(i) (values of a_i and b_i implied)
$\bar{p}$, l	If NWPPK = 2 APBAR, AL	APBAR = constant defining $W_{p.peak}$ AL = exponent defining $W_{p.peak}$
$1/\bar{q}$	AALPH	AALPH = inverse of expansive hardening exponent $\bar{q}$
λ, γ, β, K_i	AHLAM, AHGAM, AHBET, AHBLK	AHLAM, AHGAM, AHBET = unload/reload constants in ARA elastic model AHLAM = -1.0 invokes Lade and Nelson elastic model (AHGAM, AHBET not used) AHBLK = initial bulk modulus at very low pressure

Table 3.3 Fluid compressibility model constants (see Section 3.4 for definitions of constants).

Parameter	Units	Fresh Water	Sea Water
ρ_o	kg/m^3	1002.8	1026
c_i	m/s	1500	1522
S_1	-	2.00	1.97
S_2	s/m	-1.07×10^{-4}	-0.898×10^{-4}
S_3	-	1.144	1.123
v_{pt}	m/s	4000	4573
c_t	m/s	7788	8653
π_{pt}	MPa	31,240	40,600

g_p = Expansive Plastic Potential Surface
f_p' = Expansive Yield Surface (Hyperbola)
f_c' = Compressive Yield Surface (Ellipse)

Octahedral Stress Space

Principal Stress Space

Octahedral Cross Section

Note: $\psi < \dfrac{9}{7}$
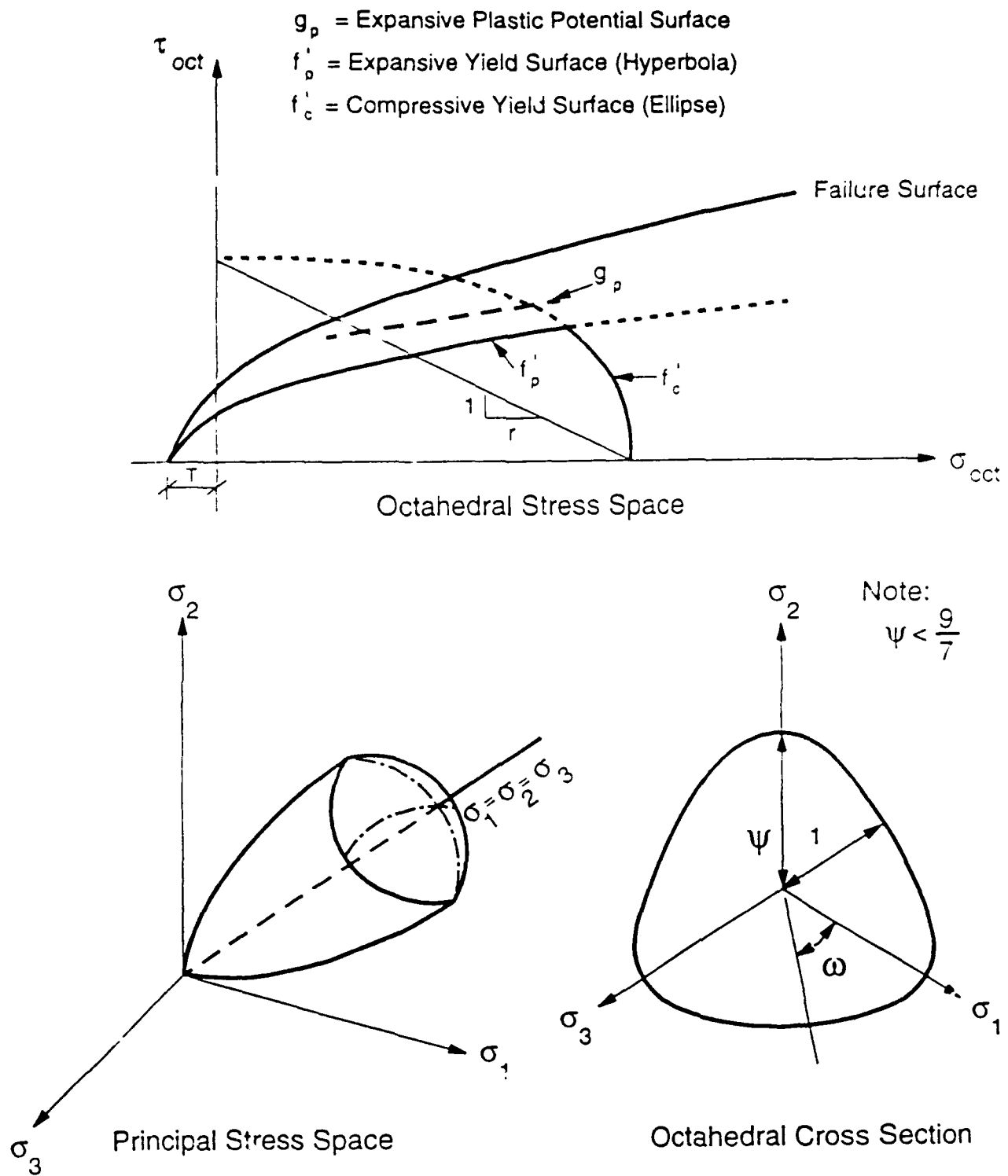
Figure 3.1. Yield surfaces used in the ARA Three Invariant
material model (after Dass and Merkle, 1986).
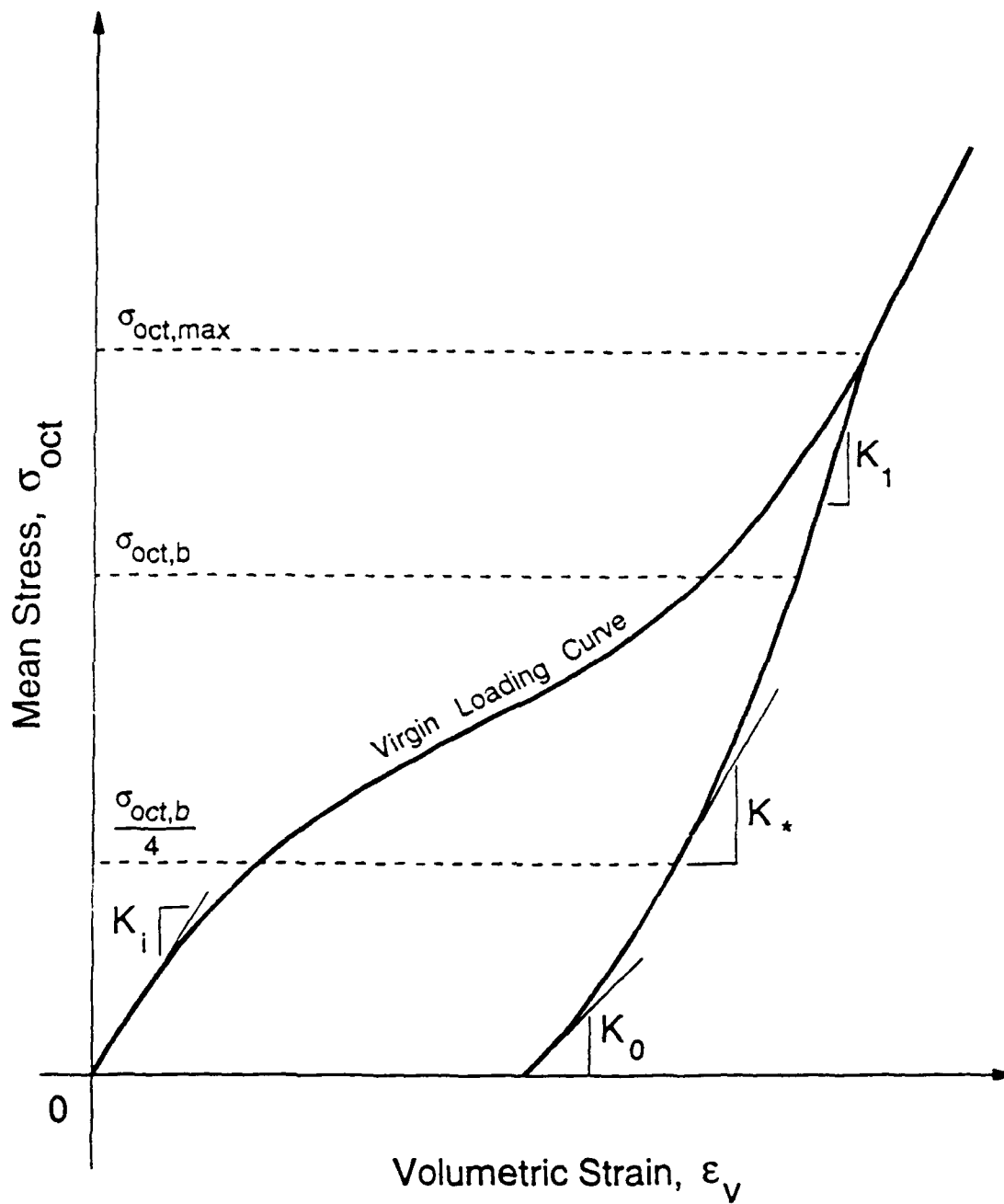
Figure 3.2. Fitting of ARA elastic formulation to unload/reload hydrostatic compression response.
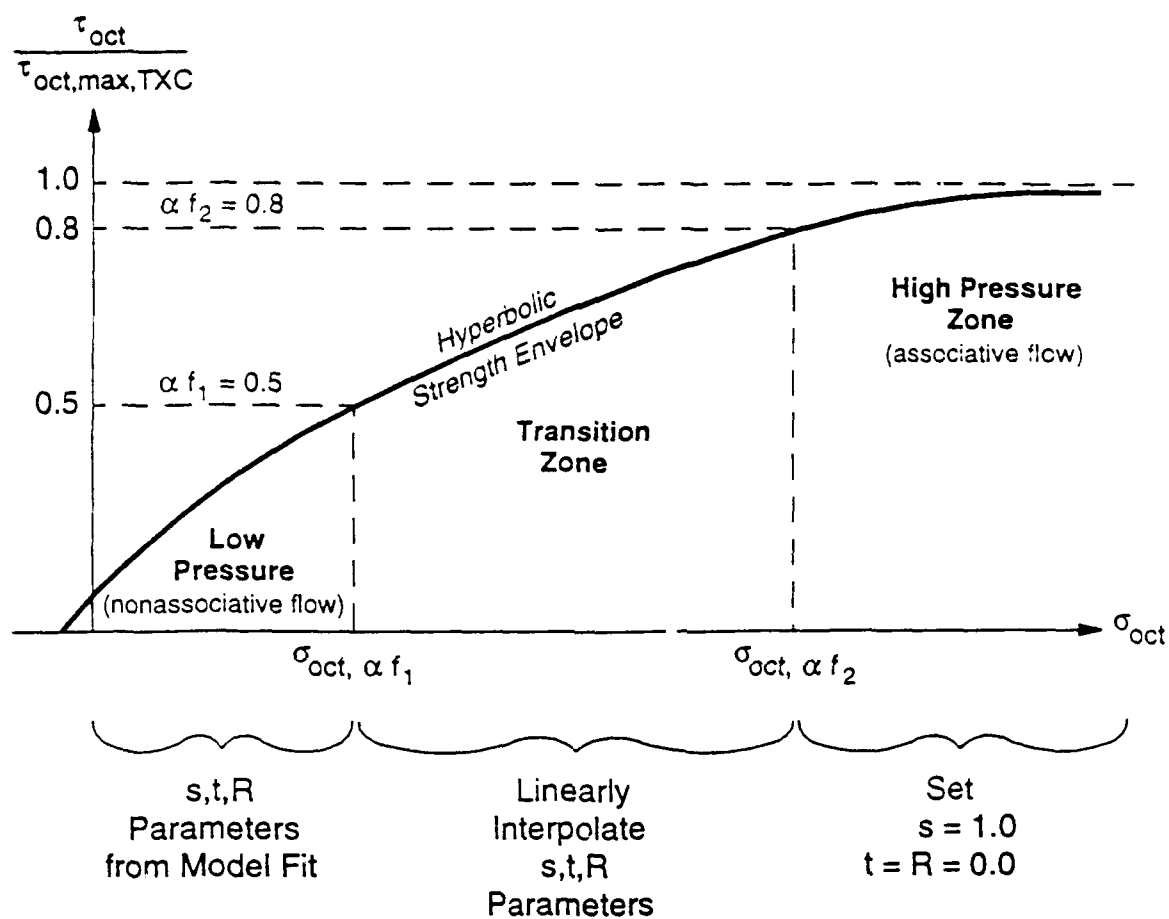
Figure 3.3 Extrapolation of plastic potential function to produce associative flow at very high pressures.
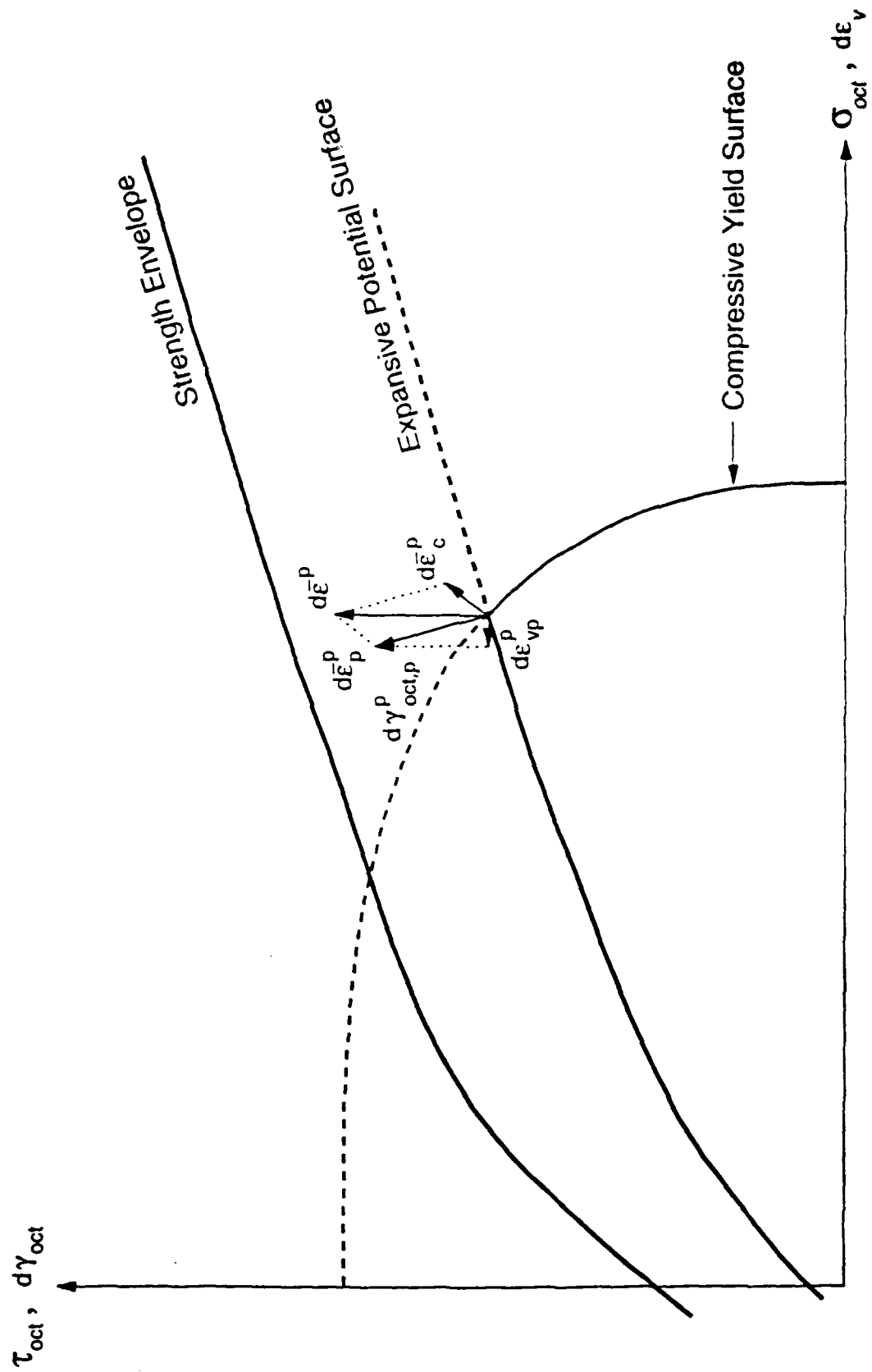
Figure 3.4. Plastic strain components in the octahedral stress/strain space.
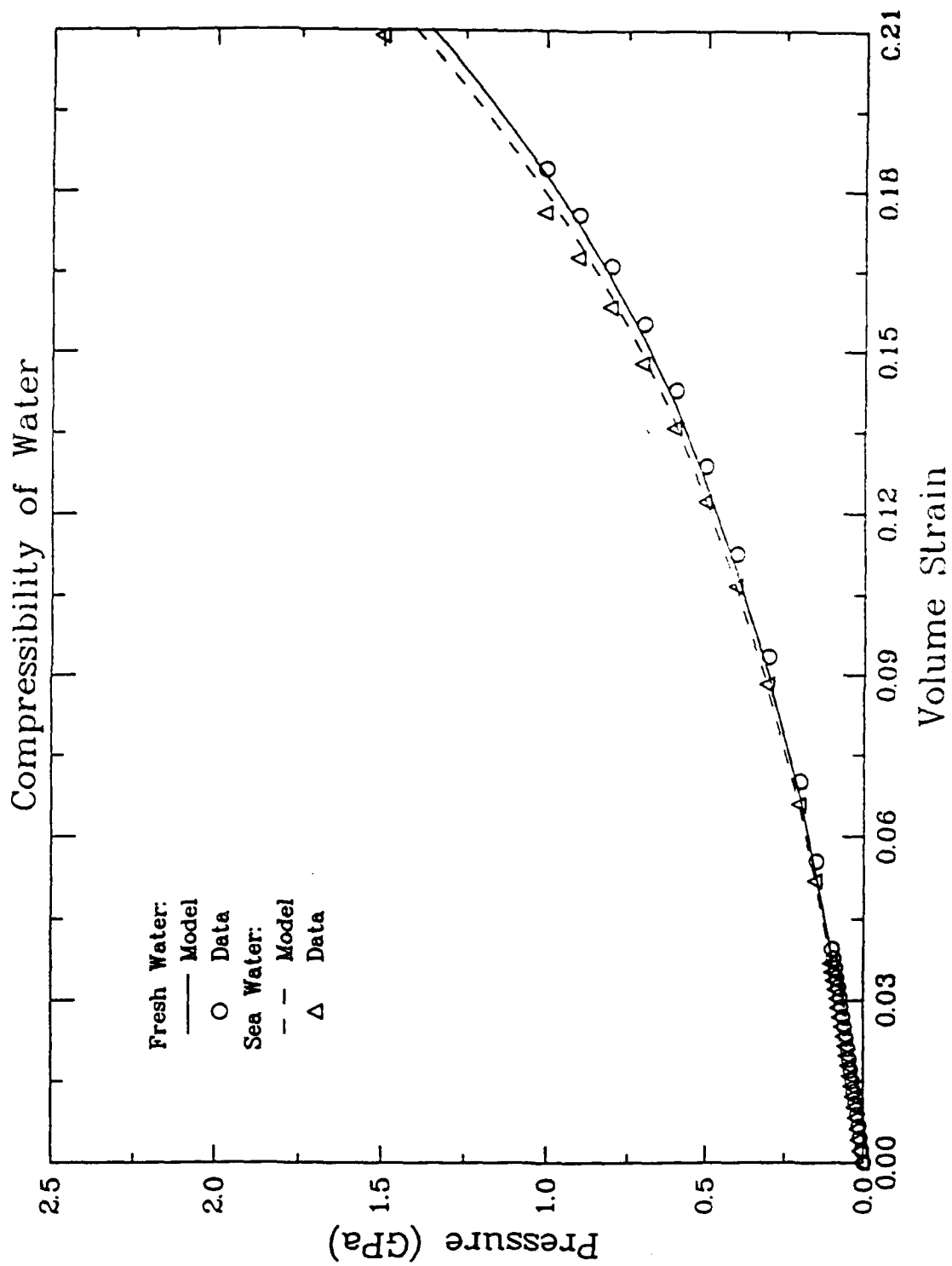
Figure 3.5a.   Pressure-volume strain relationships of fresh and sea water to 2.5 MPa.
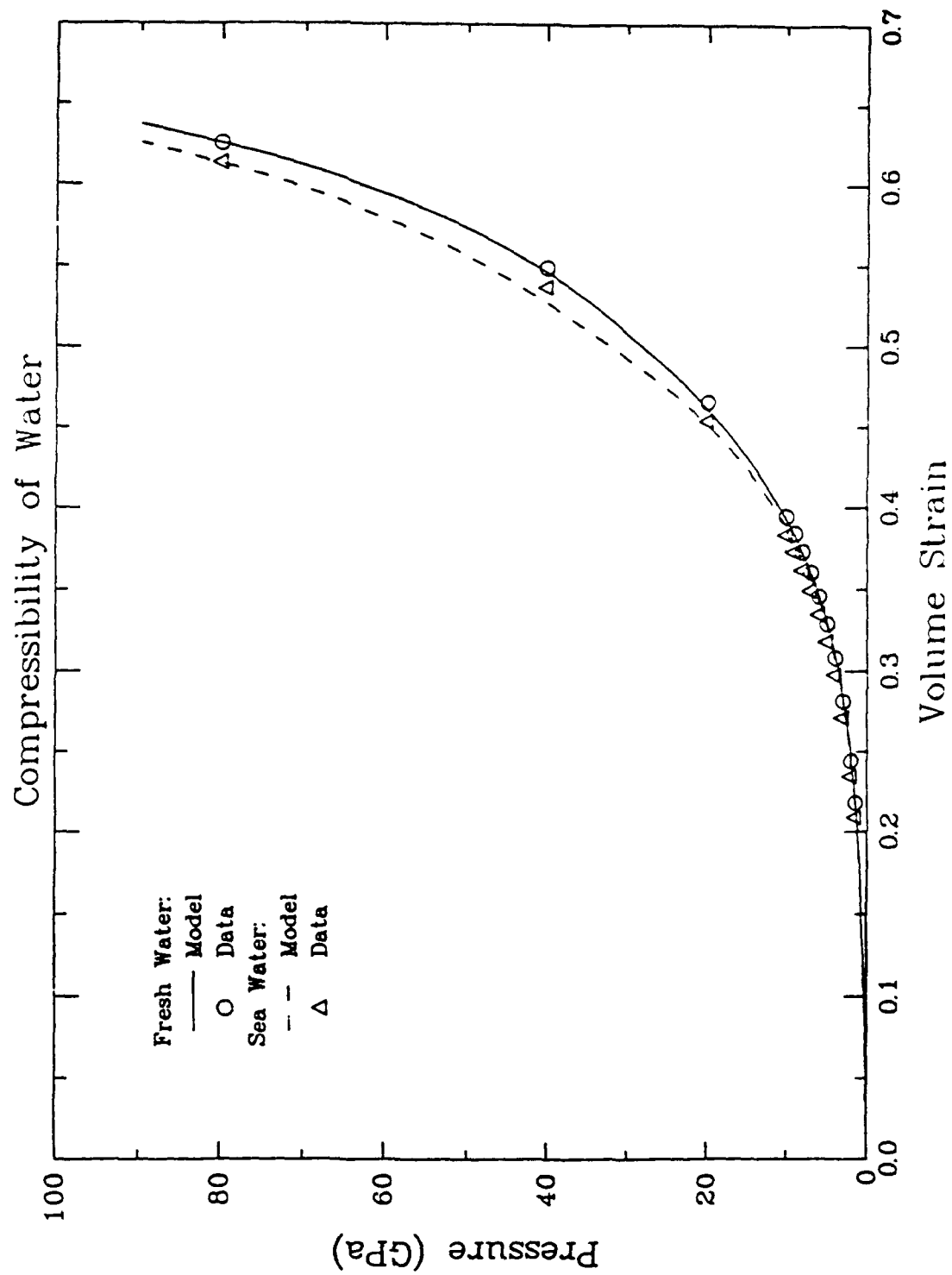
Figure 3.5b. Pressure-volume strain relationship of fresh and sea water to 90 MPa.
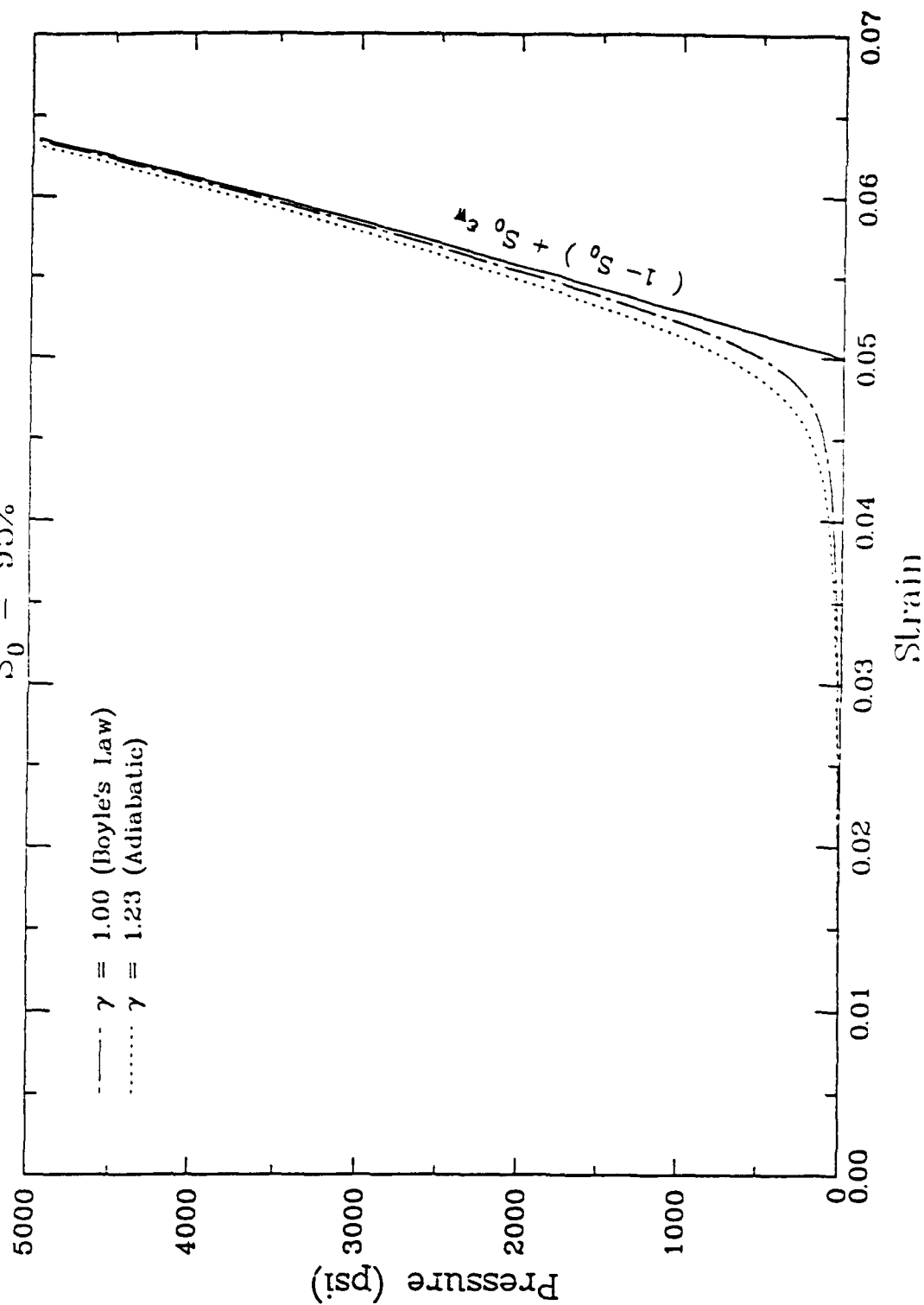
Figure 3.6. Prediction of air-water compressibility.
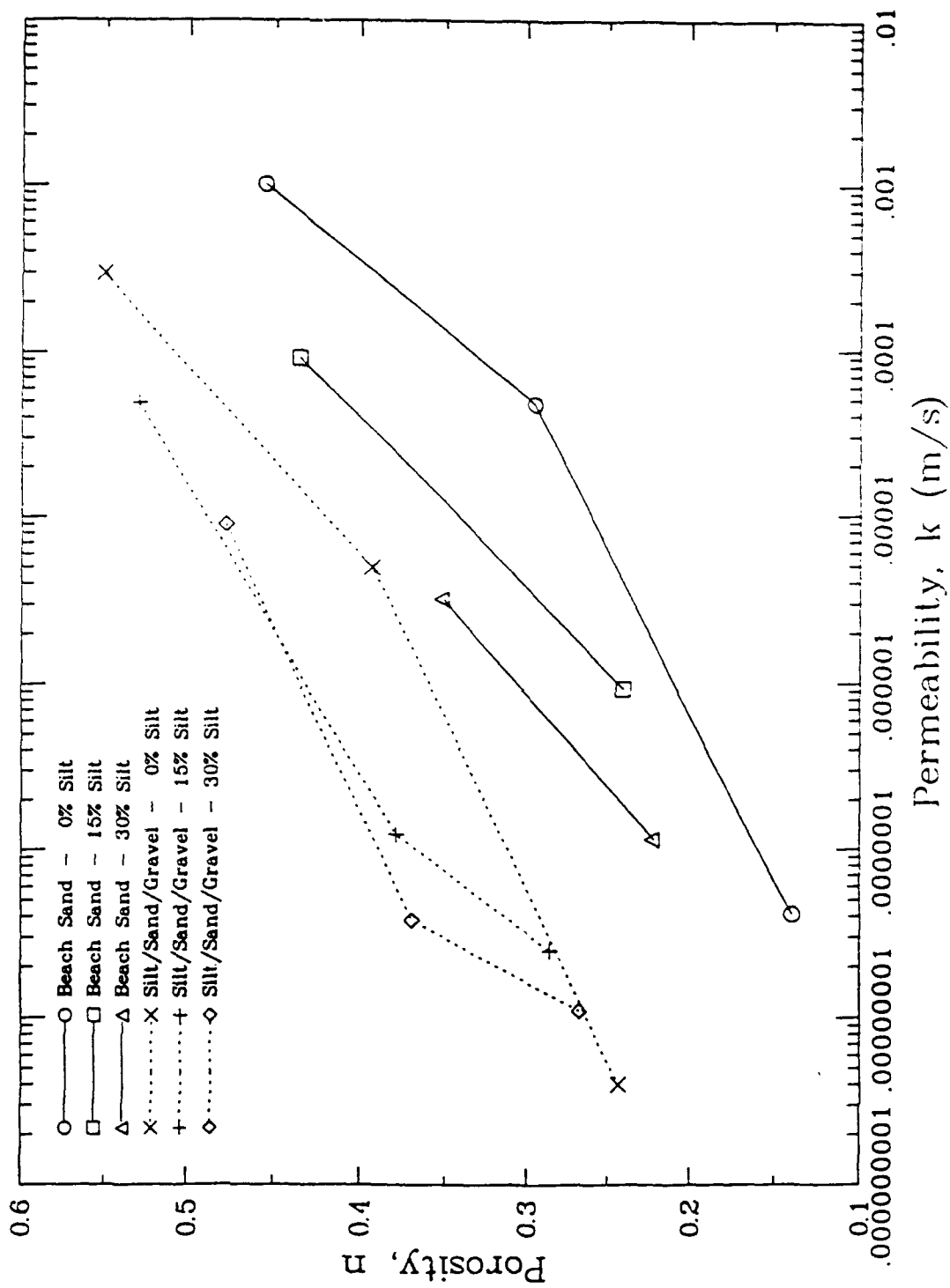
Figure 3.7. Observed variation of permeability of granular soils with changes in porosity (Blouin and Timian, 1986).

SECTION 4
RELATIONSHIP BETWEEN MICROSCOPIC
PROPERTIES AND MACROSCOPIC FLOW PARAMETERS

Section 2 of this report describes analytical formulations and their computer implementations for simulating the mechanical behavior of a saturated porous material based on knowledge of the mechanical properties of its constituent materials, i.e. the porous skeleton (possibly soil or rock), the solid grains, and the pore fluid. An advanced three-invariant plasticity model for simulating the nonlinear response of a sand or rock skeleton is presented in Section 3, along with nonlinear models for solid grains and pore water that are applicable to very high pressures. Since the fluid pressure is determined by the volume of pore space the fluid occupies, skeleton strain gradients can induce pore pressure gradients, resulting in flow of the pore fluid. The rate of pore fluid flow in response to imposed pressure gradients is a function of the properties of both the fluid and the porous (and permeable) skeleton. The flow characteristics do not strongly influence the deformation response of unsaturated materials. However, in saturated porous materials, they can be very important, particularly if the loading is dynamic.

This section begins with a discussion of the governing equation for fluid flow through a porous material. With that as a theoretical framework, fluid flow test data are presented for a range of porous materials. Included in the data set are granular materials, both spherical and angular, and porous limestone. Finally, there is a discussion of the relationship between the permeability coefficients and the microscopic geometric characteristics of the porous media.

4.1. GOVERNING EQUATIONS OF FLOW THROUGH POROUS MEDIA

Flow through porous materials has long been studied by investigators in a variety of disciplines, including hydrology, petroleum reservoir engineering, chemical engineering and filtering. In traditional civil engineering, where pressure gradients and the resulting flow

velocities are typically small, problems are almost exclusively formulated using the Darcy flow equation which assumes a linear relationship between pressure gradient and flow velocity. However, in previous AFOSR-sponsored work, Kim, et.al. (1988) reported that in dynamic problems of interest such as blast-induced liquefaction, weapons effects, and possibly earthquakes, pore pressure gradients and flow rates are of sufficient magnitude that the Darcy equation does not adequately describe the pore fluid response. To analytically treat the dynamic problems, Kim, et.al. (1988) adopted a more general expression for pressure gradient which includes a term that is proportional to the square of the fluid velocity in addition to the linear (Darcy) term, along with inertial terms related to fluid acceleration. The use of the velocity-squared term was apparently first proposed by Forchheimer (1901), and has been used in various forms by investigators over the years. Forchheimer's equation, which does not consider fluid acceleration, has the general form:

$$\pi_{,i} = a\dot{w}_i + b\dot{w}_i^2 \tag{4.1}$$

where: $\pi_{,i}$ = pore pressure gradient in the i direction

   $\dot{w}_i$ =   apparent fluid velocity in the i direction

   a,b =   constants which are functions of both skeleton and fluid properties

This formulation, with the addition of the inertial terms, was used by Kim, et.al. (1988), and again as the framework for investigating the influence of microscopic skeleton properties on fluid flow by Blouin, et.al. (1990). While Forchheimer's equation appears to be virtually unknown in the civil engineering literature, its use is widespread in chemical engineering, particularly with reference to porous metal filters. The constants, a and b, in Equation 4-1 are functions of the properties of both the pore fluid and the porous medium. A more useful form of the equation will result if it can be expressed in terms of constants that are dependent on either fluid or porous medium properties, but not both. Green and Duwez (1951) argue, based on dimensional analysis, that if the factors controlling the pressure gradient are assumed to be fluid viscosity, fluid density, a length characterizing the pore openings, and the apparent fluid velocity, then Forchheimer's equation must have the form:

$$\pi_{,i} = const_1 \frac{\mu \dot{w}_i}{\delta^2} + const_2 \frac{\rho_f \dot{w}_i^2}{\delta} \tag{4.2}$$

where: μ =   dynamic viscosity of the fluid

ρ_f =   mass density of the fluid

δ = unknown length related to pore geometry

If the constants are combined with the unknown pore dimension term, δ, and called α and β, the resulting expression has the desired separation between quantities dependent on skeleton properties and quantities dependent on fluid properties:

$$\pi_{,i} = \frac{\mu}{\alpha} \dot{w}_i + \frac{\rho_f}{\beta} \dot{w}_i^2 \tag{4.3}$$

The relationship between the two sets of coefficients is:

$$\alpha = \frac{\mu}{a}$$
$$\beta = \frac{\rho_f}{b} \tag{4.4}$$

If the term containing $\dot{w}_i^2$ is neglected the result is Darcy's equation with the constants in a different form. In some soil mechanics texts, α is called the coefficient of permeability or absolute permeability and is often represented by the symbol, K. It has units of length squared and the coefficient of the quadratic term, β, has units of length. The relationship of α to the Darcy permeability, k, is given by:

$$\alpha = \frac{k \mu}{\rho_f g} \tag{4.5}$$

4-3

where: g =   acceleration of gravity

In previous work, we have referred to the linear term as the laminar response and the quadratic term as turbulent, an analogy to flow in pipes. However, Equation 4-3 does not have the same form as the linear and turbulent flow equations for pipes. In pipes, the quality of the flow is related to the Reynolds number, Re, defined as:

$$Re = \frac{V \delta \rho_f}{\mu}$$
(4.6)

where: V = fluid flow velocity,

and the other quantities are as defined above. Laminar flow occurs in pipes at low velocity (Reynolds number), and the pressure gradient is characterized by a linear dependence on flow velocity. At some value of Reynolds number, the flow changes rather abruptly from laminar to turbulent. If the length quantity in the Reynolds number is taken as pipe diameter, then flow is sure to be laminar if Reynolds number is less than 2100, and for practical purposes, it can be assumed to be turbulent if Re is greater than 4700. In pipes, the pressure gradient in the turbulent regime is proportional to the square of the fluid velocity, and there is no linear dependence on velocity. In contrast Forchheimer's equation (4-3), retains its dependence on both the first and second powers of velocity over the full range of fluid velocities, and the relative importance of the two terms varies according to the details of each specific problem. Green and Duwez (1951) attributed the velocity squared term to inertial effects, related to the tortuosity of the flow path. Bear (1972) also concluded, based on the work of Lindquist (1933), Schneebeli (1955), Hubbert (1956), and Scheidegger (1960), that the appearance of the square term in Equation 4-3 is the effect of inertial forces associated with the flow along the tortuous path through the porous material. These forces are proportional to fluid density and independent of viscosity, consistent with the form of Equation 4-3. Thus, reference to turbulent flow has been dropped. Instead, we have adopted the nomenclature, linear and quadratic flow coefficients for the quantities α and β, respectively.

4.2 PERMEABILITY MEASUREMENTS ON GRANULAR MATERIALS

In order to investigate the relationship between the macroscopic fluid flow coefficients and the microscopic geometric properties of the porous medium, measurements of fluid flow were made in a variety of granular materials. These tests were conducted at a wide range of pressures on specimens of granular materials packed in a circular duct. The grain sizes of the materials tested span a range of more than an order of magnitude, and both spherical and angular grains shapes are represented.

The apparatus used to perform flow tests on the granular materials is shown schematically in Figure 4.1. It was fabricated from a standard hydraulic cylinder by adding a sample tube and the necessary additional ports. Screens fastened to each end of the sample tube contain the granular material. Kerosene was selected as the test fluid rather than water to avoid rusting the test apparatus. The piston of the hydraulic cylinder serves to separate the test fluid from the energy source fluid, which was either hydraulic fluid or high-pressure nitrogen. To expedite the testing, the system was equipped with solenoid operated valves so that the tests could be conducted by a single operator from the control console. Plumbing was also installed external to the test apparatus to allow the fluid to be returned from the downstream side of the test specimen to the upstream reservoir without pumping it through the test specimen.

The tests were instrumented with two pressure transducers to measure fluid pressure upstream and downstream of the test specimen. In practice, the flow resistance between the downstream end of the specimen of granular material and the low pressure reservoir was always negligible in comparison with the flow resistance of the specimen. This was verified by the negligible output of the downstream pressure transducer, and the pressure gradient was calculated as the steady state upstream pressure divided by the specimen length. A displacement transducer (a Linear Variable Differential Transformer or LVDT) was used to measure the displacement of the piston. The time derivative of the piston displacement, with the appropriate area corrections, is the fluid flow rate. The apparent fluid velocity was computed as the flow rate divided by the gross cross sectional area of the specimen.

Only the steady-state portion of each test was considered, i.e. where the pressure gradient and flow rate were constant. Previous work experimentally validated the non-steady state portion of the flow equation accounting for the acceleration of the pore fluid (Kim, et al., 1988). Figure 4.2 presents typical time histories of upstream pressure and piston displacement. The data shown for piston displacement represent the entire measurement range of the displacement transducer. The steady state piston velocity was found by a least squares fit to the portion of the LVDT output where the gage was on scale. The steady state value of upstream pressure was found by averaging the pressure transducer output over that same time window.

For each test specimen installed in the permeability apparatus, a series of flow tests was conducted at a range of pressure gradients. Each run yielded of values of steady state pressure gradient and flow rate. Data from a number of such runs are plotted in Figure 4.3. When Equation 4-1 is divided by $\dot{w}$, the resulting expression plots as a straight line on the axes shown in Figure 4.3. The slope of the line is b, or ρ_f/β, and its intercept is a, or μ/α. For each different granular material tested, least-squares fits to the data as plotted in Figure 4.3 have been used to derive the linear and quadratic flow coefficients.

Figure 4.4 is a summary plot showing all of the flow test data acquired for granular materials during the course of this effort. The characteristics of the granular materials used in each test series are presented along with the resulting flow parameters in Table 4.1. The table contains the flow coefficients both in terms of a and b, and in terms of α and β. They are most conveniently derived from the test data in terms of a and b. However, for comparison with other materials tested with different fluids, it is desirable to express the flow coefficients as α and β.

The test data were further analyzed to examine the influence of grain geometry on flow characteristics. Figure 4.5 is a log-log plot of the linear flow coefficient, α, as a function of grain size for materials consisting of spherical grains. A least squares fit to the spherical grain data results in the following relationship for between grain diameter and the linear flow coefficient, α:

$$\alpha - 8.03 \times 10^{-4} \, d^{1.94} \tag{4.7}$$

where: α = linear flow coefficient with units of in.^{2}

      d = grain diameter with units of in.

The fit given by Equation 4-7 is shown as a line on Figure 4.5. The exponent on the grain dimension in Equation 4-7 is nearly 2. If, instead of an unconstrained least squares fit, the fit is constrained to give the best fit line with a slope of 2.0, the resulting line is:

$$\alpha - 0.00104 \, d^2 \tag{4.8}$$

With the exponent of d forced to 2, α and d^2 have the same units and the coefficient, 0.00104, is dimensionless. Since α is independent of fluid properties, Equation 4.8 is applicable to flow of any fluid. Equation 4-8 is shown as a dashed line in Figure 4.5. Over the range of grain sizes tested, the difference between this equation and the unconstrained least squares fit is insignificant.

Hazen (1911) published the following approximate expression for estimating Darcy's permeability coefficient, k:

$$k - C(D_{10})^2 \tag{4.9}$$

where: k = Darcy permeability coefficient in cm/s

      C = a constant in the range 1-1.5 cm/(mm^2-s)

      D_{10} = size in mm for 10% pass on the grain size curve

Assuming for the moment that C has the value 1 cm/(mm^2-s), then in dimensionally homogeneous form, C = 10 mm^{-1}-s^{-1} = 254 in.$^{-1}$-s^{-1}. This can be converted to an expression for α using Equation 4-5. Since the Hazen expression applies to water flow, the conversion is made using and the viscosity and density values for water at 20°C, $\mu = 1.45 \times 10^{-7}$ lb-s/in.^{2} and $\rho_f = 9.35 \times 10^{-5}$ lb-s^2/in.^{4}, respectively. Substituting Equation 4-9 into 4-5, and using the value of C in inch units and g = 386.4 in./s^2, results in the following expression:

$$\alpha - 0.001 \, (D_{10})^2 \qquad\qquad (4.10)$$

For a material of uniform grain size, D_{10} is equal to d, and this is essentially the same expression as Equation 4-8. The good agreement between the data from our high pressure flow tests and the Hazen expression is an indication that the current test and analysis procedures in the high pressure gradient regime produce results consistent with conventional low pressure engineering measurement techniques for the linear part of the problem. Returning to the original range of values for C in Equation 4-9, the constant in Equation 4-10, using Hazen's range of coefficients, can have values in the range 0.001 - 0.0015.

Figure 4.6 presents values of the quadratic flow coefficient, β, derived from flow tests on spherical grain materials. The following expression represents a least squares fit to the quadratic flow coefficient data as a function of grain size:

$$\beta - 0.117 \, d^{1.125} \qquad\qquad (4.11)$$

where: β = quadratic flow coefficient with units of in.
           d = grain diameter with units of in.

If the data are fit with the exponent of d constrained to be unity, the resulting expression is:

$$\beta - 0.067 \, d \qquad\qquad (4.12)$$

Similar to Equation 4-8, the coefficient, β, and the grain size, d, both have units of length, and the constant, 0.067, is dimensionless, making the expression valid for β and d in any length units. Also, since β is independent of fluid properties, it is valid for any fluid.

Green and Duwez (1951) suggested that the ratio α/β, which has units of length, is an appropriate value to use for δ in the computation of Reynolds number (Equation 4-6). This

would mean that systems with the same Reynolds number would have the same ratio of viscous to inertial dissipative forces. This definition of Reynolds number could be used to design a scale model of a saturated porous system for laboratory experiments. If a scaled system could be developed with grain sizes much larger than the prototype materials of interest, then it might become practical to measure effects using available instrumentation that, in the prototype, would be microscopic. While it may be possible to relate the Reynolds number defined in this way to the onset of turbulence in the porous material, it would not be expected to occur at the same values of Reynolds number that apply to pipes since the geometry is completely different.

Tests were also performed on materials with non-spherical grains, including a carbonate sand from Enewetak Atoll in the Pacific, and crushed marble and granite. Figure 4.7 presents α as a function grain diameter for all of the flow tests on granular materials, including both spherical and non-spherical grains. The non-spherical grain data scatter on both sides of the fit for spherical grains. For the linear flow coefficient, α, the difference between spherical and non-spherical grains appears to be within the overall scatter of the data, indicating that its dependence on grain shape is no more significant that other uncertainties that remain unquantified.

Figure 4.8 shows the relationship between quadratic flow coefficient, β, and grain size for both spherical and non-spherical grains. Unlike the linear coefficient, quadratic flow coefficient clearly takes on lower values for the non-spherical grains than in the baseline spherical case. This means that the resistance to flow through the matrix of angular grains increases with velocity at a greater rate than through spherical grains of the same size. To first order, β for angular grains might be taken as one half the β for spherical grains of the same size.

4.3   PERMEABILITY MEASUREMENTS ON SALEM LIMESTONE

A series of permeability tests was conducted on specimens of Salem (Indiana) limestone under sponsorship of the Defense Nuclear Agency. Tests were conducted at a range of pressure gradients to define both the linear and quadratic flow coefficients for the material. To

investigate the influence of rock skeleton stress on flow properties, tests were performed on specimens under hydrostatic pressure, including pressures high enough to permanently crush the rock cementation.

For the permeability testing of noncohesive granular materials described in the previous subsection, the test specimens were prepared by packing the granular materials in a circular duct. Because of the material's granular nature, the packing process produced a test specimen in intimate contact with the wall of the cylinder, thereby minimizing any error due to flow along the cylinder wall. It would be impractical, if not impossible, to achieve a close enough fit between a rock specimen and a steel cylinder to preclude unwanted flow along the rock-cylinder interface. Thus, an alternative approach was required. Permeability testing of the porous rock was performed in a specially modified triaxial compression apparatus. Figure 4.9 is a schematic depiction of the apparatus used to conduct permeability tests on porous limestone. The tests were performed on cylindrical rock specimens approximately 1-7/8 inch in diameter by 4 inch long. An impermeable, flexible membrane of heat shrinkable polyolefin tubing was applied so that it fit tightly to the rock and was sealed on each end to a perforated steel endcap as shown in Figure 4.9. The specimen, thus prepared, was installed in the triaxial compression apparatus, which was specially equipped with fluid flow passages. As illustrated in Figure 4.9, the top and bottom endcaps were sealed to the piston and pressure vessel base, respectively, with O-rings. Pressurized water was introduced to the specimen through a port in the base of the vessel and drained to the exterior of the pressure vessel through a hole in the triaxial loading piston. In order to assure that no significant flow was allowed between the specimen and the membrane, the triaxial pressure vessel was pressurized, and the pore fluid pressures were always kept lower than the confining pressure in the vessel.

Flow generation and measurement techniques for the rock specimens were very similar to those used in the tests on granular materials described in Section 4.2. The water was pressurized and the flow rate measured with a pressure intensifier which is shown schematically in Figure 4.9. The intensifier consists of two coupled hydraulic cylinders as shown in the figure. The cylinders have an area ratio of 6.25, allowing a water pressure output of 20,000 psi with an input of hydraulic fluid at 3200 psi. The intensifier displacement was measured with

an LVDT to determine the pore fluid flow rate.

In all cases, the specimen was first loaded hydrostatically to a specified total stress level using a combination of fluid pressure and piston load. For a simple hydrostatic load, it would not be necessary to use the axial loading piston. However, for permeability testing axial loading was applied with the piston in order to maintain the seal between the perforated top cap and the piston which was necessary to prevent flow of the confining fluid into the pore space of the specimen. Once the specified level of hydrostatic total stress on the rock was reached, it was held constant while tests were performed at a series of pore pressure gradients. For each of those tests, the hydraulic fluid flow to the low-pressure side of the intensifier was quickly raised to the desired level and held constant. When the steady state condition (constant pressure gradient and flow rate) was achieved, data acquisition was initiated to measure and record the pore fluid pressure upstream of the specimen and the fluid flow rate. These measurements were processed as described in Section 4.2.

A Salem limestone specimen with porosity of 0.169 was the subject of a series of fluid flow tests. It was initially loaded to 10 MPa confining pressure. The first fluid flow test was conducted with the pressure at the upstream end of the rock specimen set to approximately 2.5 MPa. In successive tests, the upstream pore fluid pressure was incremented until it reached a value of about 90% of the confining pressure. It was not raised above that level to ensure that the confining pressure was always higher than the pore pressure to keep the membrane pressed firmly against the rock specimen. Once the pore fluid pressure reached 90% of the current confining pressure, the confining pressure was incremented and the test series was repeated with the pore pressure beginning at 2.5 MPa. Figure 4.10 presents data from tests on a single specimen at a range of confining pressure and pore pressure gradient conditions. In Figure 4.10, one line is shown for each confining pressure, and each line is identified by that pressure value. The data are plotted, as in Figure 4.3, such that the intercept and slope of the line are the linear and quadratic flow coefficients, a and b, respectively.

At pressures of 70 MPa and below, the data points fall on a straight line within each confining pressure set, and there is only slight sensitivity to changes in confining pressure. As

confining pressure is increased above 70 MPa, the cementation of the rock skeleton begins to be crushed, thereby changing the geometry of the microscopic flow paths through the rock. This results in a more pronounced variation in flow coefficients with increasing confinement. It is also apparent from Figure 4.10 that, at the higher confining pressures, the lines are no longer straight. Their slopes decrease with increasing pore pressure gradient. To understand this behavior, it is necessary to consider the stress conditions in the test specimen. The decrease in permeability of the rock specimen with increasing confining pressure is caused by compaction of the rock skeleton and the resulting reduction in the flow area through its pore space. The deformation of the skeleton is controlled, to first order at least, by the effective stress, i.e. the difference between confining pressure and pore pressure. While fluid is flowing through the specimen during the test, there is a pressure gradient in the pore fluid along the length of the specimen. As a result, there is also a gradient in the effective stress acting on the rock skeleton, with the lowest effective stress at the upstream end. If the pore pressure at the upstream end is a small fraction of the confining pressure, then the effective stress is approximately the same as the confining pressure, and the variation in effective stress along the length of the specimen is small in comparison with the confining pressure. At the other end of the spectrum, if the upstream pore pressure is nearly equal to the confining pressure, then the effective stress at the upstream end of the specimen is nearly zero, and the variation in effective stress along the specimen length is very significant, being approximately equal to confining pressure. At low confining pressures, where the rock skeleton is elastic, and the flow properties are relatively insensitive to changes in effective stress, the rock has nearly the same flow properties along its entire length and the lines in Figure 4.10 appear nearly straight. However, at the higher confining pressures where the skeleton cementation is being crushed, i.e. greater than 70 MPa, the flow properties are more sensitive to changes in effective stress and hence exhibit significant variation along the specimen length in those cases where the upstream pore pressure is significant in comparison with the confining pressure. Thus, for confining pressures above approximately 70 MPa, the curves in Figure 4.10 exhibit an initial linear range where the effective stress acting on the rock is approximately constant and equal to the confining pressure. However, with increasing upstream pore pressure, the effective stress on the upstream portion of the specimen is reduced, resulting in increased flow capacity and a downward curvature of the curves in Figure 4.10.

4-12

Values of the flow coefficients determined from the data in Figure 4.10 are presented in Table 4.2. These values were derived from the test data using an analysis approach similar to that used for sands and illustrated by Figure 4.3. The difference is that for the limestone, only data from tests in which the upstream pore pressure was less that half the confining pressure were used in the analysis. As explained above, this eliminates those tests that had large effective stress gradients along the flow path which tend to obscure the fundamental flow properties of the rock. The coefficients are presented in the table both in terms a and b, as they were derived from the test data, and in terms of α and β, which are properties only of the porous rock. The variations in the linear and quadratic flow coefficients with effective stress are illustrated in Figures 4.11 and 4.12, respectively.

4.4 RELATIONSHIP BETWEEN PERMEABILITY COEFFICIENTS AND SKELETON PROPERTIES

Section 4.2 describes relationships between the flow coefficients, α and β, and grain size for flow through porous materials consisting of spherical grains of approximately uniform size, and Figures 4.4 and 4.5 present the data from which those relationships were derived. If the relationships between flow coefficients and grain size are derived based strictly on mathematical fits to the finite sets of data points, the results are the empirical expressions for α and β given by Equations (4.7) and (4.11). If, instead, the flow coefficients are assumed proportional to integral powers of grain size, as suggested by dimensional analysis, the resulting relationships are those given by Equations (4-8) and (4-12). In the latter set of equations, the numerical constants are dimensionless.

The grain size was a convenient independent variable for analysis of granular materials. However, as attention is turned toward identifying a more fundamental relationships between microscopic geometric properties and permeability for various types of materials, it is no longer suitable. A conceptual model that is widely used for the study of flow through porous media is a matrix of openings, or pores, interconnected by smaller channels, or throats. For spherical grains, the throats have dimensions of the order of the grain size. The effective diameter of a throat was estimated as the diameter of the circle whose area is equivalent to the actual area of the throat. If the spherical grains are assumed to be close packed, the smallest throats will be

4-13

formed by the three tightly packed spheres, and the equivalent diameter of the throat is 0.23 d. Assuming that the throat diameter, t, is equal to 0.23 d, equations 4.8 and 4.12 can be rewritten in terms of t as:

$$\alpha - 0.0197 \ t^2 \qquad (4.13)$$

$$\beta - 0.509 \ t \qquad (4.14)$$

It is of interest to see how well Equations (4-13) and (4-14), which were derived from test data from granular materials, predict the permeability properties of the porous limestone. Wardlaw, et.al (1987) reported the throat dimensions of two different rock types, including Indiana limestone, derived from Wood's metal porosimetry. In this technique, molten Wood's metal, a low melting point (70 C) alloy of bismuth, is used to saturate the pore space of the rock. The Wood's metal saturated specimen is then sectioned and polished, and the rock skeleton is dissolved away with acid leaving the metal matrix in the shape of the pore space of the rock. The degree of saturation achieved is a function of the pressure applied to force the molten metal into the rock. The highest degree of saturation reported by Wardlaw, et.al. was 94%, a result of the application of 1700 psi saturation pressure. Measurements were made of the resulting metal matrix on enlarged scanning electron micrographs.

In 480 observations, Wardlaw, et.al. reported throats ranging from 2×10^{-5} to 8×10^{-4} inch with an average of 1×10^{-4}. If it is assumed that the flow is controlled by the smallest throat size, and α and β are computed using a throat size, t, of 2×10^{-5} inch in Equations 4-13 and 4-14, the resulting permeability coefficients are $\alpha = 7.88 \times 10^{-12}$ in^2 and $\beta = 1.02 \times 10^{-5}$ in. The linear permeability coefficient value of 7.88×10^{-12} in^2 is in remarkably good agreement with the measured value of 1.26×10^{-11} in^2. Admittedly, the choice of the minimum measured pore size as input to Equation 4-13 was somewhat arbitrary. However, we believe that this result suggests a strong dependence of α on the throat dimension as would be expected for a viscosity related term. In contrast, the value of the computed quadratic flow coefficient, $\beta = 1.02 \times 10^{-5}$ inch, differs by about four orders of magnitude from the measured value (at low

effective stress) of 1.2×10^{-9} inch. This limited evidence appears to suggest that β has a stronger dependence on some characteristic of the porous skeleton other than throat diameter.

This finding is consistent with the hypothesis that the quadratic flow coefficient is dependent on the tortuosity of the flow path through the porous material. For the granular materials, an approximate linear correlation was found between the grain size and the quadratic flow coefficient, β. However, if tortuosity can be characterized by a quantity with units of length, such as curvature (1/length), then it scales with grain size. Thus, if β is proportional to inverse curvature, then for granular materials, it will also be proportional to grain size, even if it is not the size of the throats that determine β. Since the pore geometry of the rock has completely different shape characteristics than the granular materials, it would not be expected to scale with throat size in the same way as the sands, and hence the expression relating β to throat dimension for granular materials would not be applicable to the rock.

4.5   RELATIVE IMPORTANCE OF LINEAR AND QUADRATIC TERMS

The existence of the quadratic term in the Forchheimer expression for relating pressure gradient to fluid flow velocity can readily be demonstrated in the laboratory. However, it is apparently not widely known or used in civil engineering. This leads to the question of where it is significant. Figure 4.13 represents an attempt to shed some light on that question. The figure shows the relative contributions of the linear and quadratic terms to the pressure gradient for two sands and a porous rock under a range of flow conditions. Table 4.3 presents the properties of the materials used to compute the data points in Figure 4.13. The two sands were assumed to have grains that would just pass U.S. Standard No. 10 and No. 100 sieves. Flow coefficients for the sands were computed using Equations 4-13 and 4-14. The limestone flow coefficients were taken from the low flow end of the test data presented in Table 4.2. In all cases, the flow coefficients were assumed to remain constant over the entire range of pressure gradients considered. The fluid was assumed to be water at 20° C, and its properties are included in Table 4.3. The variable on the vertical axis in Figure 4.13 is the ratio of the quadratic to linear terms in Equation 4-1. The figure illustrates the range of pressure gradients at which the quadratic term becomes important for the various materials.

A horizontal line is shown on Figure 4.13 at a ratio of 0.10. At this point, the contribution of the quadratic term is 10% of the linear term contribution. Taking that as a criterion for significance, flow conditions above the line on the figure are significantly influenced by the quadratic term which is missing from the traditional Darcy permeability formulation.

Table 4.1.   Summary of flow test data for samples of uniform granular materials tested with kerosene.

Material Description	U.S. Std Sieve Range	Grain Size (in)	Grain Spec. Gravity	Bulk Density (lb/ft³)	Porosity	a (lb·s/in⁴)	b (lb·s²/in⁵)	Flow Coefficients α (in.²)	β (in)
SPHERICAL GRAINS									
Steel Shot		0.0938	7.70	0.164	0.412	0.021	0.010	1.24×10^5	7.70×10^3
Glass Beads	16-18	0.0431	2.90	0.065	0.380	0.225	0.019	1.18×10^6	4.07×10^3
Glass Beads	18-20	0.0362	2.90	0.065	0.375	0.238	0.024	1.11×10^6	3.09×10^3
Glass Beads	30-40	0.0200	2.90	0.067	0.364	0.727	0.059	3.65×10^7	1.29×10^3
Glass Beads	70-100	0.0071	2.49	0.058	0.351	4.305	0.238	6.16×10^8	3.18×10^4
Glass Beads	70-140	0.0062	2.49	0.059	0.347	4.904	0.235	5.40×10^8	3.23×10^4
Glass Beads	100-140	0.0050	2.57	0.058	0.380	10.450	0.300	2.54×10^8	2.52×10^4
Glass Beads	140-200	0.0035	2.49	0.054	0.397	21.680	0.263	1.22×10^8	2.88×10^4
Glass Beads	140-200	0.0035	2.49	0.058	0.356	17.970	0.326	1.47×10^8	2.32×10^4
NON-SPHERICAL GRAINS									
Enewetak Sand	16-18	0.0431	2.82	0.055	0.462	0.234	0.043	1.13×10^6	1.78×10^3
Crushed Granite	16-18	0.0431	2.65	0.051	0.465	0.054	0.061	4.89×10^9	1.24×10^3
Enewetak Sand	30-40	0.0200	2.82	0.061	0.398	1.379	0.202	1.92×10^7	3.75×10^4
Enewetak Sand	30-40	0.0200	2.82	0.061	0.398	1.348	0.210	1.97×10^7	3.60×10^4
Ottawa Sand	30-40	0.0200	2.66	0.061	0.366	1.570	0.118	1.69×10^7	6.41×10^4
Crushed Granite	30-40	0.0200	2.65	0.050	0.481	1.007	0.129	2.63×10^7	5.89×10^4
Enewetak Sand	70-100	0.0071	2.82	0.060	0.411	3.404	0.246	7.79×10^8	3.08×10^4
Enewetak Sand	70-100	0.0071	2.82	0.055	0.458	3.795	0.253	6.98×10^8	3.00×10^4

Note: for kerosene at 20°C,

$\mu = 2.65 \times 10^{-7} \text{ lb·s/in}^2$

$\rho_l = 7.57 \times 10^{-5} \text{ lb·s}^2/\text{in}^4$

4-17

Table 4.2. Permeability Test Data for Salem Limestone

Effective Stress (psi)	a (lb-s/in^4)	b (lb-s^2in^5)	Flow Coefficients alpha (in^2)	beta (in)
1450	1.26E+04	8.79E+04	1.15E-11	1.06E-09
2175	1.33E+04	8.32E+04	1.09E-11	1.12E-09
2900	1.47E+04	7.37E+04	9.89E-12	1.27E-09
3625	1.54E+04	7.37E+04	9.41E-12	1.27E-09
4350	1.71E+04	7.13E+04	8.49E-12	1.31E-09
5800	1.86E+04	1.02E+05	7.81E-12	9.15E-10
7250	2.26E+04	1.21E+05	6.42E-12	7.72E-10
10150	3.09E+04	2.47E+05	4.71E-12	3.78E-10
13050	4.95E+04	6.91E+05	2.94E-12	1.35E+-10
15950	9.13E+04	1.49E+06	1.59E-12	6.30E-11
18850	1.41E+05	5.15E+06	1.03E-12	1.82E-11
21750	2.88E+05	1.11E+07	5.04E-13	8.39E-12

Note: for water at 20°c,

$$\mu = 1.45 \times 10^{-7} \text{ lb} \cdot \text{s/in}^2$$

$$\rho = 9.35 \times 10^{-5} \text{ lb} \cdot \text{s}^2/\text{in}^4$$

Table 4.3. Properties of materials used to create Figure 4.13.

	α (in^2)	β (in.)	a lb $\cdot$ s/in^4	b lb $\cdot$ s^2/in^5
Sand No. 10	6.20 x 10^{-6}	0.0053	0.0235	0.018
Sand No. 100	3.48 x 10^{-8}	0.00040	4.17	0.236
Salem Limestone	1.26 x 10^{-11}	1.2 x 10^{-9}	12161	71250

Note: Water at 20°c

$\mu = 1.45 \times 10^{-7}$ lb $\cdot$ s/in^2

$\rho_f = 9.35 \times 10^{-5}$ lb $\cdot$ in^4/s^2

Energy Source Fluid

Displacement Transducer
for Flow Rate
Measurement

High Pressure
Fluid Reservoir

Seals

Screen

Granular
Sample

Pressure
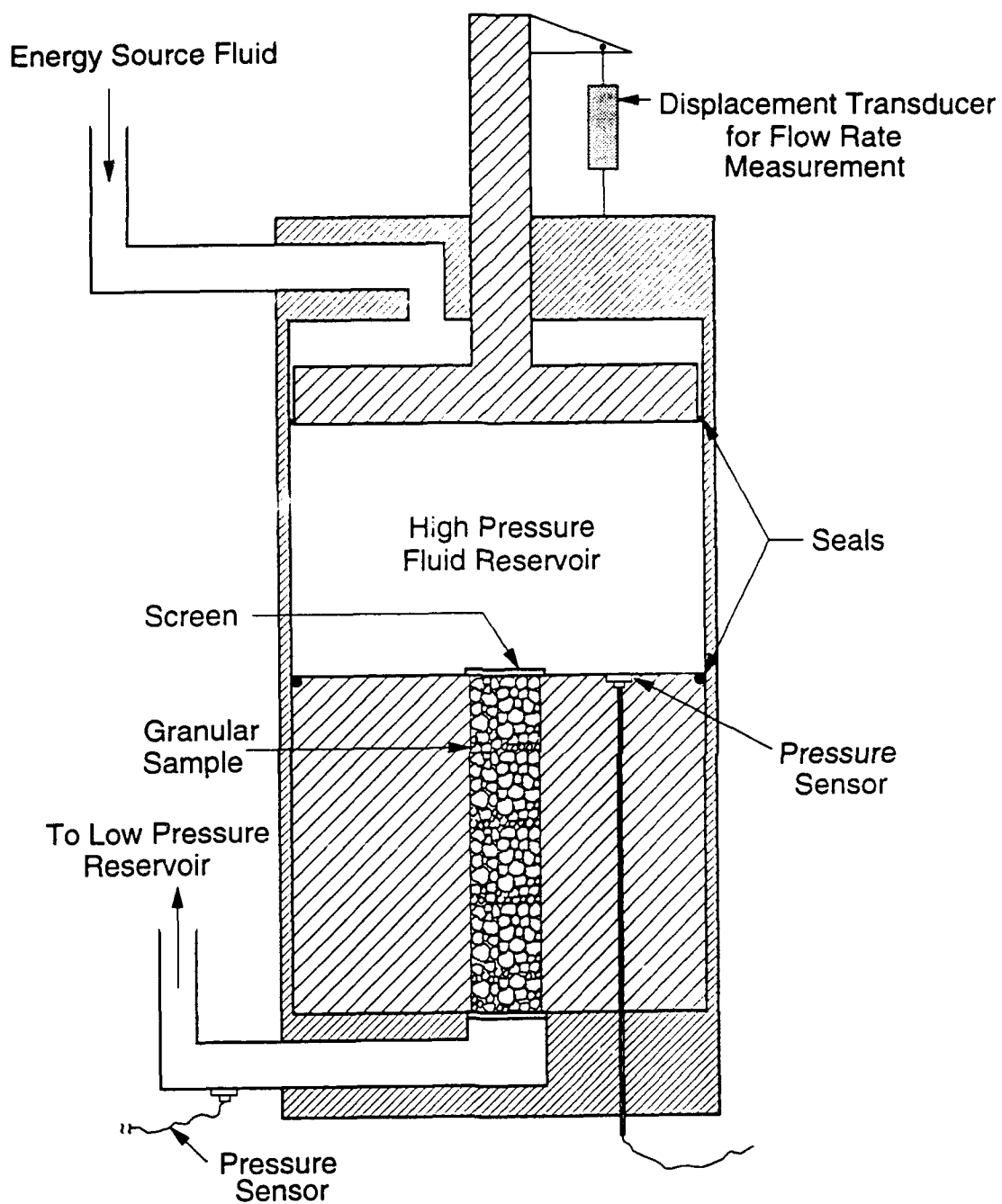Sensor

To Low Pressure
Reservoir

Pressure
Sensor

Figure 4.1.   Schematic section view of apparatus used to
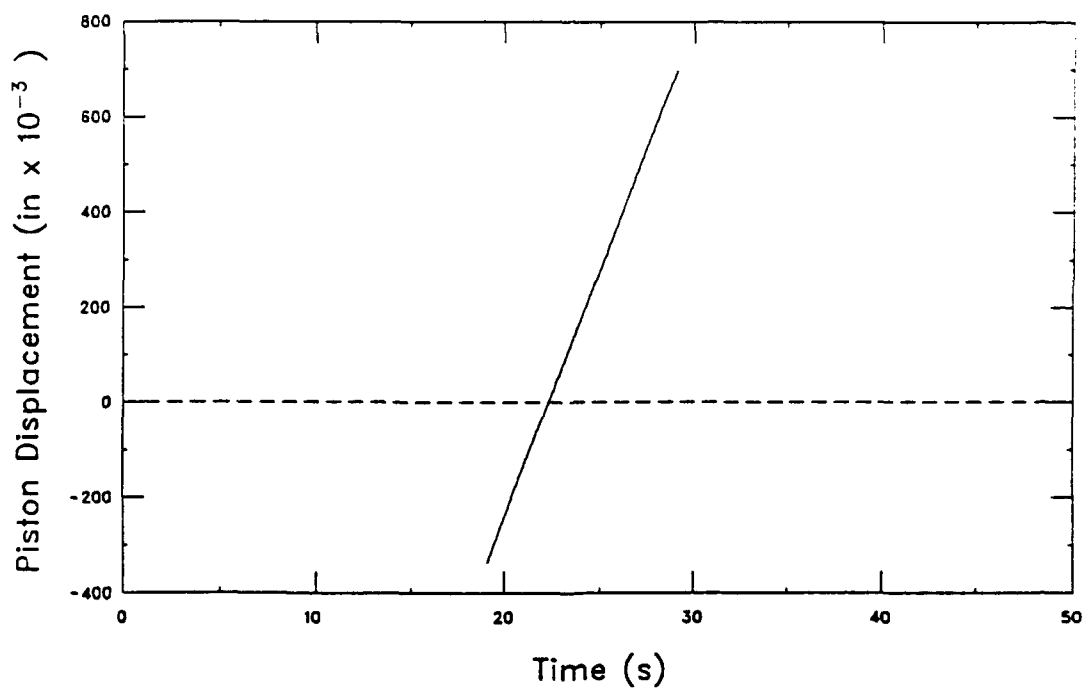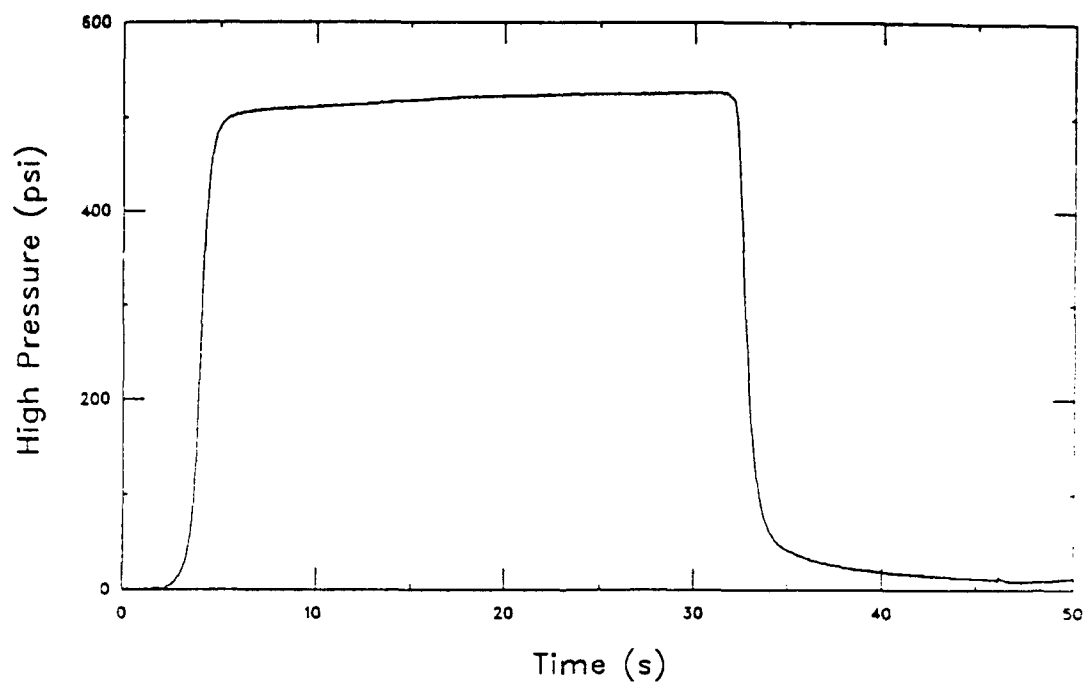measure flow through granular materials.

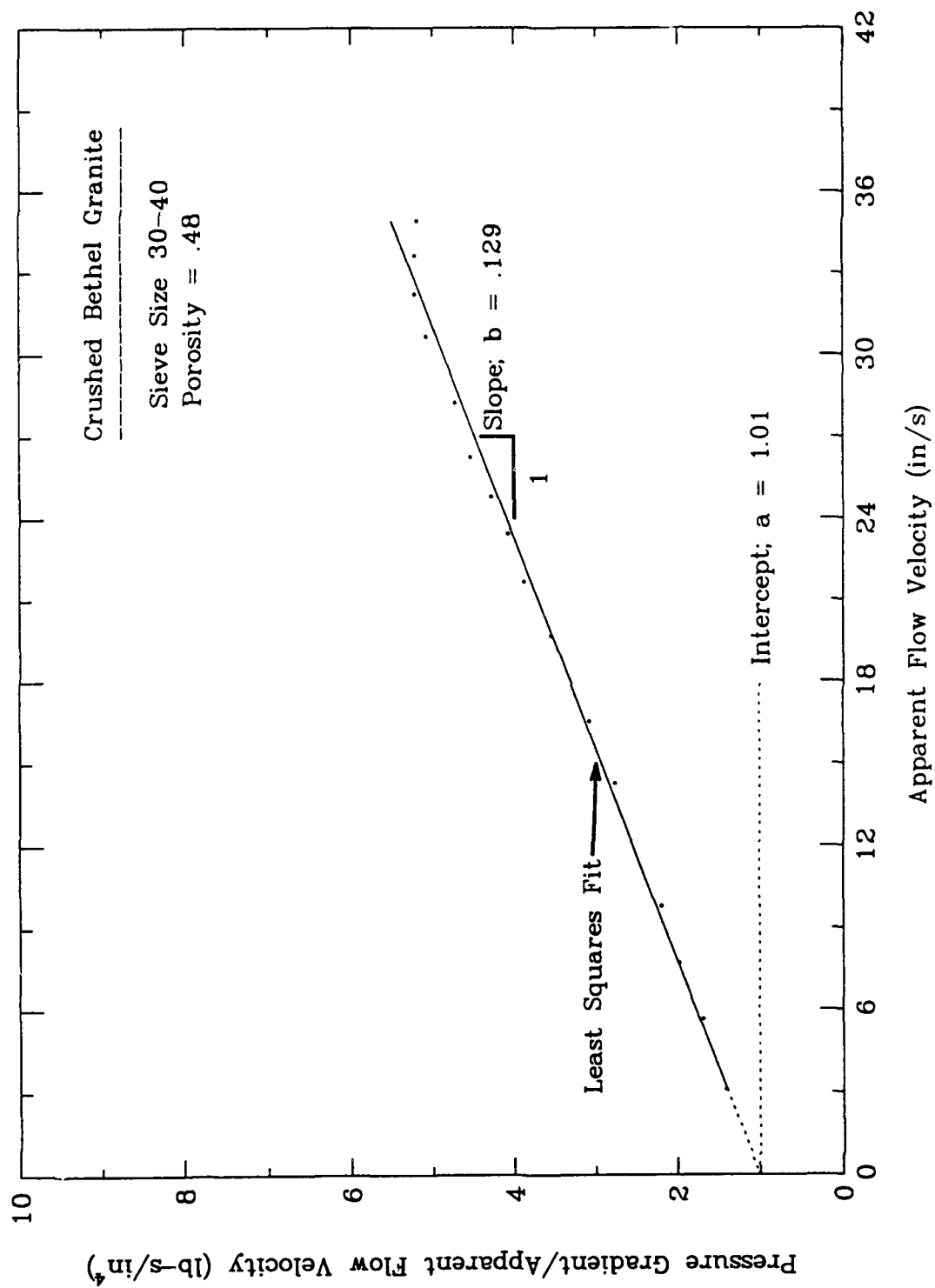Figure 4.2.   Typical raw flow test data.   Crushed Bethel granite,
30-40 sieve.

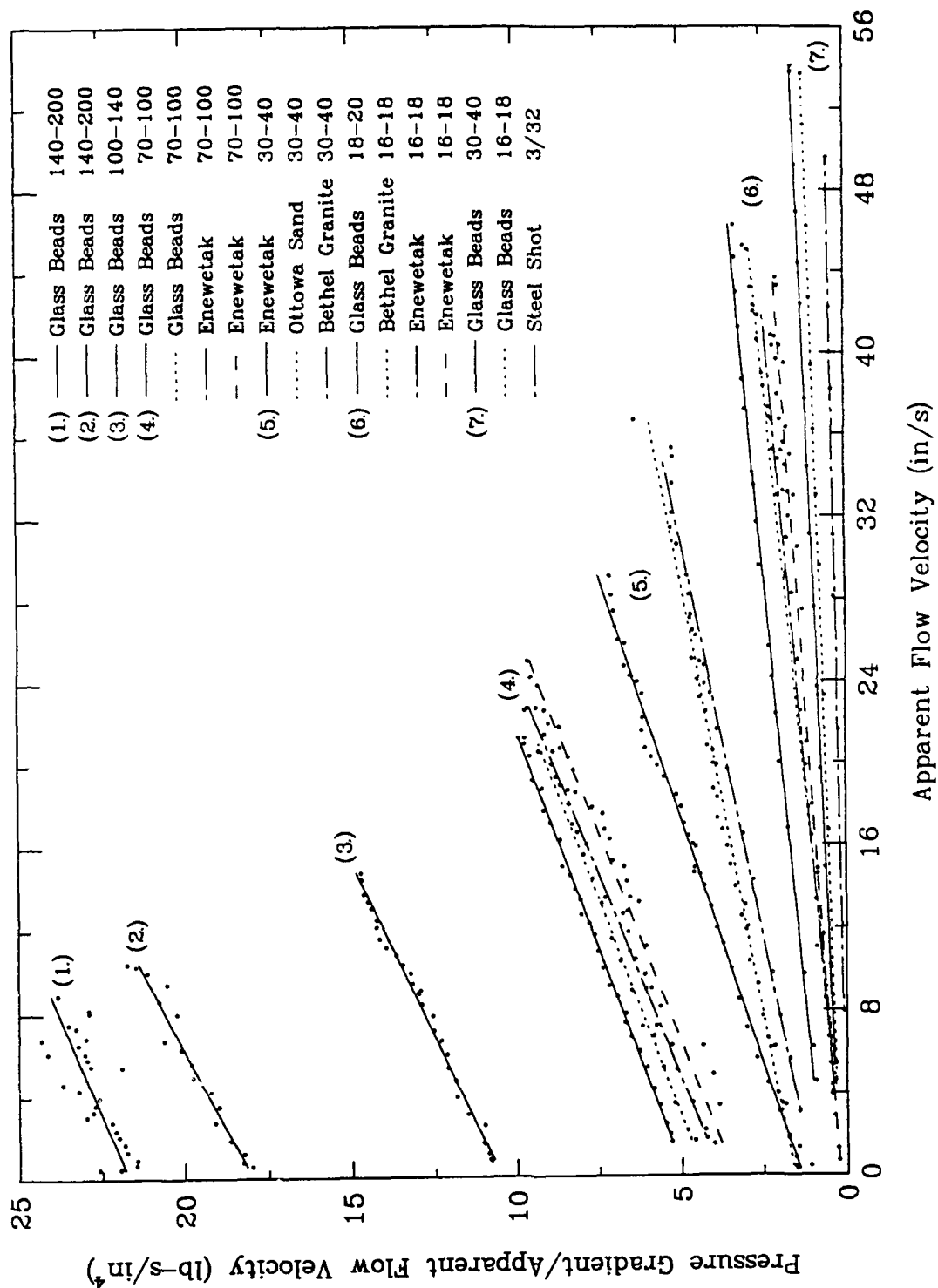Figure 4.3. Steady state flow data plotted in a format for direct determination coefficients a and b.

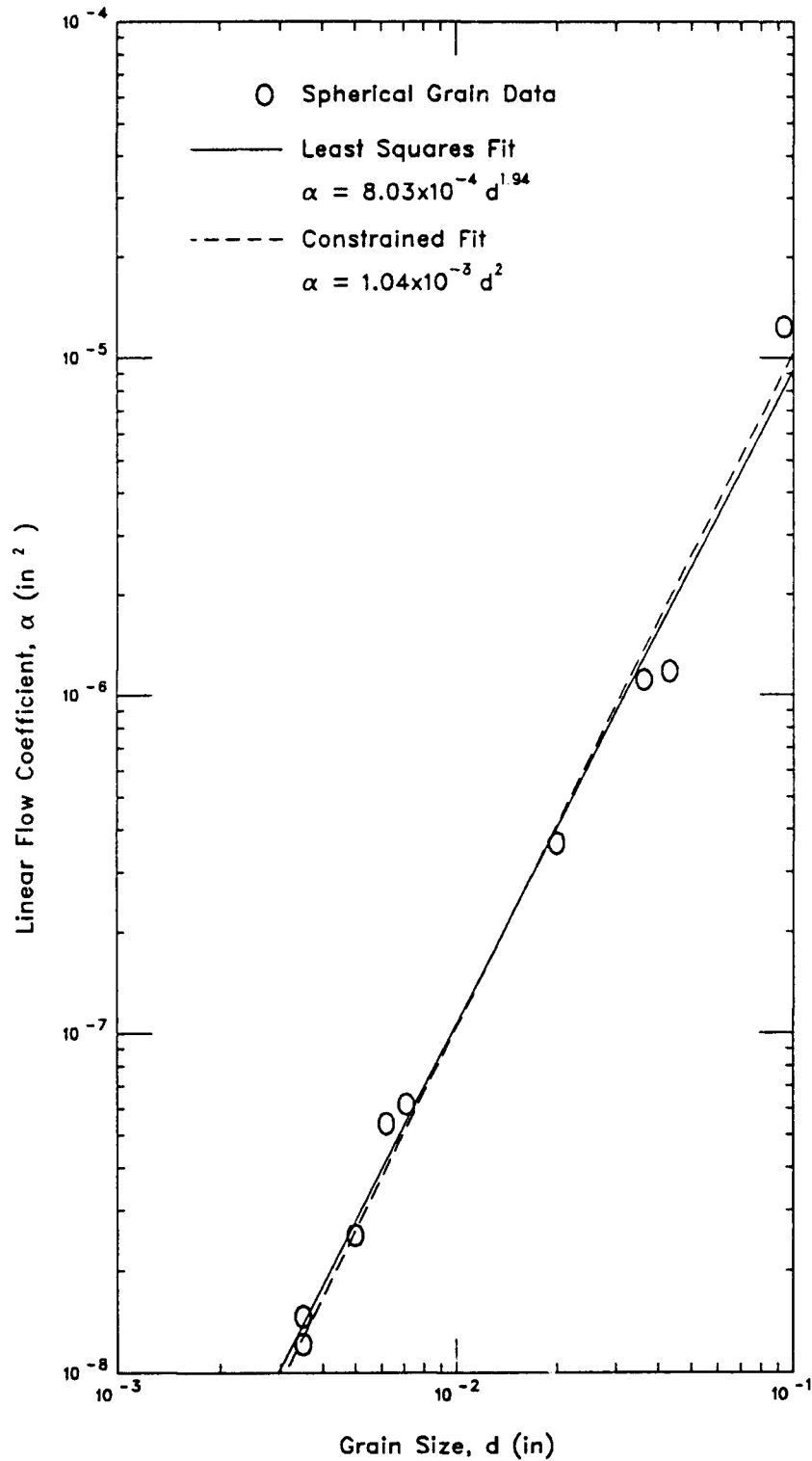Figure 4.4.   Summary plot of permeability test results on granular materials.

Legend (y-axis: Pressure Gradient/Apparent Flow Velocity (lb-s/in⁴); x-axis: Apparent Flow Velocity (in/s)):

	Material	Size
(1.)	Glass Beads	140-200
(2.)	Glass Beads	140-200
(3.)	Glass Beads	100-140
(4.)	Glass Beads	70-100
	Glass Beads	70-100
	Enewetak	70-100
	Enewetak	70-100
(5.)	Enewetak	70-100
	Ottowa Sand	30-40
	Bethel Granite	30-40
(6.)	Glass Beads	18-20
	Bethel Granite	16-18
	Enewetak	16-18
	Enewetak	16-18
(7.)	Glass Beads	30-40
	Glass Beads	16-18
	Steel Shot	3/32

Figure 4.5. Measured relationship between linear
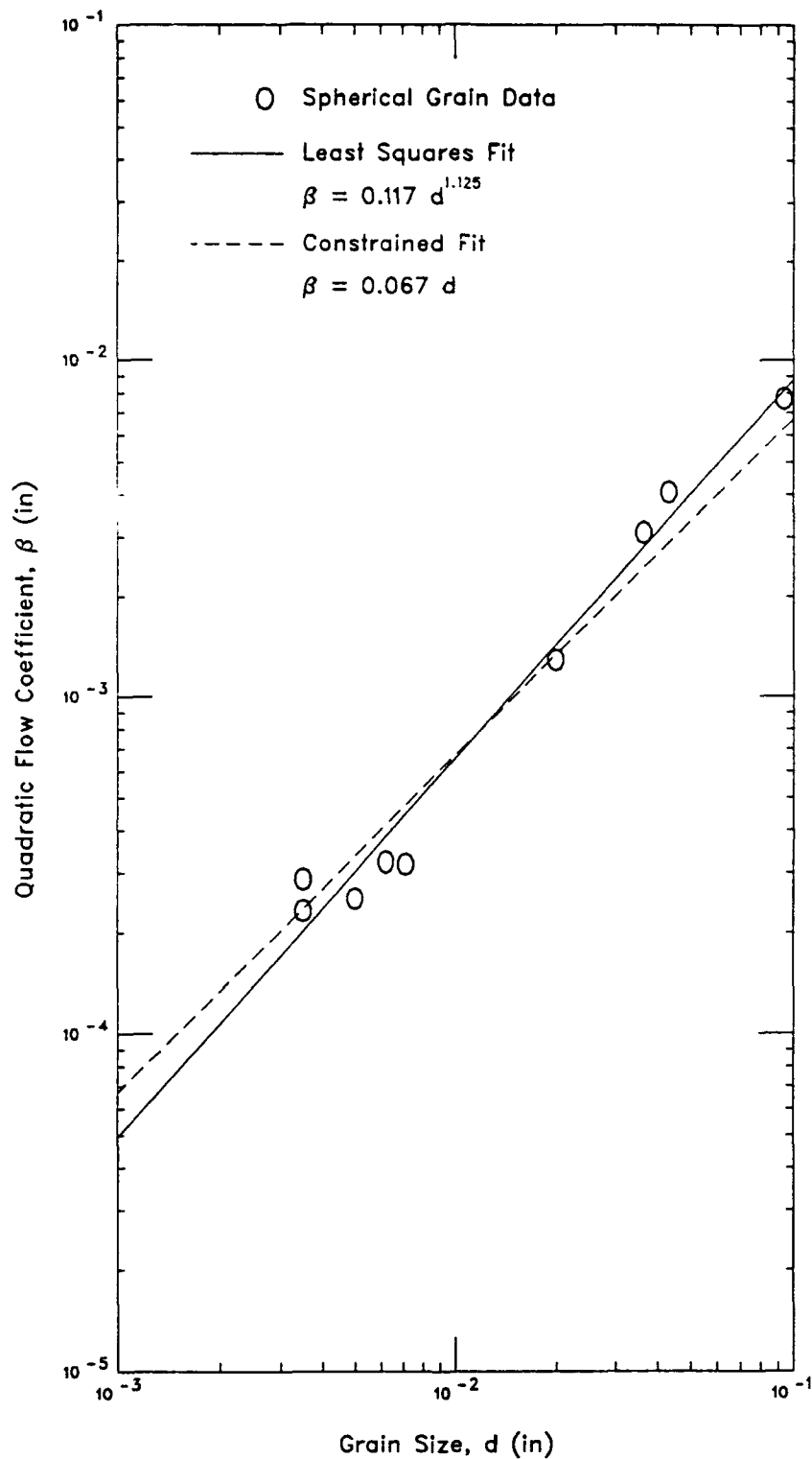flow coefficient α , and grain size for
spherical grains.

4-24

Figure 4.6. Measured relationship between quadratic flow coefficient, β, and grain size for spherical grains.
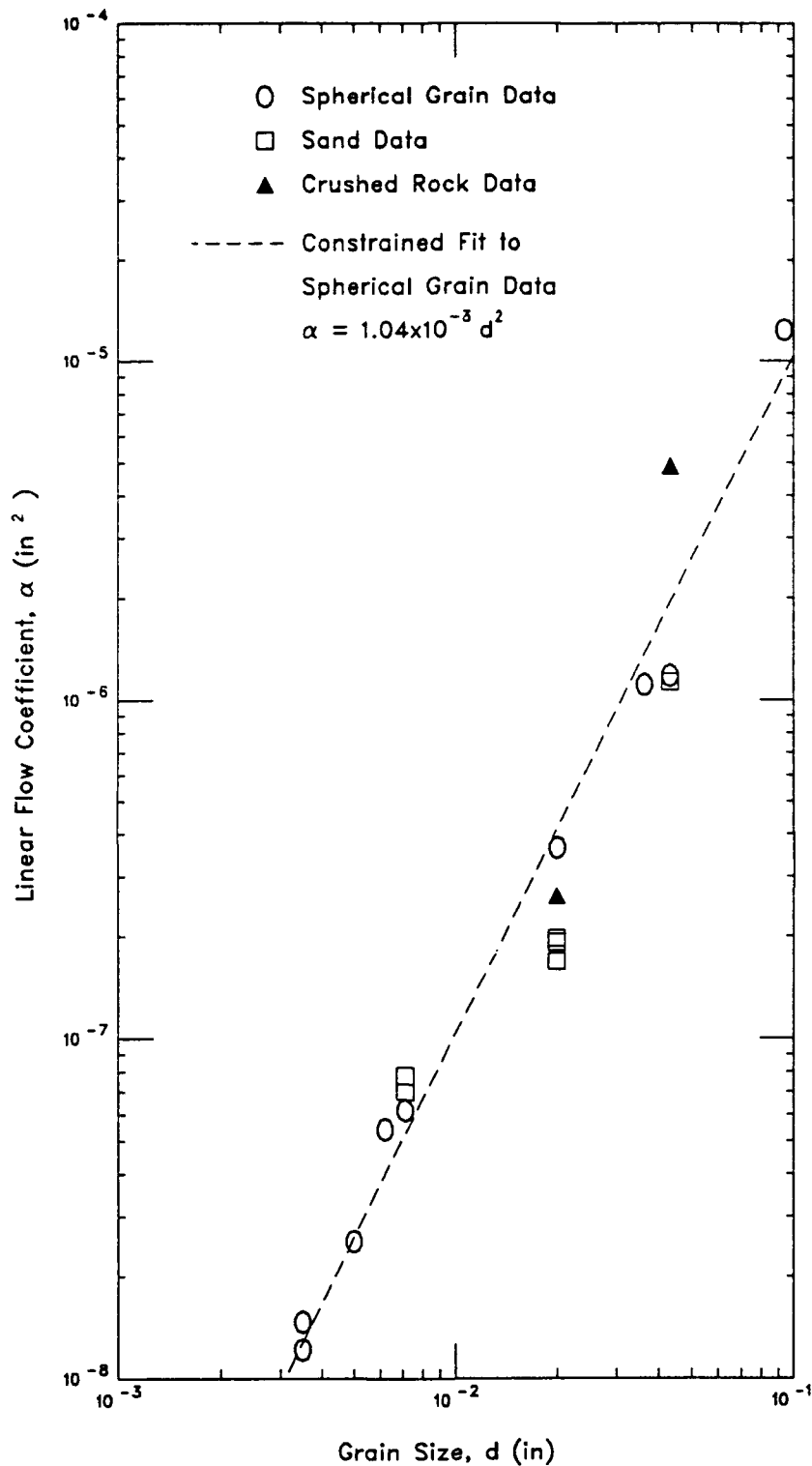
Figure 4.7. Measured relationship between linear flow coefficient, α, and grain size for all grain shapes.
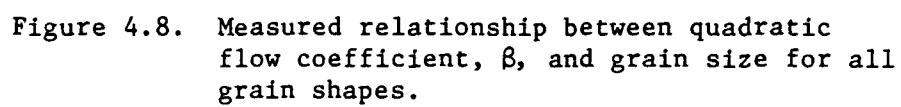
4-26

Figure 4.8. Measured relationship between quadratic flow coefficient, β, and grain size for all grain shapes.
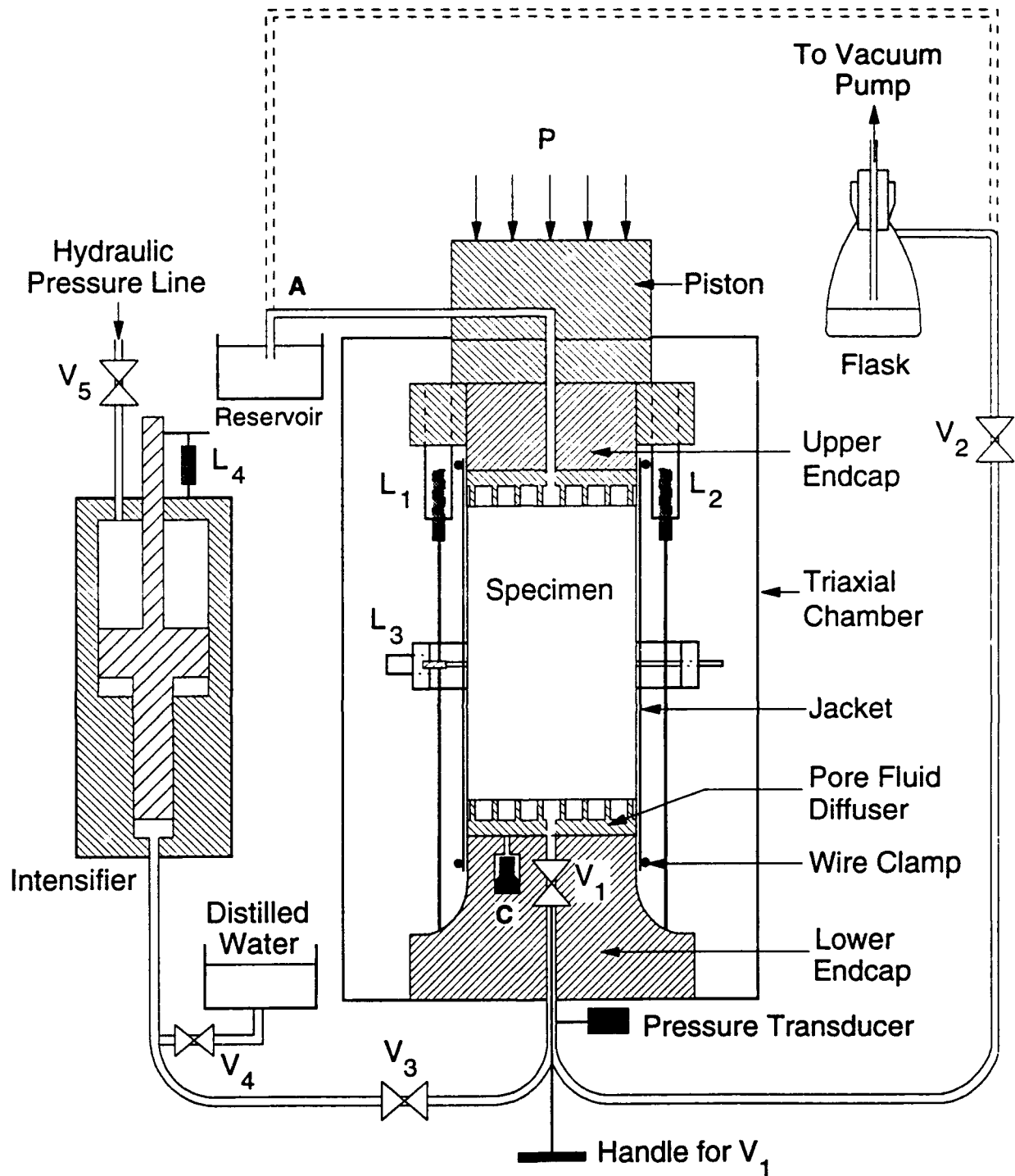
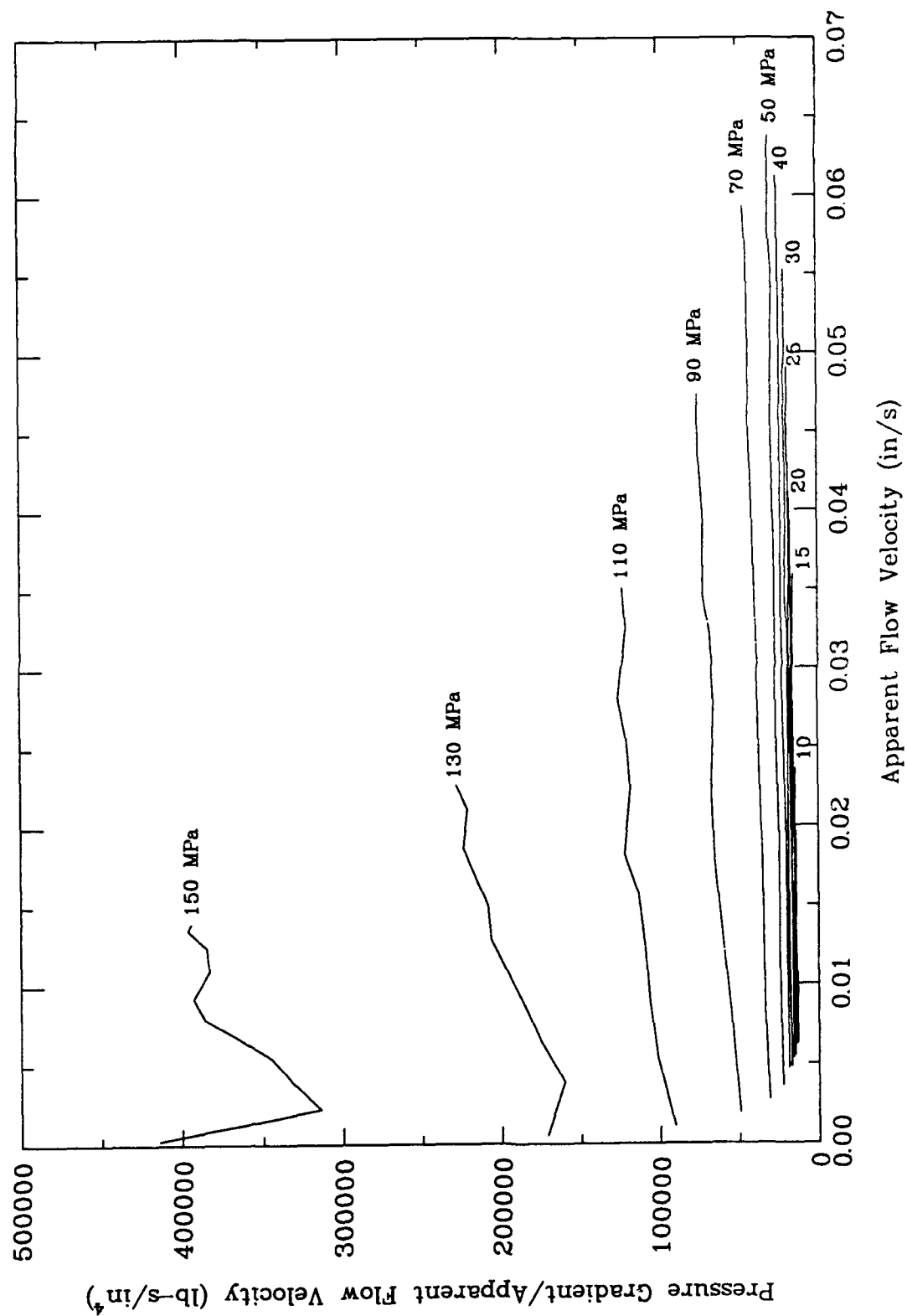Figure 4.9. Schematic of flow test apparatus for rock specimens.

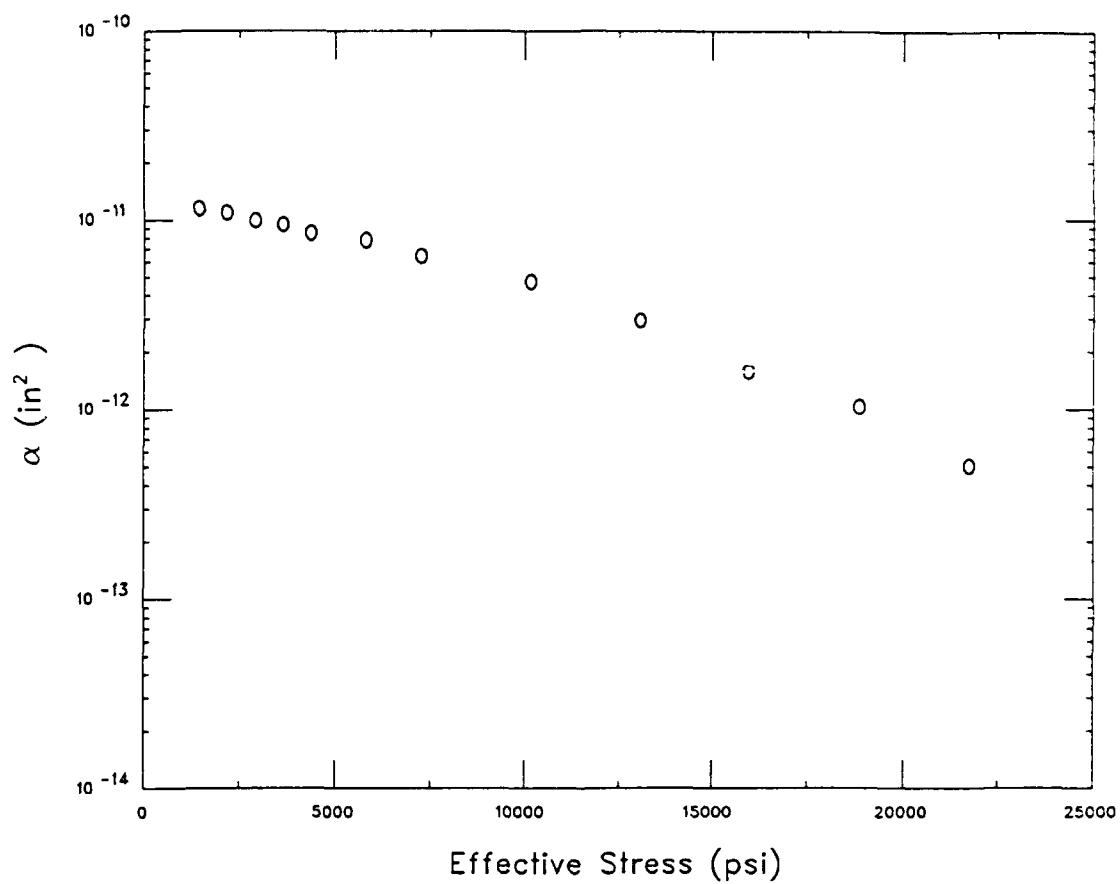Figure 4.10. Flow test data for Salem limestone.

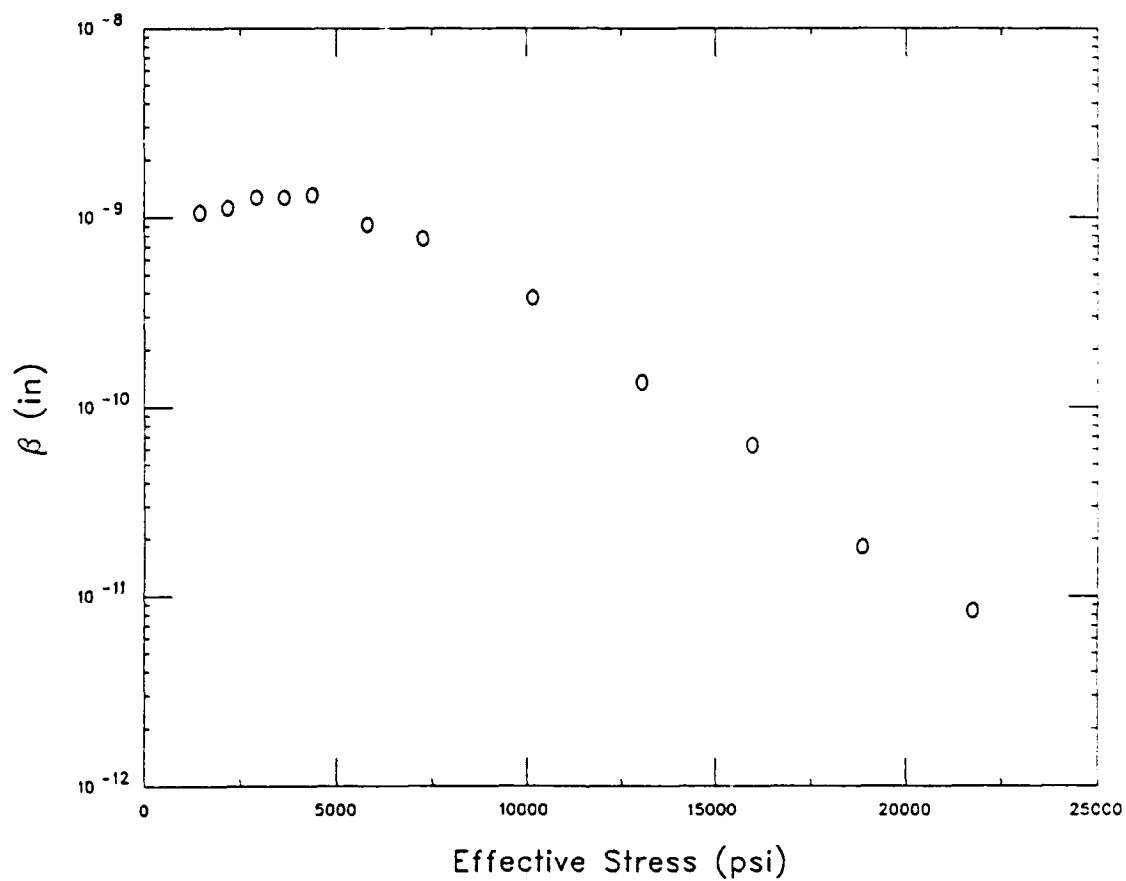Figure 4.11. Variation in linear flow coefficient, α with effective stress in Salem limestone.

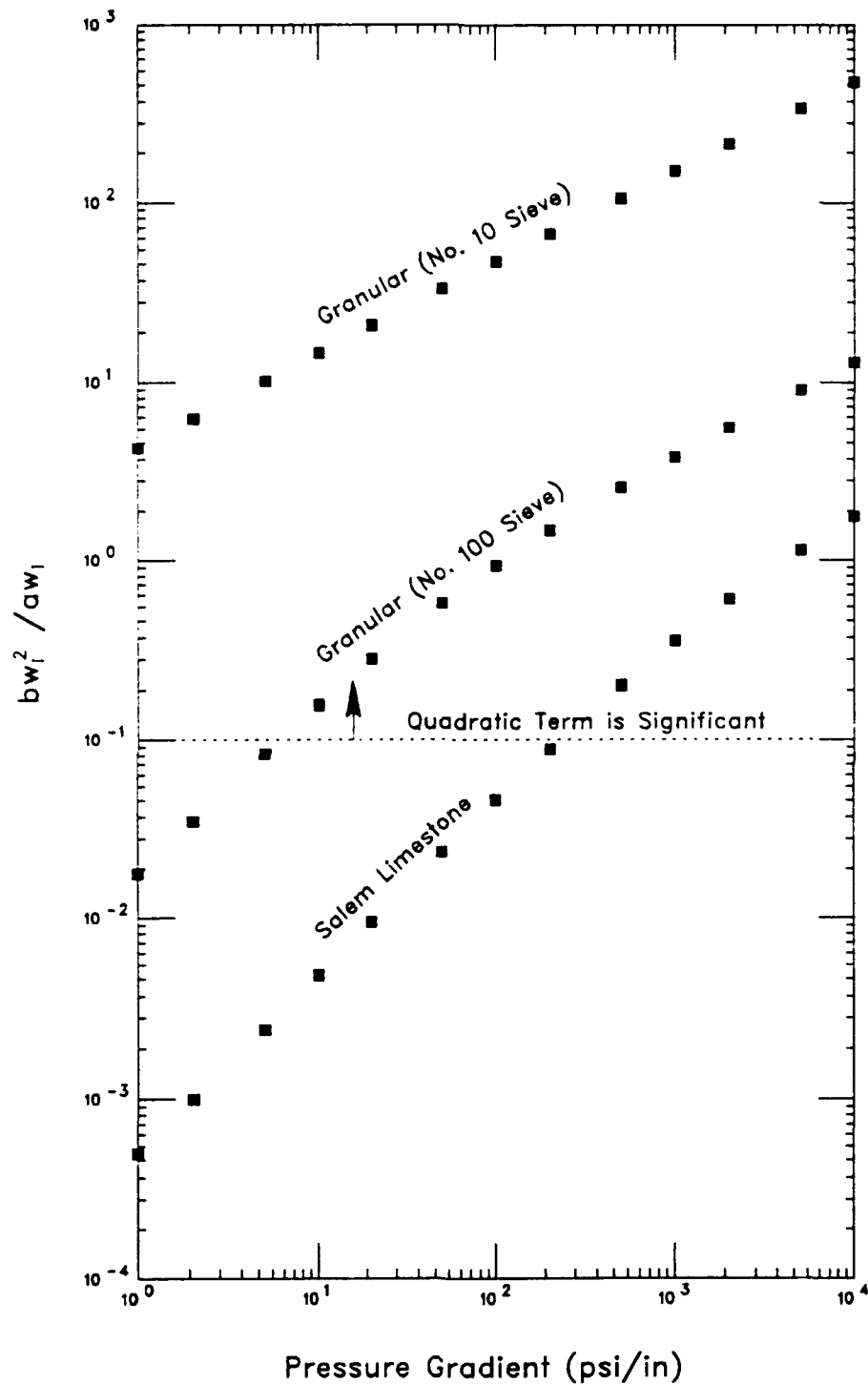Figure 4.12. Variation in quadratic flow coefficient, β, with effective stress in Salem limestone.

Figure 4.13. Relative importance of the quadratic and linear flow terms in the Forchheimer equation for two sands and a porous rock.

SECTION 5

ANALYSIS OF QUASI-STATIC UNDRAINED, TRIAXIAL

COMPRESSION RESPONSE OF SALEM LIMESTONE

Applied Research Associates conducted a series of laboratory material property tests on drained and undrained samples of porous limestone from the Salem formation in Indiana. This work was performed under sponsorship of the Defense Nuclear Agency (DNA) with the goal of providing data to formulate and validate two-phase models of the limestone response. The results of those tests, which are reported by Chitty & Blouin (1993) and summarized by Kim, Blouin, Chitty and Merkle (1988), provide an excellent opportunity to exercise the analytical formulations developed under AFOSR sponsorship.

In the DNA effort, drained tests were performed to define the rock skeleton properties. Based on those skeleton properties, two-phase analytical models were derived to characterize the saturated undrained behavior of the material. In order to validate the two-phase analytical models, tests were also performed in the saturated undrained condition, including undrained triaxial compression tests. The undrained triaxial compression test results contained apparent inconsistencies that motivated further study. Specifically, the test data showed that pore pressure remained essentially constant while the sample underwent several percent of volumetric expansion. In an effort to better understand the pore pressure and volumetric strain behavior of these tests, ARA performed a supplemental study, sponsored by the U.S. Army Engineers Waterways Experiment Station (WES), in which additional instruments were used to better define the deformed shape of the test specimens (Chitty & Blouin, 1990).

The objectives of the analysis described here were to exercise and validate the material modeling capabilities of MEM as developed for this project, and to gain a fundamental understanding of the undrained triaxial compression test and its applicability to undrained material property characterization.

This section presents an analysis of the observed response of Salem limestone in a conventional, undrained triaxial compression test. First, the appropriate model parameters used

in numerical simulations of the triaxial test are presented. Then, the assumptions and data analysis procedures that are conventionally applied to triaxial compression tests of rock are described together with the results of undrained tests on Salem limestone including special deformation measurements that were acquired. Finally, the results of a finite element simulation a the laboratory test are described followed by a discussion of the conclusions resulting from this investigation. The results presented in this section were summarized in a paper by Chitty, et. al, (1991).

5.1   MODEL PARAMETER DETERMINATION FOR SALEM LIMESTONE

Salem limestone is a porous rock of exceptional uniformity. The samples used in the undrained triaxial tests had an average porosity of 0.128. Table 5.1 summarizes the physical properties of the material used in the numerical simulations.

The solid grains of the limestone were modeled using the parameters given in Table 5.2 together with the numerical model described in Section 3.3. The limestone was saturated with fresh water in the simulations; the partial saturation model described in Section 3.5 was not used. The pore water compressibility was modeled as nonlinear corresponding to the model described in Section 3.4 and the parameters given in Table 3.3. The initial bulk modulus of the pore water is 2220 MPa. Given that the triaxial tests were quasi-static with very low pore water velocities expected, the Forchheimer permeability model was not necessary. A representative, constant Darcy permeability of 4.70×10^{-7} m/s was used in all of the numerical simulations. This value is higher by approxiately a factor of 6 than the test data presented in Section 4. The value used in the analysis was based on a very preliminary laboratory test which was shown to be significantly in error as a result of the subsequent, more precise tests described in Section 4. This error does not significantly affect the conclusions of this anlaysis because the permeabilities in both the triaxial compression test and the MEM calculation were high enough that any pore pressure gradients equilibrated essentially instantly on the time scale of the test.

5.1.1 Fitting of ARA Three Invariant Skeleton Model

The determination of the parameters for the ARA 3-I model to represent the skeleton response of Salem limestone is described in this subsection. The model was fit to the data from the drained hydrostatic and triaxial compression tests shown in Figures 5.1 and 5.2. The model parameters are summarized in Table 5.3.

Using the measured response of Salem limestone in the elastic regime during an unconfined compression test, a Poisson's ratio of 0.25 was determined. The initial bulk modulus measured in the linear portion of the drained hydrostatic loading in Figure 5.1 was 24,000 MPa. This corresponds to an initial Young's modulus of 36,000 MPa for a Poisson's ratio of 0.25. Also, from the cycled load/unload hydrostatic compression data in Figure 5.1, values of the initial unload bulk moduli at various maximum pressures were determined, converted to Young's moduli according to Equation 3.11, and plotted as shown in Figure 5.3. A least squares linear regression was then used to fit the line in log-log space as shown in Figure 5.3. This is equivalent to the procedure outlined in Section 3.2.3 and gives the elastic parameters n = 0.2286 and K_{ur} = 71,560 as given in Table 5.3.

The option for the ARA elastic model was selected to match the unloading response of the limestone as closely as possible. The unloading cycle from 200 MPa during the hydrostatic compression test (Figure 5.1) was used to obtain the parameters:

$$\lambda = 0.644$$
$$\gamma = 0.893$$
$$\beta = 0.487$$

These parameters are defined in Equations 3.4, 3.6 and 3.7. This completes the definition of the elastic response for the skeleton model.

The hydrostatic compression data from Figure 5.1 are also used to define the compressive plastic response as outlined in Section 3.2.4. The ratio of the major to minor axes of the elliptical compressive yield surface (r in Equation 3.15 and Figure 3.1) was selected to be r = 2.0 based on previous experience. The parameter fitting routines in MEM were then used to

5-3

compute the plastic compressive work from the plastic volume strains according to Equation 3.17 in the manner described in Section 3.2.4. The normalized compressive plastic work was plotted as a function of pressure as shown in Figure 5.4. Four line segments were then fit to this data defining four sets of the parameters c_i and p_i as given in Equation 3.20. The resulting parameters are given in Table 5.3 and complete the definition of the compressive plastic response.

The first step in determining the expansive plastic response parameters is to define the ultimate failure surface and the corresponding peak expansive plastic work as functions of mean stress. The failure envelope is fit to the ultimate shear strengths from the triaxial compression test data of Figure 5.2a in the conventional manner. Below the brittle ductile transition, the ultimate octahedral shear stress is used. In the ductile regime, the octahedral shear stress at 15% axial strain is used.

The expansive plastic response is fit as outlined in Section 3.2.5. The failure envelope is fit by plotting the failure points as shown in Figure 5.5 (note that $\bar{\sigma}_{oct} = \sigma_{oct} - T$ in Figure 5.5). Then, according to Equation 3.40, m is determined to be 4.203×10^{-6} from the ratio of the slope to the intercept of the straight line fit to the data in Figure 5.5. Then, from available test data on Salem limestone, a value of $\psi = 1.25$ was determined which gives $\bar{E} = 0.1111$ according to Equation 3.23. Then, substitution of m and $\bar{E}$ into the intercept value from Figure 5.5 gives $\eta_1 = 0.4197$ (refer to Equation 3.40). The tensile strength of the skeleton was measured to be T = 32 MPa. These parameters are summarized in Table 5.3.

The next step in the fitting process is to define the function for the peak plastic expansive work using a multi-segment fit (Equation 3.28) or using an exponential function (Equation 3.29). We elected to use the multi-segment function to permit as accurate a fit as possible. The peak plastic work was computed using the MEM fitting routines to integrate the plastic expansive strains up to the failure surface according to Equation 3.27. The peak plastic work from each test was then plotted as shown in Figure 5.6 and three straight line segments were fit using least-squares linear regression. The fit is specified in terms of the four pressure-peak plastic work data pairs given in Table 5.3 which correspond to the following parameters for Equation 3.28:

Segment	a_i	b_i
1	0.0037	0.118
2	0.10	-8.63
3	0.098	-8.33

The next step is to define the expansive yield hardening function given by Equation 3.25. Since the coefficient η_1 and the peak plastic expansive work have been previously defined, only the exponent $\bar{q}$ is needed to define the hardening function. In accordance with Equation 3.42, the triaxial test data is plotted as shown in Figure 5.7 using the MEM fitting routines. Then, $\bar{q}$ is computed at a value of $f_p''/\eta_1 = 0.80$ and plotted as a function of mean stress in Figure 5.8. A representative value for $\bar{q}$ is the average value of about 0.4. This yields the model relationship plotted in Figure 5.9 which is a good approximation of the test data plotted in Figure 5.7.

The final step in fitting the ARA 3-I model is defining the expansive flow rule and expansive plastic potential function as defined in Equations 3.34 and 3.35. Of the parameters in these functions, only the coefficient η_2 is yet to be determined. For Salem limestone, we elected to define η_2 as a multi-segment function of the expansive yield hardening (Equation 3.36). As outlined in Section 3.2.5, η_2 is computed from the expansive plastic strains using Equations 3.44 through 3.46 for each triaxial test.

Expansive plastic volumetric strains are plotted in Figures 5.10a through 5.10d as a function of shear strain for drained triaxial test data at confining stresses of 50, 100, 200, and 400 MPa. These plots are generated using the fitting routines in MEM. In the case of low confining stresses (50 and 100 MPa), the expansive plastic volumetric strains are initially compressive and then continuously dilative as the shear strain increases. In the case of high confining stresses (200 and 400 MPa), however, the expansive plastic volumetric strains show continuous dilation with no initial compression. To obtain representative average slopes for the computation of η_2, the expansive plastic strain data have been fit with segments described by quadratic least squares fits as shown by the solid lines in Figure 5.10. The plastic expansive strains are also compared to the total volume strain in Figure 5.10.

The plastic potential parameter η_2 (Equation 3.44) is then computed and plotted as a function of f_p'' (Equation 3.25) in Figure 5.11. The expansive plastic potential coefficients t_i and s_i (Equation 3.36) are then found by a least squares fit to the data as shown in Figure 5.11. The computed values of t_i and s_i are plotted as a function of the average mean stresses in Figures 5.12 and 5.13, respectively. Both t_i and s_i change rapidly at mean stresses near 200 MPa where the limestone undergoes a change of failure mode from brittle to ductile. Fits to these data are approximated as straight line segments with the plastic potential coefficients given in Table 5.3. This completes the specification of all the parameters required for representing the limestone skeleton with the ARA 3-I model.

5.1.2 Prediction of Drained Limestone Response

In this subsection the fit of the ARA 3-I model is verified by comparisons between numerical simulations and laboratory tests. First, MEM is used to compute a set of synthetic drained hydrostatic and triaxial compression test data for comparison to the data from which the material parameters are extracted. Next, the drained uniaxial strain response of Salem limestone is predicted and compared to drained uniaxial strain test data. This last comparison serves as a check of the model and material parameters against a set of test data obtained along a strain path not used in developing the model parameters.

The drained hydrostatic compression response computed by MEM is shown in Figure 5.14 along with the laboratory data. The calculation is in excellent agreement with the laboratory data. It should be noted that for this calculation, the expansive part of yield surface in the model is not active since material is in pure isotropic compression.

A series of four MEM calculations were performed to predict the drained triaxial compression response at confining stresses of 50, 100, 200 and 400 MPa. The computed results are presented in Figure 5.15 through 5.18 along with the corresponding laboratory test data for the corresponding confining stresses. For each confining stress, both stress differences and volumetric strains are plotted as functions of axial strain. Overall, the MEM calculations agree well with the laboratory drained triaxial compression test results. In the case of 200 MPa

confining stress, the MEM calculations shown in Figure 5.17b overpredict the peak volumetric strain by about 20%. This overprediction is probably due to the coarse linear approximation of the expansive potential parameter η_2 at the transition pressures between 150 MPa and 280 MPa.

The last MEM computation in this section is the drained uniaxial strain response prediction shown in Figure 51.9 and compared with test data. The computed axial stresses are slightly underpredicted in the elastic region and are slightly overpredicted beyond the elastic limit. Considering the ARA 3-I material parameters are solely determined fr- .. the drained hydrostatic and triaxial compression tests, such close agreement indicates strong potential applicability of the model to other more complex loading problems.

5.2   CONVENTIONAL TRIAXIAL COMPRESSION TESTING

In a triaxial compression test, a right circular cylinder of material is first loaded isotropically to a predetermined value of confining pressure. That confining pressure is then held constant while a compressive strain is imposed along the axis of the cylinder. The axial strain is applied to the sample by a hardened steel piston and the sample is supported at the opposite end by a similar hardened steel platen. Several triaxial compression tests at different confining pressures are typically used to define a strength envelope for a material.

Since the elastic modulus of the steel end caps is greater than that of a typical geotechnical sample, there is a mismatch in radial expansion between the sample and the mating steel surfaces, with the sample tending to expand more than the steel. If the interface were perfectly frictionless, this mismatch in radial deformation would not be significant since one surface would simply slide relative to the other leaving a state of pure normal stress acting across the interface. However, because there is friction, the unequal deformation imposes shear stresses on the ends of the sample in addition to the desired axial stress. These shear stresses are directed approximately toward the center of the sample and have the effect of increasing the effective confinement at the ends of the sample. As a direct result of this apparent elevated confinement near the sample ends, a typical triaxial compression sample has a nonuniform

distribution of radial strain along its axis, with substantially more radial expansion near the mid-height of the sample than at its ends, i.e. it becomes barrel shaped. This barreling effect can be sharply reduced in soils testing by lubricating the surfaces that mate with the sample. However, in rock testing, where tests are typically conducted at significantly higher pressures, lubrication was not in general use.

In order to account for nonuniform strains in test data interpretation, it is typically assumed that the test section of interest consists of the central third of the test cylinder. In that region the radial stress is equal to the confining pressure and the influence of end constraint is considered negligible. Under this assumption, the radial strain measured at sample mid-height, where radial expansion is greatest, is considered representative of the deformation under the nominal stress conditions. The strains in the radial and tangential directions are assumed to be equal as they would be if the loading were applied by a perfectly uniform normal traction on the ends and along the sides. Further, since axial strain is typically derived from a deformation measurement over the entire length of the sample, the axial strain is assumed to be uniform throughout the sample.

While there may be justification for these assumptions in dry or drained testing, they immediately lead to problems when applied to an undrained test. The strength measured in an undrained triaxial compression test is a function of the mean effective stress, which is equal to the difference between total mean stress and the pore pressure. The pore pressure depends on the change in volume of the pore spaces, which is closely related to volume strair Thus, the nonuniform radial strains and the corresponding nonuniform volume strains result in nonuniform development of pore pressures in the sample. If the sample is highly impermeable, a pore pressure gradient will be induced. If, on the other hand, the sample is sufficiently permeable to allow the pore pressure to equilibrate as the test progresses, then the pore pressure depends on the volume strain averaged over the entire sample and not at any one position. In either case, as illustrated by Figure 5.20, the volume strain measured at the center of the sample does not correspond to the pore pressure measured at one end.

5.3 SPECIAL TEST TO STUDY PORE PRESSURE AND VOLUME STRAIN

In an effort to understand the pore pressures measured in undrained triaxial compression tests, ARA conducted a small WES-sponsored test program to measure additional details of sample deformation. Limitations of available equipment precluded measurement of a complete radial strain profile during high pressure testing. Instead, the approach was to derive a shape function for the bulged shape that could be defined with a few measurements. The shape function was derived from a set of passive radial deformation measurements on triaxial test specimens. For the passive measurements, lines were scribed around the circumference of a virgin cylindrical sample of Salem limestone at approximately 6 mm spacings. The initial diameter and height above the base of each line were recorded prior to testing. The sample was then subjected to a typical triaxial compression test, and the circumfrential lines were remeasured. Active instrumentation consisted of three radial measurements, one at mid-height and two at different heights on one side of the middle, instead of the usual single gage at mid-height.

The passive radial deformation data obtained over the full sample height were used to derive a shape function which, in turn, was used to derive total volume strain estimates at each time increment from the three radial deformation measurements. As a validation of the volume strain measurement procedure, comparisons were made against total volume strain estimates derived from pore fluid displacement measurements made during saturated drained tests. Here, the volume of water drained from the sample during testing was measured and used to compute an alternative estimate of total volume strain. Throughout this procedure, the volume determination based on the shape function and three radial displacement records was found to be imperfect, but a very great improvement over the conventional technique.

Stress-strain data from a typical 200 MPa undrained triaxial compression test are shown in Figure 5.21. The figure does not include the hydrostatic loading portion of the test and begins with the initiation of the shear phase, i.e., the application of the axial strain at a constant confining pressure. The axial strain plotted in Figure 5.21 is an average over the entire sample height. Three radial strain curves are presented, corresponding to three different positions as

shown in the figure. The stress strain response is approximately linear up to an axial strain value of 0.95% where brittle failure occurs at a true stress difference of 125 MPa. As axial strain is further increased, there is a slight drop in stress difference, followed by a region of approximately constant stress. The stress difference then increases slightly at strains beyond 5%, eventually reaching almost 140 MPa before the test was unloaded at 15% axial strain.

Figure 5.22 depicts the measured pore pressure and Figure 5.23 presents volume strains determined through two different techniques from the same 200 MPa undrained test shown in Figure 5.21. Axial strain was selected as the independent variable for these plots because it is independently controlled during testing. As shown in Figure 5.22, the pore pressure increases from 105 MPa at the end of the hydrostatic phase to 145 MPa at the point of brittle failure (0.95% axial strain). From that point, there is a slight additional increase in pore pressure followed by a very slight decrease to 142 MPa at 15% axial strain. During the post failure shear, the pore pressure is nearly constant.

The volume strain determined in the conventional manner using the radial strain measured at mid-height and the average axial strain, Figure 5.23, shows an initial compressive volume strain peaking when the axial strain reaches 0.95%, corresponding to brittle failure of the sample. As axial strain increases, that measure of volume strain decreases, i.e., becomes more dilatant, until it reaches a value of approximately -7.5% at 15% axial strain. Comparison in Figure 5.20 of the relationship between pore pressure and volume strain before and after the brittle failure point leads to the conclusion that the apparent large increase in volume suggested by the conventional volume strain determination is inconsistent with the measured pore pressure. This result is to be expected since the conventional volume strain is derived from a radial deformation measurement at the largest point in a nonuniform radial strain distribution, a procedure which clearly overestimates the volume strain relative to the average total volume strain.

The total volume strain determination, based on three radial deformation measurements and the shape function, the second curve presented in Figure 5.23 shows markedly different behavior. In the small strain region, prior to brittle failure, the two curves are essentially

5-10

identical. Beyond that point, the total volume strain line stays within 0.5% of the zero volume strain line. While this is much more consistent with the pore pressure behavior, the variations are still greater than expected. Note that the variation in total volumetric strain is greater after failure (0.95% axial strain) than before but the pore pressure change occurs almost entirely before. It appears that both measures of volume strain result in a reasonably correct approximation in the region prior to brittle failure where the strains are relatively small and uniform. Subsequent to failure, both axial and radial strains grow very large with essentially zero change in stress difference. Here, it is very difficult to obtain an accurate measure of volume strain and neither method gives a volume strain determination with less than 0.5% variation in volume strain that would be required to completely resolve the details of pore pressure and volume strain behavior.

In the course of performing the passive shape measurements on the triaxial samples, it became apparent that there are nonuniform axial, as well as radial, deformations. Based on the pre- and post-test measurements, axial and radial strains were computed for each (approximately 6 mm) segment of the sample. The passive measurements were not designed to produce accurate axial deformation information. The width of the scribed lines was approximately 0.5 mm, and over the gage length of 6 mm, an error of half a line width translates to 5% axial strain. In spite of the measurement inaccuracies, the passive data clearly indicate the axial strain is larger at the center of the sample than at the ends. Figure 5.24 shows profiles of radial, axial and volume strain along the axis of a 47.5 mm diameter by 95.8 mm long sample that were computed from the passive measurements, along with an indication of the average axial strain based on the overall length change of the sample. Figure 5.25 presents a scatter plot of radial and axial strain computed from the passive measurements for the individual sample segments. Also shown is a least squares fit demonstrating the trend in the data.

The non-uniformity of axial strain is significant even in the case of drained triaxial compression where the conventional assumptions described in Section 5.3 are applicable. To the first order, the volume strain computation consists of adding the axial strain, which is positive, and twice the radial strain, which is negative. Thus, the volume strain is the difference of two numbers of like magnitude and is very sensitive to small changes in either number. In

5-11

the case where the test section is considered to be the central third of the sample and the radial strain is measured at or near the largest point on the bulged section, an underestimate of the axial strain near the mid height would result in an overestimate of the dilatancy at that measurement point. This is exactly what happens when the axial strain is measured in the conventional manner by averaging over the entire length of the specimen.

5.4 NUMERICAL SIMULATIONS OF UNDRAINED TRIAXIAL COMPRESSION TESTS

As described in the previous section, it is known that the loading conditions in real triaxial compression tests, while approximating the desired perfectly normal traction, actually include shear stresses that cause significant non-uniformities in the induced stress and strain fields. In an effort to better understand the actual behavior of the material during these tests, finite element simulations of the test were performed using MEM, the two-phase material modeling program with fluid transport that is described in Section 2. The material models discussed in Section 3 and the parameters discussed earlier in this section were used in these calculations. An effort was made to correctly model the non-ideal behavior that occurs during a real test. A ten-by-ten multi-element axisymmetric grid was used in order to model any stress and strain gradients in the sample. A symmetry boundary condition was used at sample mid-height, making it necessary to explicitly model only one half of the sample. The finite element grid and boundary conditions are shown in Figure 5.26. At the end where the hardened steel end cap bears on the sample, boundary constraints were set to allow no deformation parallel to the interface, an idealization that slightly exaggerates the physical effect observed in the tests. The flow of pore water from element to element within the mesh was modeled in these simulations.

Since the multi-element version of MEM does not currently have the capability to change from stress to displacement boundary conditions in the course of one run, the analysis was started with the hydrostatic load already in place. The initial pore pressure, porosity, and permeability were computed based on the 200 MPa confining pressure and input to the calculation. The confining pressure was held constant throughout the calculation and no pore

fluid drainage was allowed. In the axial direction the loading was strain controlled. The applied axial strain was linearly increased with time to a maximum of 15% at 3000 seconds (50 minutes), approximating the duration of an actual laboratory test.

Figure 5.27 presents radial, axial, and volume strain contours computed from the output of the MEM analysis of a 200 MPa undrained triaxial compression test. The plots in Figure 5.27 represent the end of the analysis where the average axial strain was 15% (positive strain represents compression). The contour plots exhibit the same trends observed in the test data. There is a significant variation in both axial and radial strain along the axis of the sample. The axial strain varies from 4 to 10% at the end of the sample and from 20 to 26% at mid-height. At approximately the quarter point of the sample, the axial strain is equal to the average value of 15%. Similarly, in the radial direction the strain is essentially zero at the end cap, where the boundary condition prevents radial deformation, and at mid-height radial expansion ranges from 10 to 15%. Taken together to arrive at volume strains, these data show a net compression near the end of the sample and a net expansion at the center. Another result that has been consistently obtained in the calculations, but which does not make a very interesting plot is constant pore pressure throughout the grid. This indicates that strain rates during the test are slow enough to permit pore pressures to equilibrate and that pore pressures measured at the base are representative of those throughout the specimen.

The above results are all at least qualitively in agreement with the test data. The volume strain contours clearly show that the sample undergoes a loss of void volume near the end caps with a corresponding void volume increase near the center. This is accompanied by a redistribution of pore water within the sample, with the water migrating from the ends toward the center.

One way of comparing the MEM results with test data is to assume the calculational results represent test measurement and to process them in exactly the same manner as test data. Figure 5.28 shows pore pressure plotted as a function of volume strain. Included are two different curves computed from the 200 MPa MEM simulation along with the same test data that was presented in Figure 5.20. The dashed curve was computed from the MEM output in the

same way the test data curve was computed from measurements. In both cases the conventional approach was used, with axial strain based on overall axial deformation of the sample and radial strain computed from the radial deformation at mid-height. Both curves indicate that the pore pressure initially increases to a peak, corresponding to the initial compression and cementation crushing, at a fraction of a percent positive (compressive) volume strain. In the initial loading regime where volume strains are relatively uniform and measurements are relatively accurate, the slopes of the curves representing test data and finite element analysis are reasonably consistent and are representative of the expected sensitivity of pore pressure to volume strain.

As loading continues, the pore pressure in the test data remains essentially constant while there is a steady pore pressure decrease in the calculation. This indicates that the net pore volume in the test sample stayed approximately constant through this phase of loading. In contrast, the calculation appears to have undergone a slight volumetric expansion, resulting in a pore pressure drop. The dilatancy in the computational model of the rock skeleton is not surprising considering the fact that the skeleton model was derived from test data processed in the conventional manner which has been shown to overestimate dilatancy.

Both the test data and the MEM output that was processed like test data have rates of change of pore pressure with volume strain in the post-crush-up regime that are significantly low, i.e., well below the expected sensitivity of pore pressure to volume strain as characterized by comparison with the initial loading slope. The third curve on Figure 5.28 shows volume strain computed from the MEM output by taking the actual volume change element by element and summing over the entire grid. The slope of this curve is consistent with the initial loading slope as the skeleton dilates and the pore pressure diminishes.

Figure 5.29 is a plot of volume strain as a function of axial strain, comparing experimental and analytical results for both the volume strain determined by the conventional laboratory approach and the total volume strain averaged over the entire sample. The figure shows that when the volume strains are computed consistantly, there is good agreement between the test data and the finite element simulation. The figure also clearly demonstrates the importance of correctly interpreting the strain definitions in a manner relevant to undrained

testing. Finally, comparison of Figure 5.29 to 5.28 emphasizes the sensitivity of the pore pressure to changes in volume strain and suggests that pore pressure response data from undrained tests might provide an excellent means of fine tuning the dilatancy parameters in the material model.

5.5   CONCLUSIONS RELATED TO UNDRAINED TRIAXIAL TESTING

The use of numerical calculations of laboratory tests is a powerful tool for improved understanding of test results and for obtaining more accurate material model parameters. The comparisons presented in this section have demonstrated good agreement between laboratory test results and two-phase finite element simulation with fluid transport. Because of inaccuracies in the skeleton model parameters, the simulation predicted more dilatancy than was actually observed in the laboratory. This raises the possibility of performing iterative numerical calculations of test results to better define the model parameters. Since the pore pressure response in an undrained test is very sensitive to small changes in pore volume, pore pressure response is well suited for fine tuning the volumetric strain behavior of a model.

The lab test results and the simulations are both consistent with the fundamental view that pore pressure response is a function of total volume change. In an undrained triaxial compression test, volumetric compression occurs near the ends of the sample because of the lateral constraint imposed by the end caps. Near the center of the sample, volumetric expansion occurs due to shear induced dilatancy. Because of the variation in volumetric response along the axis of the sample, pore pressure gradients are induced which in turn cause flow of pore water from the ends of the sample where the volume is being reduced to the center of the sample which is expanding.

While it is clear from post-test inspection of triaxial compression test samples that there is a non-uniform radial strain response, both laboratory measurements and finite element simulations support the less obvious conclusion that there are also non-uniform axial strains. Axial strains are smaller than average in the constrained material near the ends of the sample

5-15

and larger than average in the less constrained material at the center of the sample. Thus, the volume change response computed at the center of the sample based on radial strain at the center and average axial strain tends to be significantly more expansive than the actual behavior at any point in the sample. This introduces errors in model parameters causing the models to predict more dilatancy than actually occurs.

Table 5.1. Physical Properties of Salem limestone.

Property		Value	Units
Specific Gravity of the Solid Grains	G_s	2.72	----
Porosity	n	0.128	---
Saturation	s	100	%
Dry Bulk Density	γ_{dry}	2.37	Mg/m^3
Saturated Bulk Density	γ_{sat}	2.50	Mg/m^3

Table 5.2.   Grain compressibility parameters for Salem limestone.

Parameter		Value	Units
Initial bulk modulus of grains	K_g	69,000	MPa
Initial mass density of grains	ρ_o	2.72	Mg/m^3
Initial wave velocity at low pressure	c_o	6,760	m/s
Initial Poisson's ratio	ν_o	0.25	--
Constant relating loading wave velocity to peak particle velocity	S	1.5	--
Threshold pressure beyond which solid grains behave like a fluid	p_b	5,000	MPa

Table 5.3. ARA 3-I model parameters for Salem limestone.

Model Parameter	Input Variable	Value		[MPa]
Stress units used in fit	IUNITS	6		
T, Pa	APEX, ATMO	32.0,	0.1014	
K_{ur}, n, ν	AKUR, AN, APOI	71,560,	0.2286,	0.25
r	AR, ACRV	2.0, 4		
c_i, p_i (i = 1 to ACRV)	AACC(i), AAPC(i) —, — —, — AACC(ACRV), AAPC(ACRV)	3.228e-6,	0.7198 3.096 1.444 0.6921	
		1.534e-21,		
		1.358e-9,		
		6.458e-4,		
$\bar{E}$, m, η_1	AEY, AMY, AETA1	0.1111,	4.203e-6,	0.4197
Option for plastic potential definition	NETA2	1 [multi-segment fit for η_2]		
Number of points defining η_2	NPTS	4		
$\sigma_{oct}(i)$	SOCTA(i) . . . . SOCTA(NPTS)	76.66,	150.5,	282.1, 532.0
t_i (i = 1 to NPTS)	ATGA(i) . . . . ATGA(NPTS)	-1.481,	1.557,	0.05761, 0.07134
s_i	ASGA(i) . . . . ASGA(NPTS)	4.222,	4.166,	0.4532, 0.1666
Option for specifying $W_{p,peak}$	NWPPK	1 [multi-segment for $W_{p,peak}$]		

Table 5.3. ARA 3-I model parameters for Salem limestone (Continued).

Model Parameter	Input Variable		Value		
Pressure points defining $W_{p,peak}$ $W_{p,peak}$ corresponding to pressure points	PDPK(i) . . . . PDPK(4)	-32.0,	90.79,	165.4,	608.3
	WPDPK(I) . . . . WPDPK(4)	0.0,	0.4509,	7.844,	51.19
$1/\bar{q}$	AALPH	2.634			
λ, γ, β, K_i	AHLAM, AHGAM, AHBET, AHBLK	0.644, 0.487, [ARA elastic model]	0.893 24,000.		

5-20
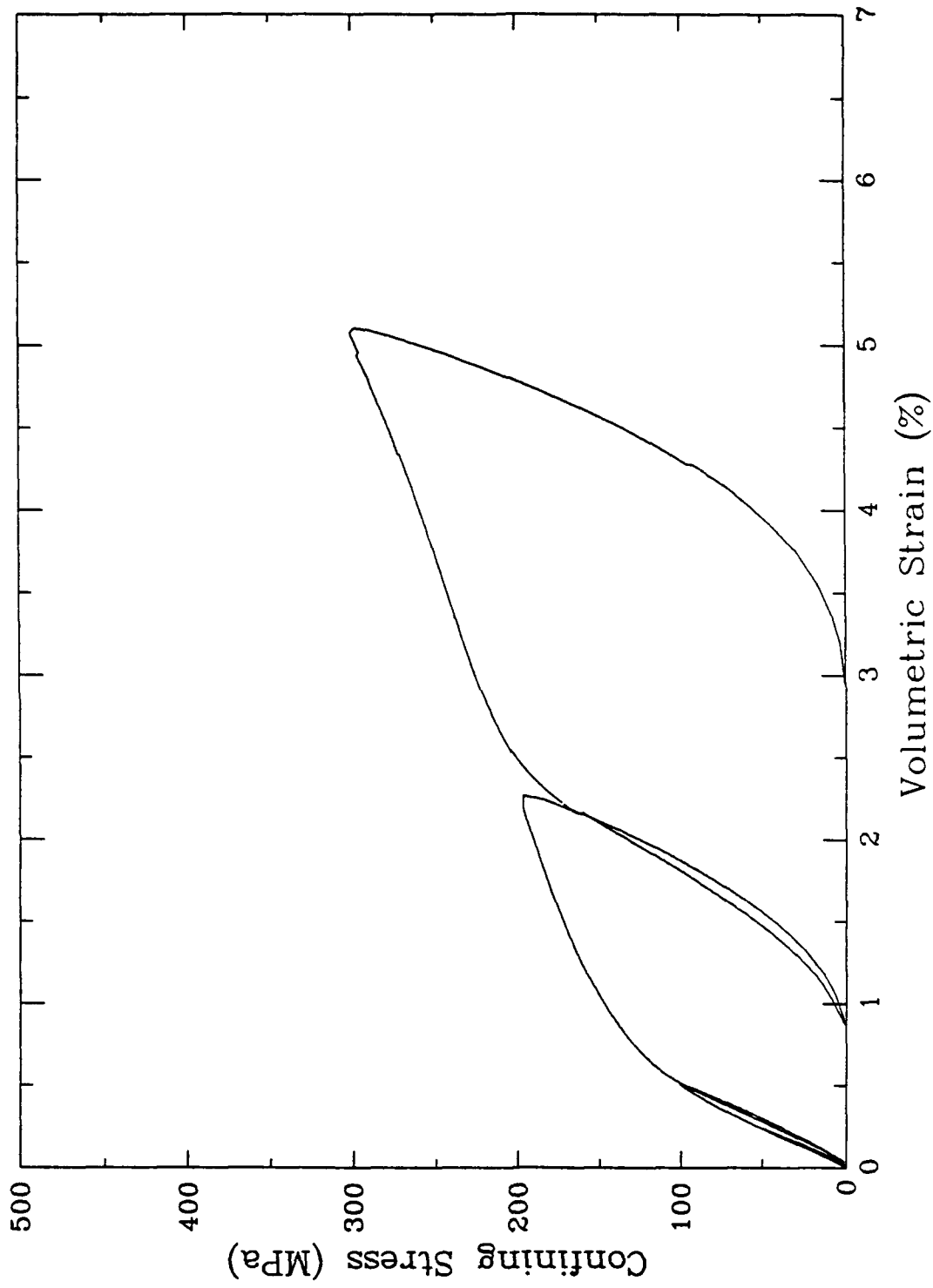
Figure 5.1. Pressure vs. volumetric strain in cycled hydrostatic compression test for Salem limestone.
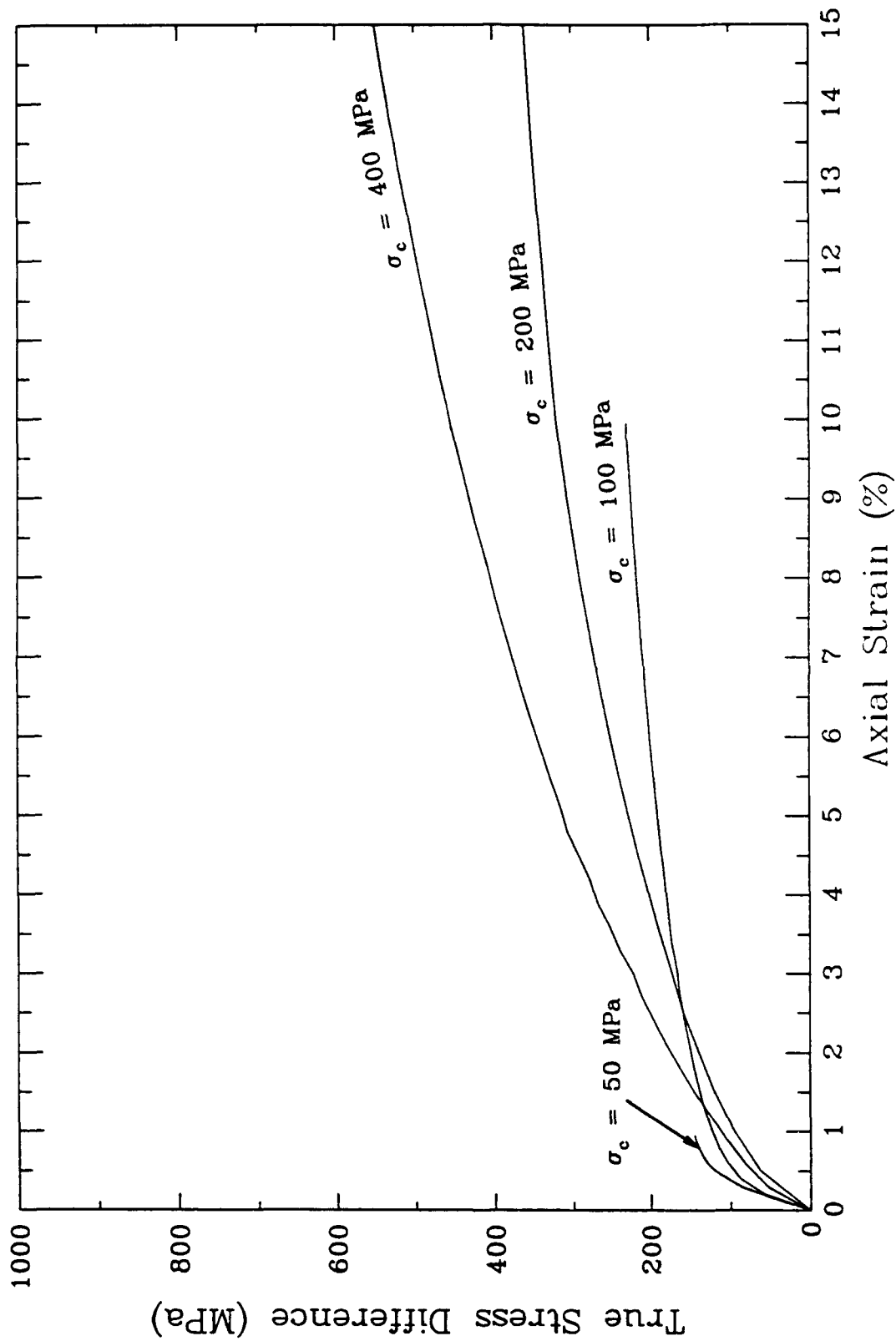
Figure 5.2a. Stress vs. axial strain in triaxial compression test for Salem limestone.
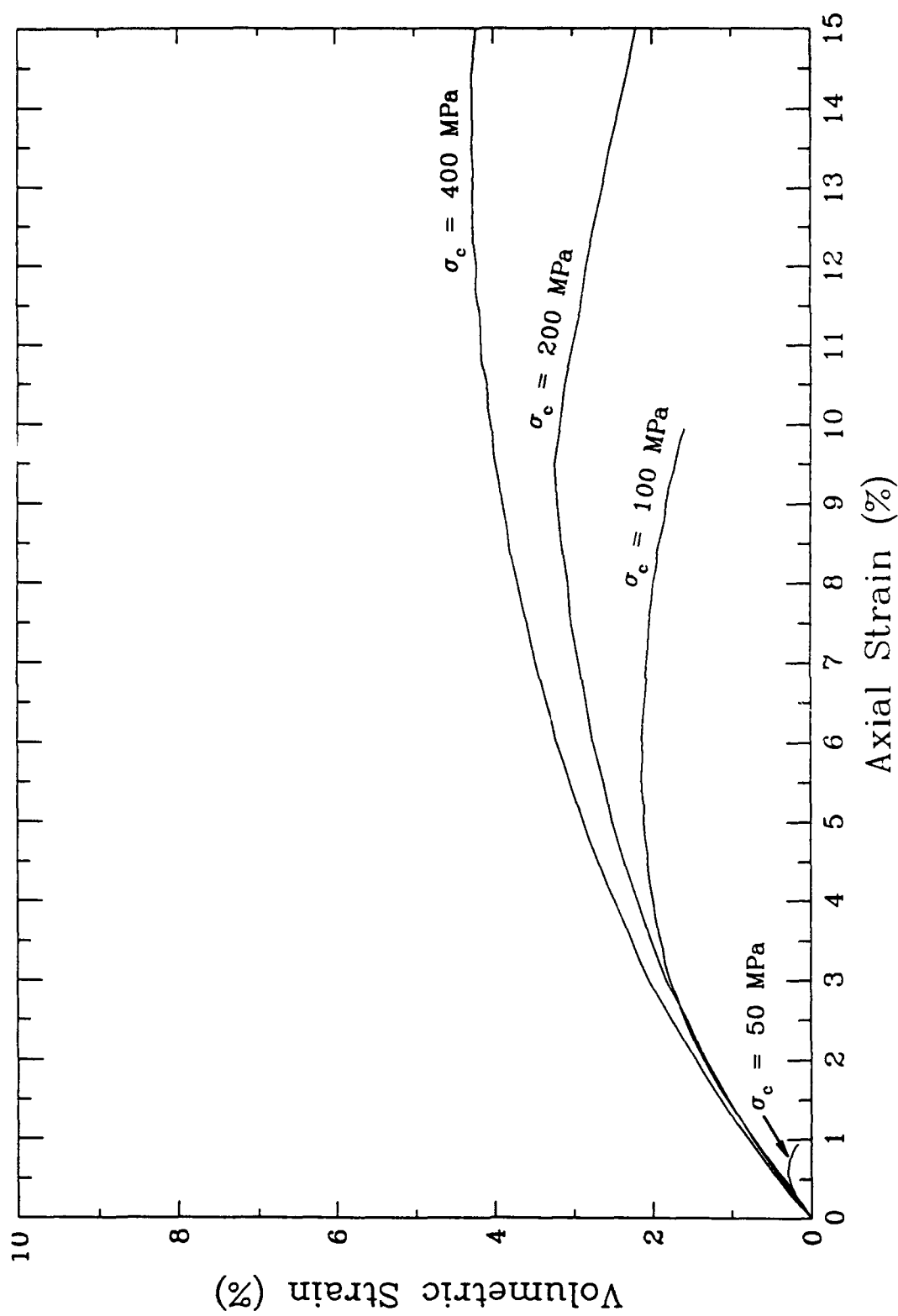
Figure 5.2b. Volumetric strain vs. axial strain in triaxial compression test for Salem Limestone.
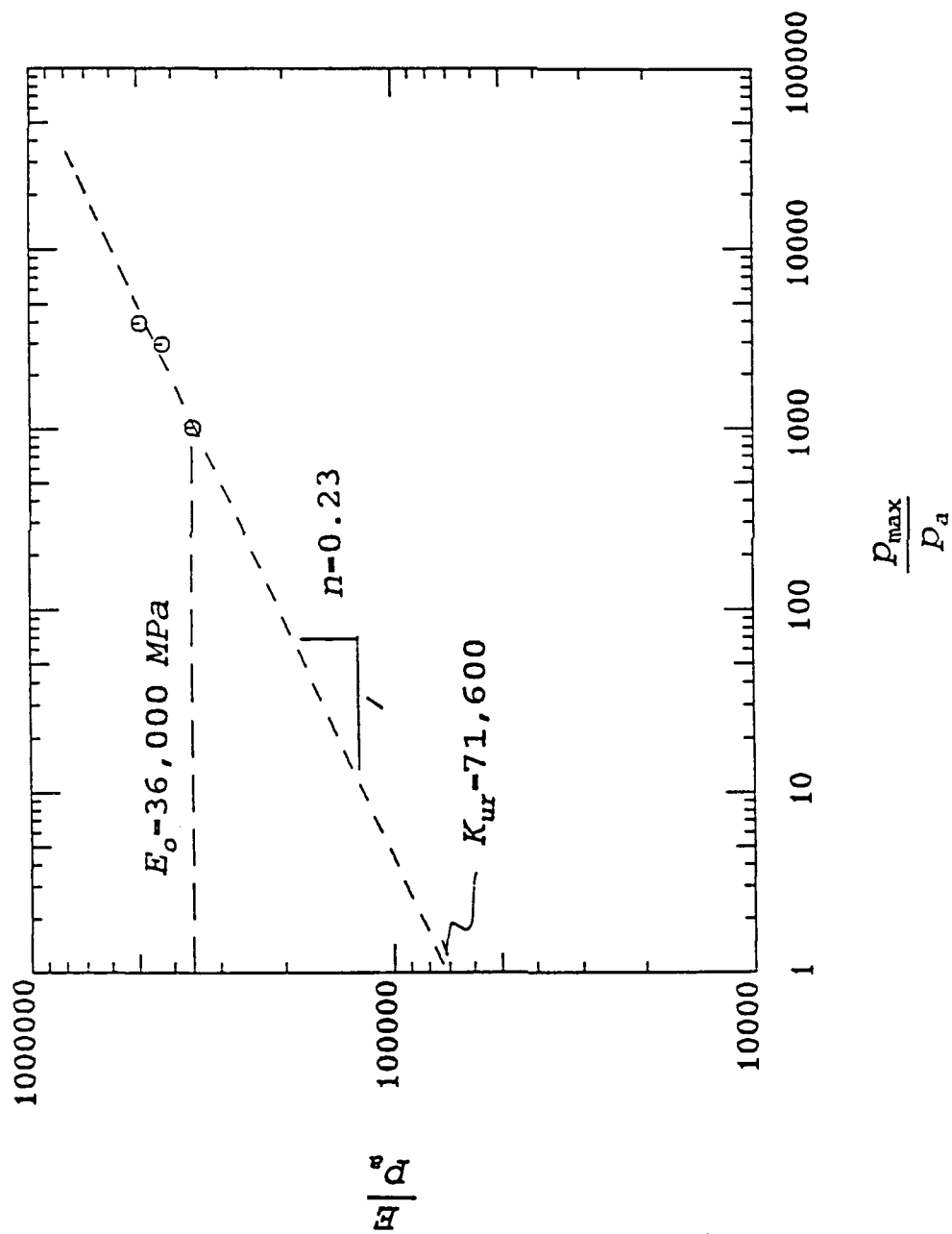
Figure 5.3.   Elastic Young's modulus as a function of previous maximum mean stress.

ARA 3-I MODEL PARAMETER FIT
MAT = SALEM LIMESTONE
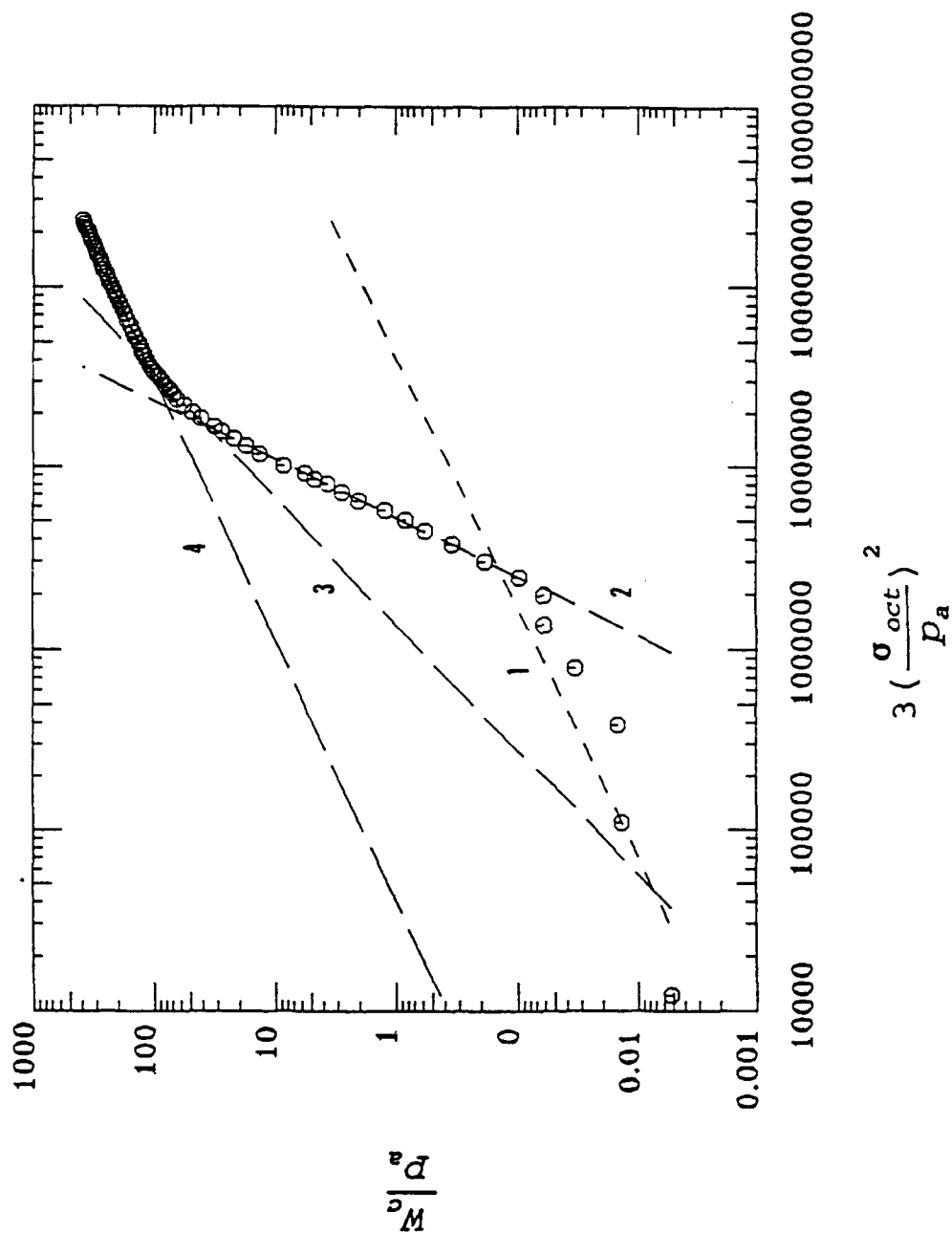
Figure 5.4. Compressive plastic work as a function of mean stress in the virgin hydrostatic compression test.
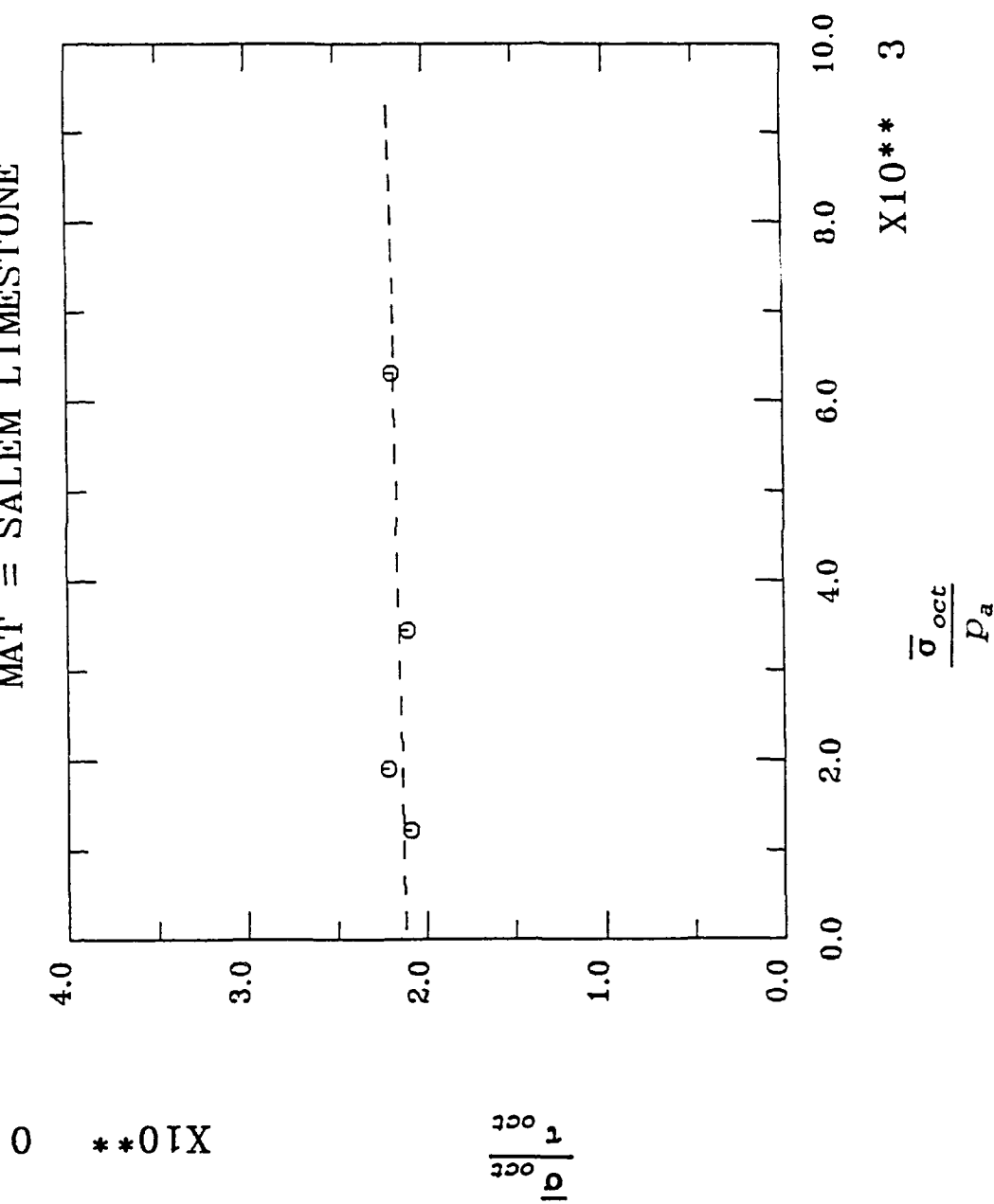
Figure 5.5. Shear strength envelope.
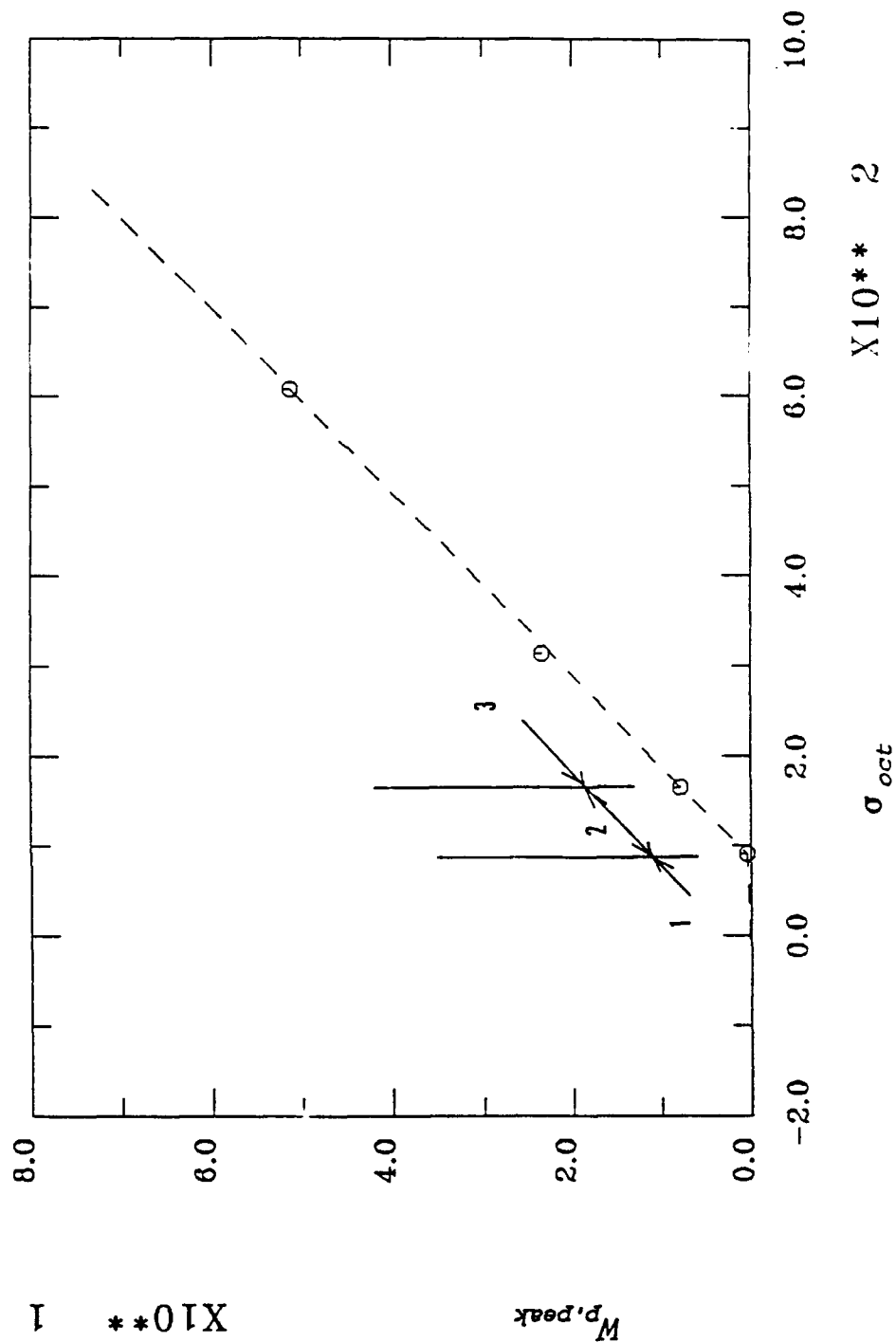
Figure 5.6. Peak expansive plastic work as a function of mean stress.
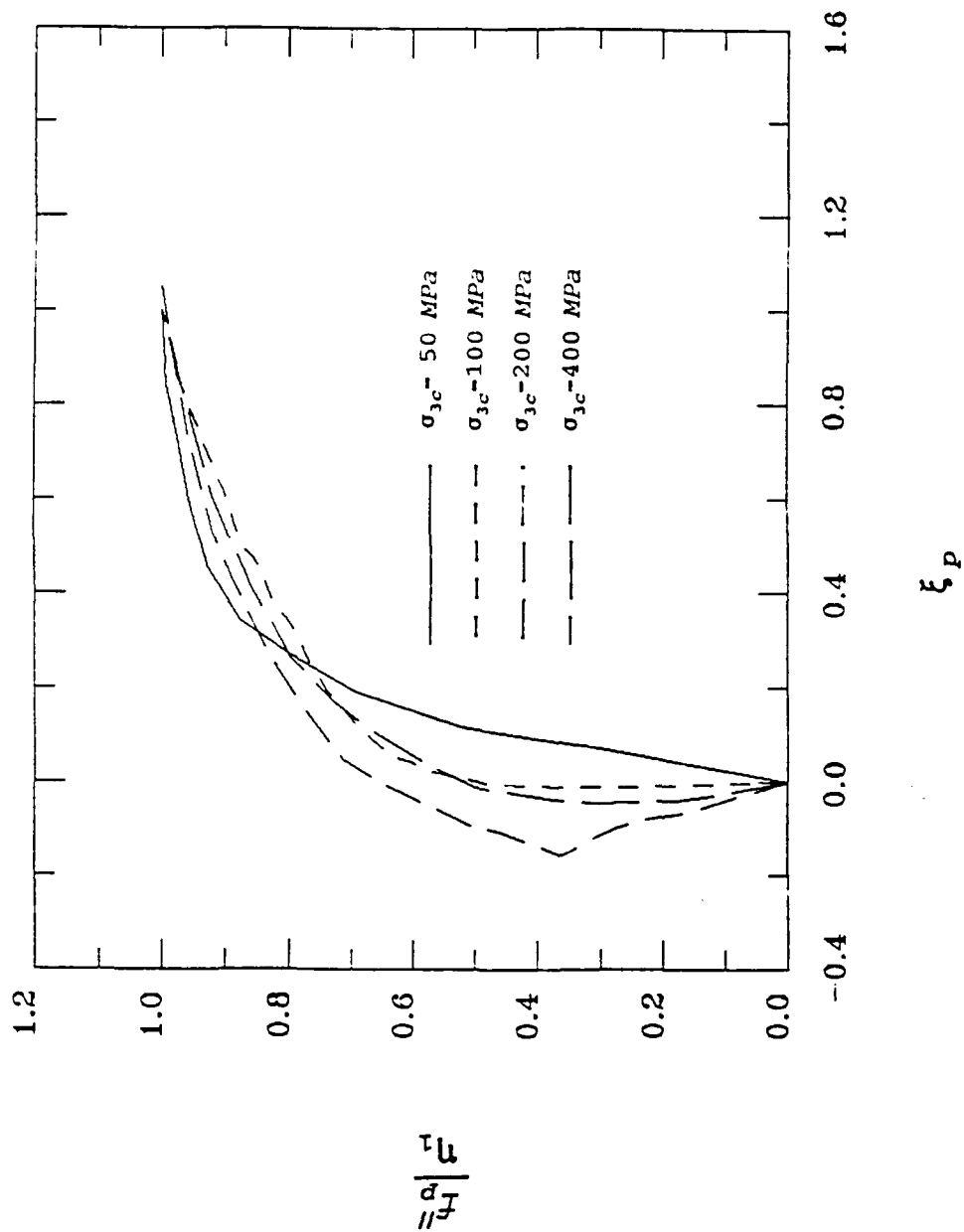
Figure 5.7. Expansive plastic hardening function as a function of normalized expansive plastic work.

ARA 3-I MODEL PARAMETER FIT
MAT = SALEM LIMESTONE
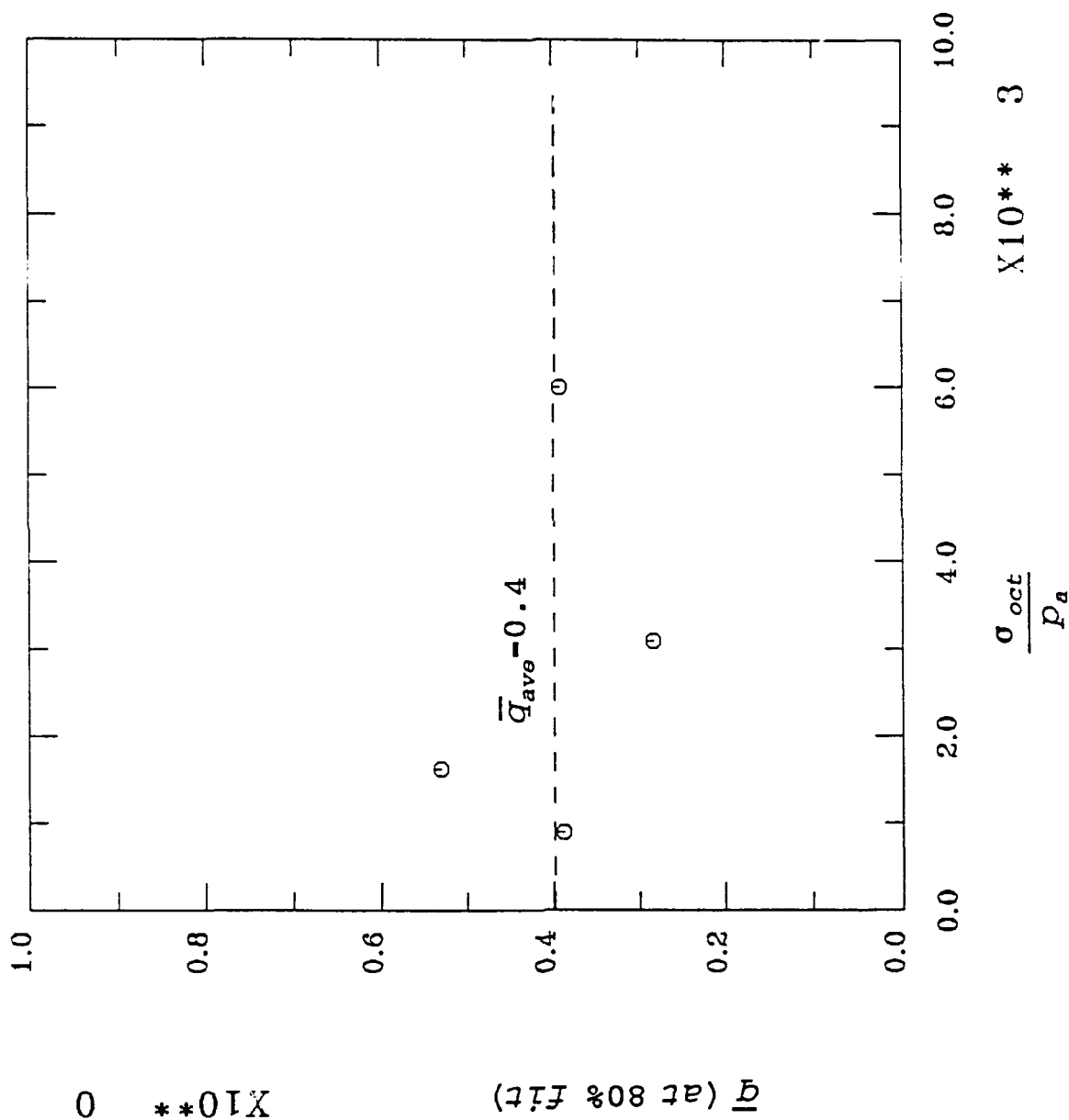
Figure 5.8. Expansive hardening parameter of $\bar{q}$ at 80% fit.

ARA 3-1 MODEL PARAMETER FIT
MAT = SALEM LIMESTONE

$$f_p'' = e^{\bar{q}(1-\xi_p)} \xi_p^{\bar{q}}$$

$$\text{where } \bar{q} = 0.4$$
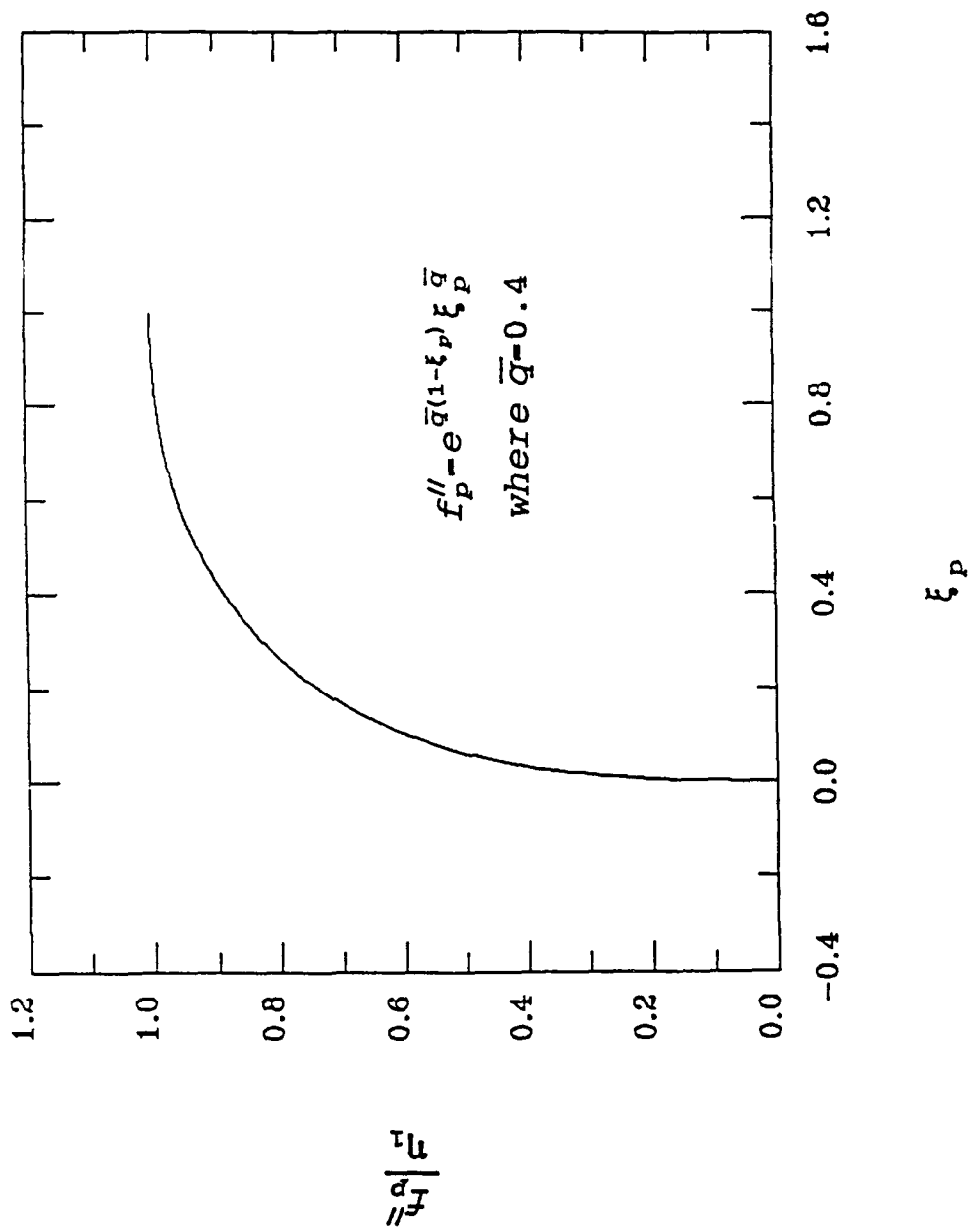
Figure 5.9. Expansive plastic hardening function vs. normalized expansive plastic work for $\bar{q} = 0.4$.
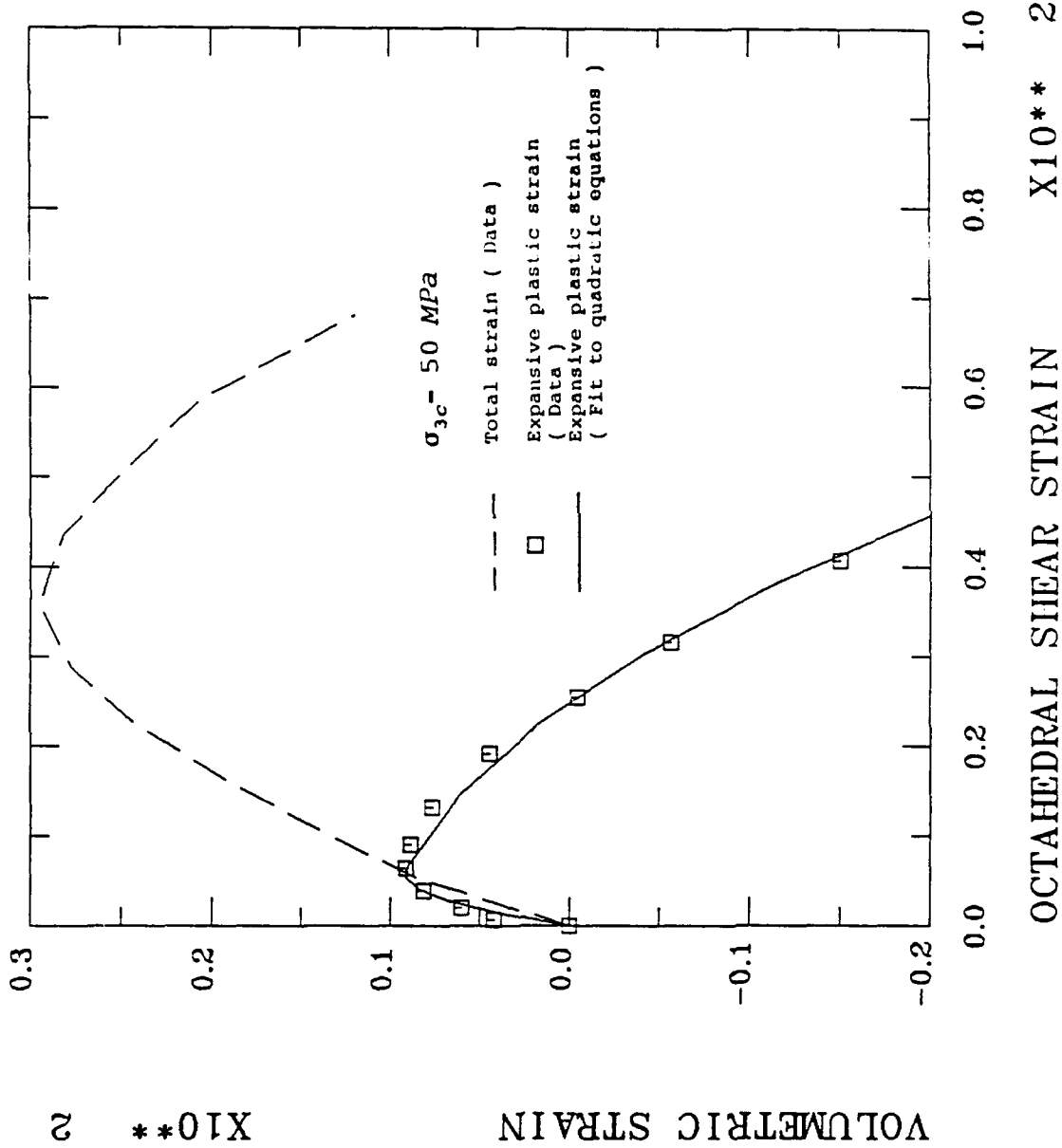
Figure 5.10a. Expansive plastic volumetric strain vs. octahedral shear strain in the drained triaxial compression test at σ_{3c} = 50 MPa.

ARA 3-1 MODEL PARAMETER FIT
MAT = SALEM LIMESTONE

σ_{3c}=100 MPa

- - - Total strain (Data)

□ Expansive plastic strain (Data)

—— Expansive plastic strain (Fit to quadratic equations)

OCTAHEDRAL SHEAR STRAIN   X10** 0

VOLUMETRIC STRAIN   X10** 0
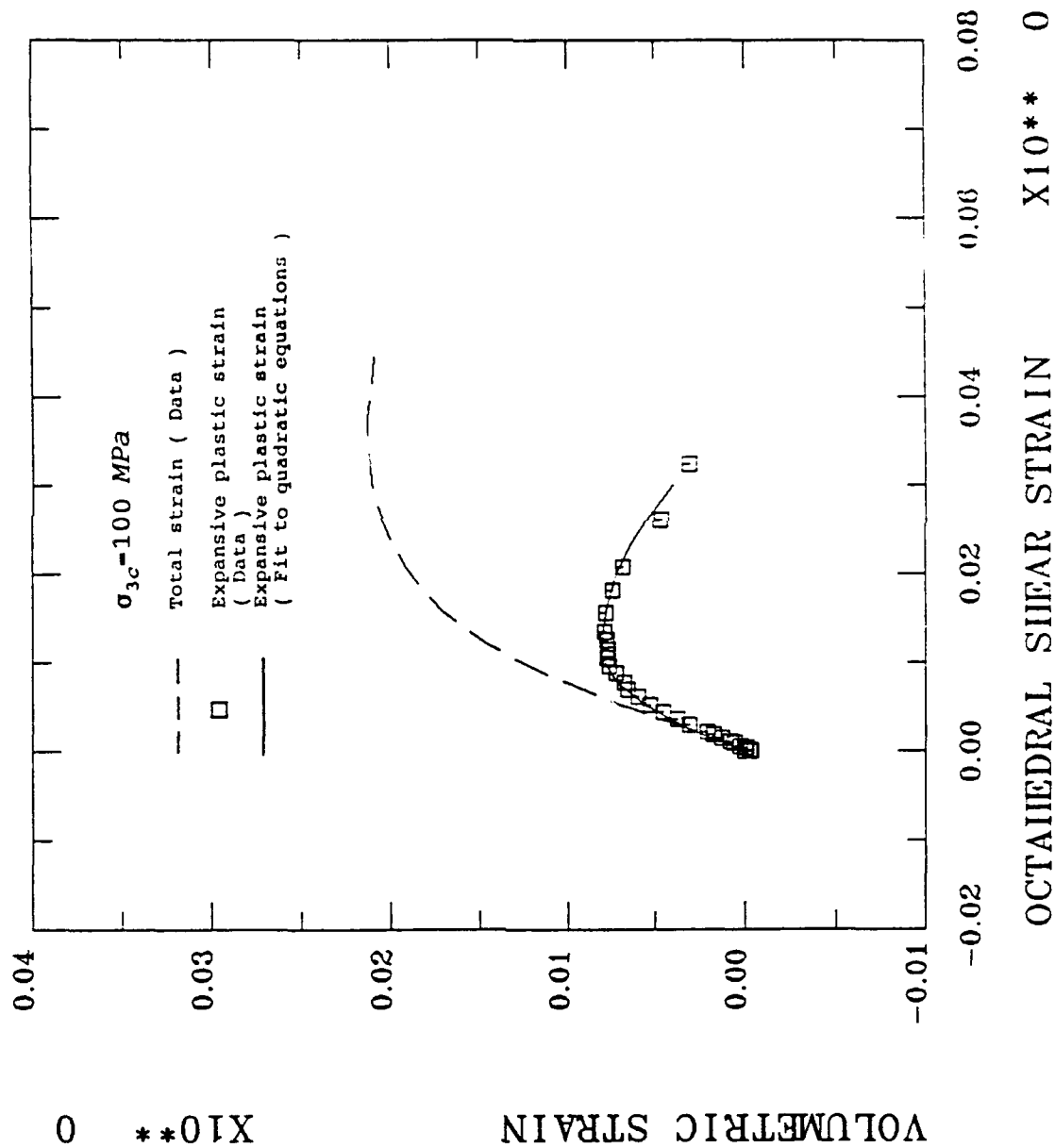
Figure 5.10b. Expansive plastic volumetric strain vs. octahedral shear strain in the drained triaxial compression test at σ_{3c} = 100 MPa.
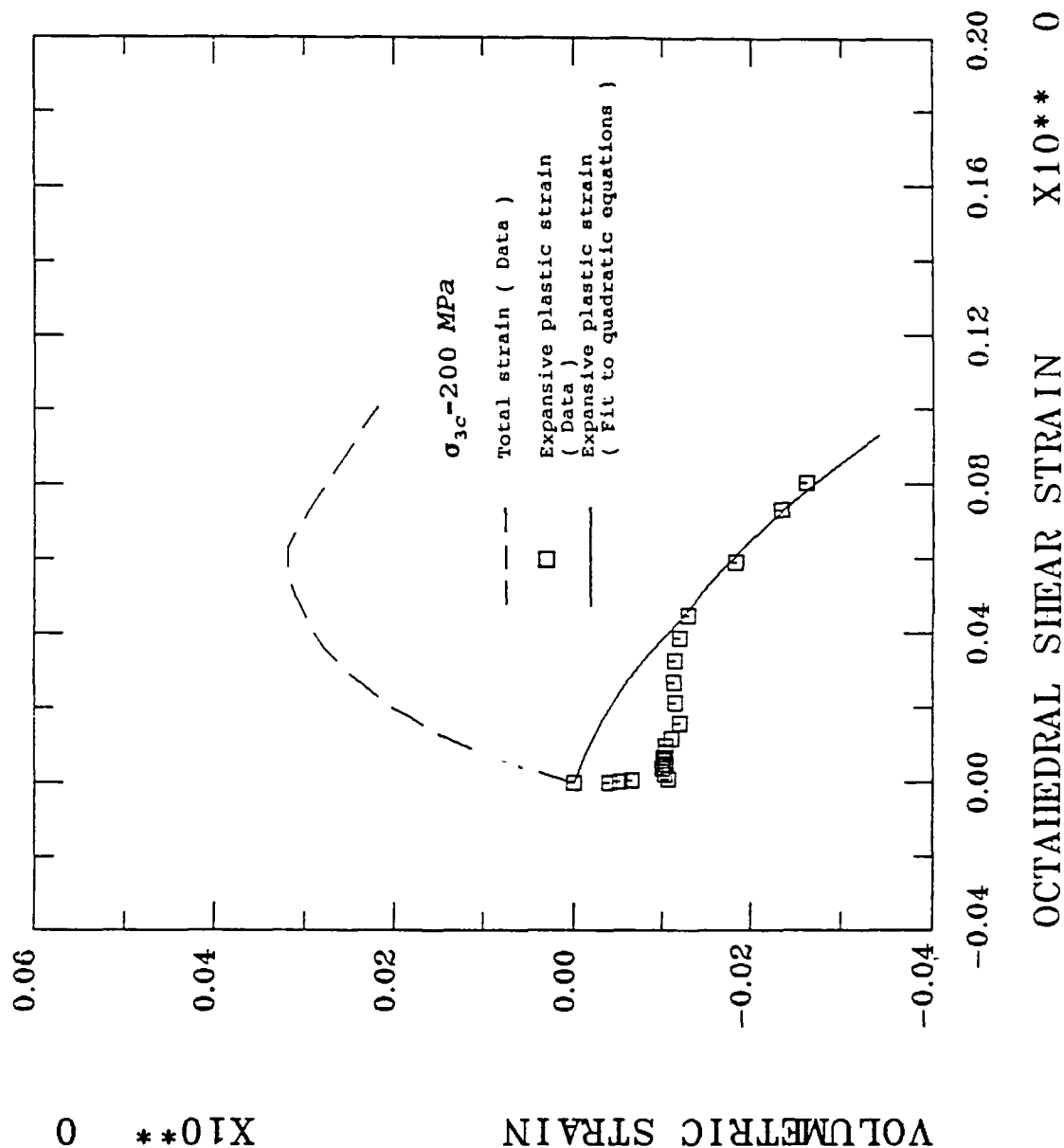
Figure 5.10c. Expansive plastic volumetric strain vs. octahedral shear strain in the drained triaxial compression test at σ_{3c} = 200 MPa.
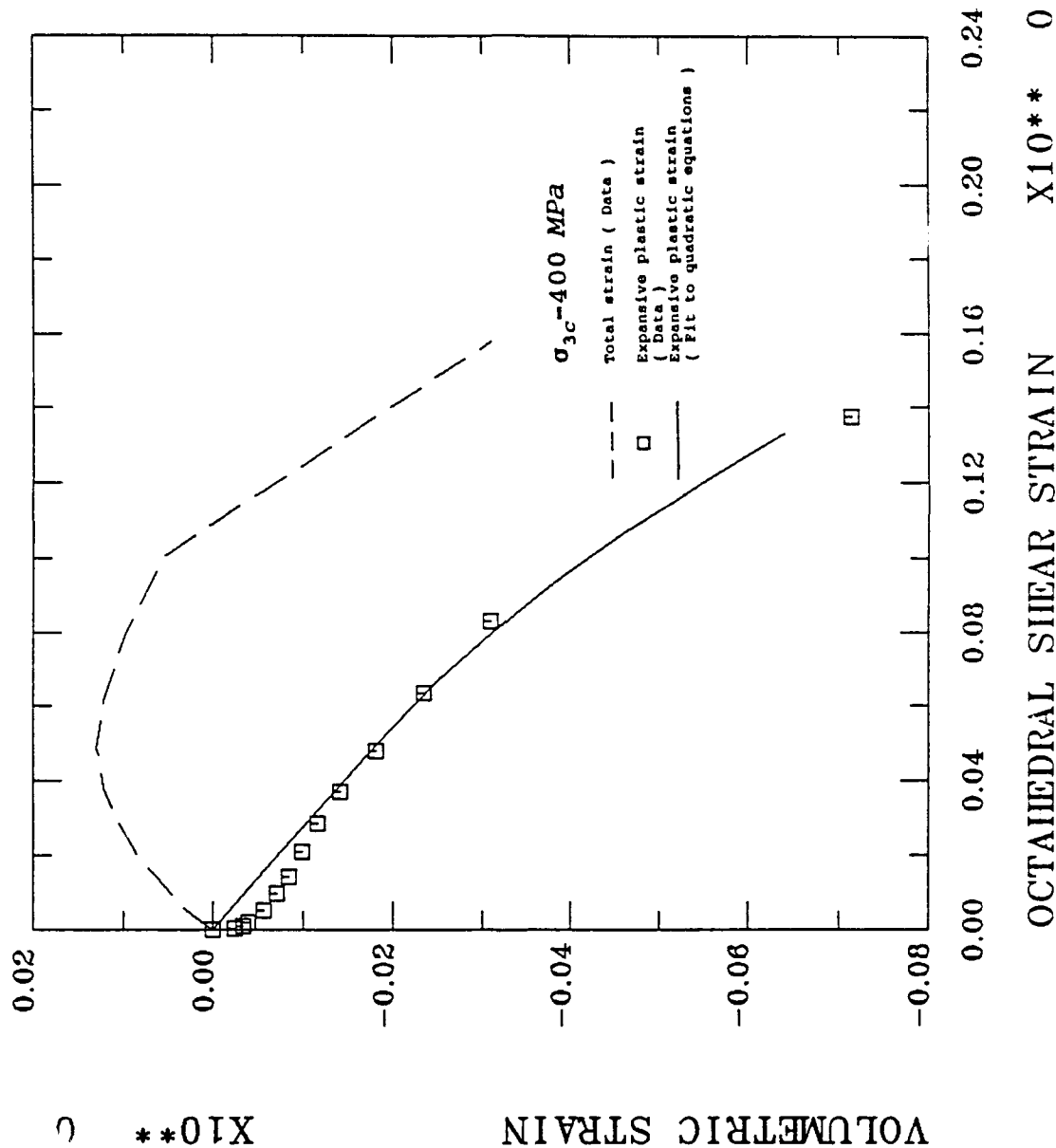
Figure 5.10d. Expansive plastic volumetric strain vs. octahedral shear strain in the drained triaxial compression test at $\sigma_{3c} = 400$ MP$_a$.

ARA 3–I MODEL PARAMETER FIT
MAT = SALEM LIMESTONE

$$\eta_2 = t_i + s_i f_p^{\prime\prime}$$
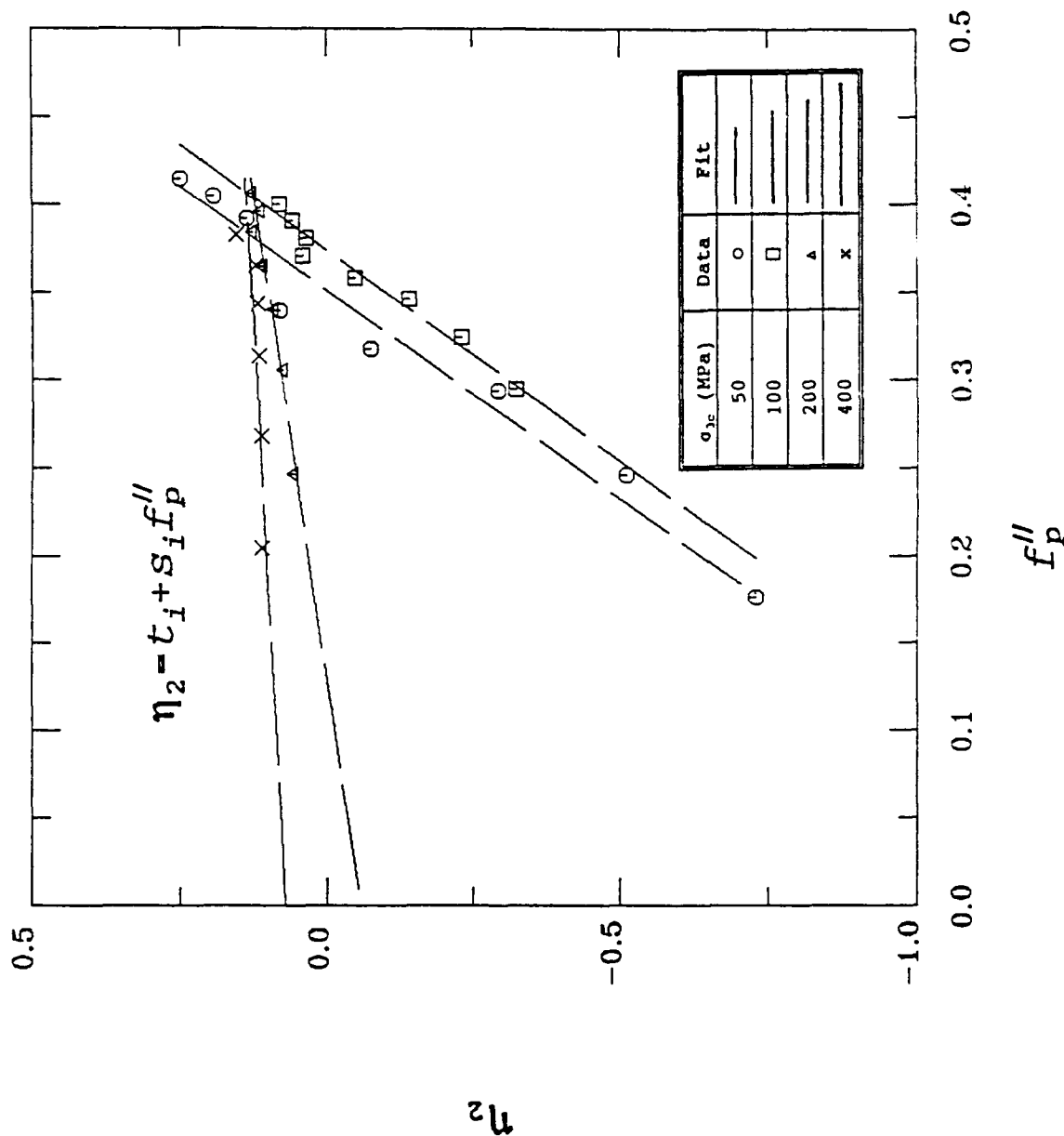
Figure 5.11. Expansive potential parameter η_2 vs. expansive hardening function $f_p^{\prime\prime}$ in the drained triaxial compression tests at $\sigma_{3c} = 50$, 100, 200, and 400 MP$_a$.

ARA 3-I MODEL PARAMETER FIT
MAT = SALEM LIMESTONE
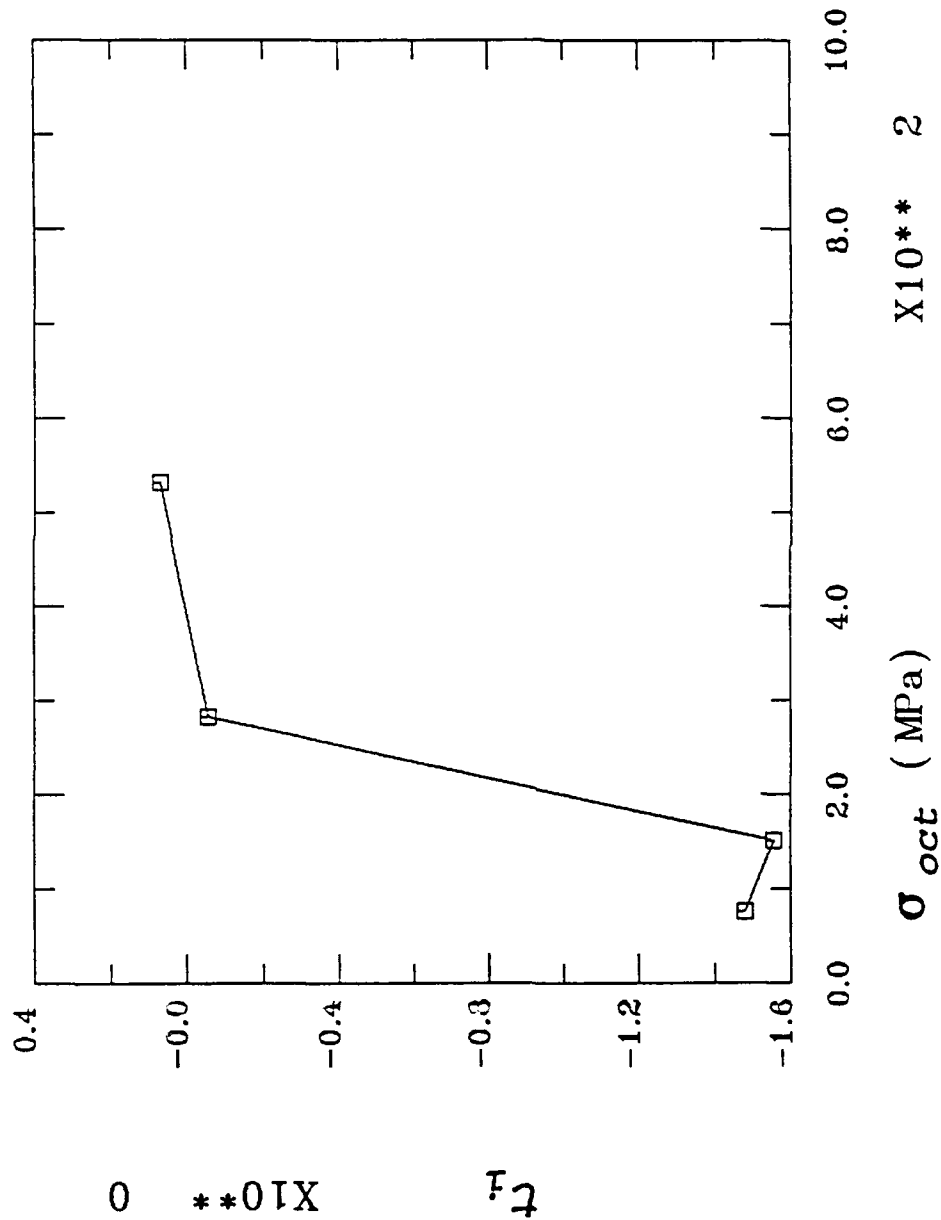
Figure 5.12. Coefficient t_1 as a function of mean stress.

ARA 3-I MODEL PARAMETER FIT
MAT = SALEM LIMESTONE
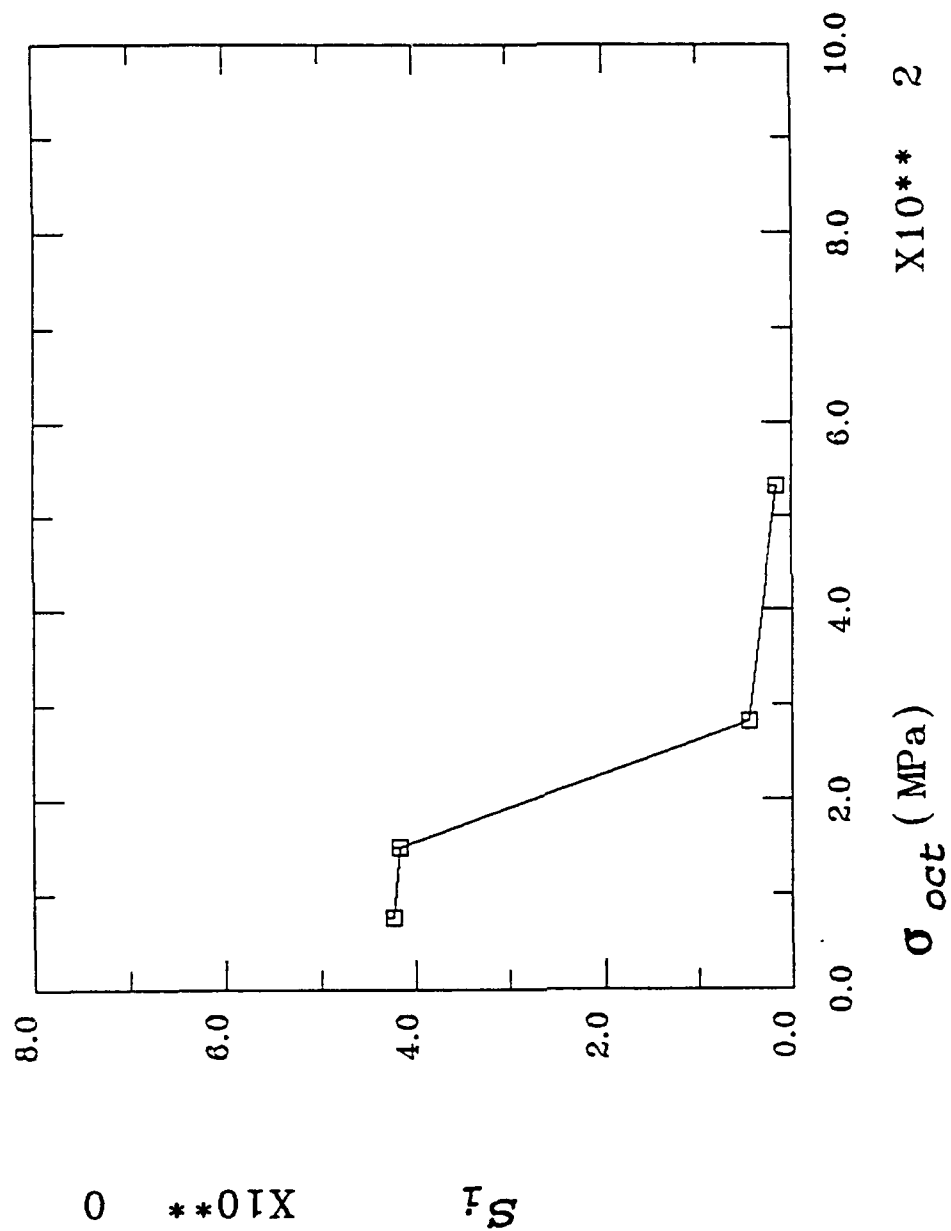
Figure 5.13. Coefficient s_i as a function of mean stress.
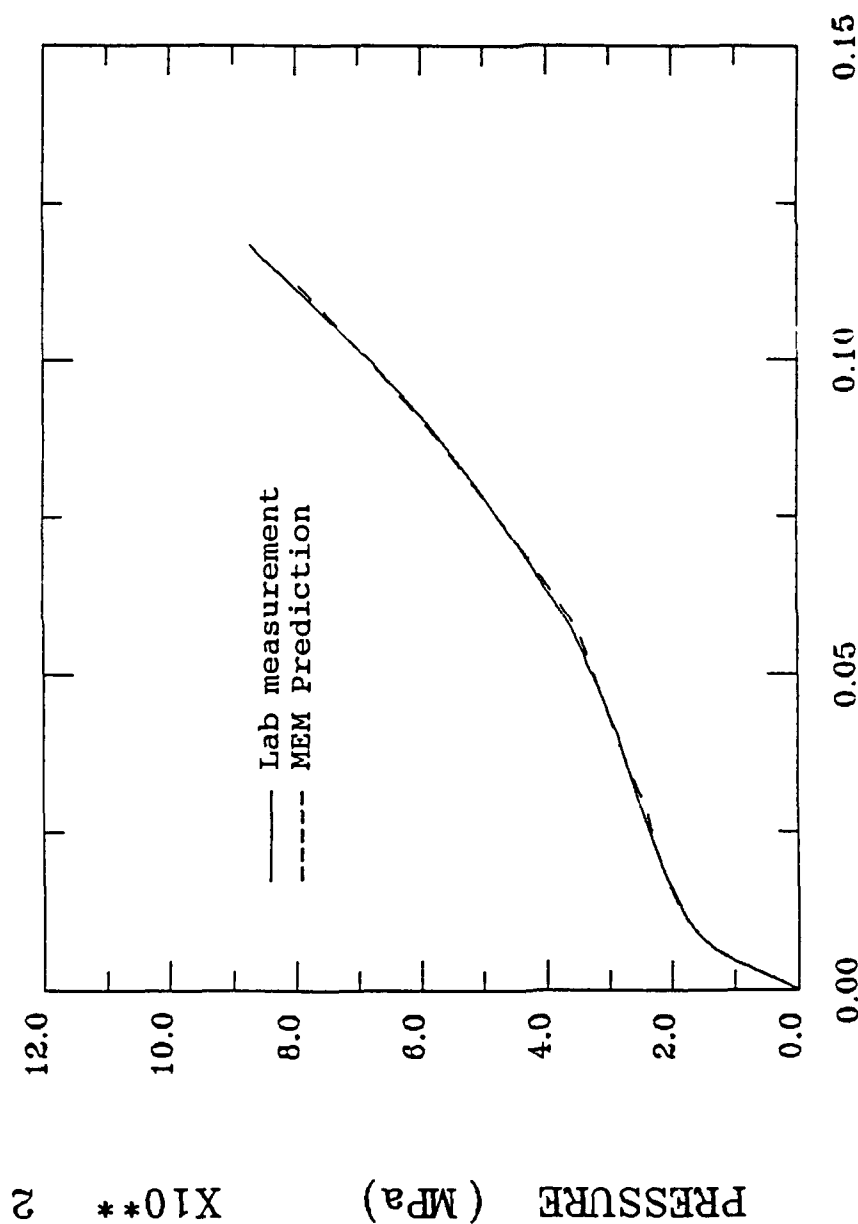
Figure 5.14. Pressure vs. volumetric strain in teh drained hydrostatic compression, MEM prediction compared with lab measurement.

MEM PREDICTION (TXC AT SIG3 = 50 MPa)
MAT = SALEM LIMESTONE
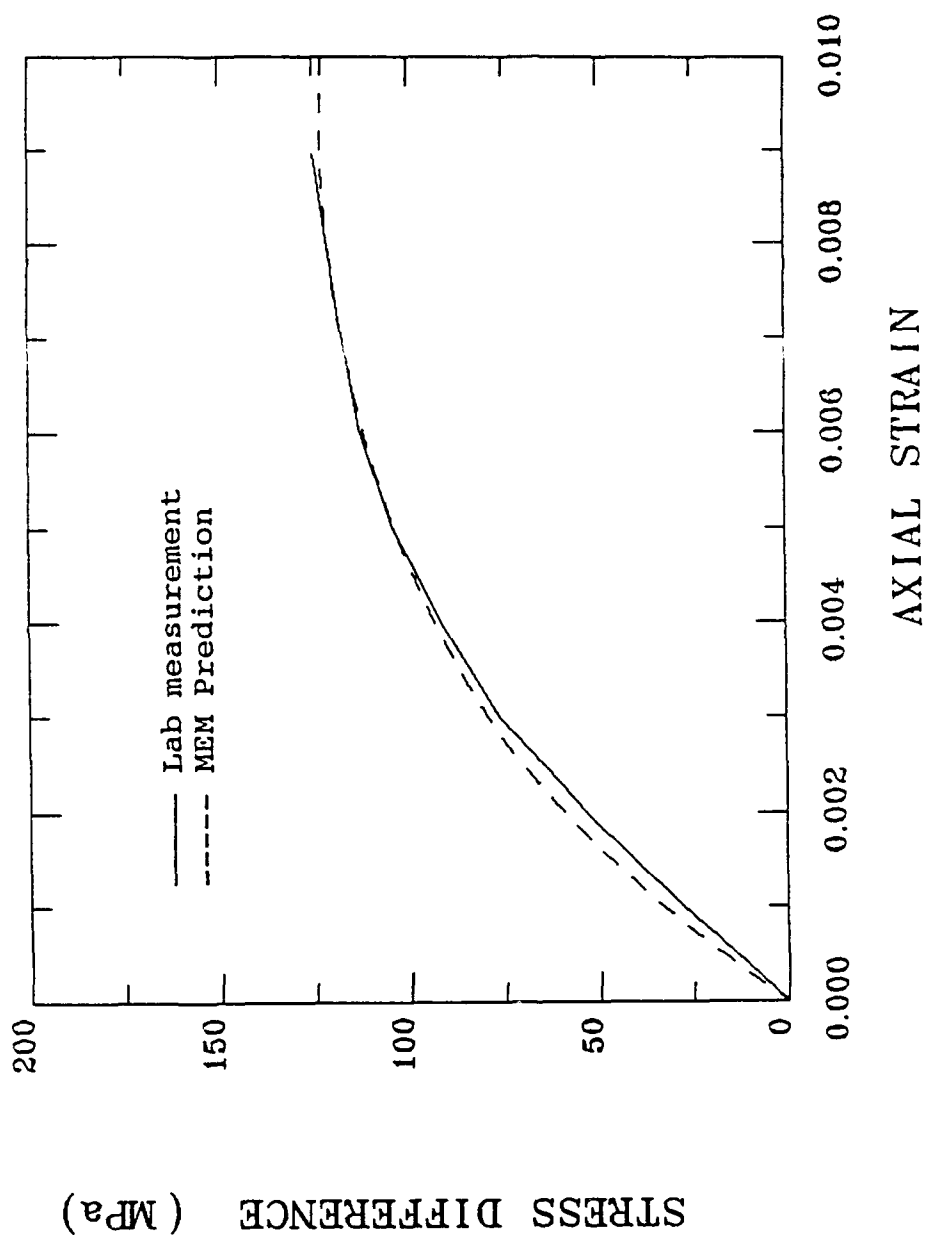
Figure 5.15a. Stress difference vs. axial strain in the drained triaxial compression at σ_{3c} = 50 MP$_a$, MEM prediction compared with lab measurement.
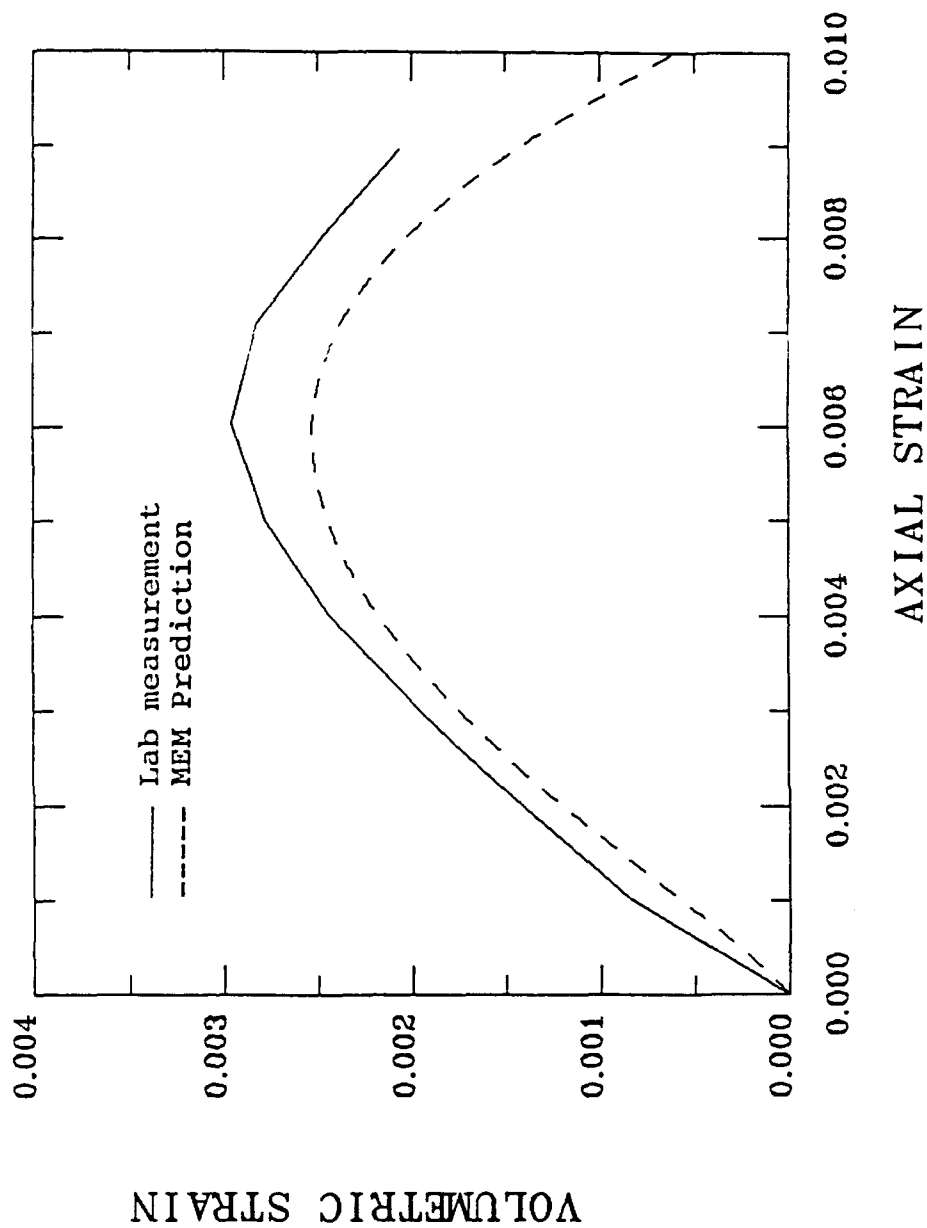
Figure 5.15b. Volumetric strain vs. axial strain in the drained triaxial compression at σ_{3c} = 50 MPa, MEM prediction compared with lab measurement.

Figure 5.16a. Stress difference vs. axial strain in the drained triaxial compression at $\sigma_{3c} = 100$ MP$_a$, MEM prediction compared with lab measurement.

MEM PREDICTION (TXC AT SIG3 = 100 MPa)
MAT = SALEM LIMESTONE

Lab measurement
MEM Prediction

AXIAL STRAIN
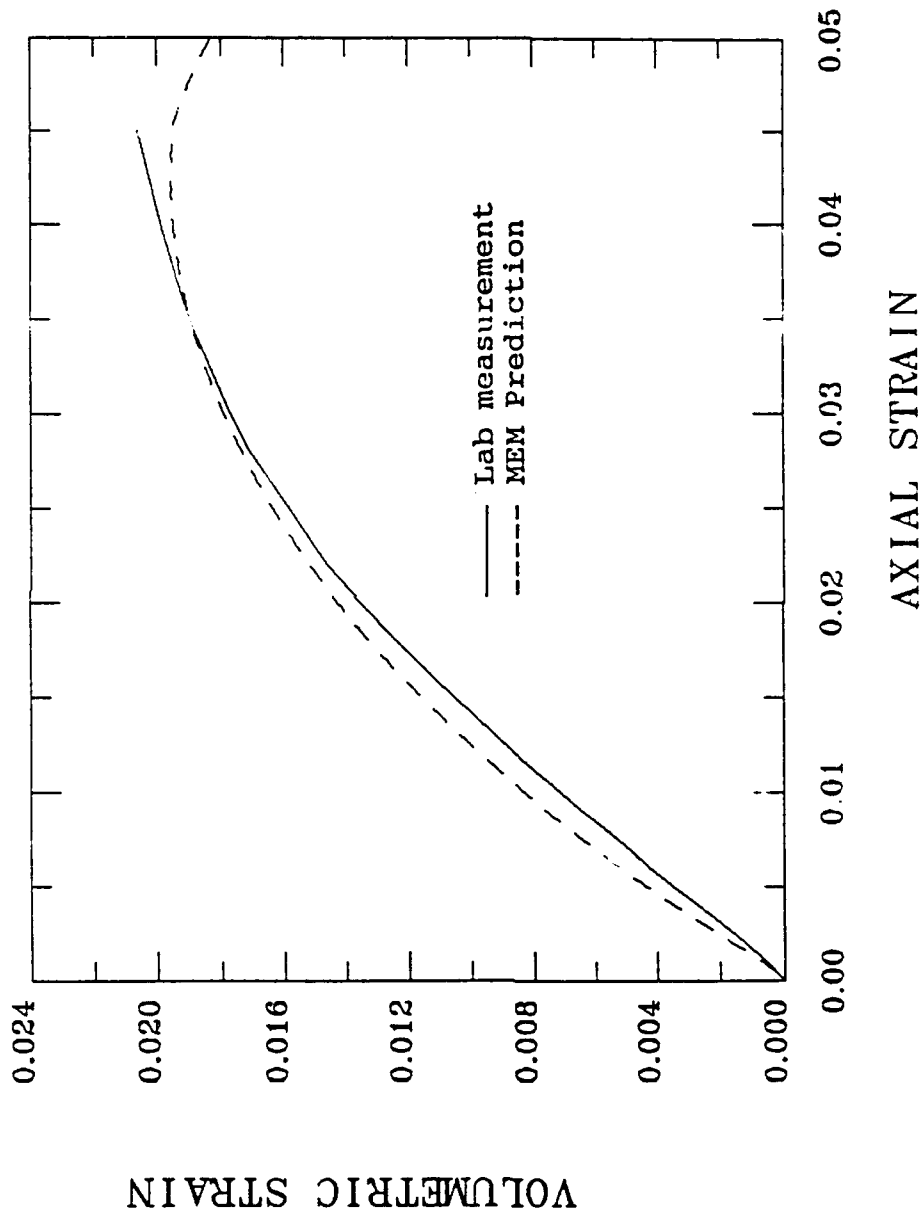
VOLUMETRIC STRAIN

Figure 5.16b. Volumetric strain vs. axial strain in the drained triaxial compression at σ_{3c} = 100 MP$_a$, MEM prediction comared with lab measurement.
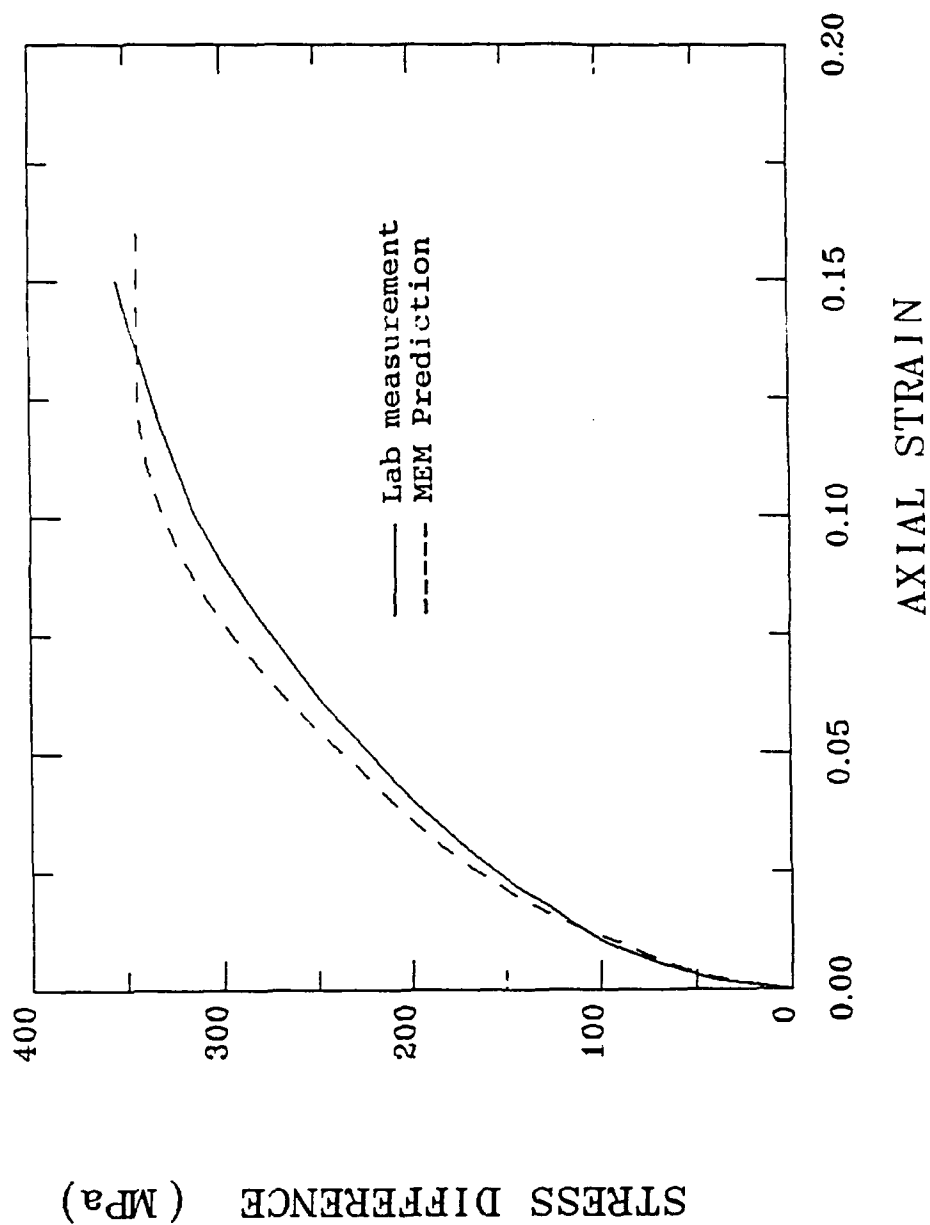
Figure 5.17a. Stress difference vs. axial strain in the drained triaxial compression at σ_{3c} = 200 MPa. MEM prediction compared with lab measurement.

Figure 5.17b. Volumetric strain vs. axial strain in the drained triaxial compression at $\sigma_{3c} = 200$ MP$_a$, MEM prediction compared with lab measurement.

MEM PREDICTION (TXC AT SIG3 = 400 MPa)
MAT = SALEM LIMESTONE
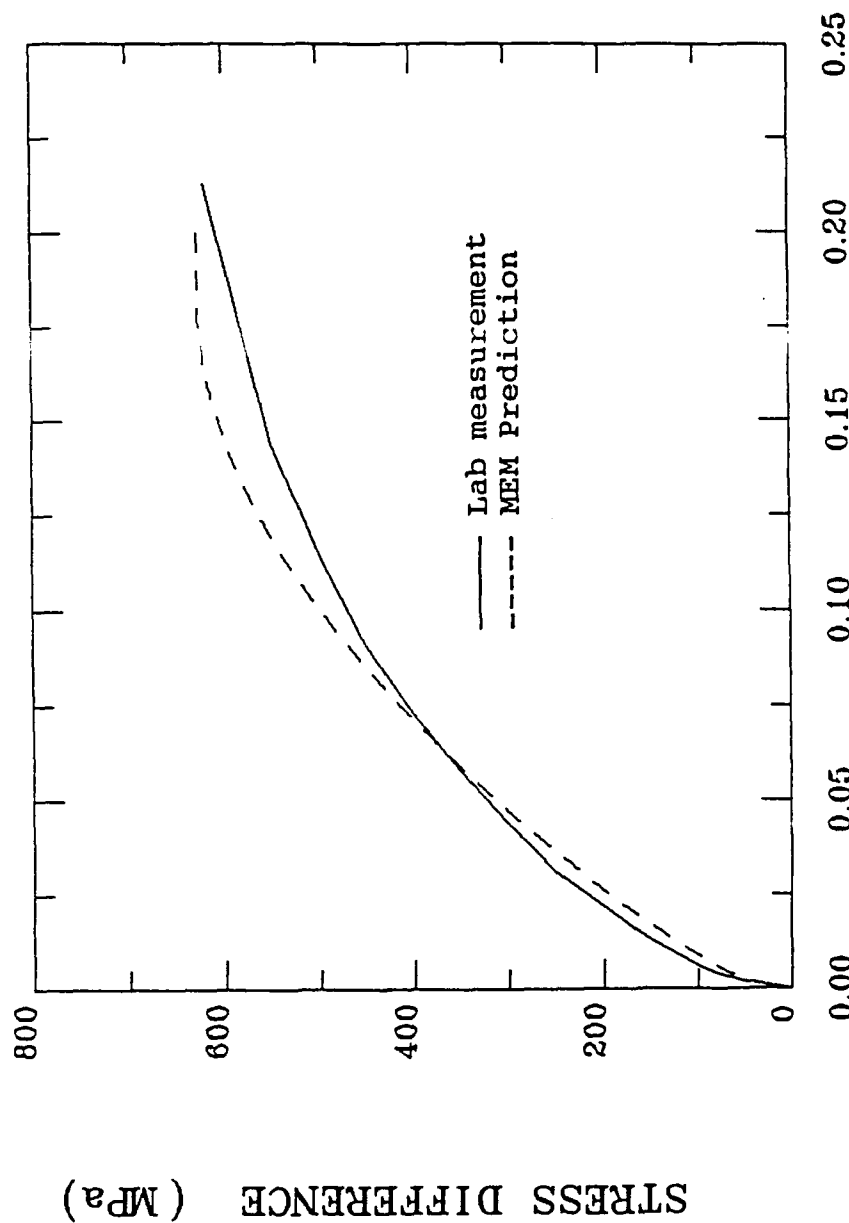
Figure 5.18a. Stress difference vs. axial strain in the drained triaxial compression at σ_{3c} = 400 MP$_a$, MEM prediction compared with lab measurement.
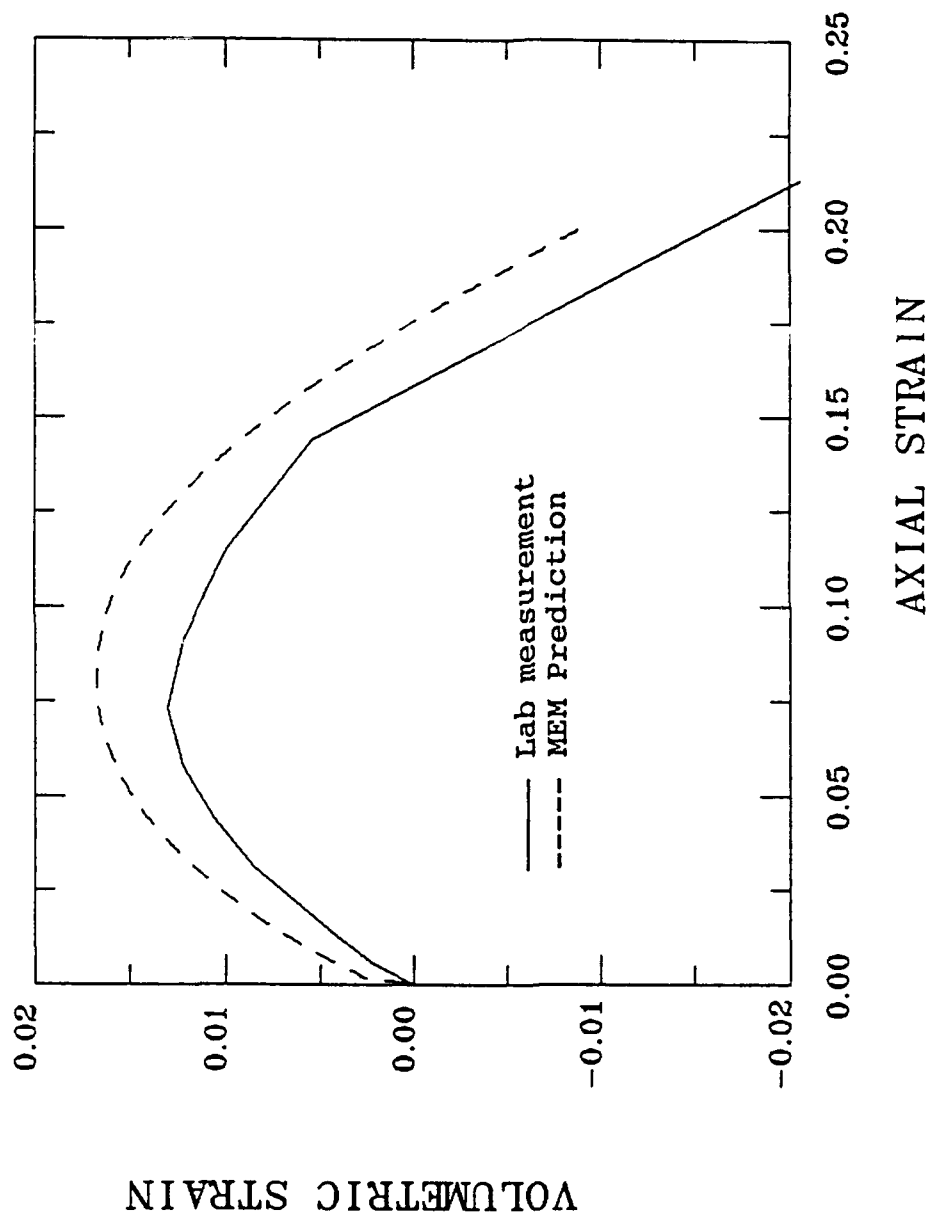
Figure 5.18b. Volumetric strain vs. axial strain in the drained triaxial compression at σ_{3c} = 400 MP$_a$, MEM prediction compared with lab measurement.
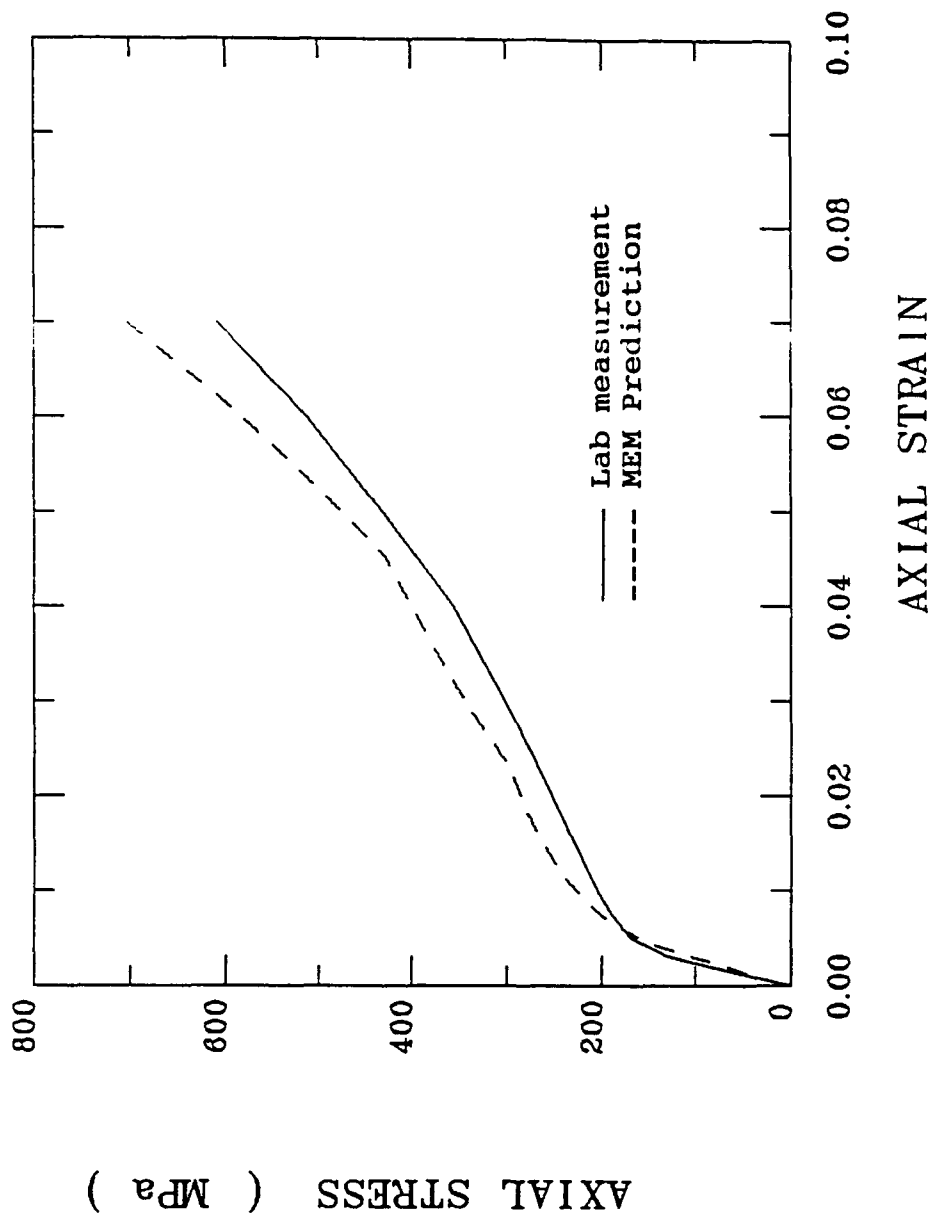
Figure 5.19. Axial stress vs. axial strain in the drained uniaxial strain loading, MEM prediction compared with lab measurement.
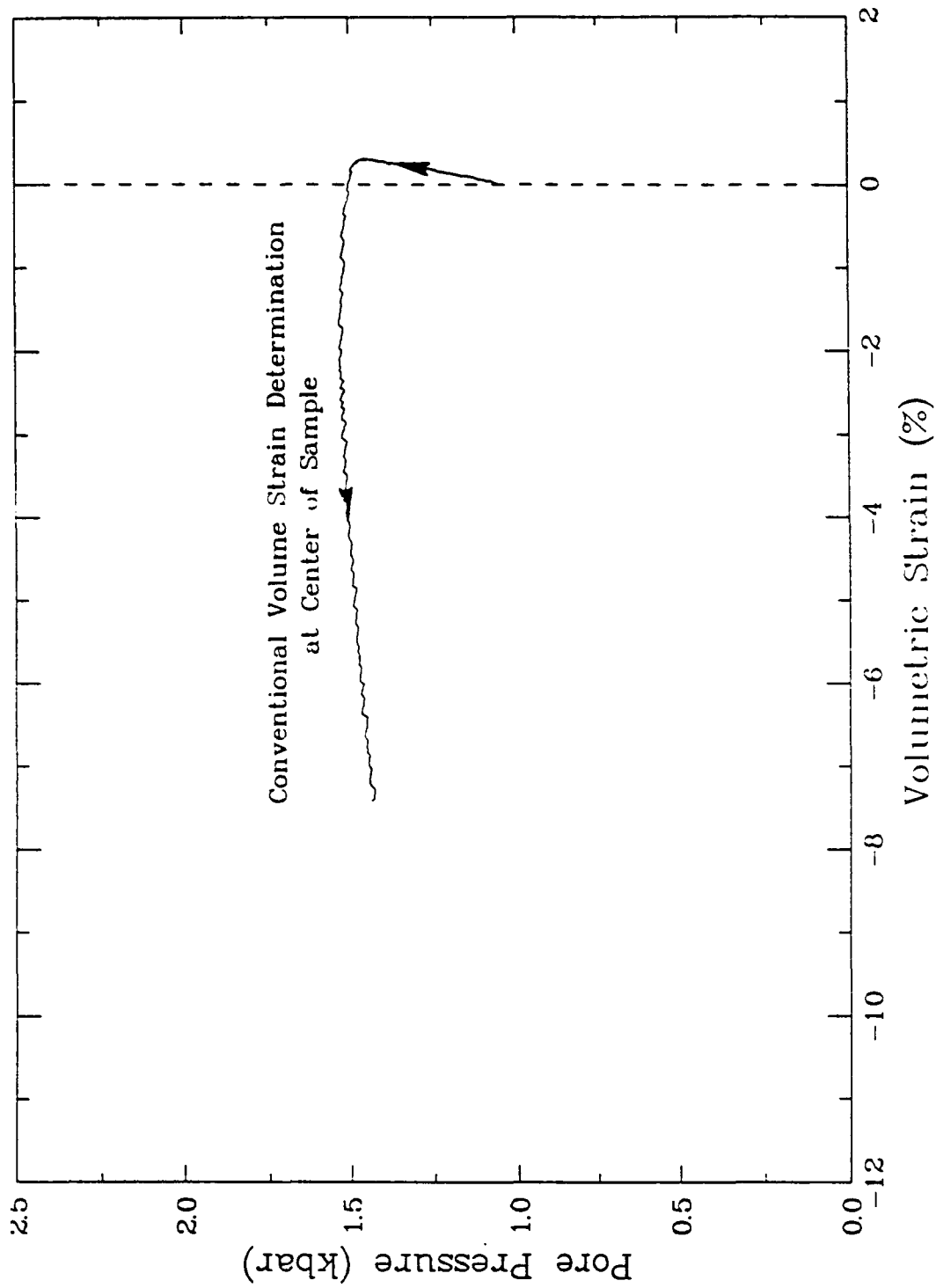
Figure 5.20. Inconsistency between pore pressure and volumetric strain in a conventional undrained triaxial test on Salem limestone (2 kb confining pressure).
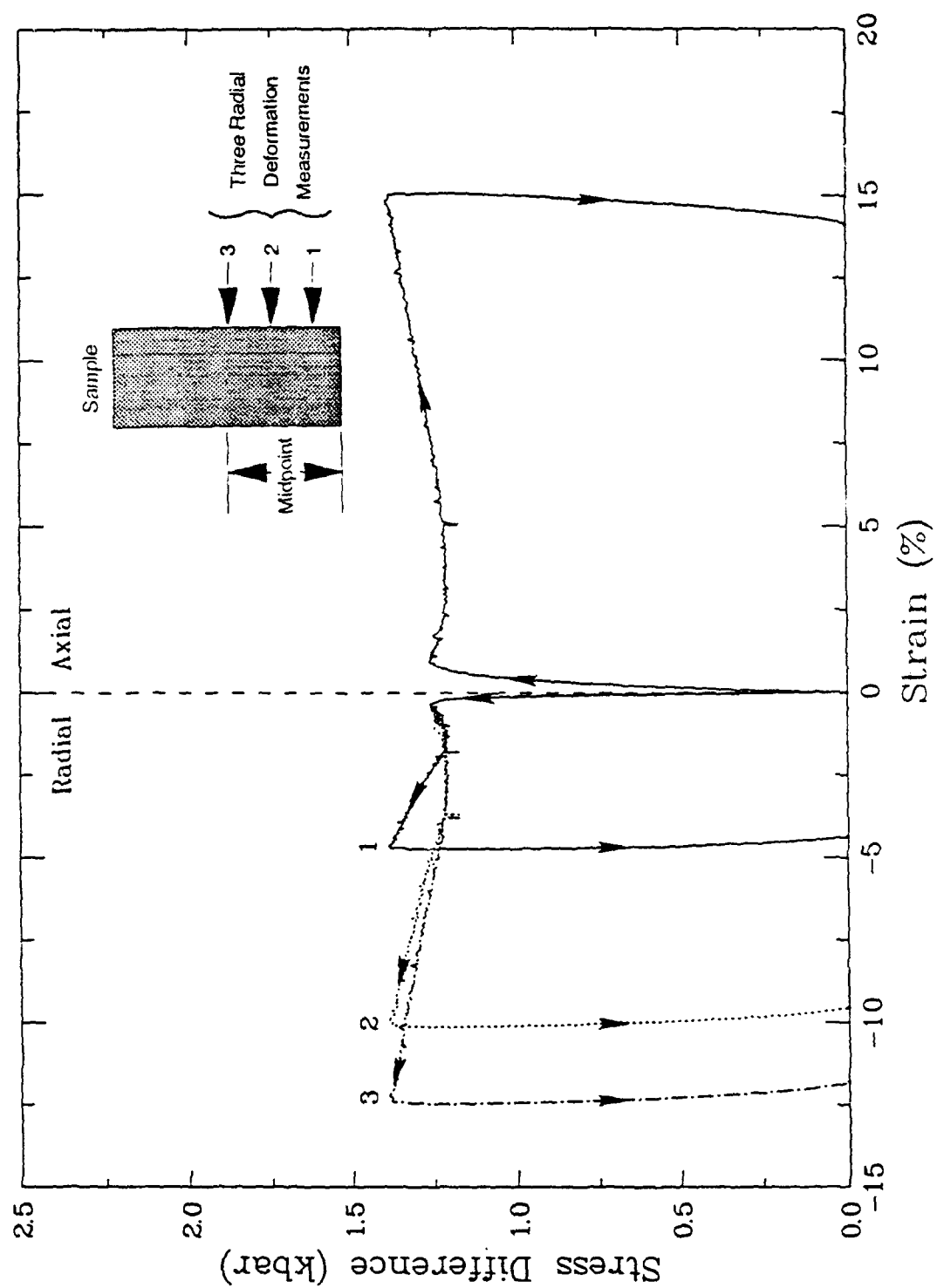
Figure 5.21. Contrast between radial strain measurements at three locations on an undrained triaxial test specimen of Salem limestone (2 kb confining pressure).
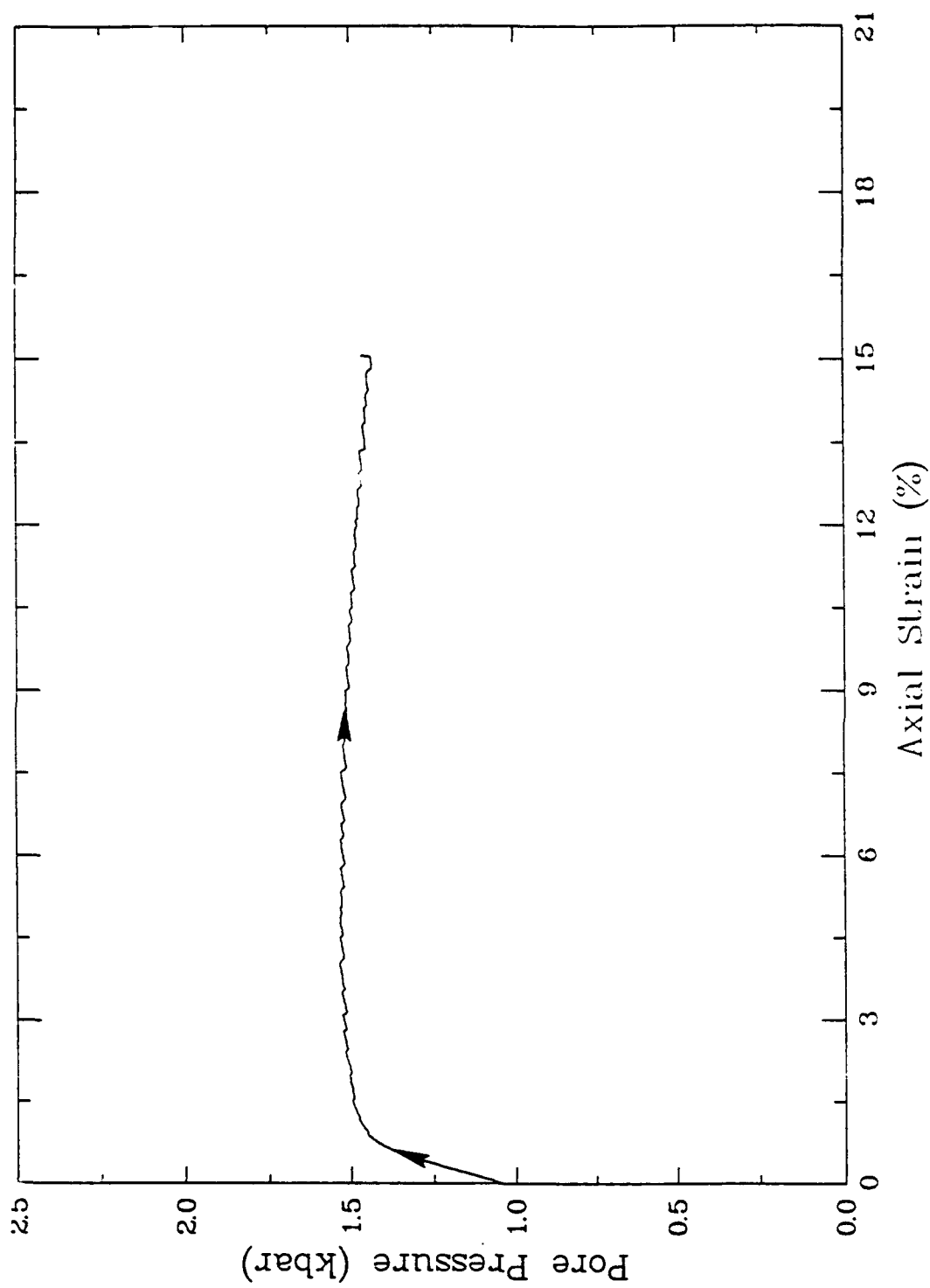
Figure 5.22. Pore pressure response as a function of axial strain for undrained triaxial loading of Salem limestone at 2 kb confining pressure.
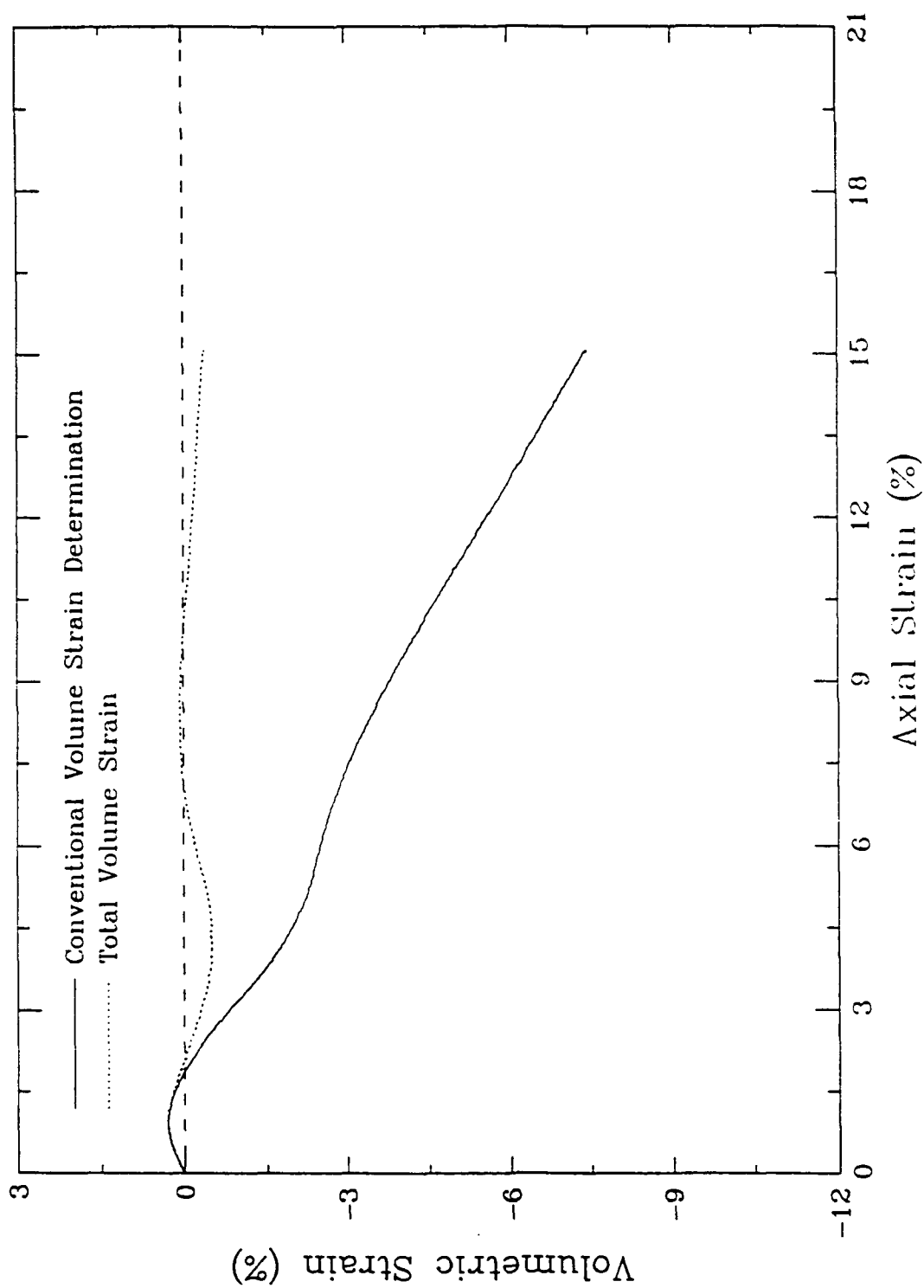
Figure 5.23. Total volume strain determined from three active radial measurements and the sample shape function compared to conventional volume strain (2 kb undrained triaxial compression of Salem limestone).
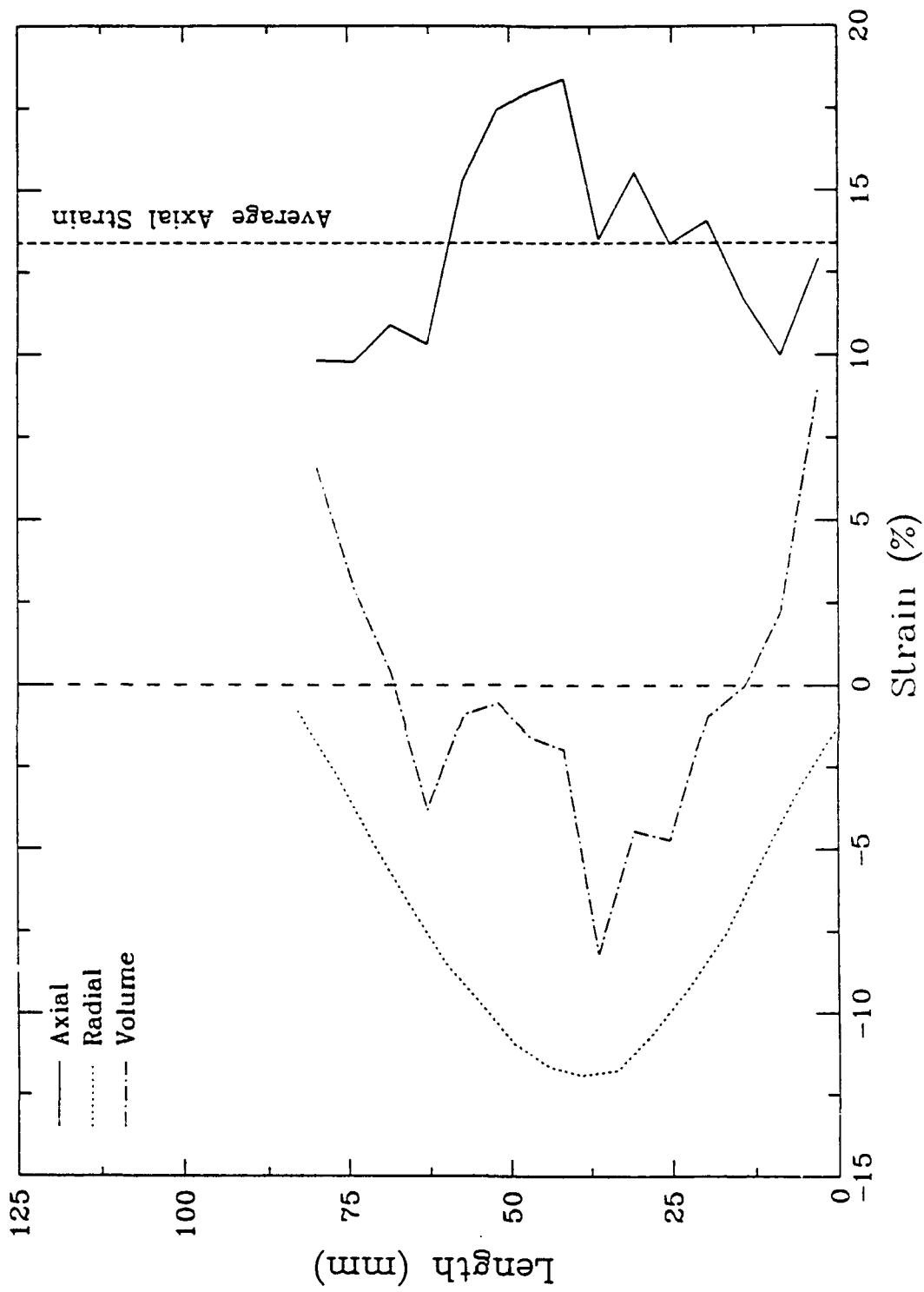
Figure 5.24. Post-test incremental passive strain measurements from an undrained Salem limestone sample in triaxial compression (2kb confining pressure).
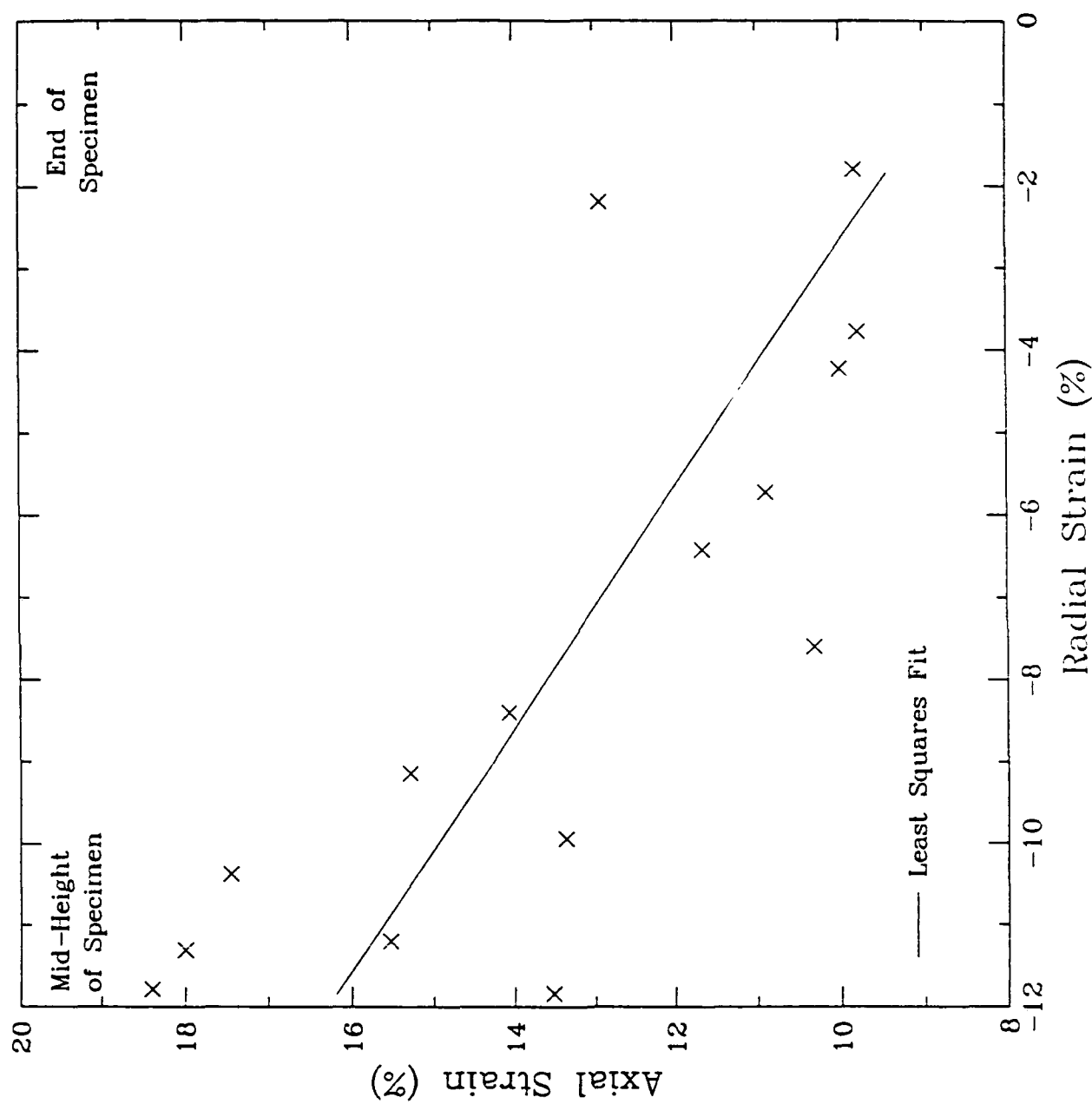
Figure 5.25. Post-test incremental passive strain measurements from an undrained Salem limestone sample in triaxial compression (2 kb confining pressure).
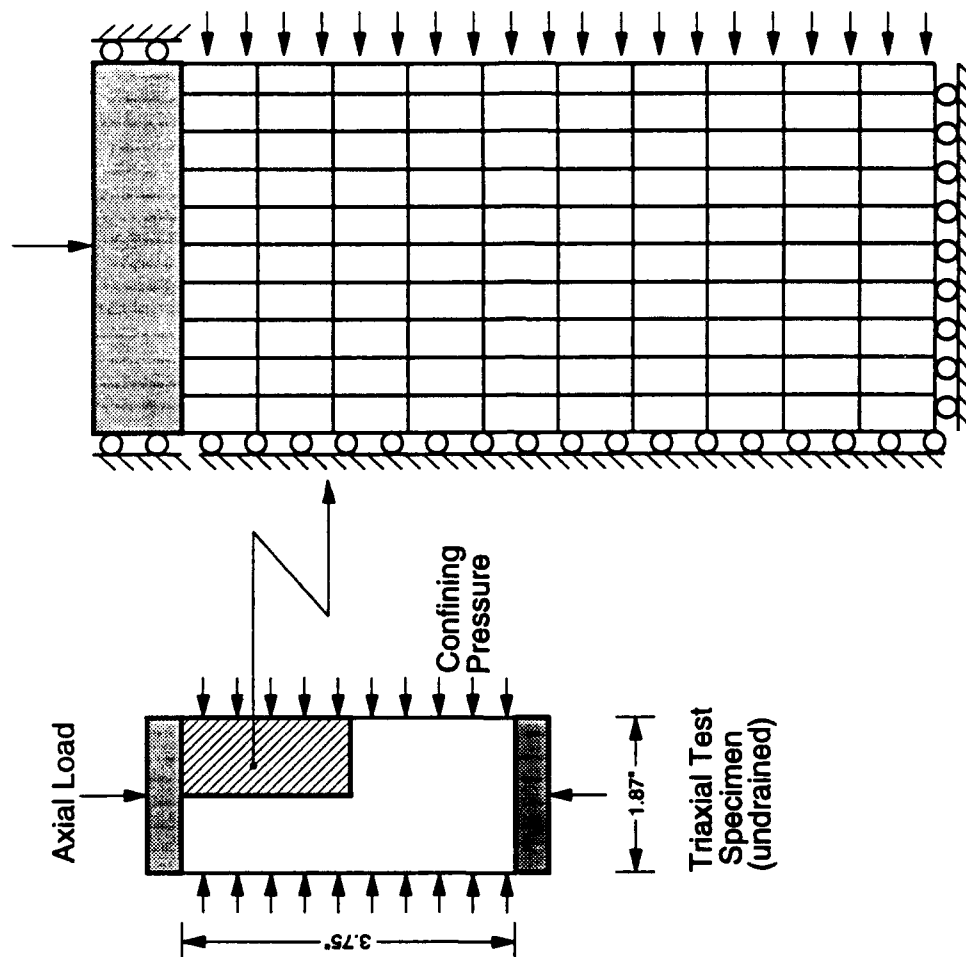
Figure 5.26. Finite element mesh and boundary constrainst used in numerical simulation of an undrained triaxial compression test.
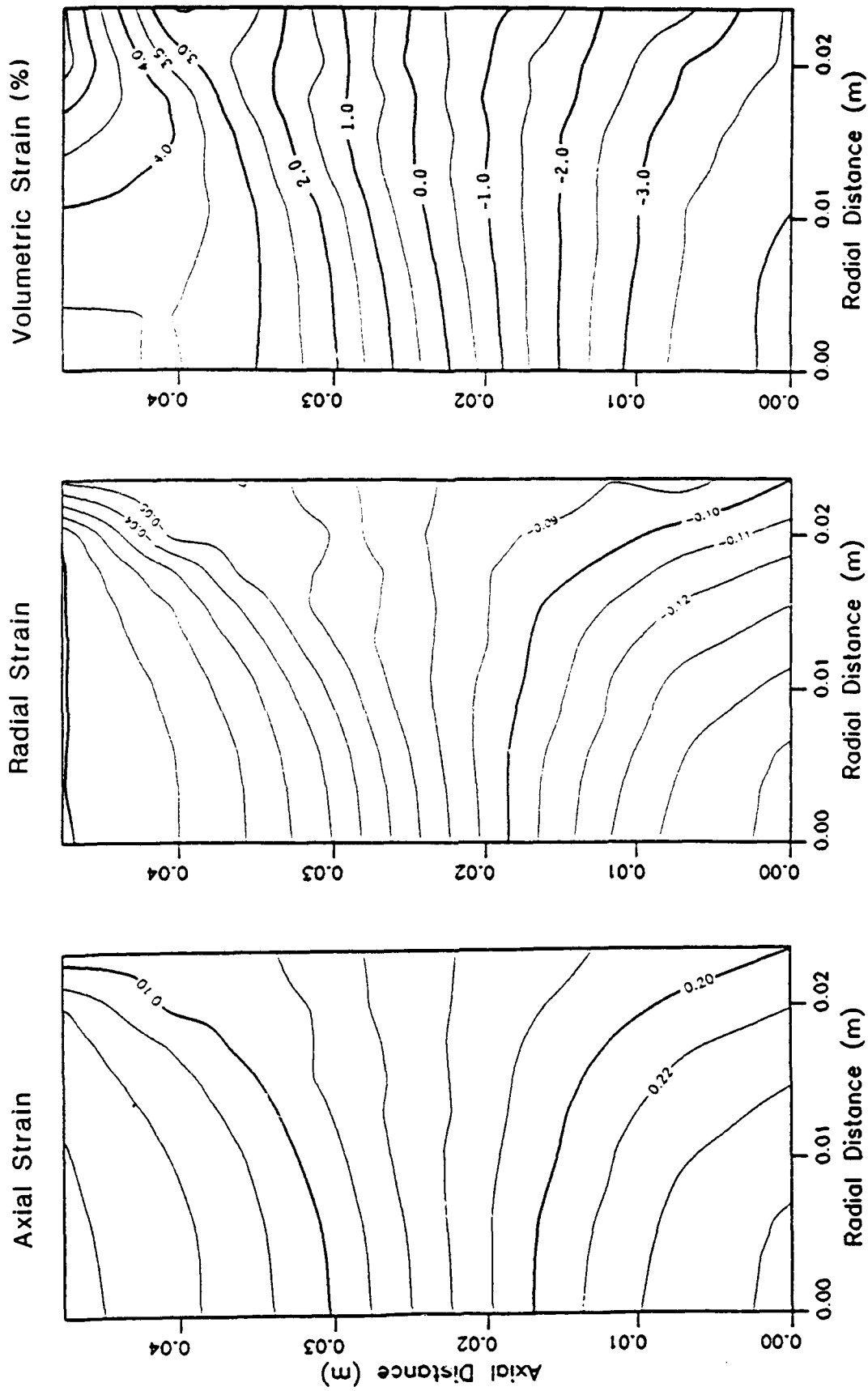
Figure 5.27. Predicted strain contours at an average axial strain of 15% for an undrained triaxial compression test of Salem limestone at 2 kb confining pressure.
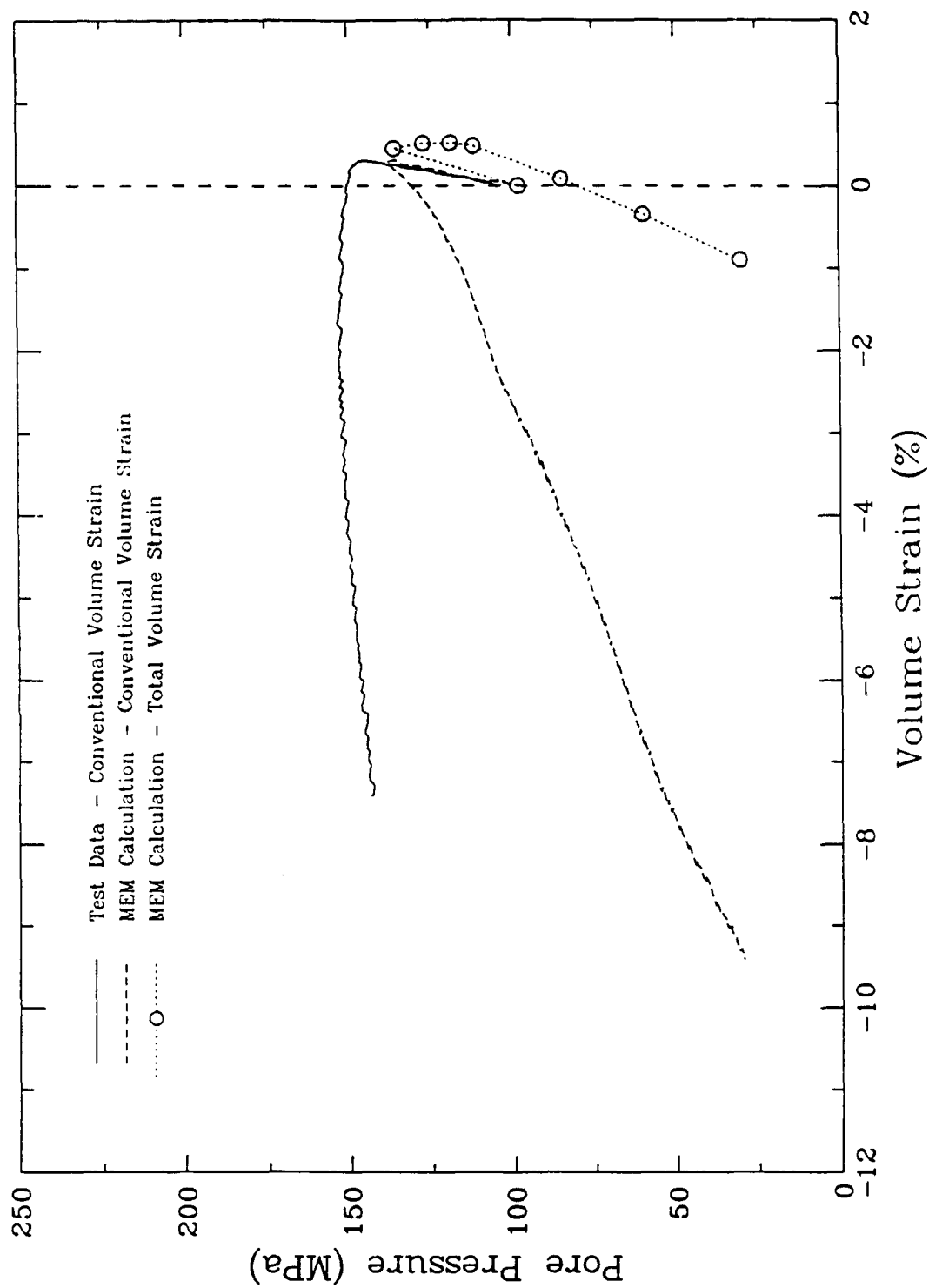
Figure 5.28. Comparison of pore pressure response computed using MEM with test data for triaxial loading of Salem limestone at 2 kb confining pressure.

5-56
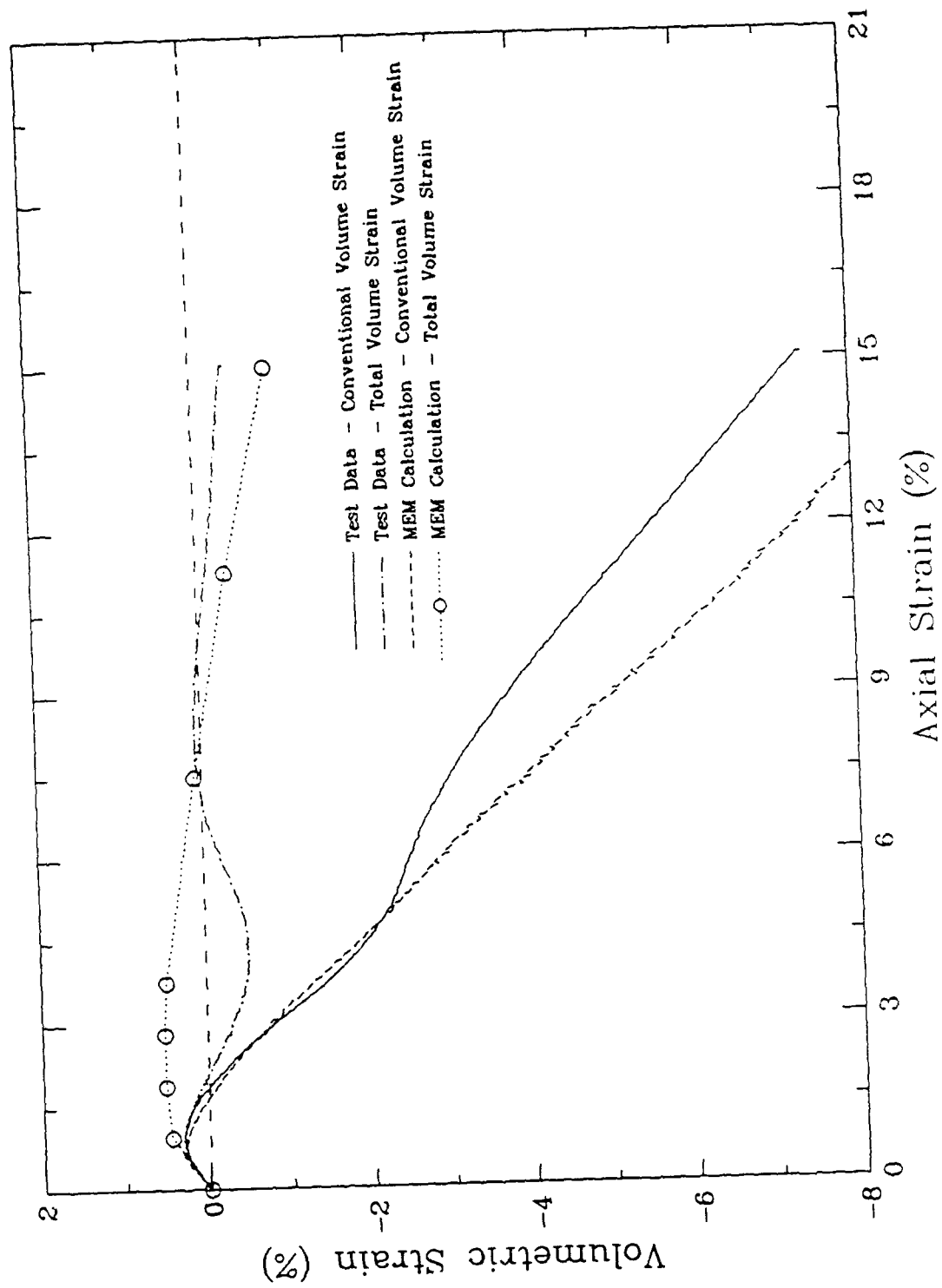
Figure 5.29. Comparison of experimental and analytic volume strains using total volume and conventional volume strain computations.

SECTION 6

DEVELOPMENT OF EQUIPMENT TO PERFORM WAVE PROPAGATION STUDIES IN SATURATED POROUS MEDIA

Both theoretical and analytical solutions for wave propagation in saturated porous media were presented by Kim, Blouin, and Timian (1987), and expanded by Kim, Blouin, Chitty, and Merkle (1988). These solutions predict two types of waves, termed waves of the first and second kinds. The wave of the first kind appears to correspond to the familiar compressional wave in a single phase medium. It is characterized by the skeleton and pore fluid, both in compression, moving in the direction of propagation. The wave of the second kind propagates at a lower velocity with compression in the pore fluid and tensile effective stress in the skeleton. These analyses also predict that certain aspects of the wave propagation behavior are dependent on the frequency of excitation, i.e. pulse duration, as illustrated in Figure 6.1. The speed of the wave of the first kind varies with excitation frequency, asymptotically approaching a lower bound at low frequencies, an upper bound at high frequencies and a having transition in the intermediate frequency range. For the particular combination of materials considered in the analysis, the transition occurs between about 10,000 and 100,000 rad/s. The energy dissipation in the wave of the first kind is significantly greater in the transition region than at frequencies either above or below. Similarly, the wavespeed and energy dissipation of the wave of the second kind are dependent on excitation frequency as illustrated in Figure 6.1.

While the analytical and numerical solutions consistently predict these phenomena, some of them have not been observed in the laboratory. Thus, in order to verify the analysis results, and gain additional insight into the physical processes involved, a program of laboratory experiments was undertaken. This involved construction of a laboratory apparatus capable of propagating compressive waves through saturated porous materials under controlled conditions. This section of the report describes the design of laboratory test apparatus and presents the results of a series of parameter calculations that were used to guide the equipment design.

The calculations presented in this section of the report were performed prior to the availability of property measurements for the porous stainless steel bars that were eventually used as test specimens. The material properties used in these calculations were estimated based on available product information supplied by manufacturers that turned out to be significantly different than the properties that were eventually measured. Section 7 presents the properties of the specimen that was tested and the results of analyses based on those updated properties.

6.1 LABORATORY TEST APPARATUS

The principal design objective of the test apparatus was to provide a means for detailed study of waves propagating through a fully saturated porous medium. Specific design objectives included requirements to: saturate a specimen of porous material with controlled boundary conditions, induce a compressive wave in the saturated specimen and measure the resulting disturbance, preferably in both the fluid and solid phases. The design that was selected for the Wave Propagation Bar (WPB) is similar in appearance to a Split Hopkinson Pressure Bar (SHPB), which is described by Nichols (1982). However, there are important differences between the two devices. The SHPB uses a sample much shorter than the wavelength of excitation so that there are several reflections through the sample in the duration of the loading and the strain field in the sample is assumed to be uniform. Strain measurements are made on metal bars on either side of the sample and a mathematical transformation is used to infer the strain in the sample. In contrast, the wave propagation bar being developed under this project uses a sample longer than the excitation wavelength so that wave propagation along the sample can be observed by strain measurements made directly on the sample. Details of the analyses that lead to the specific design decisions were presented by Blouin, et al. (1990). The resulting design is depicted in Figure 6.2 and described briefly in the following paragraphs.

The device is designed to accommodate a specimen of porous material in the shape of a cylinder 2 inches in diameter and up to 24 inches long. The specimen is held between two 50-inch long hardened steel bars, also of 2-inch diameter, designated the incident bar and

transmitter bar. On the incident bar end, is a third 2-inch diameter bar, called the striker bar. In order to induce compressive waves in the test specimen, a gas gun is used to propel the striker bar through a guide tube to a point where it impacts the incident bar. The impact results in a compressive wave that propagates through the incident bar and into the specimen. The system has been used with striker bars ranging from 5 inches to 20 inches long. This corresponds to a range in pulse durations of 50 to 200 μs. If the pulse duration is assured to be half the period of a sine wave, the resulting range of frequencies is 2,500 to 10,000 Hz or 15,700 to 62,800 rad/s. This range could be extended somewhat on either end by fabrication of different striker bars.

The duration of the excitation pulse was identified in the previous analytical work as a key variable responsible for changes in the wave propagation behavior that are under investigation. In the test apparatus, the duration of the incident wave is determined by the length of the striker bar. When the striker bar impacts the incident bar, the time before it rebounds, and hence the duration of the incident pulse, is equal to the time required for a compressive wave to travel from the point of impact to the opposite end of the striker bar and return to the impact point as a tensile wave which causes separation between the two bars.

The magnitude of the incident wave is determined by the velocity of impact, which is determined by the pressure in the gas gun. For this work, the tests were designed with the objective of keeping all material response in the elastic regime. Thus, the gas gun pressure was selected to give adequate resolution in the instrumentation without yielding the test specimen. Since the material stays elastic, the exact magnitude of the stress wave does not strongly influence the outcome of the experiments.

In order to achieve saturation of the specimen, all of the air in its pore space must be removed and replaced with fluid. Further, in order to apply the necessary boundary conditions, we impose the requirement that no fluid flow into or out of the specimen during testing. This condition is accomplished by encasing the specimen in a jacket, a tight-fitting flexible membrane, which is sealed to the solid bars on either end of the test specimen. The exterior of the jacket is pressurized to a level greater than the maximum pore pressure,

ensuring that the jacket remains tight against the test specimen and that no fluid flows across the specimen boundary.

Since the exterior of the jacketed specimen must be pressurized to maintain the required boundary conditions, it is necessary that the test apparatus include a pressure vessel to contain the specimen. In this case, the pressure vessel consists of a standard double ended hydraulic cylinder in which the piston has been replaced by the test specimen, with the incident and transmitter bars passing through the seals on either end of the cylinder.

In light of the calculational results presented in Section 6.2, a steel sleeve was added to the pressure vessel, leaving a gap of approximately 0.2 inch between the jacket covering the specimen and the inner surface of the sleeve. This results in a stiffer radial confinement condition which is intermediate in stiffness between a constant-pressure fluid confinement and a uniaxial strain condition. The latter is desirable, but is not readily achievable in the laboratory.

In addition to the radial confinement provided by the sleeve and fluid in the pressure vessel, axial confinement is required to maintain the required boundary conditions. This is provided by a hydraulic cylinder attached to the end of the transmitter bar. To react against the axial force applied by the hydraulic cylinder, a collar attached to the incident bar bears against a fixed stop.

Connection to the pore space of the installed test specimen is required to evacuate the air and introduce pore fluid. This is achieved by means of an axial hole in the transmitter bar originating at the specimen and intersecting a radial hole outside the pressure vessel. The entire apparatus is assembled on top of a 27-inch deep wide flange steel beam which provides a stiff surface to align the parts and a convenient working elevation.

6.2 CONSTRUCTION OF THE TEST EQUIPMENT

The device described above was constructed in ARA's Materials Testing Laboratory in South Royalton, Vermont. A 20-ft section of 27-inch deep by 10-inch wide steel I-beam (W27X84) was drilled for attachment of the various components, shimmed level and fastened to the floor in the laboratory. Both the pressure vessel and the axial loading cylinder were fabricated to specification by a hydraulic cylinder vendor. The pressure vessel was retrofitted with electrical penetrations to pass instrumentation signals through the pressure boundary. The pressure vessel and axial loading cylinder were carefully aligned and bolted to the top of the steel beam. Also attached to the top of the beam are the guide tube for the striker bar and a bracket to react to the axial load in the bar/specimen assembly.

The gas gun incorporated into this apparatus was available at ARA at the time of the design. While it is much larger than required for this purpose, it was the most economical choice since no additional hardware purchase was required. In order to isolate any mechanical noise developed in the gas gun from the instrumented portion of the test assembly, the gas gun is supported on a separate steel base structure. The support structure for the gas gun and the steel beam supporting the bar assembly are aligned so that the outlet of the gas gun slides a short distance into the upstream end of the striker bar guide tube without any mechanical contact.

Figures 6.3 through 6.7 are photographs of the completed test device. Figure 6.3 shows as much as possible of the entire assembly, which is over 20 ft long. The gas gun is out of the picture to the right. On the right end of the picture is the guide tube for the striker bar. Moving to the left are the incident bar, pressure vessel, transmitter bar, and the axial loading cylinder. Figure 6.4 presents a different view of the assembly, looking down axis with guide tube in the foreground. The upstream end of the incident bar is shown in Figure 6.5. Also shown in Figure 6.5 are the downstream end of the striker bar guide tube, the collar and reaction frame that support the axial load in the incident bar, and a strain gage station near the upstream end of the incident bar. Figure 6.6 shows the incident bar entering the pressure vessel that contains the test specimen. The hose and valves are for filling and

draining the pressure vessel. The downstream end of the pressure vessel is shown in Figure
6.7, with the transmitter bar passing through a seal in the end of the vessel. Also on this end
of the pressure vessel are the electrical penetrations used to transmit signals from the
instrumentation internal to the pressure vessel out to the recording equipment. Attached to
the transmitter bar, near the seal of the pressure vessel, is a tubing fitting with integral valve
which connects to the pore space in the test specimen by means of an axial hole in the end of
the transmitter bar.

6.3 PERFORMANCE TESTS

A series of performance tests were conducted prior to testing a saturated porous
specimen. For these tests the device was set up with a 2-inch diameter by 24-inch long
hardwood specimen in place of the planned saturated porous material. As with the saturated
porous metal, the hardwood specimen has a lower acoustic impedance than the steel incident
bar. The tests were conducted with no fluid and no confining pressure in the pressure vessel.
The axial loading cylinder was pressurized to hold the incident bar, the hardwood specimen,
and the transmitter bar tightly together.

A pair of electrodes with one inch separation along the axis of the bar was installed at
the end of the striker bar guide tube. Using a simple two-step voltage divider circuit, and a
20 MHz oscilloscope, measurements were made of the striker bar velocity immediately
preceding impact with the incident bar. Using this procedure, it was determined that 12 psi
pressure in the gas gun results in an impact velocity of 13 - 14 ft/s. For like materials
impacting, the magnitude of the resulting stress wave, σ_i, is given by:

$$\sigma_i = \frac{\rho \, C_p \, V}{2}$$

where: ρ = mass density of the material

C_p = compressive wavespeed of the material

V = impact velocity

A thin steel bar has mass density and compressional wavespeed of 0.00073 lb s²/in. and 200,000 in./s, respectively. At an impact velocity of 14 ft/s (= 168 in./s), the resulting computed stress is 12,300 psi. Similar velocities were obtained using 3.5 psi gas gun pressure with a 5-inch striker bar and 5 psi with a 10-inch striker bar.

Several trial runs were made with 12 psi gas gun pressure, the 20-inch striker and the hardwood specimen. There were no instruments on the specimen, but two full strain gage bridges were installed on the incident bar, one 10.5 inches from the end that is impacted by the striker and the other 2.25 inches from the specimen end, resulting in a separation distance of 37.25 inches. Both strain gage bridges were monitored with a 20 MHz digital storage oscilloscope. The data recorded in one typical run are presented in Figure 6.8 where the origin of the time scale is arbitrary. The measured voltages were converted to stresses using a calibration factor computed from the nominal values of strain gage factor, excitation voltage, amplifier gain, elastic modulus, and Poisson's ratio. The measured stress wave amplitude of approximately 12,300 psi matches the value computed from the impact velocity.

The duration of the wave should be equal to two wave transit times of the striker bar. For the 20-inch striker bar, the expected pulse duration is 200 μs. In the measured signals, the edges of the pulse exhibit some spreading due to dispersion of the wave. However, the main part of the wave very closely matches the expected value. The pulse velocity along the incident bar can be measured by comparing the signals from the two strain gage stations in Figure 6.8. There is more spreading on the leading edge of the pulse at the second strain gage station than at the first. If the propagation time between the two station is measured on the steep portion of the leading edge of the waveform, the resulting velocity is 199,000 in/s which matches the value computed using the (unconfined) elastic modulus of steel. Theoretically, this is the wave propagation velocity in a thin rod that is free to deform laterally as the wave propagates along its axis. There is also a component of the wave that is travelling faster as evidenced by the difference in first arrival times at the two stations. Based on first arrivals, a wavespeed of 213,000 in/s is computed. This is somewhat slower than the 231,000 in/s speed that is computed for the fully confined (or halfspace) case, but

apparently indicates some tendency in that direction resulting from outrunning along the central axis of the bar.

6.4 PARAMETRIC CALCULATIONS OF LABORATORY TEST APPARATUS

The propagation of stress waves in a multiphase, cylindrical bar is a complex mechanical phenomenon. In order to design laboratory experiments which can be effectively correlated with theoretical predictions, we performed a series of numerical simulations of various test specimen loading and confinement conditions to ensure that the experiments would have a maximum chance of success. These calculations were performed using the finite element code MPDAP, described in Section 2, and the material models discussed in Section 3. These calculations simulate stress wave propagation in a cylindrical bar of saturated, porous, elastic material with the primary objective of assessing various aspects of the planned experiments.

Three sets of parametric calculations were performed as shown in Table 6.1. In the first set of calculations the porous bar is loaded in uniaxial stress while confined in a fluid at constant confining pressure. Both the loaded surface at the end of the bar and the sides of the bar are sealed to prevent pore fluid from moving across these boundaries. In the experiment this would be accomplished by jacketing the sample between the incident and transmitter bars within a constant pressure gas. Two types of uniaxial stress calculations were performed. In the first, the pore fluid was free to displace within the porous skeleton as governed by a realistic permeability for the porous bar. In the second, the movement of pore fluid within the skeleton was prevented by using a very low value of permeability. The results of the uniaxial stress loading calculations showed very little influence of relative pore fluid motion because, in both the permeable and impermeable cases, excess dynamic pore pressures within the bar are relieved almost immediately by relief waves propagating into the bar from the cylindrical surface. Within the elastic regime, this phenomenon was found to be independent of the confining pressure.

A second set of calculations was performed in which the porous bar was loaded in uniaxial strain. Based on previous analyses (Kim, et al., 1988), it was expected that this loading condition would show a dramatic influence of the relative pore fluid motion. This was verified by comparing the permeable bar calculation to the companion calculation using an impermeable bar. Experimentally, however, it is extremely difficult to achieve a true dynamic uniaxial strain condition in the laboratory.

In order to approximate the uniaxial strain condition as closely as possible, so as to maximize the influence of relative pore fluid motion, an experimental configuration using a porous bar confined in a small volume of liquid within a rigid walled pressure vessel was considered. The idea of this approach is to develop dynamic confinement of the porous bar in the relatively stiff confining liquid. The thin annulus of confining liquid provides confinement with minimum shear resistance and high lateral stiffness. The third set of calculations replicates the experimental conditions using this test configuration. Two companion calculations were performed. The first accurately modeled the permeability of the porous bar and the second assumed that the bar was impermeable so as to delineate the influence of the relative pore water motion.

As described by Blouin, et al. (1990), porous stainless steel was selected for the first set of experiments because its combination of high skeleton stiffness and high permeability should accentuate the influence of the relative fluid motion. The published properties of the materials chosen for the experiment were used in these calculations and are shown in Table 6.2. The permeability properties of the porous bar were obtained from the manufacturer and the stiffness properties were estimated based on available information. Kerosene was chosen for the pore fluid because it is non corrosive.

Moduli and wavespeeds were computed from closed form solutions for the various materials and loadings used in the calculations with the properties in Table 6.2. These values are listed in Table 6.3. Both Young's modulus and the constrained modulus for the porous skeleton are listed, as appropriate, from which wavespeeds corresponding to the uniaxial stress loading and uniaxial strain loading, respectively, are computed. The wavespeed for the

6-9

uniaxial stress loading of the saturated porous bar is computed using Young's modulus of the dry skeleton because of the immediate lateral relief of the excess pore pressures. Two bounding wavespeeds are computed for the uniaxial strain loading of the saturated porous steel. As described by Kim, et al. (1987), the compressional wavespeed is a function of the permeability and the loading frequency. For low frequency excitations (or low permeabilities), a lower bound wavespeed is obtained which is that associated with the undrained fully coupled modulus computed according to procedures described by Blouin and Kim (1984). For high frequency excitations (or high permeabilities), an upper bound wavespeed is obtained according to the analytic procedures developed by Kim, et al. (1987). The computed wavespeed relationship as a function of frequency for the saturated porous steel to be used in the experimental validation is shown in Figure 6.1a. This profile was computed using the program TWAVE which is documented in Kim, et al. (1987). In part b of Figure 6.1, the damping for the compressional wave is plotted as a function of excitation frequency. In parts c and d, the wave velocity and damping for waves of the second kind are plotted as functions of excitation frequency.

A rectangular loading pulse with a peak stress of 1,000 psi was used in all the calculations listed in Table 6.1. The loading pulse had a duration of 0.1 ms with a rise time and decay time of 1.0 μs. This loading excitation frequency is on the upper bound of the wavespeed profile of Figure 6.1. As described earlier, the excitation frequency in the laboratory experiment can be varied by changing the length of the striker bar.

Schematic section views of the calculational grids and data output locations for each of the three sets of calculations are shown in Figures 6.9 through 6.11. The uniaxial stress calculations used an axisymmetric cylindrical grid of 1680 elements. There are 7 equally spaced elements in the radial direction making up the 1 inch radius porous bar and 240 elements in the axial direction making up the 24 inch total length. Data output locations are shown at points A through D spaced at 5 inch increments within the bar. The rectangular loading pulse is applied on the circular face of the bar against an impermeable free surface. There is an impermeable free boundary surrounding the bar. In the uniaxial stress calculations reported here, no confining pressure was applied to the lateral surface, simulating

an unconfined loading. Other uniaxial stress calculations, not reported, involved bars confined under constant uniform stress conditions. The response was virtually identical to that reported here for the unconfined bar.

The uniaxial strain calculations, shown schematically in Figure 6.10, consisted of the same rectangular pressure pulse applied to a 1 inch radius bar confined by an impermeable roller boundary such that no lateral motion at the boundary is allowed. The element size in the axial direction is identical to that used in the uniaxial stress calculations.

The fluid confined calculations, shown schematically in Figure 6.11, model a 1 inch radius saturated porous steel bar confined within a 0.2 inch annulus filled with kerosene. The kerosene is confined within a rigid impermeable roller boundary which approximates the steel pressure vessel. The porous steel bar is confined in the kerosene by an impermeable free boundary. The uniform rectangular pressure loading is applied to both the impermeable surface of the bar and to the confining fluid. The finite element grid for the bar is identical to that used in the uniaxial stress calculations, but an additional 720 elements are included to model the confining fluid. Additional output points, subscripted with the letter f, are included to monitor the response of the confining fluid. Selected comparisons and analysis of the calculational results are presented in the following subsection.

6.5 ANALYSIS OF PARAMETRIC CALCULATIONS

Confinement conditions have a dramatic influence on the dynamic response of the saturated porous bar. Figure 6.12 compares the total axial stress waveforms at ranges of 5, 10 and 15 inches from the point of load application (locations A, B and C of Figures 6.9 through 6.11) for the calculations in which relative fluid motion within the porous skeleton was prevented. The waveforms and propagation velocities of the uniaxial strain and fluid confined calculations are similar, but in stark contrast to those of the uniaxial stress calculation. The rectangular waveform of the loading function is well preserved throughout all ranges in the fluid confined and uniaxial strain calculations. The wave in the uniaxial stress calculation is rapidly transformed into a sinusoidal waveform with considerable

broadening of the pulse width. The propagation velocity in the uniaxial strain calculation, as measured at the half height of the initial rise to peak between the 5 and 15 inch ranges, is 1170 m/s. This is nearly identical to the calculated wavespeed for the uniaxial strain, saturated lower bound wavespeed of Table 6.3. As noted previously, this is the applicable wavespeed for the case in which there is no relative fluid motion. The propagation velocity in the uniaxial stress calculation, as measured from the peak stress arrival between the 5 and 15 inch ranges, is 835 m/s which compares to 834 m/s computed for the uniaxial stress, saturated case in Table 6.3.

The propagation velocity in the fluid confined porous bar is 1210 m/s, which is slightly faster than that for the uniaxial strain loading. This indicates that the lateral confinement in the fluid confined bar is somewhat higher than that in the uniaxial strain calculation. The propagation velocities measured from the three calculations with no relative fluid motion are listed in Table 6.4. Another indication of the excess confinement in the fluid confined bar is that the peak axial stresses are higher than those in the uniaxial strain calculation. The total axial stresses are also greater than the stress applied to the end of the bar.

Another interesting aspect of the propagation velocity of the uniaxial stress pulse is that the first arrival tends to be coincident with the first arrival of the uniaxial strain pulse. This would be expected, since some small fraction of the energy propagates to the observation point along the center of the bar at the constrained wavespeed, uninfluenced by the cylindrical unconfined boundary. Since the bar is elastic, relief waves from the unconfined boundary cannot overtake the initial waves travelling in the interior of the bar.

The pore pressure profiles, corresponding to the total stress profiles above, are shown in Figure 6.13. The shape of the profiles is similar to that of the total stresses, however, the magnitude of the pore pressure in the uniaxial stress case is relatively small because of the relief provided at the unconfined boundary of the bar. The corresponding particle velocity and displacement profiles for the calculations with no relative fluid motion are shown in Figures 6.14 and 6.15. The velocity profiles are very similar in shape to the total stress

profiles. The displacement profiles show larger displacements in the uniaxial stress case, due to the lack of confinement. At early times, displacements in the fluid confined case are greater than those in the uniaxial case because of the faster wavespeed and greater particle velocities in the former case. However, at later time the fluid confined and uniaxial strain displacements come into close agreement as the significant negative velocity phase in the fluid confined case works to reduce the late time displacements.

Comparison plots showing the influence of confinement for the three sets of calculations in which relative fluid motion is allowed, as governed by the published permeability of the porous steel bar, are shown in Figures 6.16 through 6.21. The total stress profiles at the 5, 10 and 15 inch ranges are shown in parts a, b and c of Figure 6.16. Comparison to the companion calculations with no relative fluid motion (Figure 6.12) shows that there is very little influence of relative fluid motion in the uniaxial stress case, but a dramatic influence in the uniaxial strain case. On the basis of these comparisons, we decided to replicate the uniaxial strain condition as closely as possible in our experiments. The total stress profile for the fluid confined bar proposed for the laboratory experiments is significantly altered in shape and reduced in amplitude by the relative fluid motion, though not as dramatically as are the uniaxial strain profiles.

The relative fluid motion strongly influences the development of early-time peak stress in the uniaxial strain loading as demonstrated by the comparison of the uniaxial and fluid confined waveforms in Figure 6.16a. Only 5 inches into the bar, the initially square shape of the wave has been altered considerably by the relative fluid motion. The uniaxial strain waveform is rapidly attenuated and broadened compared to that in the fluid confined bar.

The wave propagation velocities measured from the calculations with relative fluid motion are listed and compared to the velocities without fluid motion in Table 6.4. There is little change in the unconfined bar velocity because the relief from the cylindrical surface of the bar tends to minimize pore pressures and pore pressure gradients within the bar. There is a substantial increase in the velocity in the bar under uniaxial strain, from 1170 to 1375 m/s. This is in agreement with the velocity increases predicted by the analytical TWAVE

6-13

calculation of the upper bound wavespeed shown in Figure 6.1a. As explained by Kim, et al. (1987), the upper bound wavespeed is approached as either frequency or permeability becomes large. The permeability of the bar should be such that significantly higher wavespeeds will be measured than indicated by the closed form solution for the undrained fully coupled loading condition derived by Blouin and Kim (1984). The wavespeed in the fluid confined bar also shows an increase once relative motion is allowed. However, the wavespeed of 1290 m/s is 85 m/s slower than the wavespeed under pure uniaxial strain conditions.

The pore pressure time history comparisons of Figure 6.17 show some trends similar to those observed in the total stress comparisons, though the initial rapid decay of the pore pressure pulse during the uniaxial strain loading is less pronounced. The pore pressure in the uniaxial strain calculation exhibits more pulse broadening and modification than that in the fluid confined case. Pore pressures developed in the uniaxial stress case are much less than those in the other two cases because of the relief from the surface of the bar.

A comparison of the skeleton velocity time histories for the three calculations with relative fluid motion at various locations along the bar is shown in Figure 6.18. The waveforms, waveform dispersion, and other alterations in shape closely match those for the stress time histories shown in Figure 6.16. The peak velocities are significantly higher in the uniaxial stress loadings because of the lack of confinement. The peak velocity attenuation is greatest in the uniaxial strain case and least in the uniaxial stress case. The corresponding displacement time histories are shown in Figure 6.19. These reflect the differences in the velocity time histories including larger displacement in the uniaxial stress case. There is more dispersion in the uniaxial strain waveform than in that for the fluid confined case.

In order to help understand the differences in the three calculations with relative fluid motion, as well as the influence of the relative motion on the overall response, relative motion time histories at three locations along the axis of the bar are presented in Figures 6.20 and 6.21. Figure 6.20 shows average relative velocity between the pore fluid and the porous skeleton at the 5, 10 and 15 inch ranges. The relative velocity waveforms for the uniaxial

strain and fluid confined cases are similar in shape, with the fluid confined case having the highest amplitude at all ranges. Waveforms for both confined conditions jump rapidly to a peak, begin a gradual decay, and then drop suddenly into a negative phase. At the close in ranges peak relative velocities are higher than the corresponding skeleton velocities shown in Figure 6.18. At further ranges they are about equal to the peak skeleton velocities. Thus, just behind the wavefront, the pore fluid surges ahead of the skeleton as fluid is squeezed out of adjoining elements by compression of the skeleton. Then the relative velocity gradually diminishes during which time the skeleton velocity is gradually increasing (see Figure 6.18). This is followed by a sharp drop in relative velocity and a large negative phase during which the pore fluid is moving backward relative to the skeleton. The sharp drop and negative phase in the relative fluid motion corresponds with a sharp reduction in skeleton velocity. The end of the negative phase occurs at about the time the skeleton velocity drops to zero.

The relative fluid velocity in the uniaxial stress loading (Figure 6.20) is much lower in magnitude and later in time than the corresponding signal in the confined bar calculations. This is in keeping with previous analysis which showed that relief waves from the sides of the bar immediately relieve pore pressures in the fluid. The character of the uniaxial stress waveform is opposite of those in the confined bar calculations in that the relative velocity rises gradually to a peak and then decays into a negative phase, resulting in a sinusoidally shaped waveform.

The displacement of the pore fluid relative to the porous skeleton is shown in Figure 6.21 for the three ranges of interest. In the case of the uniaxial strain and fluid confined bar calculations the pore fluid shows a strong surge ahead of the porous skeleton which peaks well before the maximum skeleton displacement (see Figure 6.19 for comparison). By the time of peak skeleton displacement, the pore fluid has moved back toward its original position in the bar. The backward motion continues into a negative phase during which the pore fluid is behind its original position in the bar. The negative phase gradually lessens until the fluid returns to its original position. There is very little relative displacement in the uniaxial stress case, with only a mild oscillation developing.

In the remaining illustrations in this section we take a more detailed look at the influence of relative fluid motion on stress and motion propagation in the uniaxial stress (Figures 6.22 - 6.25) uniaxial strain (Figures 6.26 - 6.29) and fluid confined loadings (Figures 6.30 - 6.33). Comparison of total stress time histories for the uniaxial stress loadings at the three ranges of interest with and without relative fluid motion are shown in Figure 6.22. There is very little difference in the waveforms because so little relative motion develops in this loading geometry. The influence of lateral position within the bar on the total stress at a range of 10 in is shown in Figure 6.23, both without and with relative fluid motion. The waveforms are very similar, but in the case without motion slightly higher peak stresses develop toward the center of the bar. In the case with fluid motion these differences in peak stress are reduced substantially. The influence of relative fluid motion on the skeleton velocities in the uniaxial stress loading is illustrated in Figure 6.23. As was the case with total stress, there is very little influence of the relative motion for this loading condition, though the relative fluid motion appears to damp out some of the high frequency oscillations in the calculation without relative motion.

The most dramatic influence of relative fluid motion is seen in the uniaxial strain calculations. Figure 6.25 shows comparisons of total stress time-histories at the three ranges of interest with and without relative fluid motion. The relative fluid motion dramatically alters the wave shapes by increasing the propagation velocity, reducing the peak stress and smearing both the rise time and decay. As noted in the previous discussion, the increased wavespeed is predicted by the closed form solution shown in Figure 6.1 (listed in Table 6.4). Despite the rapid attenuation of peak stress due to the relative fluid motion, there appears to be very little reduction in total impulse transmitted by the stress wave. Thus, the relative fluid motion tends to spatially redistribute the energy in the wave, with very little absorption of energy due to the relative fluid motion.

The total stress waveforms for the calculation with relative fluid motion (Figure 6.25) are resolved into components of effective axial stress and pore pressure in Figure 6.26. At all ranges there is a rapid rise in pore pressure commensurate with a slower rise in effective

stress. This is followed by a levelling off in pore pressure, then a sharp decline. The sharp decline in pore pressure is accompanied by only a modest decline in effective stress with the total stress during the later portion of the waveform composed entirely of effective stress.

The waveform comparisons for axial skeleton velocity shown in Figure 6.27 are very similar to those for total stress shown in Figure 6.25. The integration of the velocity waveforms in Figure 6.28 shows that the late time displacements at all ranges are nearly identical between the two cases confirming the conclusion that little energy dissipation occurs in the case with pore fluid flow and that the changes in waveform are a result of the relative motion itself rather than due to energy dissipation mechanisms. While the late time displacements are about equal, the rise to peak displacement is much more rapid in the case of no relative fluid motion because of the large amount of dispersion in the calculations with fluid motion.

The motion of the pore fluid relative to the porous skeleton is shown in Figure 6.29 at each of the three ranges of interest. The absolute displacement of the pore fluid is much greater than that of the skeleton at early time due to the surge of pore fluid ahead of the skeleton. Eventually, the skeleton overtakes and passes the pore fluid, followed by a very gradual return of the pore fluid to its original position in the skeleton at very late times.

The fluid confined pressure bar calculation shows many of the same characteristics as the uniaxial strain calculation, but with less relative fluid motion and dispersion in the case where relative fluid motion is allowed. Comparison of the fluid confined total stresses with and without relative motion is shown in Figure 6.30. The case with relative motion has a faster wavespeed, more peak attenuation and more dispersion, all trends observed in the uniaxial strain comparisons. Figure 6.31 demonstrates that the fluid confined loading is very uniform over the entire width of the bar, both with and without relative motion. Figure 6.32 shows that the uniaxial velocity time-histories are very similar to the total stresses. Finally, the fluid displacement and skeleton displacement time histories for the case with relative fluid motion are compared in Figure 6.33. The response is again similar to that for the uniaxial strain case in that the fluid initially surges ahead of the skeleton, the skeleton overtakes and

passes the fluid, then finally the two return to their initial state of relative equilibrium.

6.6 CONCLUSIONS FROM PARAMETRIC CALCULATIONS

The set of calculations discussed in this section were of value in planning and designing the dynamic pressure bar experiments. Principal conclusions from the analysis of these calculations include the following:

1. Pore fluid within an unconfined bar or within a bar confined at a uniform pressure (such as by confining the bar within a pressurized gas) has very little influence on the dynamic response of the bar. Because of the immediate relief offered by waves propagating inward from the sides of the bar, there is almost no buildup of pore fluid pressure and only very minor relative fluid motion developed. Neither configuration was considered satisfactory for the experimental portion of this study.

2. The dynamic uniaxial strain loading condition, in which the bar is perfectly restrained to zero expansion or contraction in the lateral direction, shows dramatic influence of relative pore fluid motion on both the wavespeed and shape of the propagating wave. Allowing pore fluid motion, as governed by the stipulated porosity and permeability of the bar, results in increased wavespeed, rapid attenuation of peak velocities and stresses, and rapid dispersion in the waveform. These changes occur in conjunction with the relative fluid motion, but are not a result of the minor amount of energy dissipation due to fluid friction. During the dynamic loading with pore fluid motion, the pore fluid initially surges well ahead of the porous skeleton, followed by the skeleton overtaking and passing the pore fluid and finally the fluid and skeleton returning to their initial relative positions very late in the loading. Though the uniaxial strain loading is an ideal one for studying the influence of relative pore fluid motion, in practice it is nearly impossible to satisfactorily confine a pressure bar under such conditions.

3.   Confinement of the pressure bar within a thin annulus of liquid confined within a steel vessel around the bar appears to provide a satisfactory means of replicating all of the characteristics of the uniaxial strain loading. Even though the bar is not perfectly confined, confinement is sufficient to generate all of the phenomena observed above in the uniaxial strain case. However, these phenomena are somewhat less prominent in the case of the fluid confined bar, though they should be easily detected and measured in our test apparatus.

Table 6.1. Summary of parametric calculations.

Confined Condition	Permeable Porous Bar	Impermeable Porous Bar
Uniaxial Stress - Constant Confining Pressure	WB-U-SR	WB-U-SN
Uniaxial Strain	WB-C-SR	WB-C-SN
Liquid Confinement, Small Annulus	WB-F-SR	WB-F-SN

Table 6.2. Properties of porous skeleton and pore fluid used in parametric calculations.

Porous skeleton (316 L Stainless Steel, SIKA-R-100)		
Skeleton:		
Porosity:	$n = 0.465$	
Permeability:	$k = 0.01542$ in/sec (kerosene)	
Drained Bulk Modulus:	$K_s = 0.26 \times 10^6$ psi	
Poisson's Ratio:	$\upsilon = 0.2$	
Solid Grain:		
Specific Gravity:	$G_s = 7.8$	
Bulk Modulus:	$K_g = 16.67 \times 10^6$ psi	
Pore Fluid (Kerosene)		
Specific Gravity:	$G_s = 0.81$	
Bulk Modulus:	$K_f = 0.188 \times 16^6$ psi	

Table 6.3. Summary of wavespeeds for materials used in parametric calculations.

MATERIAL	CONDITION	MODULUS (psi)	SPECIFIC GRAVITY	WAVESPEED (m/s)
Kerosene	Confined	$.188 \times 10^6$	0.81	1265
Porous Stainless Steel	Uniaxial stress, dry skeleton	$.468 \times 10^6$	4.17	880
	Uniaxial strain, dry skeleton	$.520 \times 10^6$	4.17	927
	Uniaxial stress, saturated skeleton	$.468 \times 10^6$	4.64	834
	Uniaxial strain, saturated (low frequency)	$.909 \times 10^6$	4.64	1174
	Uniaxial strain, saturated (high frequency)	1.28×10^6	4.64	1381
Water	Confined	$.322 \times 10^6$	1.00	1490
Solid Steel	Uniaxial strain	38.0×10^6	7.80	5796

Table 6.4. Wavespeeds in saturated, porous bar determined from parametric calculations.

CALCULATION SET	RELATIVE FLUID MOTION PREVENTED (m/s)	RELATIVE FLUID MOTION ALLOWED (m/s)
Uniaxial Stress (constant confining pressure)	835	845
Uniaxial Strain	1170	1375
Liquid Confinement (small annulus)	1210	1290

$$
\begin{array}{ll}
n = 0.465 & \text{s.g.}_f = 0.81 \\
k = 0.01542 & \text{s.g.}_s = 7.8 \\
r = 0 & K_f = 0.1880E+06 \\
r = 0 & K_g = 0.1667E+08 \\
\gamma_w = 0.03611 & K_s = 0.2600E+06 \\
g = 386.4 & \nu = 0.2
\end{array}
$$
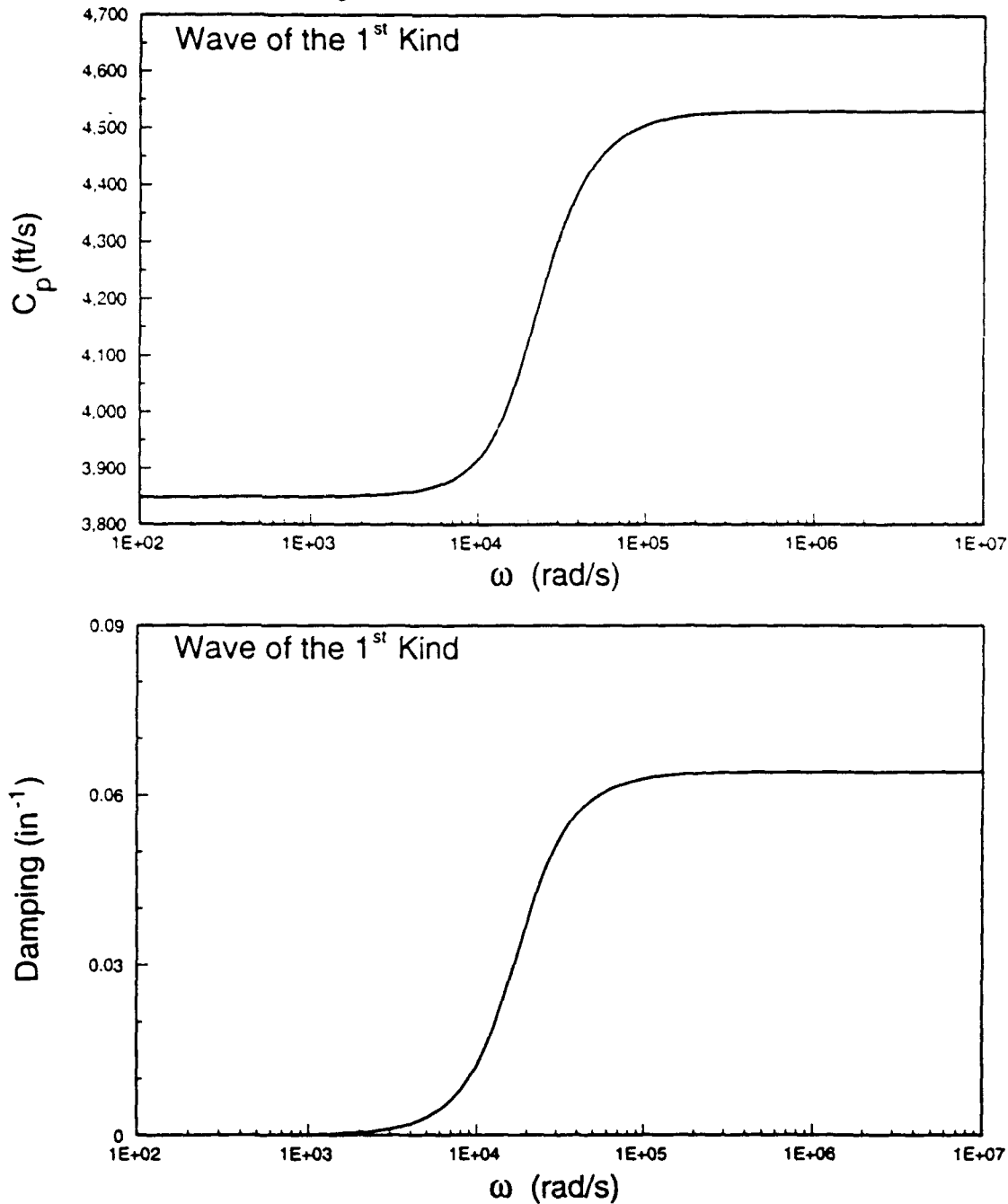
Figure 6.1a. Speed and damping of the wave of the first kind as a function of excitation frequency computed with the program TWAVE using the initial estimated properties of the porous stainless steel bar.

$$n = 0.465 \qquad s.g._f = 0.81$$
$$k = 0.01542 \qquad s.g._s = 7.8$$
$$r = 0 \qquad K_f = 0.1880E+06$$
$$r = 0 \qquad K_g = 0.1667E+08$$
$$\gamma_w = 0.03611 \qquad K_s = 0.2600E+06$$
$$g = 386.4 \qquad \nu = 0.2$$
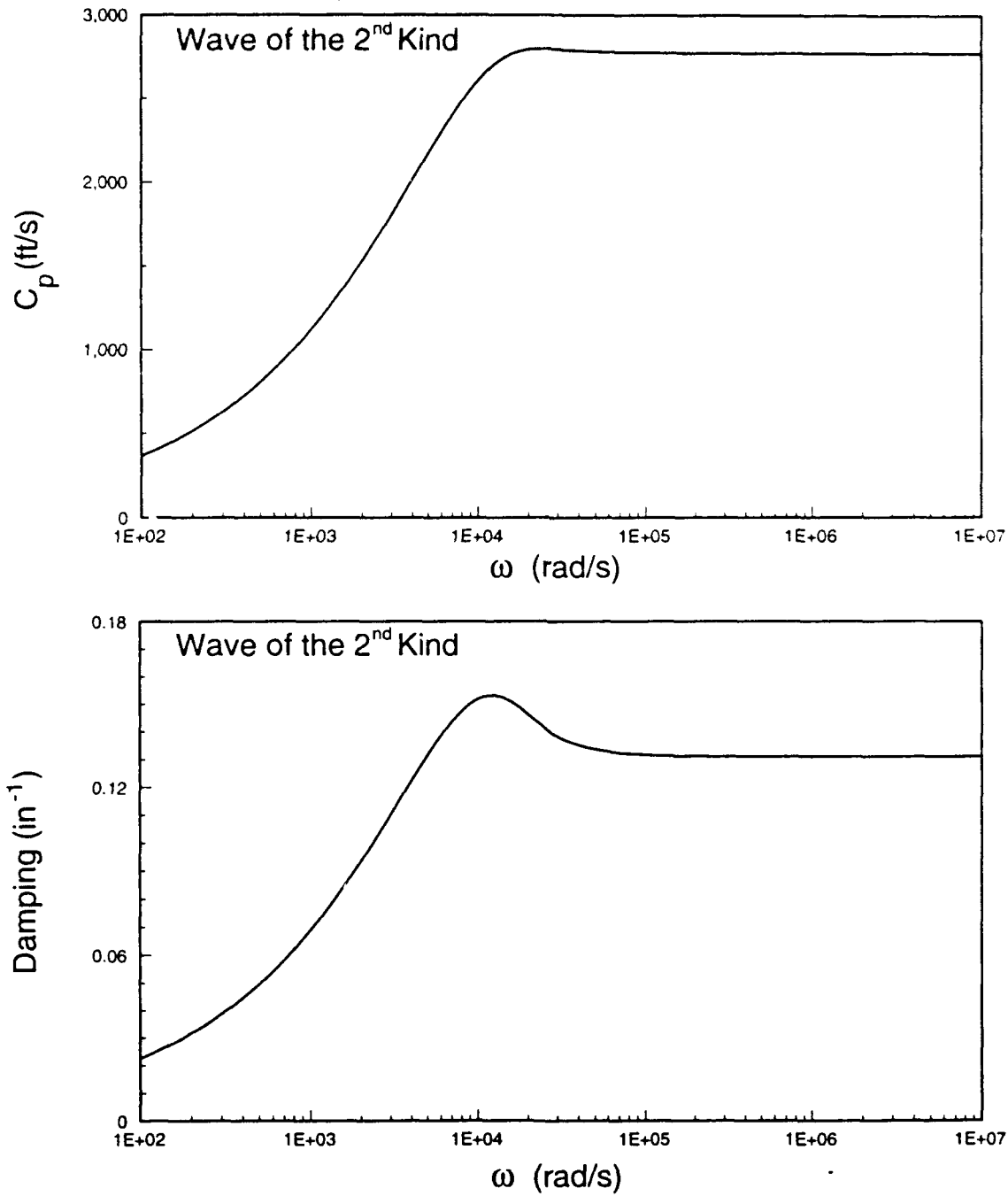
Figure 6.1b.   Speed and damping of the wave of the second kind as a function of excitation frequency computed with the program TWAVE using the initial estimated properties of the porous stainless steel bar.

NOTE: Not to Scale

Transmitter Bar
50" Long x 2" Diam

Hydraulic Cylinder
35" Stroke, 4" Bore

Incident Bar
50" Long x 2" Diam

Pressure Vessel
30" Long, 5" Bore

Barrel to Guide
2" Diameter Striker Bar

48"

Gas Gun

Steel Beam
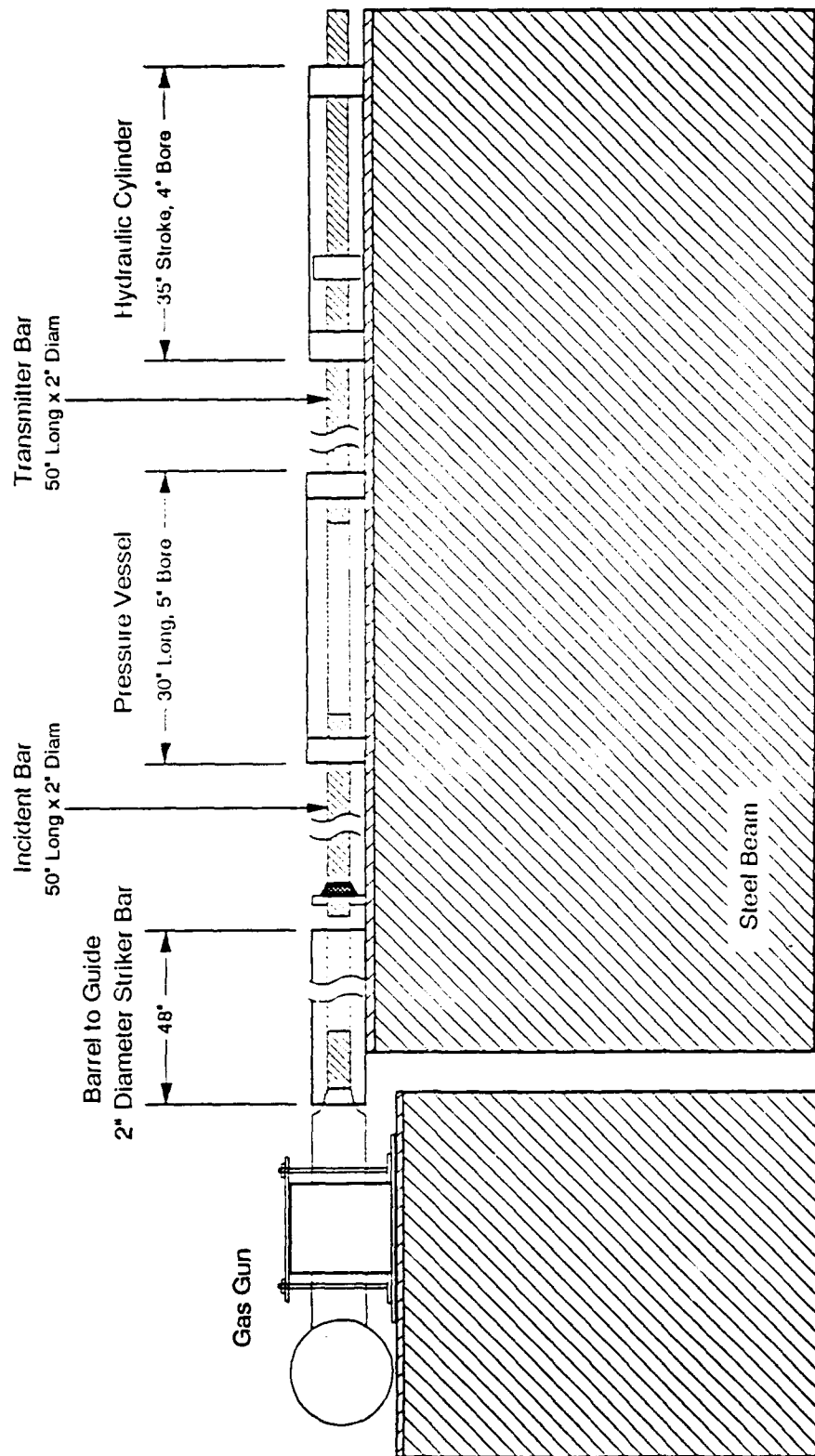
Figure 6.2. Drawing of the wave propagation bar showing dimensions of the important components.
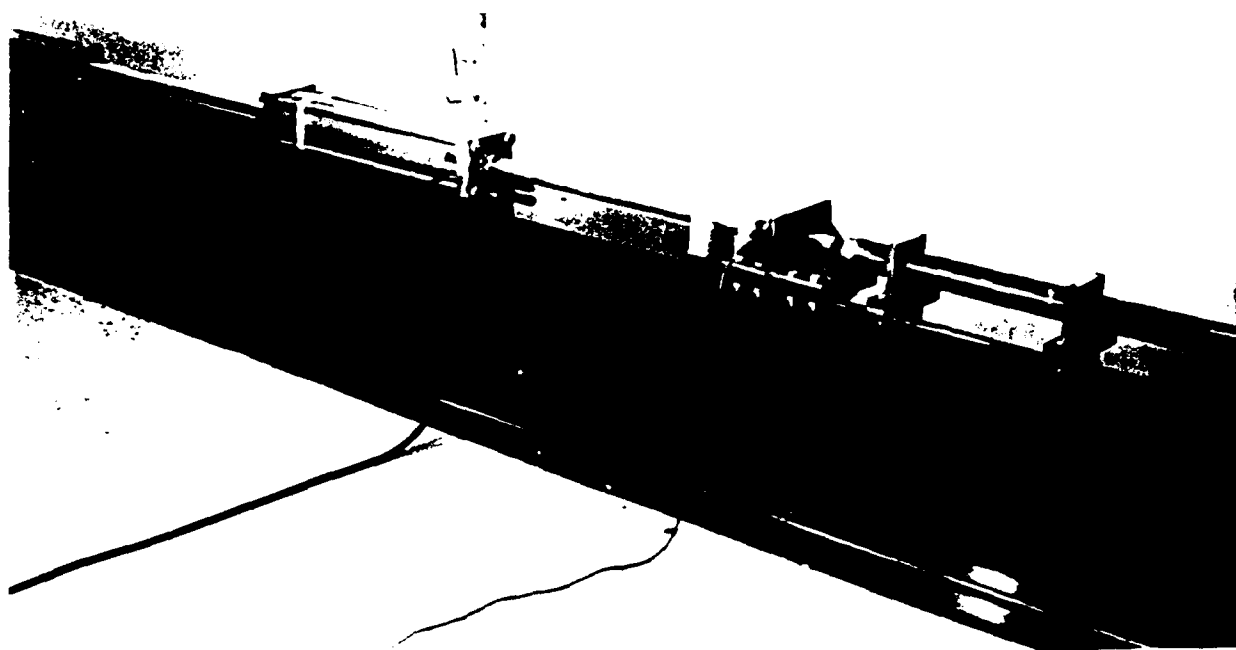
Figure 6.3.   Photograph of the wave propagation bar from the side.
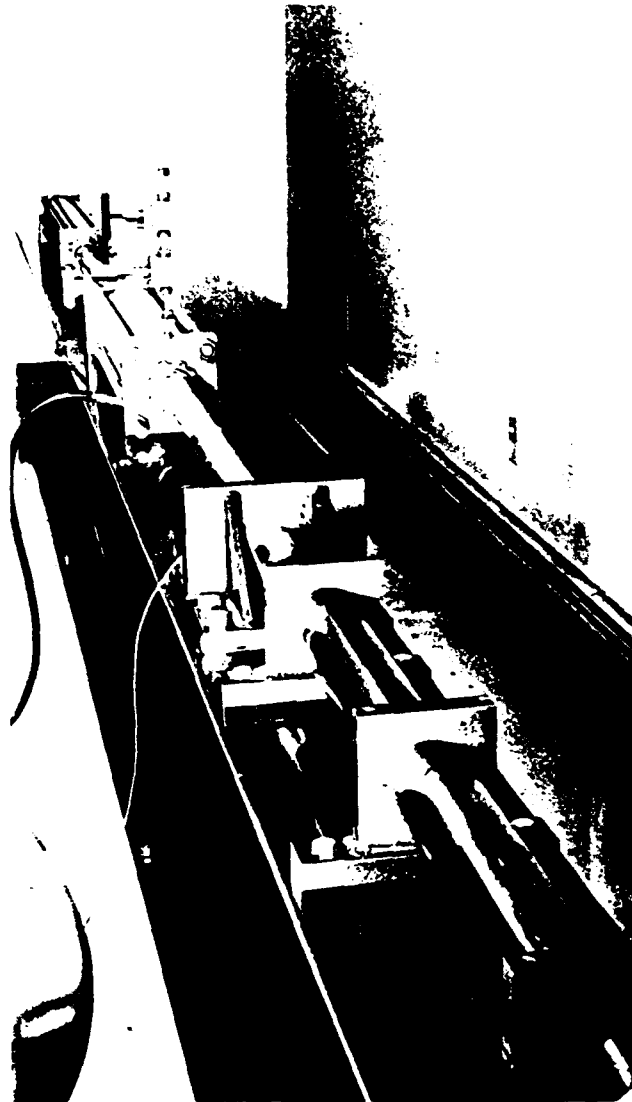
Figure 6.4.   Photograph of the wave propagation bar looking down axis.
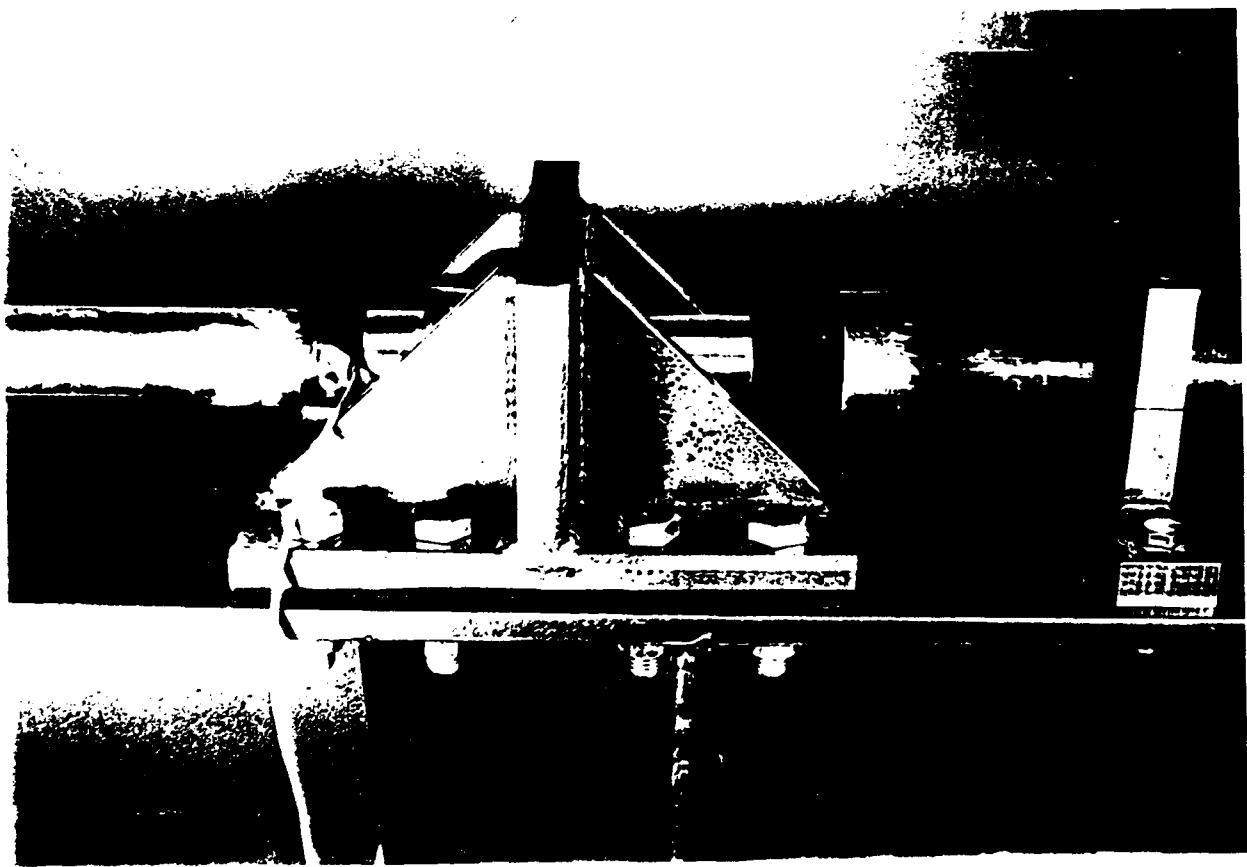
Figure 6.5. Photograph of the upstream end of the incident bar showing the axial load reaction frame.
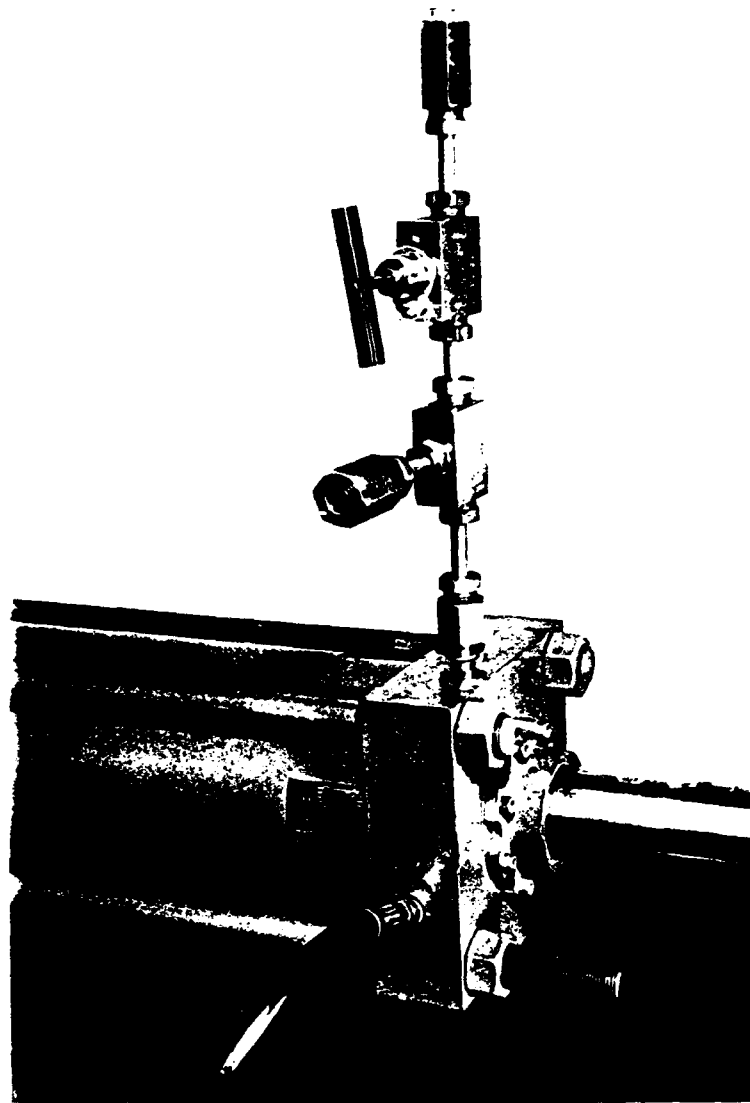
Figure 6.6. Photograph of the incident bar entering the upstream end of the pressure vessel.

Figure 6.7. Photograph of the downstream end of the pressure vessel showing the electrical penetrations and the connection to the specimen pore space.
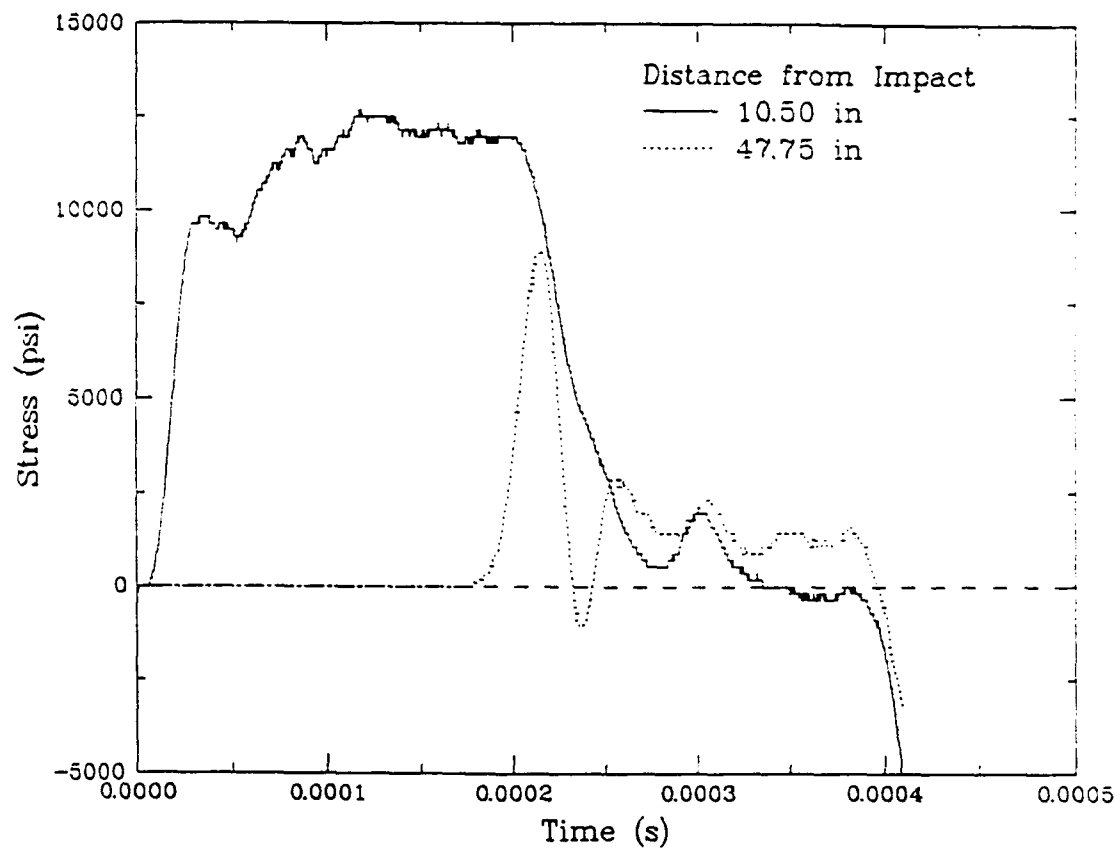
Figure 6.8.   Stress waves measured in two different locations on the
              incident bar of the wave propagation device due to impact
              of a 20-inch striker bar.

Uniaxial Stress Model
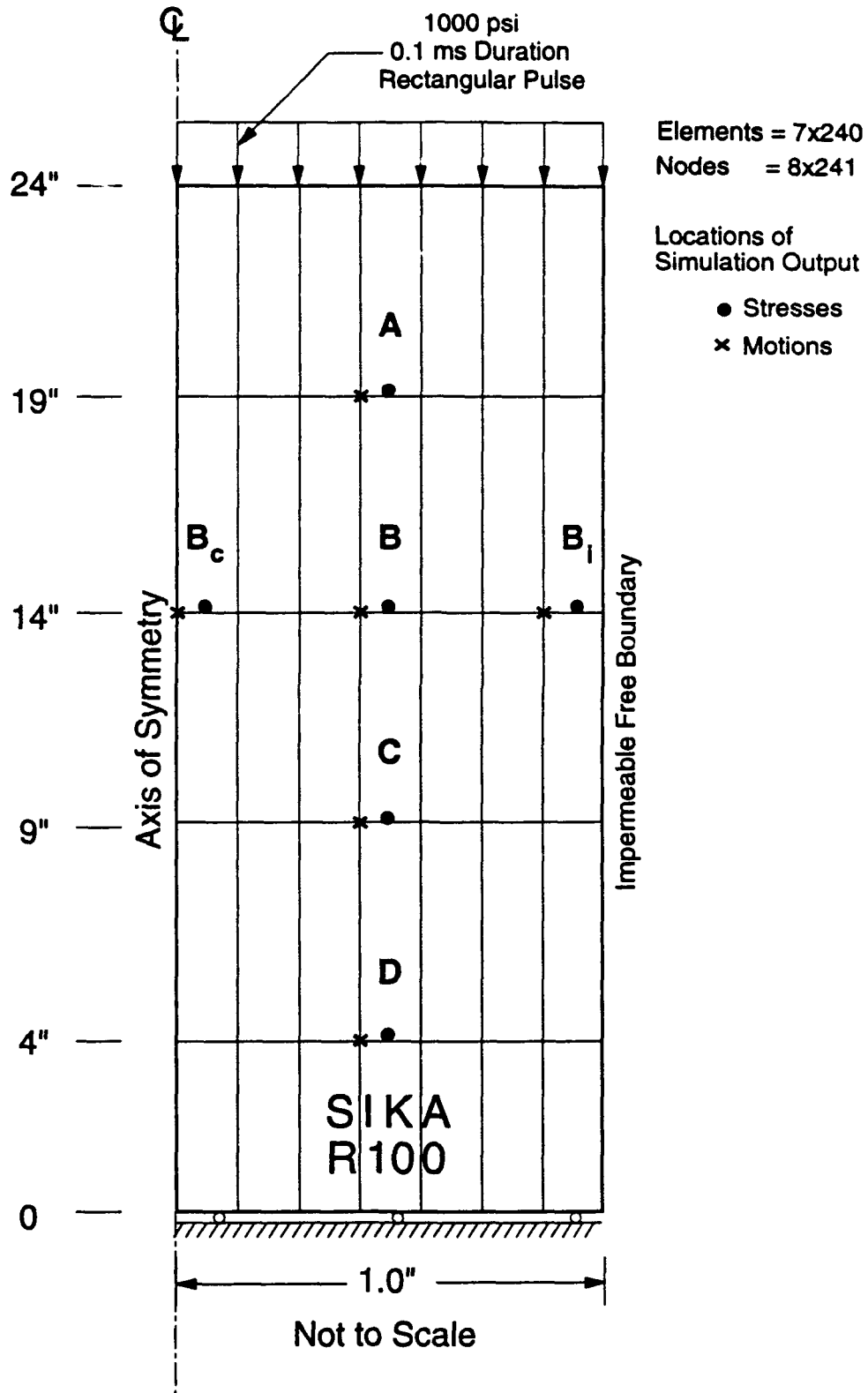
Figure 6.9.   Schematic section view of uniaxial stress calculation.

6-33

Uniaxial Strain Model
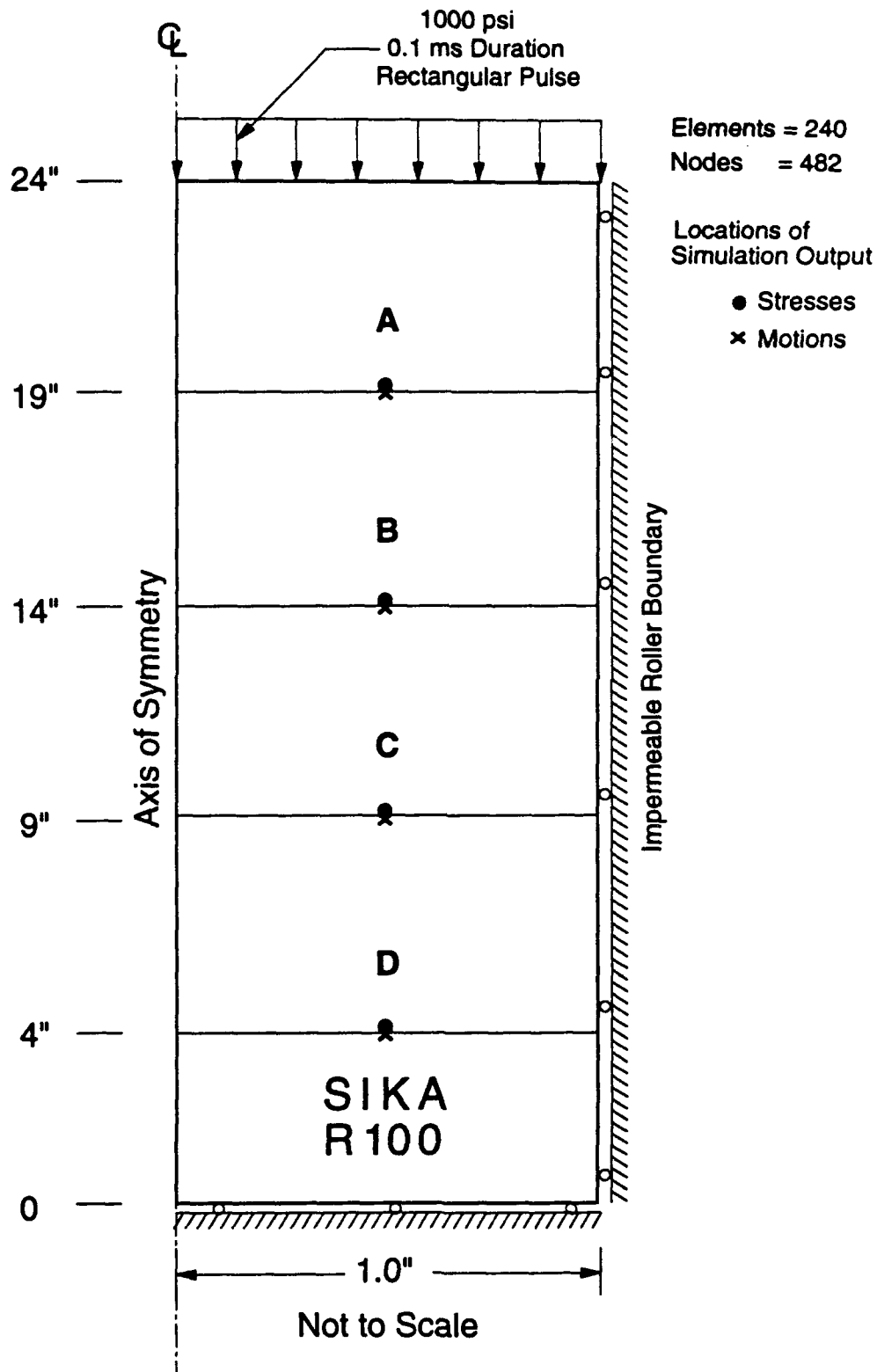
Figure 6.10. Schematic section view of uniaxial strain calculation.
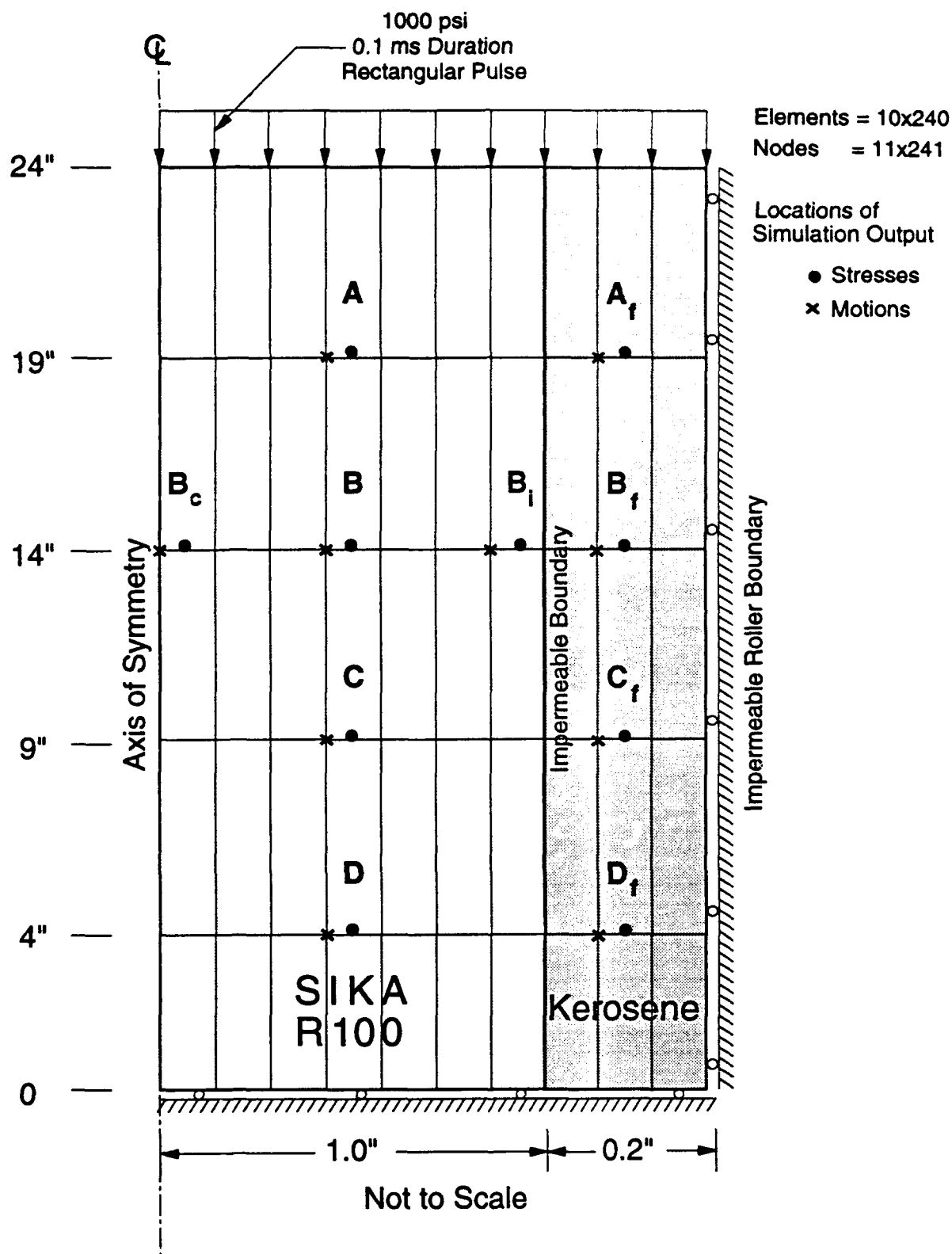
Figure 6.11. Schematic section view of fluid confined calculation.
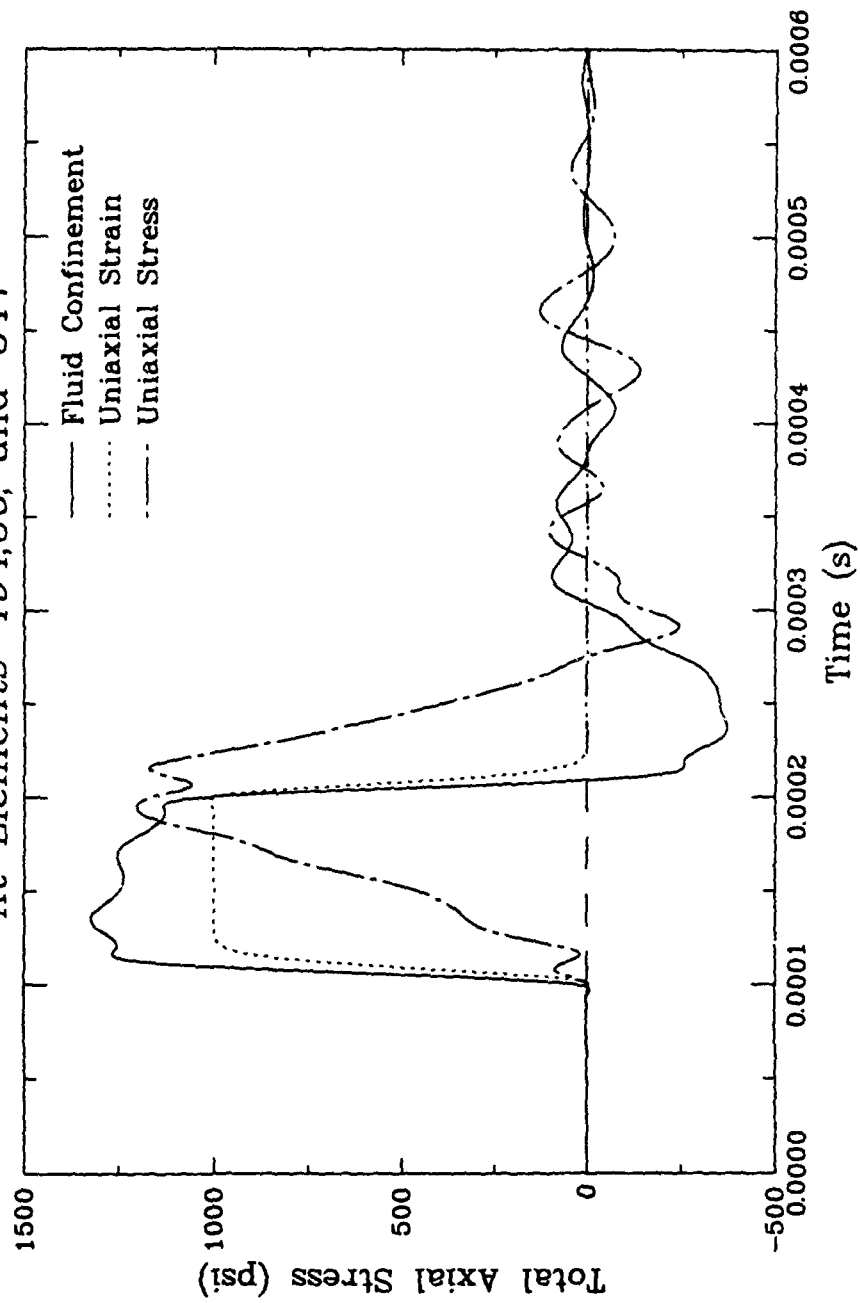
Figure 6.12a. Influence of confinement condition on total stress waveforms with no relative fluid motion at Range A (5 in.).

Figure 6.12b. Influence of confinement condition on total stress waveforms with no relative fluid motion at Range B (10 in.).

WB–F,C,U–SN

At Elements 1494,150, and 1047

Fluid Confinement
Uniaxial Strain
Uniaxial Stress

Total Axial Stress (psi)

Time (s)
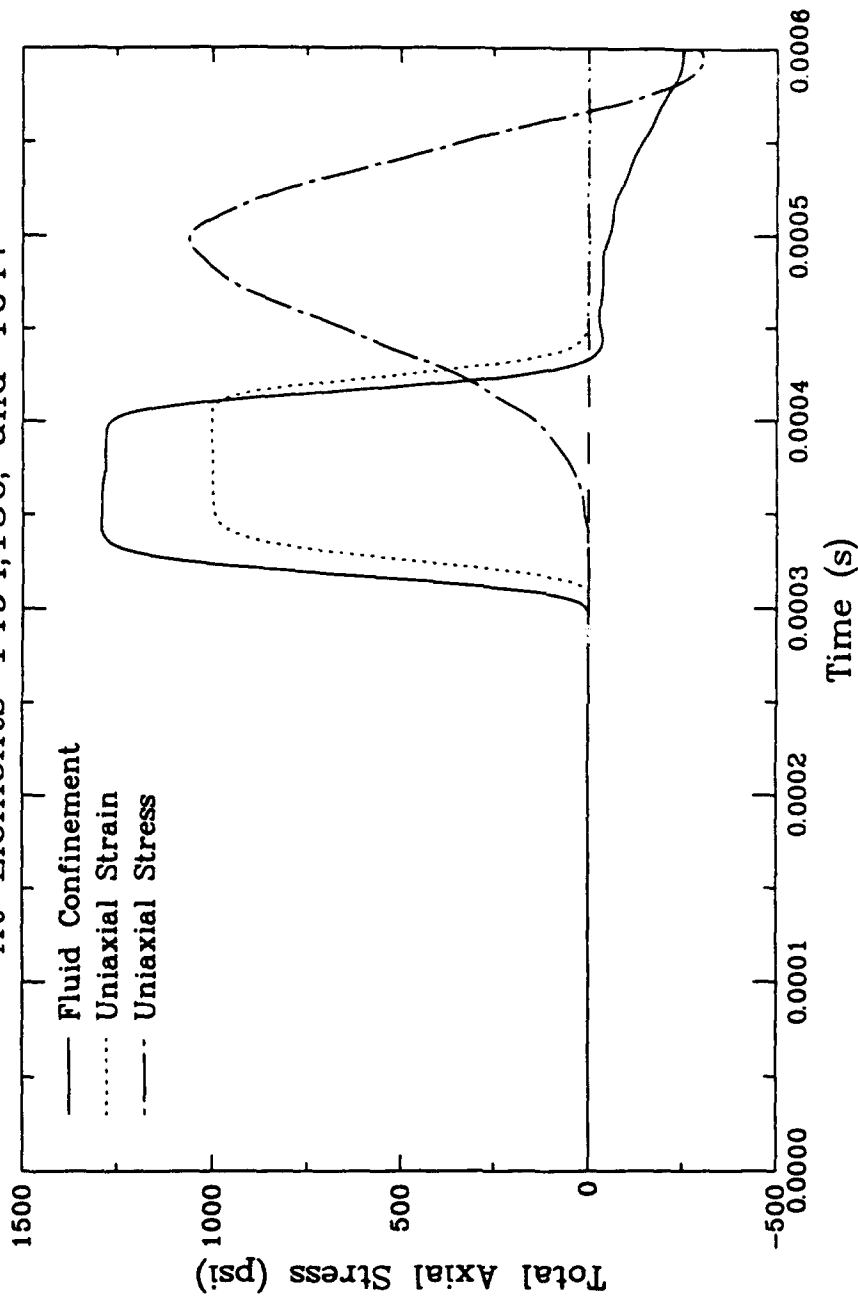
Figure 12c. Influence of confinement condition on total stress waveforms with no relative fluid motion at Range C (15 in.)

6-38
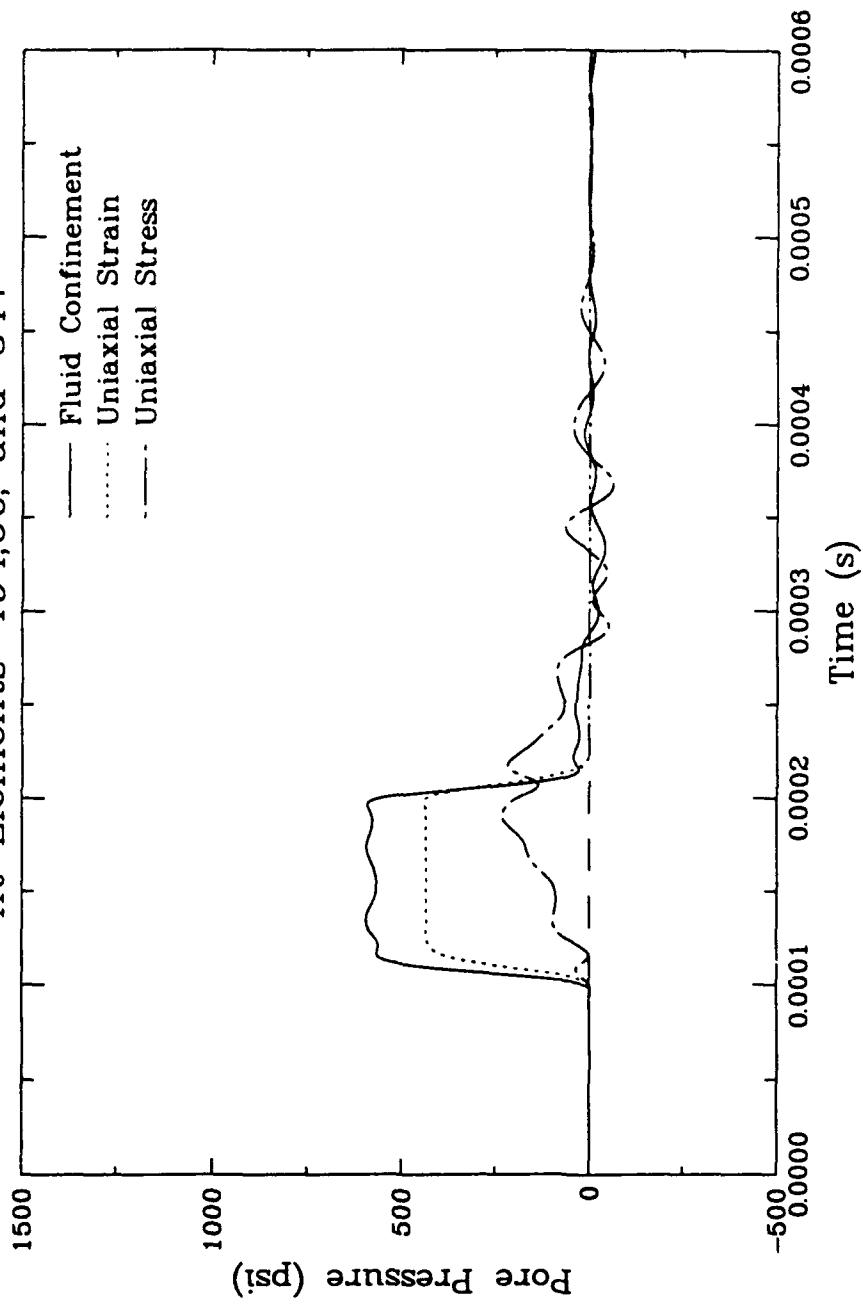
Figure 6.13a. Influence of confinement condition on pore pressure with no relative fluid motion at Range A (5 in.).

Figure 6.13b. Influence of confinement condition on pore pressure with no relative fluid motion at Range B (10 in.)

Figure 6.13c. Influence of confinement condition on pore pressure with no relative fluid motion at Range C (15 in.).
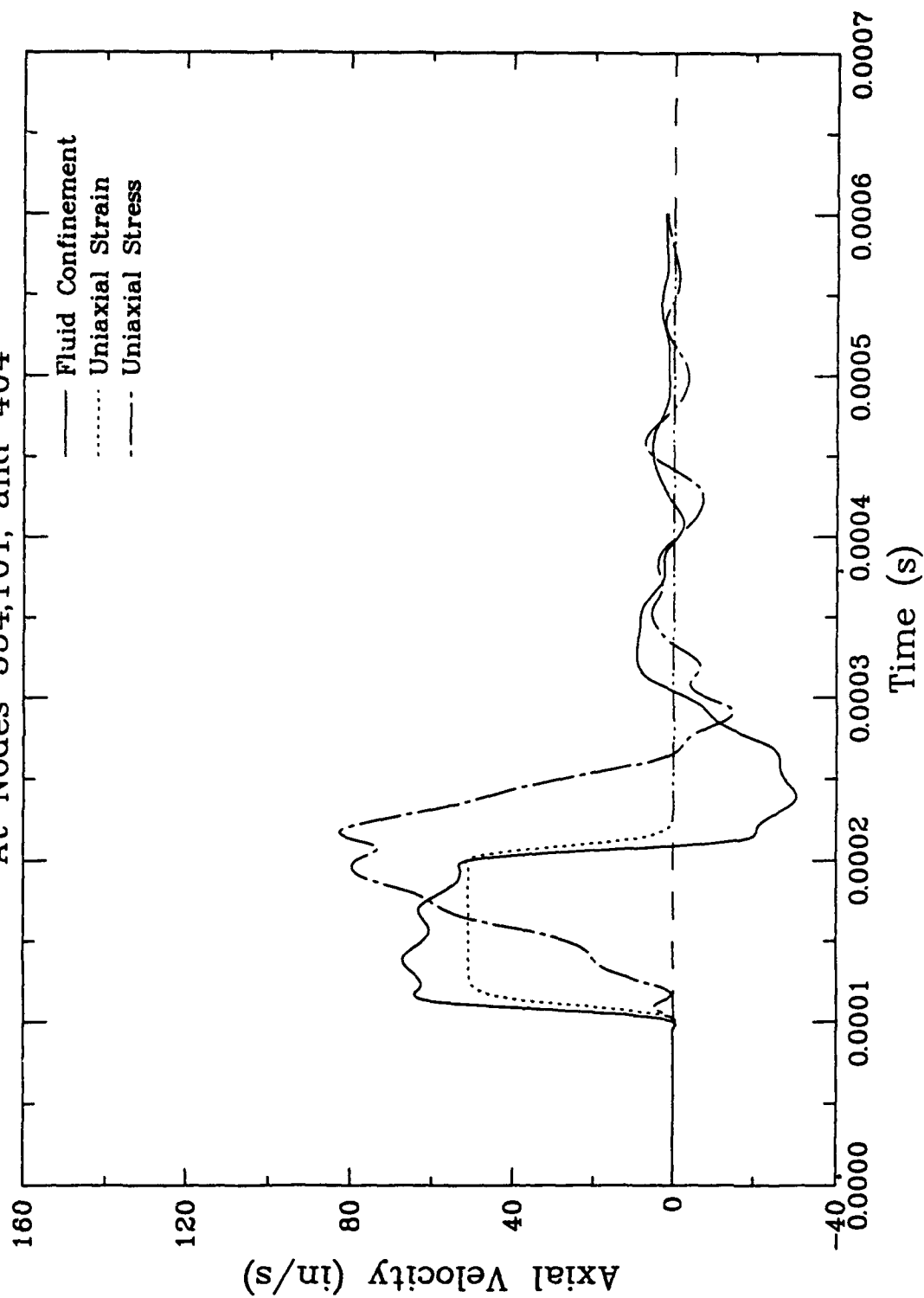
Figure 6.14a. Influence of confinement condition on particle velocity with no relative fluid motion at Range A (5 in.).

Figure 6.14b. Influence of confinement condition on particle velocity with no relative fluid motion at Range B (10 in.).
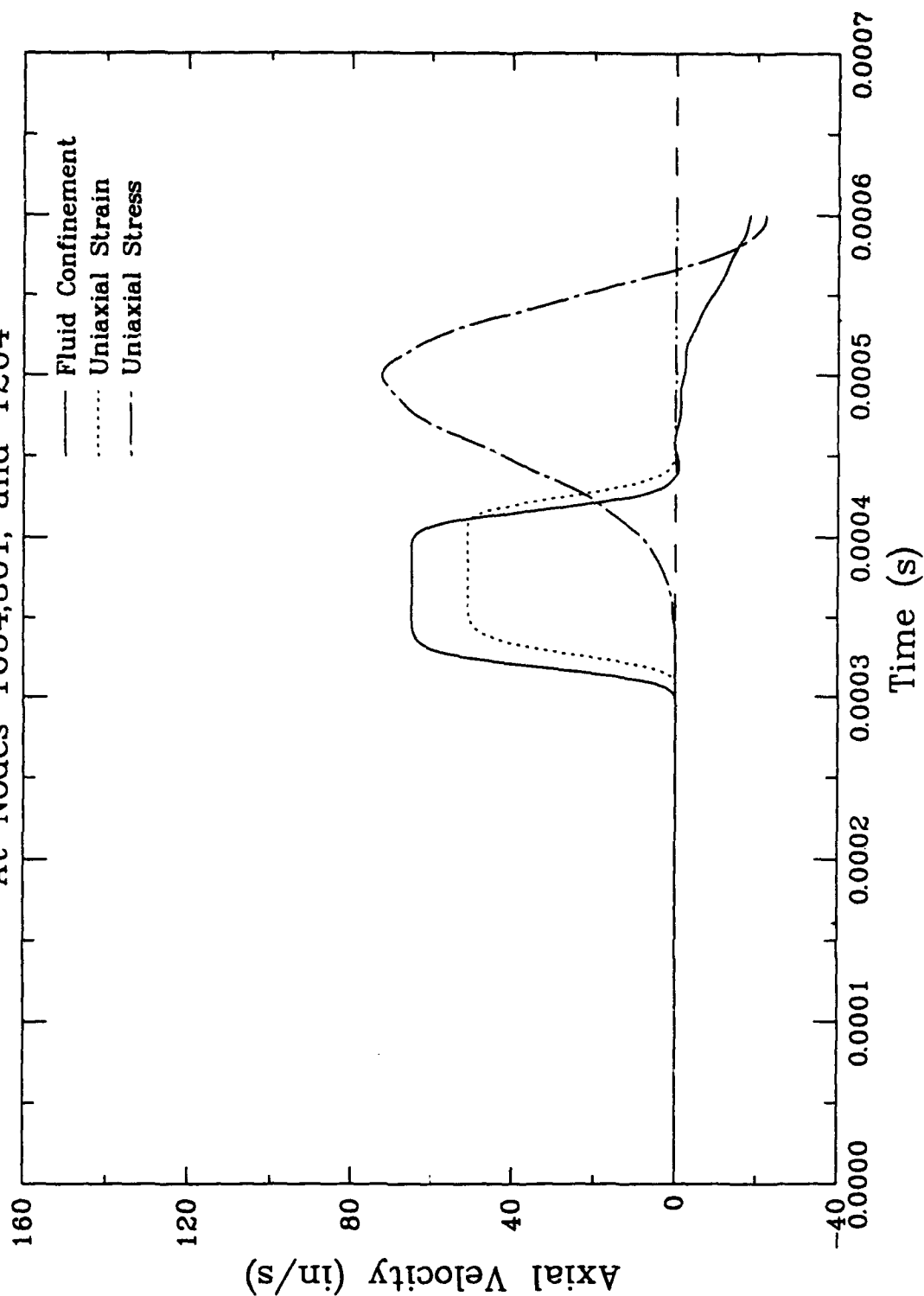
Figure 6.14c. Influence of confinement condition on particle velocity with no relative fluid motion at Range C (15 in.).

Figure 6.15a. Influence of confinement condition on particle displacement with no relative fluid motion at Range A (5 in.).

WB–F,C,U–SN

At Nodes 1104,201, and 804

— Fluid Confinement
...... Uniaxial Strain
—·— Uniaxial Stress

Axial Displacement (in)

Time (s)
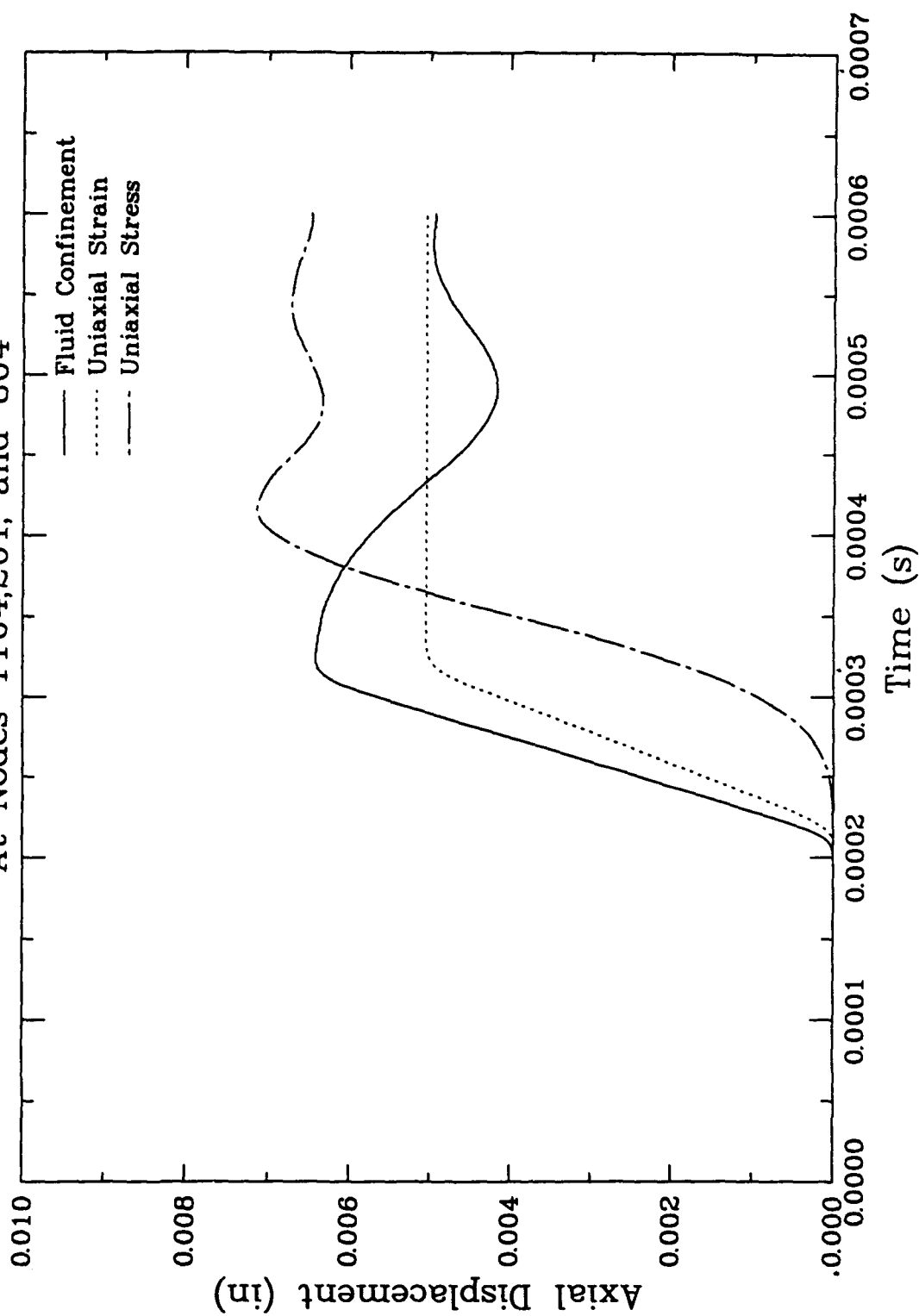
Figure 6.15b. Influence of confinement condition on particle displacement with no relative fluid motion at Range B (10 in.).

Figure 6.15c.   Influence of confinement condition on particle displacement with no relative fluid motion at Range C (15 in.)

Figure 6.16a. Influence of confinement condition on total stress waveforms with relative fluid motion at Range A (5 in.).

WB-F,CU-SR
At Elements 994,100, and 697

Fluid Confinement
Uniaxial Strain
Uniaxial Stress
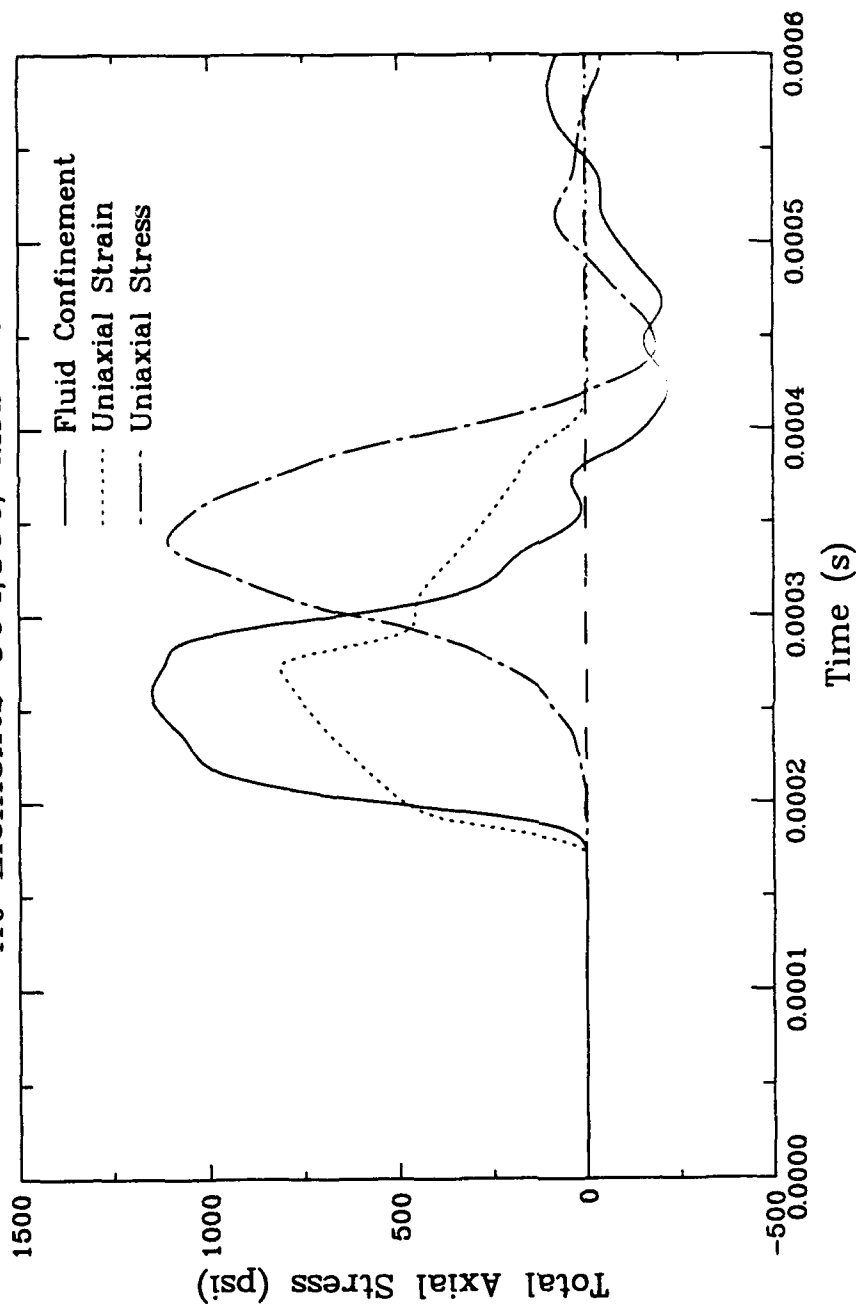
Figure 6.16b. Influence of confinement condition on total stress waveforms with relative fluid motion at Range B (10 in.)

Figure 6.16c. Influence of confinement condition on total stress waveforms with relative fluid motion at Range C (15 in.).

6-50
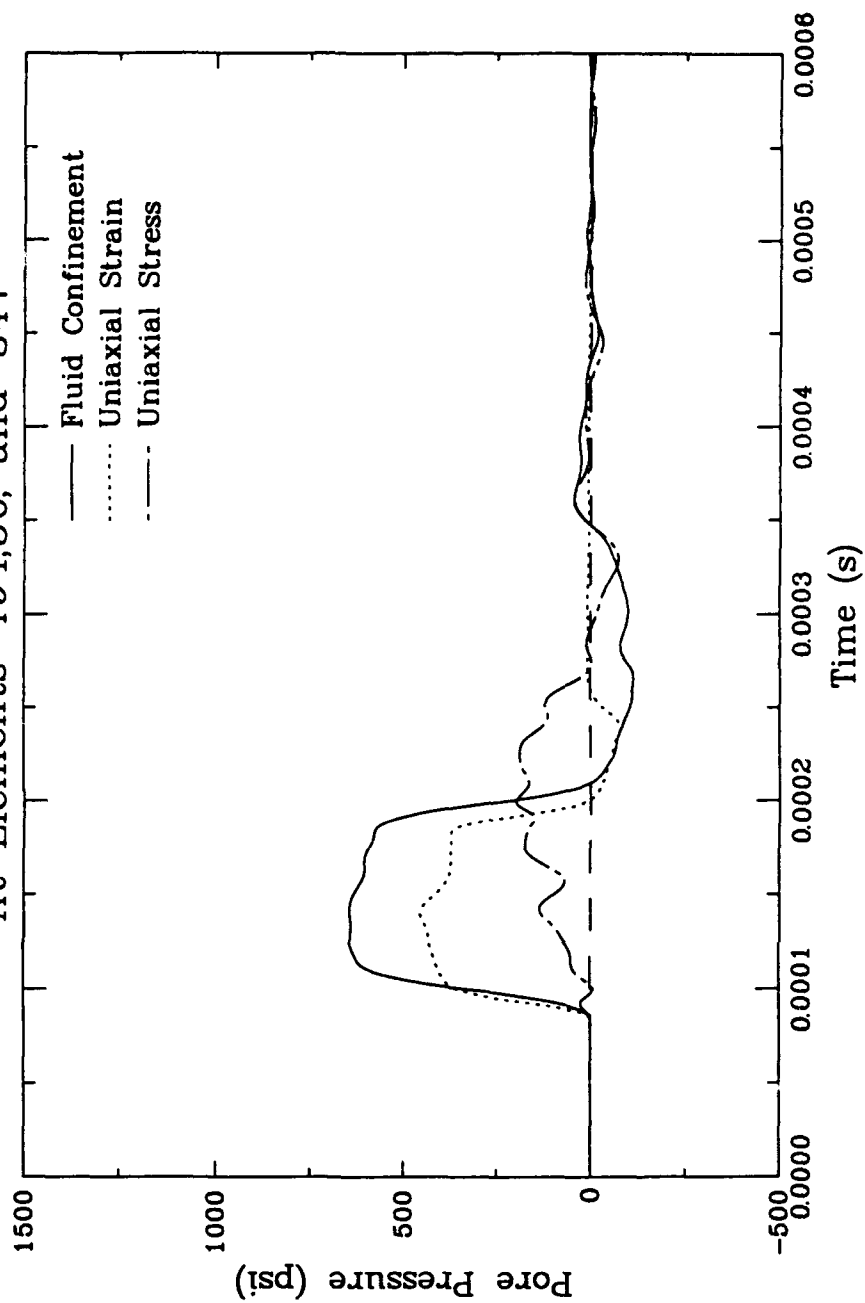
Figure 6.17a. Influence of confinement condition on pore pressure with relative fluid motion at Range A (5 in.).

Figure 6.17b. Influence of confinement condition on pore pressure with relative fluid motion at Range B (10 in.).
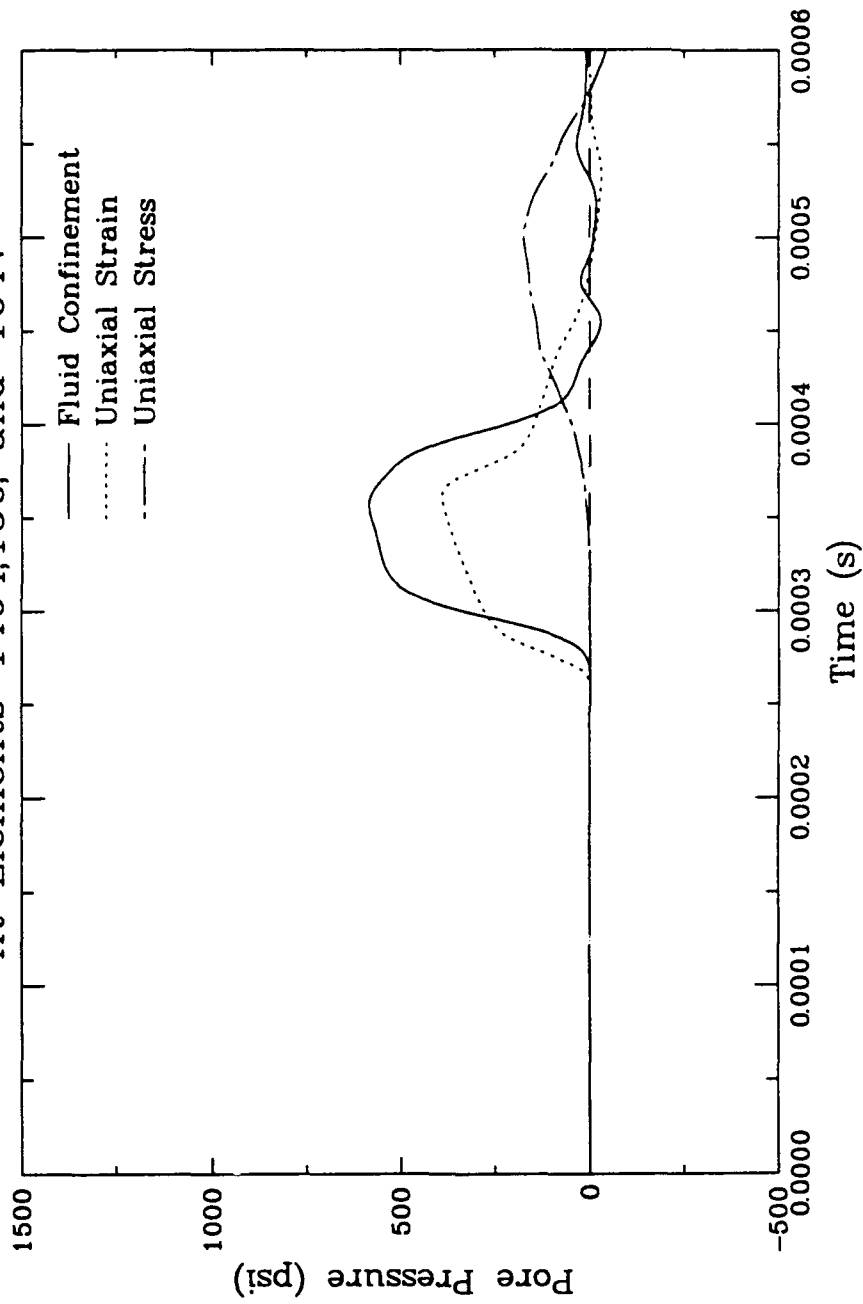
Figure 6.17c. Influence of confinement condition on pore pressure with relative fluid motion at Range C (15 in.).
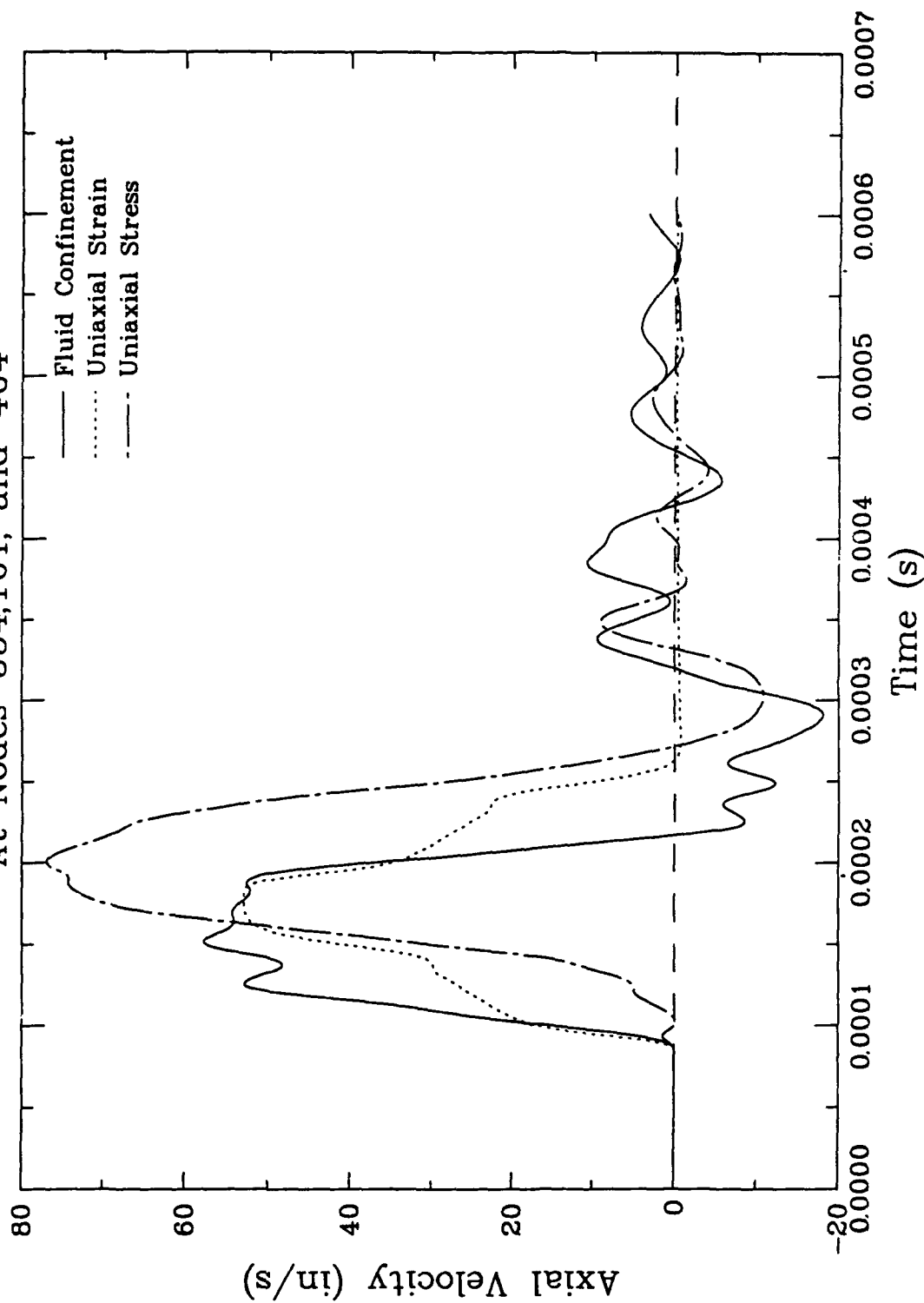
Figure 6.18a. Influence of confinement condition on skeleton particle velocity with relative fluid motion at Range A (5 in.).
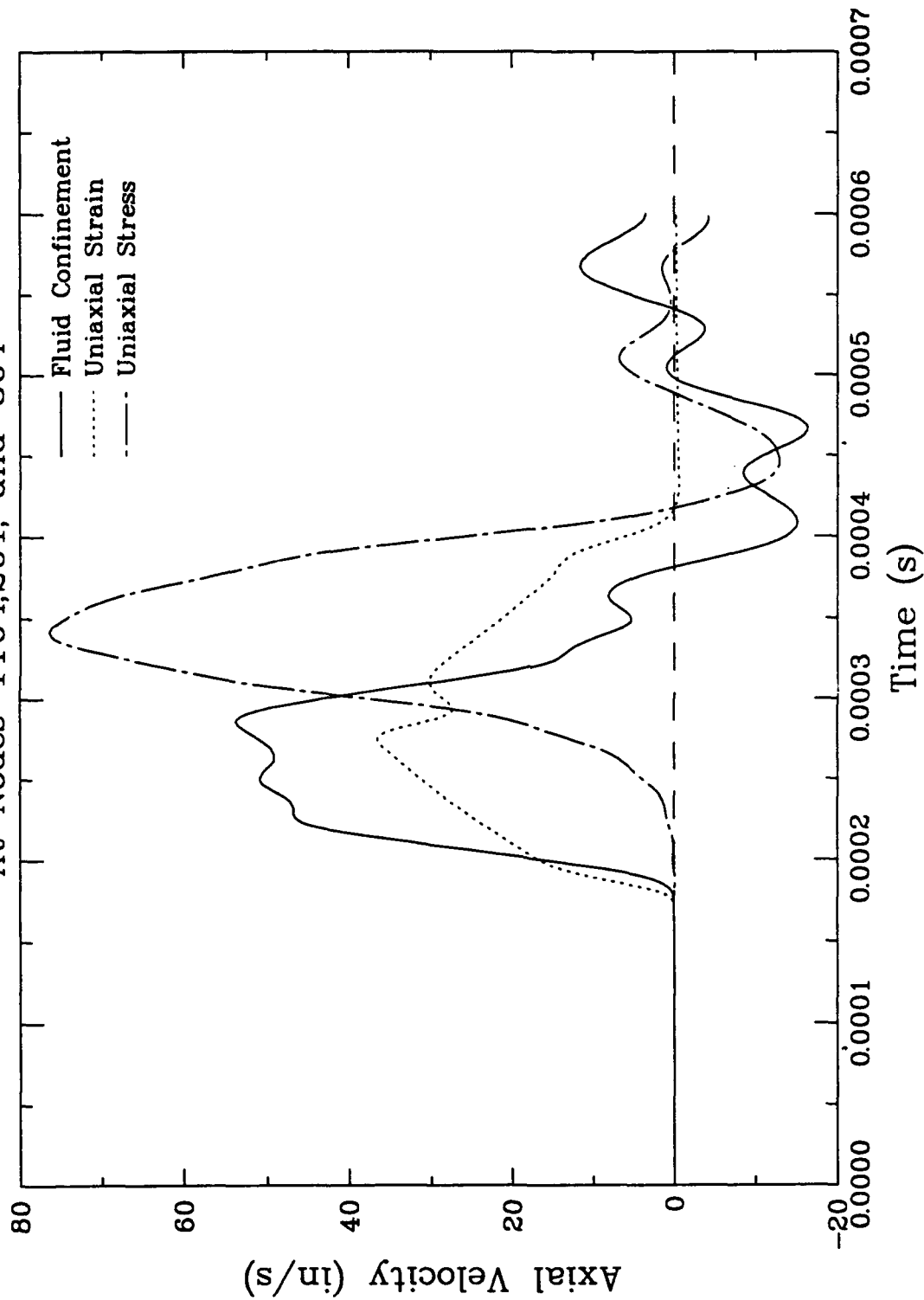
Figure 6.18b. Influence of confinement condition on skeleton particle velocity with relative fluid motion at Range B (10 in.).

Figure 6.18c. Influence of confinement condition on skeleton particle velocity with relative fluid motion at Range C (15 in.).

WB-F,C,U-SR

At Nodes 554,101, and 404

Fluid Confinement
Uniaxial Strain
Uniaxial Stress
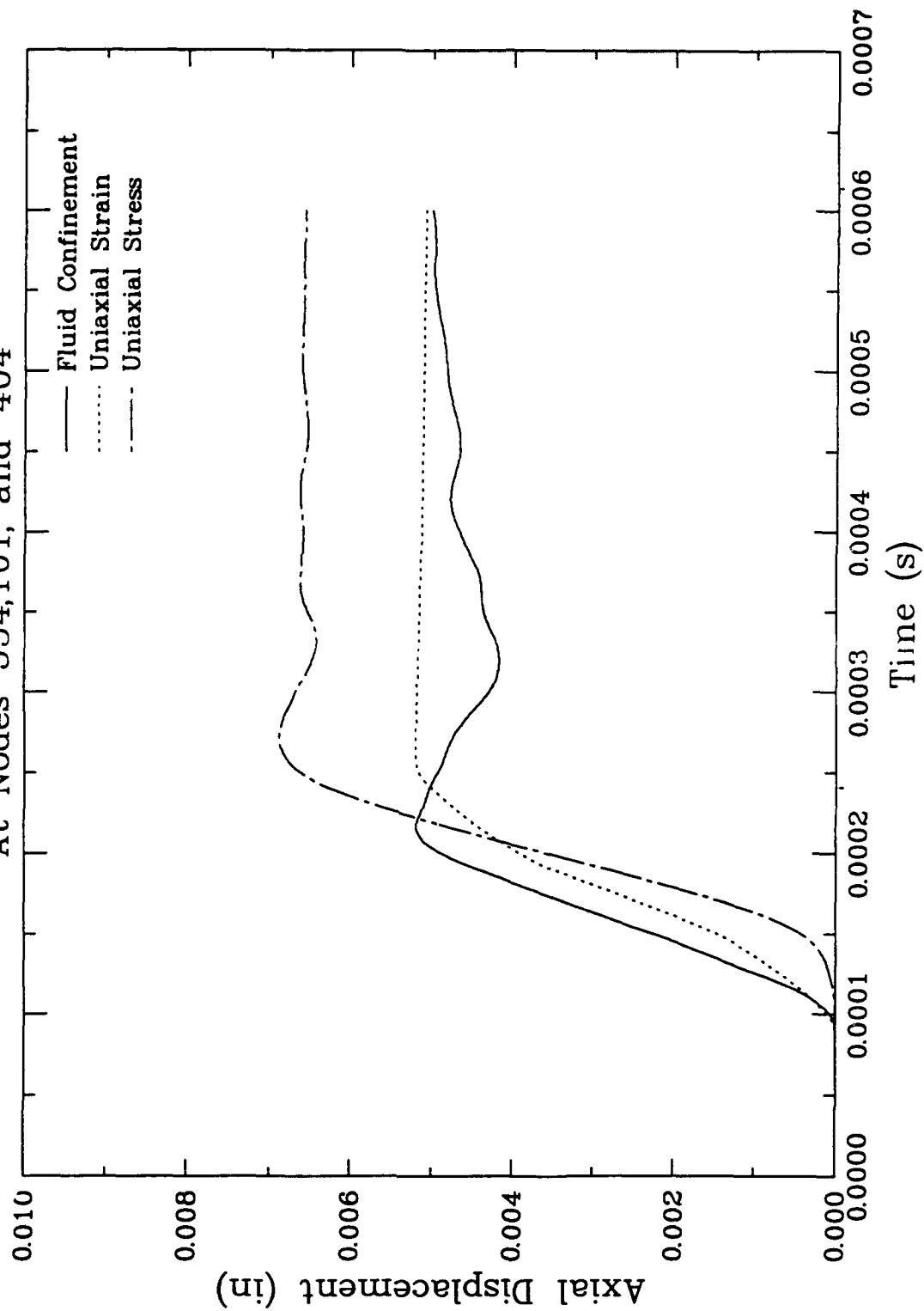
Figure 6.19a. Influence of confinement condition on skeleton particle displacement with relative fluid motion at Range A (5 in.).

Figure 6.19b. Influence of confinement condition on skeleton particle displacement with relative fluid motion at Range B (10 in.).

WB–F,C,U–SR

At Nodes 1654,301, and 1204

Fluid Confinement
Uniaxial Strain
Uniaxial Stress

Axial Displacement (in)

Time (s)
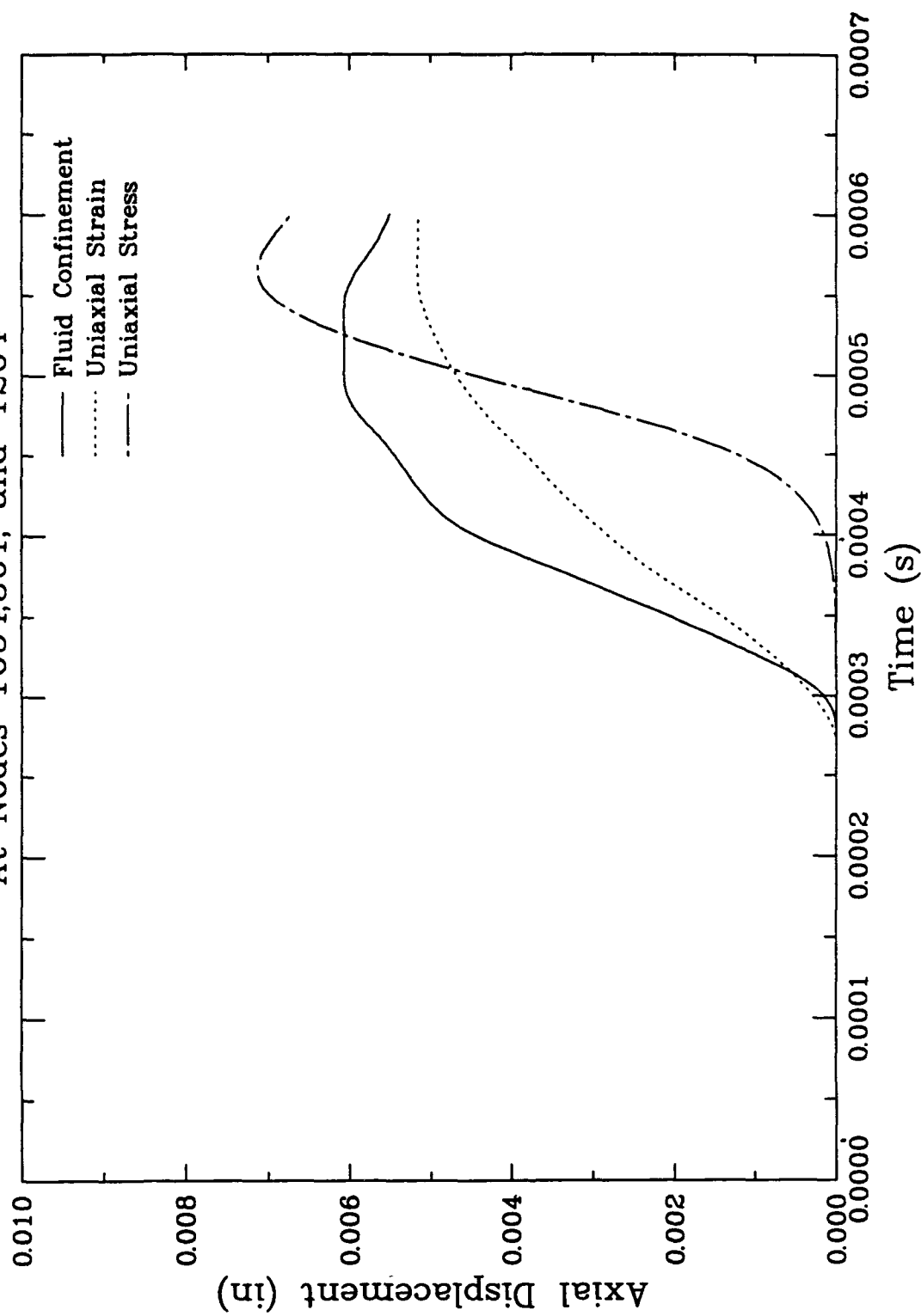
Figure 6.19c. Influence of confinement condition on skeleton particle displacement with relative
fluid motion at Range C (15 in.).

WB-F,CU-SR
At Nodes 554,101, and 404

Fluid Confinement
Uniaxial Strain
Uniaxial Stress

Absolute Relative Velocity (in/s)

Time (s)
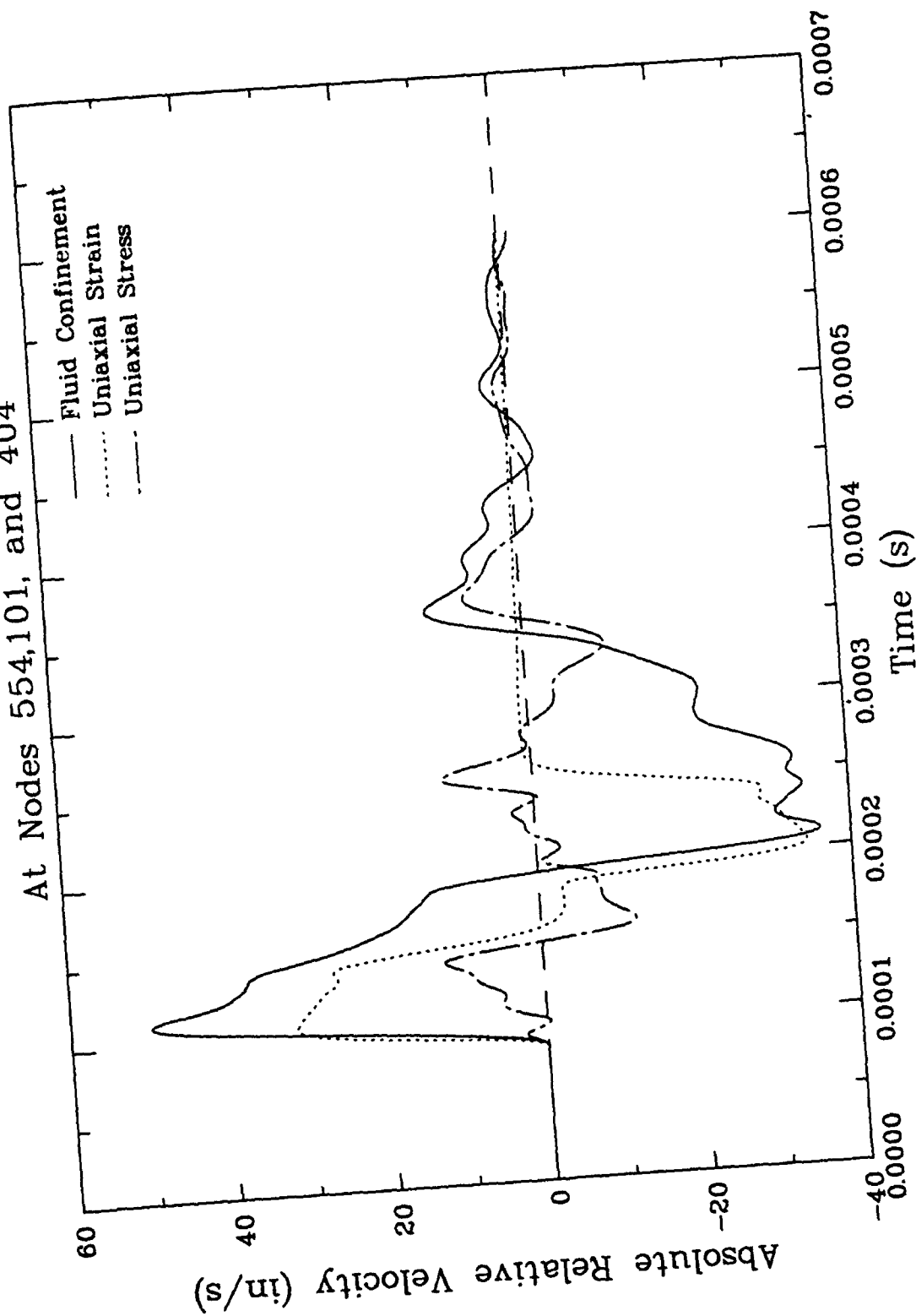
Figure 6.20a. Influence of confinement condition on axial relative fluid velocity at Range A
(5 in.).

Figure 6.20b. Influence of confinement condition on axial relative fluid velocity at Range B (10 in.).

Figure 6.20c. Influence of confinement condition on axial relative fluid velocity at Range C (15 in.).
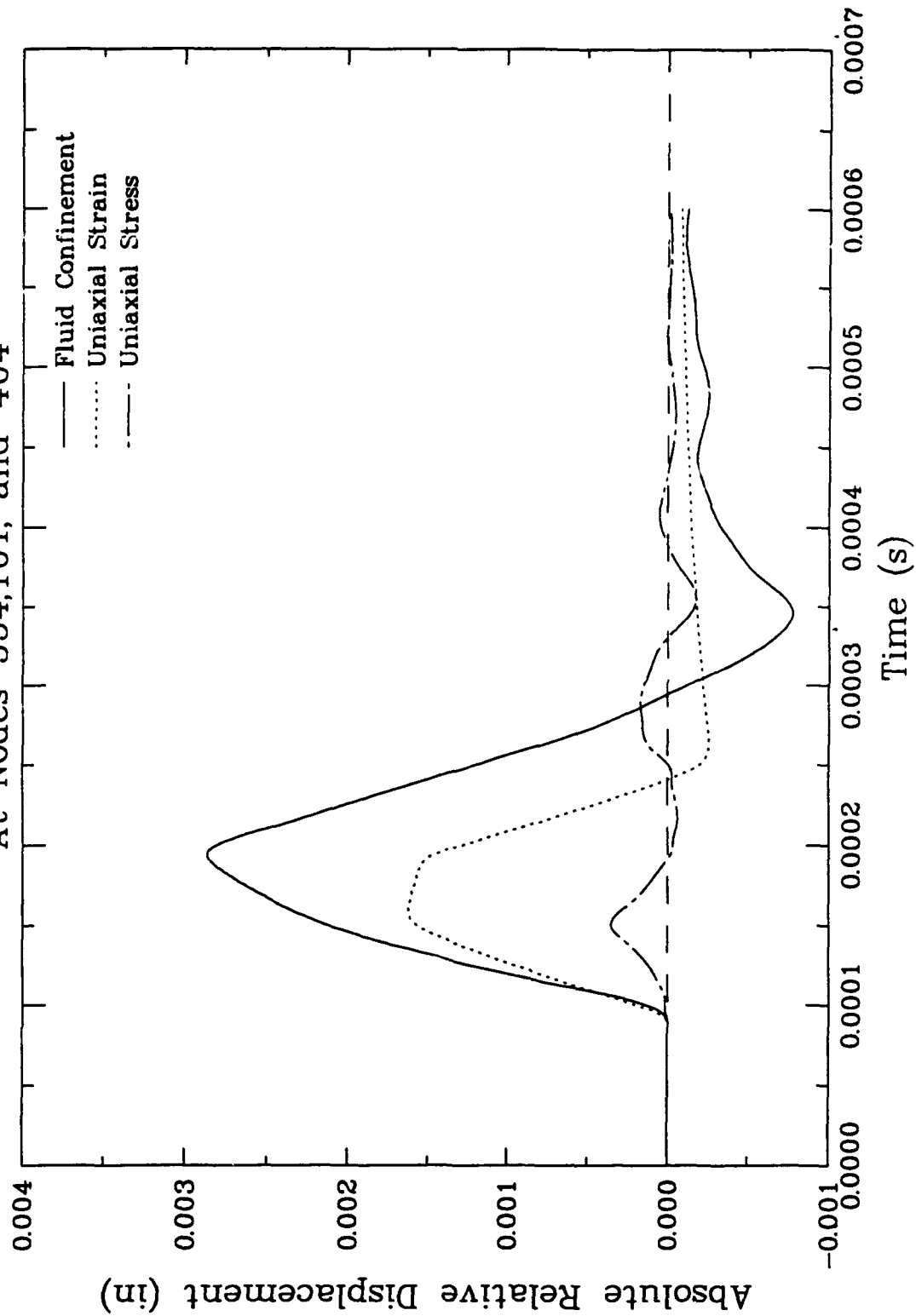
Figure 6.21a. Influence of confinement condition on axial fluid displacement at Range A (5 in.).
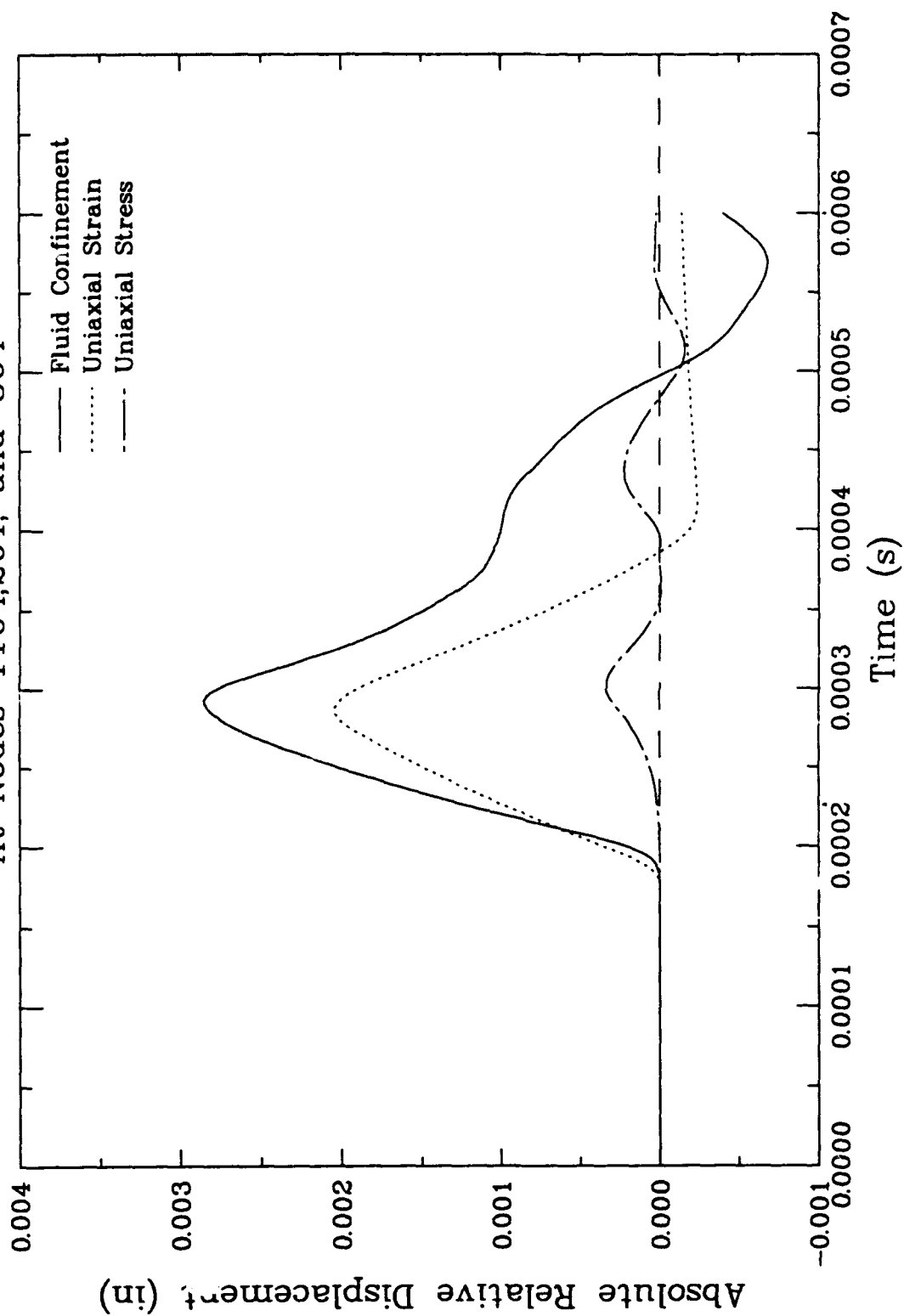
Figure 6.21b. Influence of confinement condition on axial fluid displacement at Range B (10 in.).

Figure 6.21c. Influence of confinement condition on axial fluid displacement at Range C (15 in.).

WB–U–SR,N
At Element 347

— Relative Fluid Motion
······ No Relative Fluid Motion
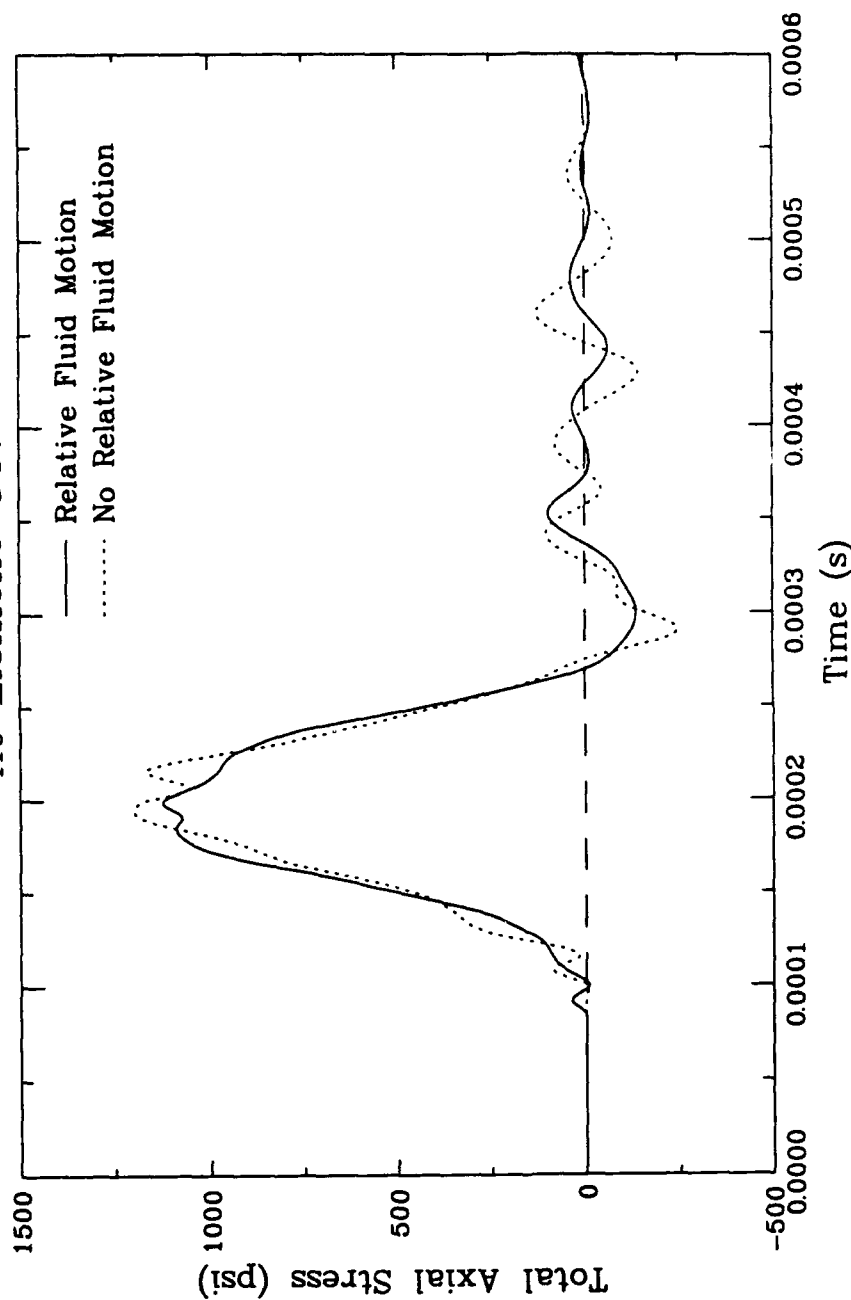
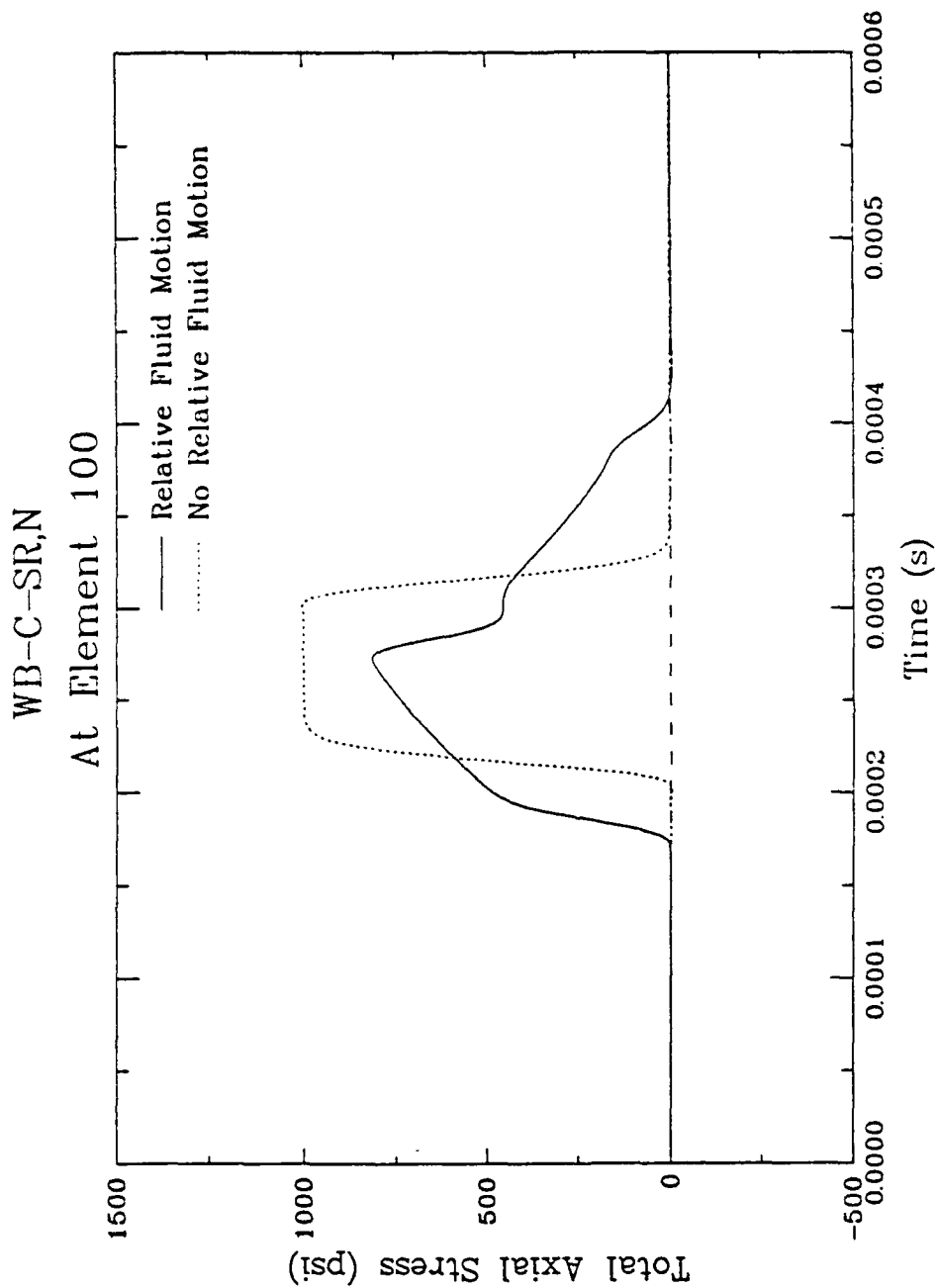Figure 6.22a. Influence of relative fluid motion on total stress for uniaxial stress loading at Range A (5 in.).
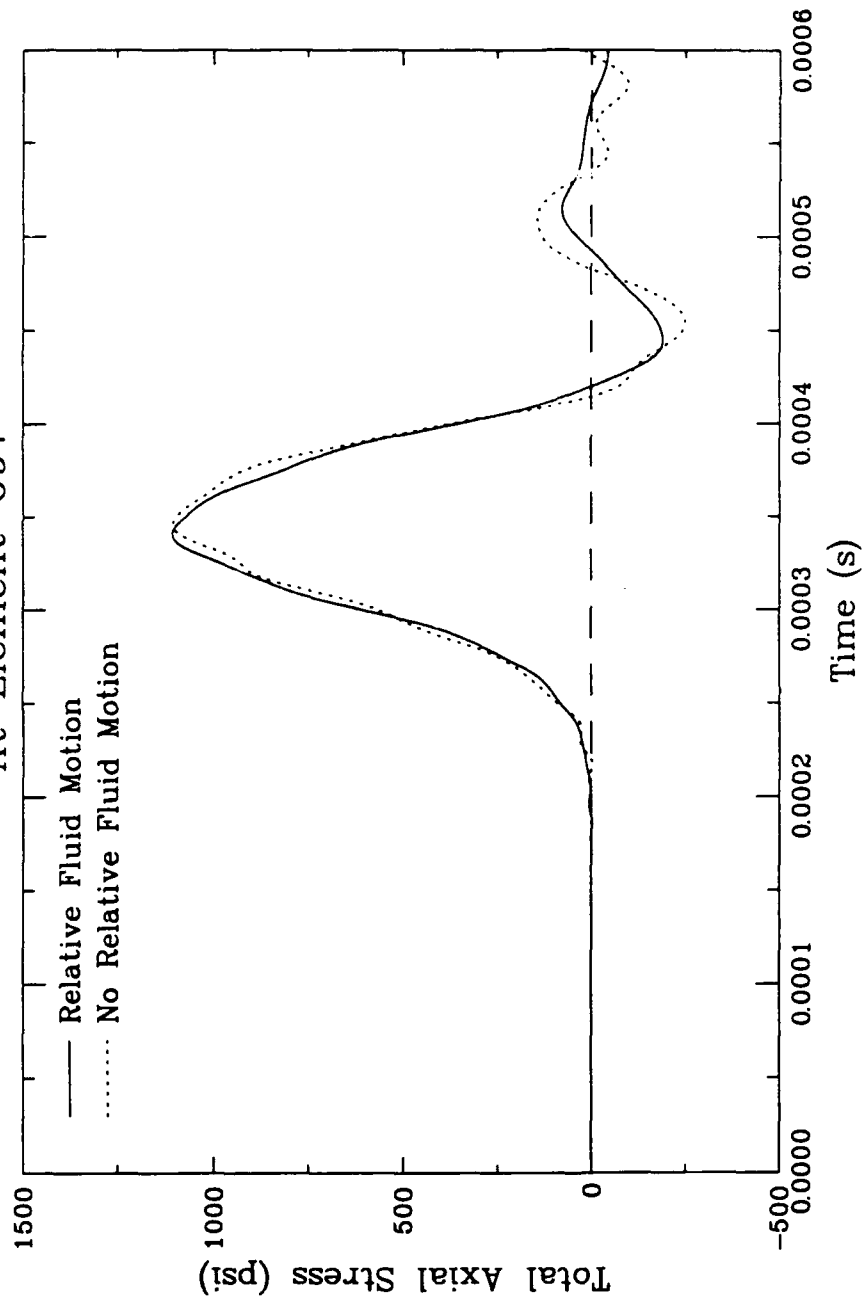
Figure 6.22b. Influence of relative fluid motion on total stress for uniaxial stress loading at Range B (10 in.).
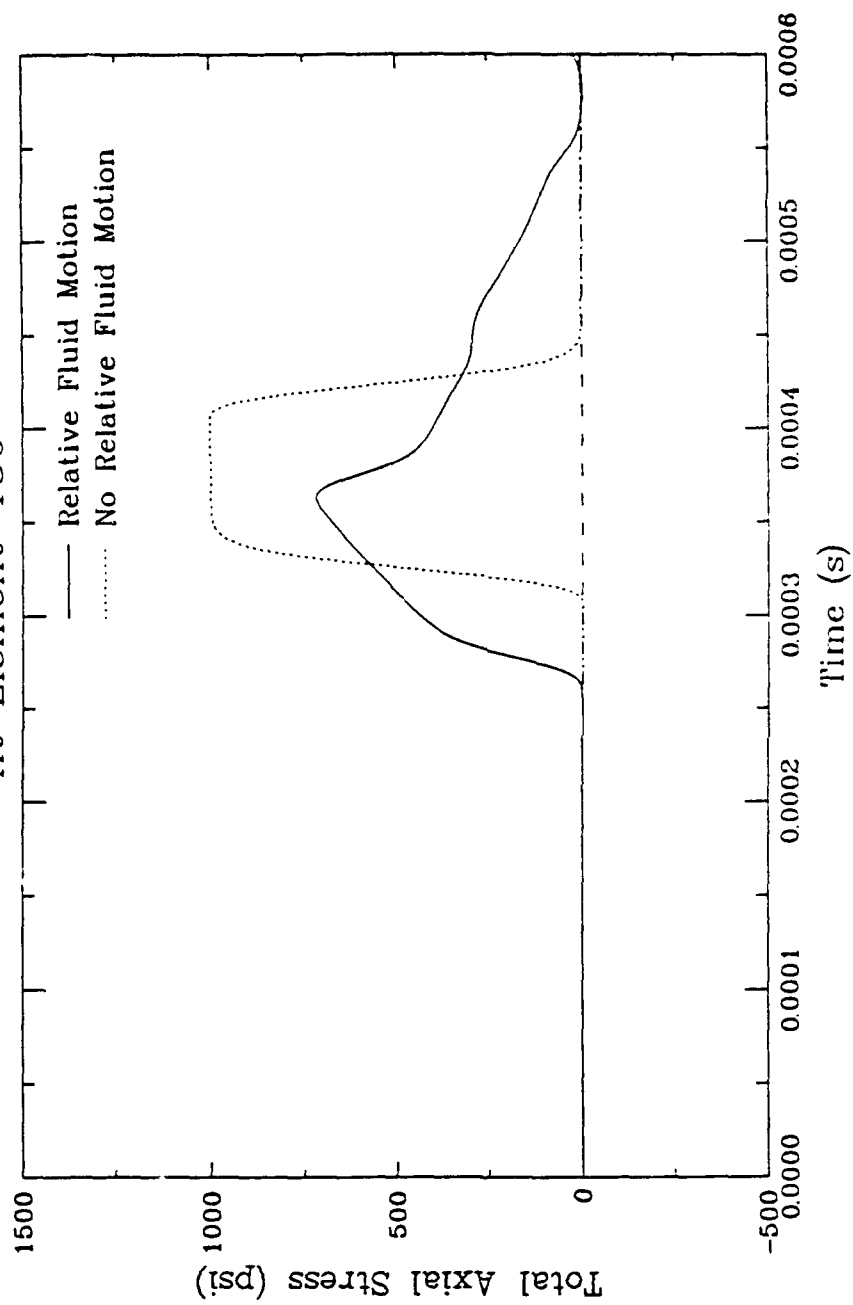
WB-U-SR,N
At Element 1047

— Relative Fluid Motion
······ No Relative Fluid Motion

Total Axial Stress (psi)

Time (s)
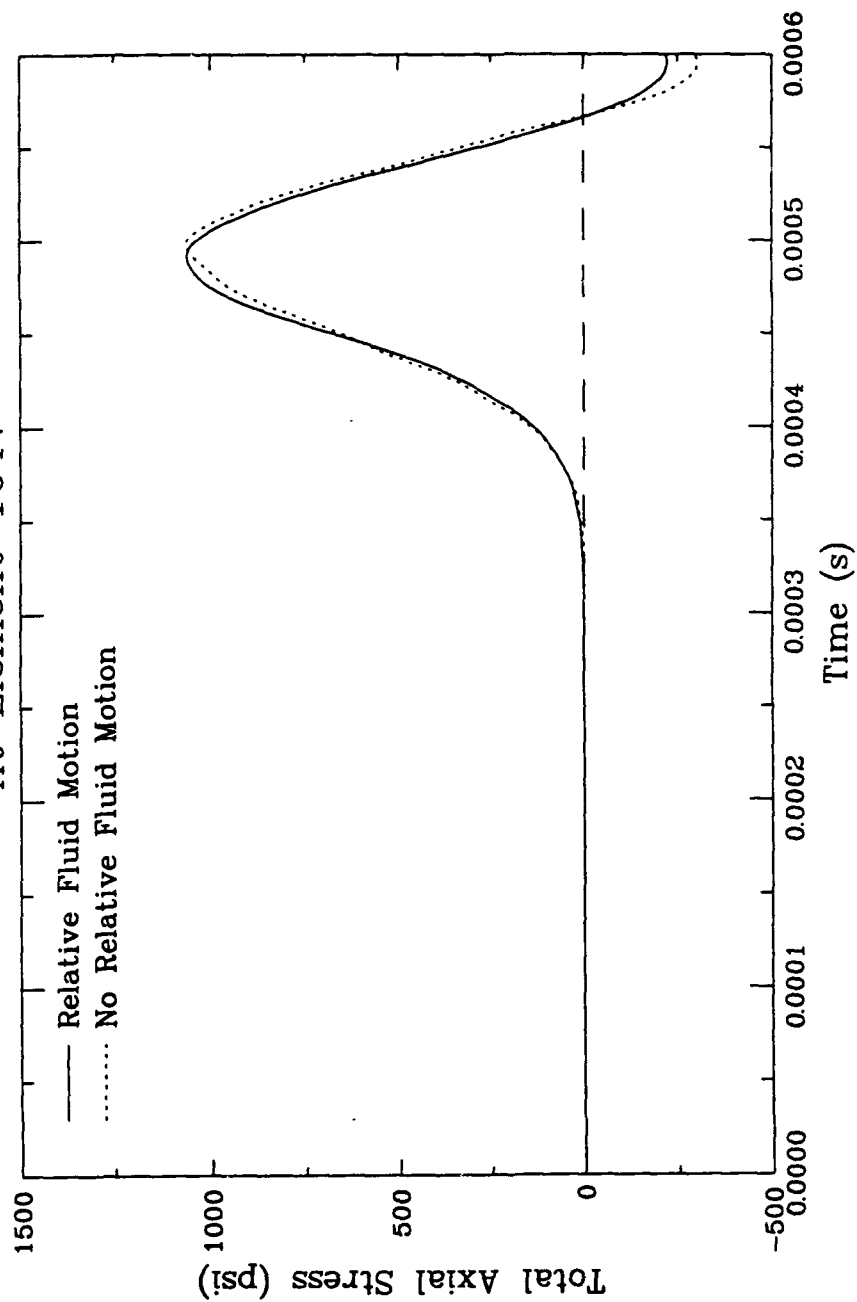
Figure 6.22c. Influence of relative fluid motion on total stress for uniaxial stress loading at Range C (15 in.).

WB–U–SN

At Elements 694,697, and 700

Location B$_c$ (Center Line),694
Location B (Mid–Radius),697
Location B$_i$ (Surface),700
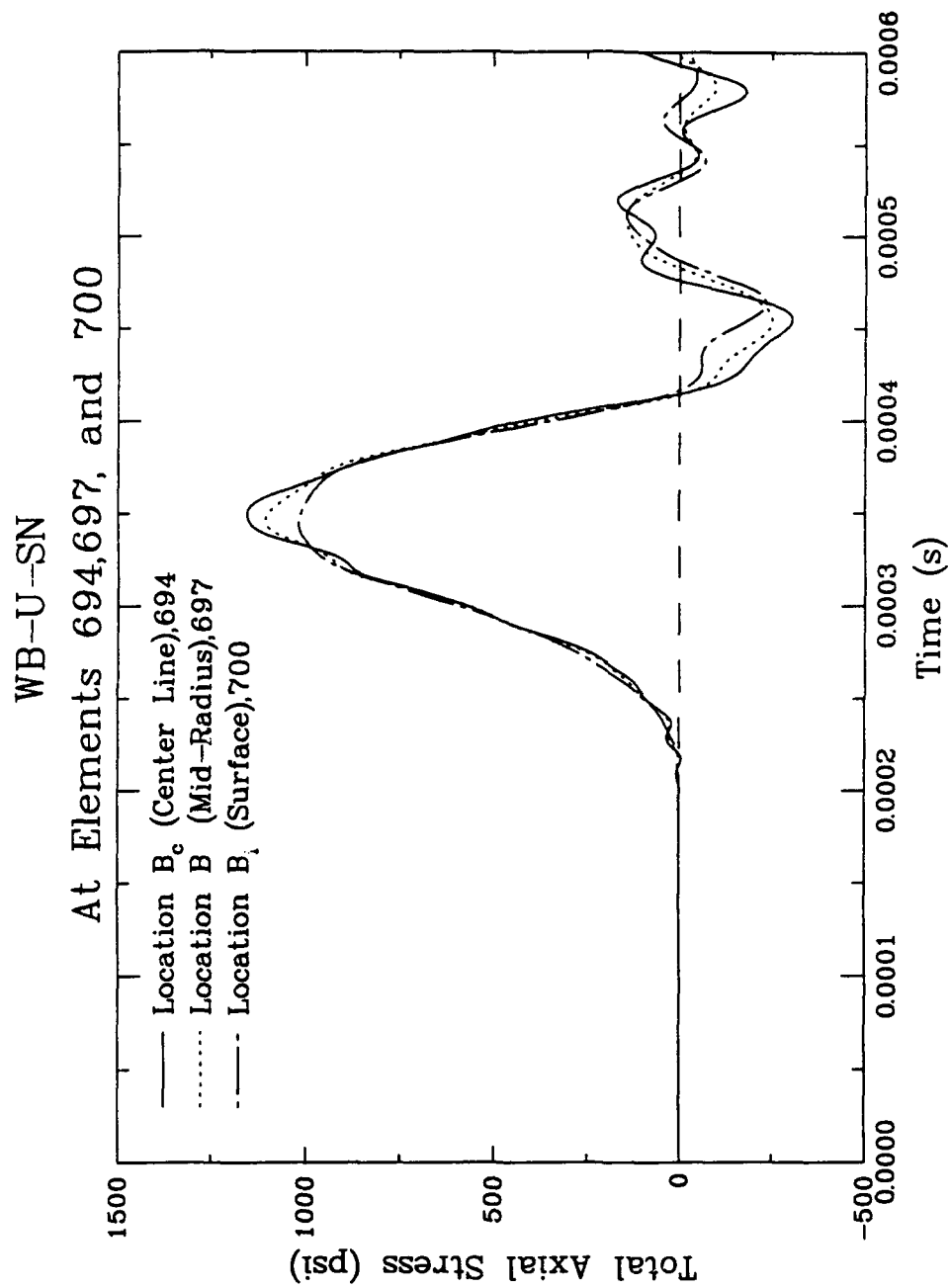
Figure 6.23a. Influence of lateral position on total stress for uniaxial stress loading without relative fluid motion, Range B (10 in.).

WB–U–SR

At Elements 694, 697, and 700

Location B_c (Center Line), 694
Location B (Mid-Radius), 697
Location B_i (Surface), 700
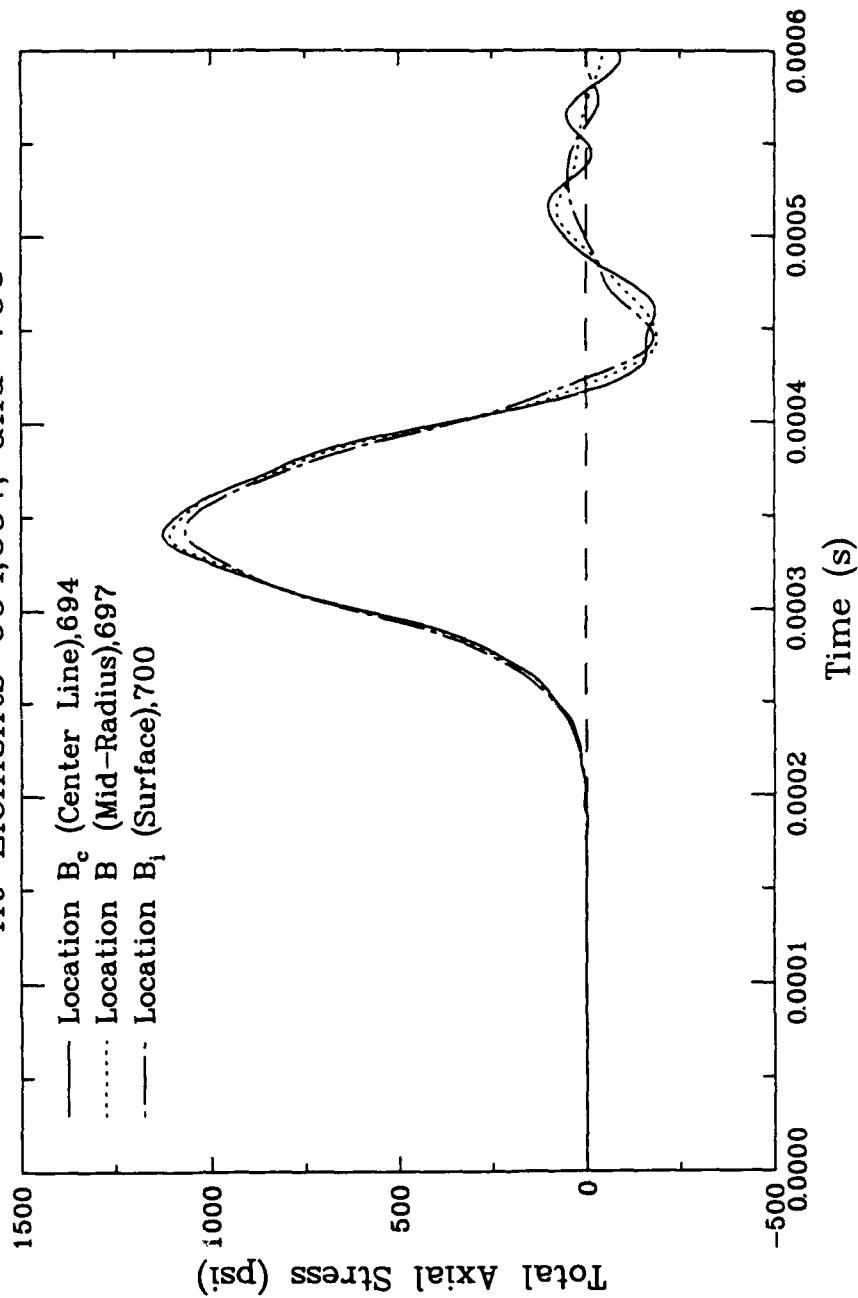
Figure 6.23b. Influence of lateral position on total stress for uniaxial stress loading with relative fluid motion, Range B (10 in.).

6-70
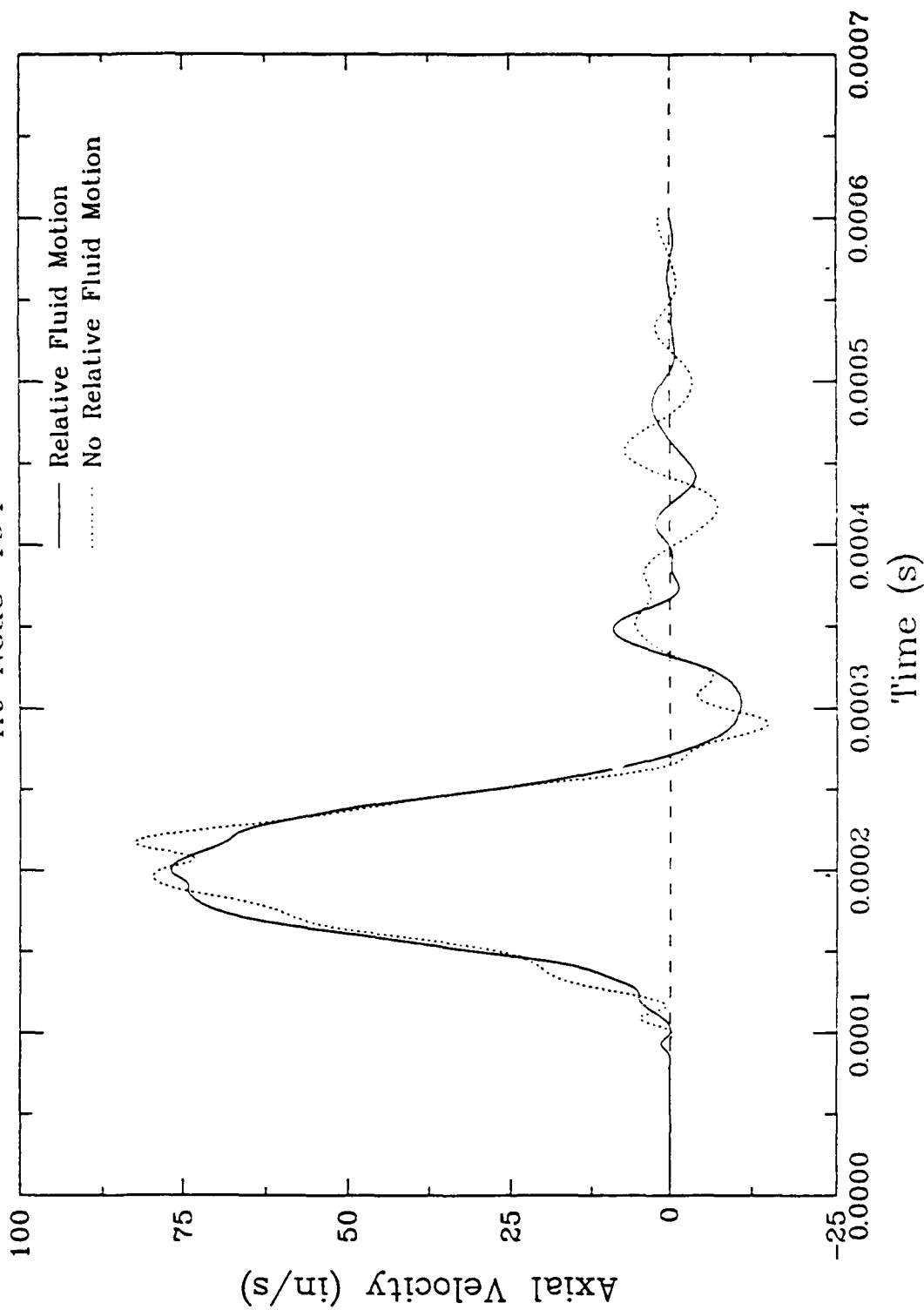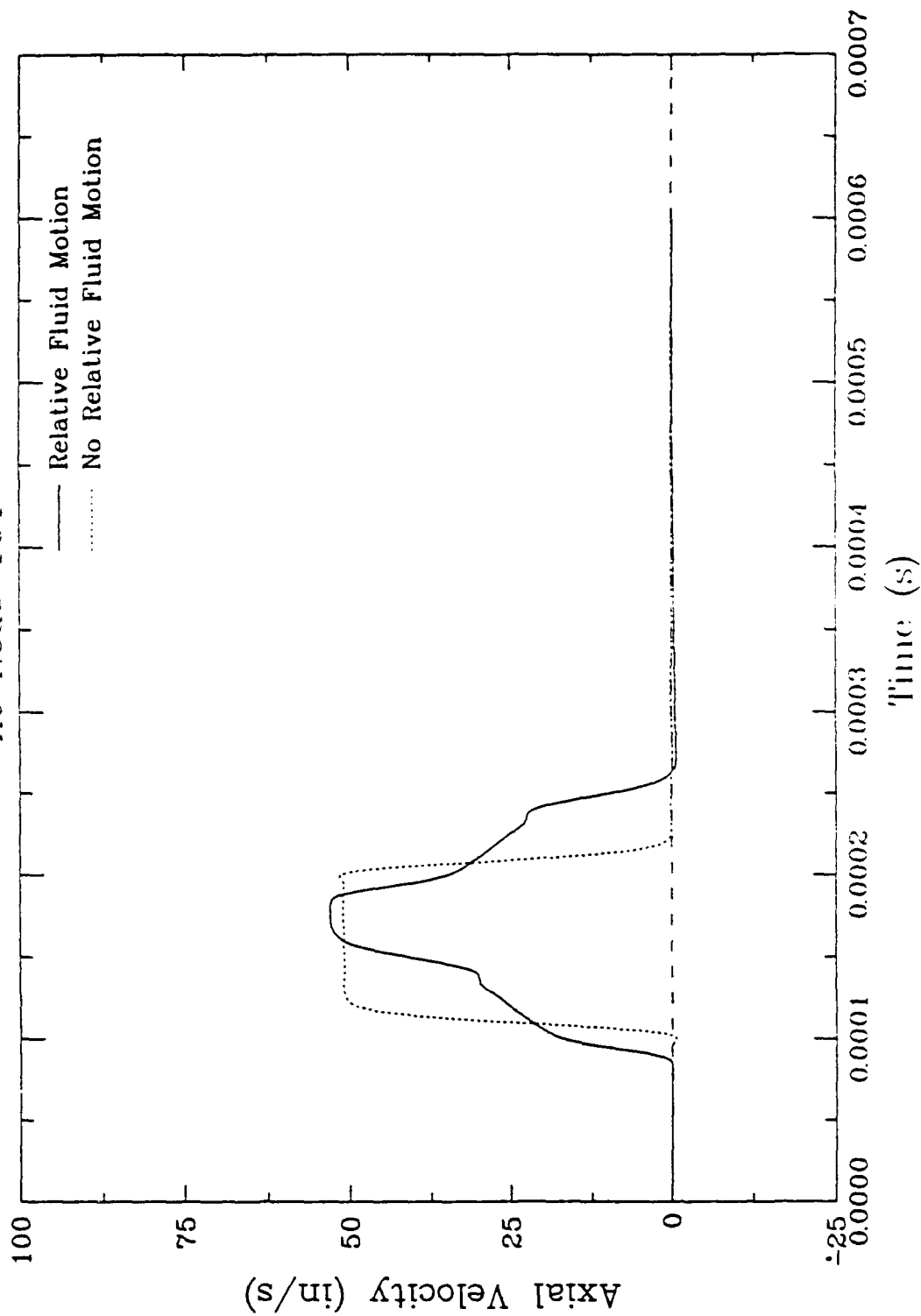
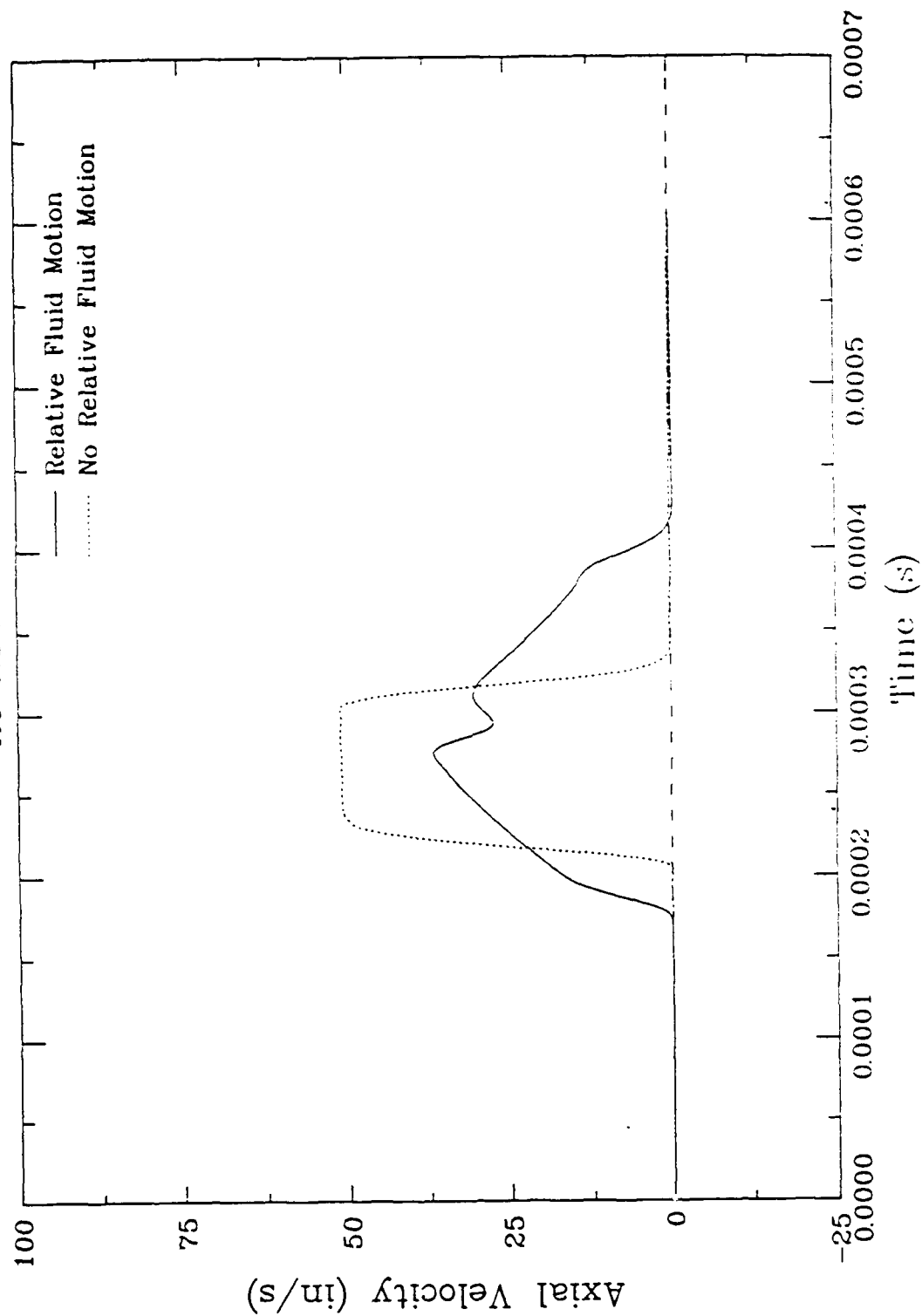Figure 6.24a. Influence of relative fluid motion on skeleton velocity for uniaxial stress loading at Range A (5 in.).
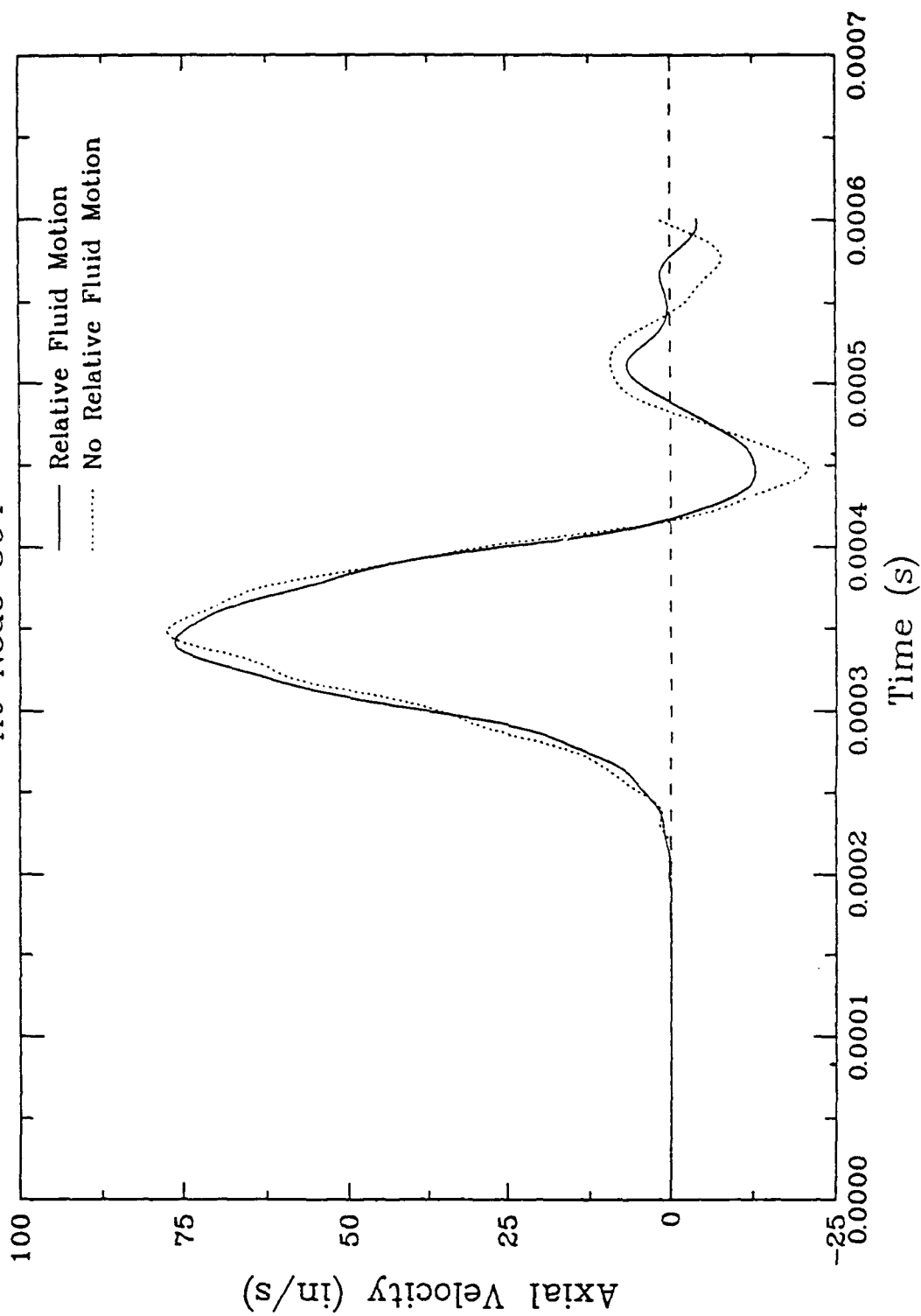
Figure 6.24b. Influence of relative fluid motion on skeleton velocity for uniaxial stress loading at Range B (10 in.).
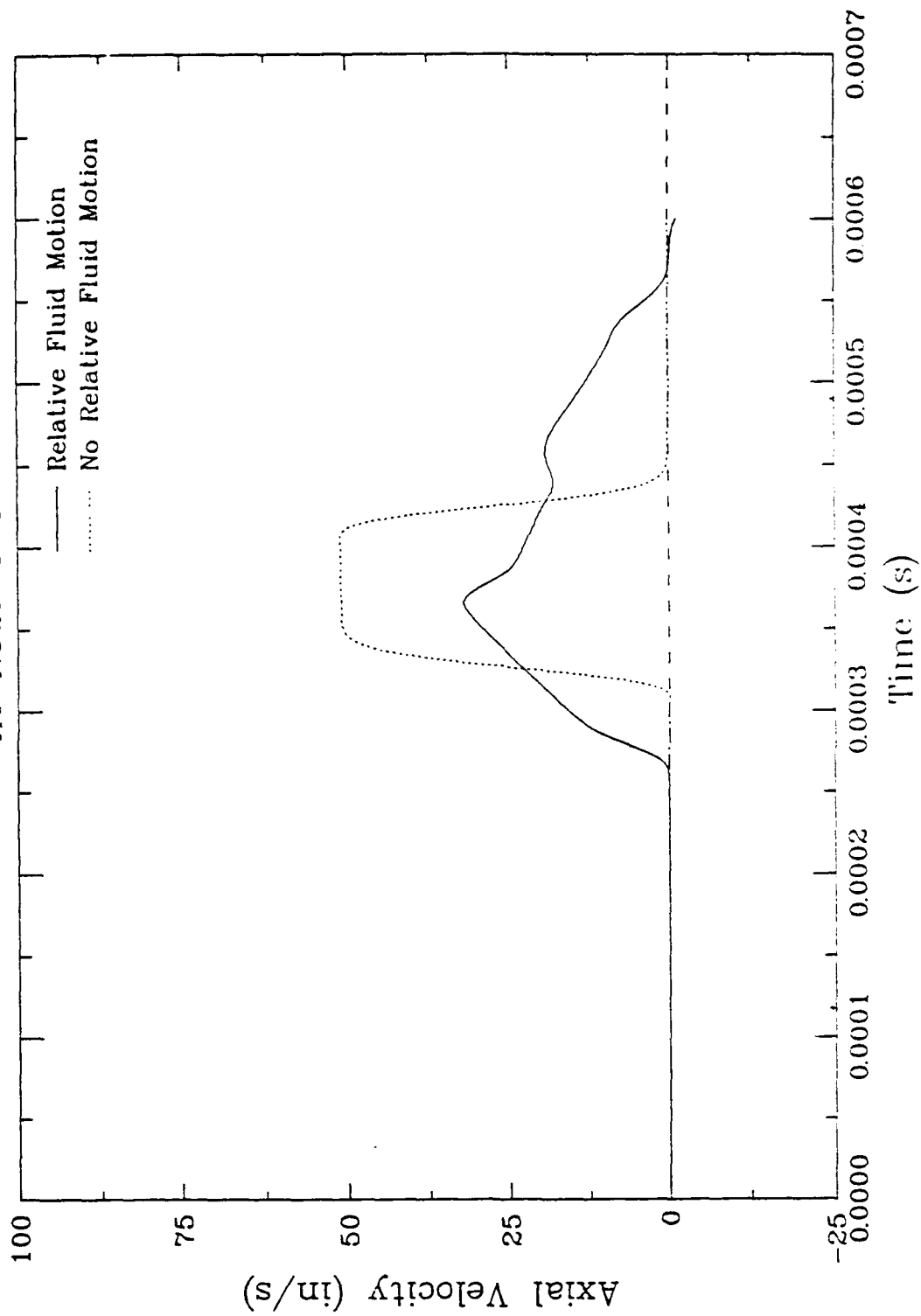
Figure 6.24c.   Influence of relative fluid motion on skeleton velocity for uniaxial stress loading at Range C (15 in.).
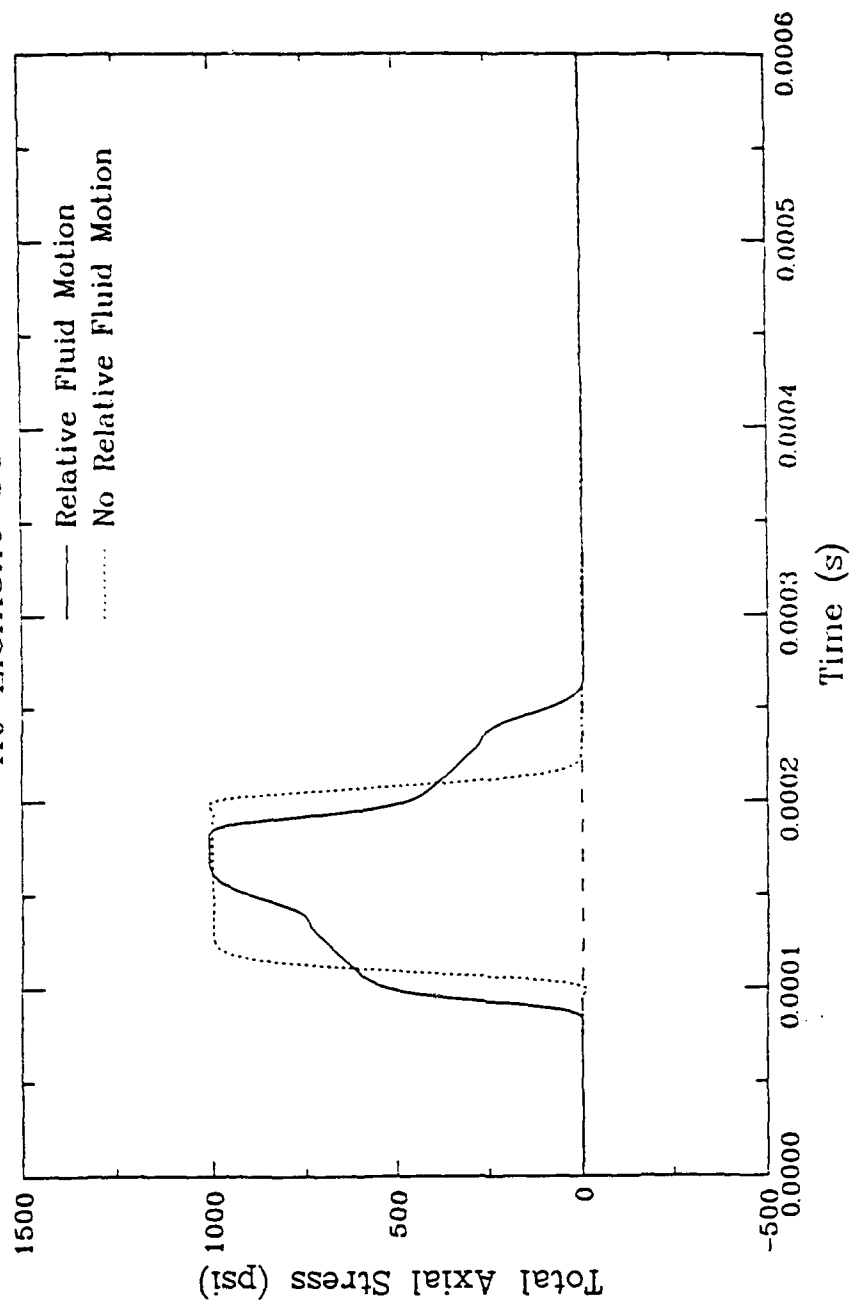
Figure 6.25a.   Influence of relative fluid motion on total axial stress for uniaxial strain loading at Range A (5 in.).

Figure 6.25b. Influence of relative fluid motion on total axial stress for uniaxial strain loading at Range B (10 in.).

Figure 6.25c. Influence of relative fluid motion on total axial stress for uniaxial strain loading at Range C (15 in.).
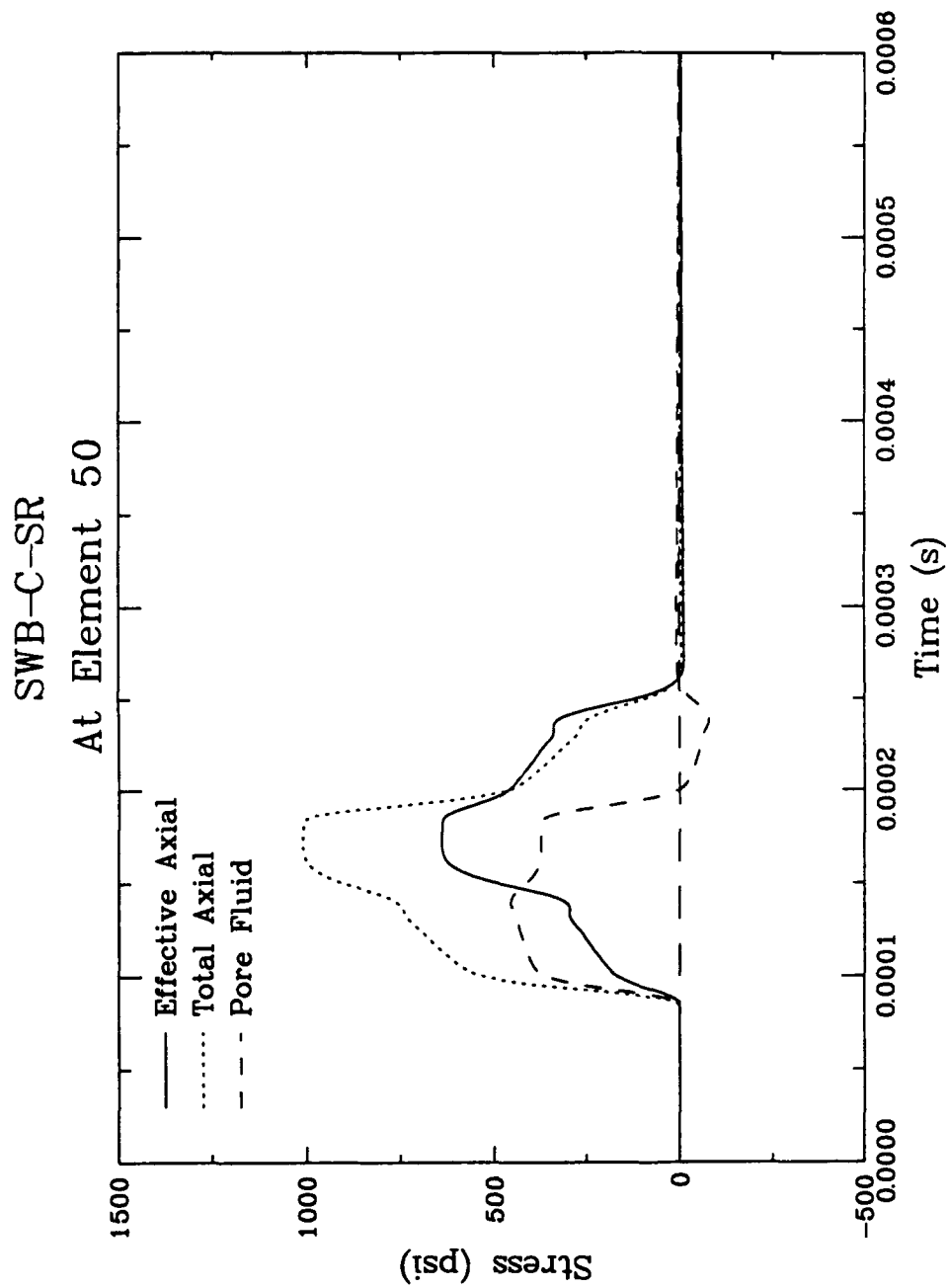
Figure 6.26a. Composite stress time-histories for uniaxial loading with fluid motion at Range A (5 in.).

SWB-C-SR
At Element 100
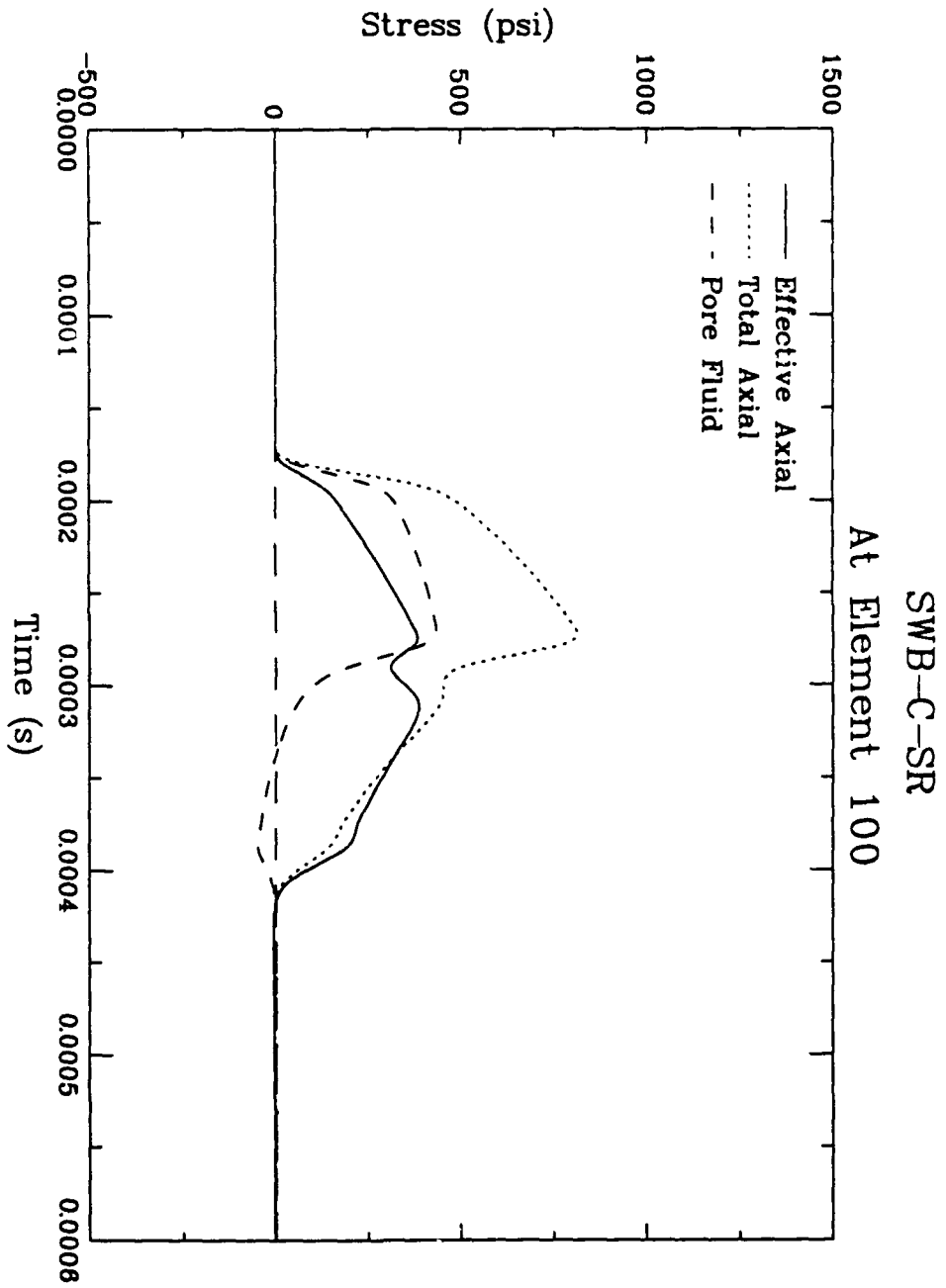
Figure 6.26b. Composite stress time-histories for uniaxial loading with fluid motion at Range B (10 in.).
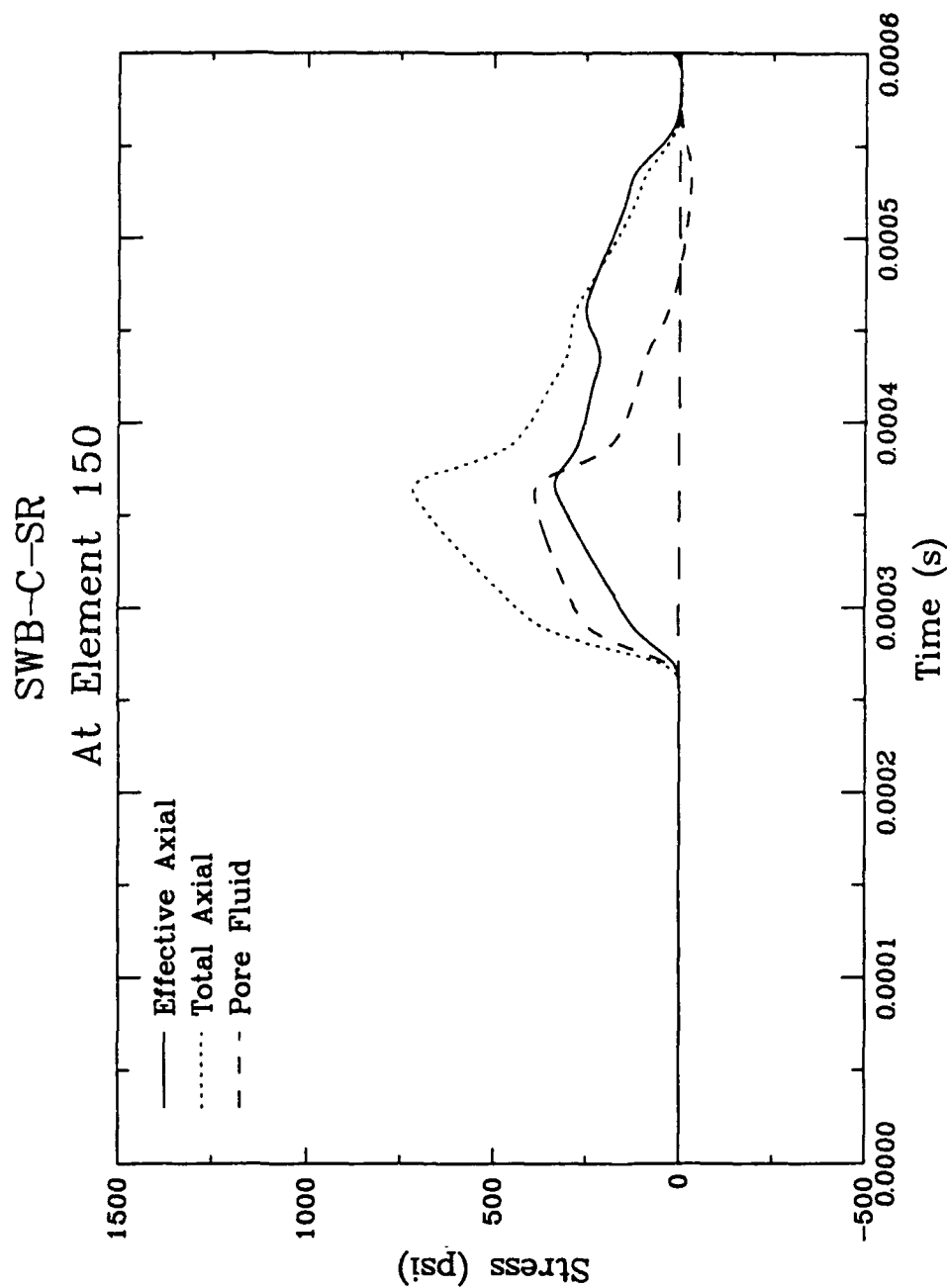
Figure 6.26c. Composite stress time-histories for uniaxial loading with fluid motion at Range C (15 in.).

Figure 6.27a. Influence of relative fluid motion on skeleton velocity for uniaxial strain loading at Range A (5 in.).

Figure 6.27b. Influence of relative fluid motion on skeleton velocity for uniaxial strain loading at Range B (10 in.).
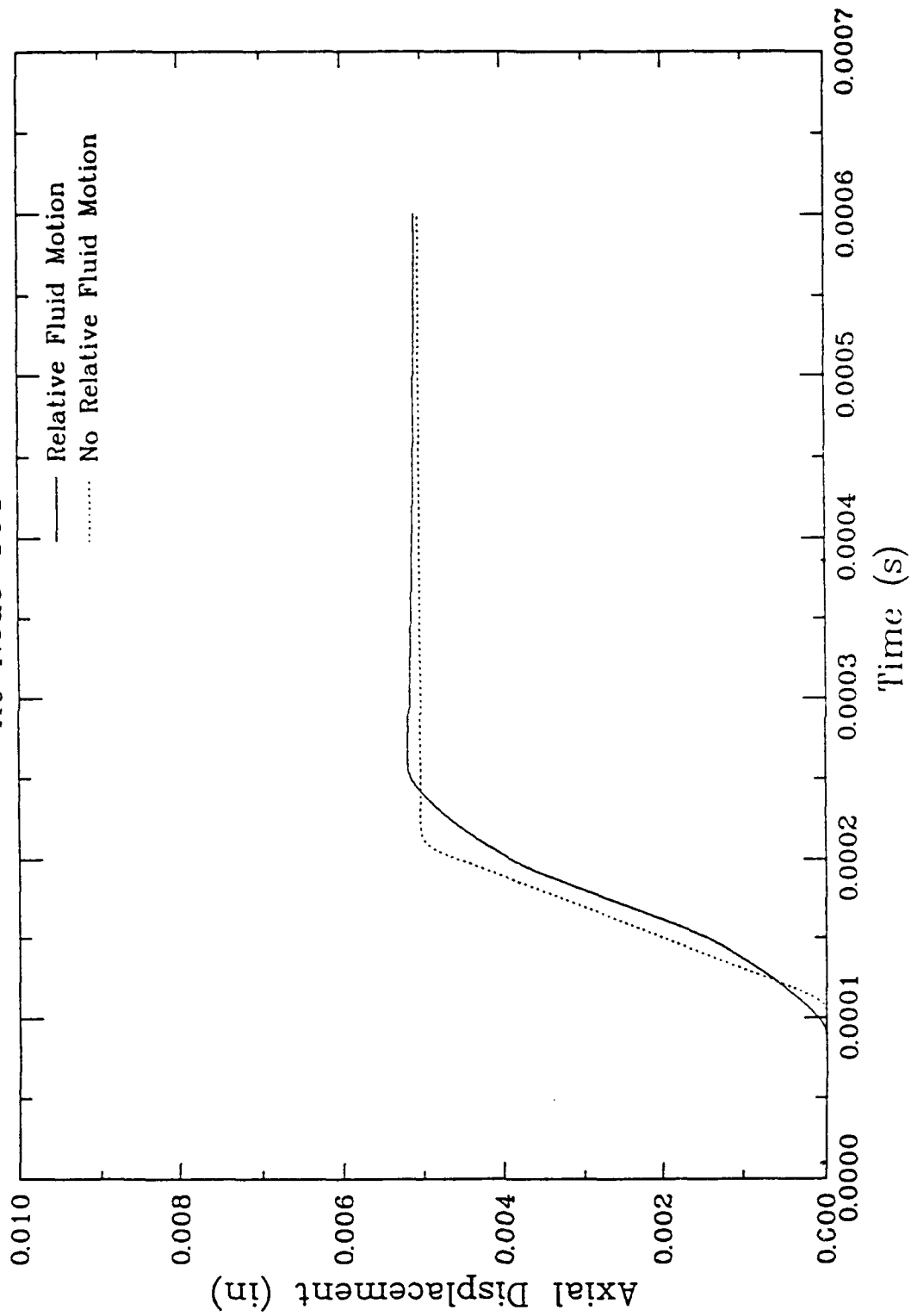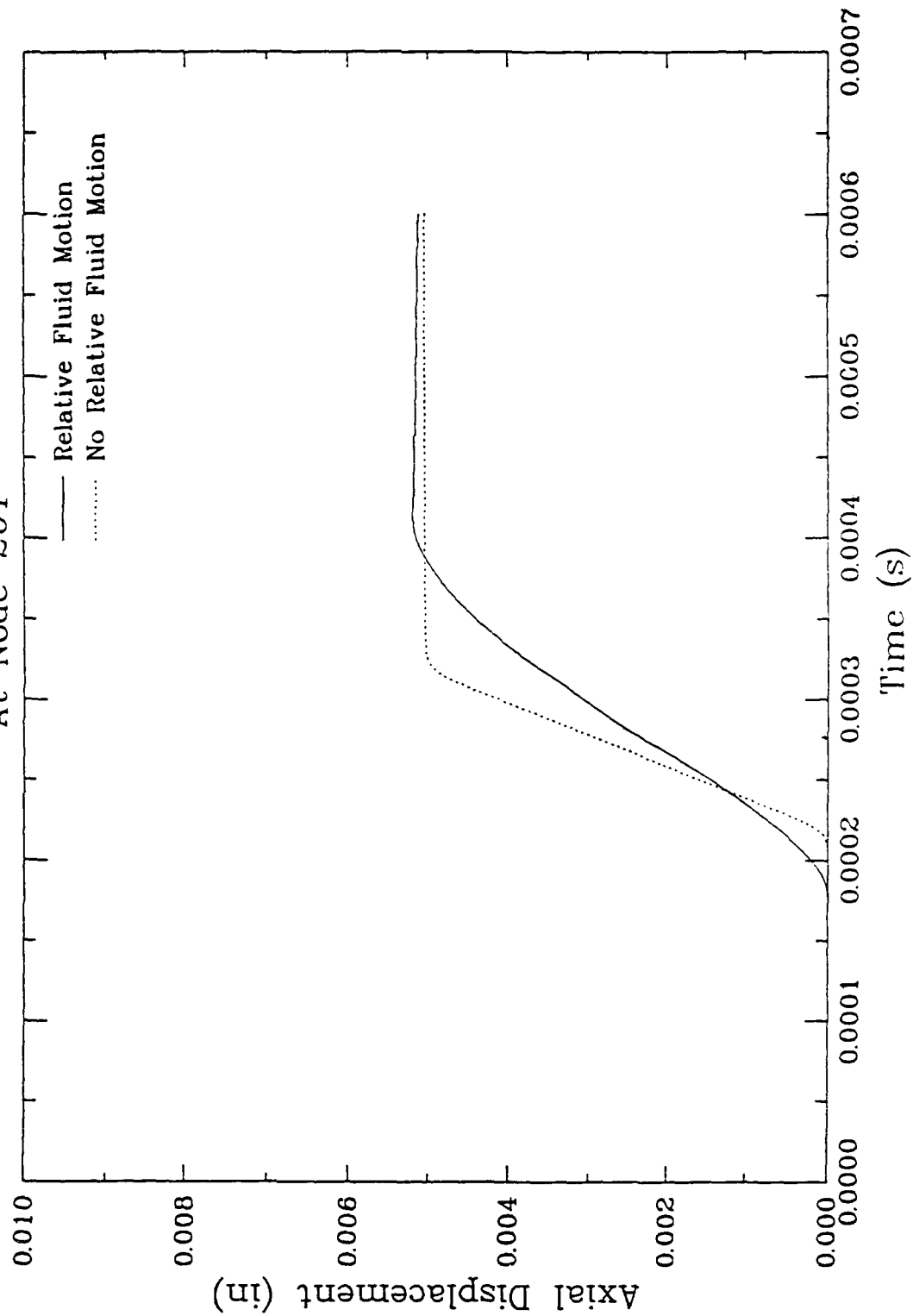
WB-C-SR,N
At Node 301

— Relative Fluid Motion
········ No Relative Fluid Motion

Figure 6.27c. Influence of relative fluid motion on skeleton velocity for uniaxial strain loading at Range C (15 in.).

Figure 6.28a. Influence of relative fluid motion on skeleton displacement for uniaxial strain loading at Range A (5 in.).

WB–C–SR,N
At Node 201

——— Relative Fluid Motion
·········· No Relative Fluid Motion

Axial Displacement (in)

Time (s)

Figure 6.28b. Influence of relative fluid motion on skeleton displacement for uniaxial strain loading at Range B (10 in.).
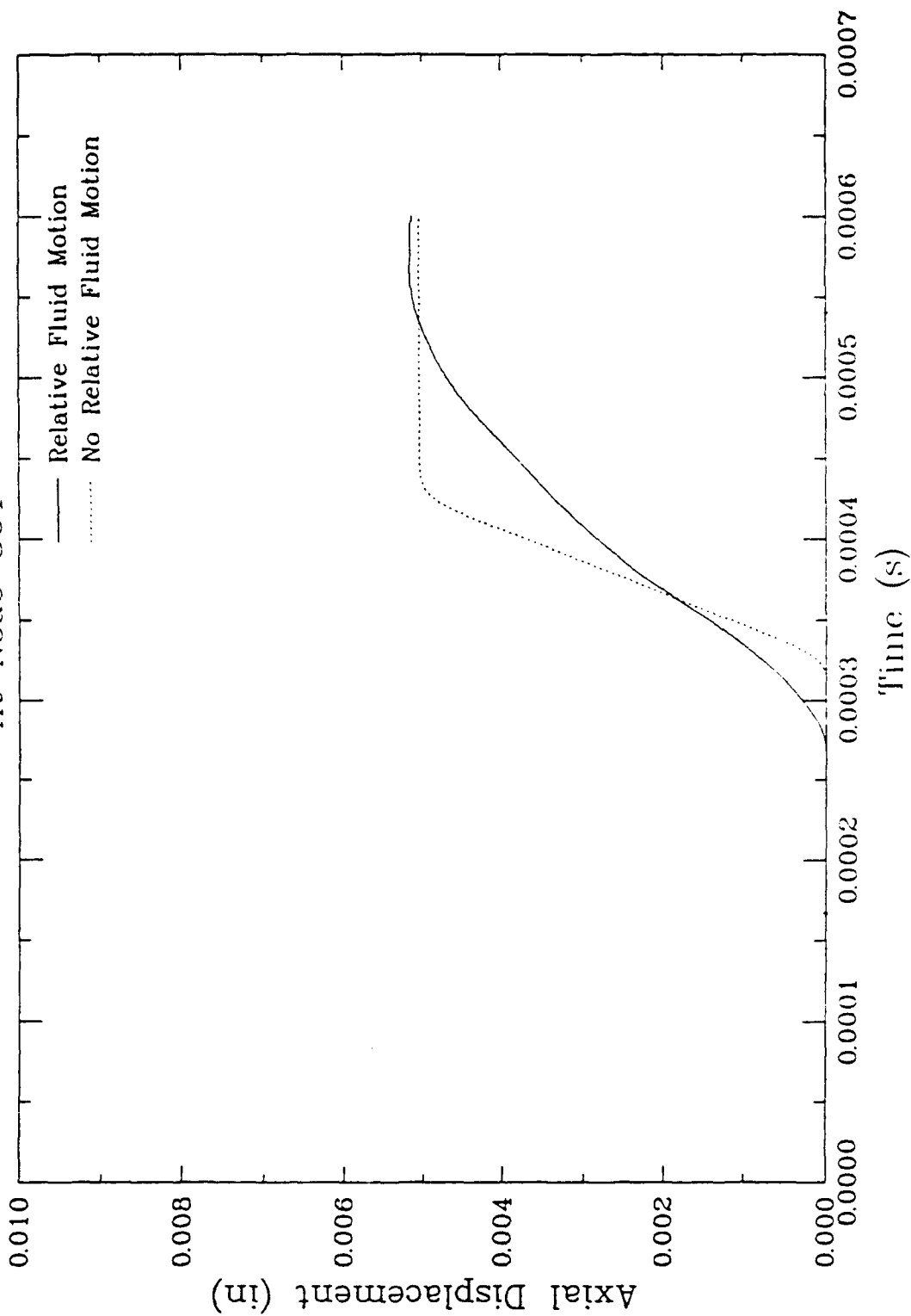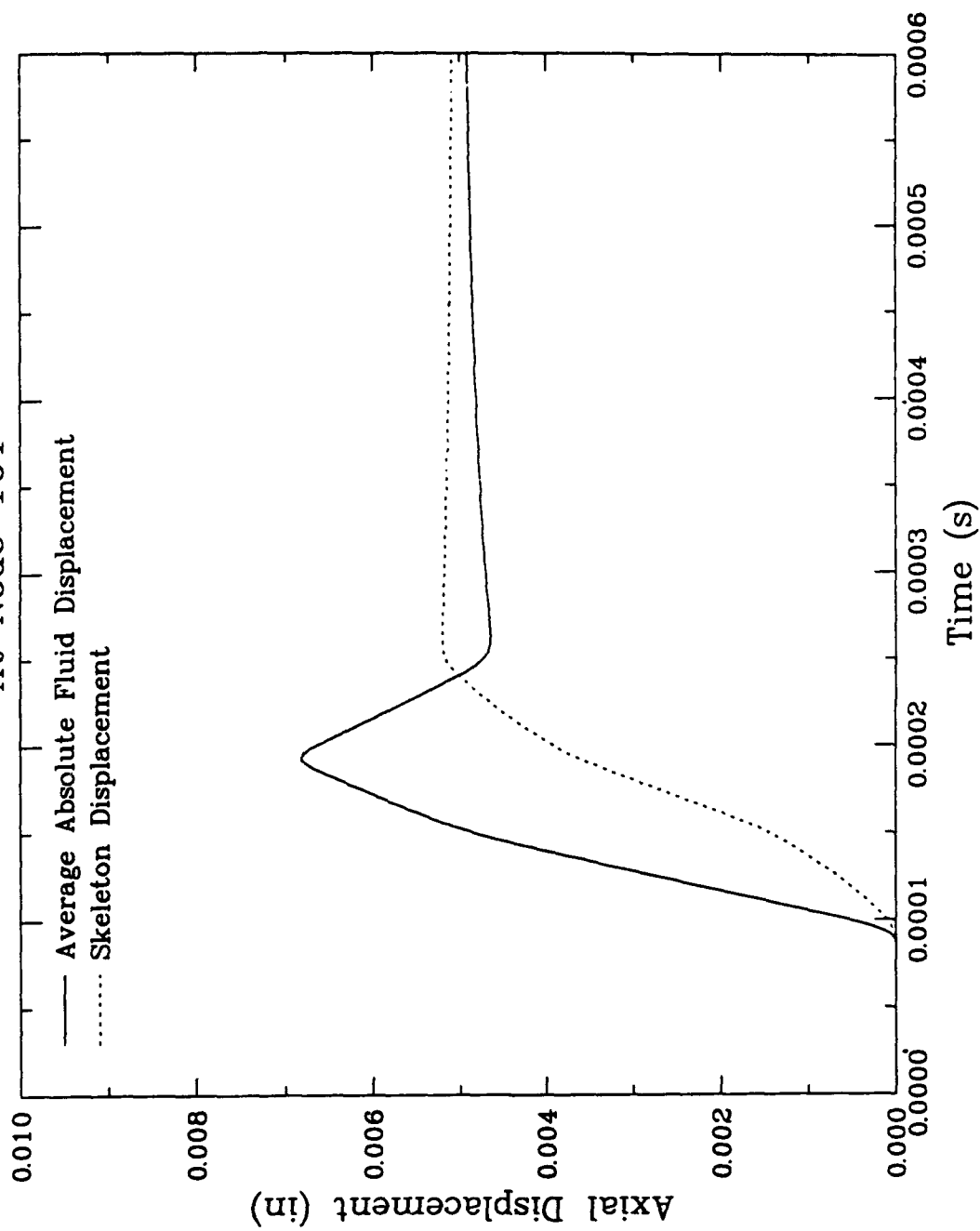
WB-C-SR,N
At Node 301

Relative Fluid Motion
No Relative Fluid Motion

Figure 6.28c. Influence of relative fluid motion on skeleton displacement for uniaxial strain loading at Range C (15 in.).

6-85

WB–C–SR
At Node 101

—— Average Absolute Fluid Displacement
········· Skeleton Displacement

Figure 6.29a. Comparison of skeleton and fluid displacements for uniaxial strain loading at Range A (5 in.).
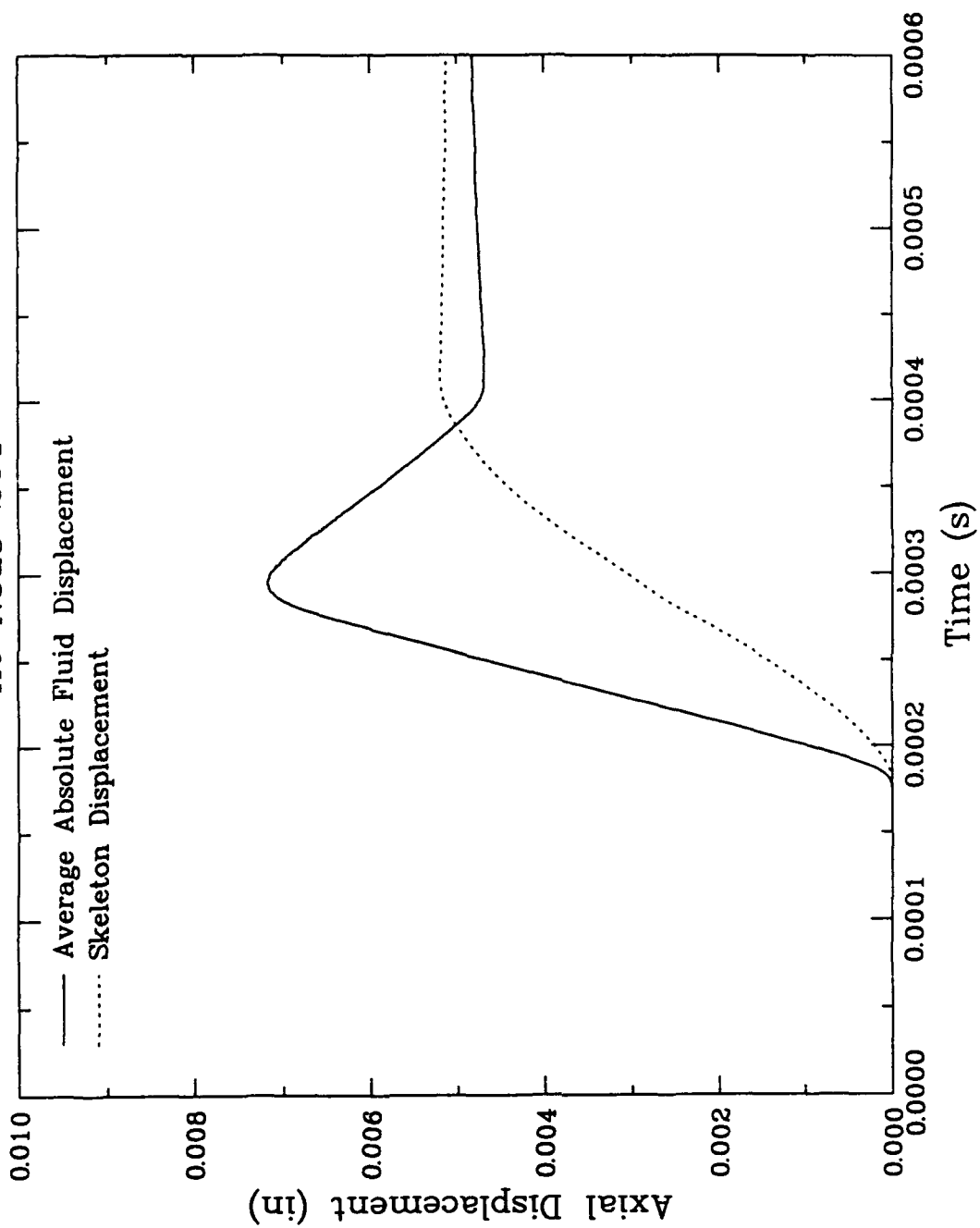
Figure 6.29b. Comparison of skeleton and fluid displacements for uniaxial strain loading at Range B (10 in.).

WB-C-SR
At Node 301

Axial Displacement (in)
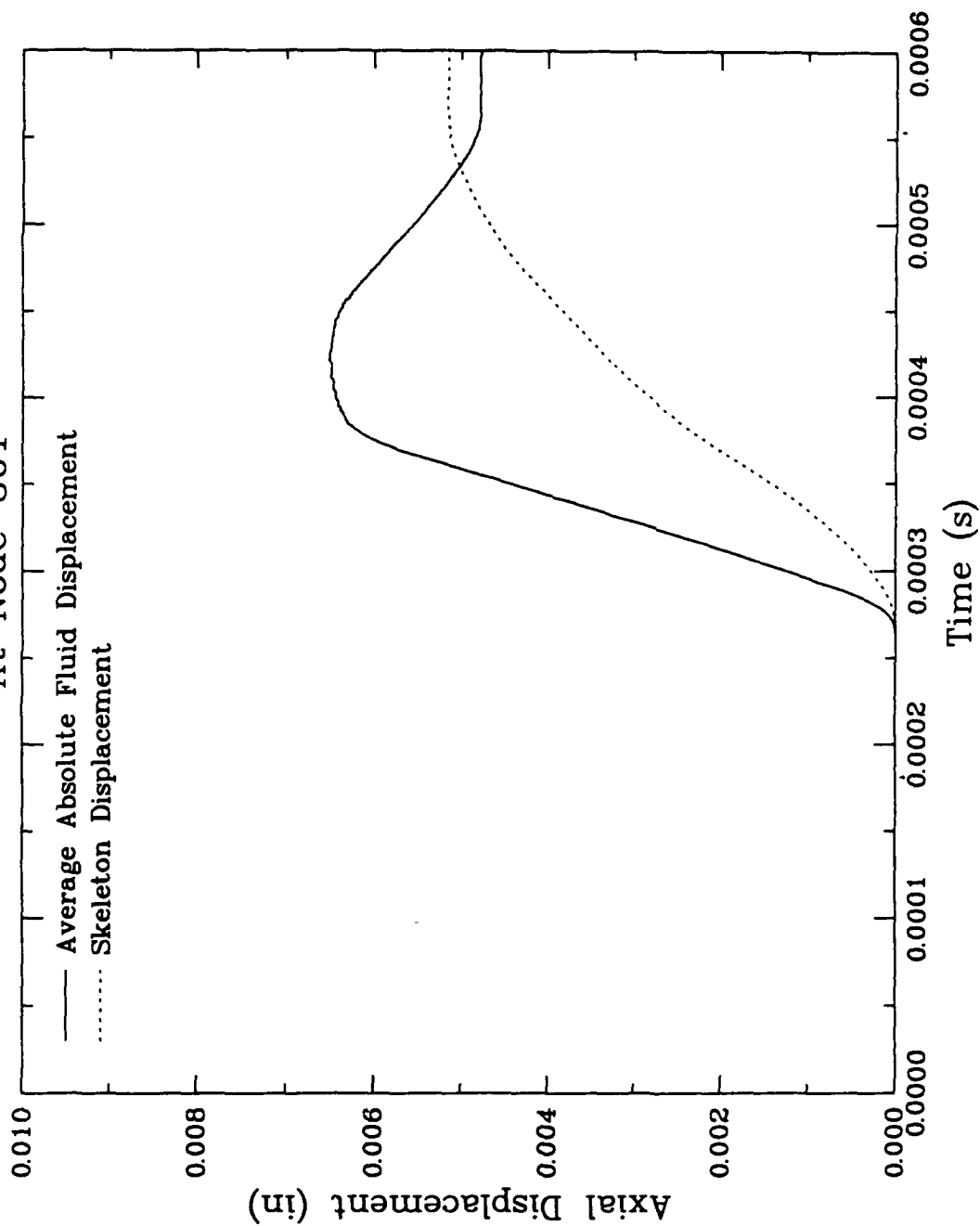
Time (s)

— Average Absolute Fluid Displacement
...... Skeleton Displacement

Figure 6.29c. Comparison of skeleton and fluid displacements for uniaxial strain loading at Range C (15 in.).

WB-F-SR,N
At Element 494

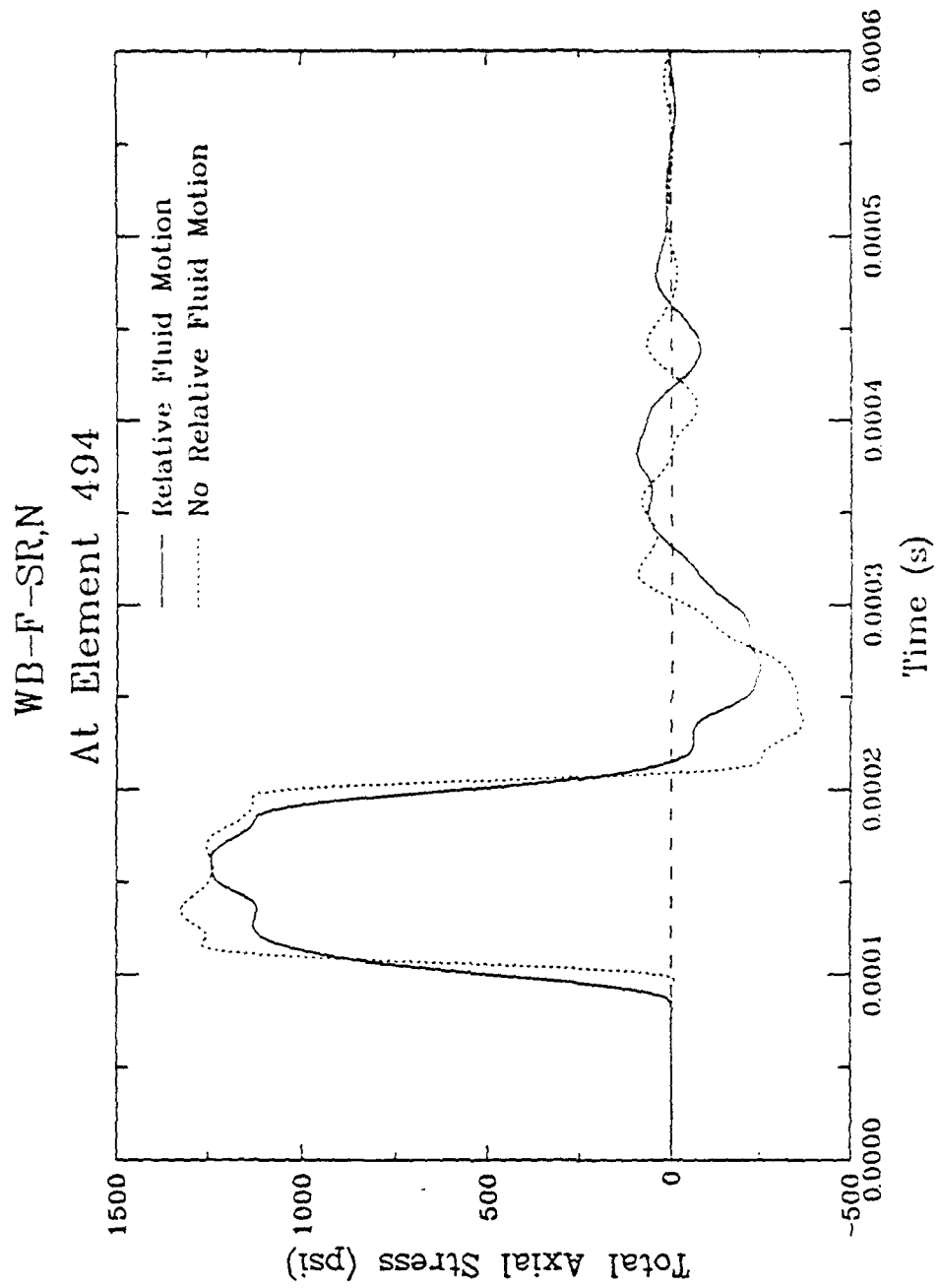Figure 6.30a. Influence of relative fluid motion on total stress for fluid confined loading at Range A (5 in.).
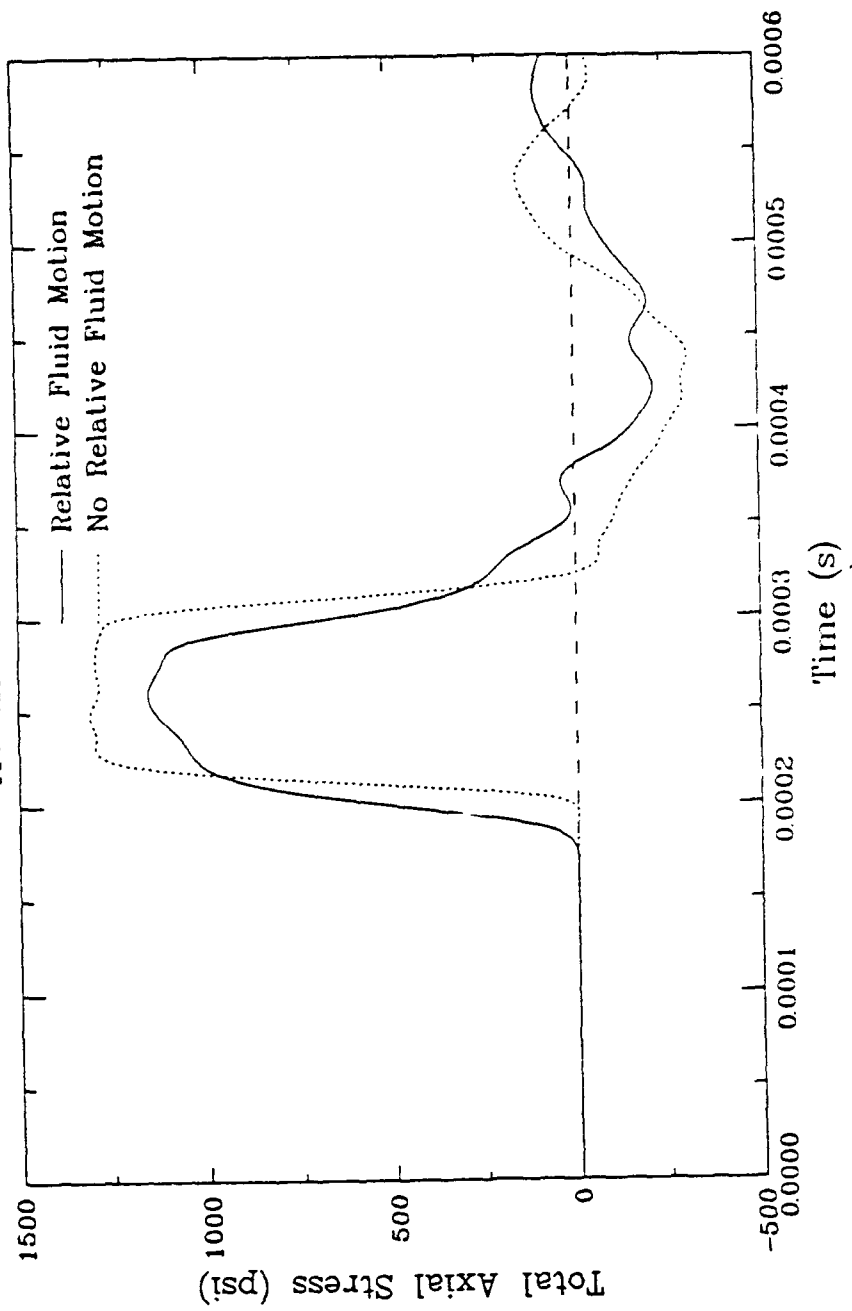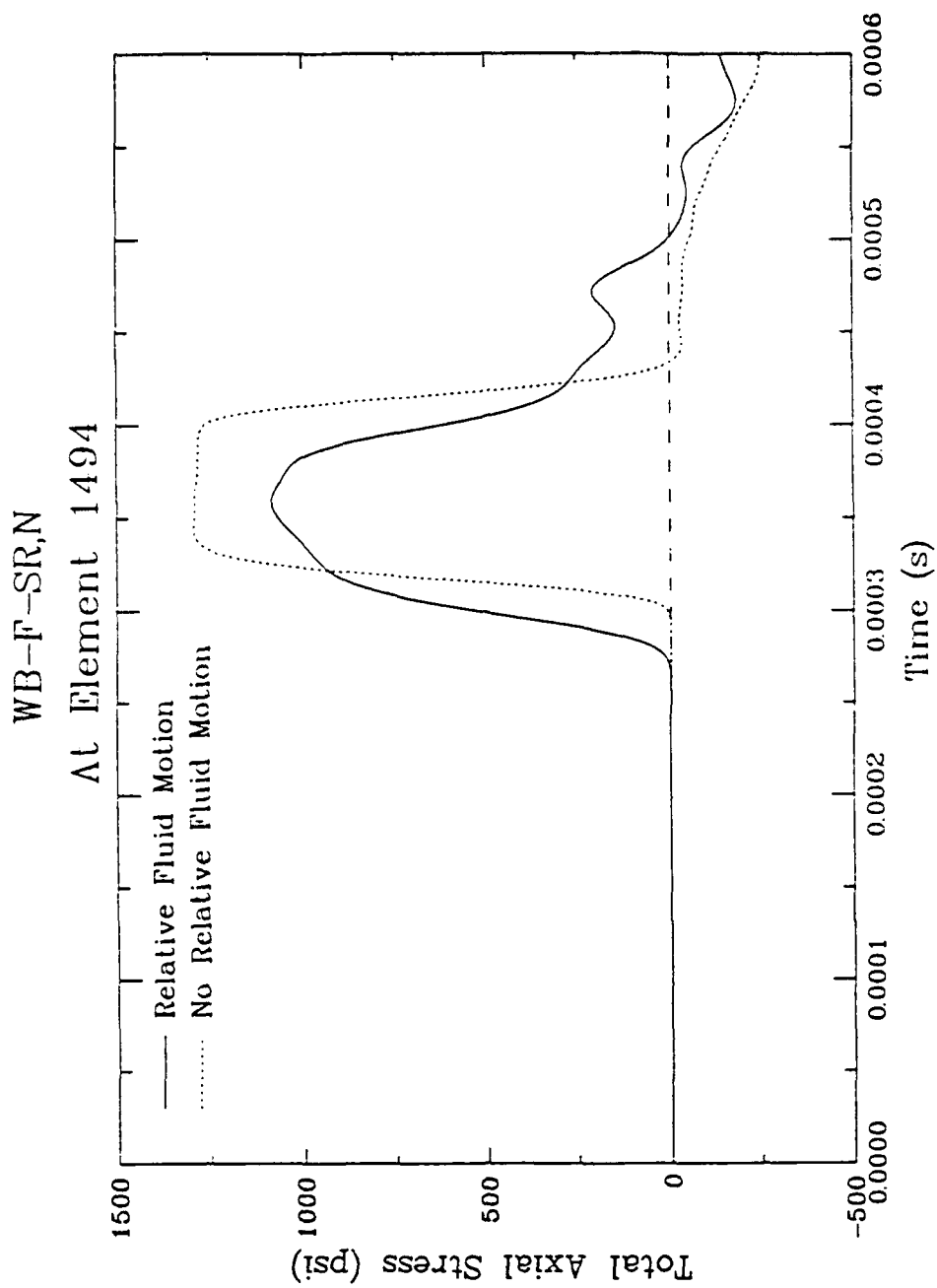
6-89

Figure 6.30b. Influence of relative fluid motion on total stress for fluid confined loading at Range B (10 in.).

Figure 6.30c.   Influence of relative fluid motion on total stress for fluid confined loading at Range C (15 in.).
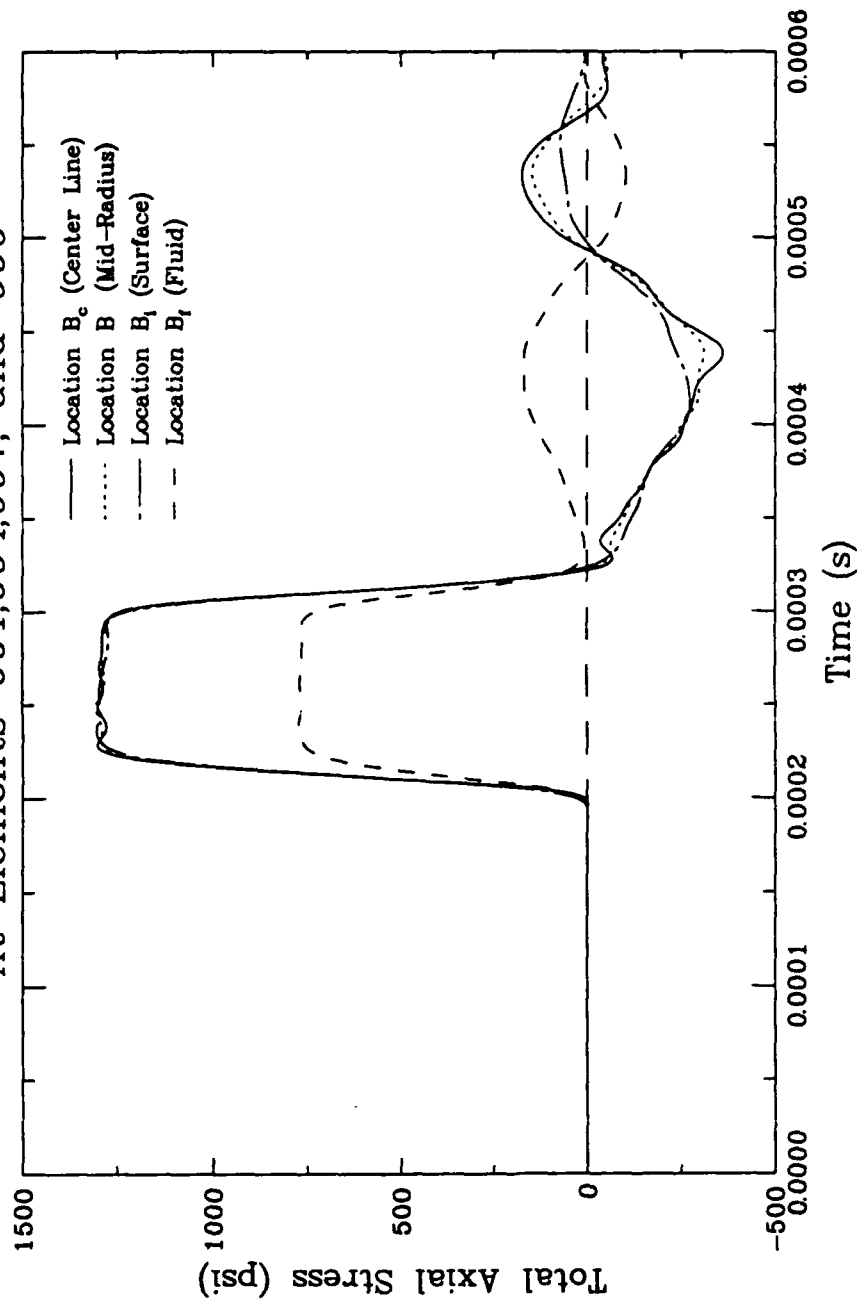
Figure 6.31a. Influence of lateral position on total stress for fluid confined loading with no relative fluid motion at Range B (10 in.).

WB–F–SR
At Elements 991,994,997, and 999
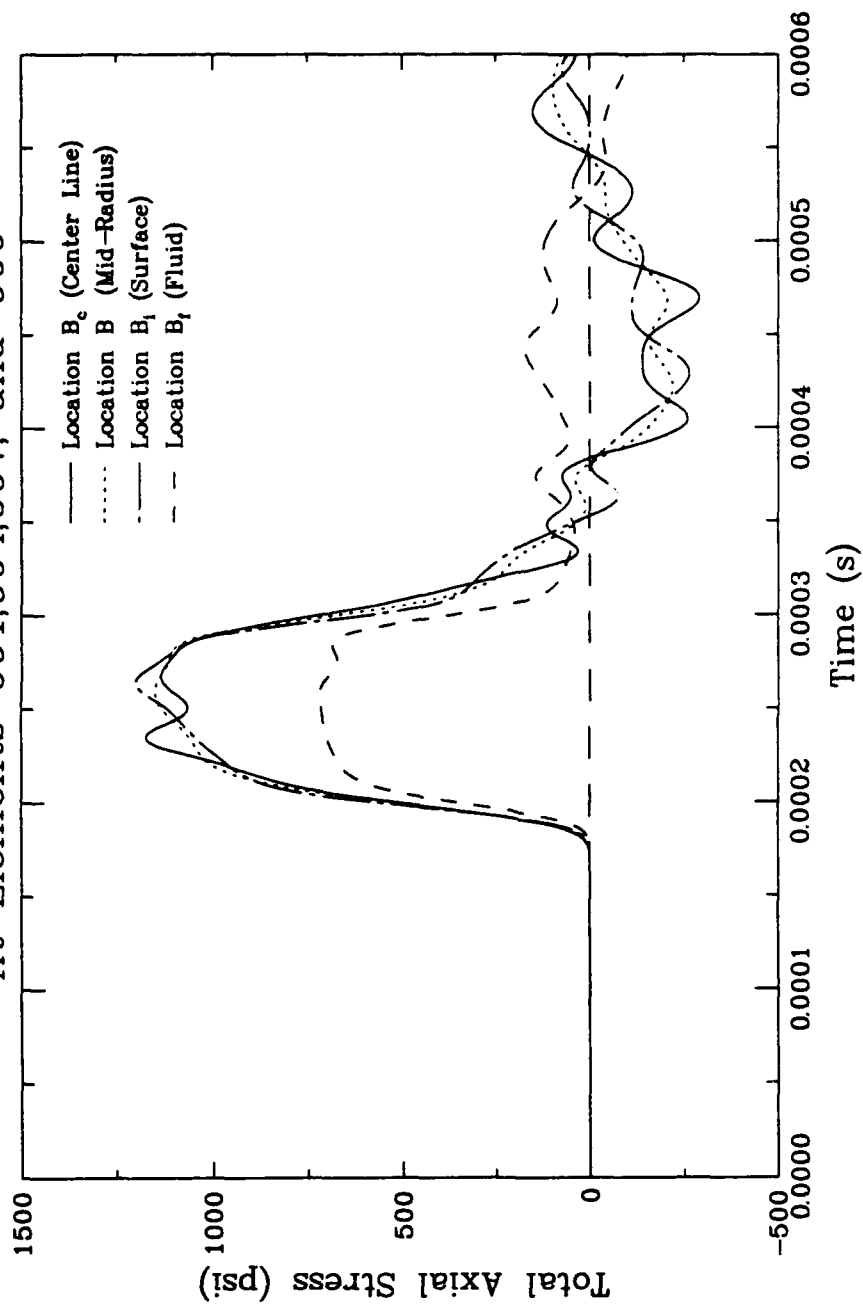
Location B_c (Center Line)
Location B (Mid–Radius)
Location B_l (Surface)
Location B_f (Fluid)

Figure 6.31b. Influence of lateral position on total stress for fluid confined loading with relative fluid motion at Range B (10 in.).

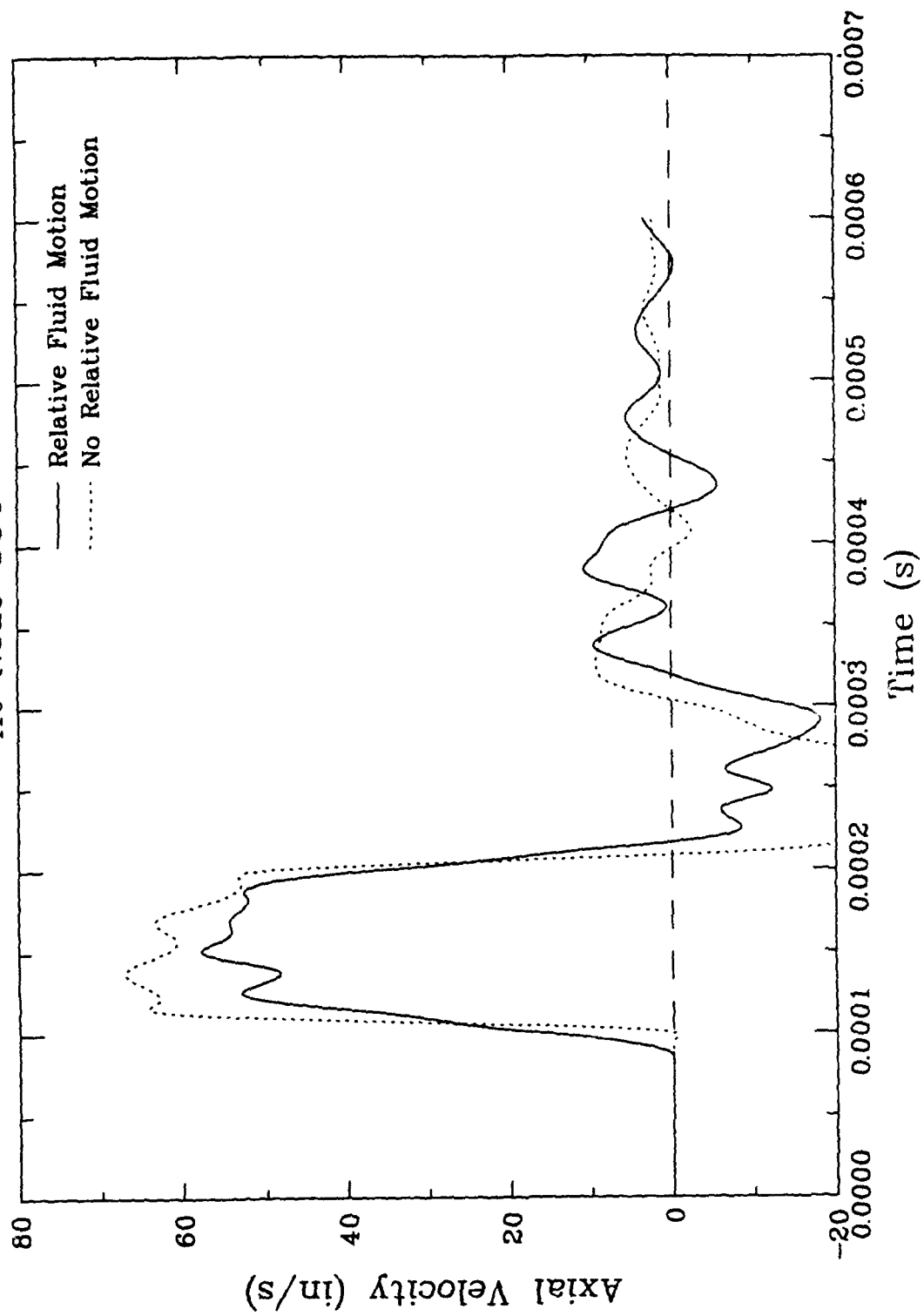Figure 6.32a. Influence of relative fluid motion on skeleton velocity for fluid confined loading at Range A (5 in.).

Figure 6.32b. Influence of relative fluid motion on skeleton velocity for fluid confined loading at Range B (10 in.).

WB–F–SR,N
At Node 1654
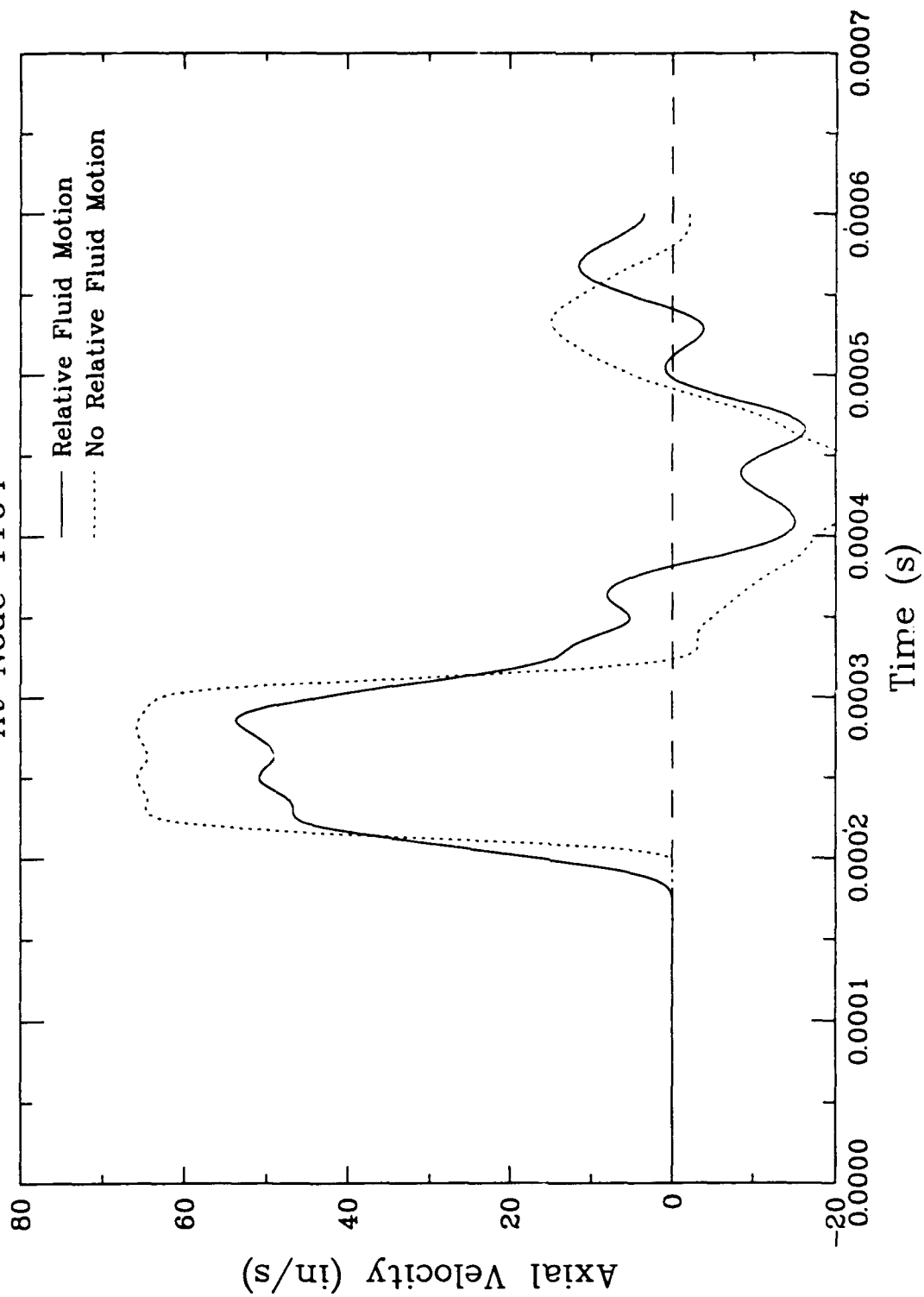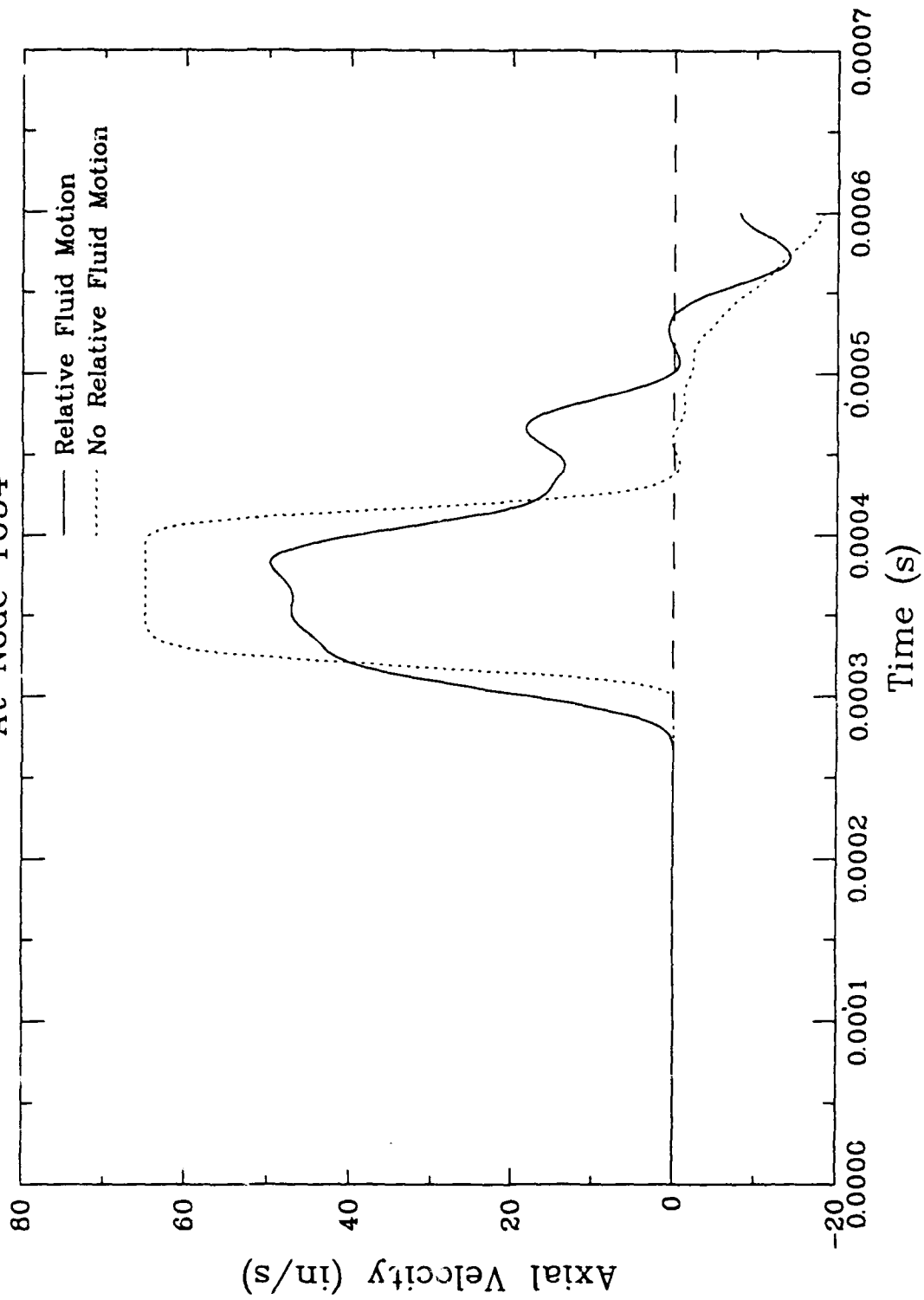
— Relative Fluid Motion
...... No Relative Fluid Motion

Figure 6.32c.   Influence of relative fluid motion on skeleton velocity for fluid confined loading at Range C (15 in.).

WB–F–SR,N
At Node 554

— Relative Fluid Motion
..... No Relative Fluid Motion

Figure 6.33a. Influence of relative fluid motion on skeleton displacement for fluid confined loading at Range A (5 in.).

WB–F–SR,N
At Node 1104

——— Relative Fluid Motion
.... No Relative Fluid Motion

Axial Displacement (in)

Time (s)
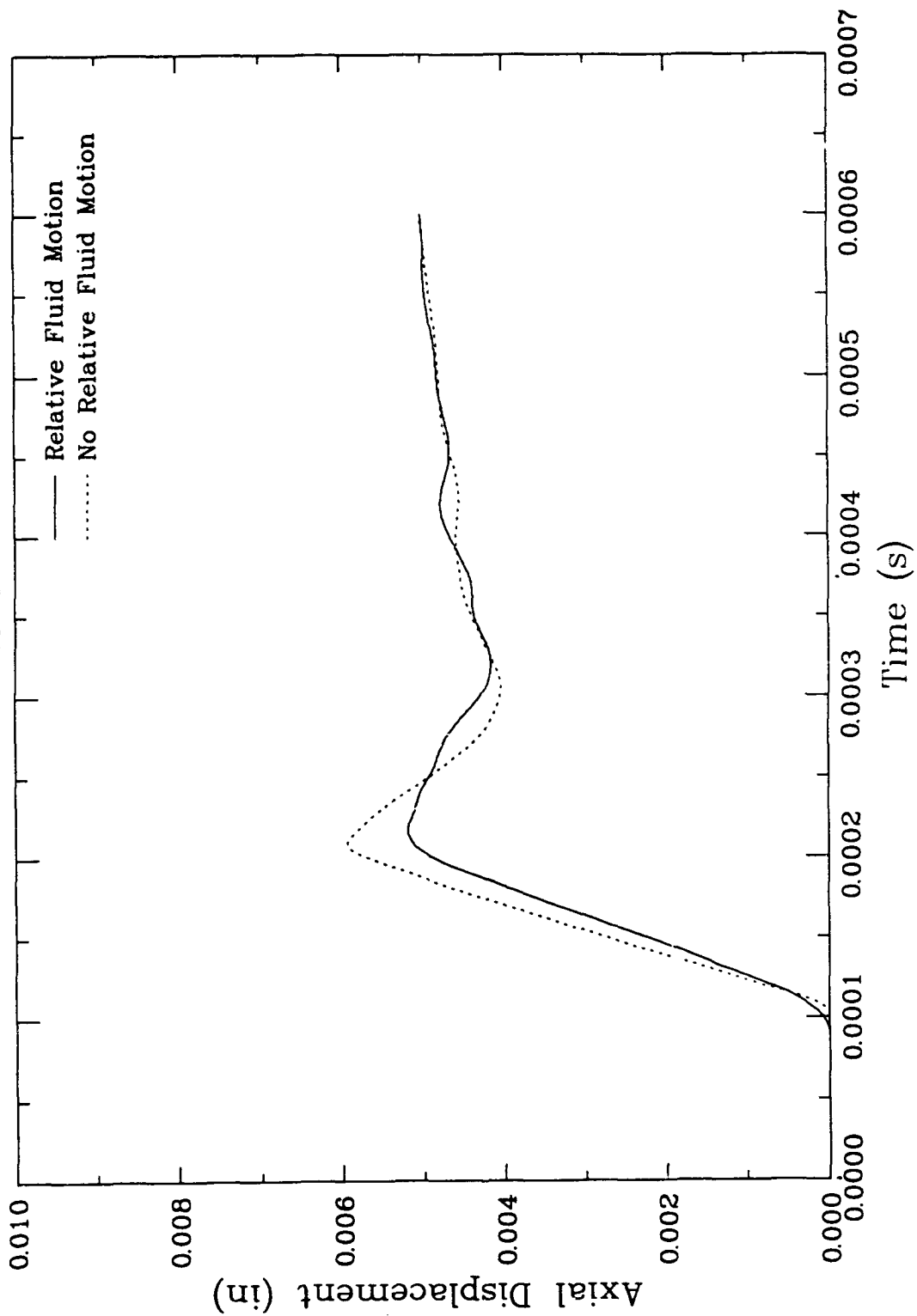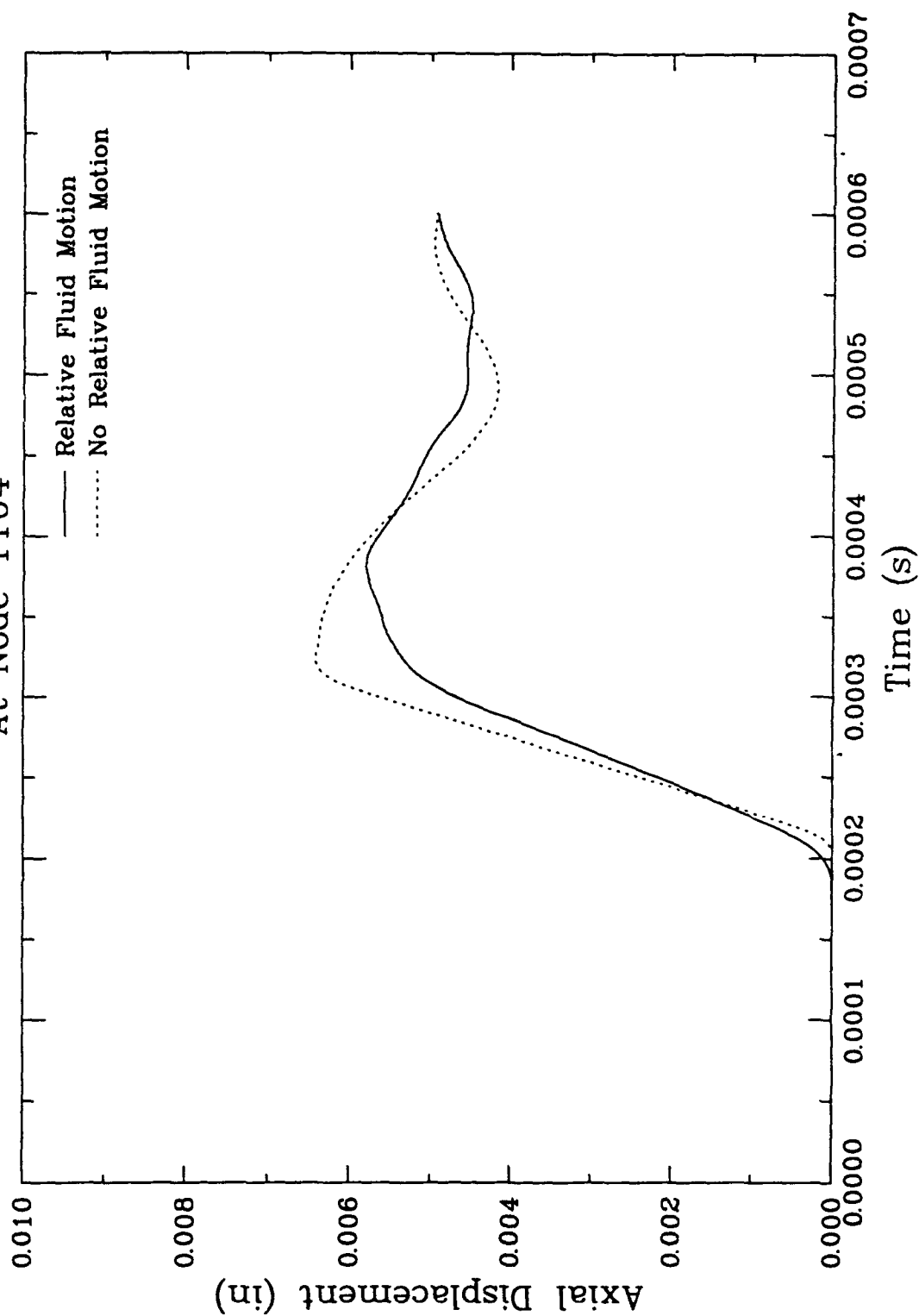
Figure 6.33b. Influence of relative fluid motion on skeleton displacement for fluid confined loading at Range B (10 in.).
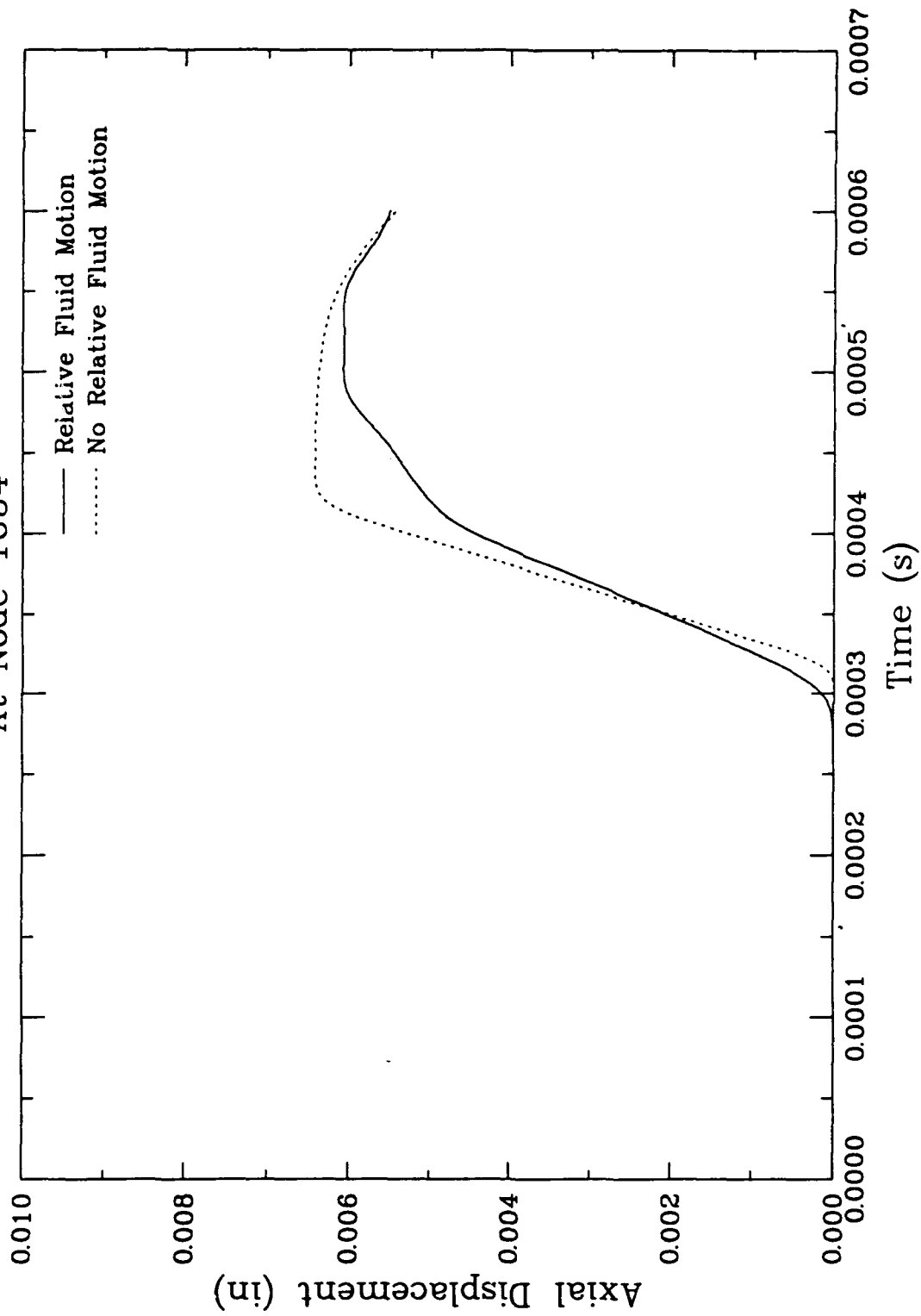
Figure 6.33c. Influence of relative fluid motion on skeleton displacement for fluid confined loading at Range C (15 in.).

SECTION 7

WAVE PROPAGATION BAR TESTS AND NUMERICAL SIMULATIONS

This section presents the results of a series of tests that was performed using the test apparatus described in Section 6 to investigate wave propagation through a fluid-saturated porous medium. Tests were performed on a specimen of sintered stainless steel under both dry and fluid-saturated conditions. This section describes the porous stainless steel specimen, including mechanical and fluid flow properties, and presents the results of the wave propagation tests. Also presented in this section are the results of a numerical simulation, performed with the finite element program, MPDAP, of one wave propagation bar test on a saturated specimen.

7.1 WAVE PROPAGATION BAR TEST DESCRIPTION

The Wave Propagation Bar (WPB) apparatus used to conduct the laboratory experiments is described in Section 6.1, and depicted in Figures 6.2 through 6.7. The subsection describes the sintered stainless steel specimen and the procedures and instrumentation used to conduct the tests.

7.1.1 Porous Stainless Steel Specimen

All of the WPB tests reported in this section were performed on a specimen of porous stainless steel. This material was selected because it has several advantages over a geologic material for studies of the fundamental mechanics of wave propagation. The metal skeleton is more nearly linear elastic than any sand or porous rock. It is very important that the properties of the constituent materials be well characterized so that the inherent complexity of the wave mechanics is not furcher confused by unknown or nonlinear skeleton response. Porous metal is formed by processing granular material at high temperature and pressure to form a solid with void spaces similar to a porous rock. Since this is a controlled process, the properties of the resulting material can be specified within some range. This, along with the fact that the skeleton

is metal, makes it possible to obtain a material that has both relatively high permeability and high skeleton stiffness, a combination that was expected to accentuate the phenomenology of interest. Blouin, et.al. (1990) listed fifteen grades of porous stainless steel that are commercially available, covering a broad range of porosity and permeability. Since the elastic modulus is apparently not of interest in the normal commercial uses of the material, no data on compressibility properties were available at the time of the initial design. The original equipment design and calculations of specimen response were based on estimates of the mechanical properties of the various grades of porous stainless steel, as described in Section 6.

Two bars of porous stainless steel were fabricated for use as test specimens by Newmet Krebsoge of Terryville, CT. The nominal dimensions of the bars were 2 inches diameter and 24 inches long. One bar was cut into shorter lengths for mechanical property and fluid flow testing, and the other was used at almost full length for WPB tests. In order to avoid closing the pore spaces on the cut as would happen with conventional cutting techniques, the bars were cut using a modern machining technique known as wire electric discharge machining.

The bars were specified to be Sika R 100. However, since the material is not normally manufactured in such large sizes, some variation from the normal R 100 specifications was expected. The nominal porosity of the Sika R 100 based on the specified density is 0.465, and it was estimated to have an elastic modulus of 4.7×10^5 psi and Poisson's ratio of 0.2. In order to determine the actual properties of the test specimens, an unconfined compression test was performed on a cylindrical specimen of the porous stainless steel (approx. 2 in. diameter by 4 in. long). Plots of the resulting axial and radial strain against axial stress are presented in Figure 7.1. From the data in Figure 7.1 the elastic modulus and Poisson's ratio were found to be 3.6 $\times 10^6$ psi and 0.25, respectively. Thus, the stiffness of the porous bars as fabricated was nearly and order of magnitude greater than originally estimated. Confirmation of the unconfined compression test result is provided by data acquired while preparing the full length specimen for wave propagation testing. The strain gage circuits on the porous specimen and axial load measurement gages on the incident bar were monitored during initial static axial preloading of the specimen. The elastic modulus computed from those measurements was found to be essentially identical to the value determined from the unconfined compression test on the

specimen cut from the other bar of porous material. The physical and mechanical properties of the porous specimen are summarized in Table 7.1.

The results of a series of permeability tests on a specimen of the porous stainless steel are presented in Figure 7.2. A straight line was fit using the complete data set, as depicted in the figure. The intercept and slope of the line were used to define flow coefficients a and b, respectively, as defined in Section 4. The permeability is lower by approximately a factor of five than the value given by the manufacturer, reported by Blouin, et al., (1990), and used in the parametric calculations reported in Section 6.2.

The expected wavespeed and damping for compressional waves of the first and second kinds in kerosene saturated porous stainless steel with the measured material properties were computed as a function of the frequency of the excitation pulse with the computer program TWAVE, as described in Section 6. The results of those calculations are presented graphically in Figure 7.3. Table 7.2 presents the wavespeeds of the saturated material and its various constituents, computed from the properties listed in Table 7.1, using the procedures described in Section 6.6. Comparison of the values in Table 7.2 with the corresponding quantities in Table 6.3 reveals that the wavespeeds computed based on the initial estimates of specimen stiffness are significantly in error.

The transition in the wave of the first kind occurs in the range of approximately 10,000 to 100,000 rad/s. Thus, the range of frequencies possible with the wave propagation apparatus as fabricated (15,700 to 62,800 rad/s) falls within the transition region for the specimen material.

7.1.2 Test Procedures

The specimen was 21.3 inches long, and its cylindrical surface was rough due to the fabrication process, having a diameter of 1.90 ± 0.02 inches. Prior to installation of the specimen in the test apparatus, two foil strain gages, one each in the axial and circumferential directions, were bonded to the bar at specially prepared locations on its surface at distances of 5, 10, and

15 inches from the upstream end of the specimen and a pore pressure gage was also placed on the surface of the specimen at the 5-inch station, as described in Section 7.1.3. The specimen was then placed inside a heat-shrinkable polyolefin tube and installed between the incident bar and transmitter bar as illustrated in Figure 6.2. The tubing was shrunk to a tight fit around the specimen. The tubing also extended approximately 1 inch onto the bars on either end and was sealed to the incident and transmitter bars with epoxy adhesive and wire clamps. At this point, the pressure vessel was closed, and all of the instrumentation was connected and checked. Wave propagation measurements were made on the dry specimen with no confining pressure. During these tests, approximately 350 psi average axial stress was applied to the specimen to tightly seat the various components of the WPB assembly.

Upon completion of the dry tests, the pressure vessel was evacuated and then filled with de-aired kerosene. Access to the pore space of the specimen was by means of an axial hole drilled in the transmitter bar and an intersecting radial hole outside the pressure vessel. In preparation for saturation, the pore space was evacuated. It was then filled with de-aired kerosene. A quantity of kerosene slightly larger than the void space of the specimen was introduced, resulting in a layer of fluid between the specimen and the polyolefin membrane. The confining fluid in the pressure vessel surrounding the specimen was then pressurized to 1000 psi. Axial load equivalent to 1000 psi average axial stress was also applied to the specimen. Because of the excess fluid surrounding the specimen, this also had the effect of pressurizing the pore fluid. This tends to force any remaining pore air into solution. The pore fluid valve was then opened momentarily, allowing the excess pore fluid to drain. The quantity of fluid drained was manually controlled to obtain the desired initial pore pressure of 500 psi. These initial stress conditions of 1000 psi confining pressure and axial stress, and 500 psi pore pressure were maintained throughout the wave propagation tests on saturated specimens.

7.1.3 Instrumentation

During each test, a high-speed digital data acquisition system was used to record eight channels of instrumentation, consisting of strain gages on the porous stainless steel specimen, pore pressure at the surface of the specimen, and a strain gage bridge on the incident bar to measure the loading applied to the test specimen. The locations of the instruments on the porous specimen and on the incident bar are shown in Figure 7.4.

Standard foil strain gages were bonded to the stainless steel were used to monitor skeleton deformation. As manufactured, the surface of the porous stainless steel is much too rough to be strain gaged. However, experimentation in the laboratory showed that by grinding the surface, it is readily possible to obtain a surface that can be strain gaged. The grinding not only smooths the roughness but also smears some material into the void spaces, creating a surface with an appropriate texture for strain gaging. Axial and radial strains were measured at there stations. The three stations, designated A, B, and C were located at distances of 5, 10, and 15 inches, respectively, from the incident end of the test specimen.

One pore pressure measurement was made at the surface of the porous bar at Station A, located 5 inches from the upstream end of the specimen. A special instrumentation package was devised for that purpose. An ENTRAN Model EPL6-125-5000X pressure transducer (0.125 inch diameter and 0.07 inch thick) was installed under a specially designed aluminum shroud which distributed the confining pressure load around the pressure transducer so that it was exposed only to pore pressure.

The load applied to the test specimen was measured with a full strain-gage bridge on the incident bar external to the pressure vessel. The foil strain gages were bonded to the incident bar 37.5 inches upstream from the contact with the test specimen. They were arranged and wired in the conventional manner for a column load cell.

All channels were digitized at a sampling interval of 1 μs. In each test, the start time for data acquisition was initiated when the striker bar made contact with a switch in advance of

impacting the incident bar. Due to variations in switch positioning and bar velocity, this is not a reliable zero-time indication. In all of the test data plots, zero time has been set to approximately the time the stress wave arrived at the interface between the incident bar and the test specimen. This was done by choosing a point 55 µs before arrival of the wave at strain gage Staion A. It is estimated that the difference between the zero time selected in this manner and the actual arrival of the stress wave is less than 5 µs. All of the traces for each test are plotted with respect to the same time reference.

7.2 WAVE PROPAGATION BAR TEST RESULTS

This subsection presents the results of the WPB tests on a porous stainless steel specimen described in Section 7.1. Table 7.3 presents a summary of all the tests performed. The results of tests on the porous specimen in the dry condition are presented in Section 7.2.1, and Section 7.2.2 presents the tests performed with the specimen saturated.

7.2.1 Wave Propagation Tests on Dry Specimen

As indicated in Table 7.3, tests on dry porous stainless steel specimens were performed with three different length striker bars, 5-, 10-, and 20-inch. Three nominally identical tests were performed with each striker bar. There were no significant differences between tests with a given bar type, and a typical test of each type was selected for further analysis. Figures 7.5 through 7.7 present the results of three typical tests on dry specimens, one with each striker bar length. Each of Figures 7.5 through 7.7 has three parts, designated a, b, and c. Part a of each figure presents the input force time history measured on incident bar for that test. Parts b and c of Figures 7.5 through 7.7 present axial and radial strains, respectively, on the test specimen. Each of the strain plots shows three strain histories, corresponding to the three strain measurement stations as defined above and illustrated in Figure 7.4.

By examining parts a of Figures 7.5 through 7.7, it can be seen that, as expected, durations of the applied stress pulses are proportional to their respective striker bar lengths. The

5-, 10-, and 20-inch striker bars produced pulse durations, as measured from the beginning of the rise to the onset of unloading, are 50, 100, and 200 µs, respectively. All three tests exhibit wavespeeds of about 90,000 in./s (2300 m/s) when determined from first arrivals and approximately 80,000 in./s (2000 m/s) when measured from the mid-points of the initial rise portions of the stress wave signals. The wavespeed determined from first arrivals is in good agreement with the rod (uniaxial stress) wavespeed listed in Table 7.2. This result differs from the numerical simulation results presented in Section 6, in which the wavespeed at mid-height of the first rise to peak was in reasonable agreement with the computed uniaxial strain wavespeed. Recall that the actual elastic modulus of the porous stainless steel is almost a factor of eight larger than the elastic modulus used in the calculations presented in Section 6. The difference in wavespeeds is an indication that the fluid confinement is not as effective in maintaining a uniaxial strain condition with the real material as it was computed to be with the erroneously soft porous skeleton.

The reflections from the downstream end of the specimen are evident in the strain data presented in Figures 7.5 through 7.7 (parts b and c). The reflection arrives first at Station C, at approximately 350 µs. It is followed by arrivals at Stations B and A at times of approximately 400 and 450 µs, respectively.

7.2.2 Wave Propagation Tests on Saturated Specimen

Wave propagation bar tests were performed on the same porous stainless steel specimen fully saturated with kerosene, as described in Section 7.1. Those tests are summarized in Table 7.3. In addition to tests with the 5-, 10-, and 20-inch striker bars, a test was performed on the saturated specimen with a 1/8-inch thick rubber pad attached to the front of the 20-inch striker bar to produce an input stress pulse with a longer rise time to peak. Figures 7.8 through 7.11 present data plots for one representative test with each type of excitation. Figures 7.8 through 7.11 correspond respectively to excitation by 5-inch striker, 10-inch striker, 20-inch striker, and 20-inch striker with rubber pad. As with the dry specimens, each figure has parts a, b, and c showing the input force pulse, axial strains, and circumferential strains, respectively. In addition, each figure for the saturated tests has a part d which presents the pore pressure time history at

7-7

Station A, 5 inches from the interface with the incident bar.

The wavespeed in the saturated porous bar, as determined from the first arrivals is 90,000 in./s (2300 m/s). When determined by the mid-points of the initial rise portions of the waves at the first and last strain gage stations, the wavespeed is 80,000 in./s (2000 m/s). These values are the same as the corresponding measurements for the dry porous bar. This is consistent with the calculated wavespeeds presented in Table 7.2, which show no significant difference in computed wavespeeds between the dry and saturated cases. This lack of sensitivity of wavespeed to the degree of saturation results from the dominant stiffness of the material skeleton.

One measure of the consistency between the experimental results and the analytical understanding of the physics of the problem is the amount of the load carried by the water relative to the porous skeleton. Blouin and Kim (1984) present the following expression for the ratio, β_m, of effective stress to pore pressure under uniaxial strain loading given by:

$$\beta_m = \frac{K_g^2 M_s + K_m K_s^2 - M_s K_m K_s - K_g K_m K_s}{K_m K_g (K_g - K_s)} \qquad (7\text{-}1)$$

where:

K_m = mixture modulus = $(K_g K_f) / [K_f + n(K_g - K_f)]$

K_g, K_m, K_s = bulk modulus of grains, fluid, skeleton

M_s = constrained modulus of skeleton = $3K_s(1-v)/(1+v)$

v = Poisson's ratio of skeleton

n = porosity of skeleton

Using the properties for the porous stainless steel skeleton, solid grains, and kerosene given in Table 7.1, the resulting value of β_m is 9.75. For comparison, consider the test data from a saturated specimen impacted by a 10-inch striker bar which are shown in Figures 7.9b-7.9d. The peak in the pore pressure history occurs at approximately 120 μs. The initial peaks in both skeleton strains at Station A occur at the same time. Using the axial and circumferential strains at 120 μs and the elastic constants given in Table 7.1, the axial stress in the stainless steel skeleton is found to be approximately 3500 psi. At the same time the pore pressure was

7-8

approximately 345 psi. The ratio of effective stress in the skeleton as derived from strain measurements to the measured dynamic pore pressure at the same time is 10.1. This quantity is comparable, although not exactly the same, as the β_m derived from theory. The ratio, β_m, is derived assuming a uniaxial strain condition. While this is known not to be the case in the experiment, the close match between measured and calculated values is a clear indication that the porous skeleton was fully saturated and that the partitioning of load between skeleton and pore fluid was approximately as predicted by theory.

7.2.3 Comparison between Dry and Saturated Test Results

Figures 7.12 through 7.14 present comparisons of strain records from dry and saturated tests for striker bar lengths of 5, 10, and 20 inches, respectively. Parts a of Figures 7.12 through 7.14 show axial strains and parts b present circumferential strains. The traces have been shifted, as necessary so that the initial arrivals occur at the same time. The records from the dry tests in Figures 7.13 and 7.14 were also scaled in amplitude by the ratios of the loading amplitudes so that they are approximately the same size on the comparison plots. The loading amplitudes for the dry and saturated tests were within 2% of each other for the records shown in Figure 7.12, and no scaling was done. In all three tests, the arrivals of the waves at Stations B and C occurred at essentially the same times in both dry and saturated specimens. This shows, as noted in the preceding subsections, that the wavespeeds in the saturated tests were essentially identical to those in the dry tests.

In the tests with the 5-inch striker bar, shown in Figure 7.12, the wave propagating through the dry specimen exhibited more dispersion than saturated specimen, as evidenced by the longer durations of the strain pulses. This trend does not appear to carry over to the tests with the longer striker bars shown in Figures 7.13 and 7.14.

7.3   NUMERICAL SIMULATION OF LABORATORY EXPERIMENT

To improve our understanding of the laboratory results and to validate our numerical models, a detailed finite element calculation was performed to simulate wave propagation test number D31K1. The calculation was completed using the MPDAP code and was similar to the parametric calculations discussed in Section 6. The finite element mesh geometry and boundary conditions were the same as used in the parametric calculations of the fluid confined bar as depicted in Figure 6.11. For this simulation, however, the material properties, initial stress conditions, and input loading wave were carefully selected to model the actual test conditions as closely as possible.

The porous, stainless steel test specimen and the kerosene fluid were modeled as linear elastic materials. This is an appropriate assumption for the stress wave amplitudes induced in the tests. Properties for the test specimen and pore fluid are summarized in Table 7.1. Elastic properties for the porous steel skeleton were obtained from the unconfirmed compression test on a sample of the specimen material, as described in Section 7.1.1 and shown in Figure 7.1. The specific gravities and bulk moduli for the solid steel grains and the kerosene were obtained from standard references on material properties. Note that kerosene is used for both the pore fluid inside the porous skeleton and the confining fluid. The permeability parameters for the porous-steel test specimen are also given in Table 7.1. They were derived from the test data presented in Figure 7.2. Since the porosity of the bar is practically unchanged during passage of the stress wave, the permeability parameters were considered as constant.

The parametric calculations described in Section 6.4 were started with a zero stress condition in the specimen. In test number D31K1, an axial stress of 1000 psi was applied to the test specimen to ensure full contact with the incident and transmitter bars. Furthermore, a 500 psi initial pore pressure was applied to the specimen to maintain saturation necessary for accurate pore pressure measurements. Both the initial axial stress of 1000 psi and pore pressure of 500 psi were applied at the start of the numerical simulation to maintain a complete simulation of the test. However, since only linear elastic material models were used, modeling the initial stress condition should have no effect on the simulation results.

To permit a direct comparison between the simulation and test results, it was necessary to match, as closely as possible, the loading conditions in the test. First, the loading was modeled by specifying uniform velocity time history across the end of the bar. The velocity boundary ensures that the end of the specimen will displace uniformly in the simulation. This is a more accurate model of the actual loading condition than the pressure loading used in the parametric calculations. Further, the input loading was applied only to the end of the specimen and not to the confining fluid as was done in the parametric calculations reported in Section 6.4.

To develop an appropriate boundary velocity-time history to simulate the stress wave loading, the input stress pulse was recorded using a load cell on the incident bar. From the recorded stress wave, seven time points were used directly in the load history for the simulation. To determine the appropriate velocity magnitude at each point, a trial and error procedure was used to determine a correlation factor between the recorded axial load and the corresponding particle velocity to be used in the simulation. In this manner, a seven-point, velocity time history was developed that accurately simulated the input pulse in test number D31K1. This loading condition is plotted in Figure 7.15.

The calculated axial strains in the test specimen are overlaid with the actual test data from D31K1 in Figure 7.16a, b, and c for ranges of 5 inch, 10 inch, and 15 inch, respectively. Considering the complexity of the problem, the overall agreement between the calculation and the data is excellent. The wavespeeds in the simulation are slightly higher than those measured in the experiments. The wavespeed calculated based on initial arrival is 95,000 in./s (2410 m/s), as compared with 90,000 in./s (2290 m/s) measured in the experiments. Similarly, at the mid-points of the initial rise to peak in the strain signals, the calculation shows a speed of 92,000 in./s (2340 m/s) while the rise to peak in the tests was slower, exhibiting a wavespeed at the mid-point of approximately 80,000 in./s (2030 m/s). The amplitudes of both the initial peak and the overall peak are in quite good agreement between calculation and experiment.

Figures 7.17a, b, and c present comparisons of circumferential strain records at Stations A, B, and C, respectively. The numerical simulation under-predicted the circumferential strain

at every station relative to the test measurements. This is an indication that the confinement system was somewhat more effective than the calculation would suggest.

In Figures 7.16a and 7.16b is evidence of what may be the wave of the second kind. The simulation clearly shows an initial peak in axial strain followed by a second significant rise. At Station A (Figure 7.16a), the second rise begins at 105 μs, which is 10 μs after the initial peak. At Station B (Figure 7.16b), the second rise begins at 205 μs, which is about 55 μs after the initial peak. This secondary strain pulse is propagating at a velocity of 50,000 in./s (4170 ft/s = 1270 m/s), which agrees very well with the computed velocity of the wave of the second kind (4100 ft/s) at the high frequency end of Figure 7.3b. At the time where this wave pulse would be expected at Station C (approx. 350 μs), the reflection from the far end of the bar dominates the waveform, making it impossible to detect the slow moving forward propagating pulse. The same phenomenon is present in the lab test data, although somewhat less pronounced. The arrival of the secondary wave is easier to observe in the circumferential strain data shown in Figures 7.17a and 7.17b than in the axial strain records. In the test data, the second wave is propagating at about 40,600 in/s (3380 ft/s = 1030 m/s). As with the wave of the first kind, this is somewhat lower than the speed predicted by analysis for the case where radial strains are fully constrained.

If the secondary wave discussed in the previous paragraph is in fact the wave of the second kind, which is associated with a fluid saturated porous material, then it should not appear in the tests performed on the dry bar. Attention is referred back to Figures 7.14a and 7.14b. At Station A, the saturated waveforms for both axial and radial strains clearly exhibit a secondary pulse that is different than those for the dry material. At Station B, which is 5 inches further downstream, the secondary wave is significantly attenuated, but still appears in the records from the saturated specimen and not those for the dry condition.

Figure 7.18 compares the measured and calculated dynamic pore pressures. (In this figure, zero dynamic pore pressure corresponds to the initial pore pressure of 500 psi). In this case, the calculated pore pressures are about one half of the measured values. Only one pore pressure measurement location was available in this test, so only the comparison in Figure 7.18

is possible. The computed pore pressure responses at 5, 10, and 15 inch ranges are compared in Figure 7.19. At the times of the secondary strain pulses discussed in the previous two paragraphs, simulation results exhibit a sharp drop in pore pressure at both locations. In the measured strain records shown in Figure 7.14, the arrival of the secondary wave occurs at approximately 130 μs. Consistent with the analysis results, the one measured pore pressure record also has a major negative-going excursion at that time. However, in the simulations, the first negative-going pulse in the pore pressure corresponds with the arrival of the secondary wave in the strain records. In contrast, in the laboratory test records, the pore pressure contains a prior negative-going pulse.

Figures 7.20a through 7.20c present time histories of particle velocity of the porous skeleton and of velocity of the pore fluid relative to the skeleton at Stations A, B, and C, respectively. Particularly at Stations A and B, the skeleton velocities exhibit secondary pulses of the same form as the strain records. In the apparent relative fluid velocity records, both the arrival of the initial wave and the secondary wave, there are short duration (less than 50 μs) negative pulses of relative fluid velocity, i.e. the fluid momentarily lags behind the skeleton. Unfortunately, there are no analogous laboratory measurements for comparison.

Figures 7.21 and 7.22 compare the computed axial strains and dynamic pore pressures at various locations within the bar at a range of 10 inches. Since measurements can only be acquired at the surface of the specimen in the test, the finite element simulation can be used to study variations in the stress wave with distance from the surface of the bar. From Figures 7.21 and 7.22, it appears that a very uniform stress condition is propagating through the bar in this simulation.

7.4 DISCUSSION OF WAVE PROPAGATION BAR TESTS

The research effort described in this section involves both laboratory experiments and numerical simulations of wave propagation through saturated porous media. A laboratory test apparatus was designed and assembled and a series of tests was performed on a specimen of

7-13

porous (sintered) stainless steel. The tests were conducted with the specimen both dry and fully saturated with kerosene. Instrumentation on the specimen was used to measure axial and circumferential strains at three stations and pore fluid pressure at one station. Mechanical waves were induced in the test specimen by impacting a hardened steel bar that was in contact with the specimen by second hardened steel bar called the striker bar. The duration of the stress pulse was determined by the length of the striker bar, and strikers of three different lengths were used in the tests to produce stress pulses of nominally 50, 100, and 200 μs duration.

The numerical simulations were performed with MPDAP, a special purpose finite element computer program specifically designed for the analysis of fully or partially saturated porous materials. A simulation was performed with the test apparatus and input boundary conditions carefully defined to match, as closely as possible, one of the laboratory experiments. Comparisons were made between the measured and computed response, and between measured response of the porous stainless steel specimen in the dry and fully saturated conditions.

In a saturated porous material, the stress resulting from an imposed load is partitioned between the porous skeleton and the pore fluid. In the test apparatus, the stresses carried in by the solid and fluid phases were measured and the distribution of stresses between the two was found to be consistent with theoretical predictions. Unfortunately, because of the very high stiffness of the porous stainless steel specimen with respect to the pore fluid, approximately 90% of the load was carried by the steel skeleton. Thus, while the saturated specimen did behave as expected, its response was, in many ways, not very different from that of a dry specimen. However, using the results of the numerical simulations for guidance, we were able to find evidence in the both the strain and pore pressure records from the laboratory experiments of the wave of the second kind that has been theoretically predicted to exist in saturated porous materials.

We believe that our ability to resolve the phenomena of interest in the test data was limited because of the very high stiffness of the porous skeleton that we inadvertently chose for the experiment. In future work it is recommended that softer (less stiff) skeleton materials be used in order to accentuate the effect of the pore water on the overall response of the saturated

7-14

porous material. Further, it would be very desirable to devise an instrumentation scheme that would measure the velocity of the pore fluid relative to the porous skeleton.

Table 7.1. Properties of test specimen used in numerical simulation of laboratory test.

Porous Stainless Steel		
Model: linear elastic		
porosity	n	0.42
Poisson's ratio	ν	0.25
Young's modulus	E	3.6×10^6 psi
bulk modulus	K	2.4×10^6 psi
shear modulus	G	1.44×10^6 psi
constrained modulus	M	4.32×10^6 psi
Solid Stainless Steel Grains		
Model: linear elastic		
specific gravity	G_s	7.8
bulk modulus	K_g	16.67×10^6 psi
Kerosene Pore Fluid and Confining Fluid		
Model: linear elastic		
specific gravity	G_s	0.81
bulk modulus	K_f	0.188×10^6 psi
viscosity	μ	2.65×10^{-7} lb-s/in^2
Permeability of Skeleton		
Permeability coefficient	a	7.8 lb-s/in^4
Permeability coefficient	b	2.3 lb-s^2/in^5
Permeability coefficient	$\beta = \rho_f / b$	3.4×10^{-8} in^2
Permeability coefficient	$\alpha = \mu / a$	4.1×10^{-5} in

Table 7.2. Summary of computed wavespeeds for materials used in laboratory tests.

MATERIAL	CONDITION	MODULUS (psi)	SPECIFIC GRAVITY	WAVESPEED (m/s)
Kerosene	Confined	$.188 \times 10^6$	0.81	1265
Porous Stainless Steel	Uniaxial stress, dry skeleton	3.60×10^6	4.52	2344
	Uniaxial strain, dry skeleton	4.32×10^6	4.52	2566
	Uniaxial stress, saturated skeleton	3.60×10^6	4.86	2260
	Uniaxial strain, saturated (low frequency)	4.69×10^6	4.86	2567
	Uniaxial strain, saturated (high frequency)	4.76×10^6	4.86	2600
Water	Confined	$.322 \times 10^6$	1.00	1490
Solid Steel	Uniaxial strain	38.0×10^6	7.80	5796

7–17

Table 7.3. Wave propagation bar test summary.

Confining pressure (psi)	Confining Pressure (psi)	Pore Pressure (psi)	Axial Preload (psi)	Striker Length (in.)	Gun Pressure (psi)	
D30A1	0	0	318	20	7.5	Overload on axial strains
D30B1	0	0	318	20	7.5	
D30C1	0	0	318	20	7.5	
D31A1	0	0	318	5	4	
D31B1	0	0	318	5	3.6	
D31C1	0	0	318	5	3.6	
D31D1	0	0	318	10	7	
D31E1	0	0	318	10	5.5	
D31F1	0	0	318	10	4	
D31G1	1000	500	1000	10	5	
D31H1	1000	500	1000	10	5	
D31I1	100	500	1000	10	5	
D31J1	1000	500	1000	20	12	
D31K1	1000	500	1000	20	12	
D31L1	1000	500	1000	20	12	
D31M1	1000	500	1000	5	3.5	
D31N1	1000	500	1000	5	3.5	
D31O1	1000	500	1000	5	3.5	
D31P1	1000	500	1000	20	15	w/0.112-in. thick rubber pad
D31Q1	1000	500	1000	20	15	w/0.112-in. thick rubber pad
D31R1	1000	500	1000	20	15	w/0.112-in. thick rubber pad
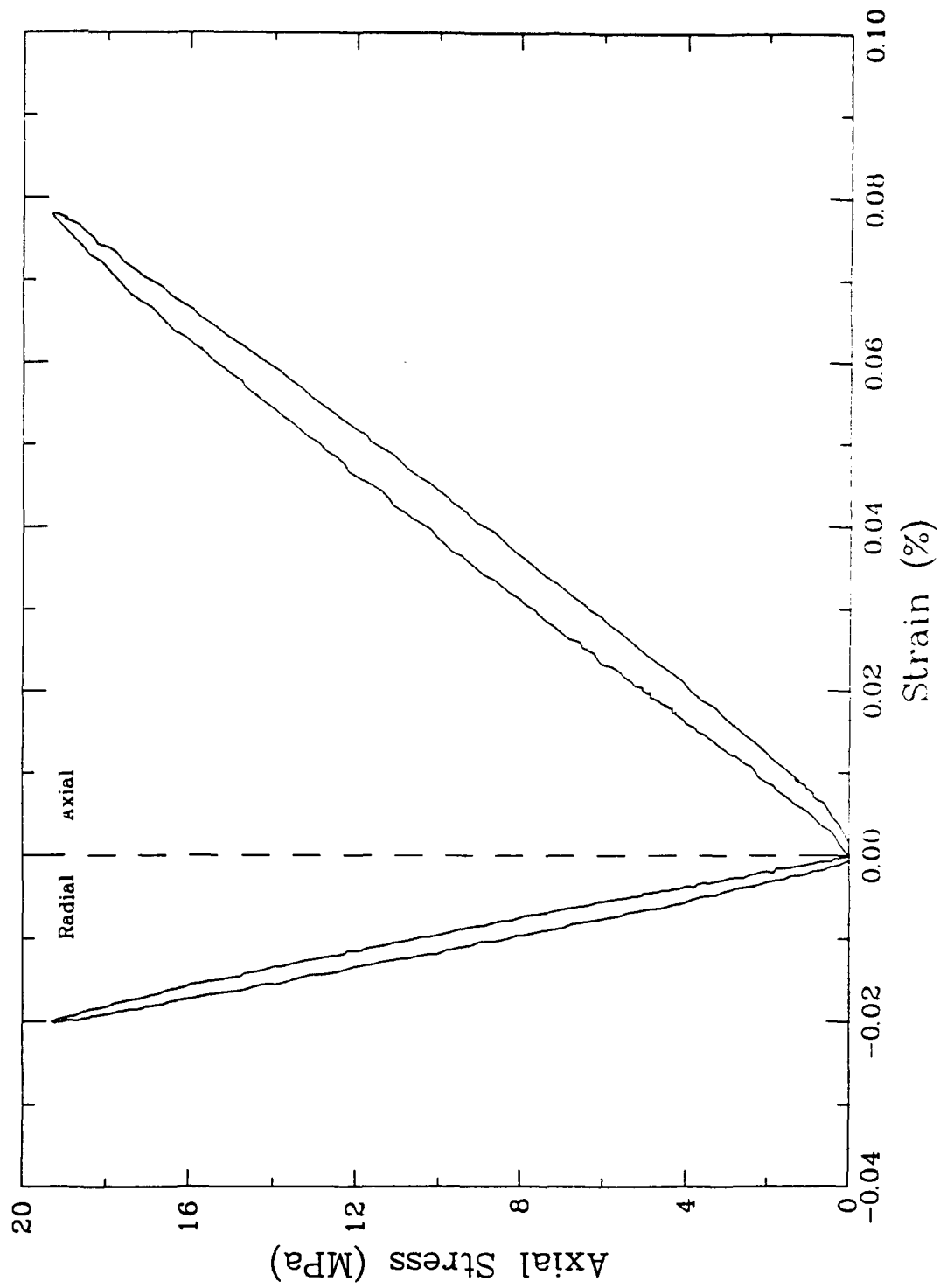
Figure 7.1. Unconfined compression test data for a specimen of the porous stainless steel that was used in the wave propagation bar tests.

Sintered Stainless Steel

Permeability Tests with Kerosene

Apparent Flow Velocity (in/s)

Pres. Gradient/App. Flow Velocity (lb-s/in⁴)

500 psi, 1gpm
500 psi, 2gpm
1000 psi, 2gpm
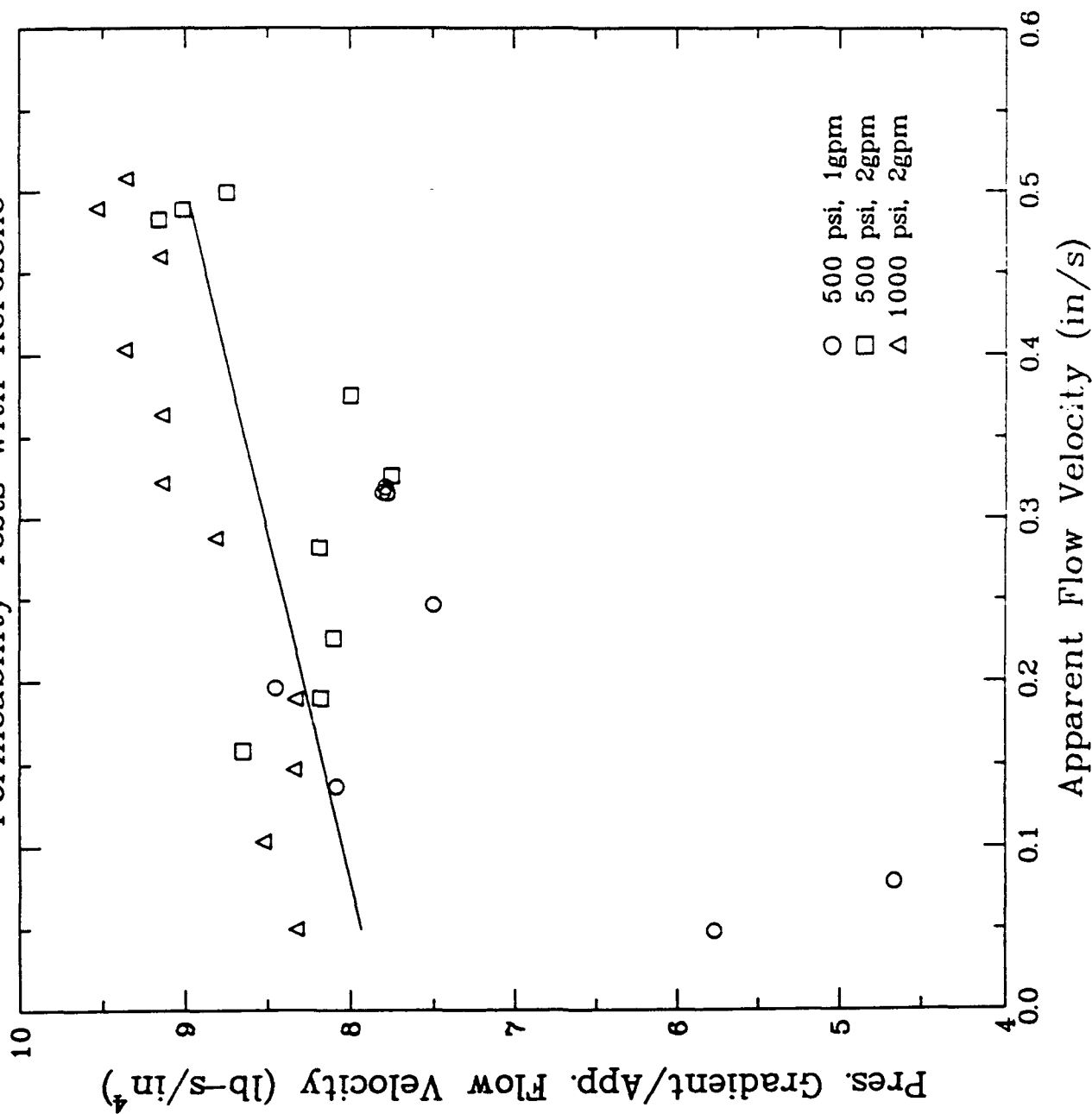
Figure 7.2. Permeability test results for a specimen of the porous stainless steel that was used in the wave propagation tests; intercept = a = 7.8 lb-s/in⁴; slope = b = 2.3 lb-s²/in⁵.

$n = 0.4200$ s.g.$_f$ = 0.810

$k = 0.00373$ s.g.$_s$ = 7.800

$r = 0$ $K_f = 0.1880E+06$

$r = 0$ $K_g = 0.1667E+08$

$\gamma_w = 0.03611$ $K_s = 0.2400E+07$

$g = 386.4$ $\nu = 0.250$
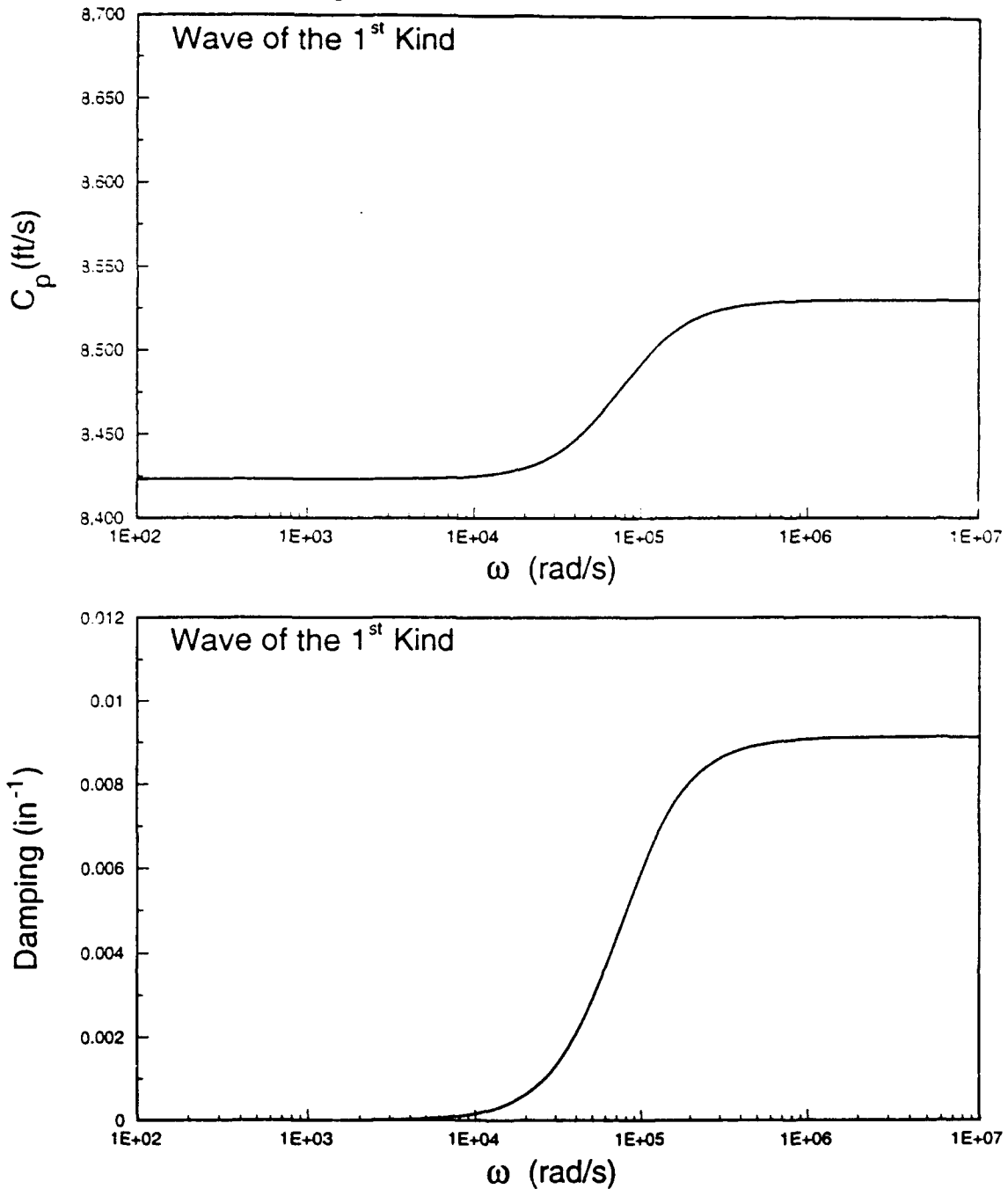
Figure 7.3a.   Speed and damping of the wave of the first kind as a function of excitation frequency computed with the program TWAVE using the measured properties of the porous stainless steel bar.

$$n = 0.4200 \qquad s.g._f = 0.810$$
$$k = 0.00373 \qquad s.g._s = 7.800$$
$$r = 0 \qquad K_f = 0.1880E+06$$
$$r = 0 \qquad K_g = 0.1667E+08$$
$$\gamma_w = 0.03611 \qquad K_s = 0.2400E+07$$
$$g = 386.4 \qquad \nu = 0.250$$
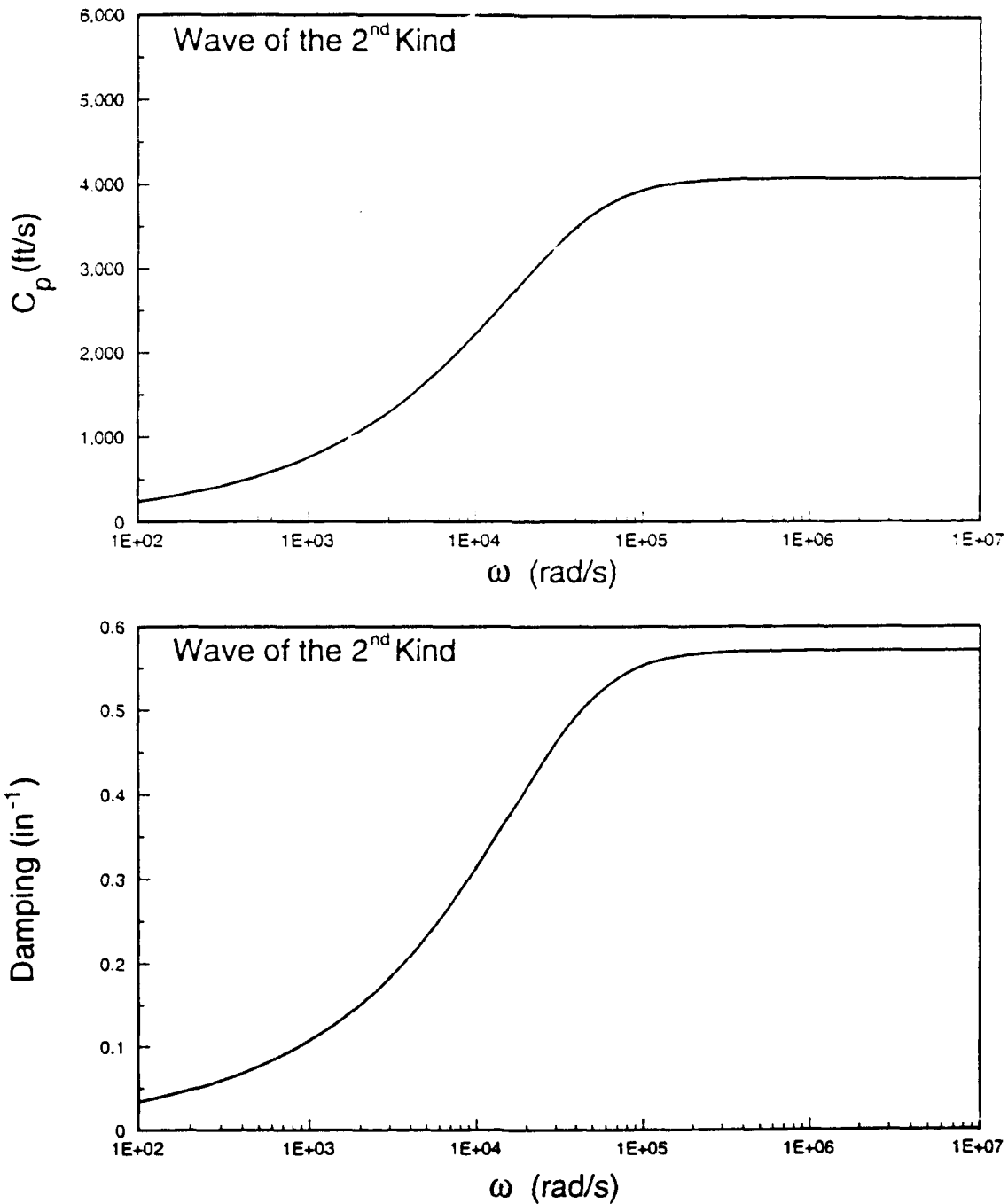
Figure 7.3b. Speed and damping of the wave of the second kind as a function of excitation frequency computed with the program TWAVE using the measured properties of the porous stainless steel bar.
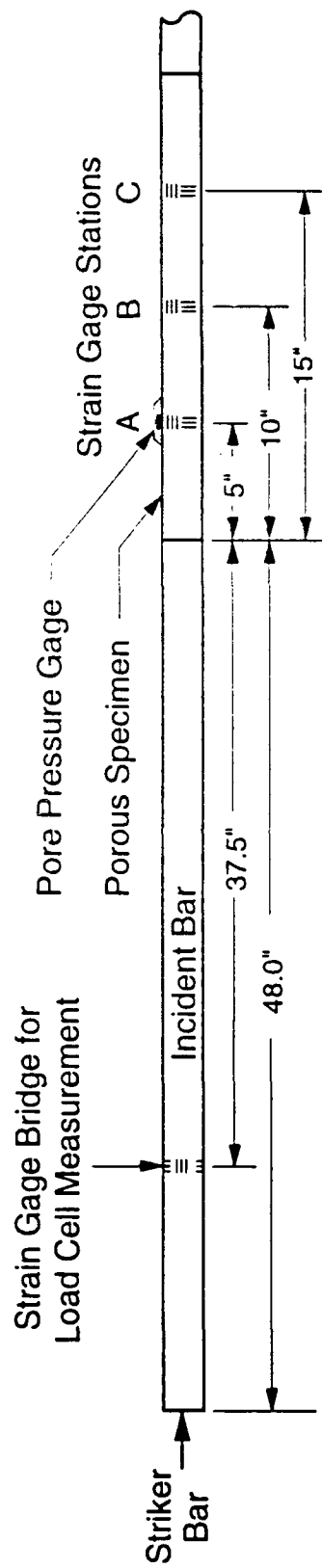
Figure 7.4. Instrument locations on porous specimen and incident bar.
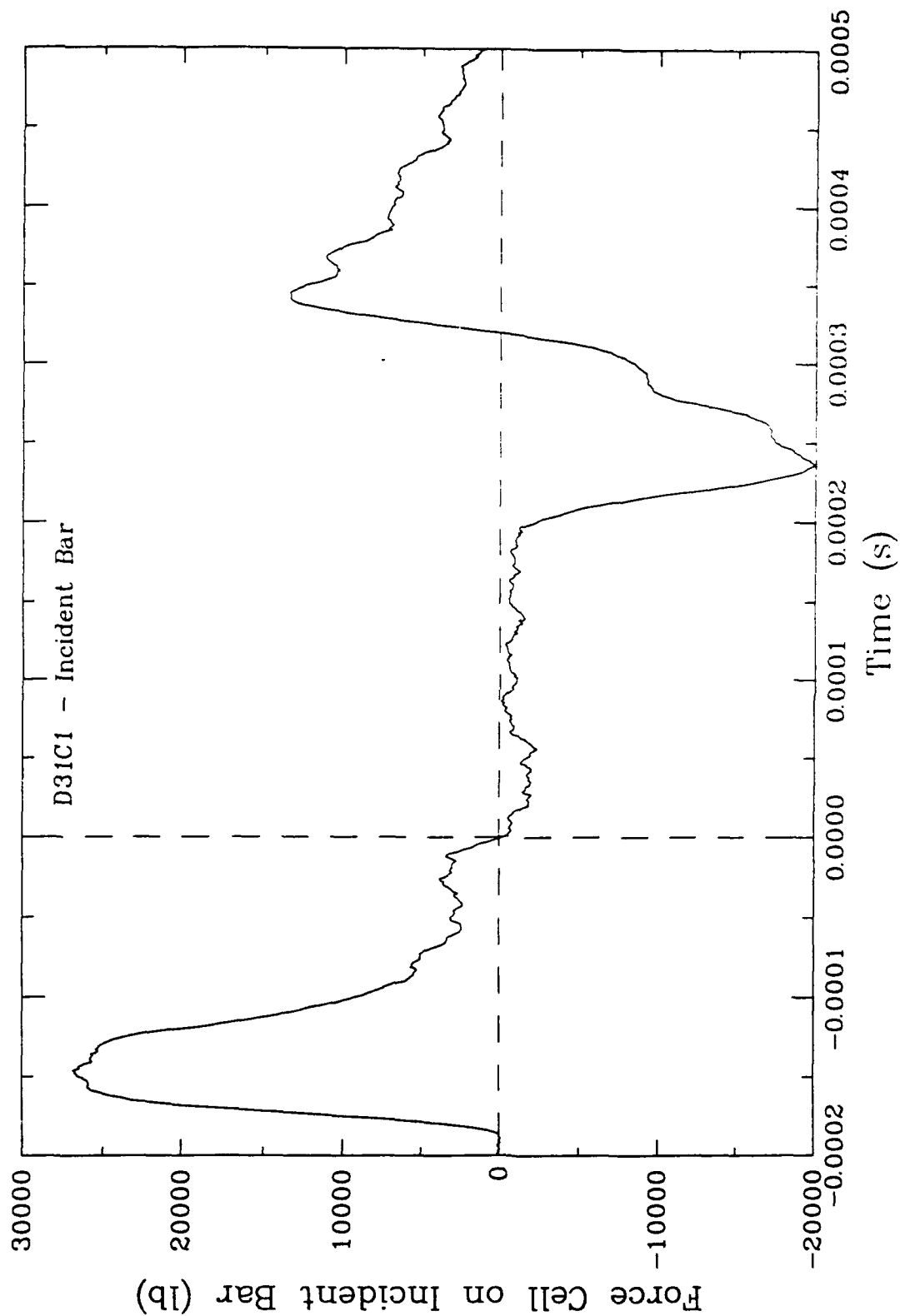
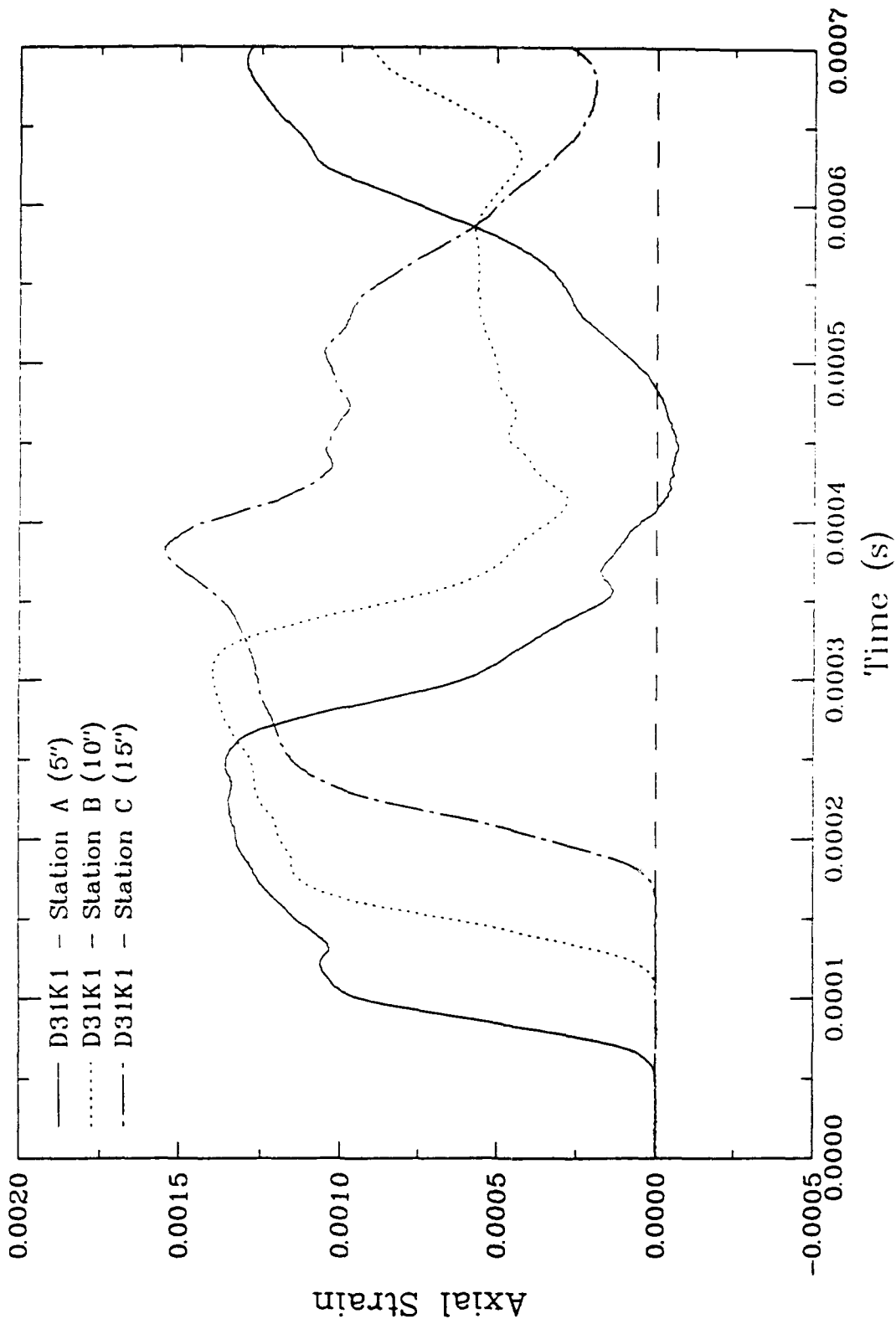**Figure 7.5a.** Input force data from a WPB test on dry porous stainless steel with a 5-inch striker bar.

7-24
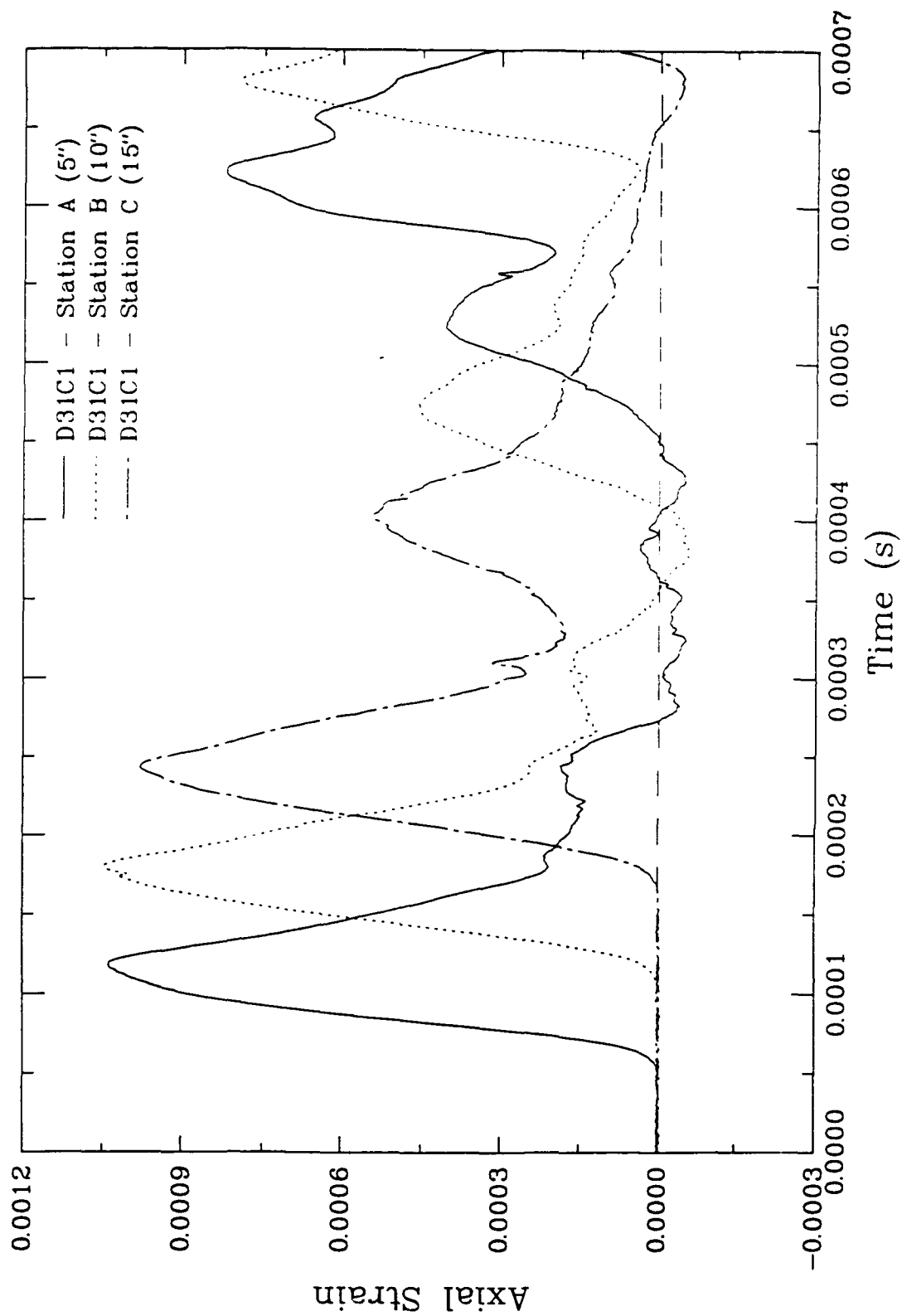
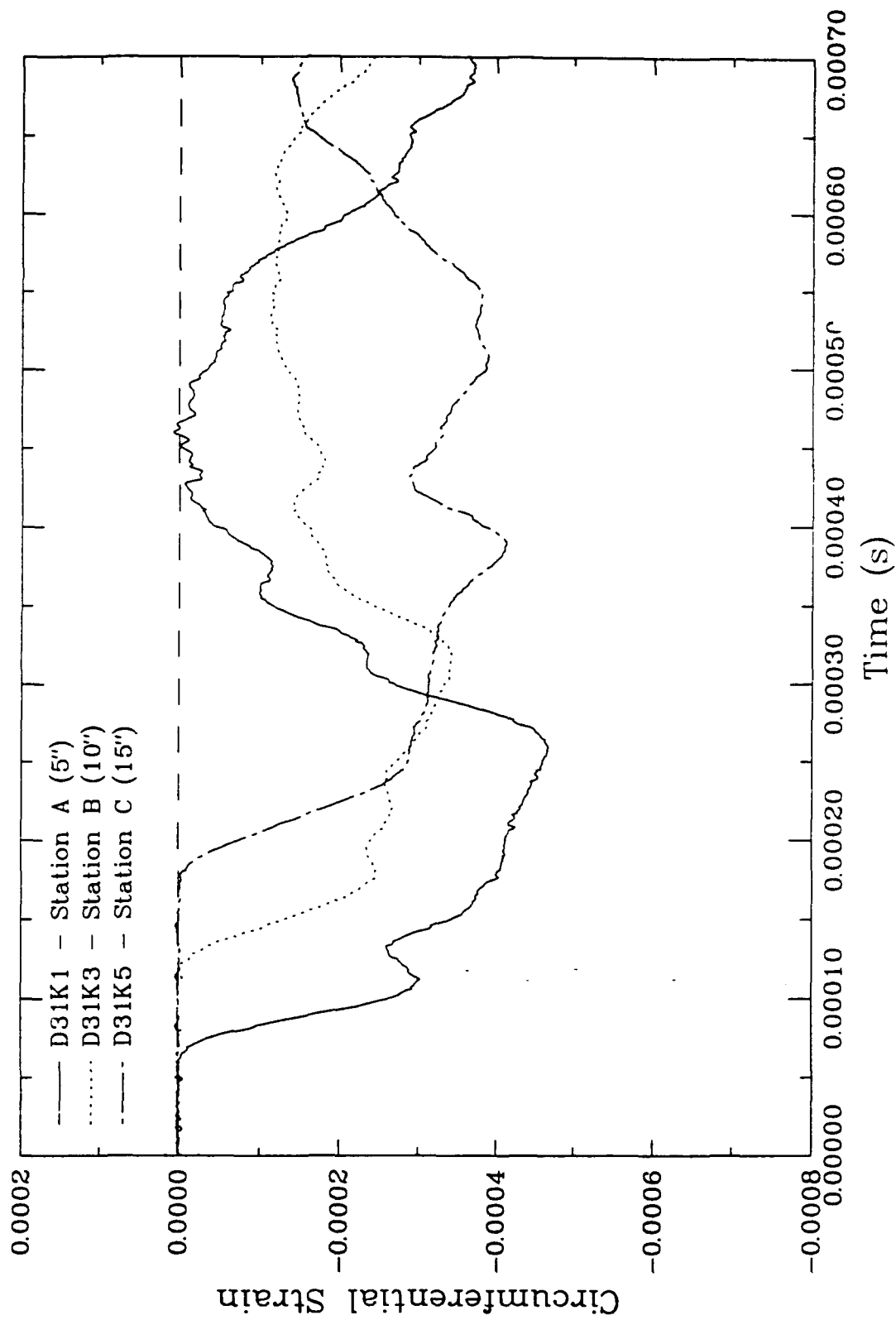Figure 7.5b. Axial strain data from a WPB test on dry porous stainless steel with a 5-inch striker bar.
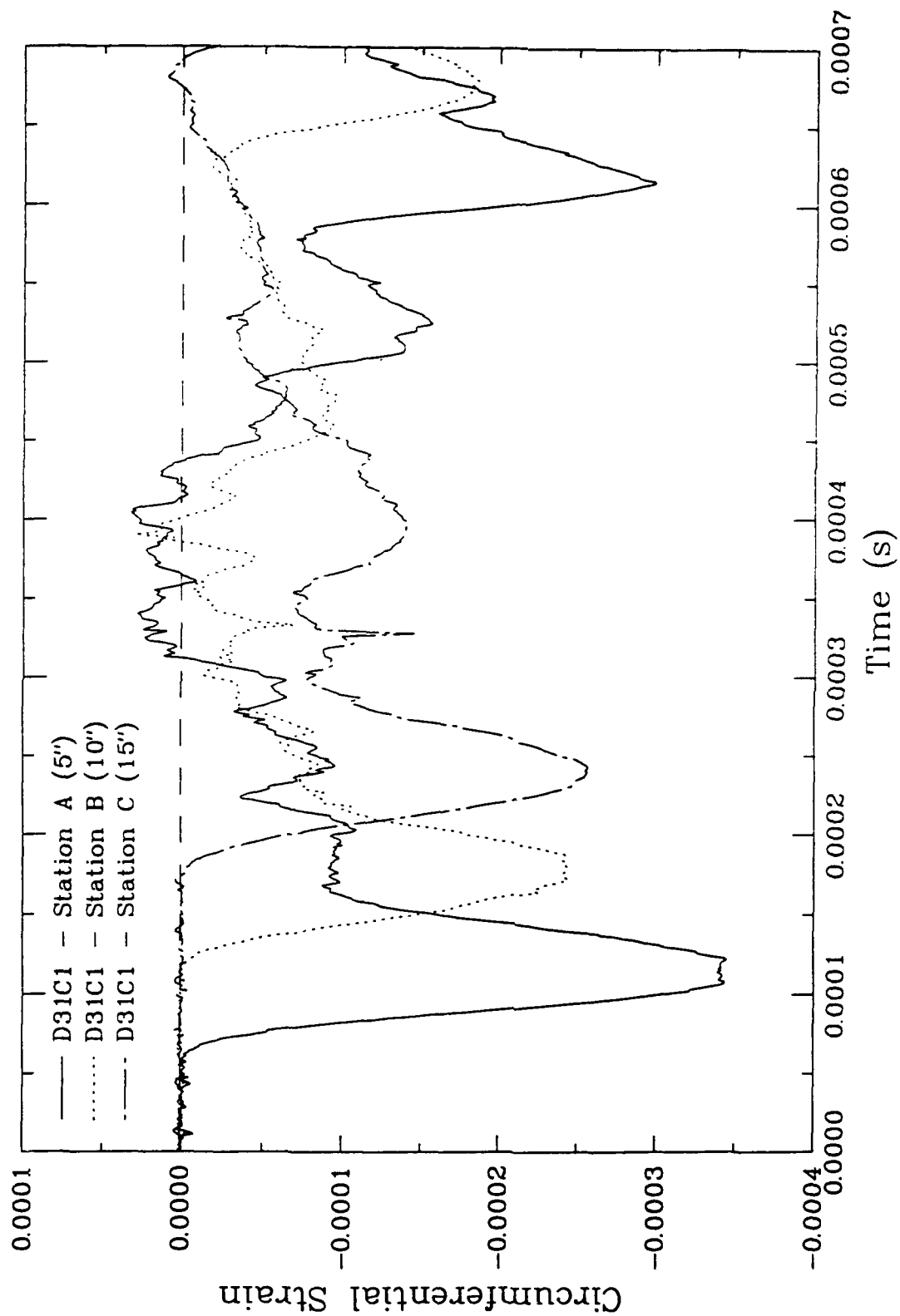
Figure 7.5c. Circumferential strain data from a WPB test on dry porous stainless steel with a 5-inch striker bar.

7-26
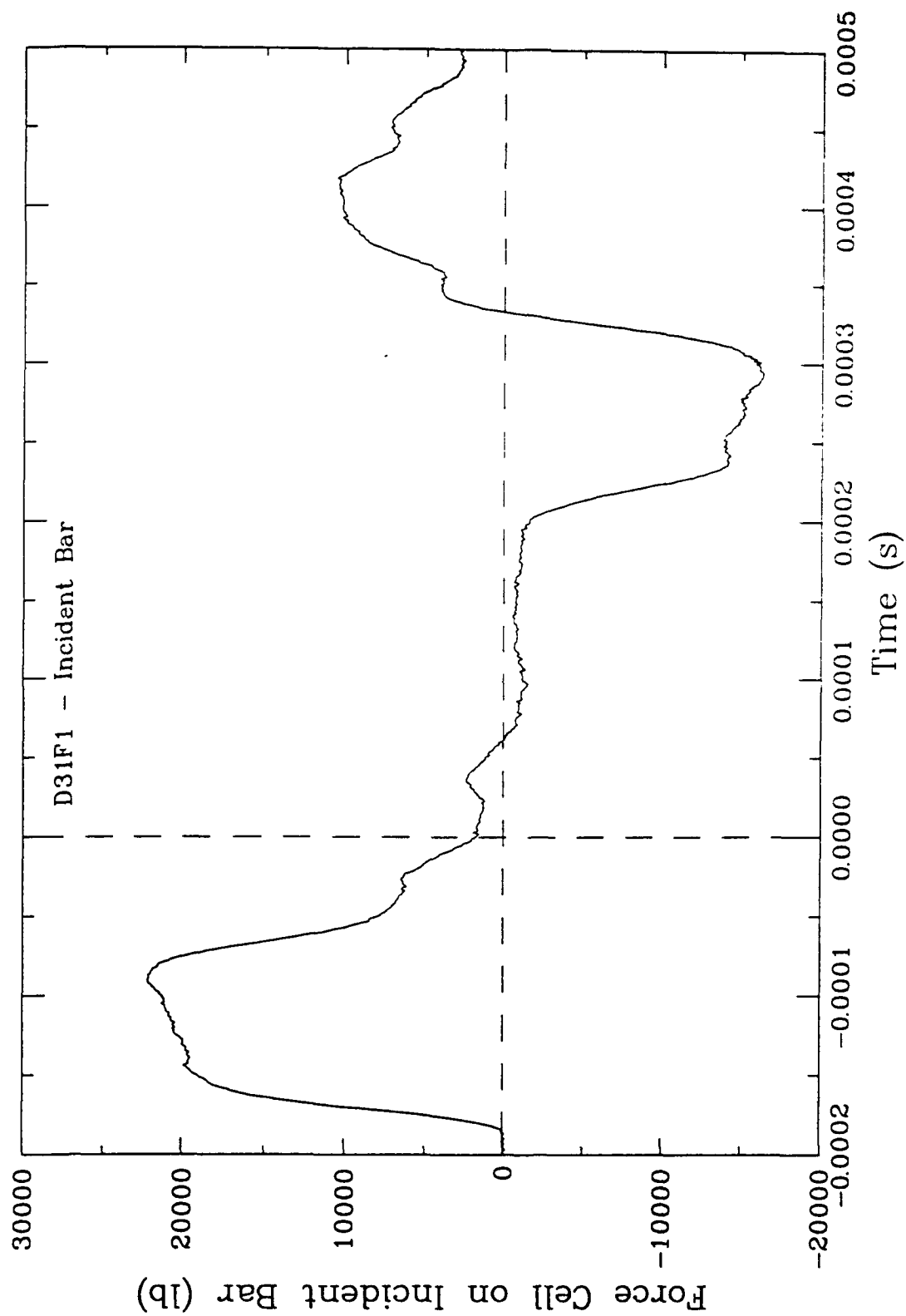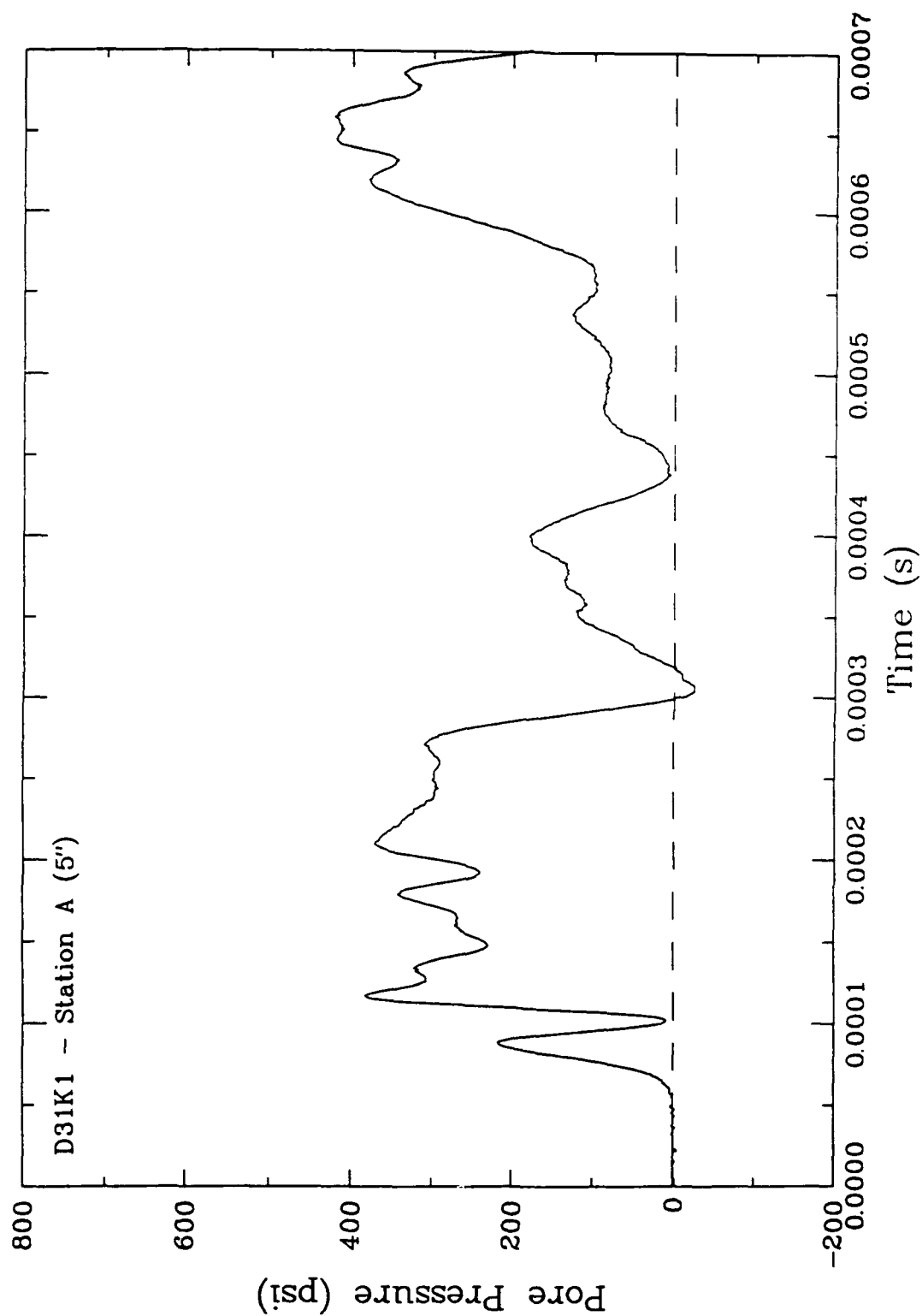
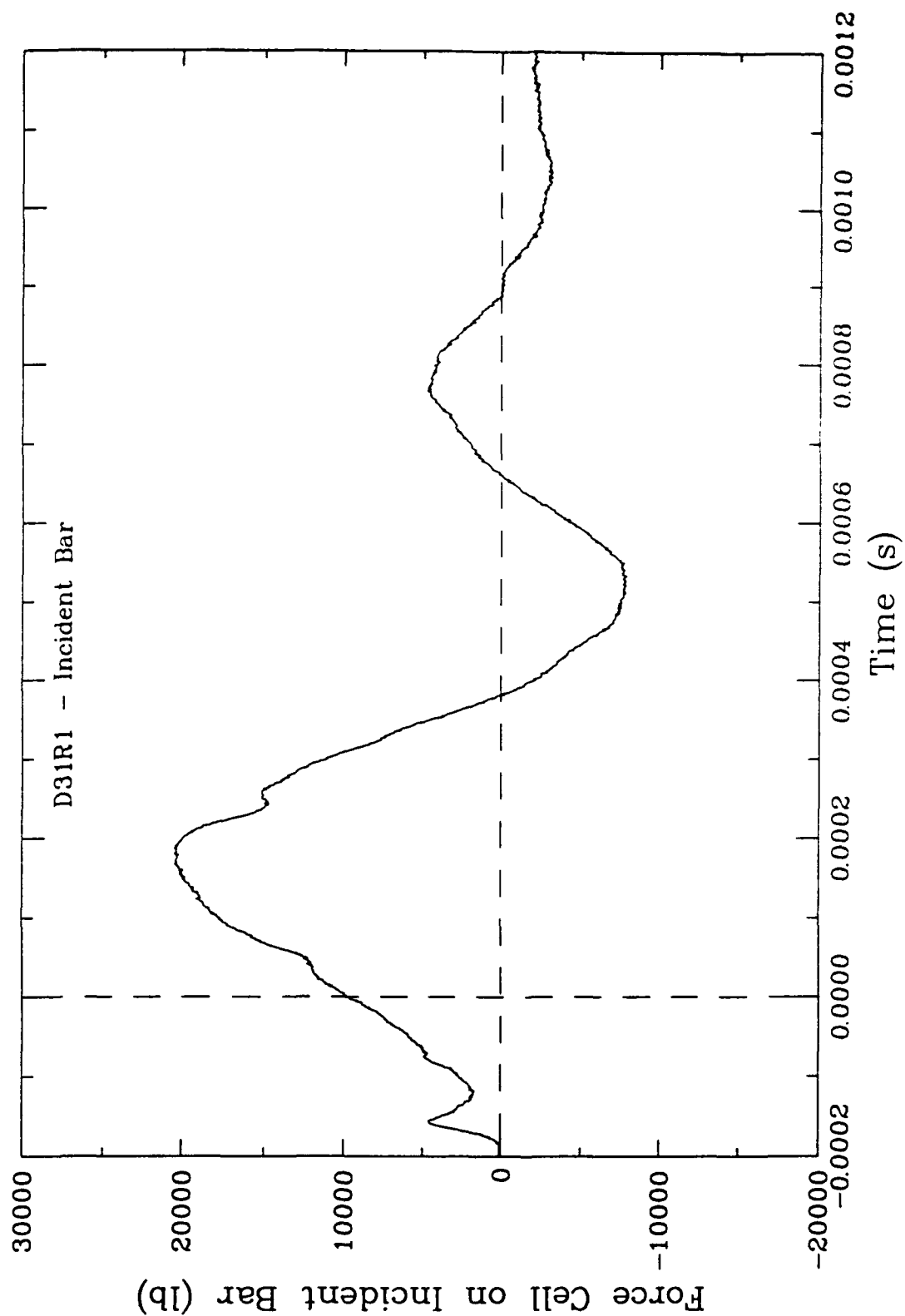Figure 7.6a. Input force data from a WPB test on dry porous stainless steel with a 10-inch striker bar.
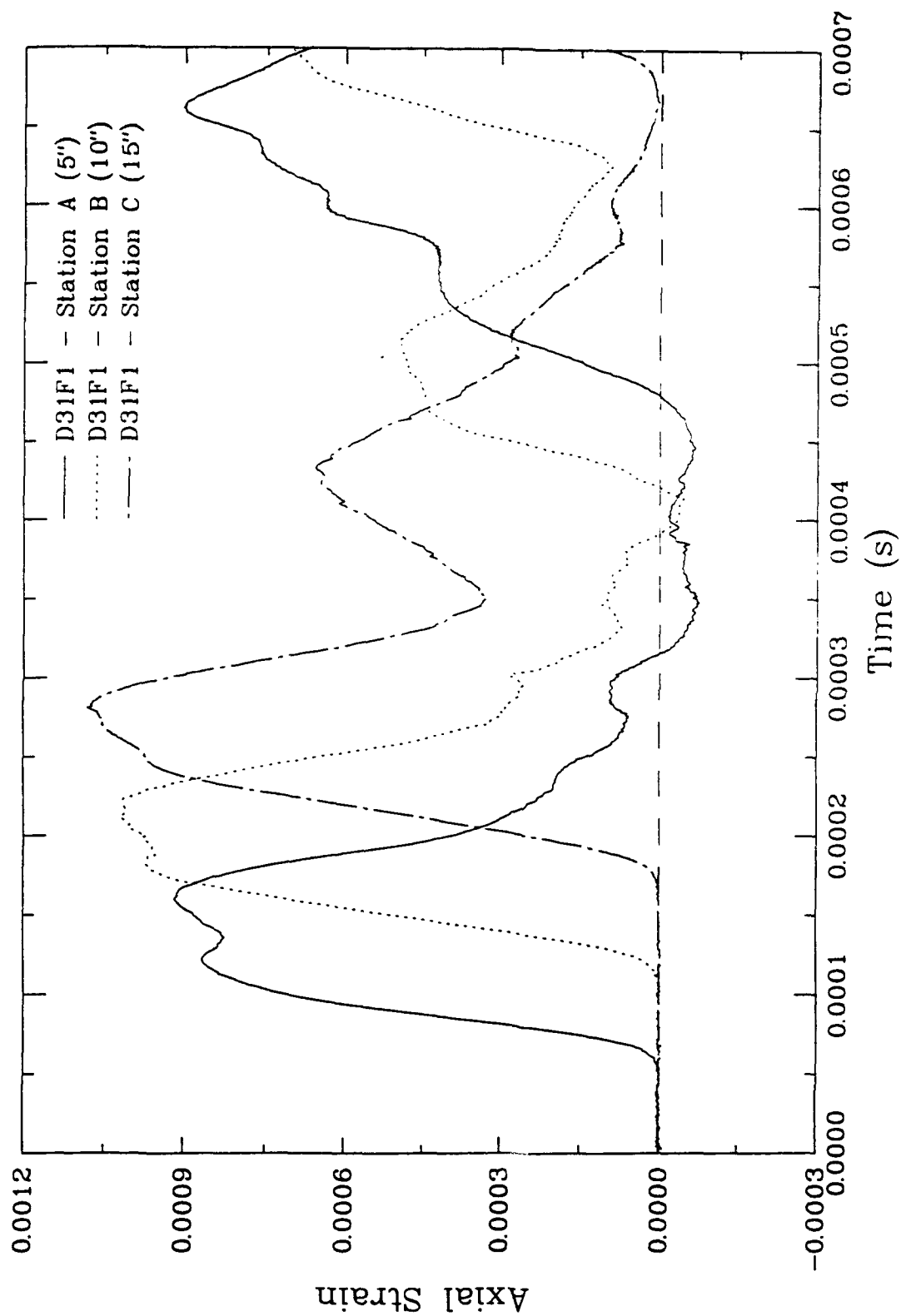
Figure 7.6b. Axial strain data from a WPB test on dry porous stainless steel with a 10-inch striker bar.
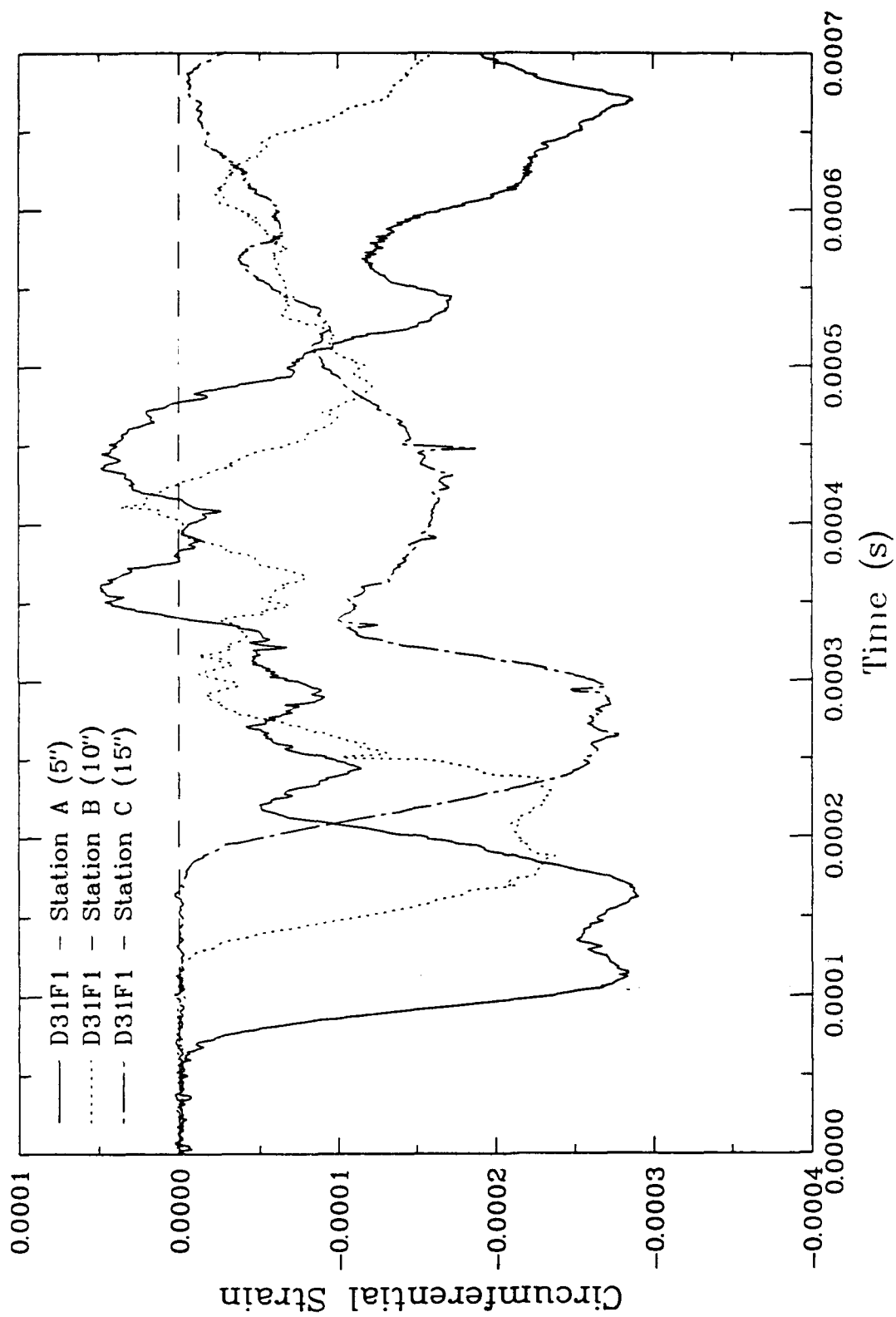
Figure 7.6c. Circumferential strain data from a WPB test on dry porous stainless steel with a 10-inch striker bar.
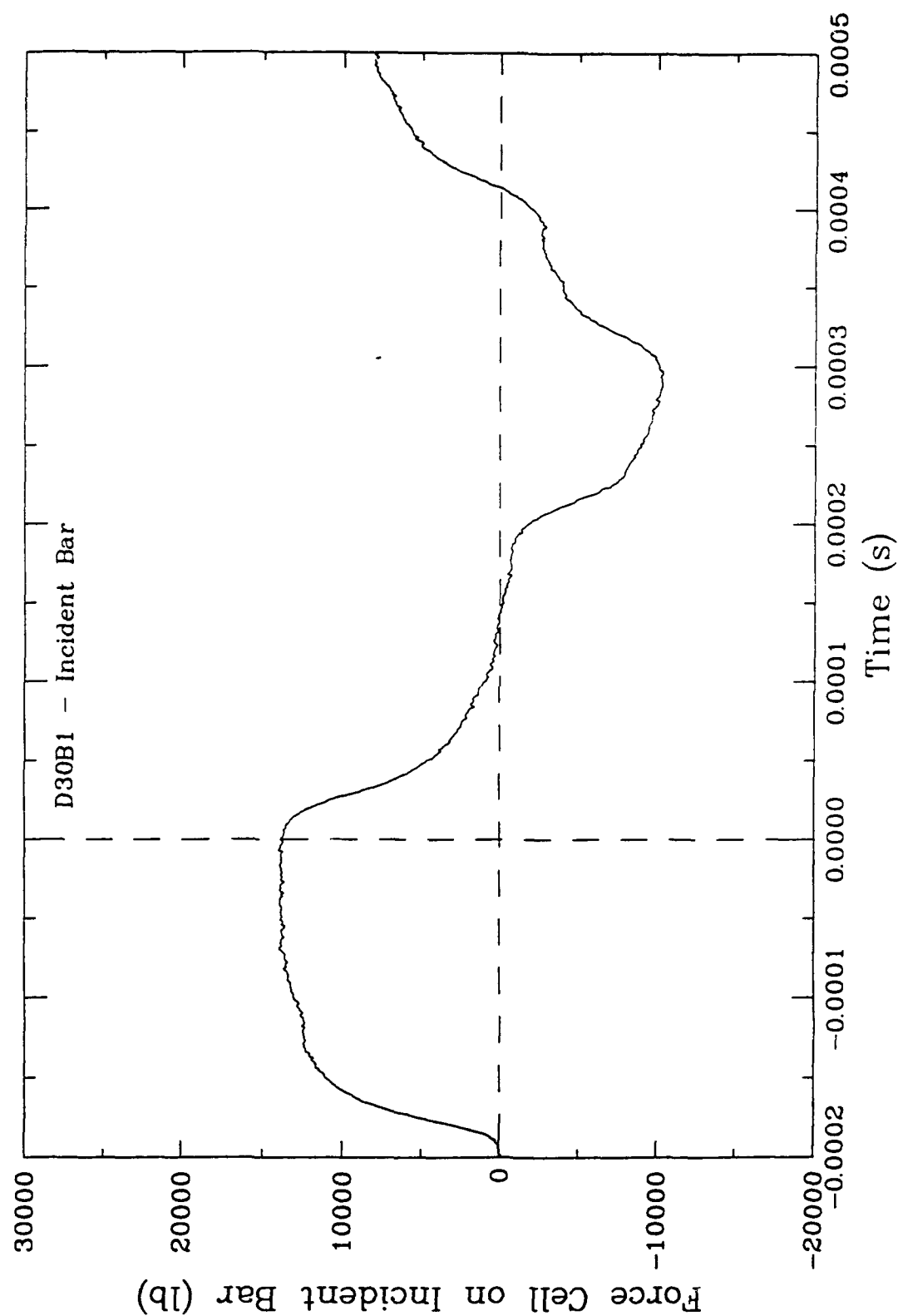
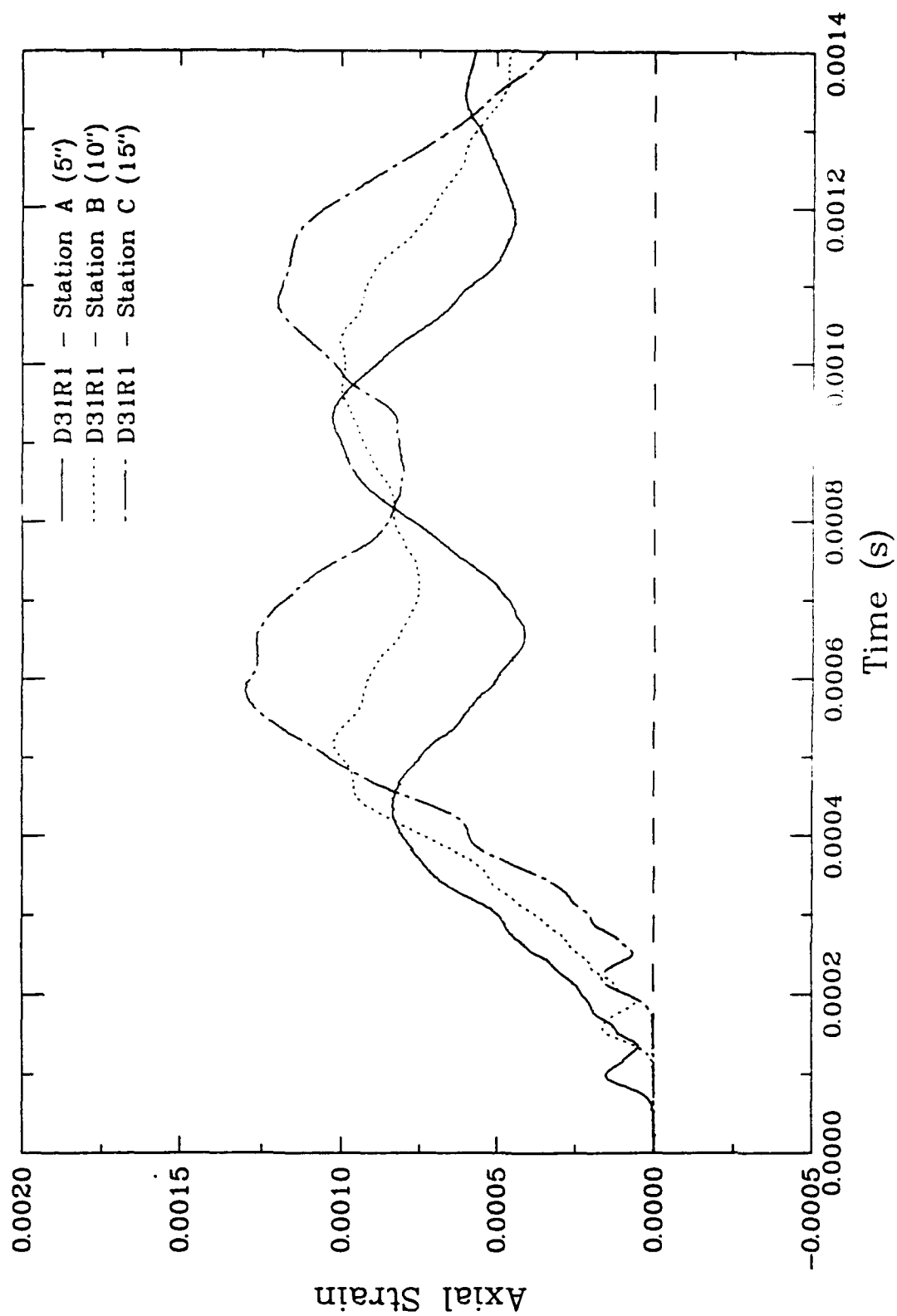Figure 7.7a. Input force data from a WPB test on dry porous stainless steel with a 20-inch striker bar.
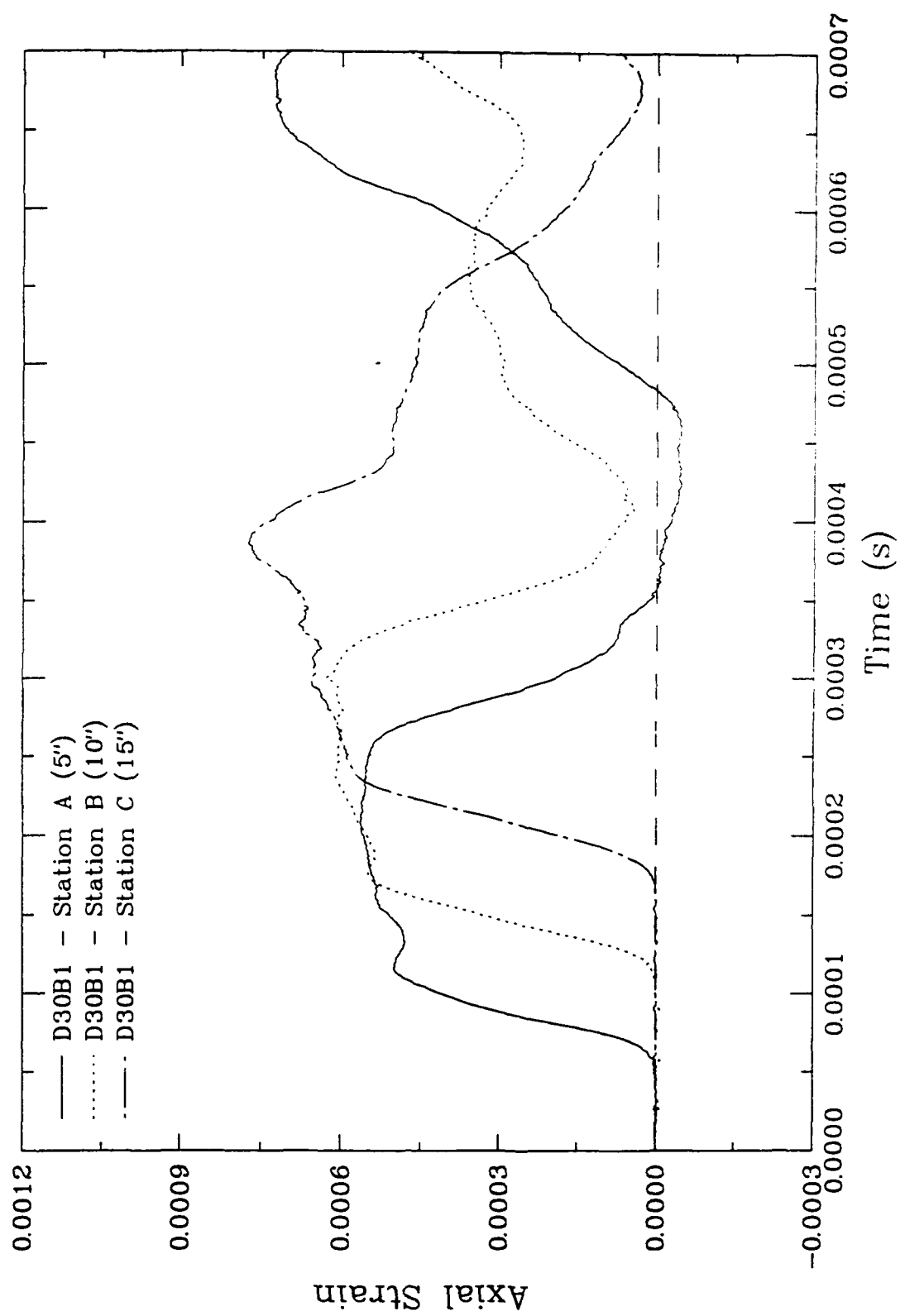
Figure 7.7b. Axial strain data from a WPB test on dry porous stainless steel with a 20-inch striker bar.
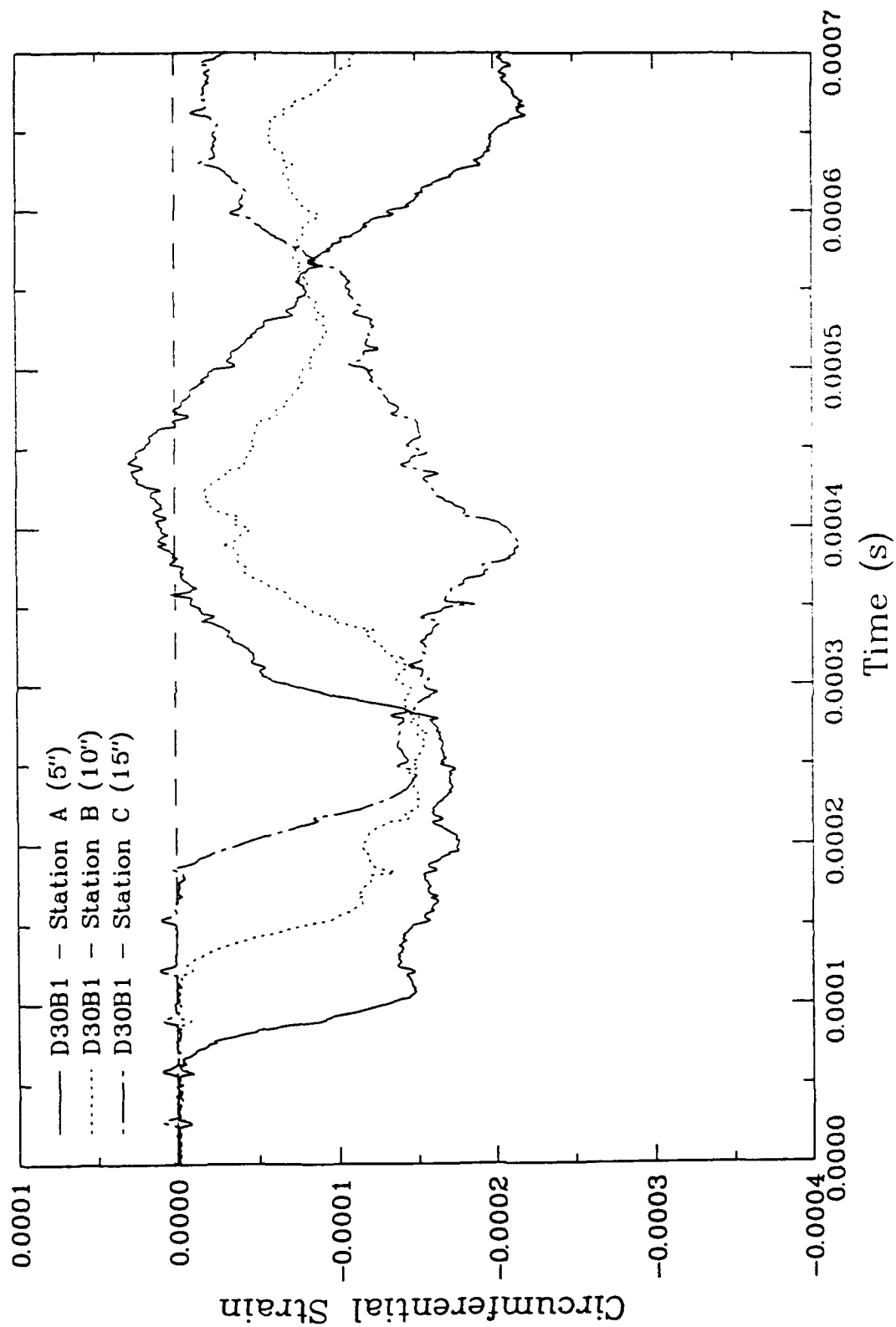
Figure 7.7c. Circumferential strain data from a WPB test on dry porous stainless steel with a 20-inch striker bar.

7-32
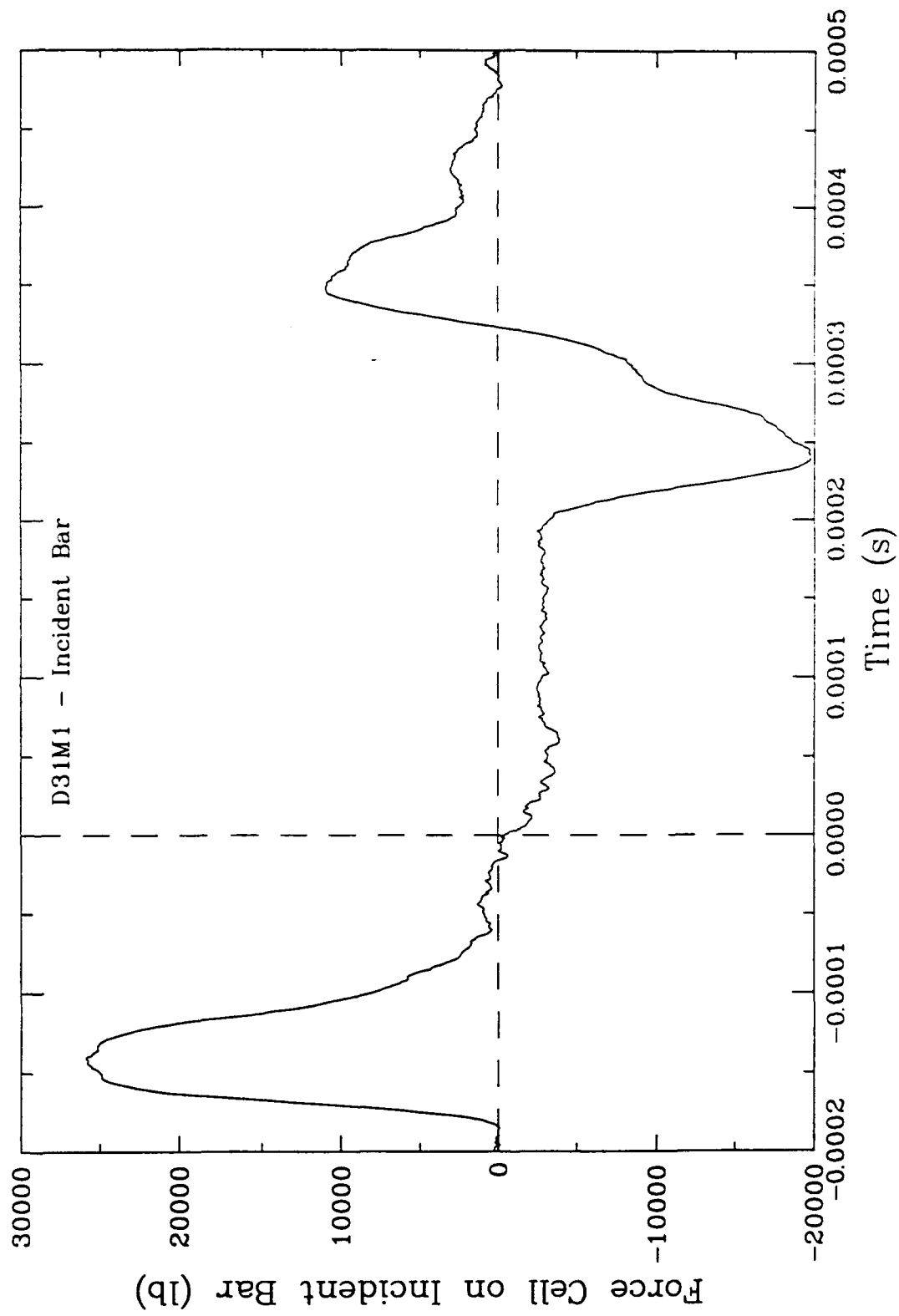
Figure 7.8a. Input force data from a WPB test on saturated porous stainless steel with a 5-inch striker bar.
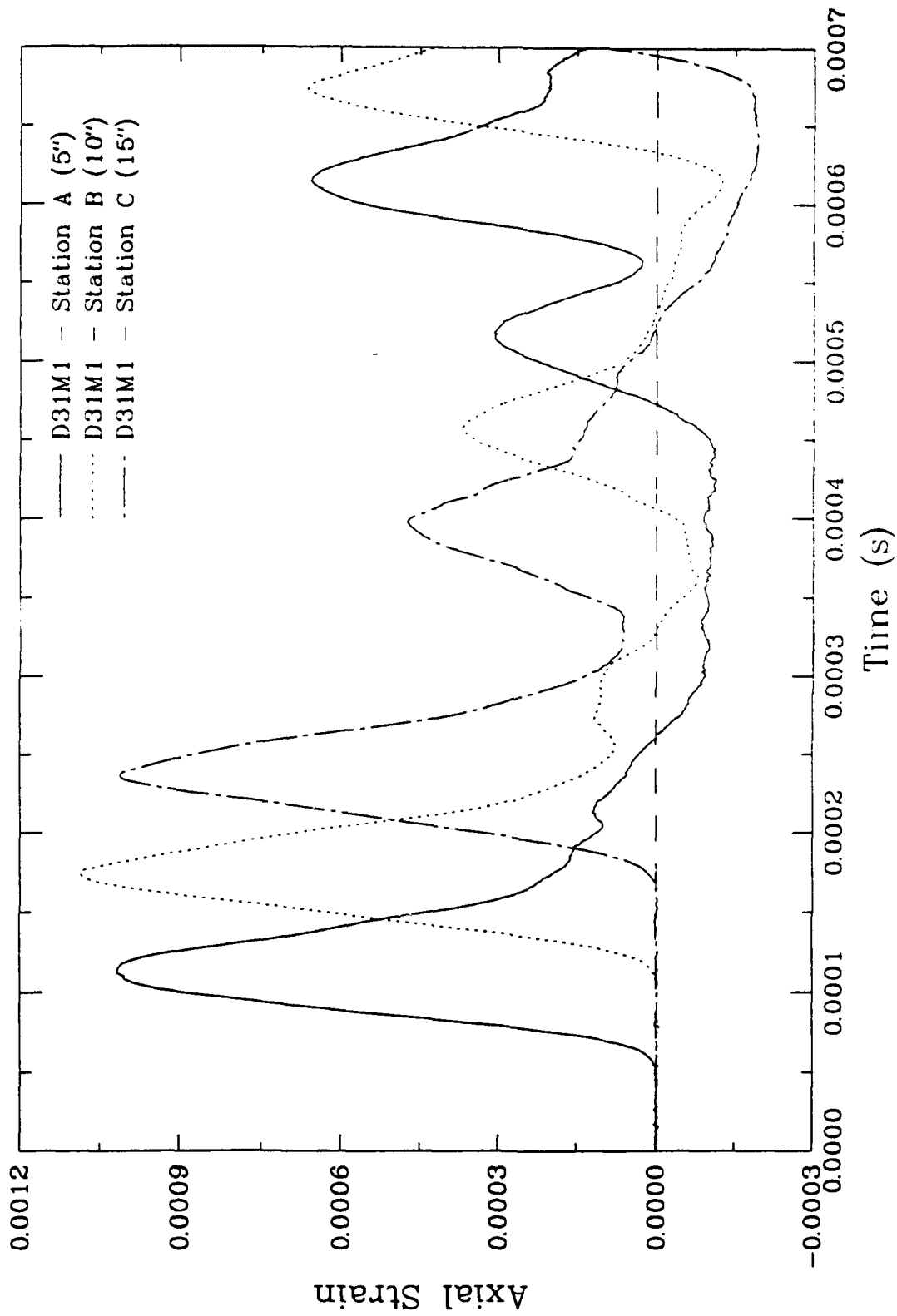
Figure 7.8b. Axial strain data from a WPB test on saturated porous stainless steel with a 5-inch striker bar.

7-34
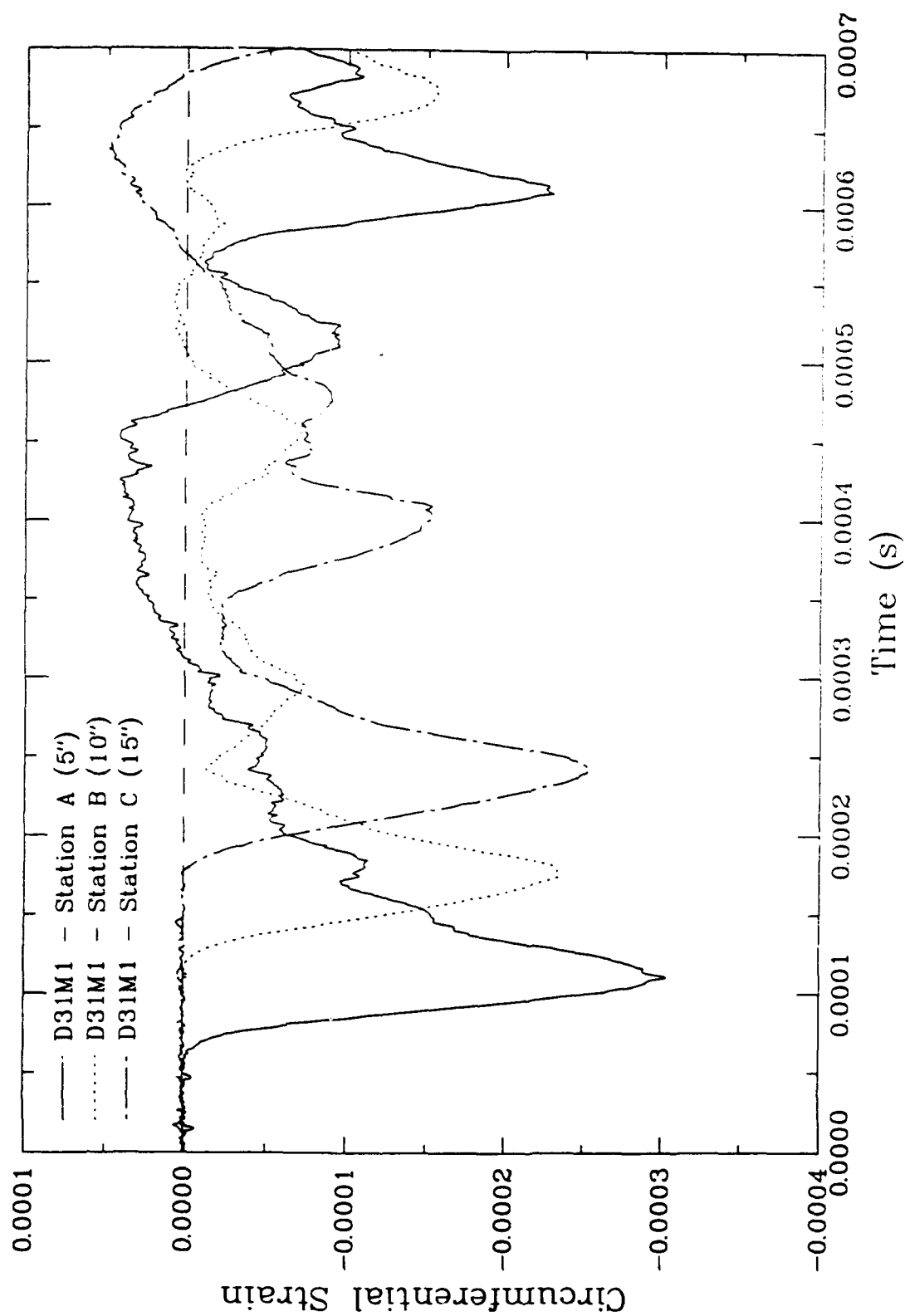
Figure 7.8c. Circumferential strain data from a WPB test on saturated porous stainless steel with a 5-inch striker bar.
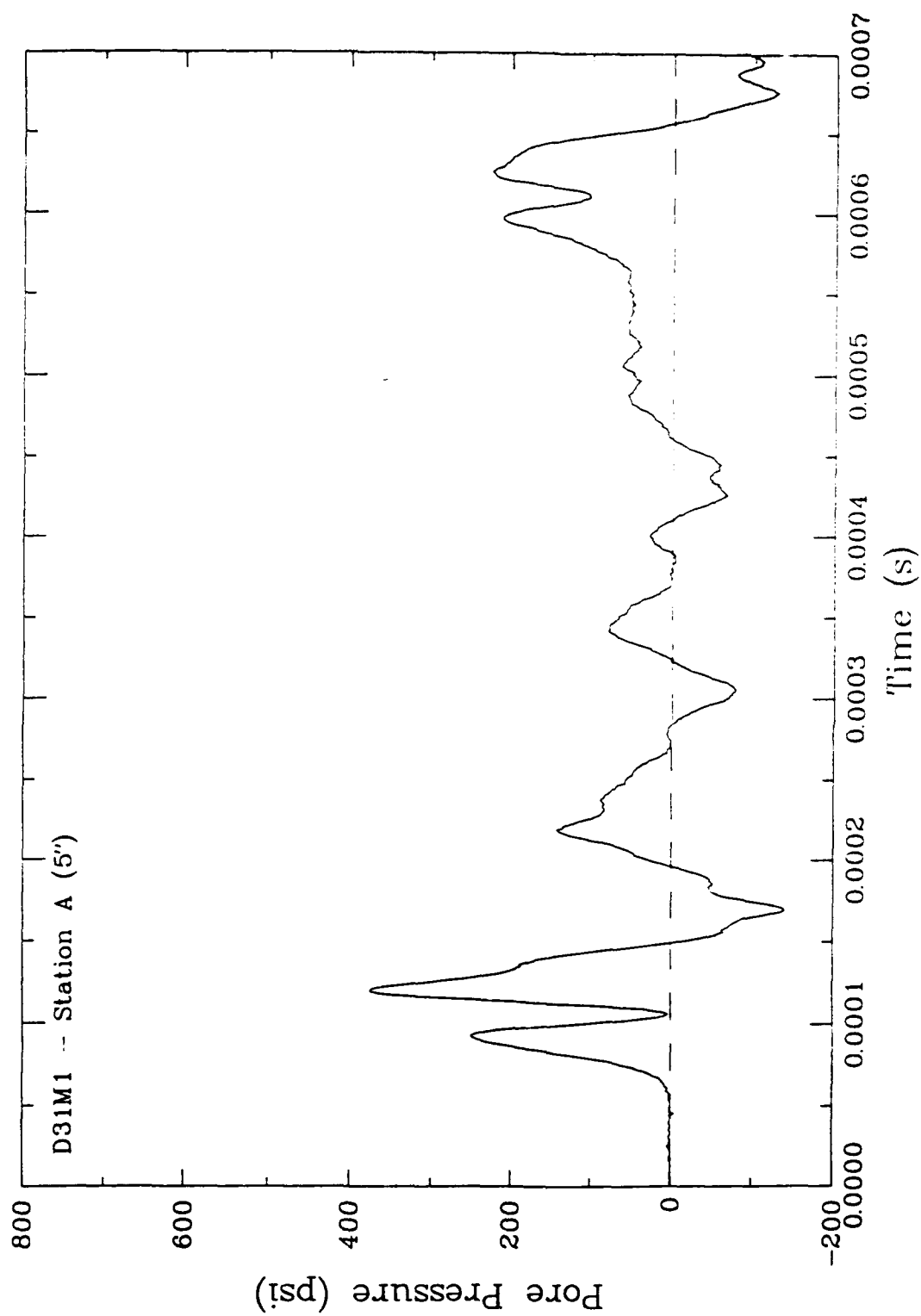
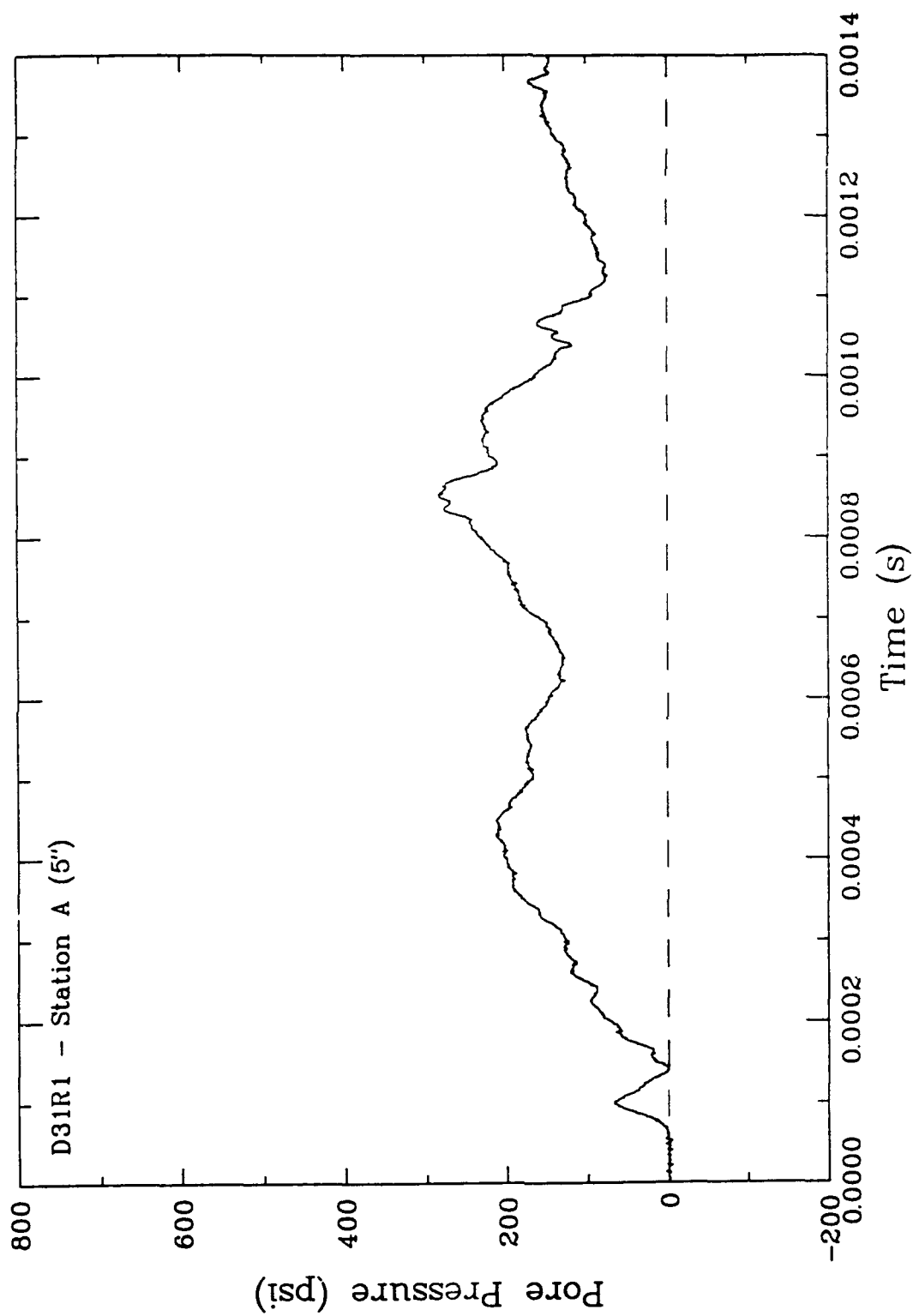**Figure 7.8d.** Pore pressure data from a WPB test on saturated porous stainless steel with a 5-inch striker bar.
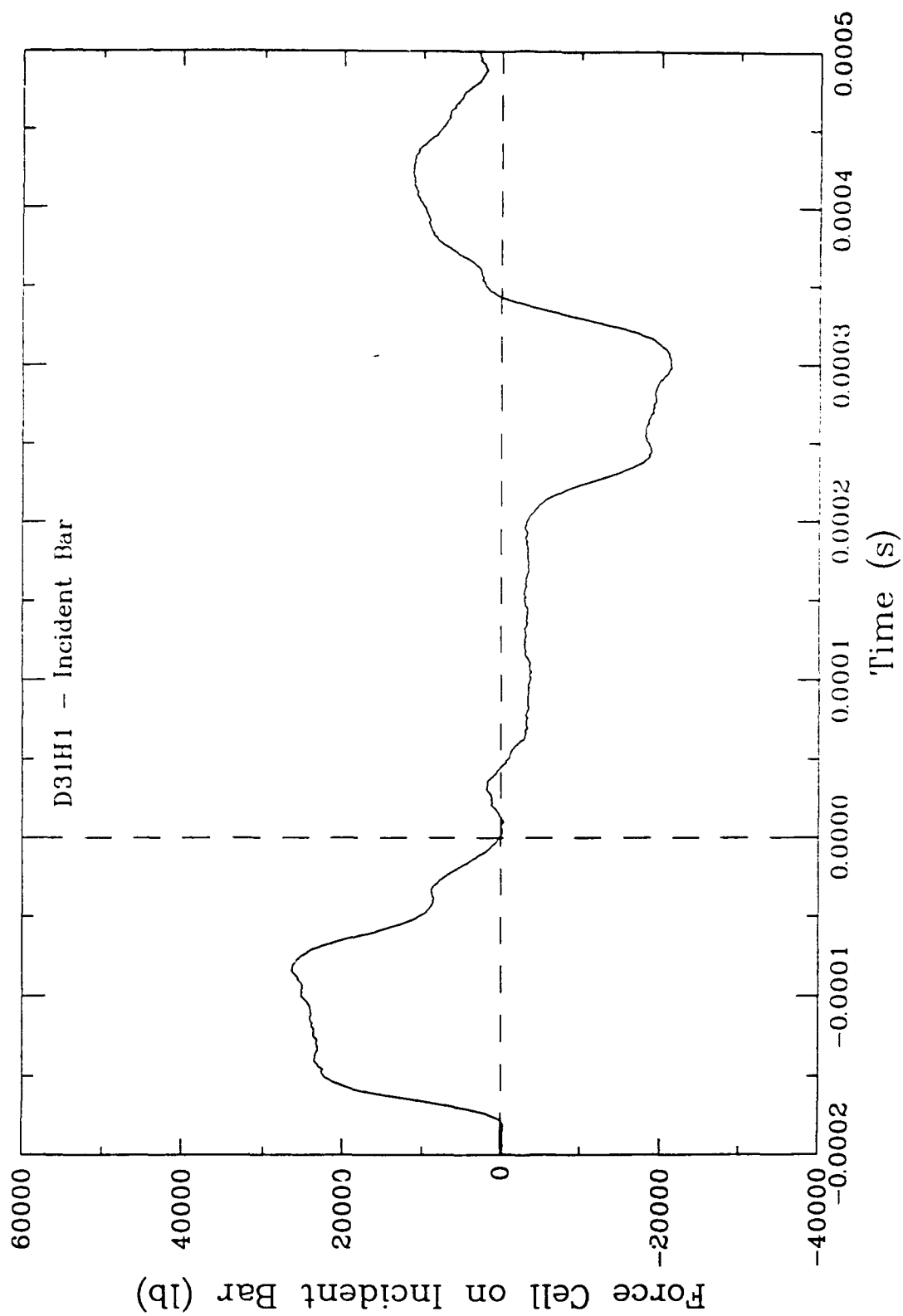
Figure 7.9a. Input force data from a WPB test on saturated porous stainless steel with a 10-inch striker bar.
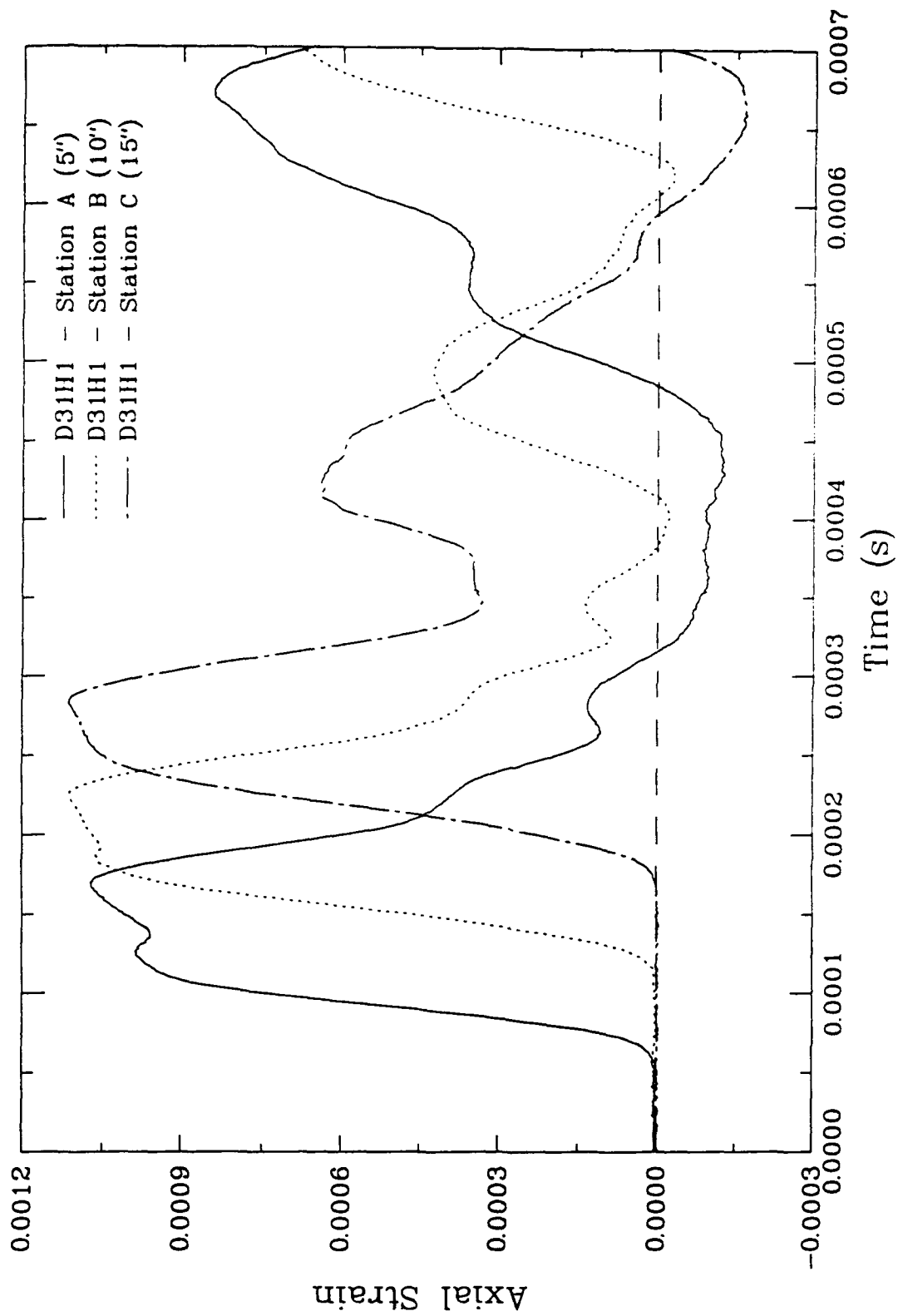
Figure 7.9b. Axial strain data from a WPB test on saturated porous stainless steel with a 10-inch striker bar.
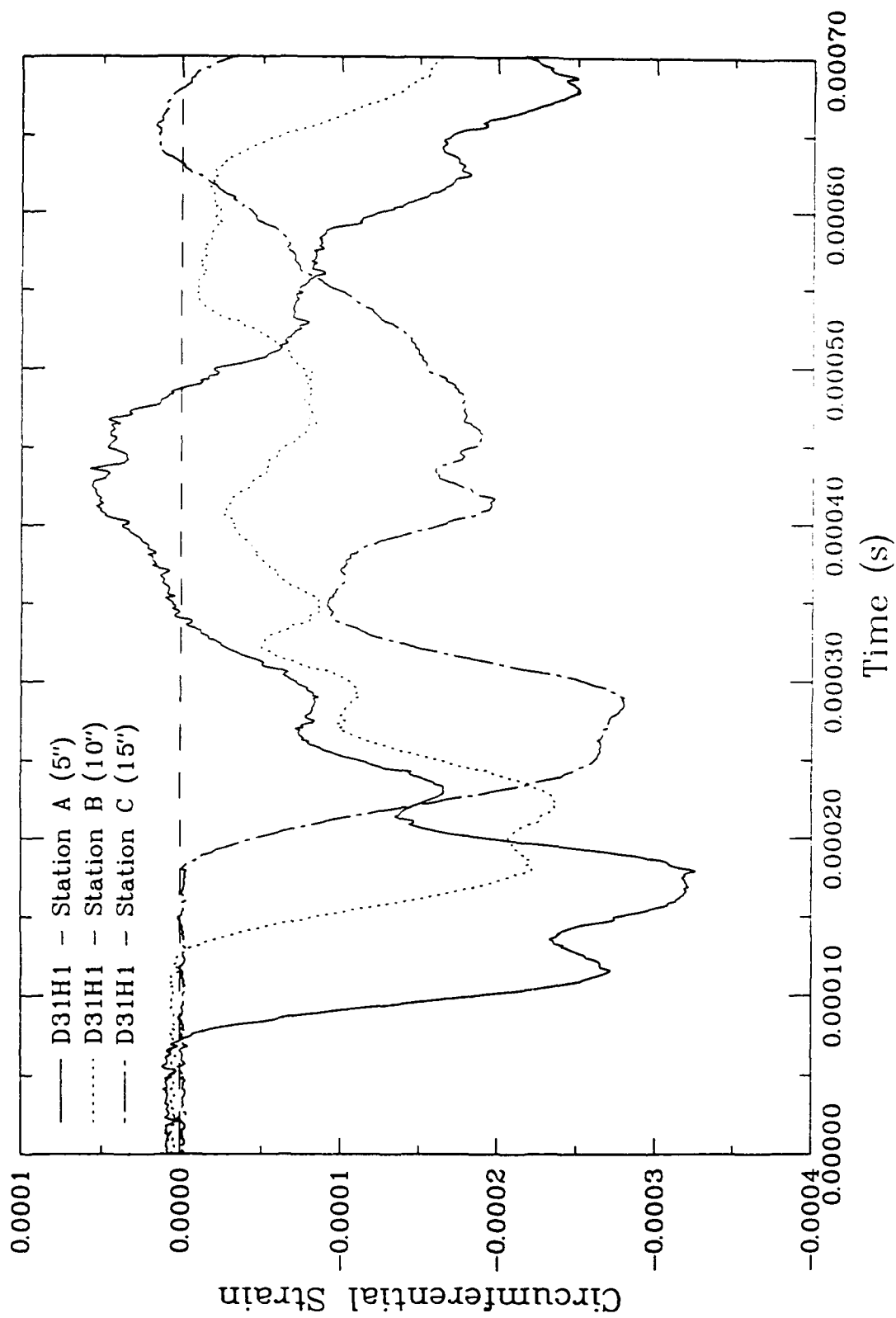
Figure 7.9c. Circumferential strain data from a WPB test on saturated porous stainless steel with a 10-inch striker bar.
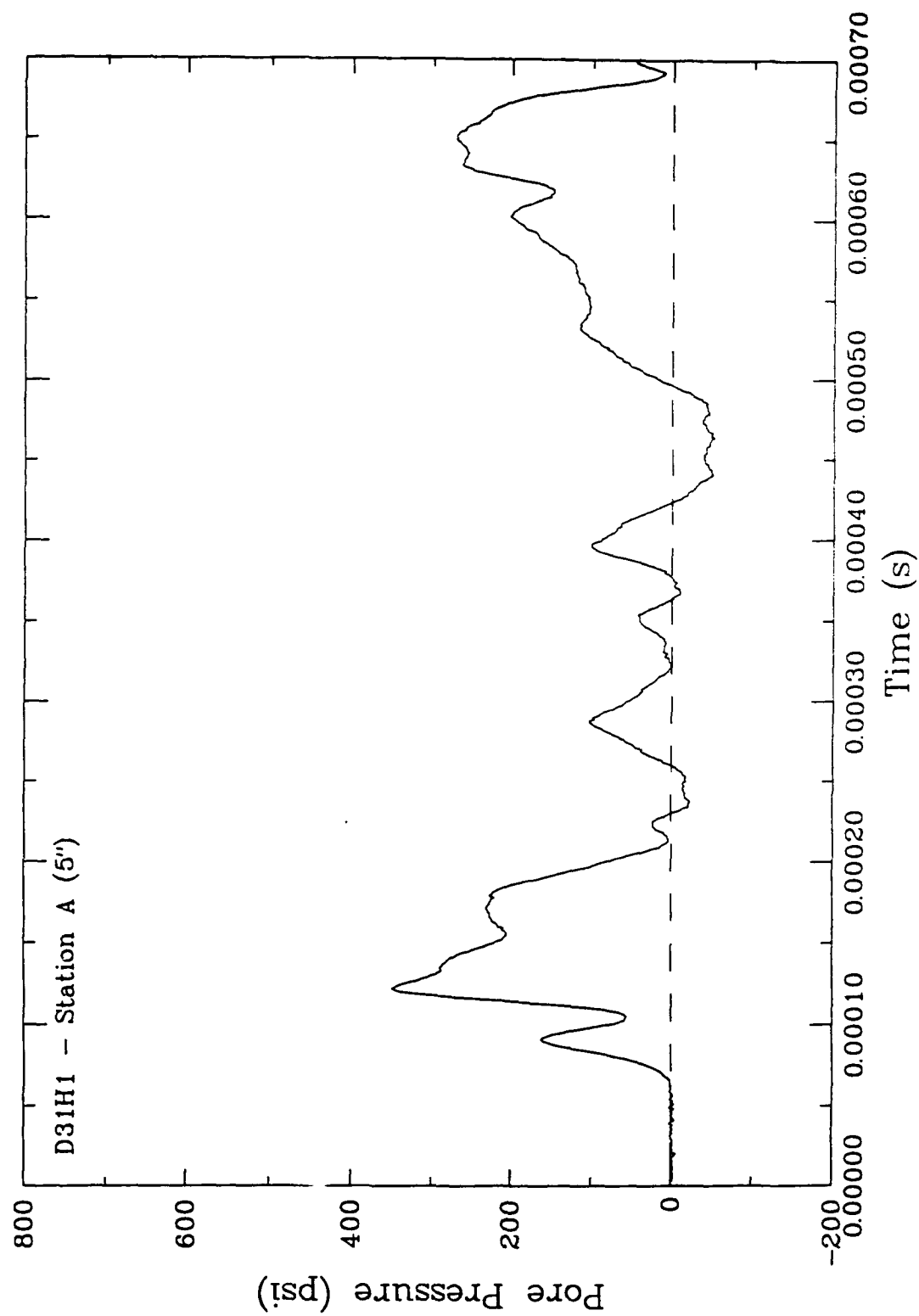
Figure 7.9d. Pore pressure data from a WPB test on saturated porous stainless steel with a 10-inch striker bar.
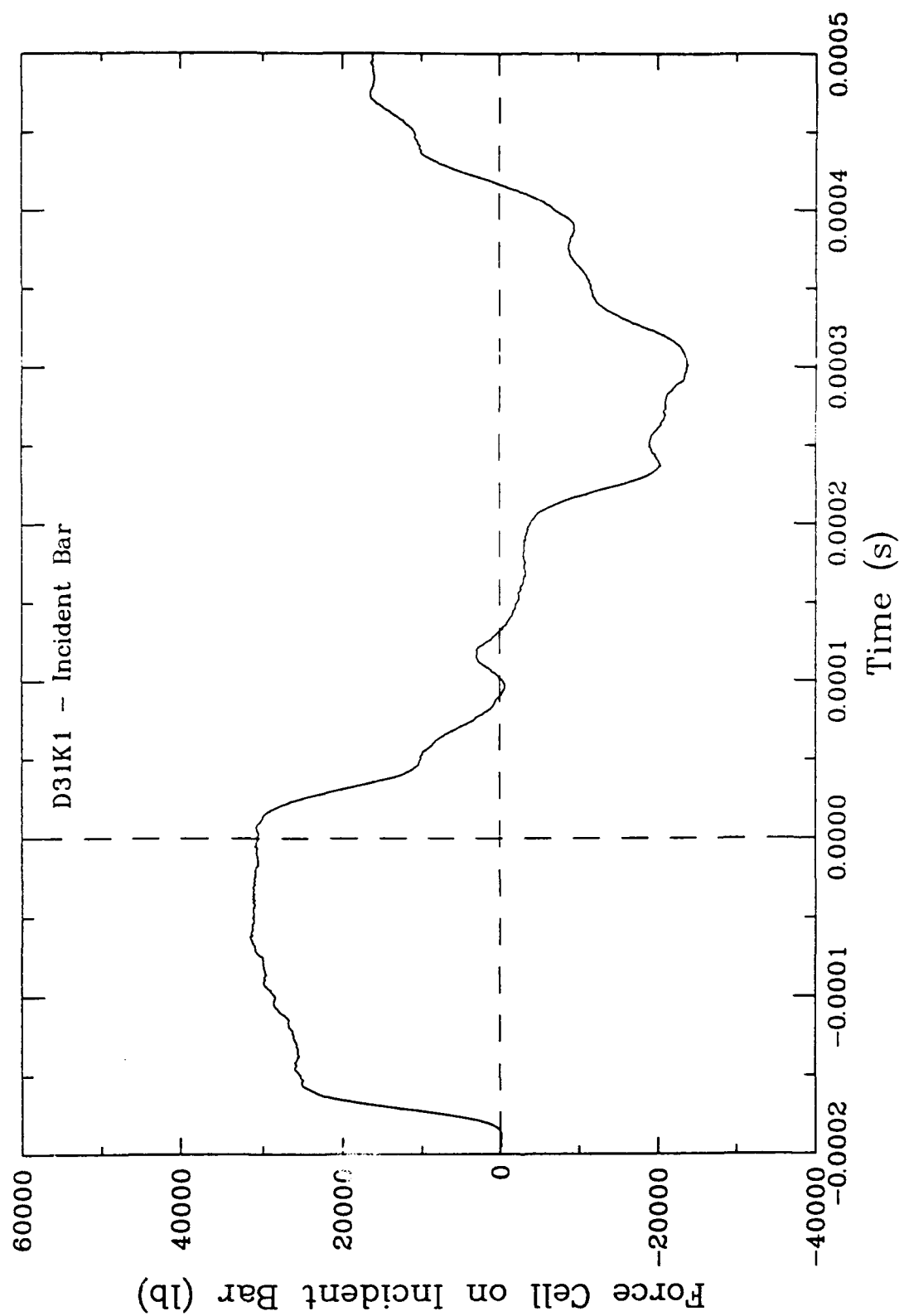
Figure 7.10a. Input force data from a WPB test on saturated porous stainless steel with a 20-inch striker bar.

7-41

Figure 7.10b. Axial strain data from a WPB test on saturated porous stainless steel with a 20-inch striker bar.

Figure 7.10c. Circumferential strain data from a WPB test on saturated porous stainless steel with a 20-inch striker bar.

Figure 7.10d. Pore pressure data from a WPB test on saturated porous stainless steel with a 20-inch striker bar.

7-44

Figure 7.11a. Input force data from a WPB test on saturated porous stainless steel with a 20-inch striker bar and a 1/8 inch rubber pad.

7-45

Figure 7.11b. Axial strain data from a WPB test on saturated porous stainless steel with a 20-inch striker bar and a 1/8 inch rubber pad.

7-46
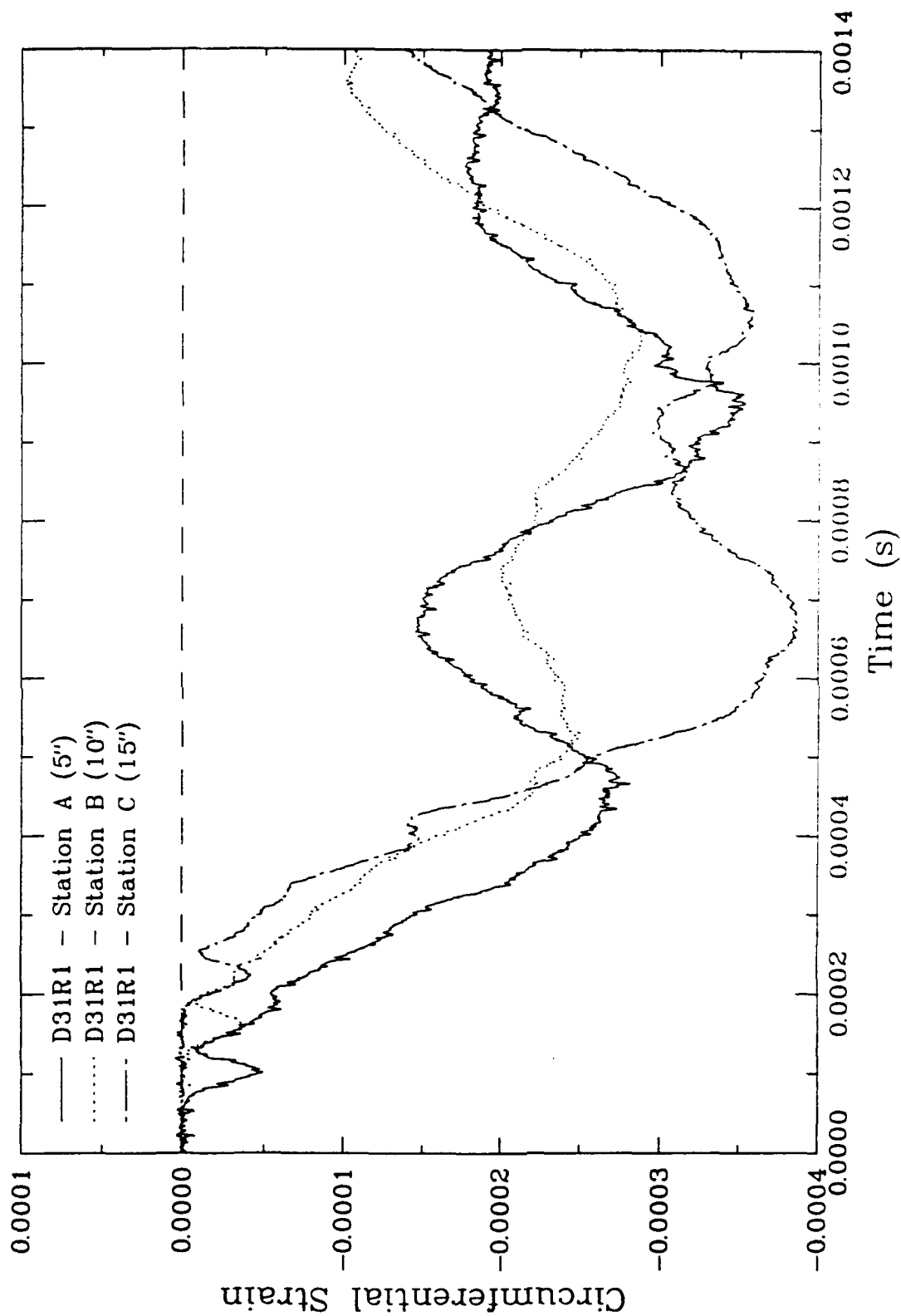
Figure 7.11c. Circumferential strain data from a WPB test on saturated porous stainless steel with a 20-inch striker bar and a 1/8 inch rubber pad.

Figure 7.11d. Pore pressure data from a WPB test on saturated porous stainless steel with a 20-inch striker bar and a 1/8 inch rubber pad.
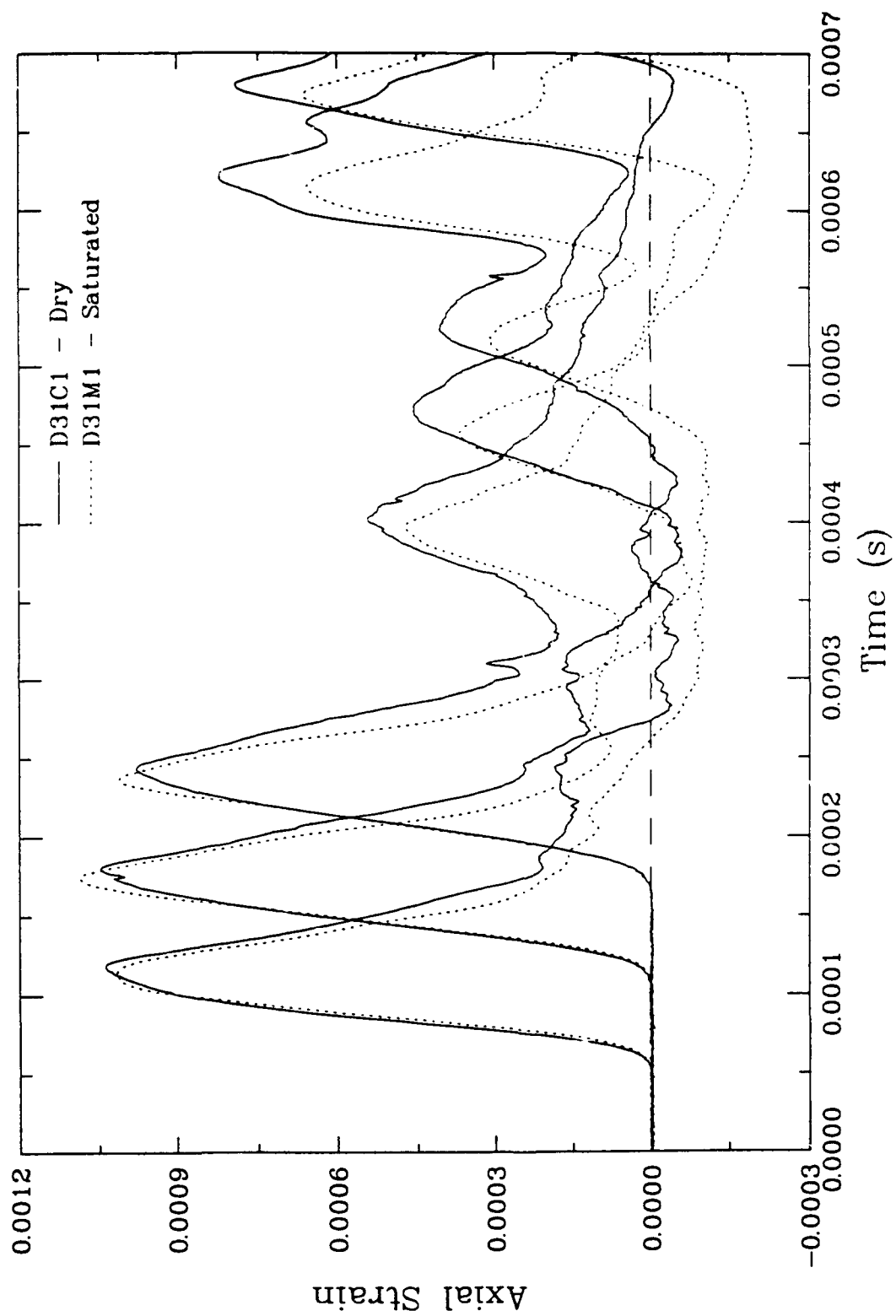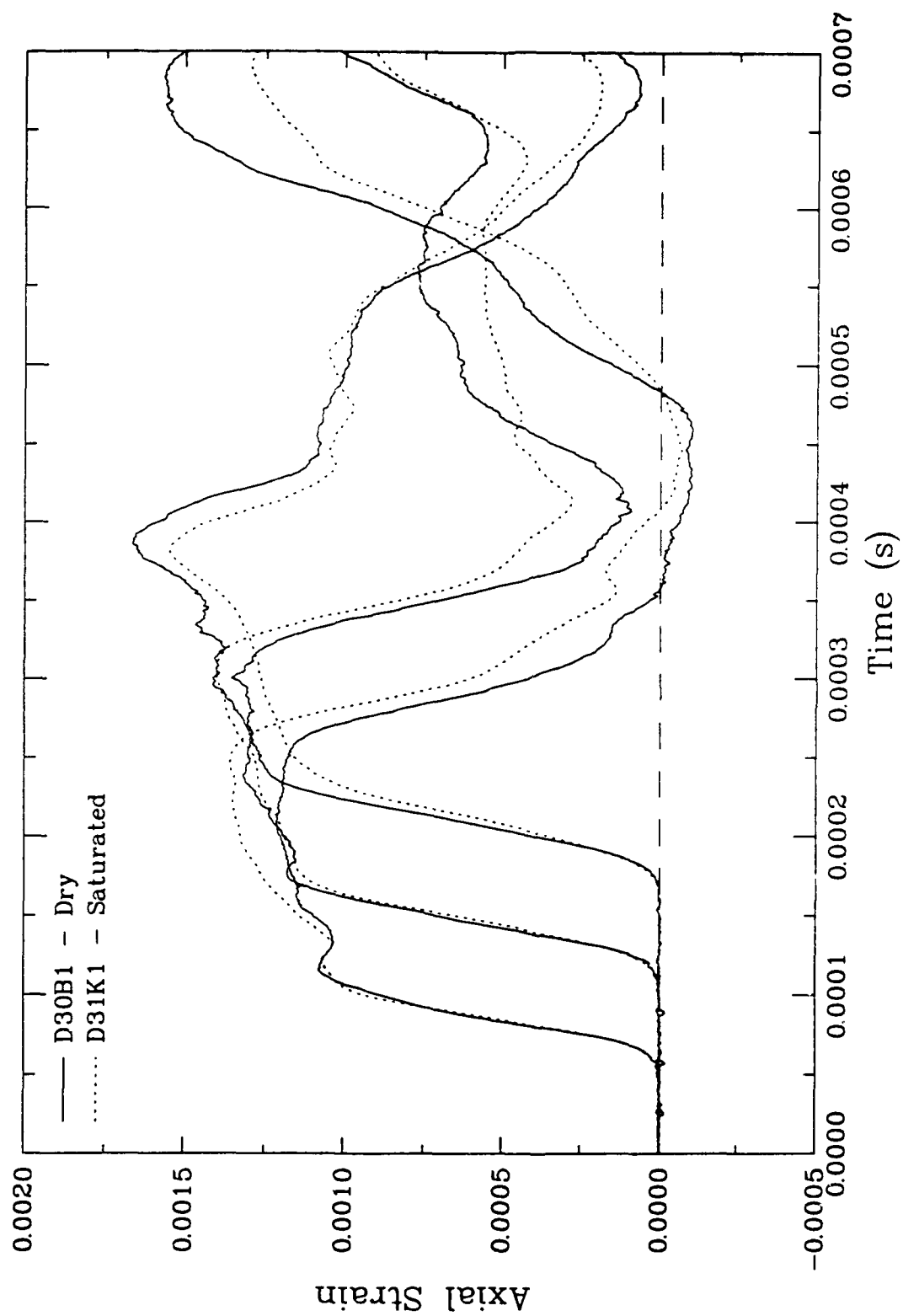
Figure 7.12a. Comparison between axial strain records from tests conducted on dry and fluid-saturated porous stainless steel specimens with a 5-inch striker bar.
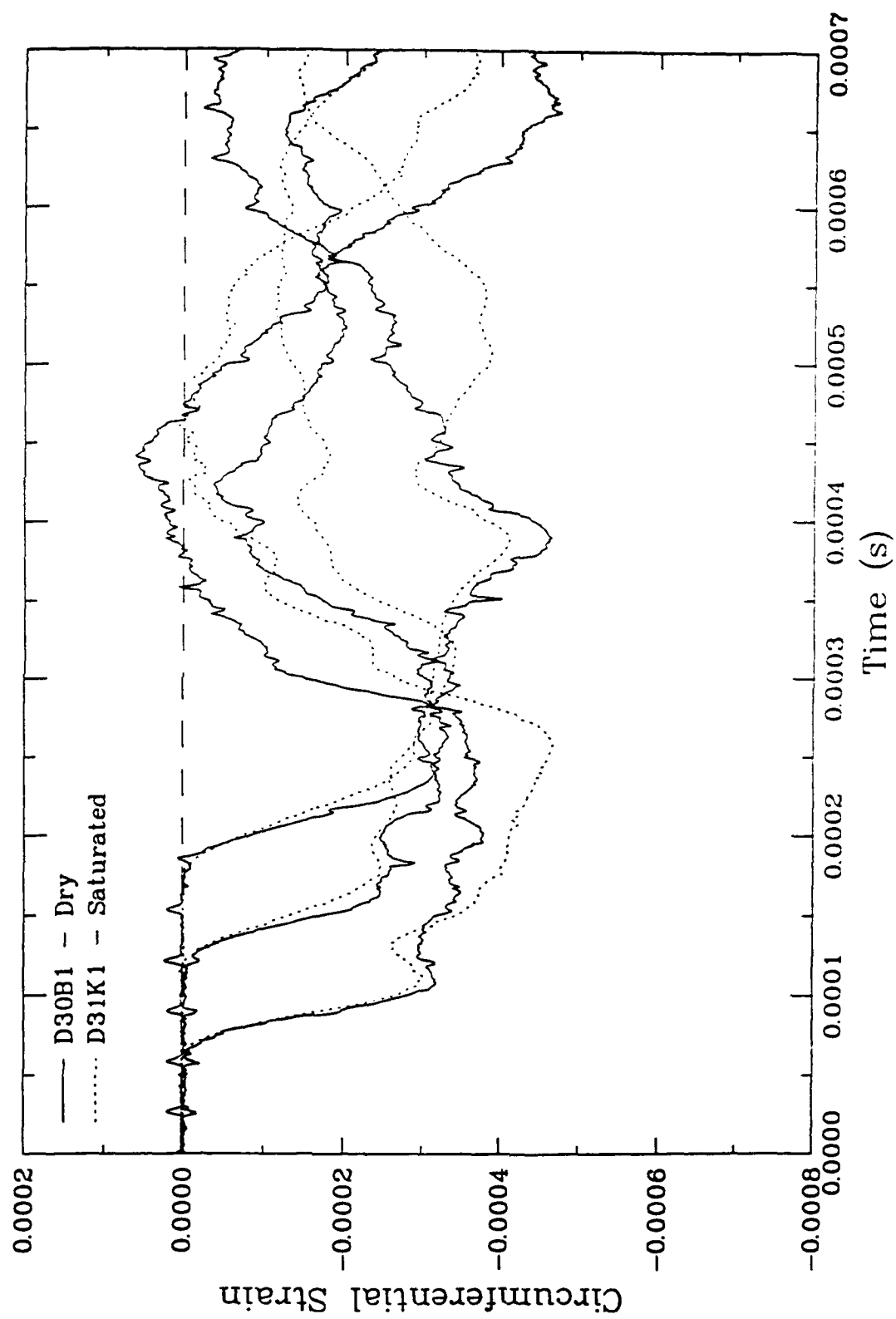
7-49
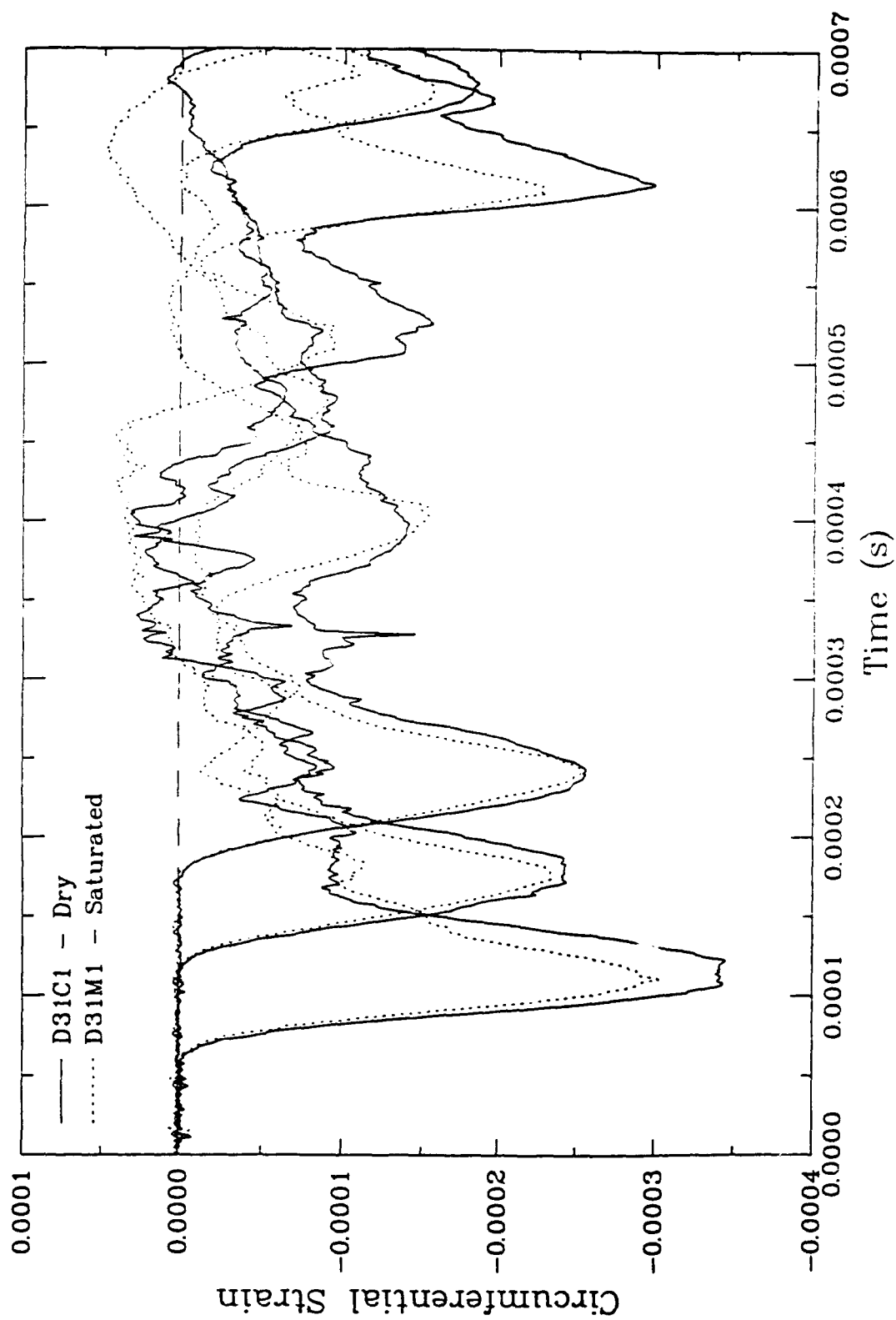
Figure 7.12b. Comparison between circumferential strain records from tests conducted on dry and fluid-saturated porous stainless steel specimens with a 5-inch striker bar.
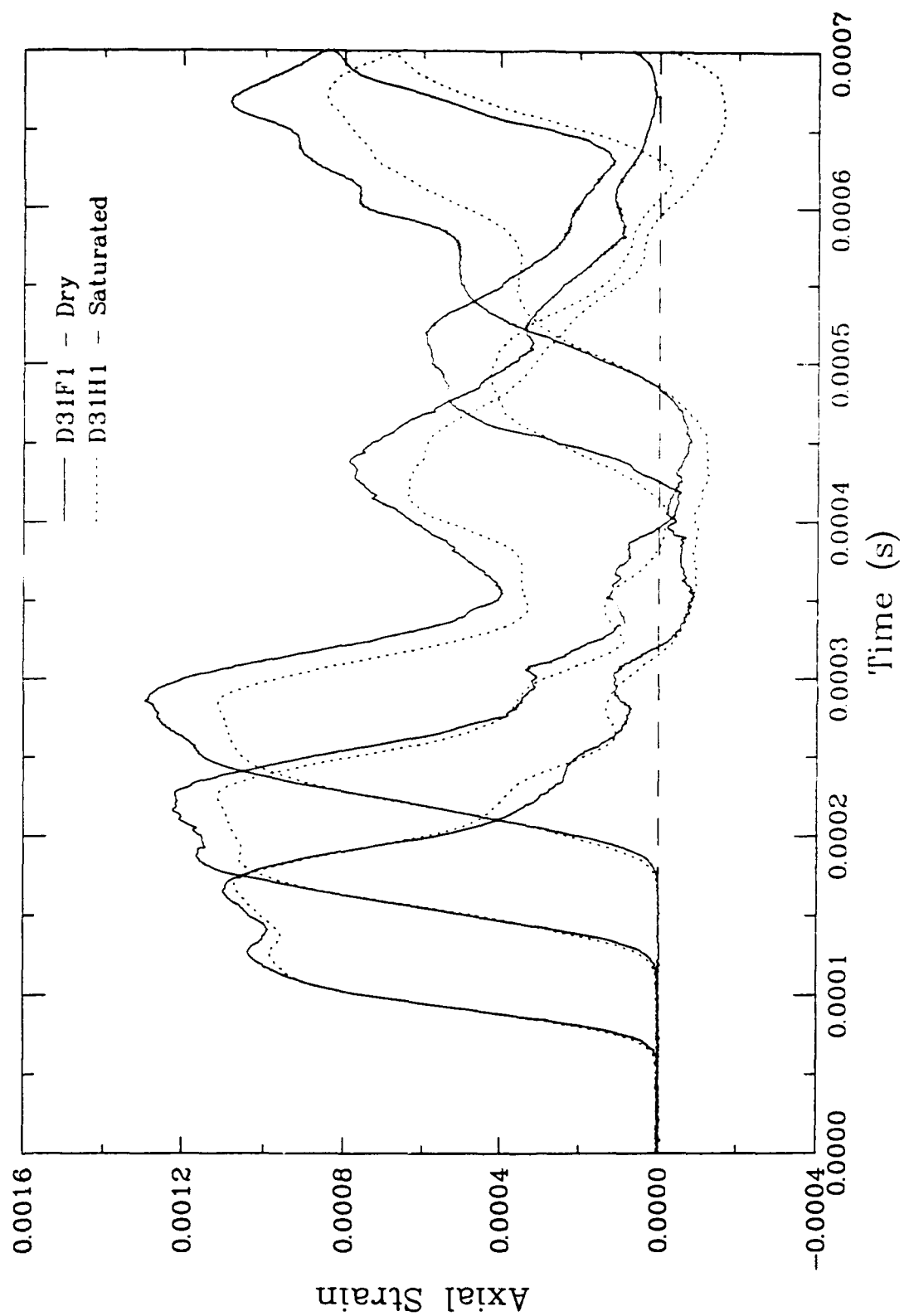
Figure 7.13a. Comparison between axial strain records from tests conducted on dry and fluid-saturated porous stainless steel specimens with a 10-inch striker bar.
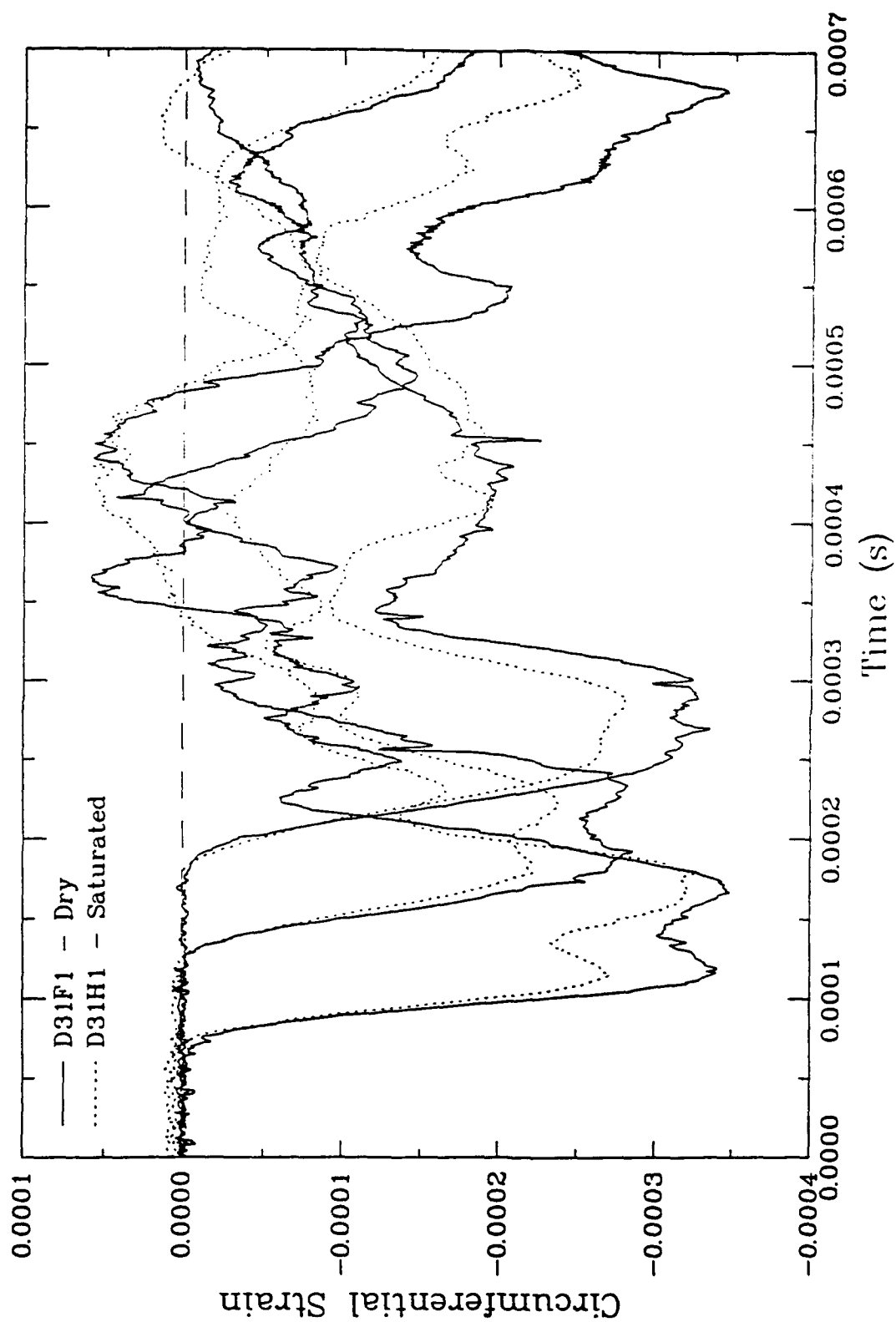
Figure 7.13b. Comparison between circumferential strain records from tests conducted on dry and fluid-saturated porous stainless steel specimens with a 10-inch striker bar.

Figure 7.14a. Comparison between axial strain records from tests conducted on dry and fluid-saturated porous stainless steel specimens with a 20-inch striker bar.

Figure 7.14b. Comparison between circumferential strain records from tests conducted on dry and fluid-saturated porous stainless steel specimens with a 20-inch striker bar.

7-54

Input Velocity Time History
MPDAP Simulation WFR-V
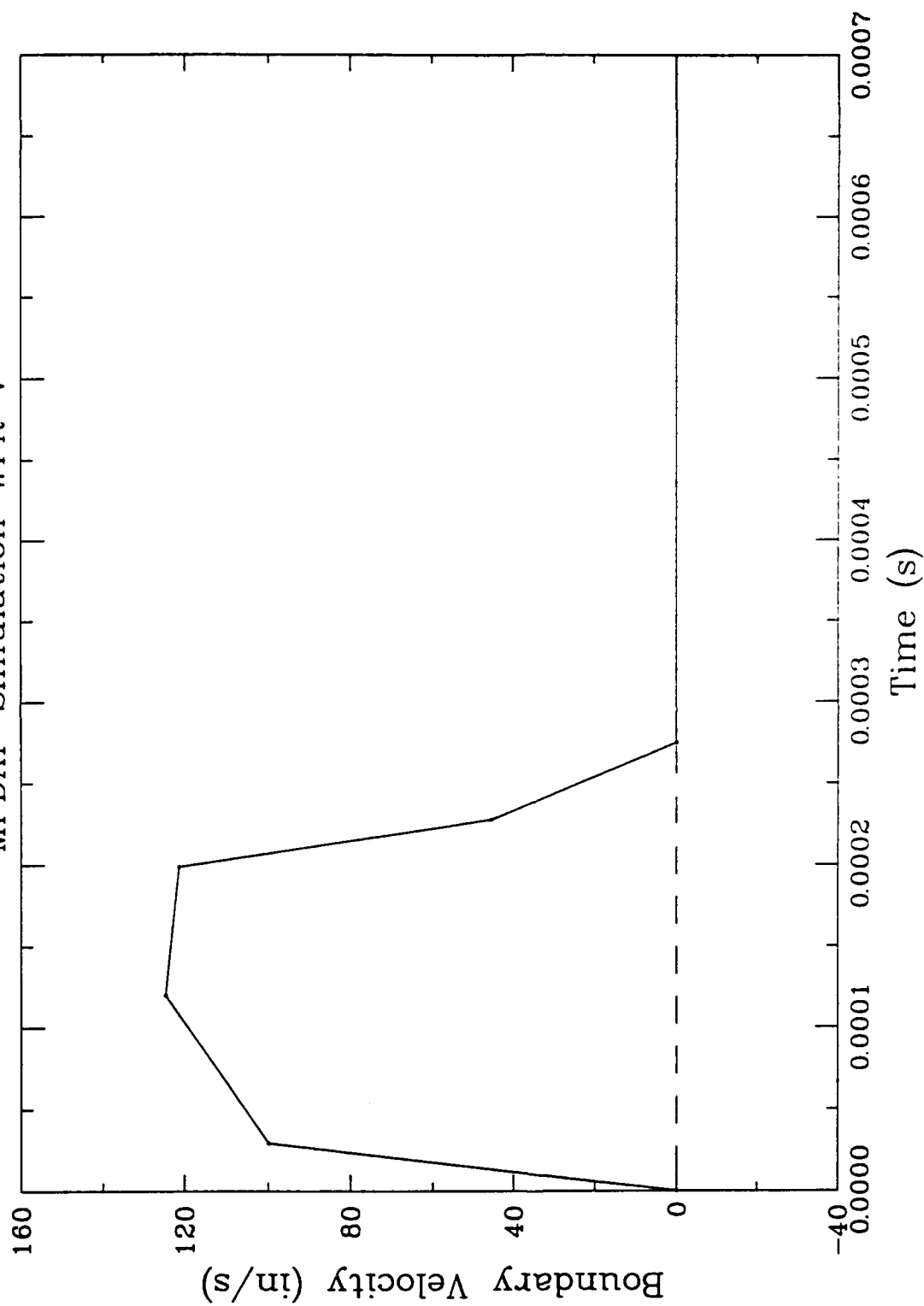
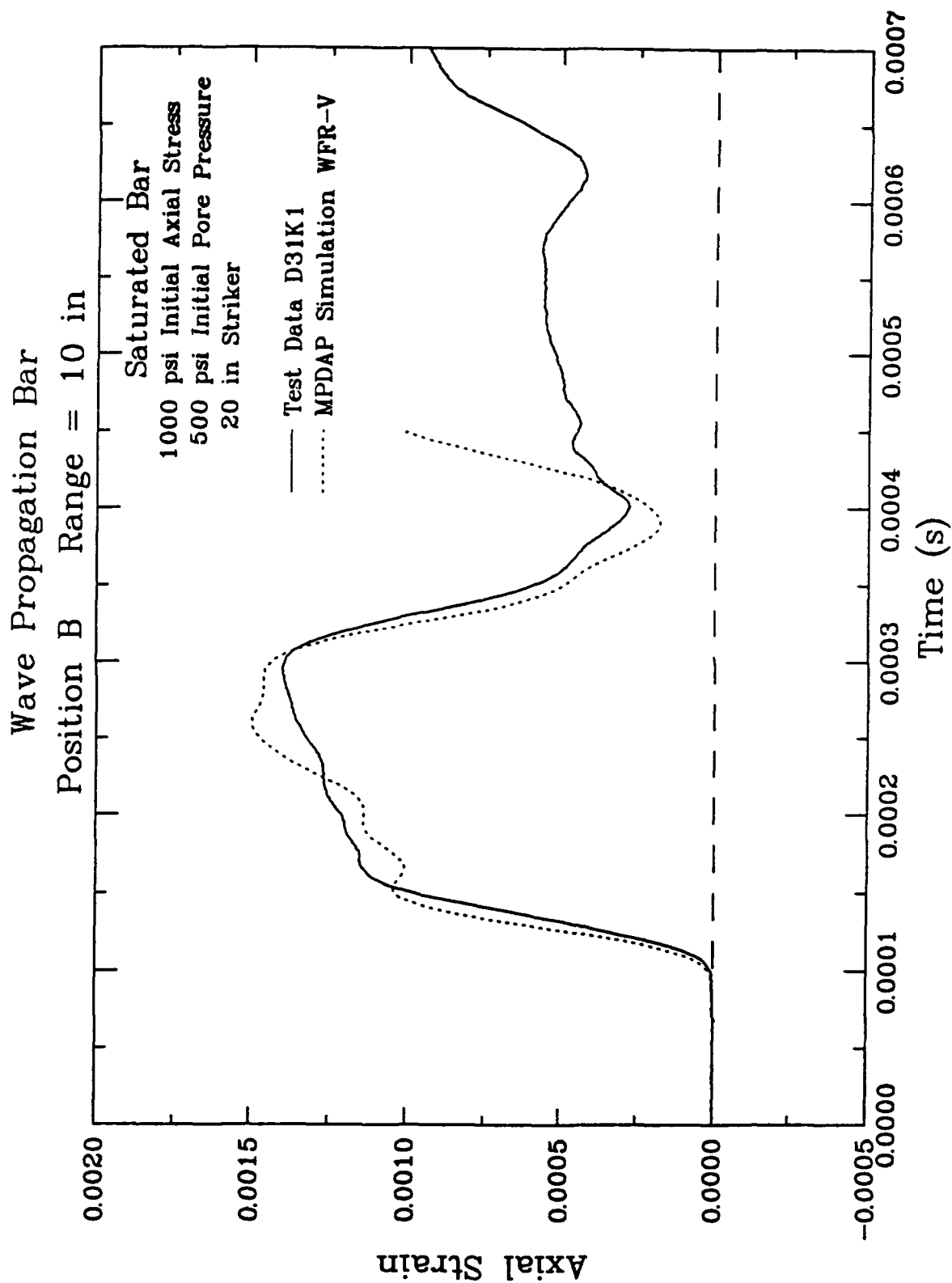Figure 7.15. Velocity history that was used as the loading function for the numerical simulation of test D31K1.
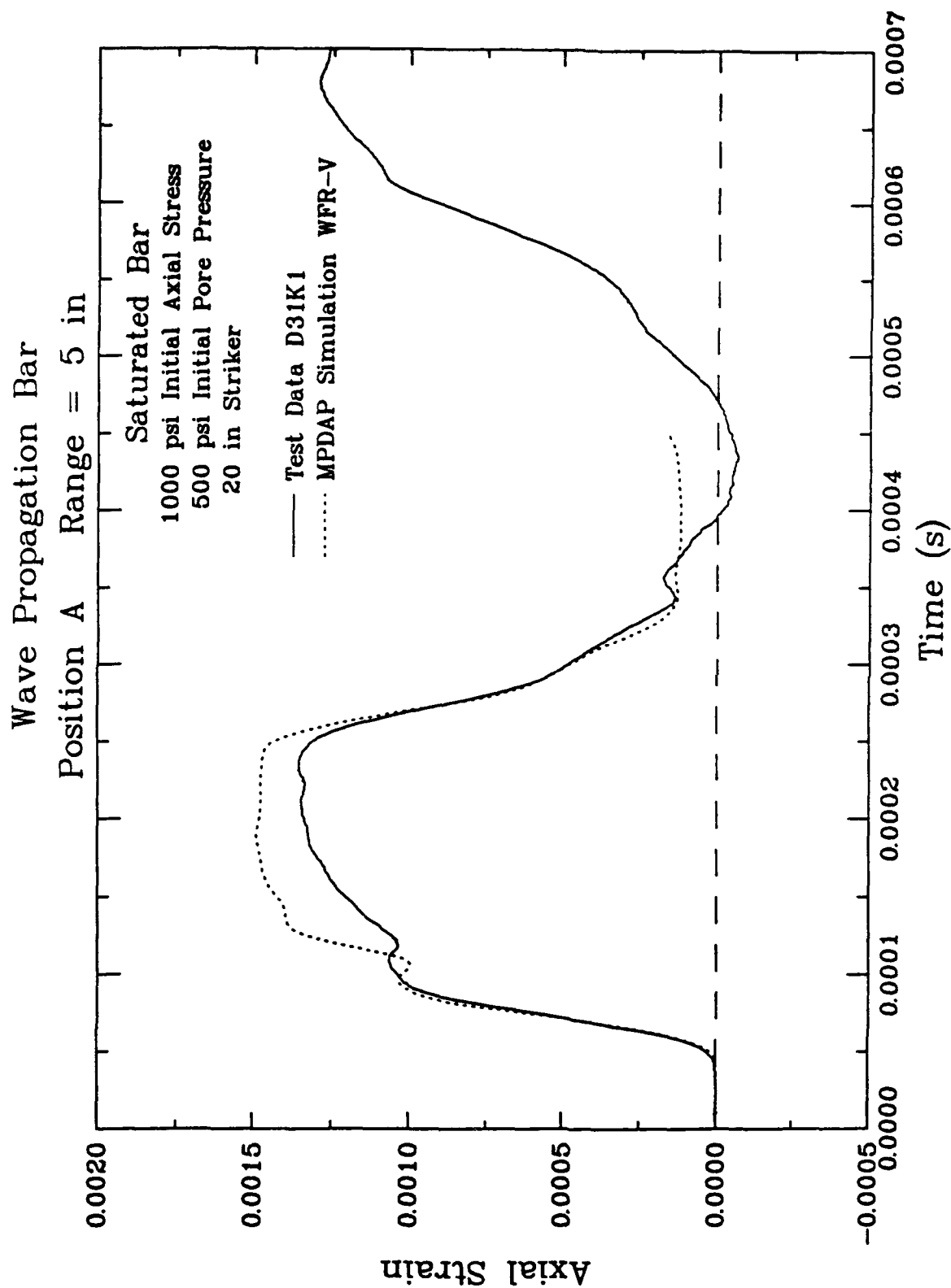
Figure 7.16a. Comparison of the axial strain at the 5-inch point (Station A) computed in the numerical simulation with the corresponding quantity from test D31K1.
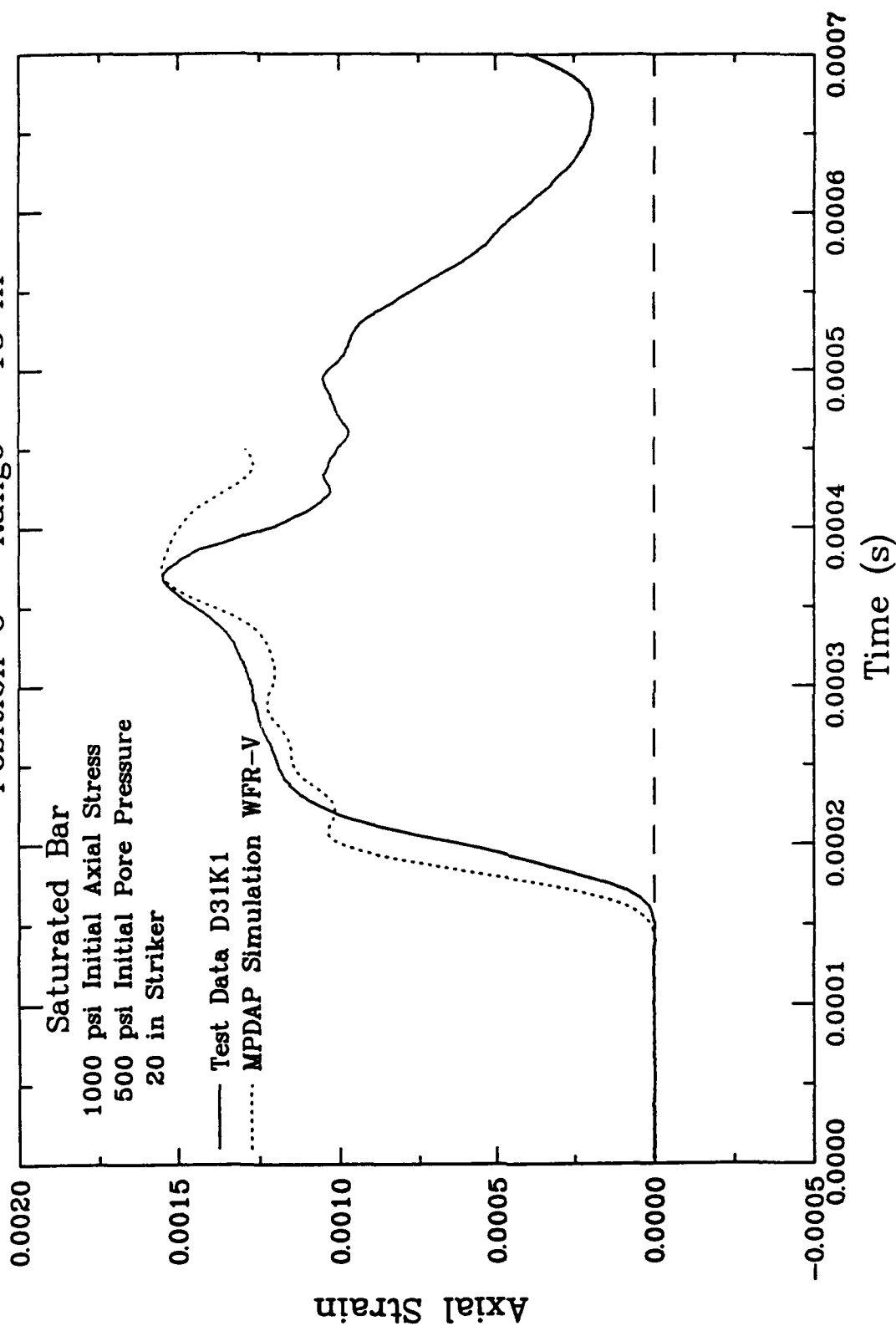
Figure 7.16b. Comparison of the axial strain at the 10-inch point (Station B) computed in the numerical simulation with the corresponding quantity from test D31K1.

Figure 7.16c. Comparison of the axial strain at the 15-inch point (Station C) computed in the numerical simulation with the correponding quantity from test D31K1.
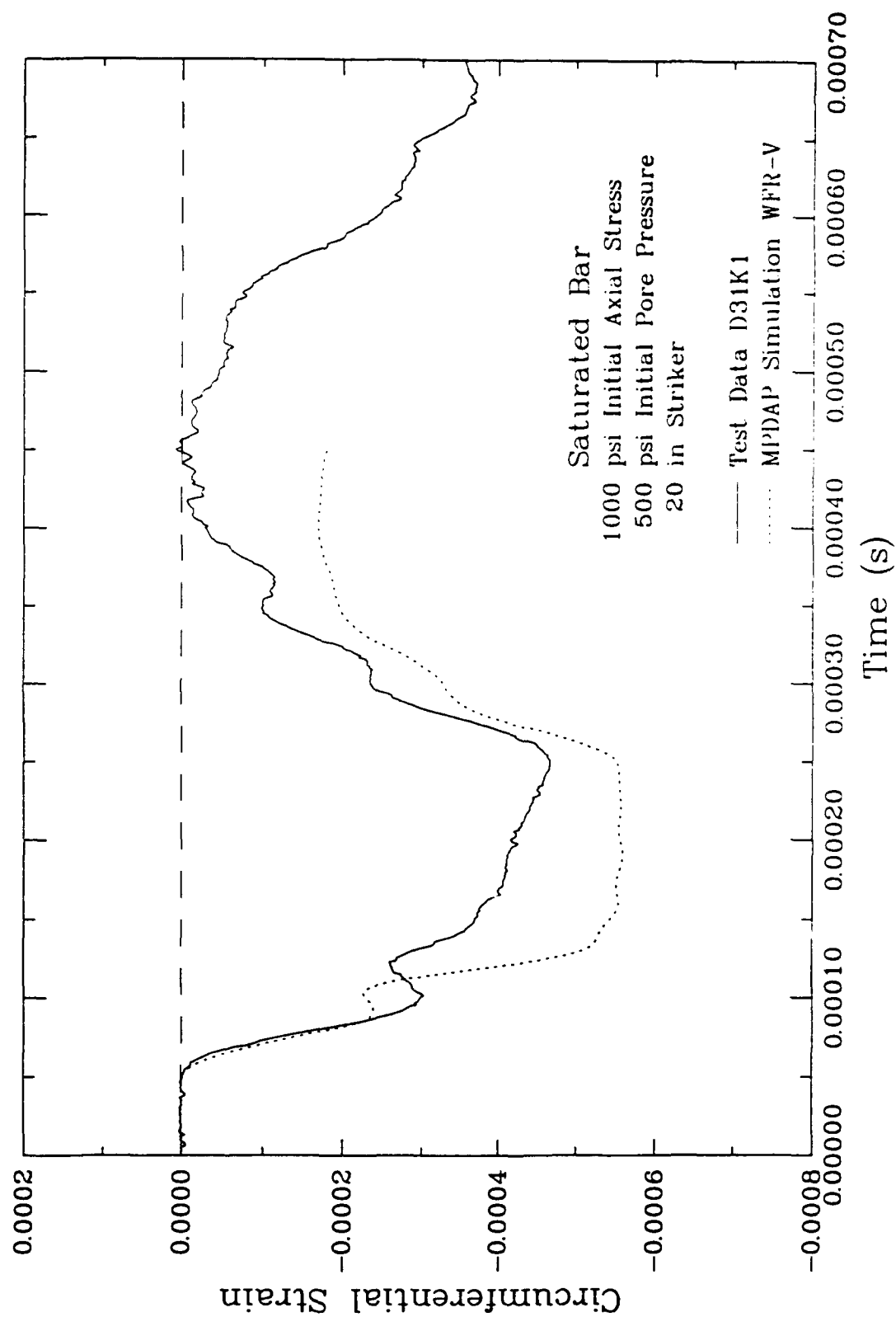
Figure 7.17a. Comparison of the circumferential strain at the 5-inch point (Station A) computed in the numerical simulation with the corresponding quantity from test D31K1.
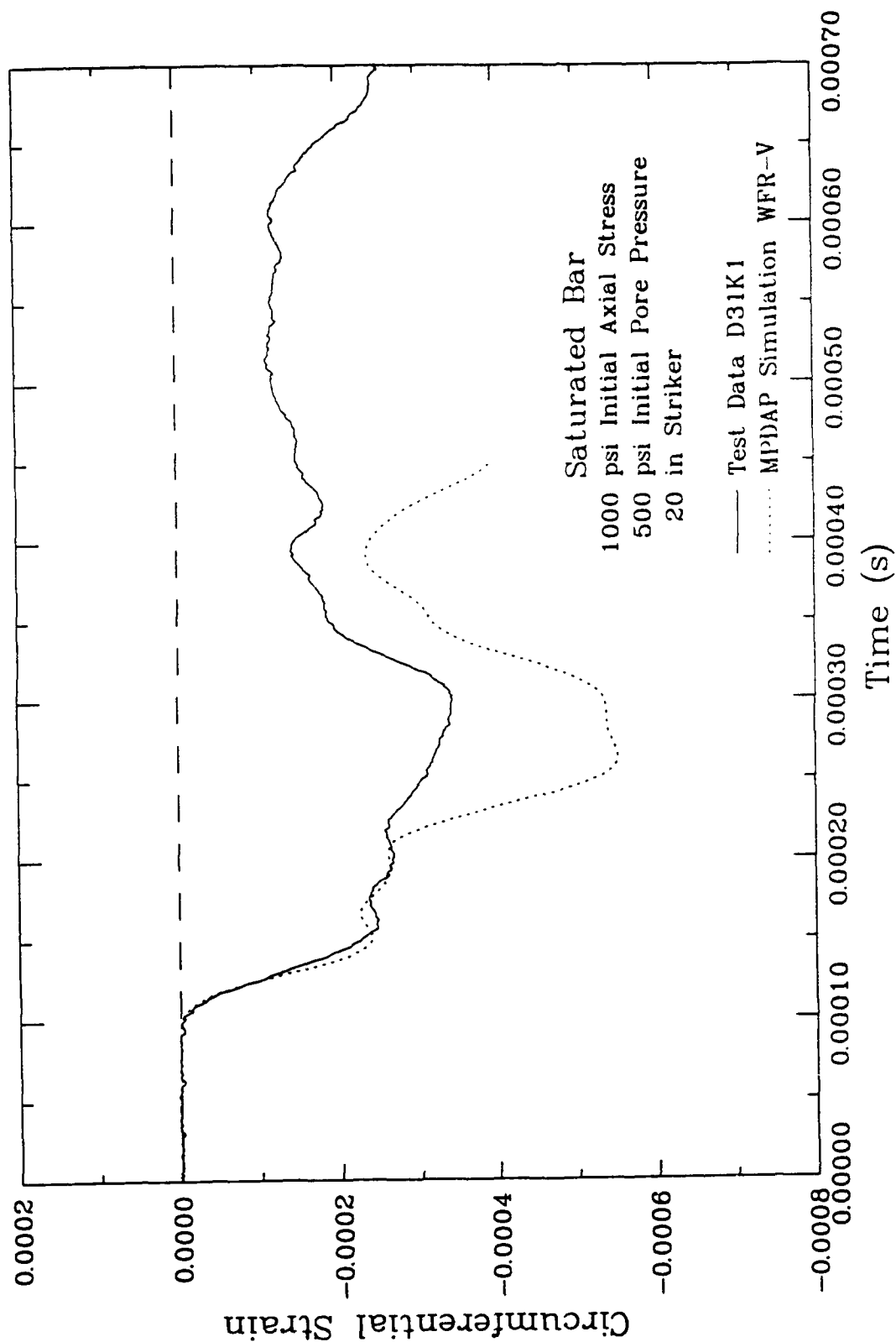
Figure 7.17b. Comparison of the circumferential strain at the 10-inch point (Station B) computed in the numerical simulation with the corresponding quantity from test D31K1.

Wave Propagation Bar

Position A   Range = 5 in

Saturated Bar

1000 psi Initial Axial Stress
500 psi Initial Pore Pressure
20 in Striker

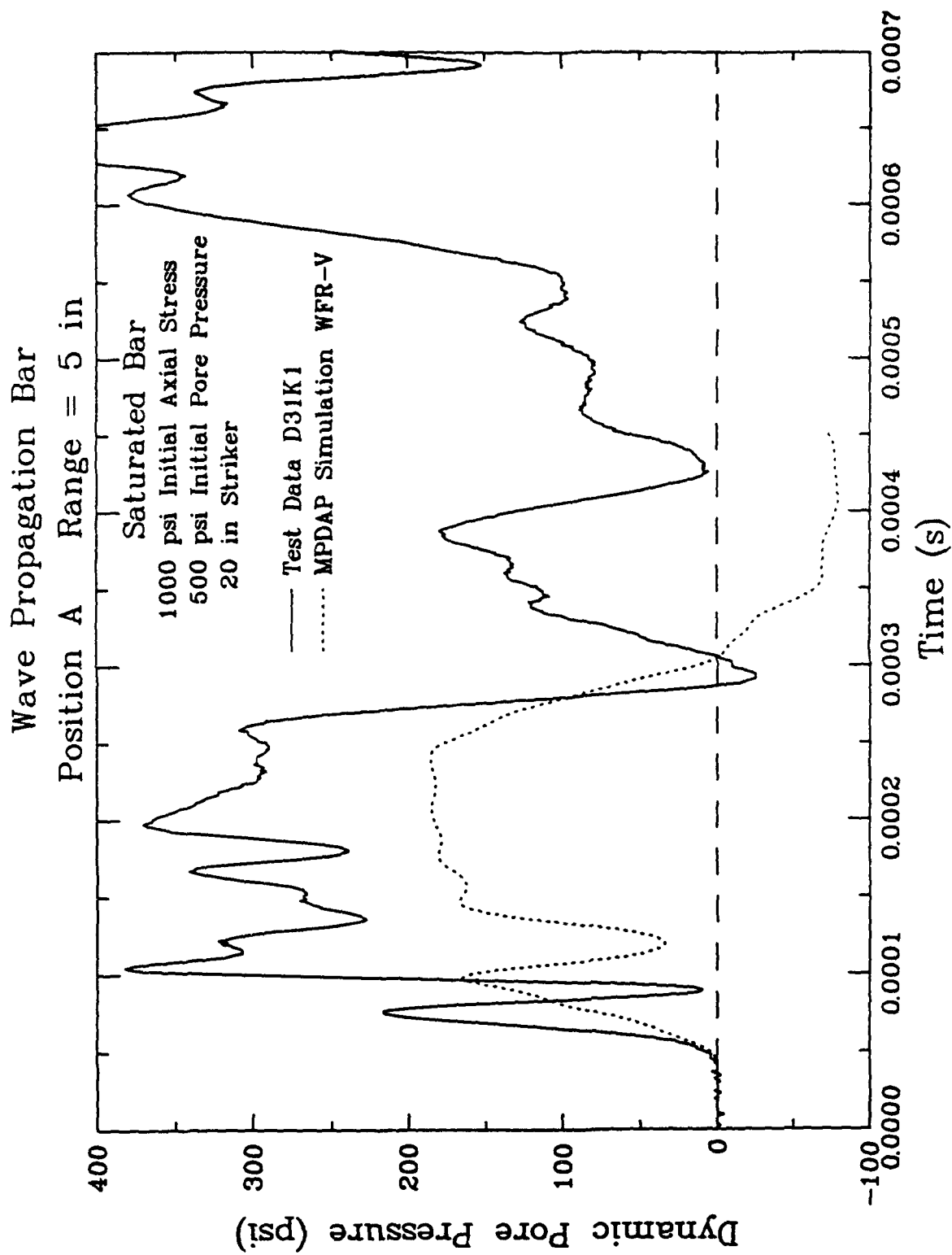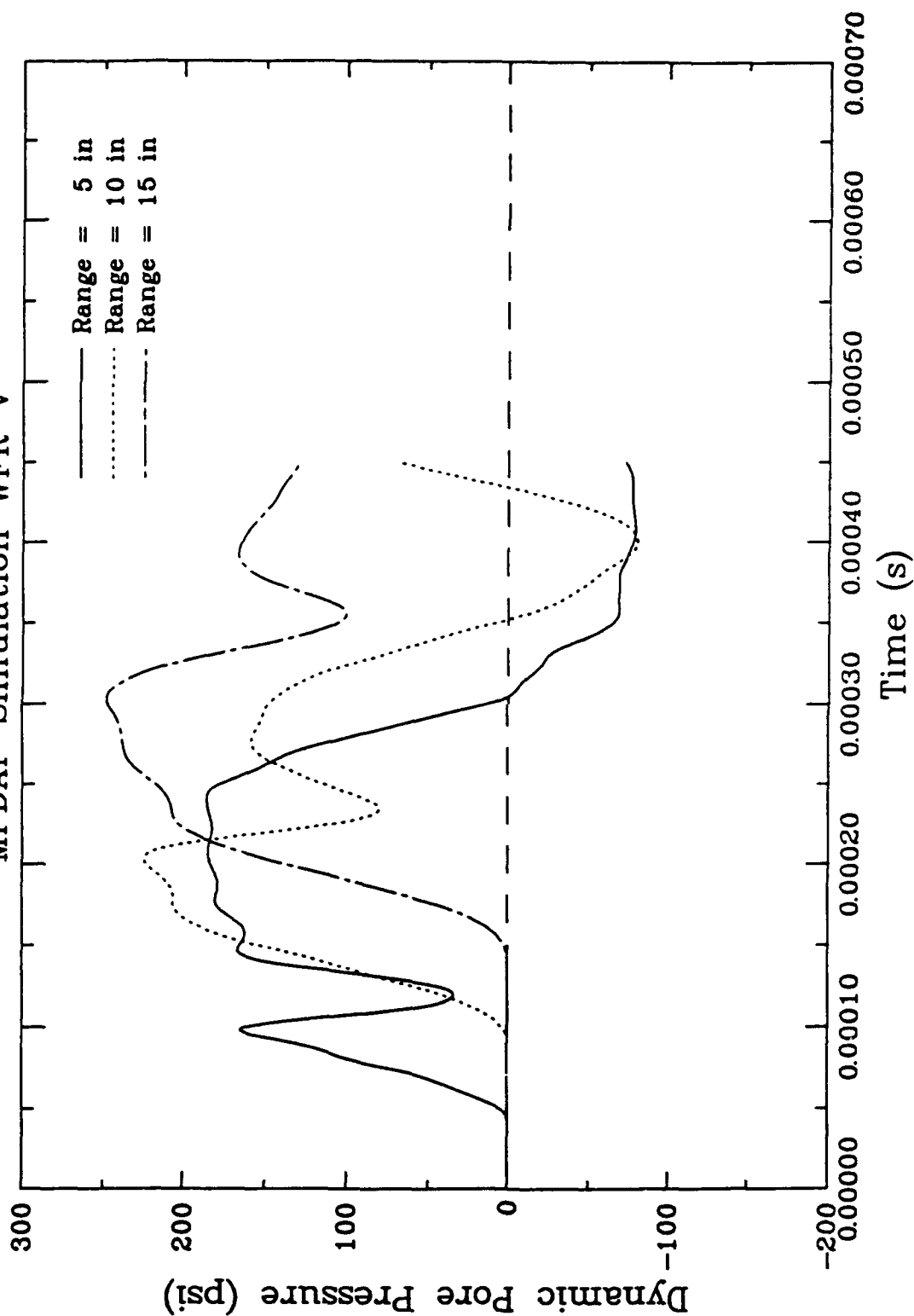—— Test Data D31K1
········ MPDAP Simulation WFR-V

Figure 7.18.   Comparison of the pore pressure at the 5-inch point (Station A) computed in the numerical simulation with the corresponding quantity from test D31K1.

7-61

Figure 7.19. Pore pressures computed by the numerical simulation at the 5-, 10-, and 15-inch points on the saturated porous specimen.

Figure 7.20a. Skeleton velocity and apparent relative fluid velocity computed by the numerical simulation at the 5-inch point (Station A).

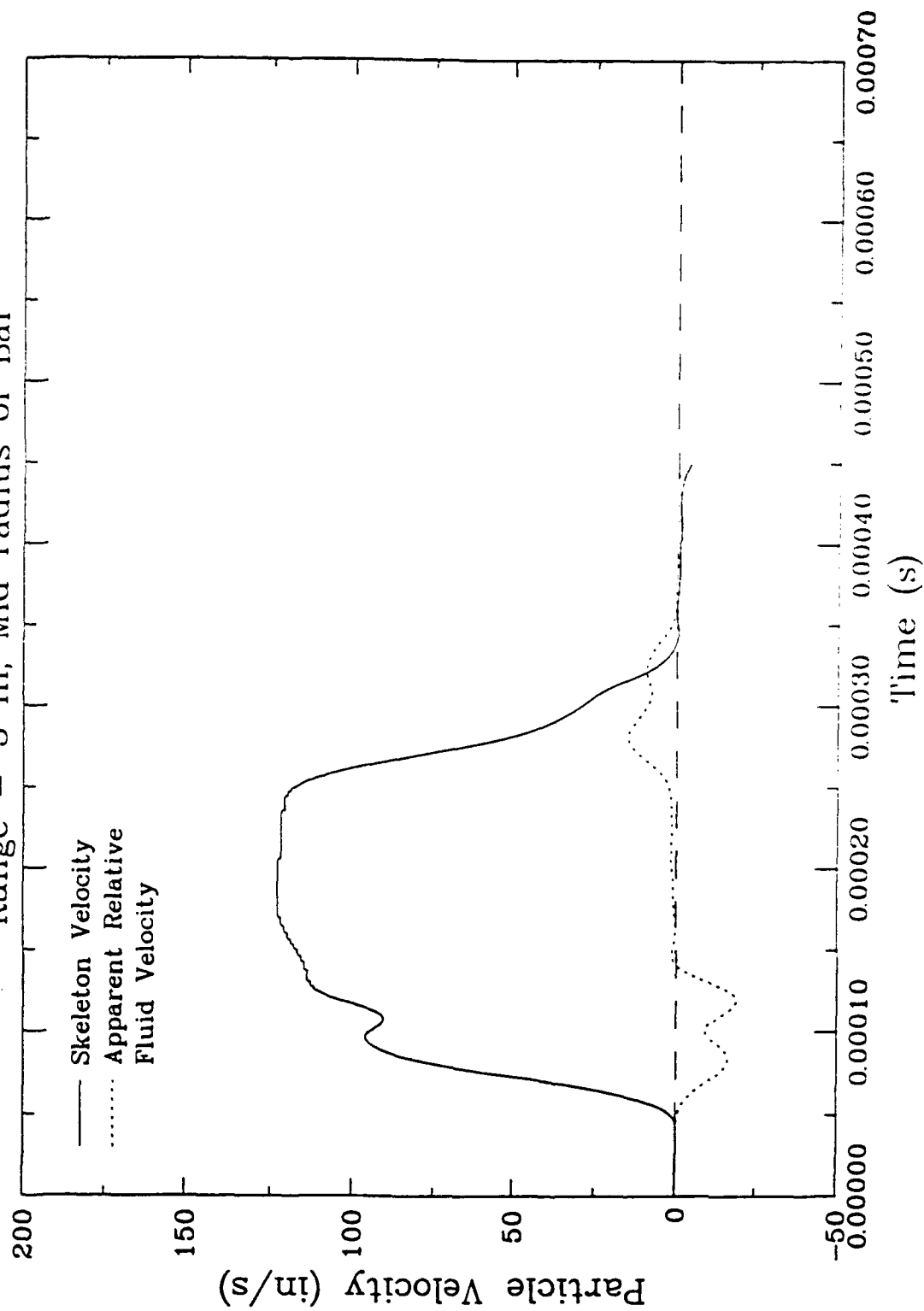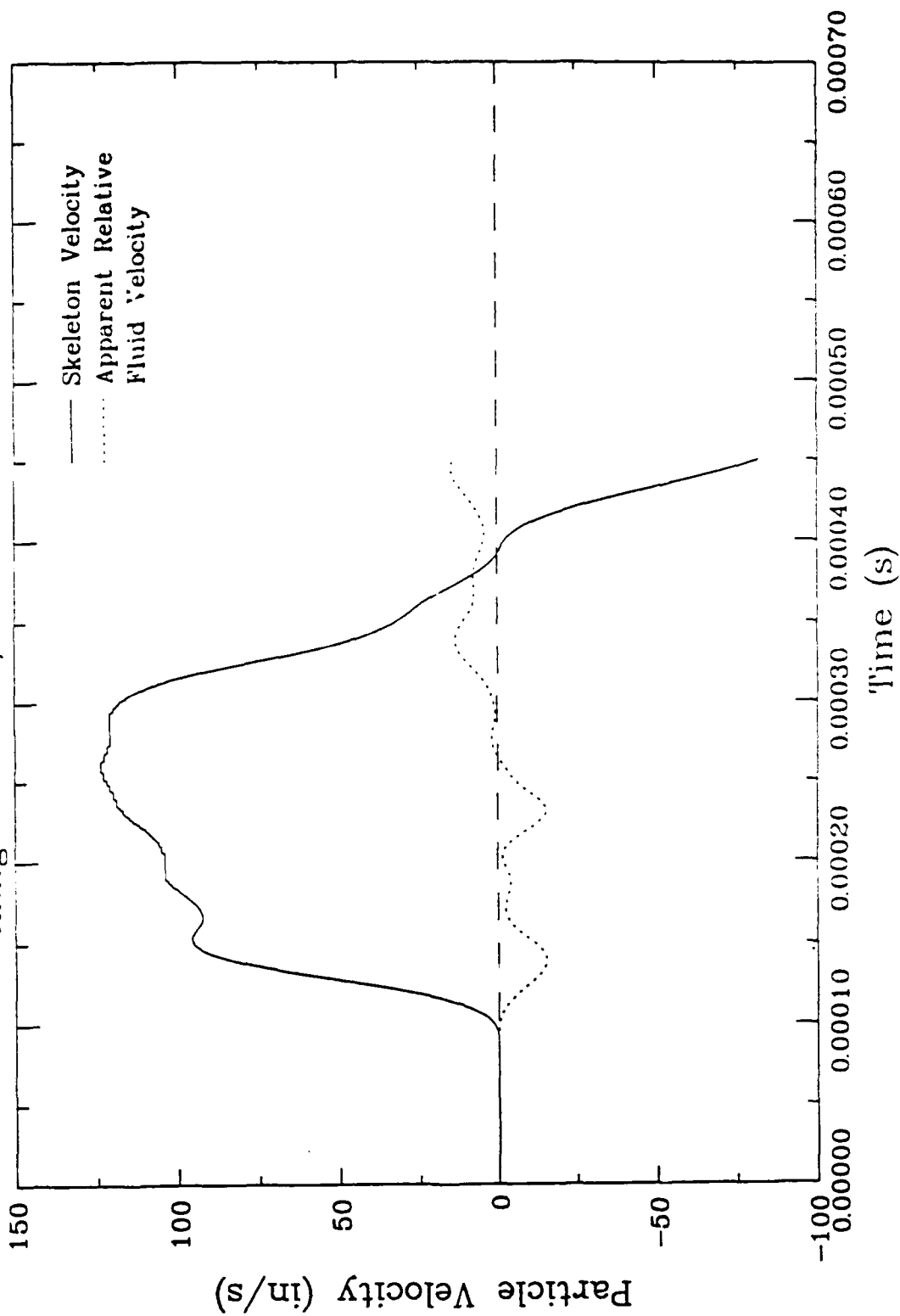Figure 7.20b. Skeleton velocity and apparent relative fluid velocity computed by the numerical simulation at the 10-inch point (Station B).
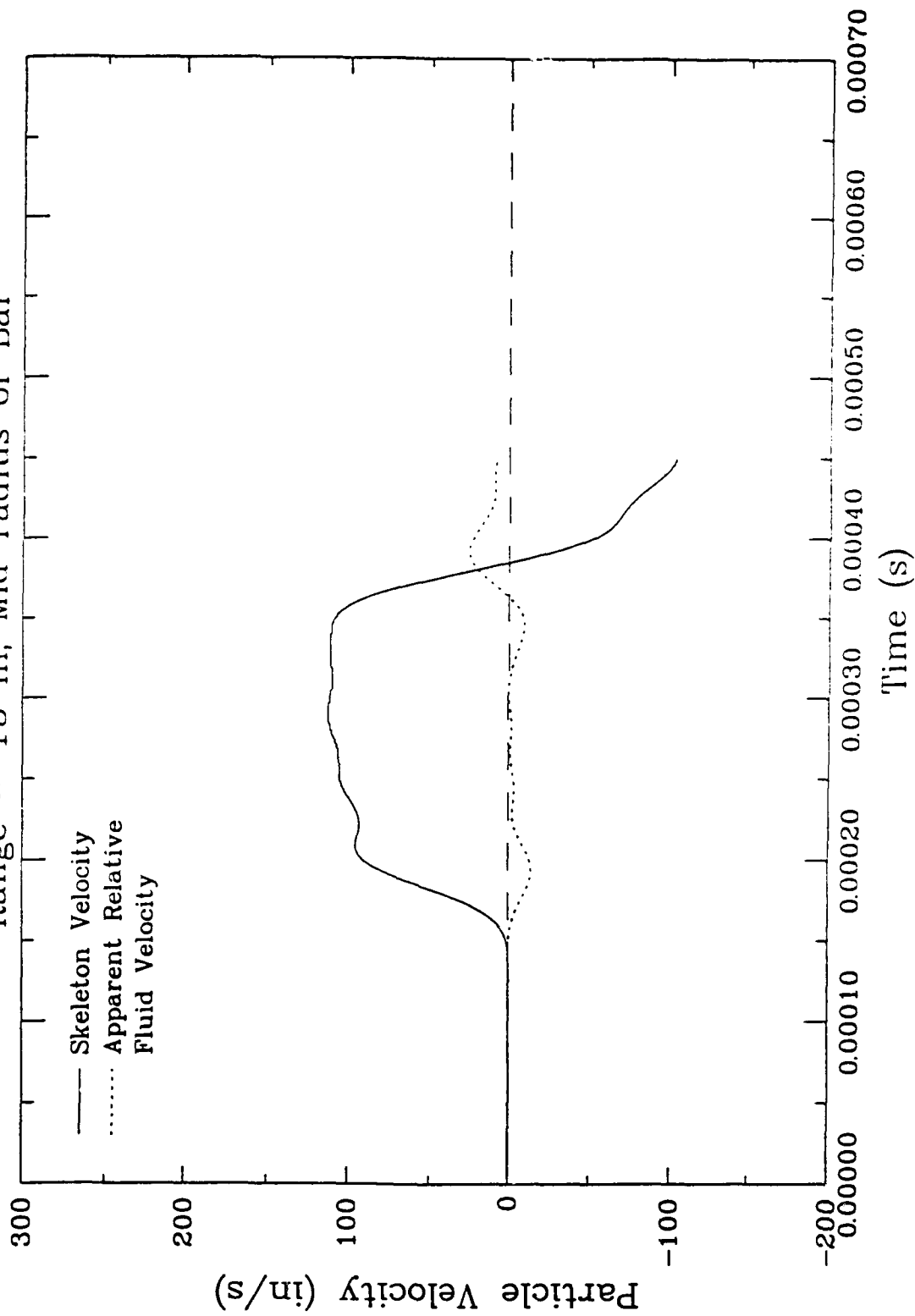
Figure 7.20c. Skeleton velocity and apparent relative fluid velocity computed by the numerical simulation at the 15-inch point (Station C).
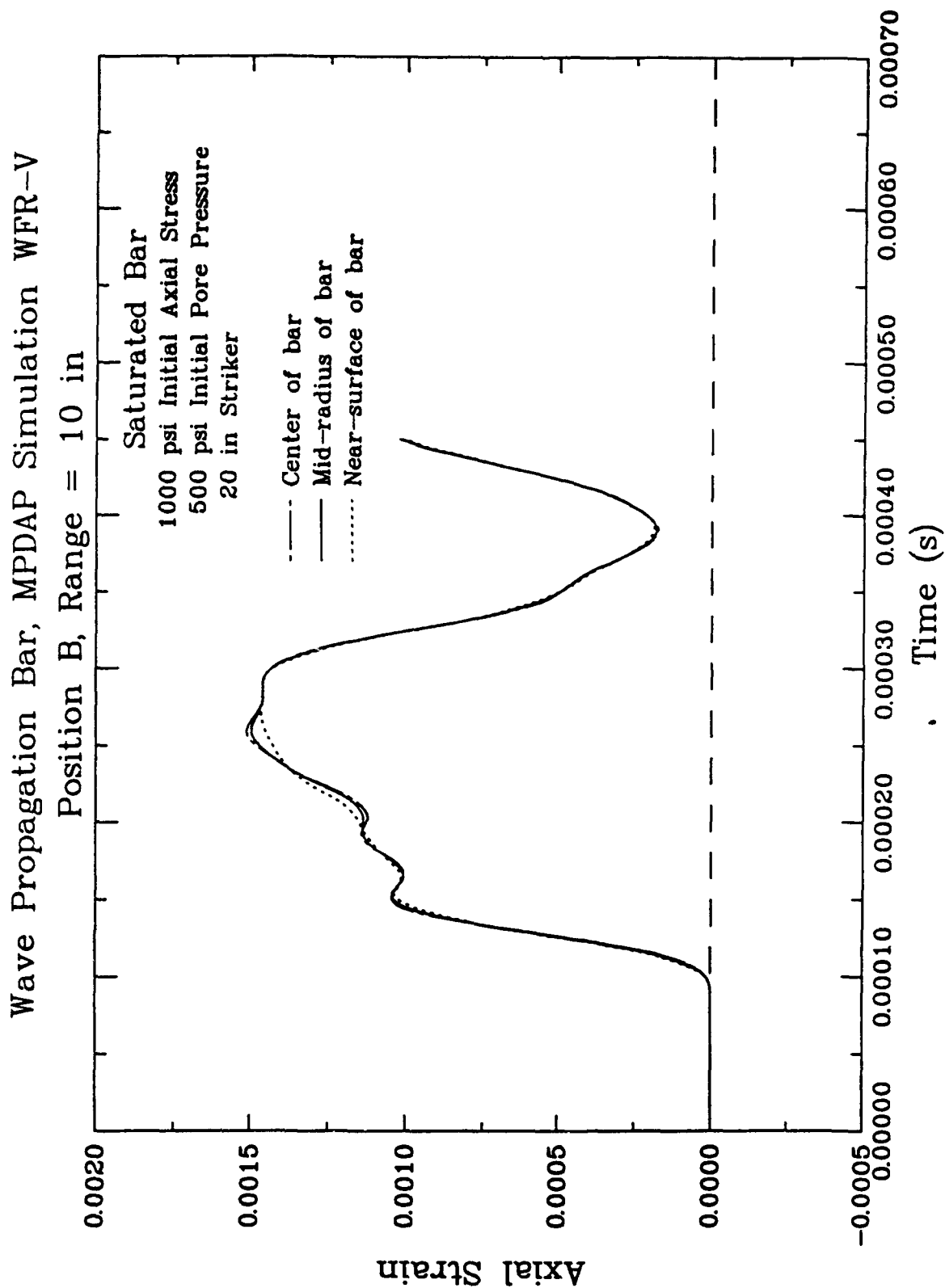
Figure 7.21. Comparison of axial strains computed by the numerical simulation at the 10-inch point at various radial distances from the center of the test specimen.
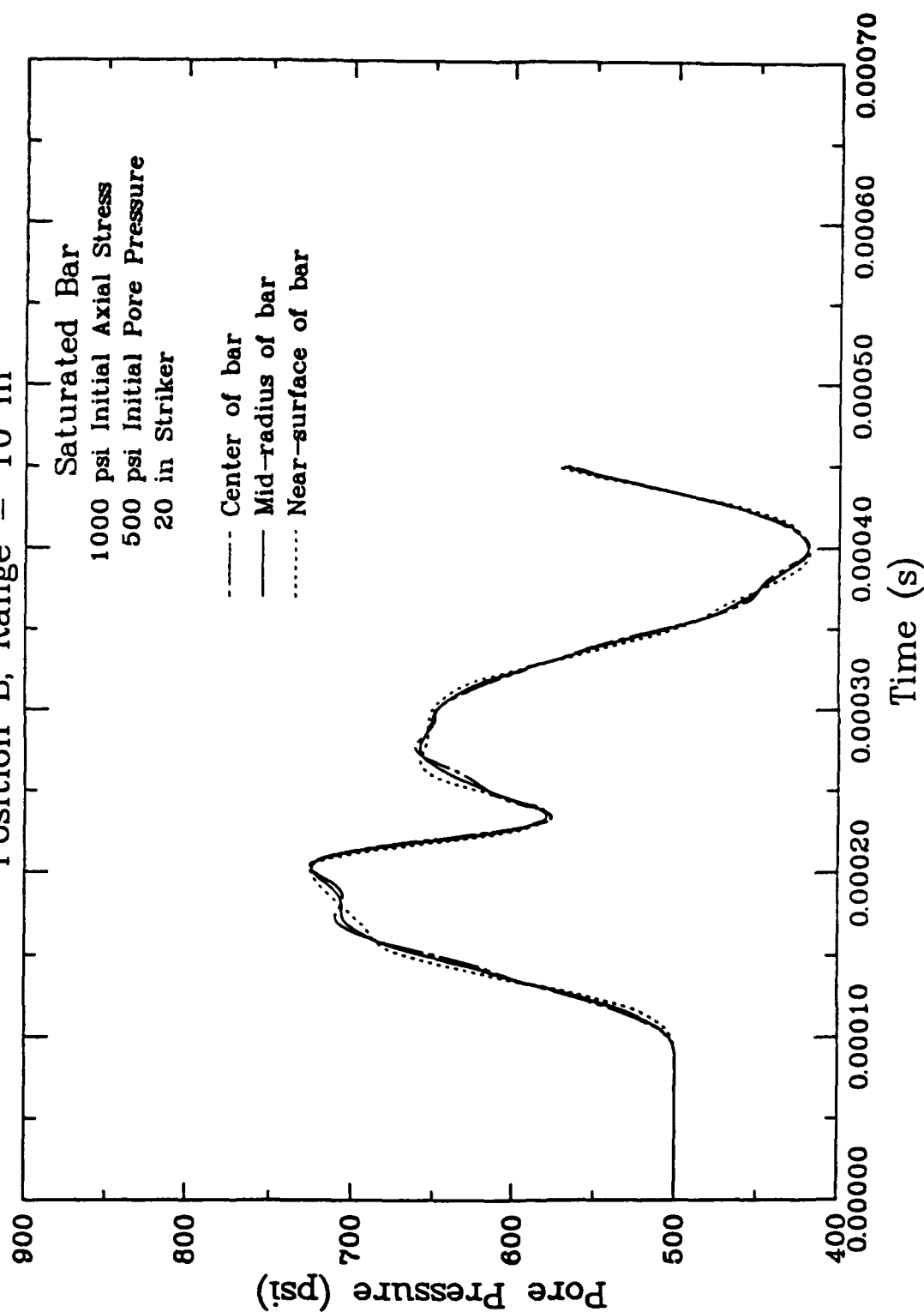
Figure 7.22. Comparison of pore pressures computed by the numerical simulation at the 10-inch point at various radial distances from the center of the test specimen.

SECTION 8

LIST OF REFERENCES

Ahrens, T. J., "Equation of State of Earth Media," Report to Defense Nuclear Agency, DNA-TR-88-265, Washington, D.C., November 1988.

Allen, R.T., "Equation of State of Rocks and Minerals," Defense Atomic Support Agency, DA49-146-XZ-462, Project No. 532, March 1967.

Applied Research Associates, Inc., "Proposal to Provide Laboratory Investigation and Analysis of Rock Properties in Support of Rock-Liner Interaction," proposal to Defense Nuclear Agency, Washington, D.C., November 1991.

Bakanova, A.A, V.N. Zubarev, Y.N. Sutulov, and R.F. Trunin, "Thermodynamic Properties of Water at High Pressures and Temperatures," *Soviet Phys. JETP*, 41, 544, 1976.

Bear, J., Dynamics of Fluids in Porous Media, American Elsevier Publishing Company, Inc., New York, 1972.

Blouin, S.E., and K.J. Kim, "Undrained Compressibility of Saturated Soil", DNA-TR-87-42, Defense Nuclear Agency, Washington, D.C., February 1984.

Blouin, S.E., and D.A. Timian, "Material Properties Testing in Support of PEACE Program, Enewetak Atoll," Report to Defense Nuclear Agency, June 1986.

Blouin, S.E., D.E. Chitty, A.F. Rauch, and K.J. Kim, "Dynamic Response of Multiphase Porous Media," Annual Technical Report 1, Report to U.S. Air Force Office of Scientific Research, Washington D.C., March 1990.

Blouin, S.E., D.E. Chitty, A.F. Rauch, and K.J. Kim, "Dynamic Response of Multiphase Porous Media," Annual Technical Report 2, Report to U.S. Air Force Office of Scientific Research, Washington, D.C., June 1991.

Britt, J.R., "Behavior of Water in Low Pressure Region," unpublished manuscript, 1985.

Chitty, D.E., and S.E. Blouin, "Special-Purpose Mechanical Property Tests of Salem Limestone," Final Report to U.S. Army Engineer Waterways Experiment Station, Vicksburg, MS, Februrary 1990.

Chitty, D.E., S.E. Blouin, A.F. Rauch, K.J. Kim, and D.H. Merkle, "Undrained Triaxial Compression Behavior of Saturated Indiana Limestone," in C.S.Desai, E. Krempl, G. Frantziskonis, and H. Saadatmanesh, eds., Constitutive Laws for Engineering Materials, Recent Advances and Industrial and Infrastructure Applications, Proceedings of the Third International Conference on Constitutive Laws for Engineering Materials: Theory and Applications, held January 7-12, 1991 in Tucson, Arizona, USA, ASME Press, New York, 1991.

LIST OF REFERENCES (CONTINUED)

Chitty, D.E., and S.E. Blouin, "Laboratory Investigation of the Strength and Deformation Properties of Carbonate Rocks and Soils," DNA-TR-92-45, Defense Nuclear Agency, Alexandria, VA, June 1993.

Dass, W.C., and D.H. Merkle, "Computational Aspects of the ARA Three Invariant Constitutive Model," Report to U.S. Air Force Office of Scientific Research, Washington, D.C., May 1986.

Forchheimer, P., "Wasserbewegung durch Boden," Z. Ver. *Deutsch Ing.*, 45, pp. 1782-1788, 1901.

Green, L., Jr., P. Duwez, "Fluid Flow Through Porous Metals," Journal of Applied Mechanics, Vol. 18, pgs 39-45, March 1951.

Hazen, A., "Discussion 'Dams on Sand Foundations'," Transactions of American Society of Civil Engineers, 1911.

Hoek, E. and E.T. Brown, *Underground Excavations in Rock*, The Institution of Mining and Metallurgy, London, England, 1982.

Hubbert, M.K., "Darcy law an the field equations of the flow of underground fluids," *Trans. Amer. Inst. Min. Metal. Eng..* **207**, pp. 222-239, 1956.

Kim, K.J., "Finite Element Analysis of Nonlinear Consolidation," Thesis submitted in partial fulfillment of the requirements for the degree of Doctor of Philosophy in Civil Engineering, University of Illinois at Urbana-Champaign, 1982.

Kim, K.J., and S.E. Blouin, "Influence of Pore Water on the Calculated Response of Porous Limestone to a Contained Explos :1," DNA-TR-89-232, Defense Nuclear Agency, Alexandria, VA, September 1990.

Kim, K.J., D.D. Piepenburg, and D.H. Merkle, "Influence of the Intermediate Principal Stress on Rock Tunnel Behavior," Draft Report to Defense Nuclear Agency, Washington, DC, November 1985.

Kim, K.J., S.E. Blouin, and D.A. Timian, "Experimental and Theoretical Response of Multiphase Porous Media to Dynamic Loads," Annual Technical Report 1, Report to U.S. Air Force Office of Scientific Research, Washington, D.C., August 1986.

Kim, K.J., S.E. Blouin, and D.A. Timian, "Experimental and Theoretical Response of Multiphase Porous Media to Dynamic Loads," Annual Technical Report 2, Report to U.S. Air Force Office of Scientific Research, Washington, D.C., September 1987.

LIST OF REFERENCES (CONTINUED)

Kim, K.J., S.E. Blouin, D.E. Chitty, and D.H. Merkle, "Experimental and Theoretical Response of Multiphase Porous Media to Dynamic Loads," Final Report to U.S. Air Force Office of Scientific Research, Washington, D.C., September 1988.

Lade, P.V. and R.B. Nelson, "Modelling the Elastic Behavior of Granular Materials," *International Journal for Numerical and Analytical Methods in Geomechanics*, Vol. II, pp. 521-542, 1987.

Lindquist, E., "On the flow of water through porous soil," Premier Congrès des Grands Barrages, Stockholm, 5, pp. 81-101, 1933.

Merkle, D.H, and W.C. Dass, "Fundamental Properties of Soils for Complex Dynamic Loadings: Development of a Three Invariant Constitutive Model," Report to the U.S. Air Force Office of Scientific Research, Washington, D.C., April 1985.

Nicholas, T., "Material Behavior at High Strain Rates," Chapter 8 of *Impact Dynamics*, Zukas, J.R., Ed., John Wiley & Sons, NY, p. 280, 1982.

Rischbieter, F., et. al., "Studies of Soil Liquefaction by Shock Wave Loading," *Fifth International Symposium on Military Applications of Blast Simulation*, Vol. III, Royal Swedish Fortifications Administration, Stockholm, Sweden, May 1977.

Simons, D.A., "Comparison of Several Two-Phase Models for Saturated Porous Media," RDA-TR-0264238903-09, Report to Defense Nuclear Agency, March 1989.

Scheidegger, A.E., The Physics of Flow Through Porous Media, 2nd ed., University of Toronto Press, Toronto, 1960.

Schneebeli, G., "Experiences sur la limite de validite de la loi de Darcy et l'apparition de la turbulence dans un ecoulement de filtration", La Huille Blanche, No. 2, 10, pp. 141-149 (1955).

Wardlaw, N.C., Y. Li, and D. Forbes, "Pore-throat Size Correlation from Capillary Pressure Curves", Transport in Porous Media, D. Reidel Publishing Co., 1987.